MPM SCIENTIFIC JOURNAL

ISSN 1605-2730
E-ISSN 1605-8119

MATERIALS PHYSICS AND MECHANICS

Vol. 53, No. 6, 2025

MATERIALS PHYSICS AND MECHANICS

"Materials Physics and Mechanics" Editorial Office:
Phone: +7(812)552 77 78, ext. 224 **E-mail:** mpmjournal@spbstu.ru **Web-site:** http://www.mpm.spbstu.ru

International scientific journal "**Materials Physics and Mechanics**" is published by Peter the Great St. Petersburg Polytechnic University in collaboration with Institute for Problems for Mechanical Engineering in the Russian Academy of Sciences in both hard copy and electronic versions. The journal provides an international medium for the publication of reviews and original research papers written in English and focused on the following topics:

- Mechanics of composite and nanostructured materials.
- Physics of strength and plasticity of composite and nanostructured materials.
- Mechanics of deformation and fracture processes in conventional materials (solids).
- Physics of strength and plasticity of conventional materials (solids).
- Physics and mechanics of defects in composite, nanostructured, and conventional materials.
- Mechanics and physics of materials in coupled fields.

Owner organizations: Peter the Great St. Petersburg Polytechnic University; Institute of Problems of Mechanical Engineering RAS.

Materials Physics and Mechanics is indexed in Chemical Abstracts, Cambridge Scientific Abstracts, Web of Science Emerging Sources Citation Index (ESCI) and Elsevier Bibliographic Databases (in particular, SCOPUS).

МЕХАНИКА И ФИЗИКА МАТЕРИАЛОВ

Materials Physics and Mechanics

Том 53, номер 6, 2025 год

Учредители:
ФГАОУ ВО «Санкт-Петербургский политехнический университет Петра Великого»
ФГБУН «Институт проблем машиноведения Российской академии наук»

Тел.: +7(812)552 77 78, доб. 224 **E-mail:** mpmjournal@spbstu.ru **Web-site:** http://www.mpm.spbstu.ru

Тематика журнала

Международный научный журнал "Materials Physics and Mechanics" издается Санкт-Петербургским политехническим университетом Петра Великого в сотрудничестве с Институтом проблем машиноведения Российской академии наук в печатном виде и электронной форме. Журнал публикует обзорные и оригинальные научные статьи на английском языке по следующим тематикам:

- Механика композиционных и наноструктурированных материалов.
- Физика прочности и пластичности композиционных и наноструктурированных материалов.
- Механика процессов деформации и разрушения в традиционных материалах (твердых телах).
- Физика прочности и пластичности традиционных материалов (твердых тел).
- Физика и механика дефектов в композиционных, наноструктурированных и традиционных материалах.
- Механика и физика материалов в связанных полях.

Редколлегия принимает статьи, которые нигде ранее не опубликованы и не направлены для опубликования в другие научные издания. Все представляемые в редакцию журнала "Механика и физика материалов" статьи рецензируются. Статьи могут отправляться авторам на доработку. Не принятые к опубликованию статьи авторам не возвращаются.

Журнал "Механика и физика материалов" ("Materials Physics and Mechanics") включен в систему цитирования Web of Science Emerging Sources Citation Index (ESCI), SCOPUS и РИНЦ.

Contents

MATERIALS PHYSICS AND MECHANICS RESEARCH ARTICLE

Submitted: October 15, 2025 **Revised: November 11, 2025** **Accepted: November 20, 2025**

Temperature dependence of linear fracture mechanics parameters in ceramics: a finite element study

Yu.V. Ermolaeva [1], S.A. Krasnitckii [2]✉, M.Yu. Gutkin [1]

[1] Institute for Problems in Mechanical Engineering, Russian Academy of Sciences, St. Petersburg, Russia

[2] ITMO University, St. Petersburg, Russia

✉ krasnitsky@inbox.ru

ABSTRACT

Parametric finite element simulations are conducted to investigate the steady-state growth of a crack in ceramic material under various temperature conditions. The temperature dependences of elastic moduli and specific surface energy are incorporated to compute the critical fracture parameters such as the crack length, the failure stress and the energy release rate. The finite element modelling is first verified against Griffith's theory and then implemented to practical case of cracks growing from a pore. It is demonstrated that crack growth can be energetically favorable at elevated temperatures, whereas it can be inhibited at low temperatures.

KEYWORDS

high-temperature ceramics • cracks • pores • linear fracture mechanics • finite element method

Funding. *This work was supported by the Russian Science Foundation (grant No. 23-19-00236).*

Citation: Ermolaeva YuV, Krasnitckii SA, Gutkin MYu. Temperature dependence of linear fracture mechanics parameters in ceramics: a finite element study. *Materials Physics and Mechanics*. 2025;53(6): 1–11. http://dx.doi.org/10.18149/MPM.5362025_1

Introduction

The exceptional mechanical properties of ceramic materials, such as high strength, hardness, and wear resistance at elevated temperatures, make them perfect candidates for applications in extreme environments, including aerospace, energy, and manufacturing industries [1–3]. However, the widespread use of structural ceramics is often limited by their inherent brittleness and sensitivity to fracture associated with the presence of intrinsic microstructural defects introduced during manufacturing [4,5]. Among these defects, pores being one of the most common stress concentrators are effective sites for crack nucleation [6,7].

The fracture behavior of ceramics is strongly dependent on the operating temperature [8,9]. At lower temperatures, the material exhibits classic brittle fracture, where crack propagation is the dominant relaxation mechanism. In contrast, at elevated temperatures, the activation of dislocation and grain boundary (GB) sliding can induce a brittle-to-ductile transition (BDT), often accompanied by crack-tip blunting, which significantly enhances fracture toughness [10]. This transition is critical for determining the service limits and reliability of ceramic components. The problem of BDT has been extensively studied in the literature, with numerous works focused on the critical conditions of GB dislocation emission [11–14], the toughening effect of crack blunting [15–17], GB sliding [18–20] and GB segregations [21–23]. Nevertheless, a comprehensive analysis

Publisher: Peter the Great St. Petersburg Polytechnic University

linking the temperature-induced evolution of material parameters to the critical conditions for crack growth from specific defects, such as pores, remains an essential issue.

In our previous research, we have systematically investigated stress concentration and fracture initiation in ceramic composites. We analyzed local stress distributions near pores and inclusions using both analytical perturbation techniques and finite element (FE) simulations [24,25]. Furthermore, we employed FE modeling to reveal the energetical favorability of various crack configurations near lamellar inhomogeneities [26] and to study the competition between brittle and ductile fracture behavior at elevated temperatures [27].

In the present work, the effect of operating temperature on the crack tolerance of α-Al_2O_3 ceramics is investigated to assess the energy favorability of the following different fracture scenarios: (i) the homogenous scenario of crack growth without any extra source of stress disturbance, and (ii) the heterogeneous scenario of crack growth accelerated by stress concentration around a circular pore. The first scenario can be attributed to fracture initiated inside the grains (transgranular fracture), while the second scenario is addressed to intergranular fracture initiated by pre-existing defects at GBs. Some empirical temperature dependences of α-Al_2O_3 ceramics properties are involved in FE analysis in assumption of the steady-state crack growth. The elastic response of an FE model containing flaws is obtained through parametric FE simulations that account for variations in flaw lengths, applied stress and operating temperature. The resulting strain energy data are utilized to evaluate some fracture parameters including the critical crack length, the critical failure stress and the energy release rate. The validity of FE data is proved by comparison with the results of Grifith's theory for the homogeneous scenario. The obtained results allow to assess the deterioration in fracture tolerance in ceramics due to temperature rise and presence of pores as well.

Model

We consider a ceramic material subjected to a remote tensile load S under the plane strain condition. The material response is supposed to be linearly elastic and isotropic defined by the Young modulus E and the Poisson ratio ν with respect to the operating temperature T. Figure 1 illustrates two possible scenarios of crack generation in polycrystal material: (i) homogenous crack nucleation (HmCN) inside a grain with no stress concentration effect; (ii) heterogeneous crack nucleation (HtCN) initiated by the stress concentration induced by such a manufacturing defect as a circular pore of radius R_0 located at a GB.

The favorability of these scenarios can be analyzed within the framework of linear elastic fracture mechanics (LEFM) considering the following parameters: the critical crack length L_{cr}, the critical stress for crack growth S_{cr} and the energy release rate G due to the crack advance. According to Griffith's theory [10], the total energy change due to crack formation is given by the sum:

$$\Delta W = \Delta W_{st} + \Delta W_{sf}, \quad (1)$$

where ΔW_{st} is the change in the strain energy of the body and ΔW_{sf} is the energy to create new free surfaces.

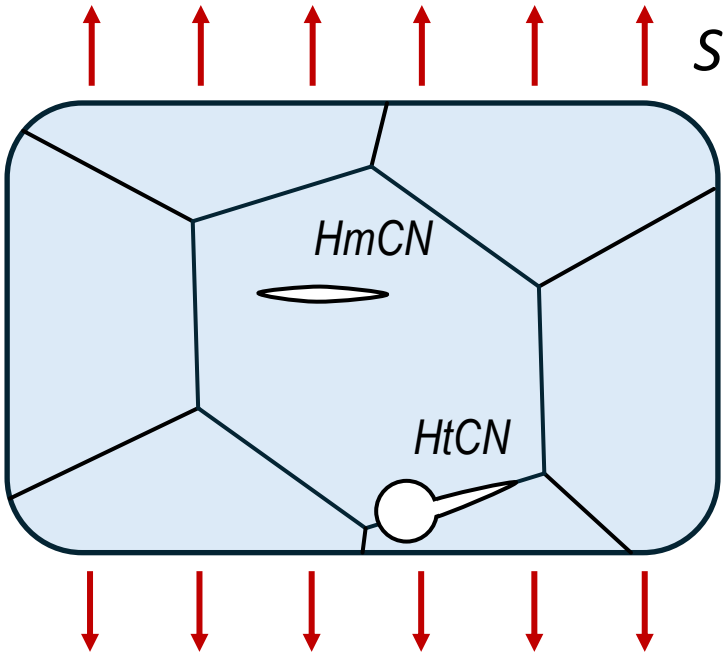

Fig. 1. Typical fracture scenarios in a polycrystalline ceramics: a transgranular crack under the homogenous stress condition (HmCN) and an intergranular crack under the heterogeneous stress condition induced by a GB pore (HtCN)

In the case of HmCN, the strain energy change due to a crack of length L (per unit length of the crack in the direction normal to Fig. 1 plane) is:

$$\Delta W_{st} = -\frac{\pi}{4}\frac{1-\nu^2}{E}L^2S^2. \quad (2)$$

The surface energy term reads:

$$\Delta W_{st} = 2L\gamma, \quad (3)$$

where γ is the specific surface energy of the ceramics.

It is supposed that a crack becomes unstable under a constant applied stress S if the crack length exceeds some critical value L_{cr} defined by the following equilibrium criteria:

$$\frac{d}{dL}\Delta W|_{S=const} = 0, \quad \frac{d^2}{dL^2}\Delta W|_{S=const} \leq 0. \quad (4a,b)$$

For instance, the critical crack length L_{cr} determined from Eqs. (4) in the case of HmCN is well-known and given by:

$$L_{cr} = \frac{4}{\pi}\frac{E\gamma}{(1-\nu^2)S^2}. \quad (5)$$

Unlike the equilibrium criteria given by Eqs. (4), the negative energy change ($\Delta W < 0$) accompanied by crack advance is considered as an alternative fracture criterion to obtain the critical parameters. For instance, the threshold stress S_{cr} can be determined from the critical condition:

$$\Delta W|_{L=const} = 0. \quad (6)$$

Substituting Eqs. (1–3) in Eq. (6), one obtains the following expression for the critical stress in the case of HmCN:

$$S_{cr} = \sqrt{\frac{8}{\pi}\frac{E\gamma}{(1-\nu^2)L}}. \quad (7)$$

It is worth noting that the value of the critical stress determined by Eq. (7) is overestimated in comparison with the one prescribed by Griffith's theory [10]. In the present work, the critical condition given by Eq. (6) is employed because it qualitatively reflects the physical aspects of fracture process. Besides, it is more adaptable to evaluate the critical values of stress from FE numerical data.

Another key parameter of fracture mechanics is the energy release rate G defined as the energy available for a crack advance. In the case of displacement-controlled loading (where the work done by an external force is zero), the energy release rate can be figured out from the expression:

$$G = -\frac{dW_{st}}{dL}, \quad (8)$$

whence for the HmCN scenario one can obtain G with respect to Eq. (2):

$$G = \frac{1-\nu^2}{E} {K_1}^2, \quad (9)$$

where K_1 is the stress intensity factor of the crack-tip, so that $K_1 = S\sqrt{\pi L/2}$. In contrast to the temperature independent parameter K_1, the energy release rate G can be strongly affected by the temperature conditions as the elastic moduli depend on the operating temperature.

Along with the analytical approach, FE simulations can be employed to evaluate the critical fracture parameters. FE method is particularly useful for studying objects with complex geometry, as is the case with HtCN where the strict analytical solution is not feasible [28]. Furthermore, standard post-processing modules in commercial FE software readily provide the values of the strain energy for the entire model. In addition, pre-processing operations directly allow to input the temperature dependences for elastic moduli.

To investigate the energy favorability of the HmCN and HtCN fracture scenarios with respect to temperature conditions, the parametric FE simulations were conducted. For this purpose, FE models comprising four-node plane strain elements were created using

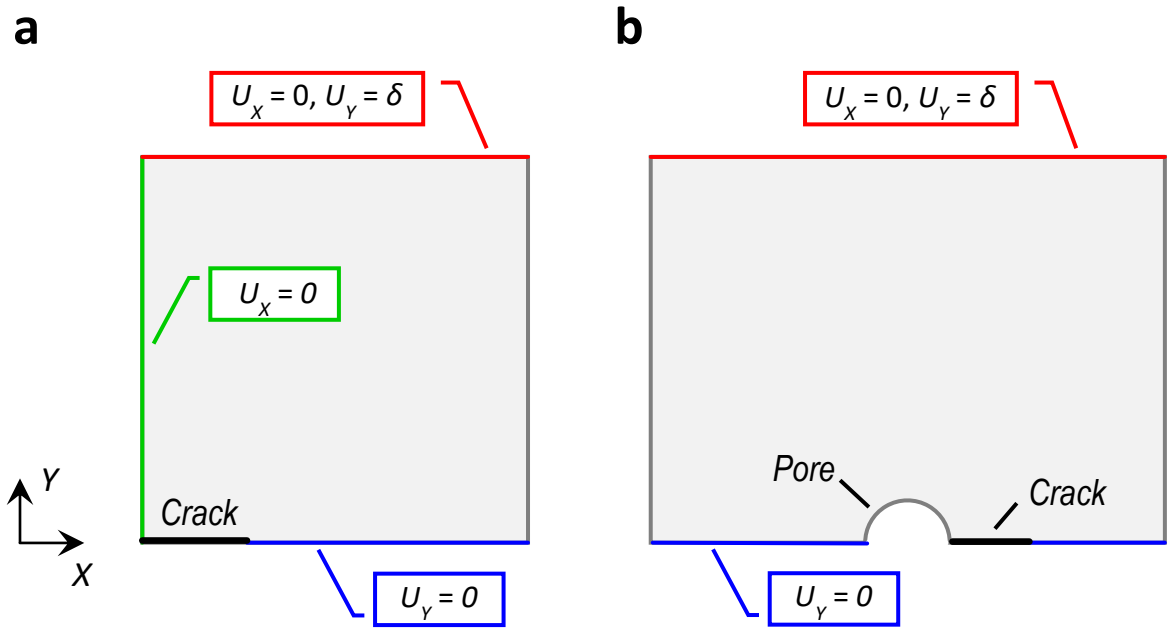

Fig. 2. The kinematic boundary conditions implemented in FE analysis of (a) homogenous crack nucleation (HmCN), and (b) heterogeneous crack nucleation (HtCN) initiated by the circular pore

ANSYS Academic Research software. Each node had two degrees of freedom corresponding to node-displacements U_X and U_Y. Figure 2 depicts the boundary conditions applied to the model with respect to the geometry and loading symmetry. The loading was assumed to be displacement-controlled by the prescribing displacement δ. The associated value of the remote stress S was subsequently calculated from the model's force reaction. The crack was treated as a flat cut with free surfaces. The model size was supposed to be an order of magnitude larger than those of both the pore and crack to eliminate boundary effects on the crack-tip stress field. For instance, the considered FE model has a size of ~ 1 μm, the average size of element in the vicinity of crack and pore is ~ 1 nm.

Since the elastic properties of corundum ceramic (α-Al_2O_3) are well-established in the literature for a wide temperature range, they were adopted to define the material behavior in the models. The following empirical approximation from [29] valid up to 1400 °C was employed in the simulations:

$$E\,[\text{GPa}] = 417 - 0.0525\,T\,[^\circ\text{C}]. \quad (10)$$

The Poisson ratio was taken as $\nu = 0.23$, as its dependence on temperature is negligible. It is worth mentioning that the FE model considers neither anisotropy of mechanical properties nor plastic response of materials. These limitations should be an issue of further investigations.

For the subsequent calculations, the temperature dependence of the specific surface energy had to be taken into account. Based on experimental data for α-Al_2O_3 ceramics [30], the following linear approximation was used:

$$\gamma = \gamma_0 - \beta T, \quad (11)$$

where the temperature T is given in K, $\beta \approx 0.83$ mJ/(m^2 K) and $\gamma_0 \approx 2138$ mJ/m^2.

Results

The parametric FE simulations considering the variations in the crack length L, the rigid displacement δ and the operating temperature T were employed to compute the change in the strain energy, $\Delta W_{st} = \Delta W_{st}|_{L>0} - \Delta W_{st}|_{L=0}$, due to both the HmCN and HtCN scenarios in the α-Al_2O_3 ceramic. The corresponding total energy change of the systems was evaluated using Eq. (1), where the strain energy term was obtained via FE modeling, while the surface energy term was determined by Eq. (3).

Figure 3 illustrates the obtained profiles of the total energy change $\Delta W(L)$ under the remote stress $S = 2.8$ GPa given for the HmCN and HtCN scenarios undergoing the temperature conditions $T = 300$ °C (Fig. 3(a)) and 1000 °C (Fig. 3(b)). One can note that the higher the temperature the lower the energy-consumption for crack growth in both scenarios. Besides, the energy values are significantly affected by the occurrence of pore. For instance, in the case of HmCN under 300 and 1000 °C the energy barriers ~ 1.2 and ~ 0.5 keV/nm should be surmounted, respectively. As for the case of HtCN, the energy barriers are significantly lower: ~ 0.3 keV/nm at 300 °C and ~ 0.1 keV/nm at 1000 °C. It is worth mentioning that the curves in Fig. 3 obtained analytically within Griffith's theory practically coincide with those computed for HmCN via FE simulations.

The maxima on the energy curves in Fig. 3 correspond to the cracks with the critical size above which the crack growth is facilitated by energy relief. The critical crack length

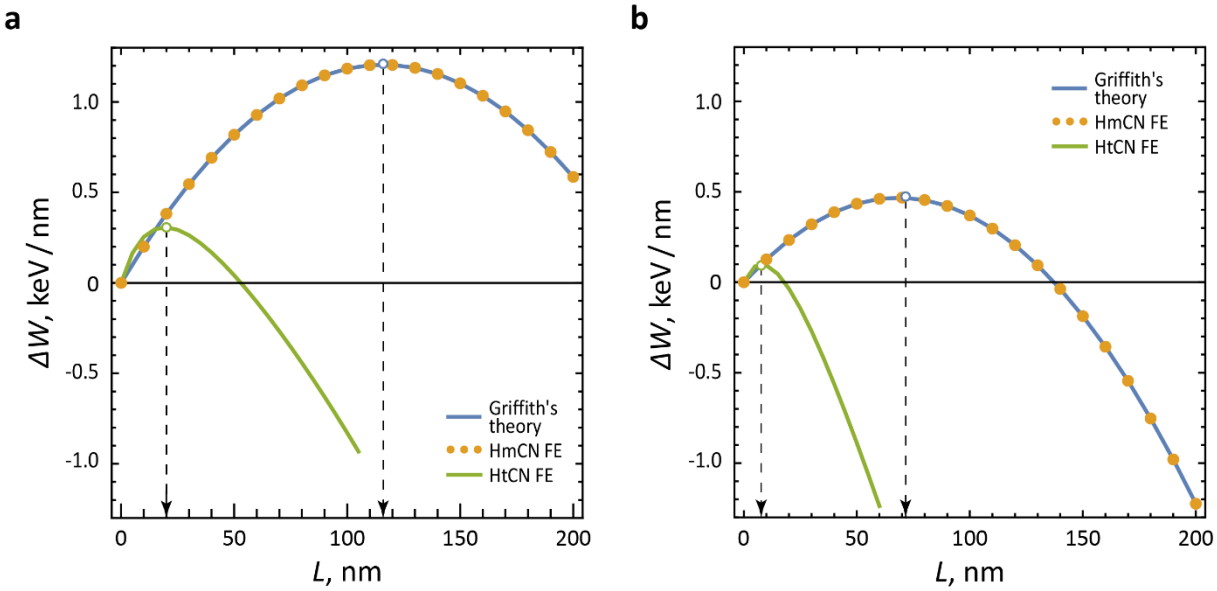

Fig. 3. Dependences of the total energy change ΔW on the crack length L given for the remote stress S = 2.8 GPa and the two operating temperatures, T = 300 °C (a) and 1000 °C (b). The curves were obtained analytically by Eqs. (1–3) (Griffith's theory) and numerically for the scenarios of homogeneous crack nucleation (HmCN FE) and heterogeneous crack nucleation initiated by the pore of radius R_0 = 100 nm (HtCN FE)

obtained by FE modeling is in good agreement with theoretical results. For example, the critical crack length indicated from the HmCN FE data in Fig. 3(a) is approximately 121 nm, that is about 4 % greater than the value ~ 116 nm prescribed by Griffith's theory.

The effect of temperature on the critical crack length is depicted in Fig. 4 for different values of the remote stress S = 2.8 and 3.6 GPa. The data reveal that L_{cr} almost linearly decreases with temperature rise in both the HmCN and HtCN scenarios. This graph can be employed to define the threshold temperature as well. In the case of HmCN under remote stress S = 2.8 GPa, the critical crack length 90 nm corresponds to

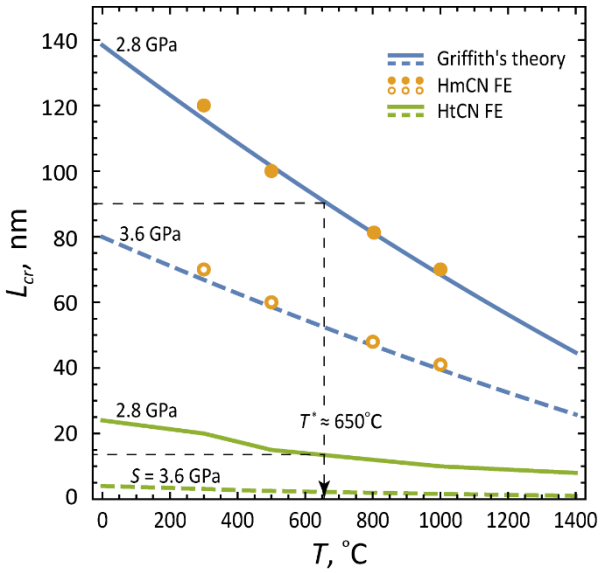

Fig. 4. Dependences of the crack critical length L_{cr} on the operating temperature T under the remote stress S = 2.8 GPa (solid curves and solid circles) and 3.6 GPa (dashed curves and hollow circles). The data were obtained analytically by Eq. (5) (Griffith's theory) and numerically for the scenarios of homogeneous crack nucleation (HmCN FE) and heterogeneous crack nucleation initiated by the pore of radius R_0 = 100 nm (HtCN FE)

the threshold temperature T^* approximately 650 °C. It means that the cracks with L = 90 nm are expected to be energetically stable if the operating temperature is lower than the threshold one ($T \leq T^*$) whilst to easily propagate at a higher temperature ($T > T^*$). In addition, it is apparent from the data for the HtCN scenario (crack growth from a circular pore of R_0 = 100 nm) acting under the same remote stress S = 2.8 GPa, that the cracks with L > 14 nm should exhibit the unstable growth under the temperature greater than ~ 650 °C.

It is worth noting that according to estimation in [25], the cleavage stress for crack advance (theoretical strength) reaches approximately 35 GPa at 1000 °C which significantly exceeds the considered values of remote stress S = 2.8 and 3.6 GPa. However, in practical cases the dislocation sliding is expected to occur under lower stress values ~1 GPa. This issue is beyond the scope of this study.

Turning now to a critical condition for the remote stress S, the energy change profiles $\Delta W(S)$ given at operating temperatures T = 300 and 1000 °C in the frame of the HmCN and HtCN scenarios are illustrated in Fig. 5(a). In accordance with the criteria introduced in the previous section, the critical stress for crack growth is prescribed by the equation $\Delta W(S_{cr}) = 0$. As is seen from Fig. 5(a) at a fixed temperature in the unloaded state (when the remote stress vanishes, S = 0), the energy change is determined by the surface energy term (see Eqs. (1–3)) predicting the identical energy values for cracks of the same length regardless of the crack initiation scenarios (HmCN and HtCN). As the remote stress S rises, the energy change ΔW drops more rapidly for HtCN than for HmCN. For example, for L = 100 nm and T = 300 °C the critical stress S_{cr} is ~1.8 GPa in the case of HtCN, that is almost two times lower than the value ~ 4.2 GPa for HmCN. Besides, the higher the temperature T the lower the critical stress S_{cr}.

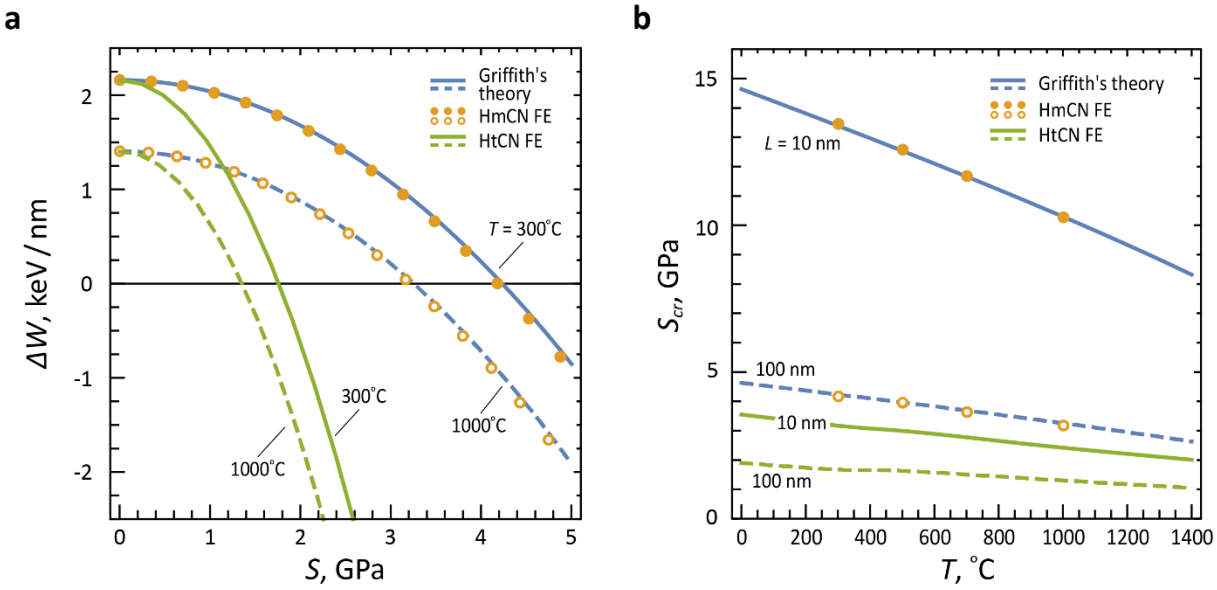

Fig. 5. (a) Dependences of the total energy change ΔW on the remote stress S given for a crack with L = 100 nm under the two operating temperatures, T = 300 °C (solid curves and solid circles) and 1000 °C (dashed curves and hollow circles). (b) Dependences of the critical remote stress S_{cr} on the operating temperature T given for cracks with L = 10 nm (solid curves and solid circles) and 100 nm (dashed curves and hollow circles). The data in (a) and (b) were obtained analytically by Eqs. (1–3,7) (Griffith's theory) and numerically for the scenarios of homogeneous crack nucleation (HmCN FE) and heterogeneous crack nucleation initiated by the pore of radius R_0 = 100 nm (HtCN FE)

The insignificant discrepancy between analytical and FE results emerges as the stress S increases (see Fig. 5(a)). Apparently, this discrepancy is caused by numerical inaccuracies accumulating due to the iterative adjustment of the displacement δ in order to maintain a constant value of the remote stress S.

Figure 5(b) demonstrates the temperature dependence of the critical stress S_{cr} provided for the crack lengths of 10 and 100 nm. What stands out from Fig. 5(b) is an approximately linear decrease of the critical stress S_{cr} with increasing T in a similar manner with the curves $L_{cr}(T)$ (see Fig. 4). In the case of HmCN, the temperature conditions remarkably affect the critical stress for relatively small cracks (L ~ 10 nm), *e.g.* $S_{cr} \approx 14$ GPa for T = 100 °C *vs.* $S_{cr} \approx 10$ GPa for T = 1000 °C. In contrast, in the case of HtCN scenario with similar small cracks (L = 10 nm) induced by a circular pore with R_0 = 100 nm, the drop is significantly less exhibited, *e.g.* $S_{cr} \approx 3.5$ GPa for T = 100 °C *vs.* $S_{cr} \approx 2.5$ GPa for T = 1000 °C. Therefore, not only does the presence of the pore lower the values of the critical stress S_{cr} but also essentially reduces its sensitivity to temperature fluctuations compared to HmCN scenario.

Further analysis of the fracture in α-Al_2O_3 ceramics concerns with computing the crack energy release rate G via FE modeling. The strain energy data obtained by FE parametric simulations can be employed to approximate the energy release rate G regarding Eq. (8) as follows:

$$G = -\frac{W_{st}|_{L+\delta L} - W_{st}|_L}{\delta L}, \tag{12}$$

where δL is the crack extension. The smaller δL utilized in numerical computations the more accurate the estimation of G by Eq. (12).

According to LEFM, the stability of a crack is defined by the value of its energy release rate G. If G is less than a critical value G_{cr} then the energy release rate is not sufficient enough to promote cracking. On the contrary, a crack tends to catastrophic grow if the inequality $G > G_{cr}$ is valid. The critical value of G directly yields from the energy criteria (Eqs. (1–4)) as $G_{cr} = 2\gamma$.

Figure 6 shows the temperature dependence of the energy release rate G for various cracks subjected to the remote stress S = 2.8 GPa. The diagrams reveal two complementary effects of the temperature increase on the fracture tolerance: an increase in the energy release rate G accelerating the growth of cracks is accompanied by a decrease in the fracture resistance G_{cr} of α-Al_2O_3 ceramics.

As it is shown in Fig. 6(a) for the HmCN scenario in the temperature range 0 < T < 1400 °C, the relatively long cracks (here with L ~ 200 nm) have a tendency to propagate since their energy release rate G is greater than the critical one, while G for relatively small cracks (here with L ~ 10 nm) is not sufficient enough to encourage their propagation. Of interest here are cracks of a middle length (here with L ~ 100 nm): as is seen, the crack growth is suppressed for T < 500 °C, whilst expected to be provided under an elevated temperature T > 500 °C.

Analogous temperature dependences of the energy release rate G are demonstrated in Fig. 6(b) for the HtCN scenario considering the generation of a crack with length of 10 nm near pores with different sizes (R_0 = 0, 10 and 100 nm). As is seen from Fig. 6(b), the presence of a pore significantly affects the value of the energy release rate for crack

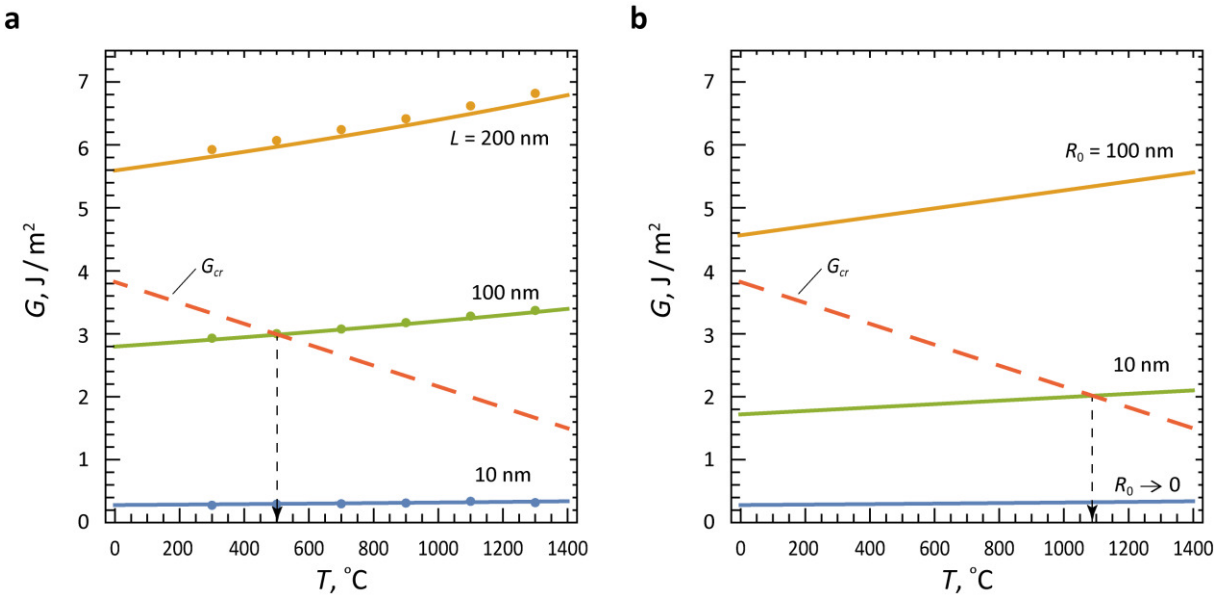

Fig. 6. Dependences of the energy release rate G on the operating temperature T under the remote stress S = 2.8 GPa in the case of (a) HmCN scenario considering the cracks of various lengths L = 10, 100 and 200 nm; here the analytical dependences given by Eq. (9) and the FE data are depicted with solid curves and circles, respectively, and (b) HtCN scenario considering a crack with L = 10 nm initiated by circular pores of different radii R_0 = 0, 10 and 100 nm. The temperature dependent critical value $G_{cr} = 2\gamma$ is given by dashed lines

advance. This effect rises with an increase in the pore radius. For instance, at the operating temperature T = 1000 °C, the energy release rate G reaches the values ~ 2 and ~ 5 J/m² for a crack initiated by a pore of the same radius as the crack length (L/R_0 = 1.0) and a pore of radius much larger than the crack length (L/R_0 = 0.1), respectively. These values are an order of magnitude higher than that for the HmCN scenario (~ 0.3 J/m² for $R_0 \to 0$). One can suggest that in the limiting case of a relatively small crack ($R_0 \gg L$), the energy release rate G tends to the value prescribed for the crack initiated at a flat surface of a semi-infinite body.

Thus, the results of FE simulations presented above clearly evidence that thermal loading and pre-existing inhomogeneities, particularly pores, are critical factors for controlling the fracture tolerance of ceramic materials.

Conclusions

In summary, the FE analysis was provided to investigate the reduction in fracture tolerance under elevated temperatures in ceramics in the frameworks of LEFM. In doing so, the linear temperature approximations of the Young module E and the specific surface energy γ was employed to compute the elastic response of FE models containing flaws and pores under remote tensile stress. The following FE models were considered: those containing a single flat flaw were utilized to describe the homogeneous nucleation of cracks (HmCN), and those considering flat flaw near a circular pore were implemented to study the heterogeneous scenario of crack nucleation accelerated by the stress concentration of inhomogeneities (HtCN). The HmCN scenario was also employed to verify the validity of the FE models against Griffith's theory. The data obtained within parametric FE simulations were used to anticipate the effect of increasing temperature

on the parameters of fracture including the critical crack length L_{cr}, the failure stress S_{cr}, the total energy change ΔW, and the rate of strain energy release G due to crack extension.

The results performed for the α-Al_2O_3 ceramics clearly demonstrate the deterioration in the fracture toughness (L_{cr}, $S_{cr}$and G_{cr}) at elevated temperatures as well as the reduction in the total energy change ΔW due to flaw generation. An opposite effect is indicated for the crack driving force, the decrease in material stiffness (the Young modulus) stimulates the rise of G as operating temperature T increases. The most obvious finding to emerge from obtained data is that the linear approximations can be employed to estimate quite accurately the aforementioned parameters with temperature change. The temperature slope of these approximations significantly depends on the crack and pore sizes, and the applied stress. The increase of these parameters drives the decrease of the temperature slope of fracture toughness criteria (L_{cr}, S_{cr}), while the temperature slope of energy release rate G increases.

CRediT authorship contribution statement

Yulia V. Ermolaeva: data curation, investigation; **Stanislav A. Krasnitckii**: conceptualization, writing – original draft; **Mikhail Yu. Gutkin**: supervision, writing – review & editing.

Conflict of interest

The authors declare that they have no conflict of interest.

References

1. Ramachandran K, Boopalan V, Bear JC, Subramani R. Multi-walled carbon nanotubes (MWCNTs)-reinforced ceramic nanocomposites for aerospace applications: a review. *Journal of Materials Science.* 2022;57(6): 3923–3953.
2. Shvydyuk KO, Nunes-Pereira J, Rodrigues FF, Silva AP. Review of ceramic composites in aeronautics and aerospace: A multifunctional approach for TPS, TBC and DBD applications. *Ceramics.* 2023;6(1): 195–230.
3. Wyatt BC, Nemani SK, Hilmas GE, Opila EJ, Anasori B. Ultra-high temperature ceramics for extreme environments. *Nature Reviews Materials.* 2024;9(11): 773–789.
4. Zhang K, Meng Q, Qu Z, He R. A review of defects in vat photopolymerization additive-manufactured ceramics: Characterization, control, and challenges. *Journal of the European Ceramic Society.* 2024;44(3): 1361–1384.
5. Gavalda-Diaz O, Saiz E, Chevalier J, Bouville F. Toughening of ceramics and ceramic composites through microstructure engineering: A review. *International Materials Reviews.* 2025;70(1): 3–30.
6. Li Z, Wang KF, Wang BL, Li JE. Size effect on the punch performance of brittle porous ceramics: theoretical analysis and numerical simulation. *International Journal of Mechanical Sciences.* 2021;207: 106674.
7. Liang C, Gao X, Fu L, Mei H, Cheng L, Zhang L. Pore evolution and mechanical response under locally varying density defects in ceramic matrix composites. *Composites Part B: Engineering.* 2024;279: 111459.
8. Jin H, Zhang S, Hao Y, Yang Y, Xu C. Mechanical properties and fracture behavior of ultrahigh temperature ceramics at ultrahigh temperatures. *Ceramics International.* 2023;49(17): 28532–28537.
9. Sheinerman AG. Model of enhanced flexural strength of ceramics at elevated temperatures. *Mechanics of Materials.* 2025;208: 105398.
10. Anderson TL. *Fracture mechanics: fundamentals and applications*. Boca Raton: CRC press; 2017.
11. Bobylev SV, Mukherjee AK, Ovidko IA. Emission of partial dislocations from amorphous intergranular boundaries in deformed nanocrystalline ceramics. *Scripta Materialia.* 2009;60(1): 36–39.

12. Zeng XH, Hartmaier A. Modeling size effects on fracture toughness by dislocation dynamics. *Acta Materialia.* 2010;58(1): 301–310.
13. Armstrong RW. Material grain size and crack size influences on cleavage fracturing. *Philosophical Transactions of the Royal Society A: Mathematical, Physical and Engineering Sciences.* 2015;373(2038): 20140124.
14. Reiser J, Hartmaier A. Elucidating the dual role of grain boundaries as dislocation sources and obstacles and its impact on toughness and brittle-to-ductile transition. *Scientific Reports.* 2020;10(1): 2739.
15. Beltz GE, Lipkin DM, Fischer LL. Role of crack blunting in ductile versus brittle response of crystalline materials. *Physical Review Letters.* 1999;82(22): 4468.
16. Fischer LL, Beltz GE. The effect of crack blunting on the competition between dislocation nucleation and cleavage. *Journal of the Mechanics and Physics of Solids.* 2001;49(3): 635–654.
17. Ovidko IA, Sheinerman AG. Grain size effect on crack blunting in nanocrystalline materials. *Scripta Materialia.* 2009:60(8): 627–630.
18. Sheinerman AG, Ovidko IA. Grain boundary sliding and nanocrack generation near crack tips in nanocrystalline metals and ceramics. *Materials Physics and Mechanics.* 2010:15(1/2); 37–46.
19. Sheinerman AG, Morozov NF, Gutkin MYu. Effect of grain boundary sliding on fracture toughness of ceramic/graphene composites. *Mechanics of Materials.* 2019;137: 103126.
20. Gutkin MYu, Krasnitckii SA, Skiba NV. Formation of liquid-like inclusions near pores in amorphous intercrystalline layers in high-temperature ceramics. *Materials Physics and Mechanics.* 2024;52(6): 8–16.
21. Sheinerman AG. Strengthening of nanocrystalline alloys by grain boundary segregations. *Materials Physics and Mechanics.* 2022;50(2): 193–199.
22. Sheinerman AG. Modeling the effect of grain boundary segregations on the fracture toughness of nanocrystalline and ultrafine-grained alloys. *Metals.* 2023;13(7): 1295.
23. Sheinerman AG, Shevchuk RE. Toughening of nanocrystalline alloys due to grain boundary segregations: finite element modeling. *Materials Physics and Mechanics.* 2023;51(7): 34–41.
24. Vakaeva AB, Krasnitckii SA, Smirnov A, Grekov, MA, Gutkin MYu. Stress concentration and distribution at triple junction pores of three-fold symmetry in ceramics. *Reviews on Advanced Materials Science.* 2018;57(1): 63–71.
25. Vakaeva AB, Krasnitckii SA, Grekov MA, Gutkin MYu. Stress field in ceramic material containing threefold symmetry inhomogeneity. *Journal of Materials Science.* 2020;55(22): 9311–9321.
26. Ignateva EV, Krasnitckii SA, Sheinerman AG, Gutkin MYu. The finite element analysis of crack tolerance in composite ceramics. *Materials Physics and Mechanics.* 2023:51(2): 21–26.
27. Krasnitckii SA, Sheinerman AG, Gutkin MYu. Brittle vs ductile fracture behavior in ceramic materials at elevated temperature. *Materials Physics and Mechanics.* 2024;52(2): 82–89.
28. Murakami Y. (Ed.) *Stress Intensity Factors Handbook. In 2 Volumes.* Oxford: Pergamon press; 1987.
29. Munro RG. Evaluated material properties for a sintered alpha-alumina. *Journal of the American Ceramic Society.* 1997;80(8): 1919–1928.
30. Weirauch DA, Ownby PD. Application of the Zisman critical surface tension technique to ceramic surfaces at high temperature. *Journal of Adhesion Science and Technology.* 1999;13(11): 1321–1330.

MATERIALS PHYSICS AND MECHANICS RESEARCH ARTICLE

Submitted: October 29, 2025 **Revised: November 13, 2025** **Accepted: December 5, 2025**

Influence of bending deformation in spherulitic films of lead zirconate titanate on the formation of the internal field and self-polarization

A.R. Valeeva [1], M.V. Staritsyn [2], S.V. Senkevich [1], E.Yu. Kaptelov [1], I.P. Pronin [1]✉, D.A. Kiselev [3], S.A. Nemov [4]

[1] Ioffe Institute, St.-Petersburg, Russia

[2] NRC "Kurchatov Institute" — CRISM "Prometey", St.-Petersburg, Russia

[3] National University of Science and Technology MISIS, Moscow, Russia

[4] Peter the Great Saint-Petersburg Polytechnic University, St. Petersburg, Russia

✉ Petrovich@mail.ioffe.ru

ABSTRACT

Experimental studies of the internal field and self-polarization in thin lead zirconate titanate films formed on platinized silicon substrates using a two-stage radio-frequency magnetron sputtering of a ceramic target were conducted. In the first stage, amorphous films were deposited on a cold substrate, and in the second stage, high-temperature annealing was performed, accompanied by crystallization of the perovskite phase and the formation of a spherulitic microstructure. The aging characteristics of these films, associated with the formation of non-uniform mechanical stresses leading to the upward diffusion of oxygen vacancies (the Gorsky effect), were studied. Estimates were made of the diffusion rate of oxygen vacancies, as well as their concentration, necessary for the formation of an internal field in thin films. It was shown that a change in the crystallization (synthesis) temperature of the perovskite phase can lead to a change in the direction of the gradient vector of non-uniform mechanical stresses and the direction of diffusion of oxygen vacancies towards the substrate.

KEYWORDS

lead zirconate titanate • thin films • spherulitic microstructure • rotational crystals • self-polarization internal field • bending mechanical deformation • Gorsky effect

Funding. *The work was supported by the Russian Science Foundation grant No. 24-22-00631.*

Citation: Valeeva AR, Staritsyn MV, Senkevich SV, Kaptelov EYu, Pronin IP, Kiselev DA, Nemov SA. Influence of bending deformation in spherulitic films of lead zirconate titanate on the formation of the internal field and self-polarization. *Materials Physics and Mechanics*. 2025;53(6): 12–24.
http://dx.doi.org/10.18149/MPM.5362025_2

Introduction

Thin ferroelectric films are finding increasing use in applied fields [1–6]. One of the main areas of their application is microelectromechanics (MEMS), where lead zirconate titanate (PZT) films occupy a niche of approximately 95 % [7,8]. The most effective is the use of naturally unipolar or self-polarized films, in which the macroscopic polar state is formed during their crystallization. Such films eliminate the need for labor-intensive polarization procedures. Furthermore, as practice has shown, an additional advantage is the increased stability of their polar state to external influences [9–11].

Although the mechanisms of self-polarized state formation have been studied for decades, there is still no consensus on their nature. Several physical causes of its formation are considered. These mechanisms can be roughly divided into electrical and mechanical ones. Electrical mechanisms are associated with:

1. the polarizing effect of the space charge localized at the lower interface of the ferroelectric film [9,10], the electrochemical potential on the thin film surface (Mott potential) [12], and ordered charged defects, in particular, oxygen vacancies [13];
2. differences in the work functions of the lower and upper film interfaces when using different materials as electrodes [14].

Depending on the nature of their action, mechanical mechanisms are divided into (a) tensile or compressive deformation of a thin film in the plane of the substrate, and (b) bending deformation. In the first case, the action of tensile or compressive forces on a thin film can be caused by a difference in the temperature coefficients of linear expansion of the polycrystalline film and the substrate [15,16], and in the case of epitaxial growth of a thin film, by a difference in the parameters of their crystal lattices (misfit) [17]. However, since polycrystalline films are used in the vast majority of practical applications, we will not consider misfit further. The difference in the temperature coefficients of linear expansion of the film and the substrate also leads to bending deformation of this structure, and thus to a deformation gradient.

By its nature, linear deformation (under the action of compression/expansion forces) leads to a reorientation of the ferroelectric polarization vector in directions either as close as possible to the normal to the substrate plane, or to its plane [16,18]. Thus, in thin PZT films deposited on a silicon substrate, the composition of which corresponds to the region of the morphotropic phase boundary (MPB), where the maximum values of electromechanical/piezoelectric coefficients are achieved, the magnitude of tensile mechanical stresses can reach 100–150 MPa, which leads to a partial reorientation of the polarization vector and, accordingly, a decrease in the degree of unipolarity [15,16]. In this case, the deformation itself, being a scalar quantity, cannot be the cause of macroscopic polarization, unlike bending deformation, characterized by a deformation gradient, which is a vector quantity. According to [19,20], such deformation leads to an asymmetric shift of atoms within a unit cell in a multicomponent crystal lattice, the appearance of an internal field and, as a consequence, a macroscopic polar state – an effect subsequently called flexoelectrical one. A similar effect in thin PZT films was observed under strong bending, close to the plastic limit of the silicon substrate (with a curvature radius of about 30 cm) and a lattice deformation of ~ 1 % [21], which is usually not realized in real structures.

Studies conducted in recent years have shown that strong non-uniform deformation is observed in thin films characterized by a spherulitic microstructure. The crystalline phase of these films is formed by the growth and subsequent fusion of individual spherulitic islands from the amorphous phase during high-temperature annealing. In such polycrystalline formations, which are often referred to as rotational crystals, a rotation of the crystal lattice (or growth axis) in radial directions is observed, accompanied by bending deformation [22–28]. In this case, the integral angle of rotation can reach tens and hundreds of degrees, and the rotation rate is hundreds of degrees per micron and more [22–24]. Similar spherulitic formations with a radial-

radiant microstructure are often observed in PZT thin films, and recently attempts have been made to study the relationship between their microstructure and physical properties [28–30]. In particular, it was shown that tensile mechanical stresses can lead to a reorientation of the ferroelectric polarization in directions as close as possible to the plane of the substrate, and in individual spherulitic islands the effect of radially oriented lateral self-polarization was detected [28,29].

It is assumed that in such rotational structures, due to non-uniform deformation, a mechanism for the formation of thickness self-polarization associated with the directional diffusion of charged defects (the Gorsky effect) can be realized [31,32]. Positively charged oxygen vacancies can act as such point defects in PZT films; their directional diffusion can lead to the formation of an internal field and a stable macroscopic polar state. The aim of this work was to identify the role of oxygen vacancies and their diffusion capacity in the formation of an internal field under conditions of non-uniform deformation and to evaluate their contribution to the stability internal field and of self-polarization in thin spherulitic PZT films.

Sample preparation and research methods

The PZT films were deposited on platinized silicon substrates ($Pt/TiO_2/SiO_2/Si$) using a two-stage high-frequency magnetron sputtering method. The composition of the sputtered ceramic target corresponded to the region of the morphotropic phase boundary and corresponded to the elemental ratio of zirconium and titanium atoms Zr/Ti = 54/46 [28]. To obtain a two-phase structure in the form of perovskite islands with transverse dimensions in the range of 30–40 μm surrounded by a matrix of the low-temperature pyrochlore phase, or a single-phase block structure, the amorphous films deposited at a low substrate temperature were annealed at a temperature of 535–570 °C. The thickness of the PZT films was ~ 500 nm. To carry out electrophysical measurements, platinum electrons with dimensions of 200 × 200 μm^2 were formed on the surface of the films.

The crystal structure and phase state of the films were monitored using X-ray diffraction analysis (Rigaku Ultima IV). Microimages of spherulitic islands were obtained using a scanning electron microscope (Tescan Lyra 3) equipped with an electron backscatter diffraction (EBSD) detector. Processing of the diffraction patterns allowed for the point-by-point generation of orientation maps of the spherulitic islands, along with crystallographic orientation data, and the determination of lattice rotation rates.

To assess the self-polarized state, piezoelectric response force microscopy (PFM) was used on an MFP-3D SA atomic force microscope (Asylum Research). Measurements of the normal component of the piezoresponse were performed in contact mode by applying an alternating voltage of 5 V at 50 kHz to the cantilever. The scanned surface area was 40 × 40 μm^2. The dielectric properties of thin films were studied using an E7-30 immittance meter. Dielectric hysteresis loops and internal field were measured using a modified Sawyer-Tower scheme. Measurements were performed at a frequency of 1 kHz.

Experimental results

Figure 1 shows electron micrographs of the spherulitic microstructure observed in thin PZT films. Crystallization of the perovskite phase in such films occurs through the nucleation and growth of individual perovskite islands, which are nearly circular in shape, in a matrix of the low-temperature non-polar pyrochlore phase (Fig. 1(a)). Further island growth leads to the formation of a polyhedral block structure (Fig. 1(b)). Typically, the spherulitic microstructure consists of distinct regions separated by radial rays, in which new growth centers emerge as growth proceeds. In the studied PZT films, the diameter of individual spherulitic islands (or the linear size of the blocks) reached several tens of micrometers. This pattern of spherulitic growth indicates so-called low-angle non-crystalline (growth) branching.

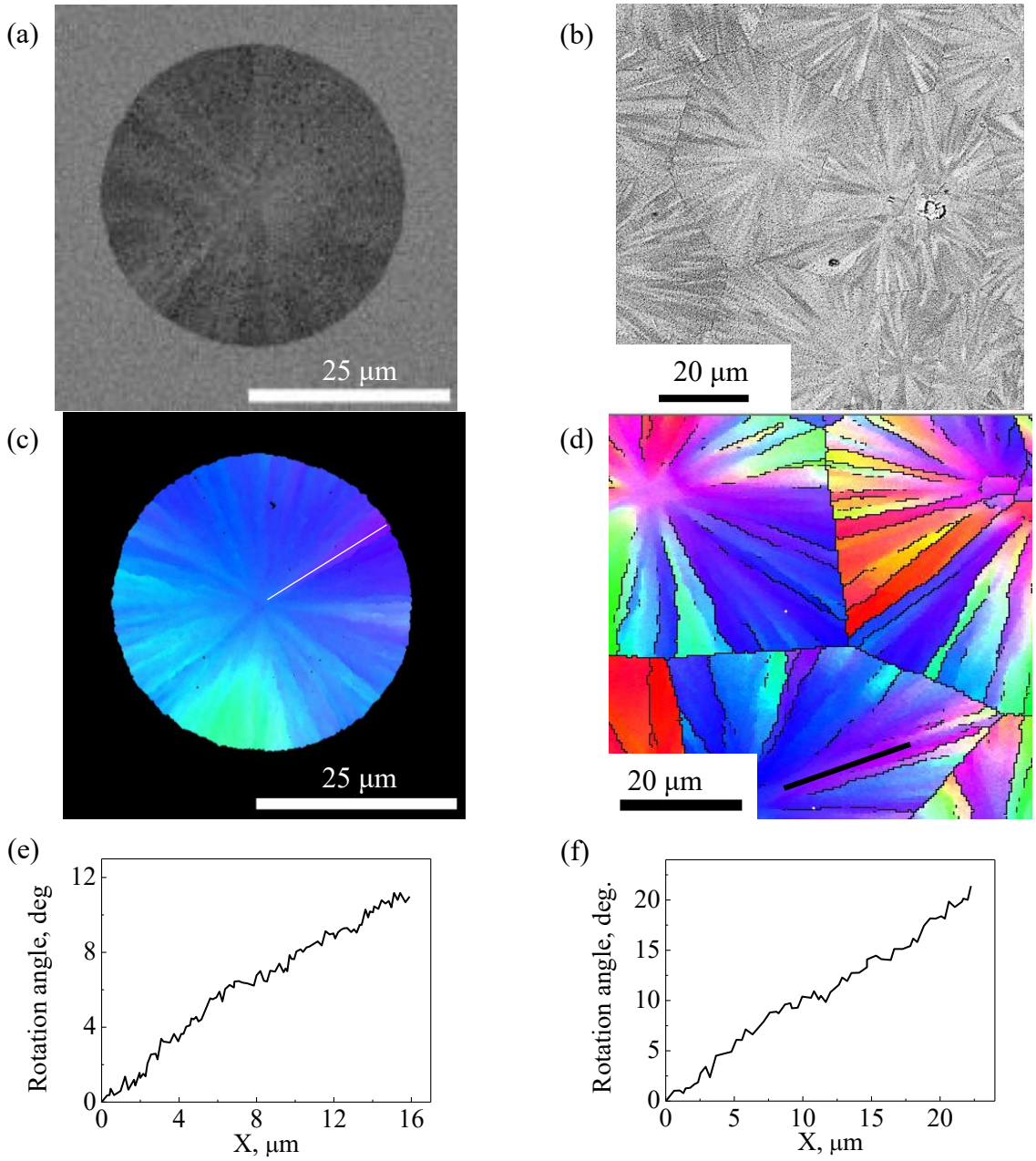

Fig. 1. Electron images of the spherulitic microstructure (a,b), EBSD maps (c,d) and dependence of the rotation angle (φ) of the lattice along the marked radial directions (e,f), the application of strong alternating fields, and long-term aging at room temperature

It is believed that one of the microstructural features of radial-rayed spherulites is the rotation of the growth axis (crystal lattice) around a direction perpendicular to the radial rays. In EBSD images, this manifests itself as a smooth change in color gamut with radial movement from the center of the spherulites to their periphery (Fig. 1(c,d)). Figure 1(e,f) shows near-linear dependences of the lattice rotation angle (φ) along the indicated radial directions. The rotation angle in the studied films reached 20–30°, and the rotation rate (gradient) varied from 0.5 to 1.2 deg/μm.

In the works devoted to the study of the properties of rotational crystals, it was noted that such non-uniform deformation of the crystal lattice is a consequence of the action of mechanical stresses arising during the formation of the crystalline phase from the amorphous phase during high-temperature annealing, which is accompanied by a change in the density of the thin film [22–28]. The results of the study of dielectric hysteresis loops and piezoelectric response presented below revealed changes in the polar characteristics of self-polarized PZT thin films during the influence of temperature (high-temperature annealing above the Curie).

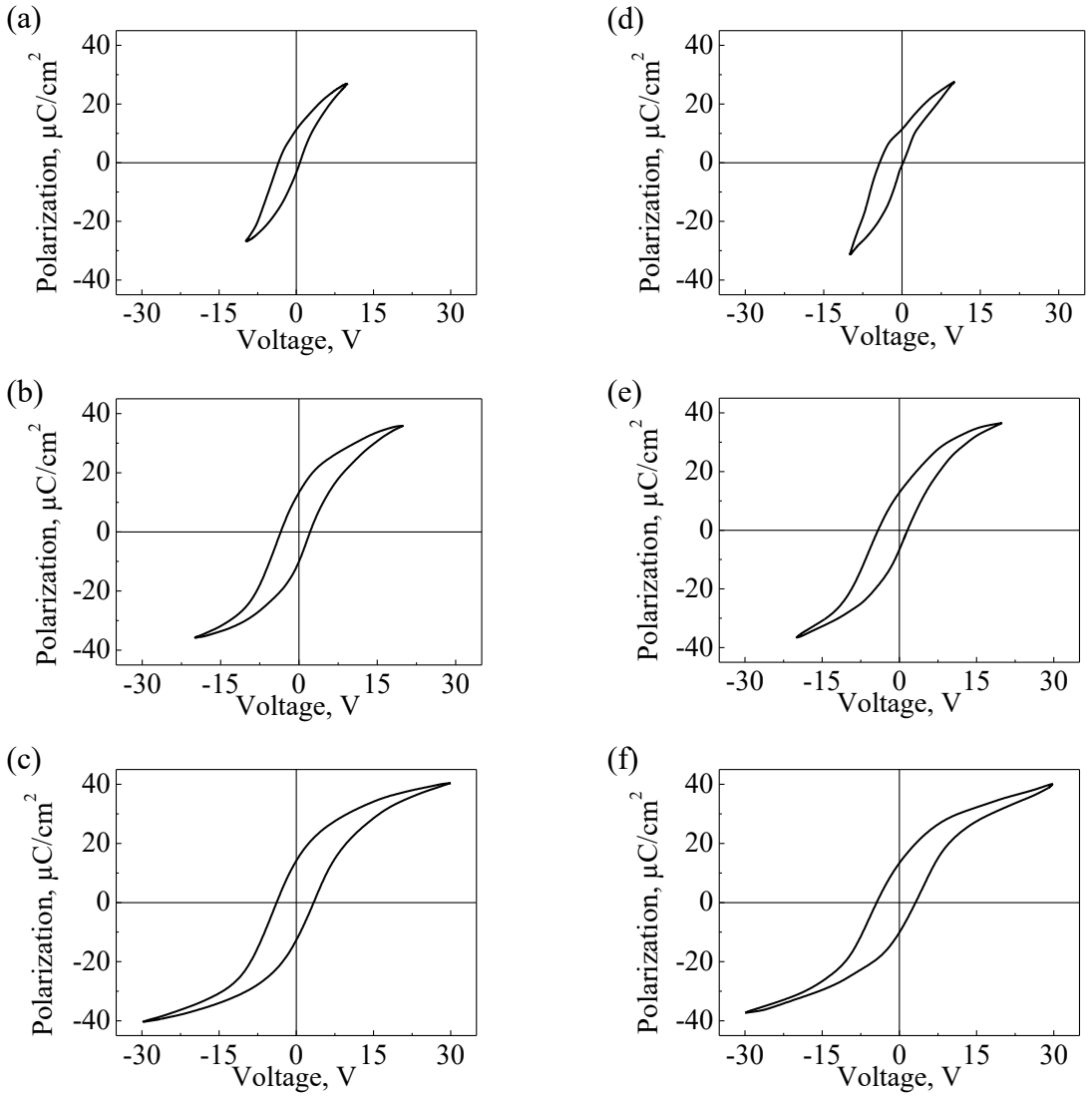

Fig. 2. Dielectric hysteresis loops of perovskite films at voltages of 10, 20 and 30 V, formed at a distance from the target to the substrate of 30 mm, immediately after deposition (a,b,c) and after long-term exposure (d,e,f)

Figure 2 shows the dielectric hysteresis loops (*P-V*) of an as-prepared film (Fig. 2(a–c) and one subjected to long-term aging (more than 4 years) (Fig. 2(d–e)) under the application of an alternating field with an amplitude from 200 to 600 kV/cm. The magnitude of the internal field (E_{int}) in the films was estimated from the shift of the *P-V* loops along the abscissa axis. It is evident that in as-prepared films the value of E_{int} was ~ 14 kV/cm. The application of a strong field (600 kV/cm) resulted in almost complete symmetrization of the hysteresis loop, that is, the disappearance of the internal field (Fig. 2(c)). A similar symmetrization of the P-V loops (even in relatively weak fields) was also observed during annealing of the sample at temperatures close to the Curie temperature (~ 380 °C) or higher [33,34]. Long-term aging of such samples resulted in the appearance of strong asymmetry in the *P-V* loops and an increase in E_{int} to ~ 23 kV/cm when an alternating field of 400 kV/cm was applied. However, no loop symmetrization occurred in a strong field (Fig. 2(e)).

Figure 3 shows the hysteresis loops of self-polarized films after long-term aging (Fig. 3(a)), as well as their changes after high-temperature annealing above the Curie temperature (~400 °C) and subsequent aging. It is evident that in such films, the internal field was maintained even in a strong field (400 kV/cm) after annealing of the samples, although the value of E_{int} decreased significantly, Fig. 3(b). Further aging of the samples (for ~ 10^7 s) at room temperature led to an increase in asymmetry, i.e., an increase in E_{int} by ~ 6 kV/cm (Fig. 3(c)).

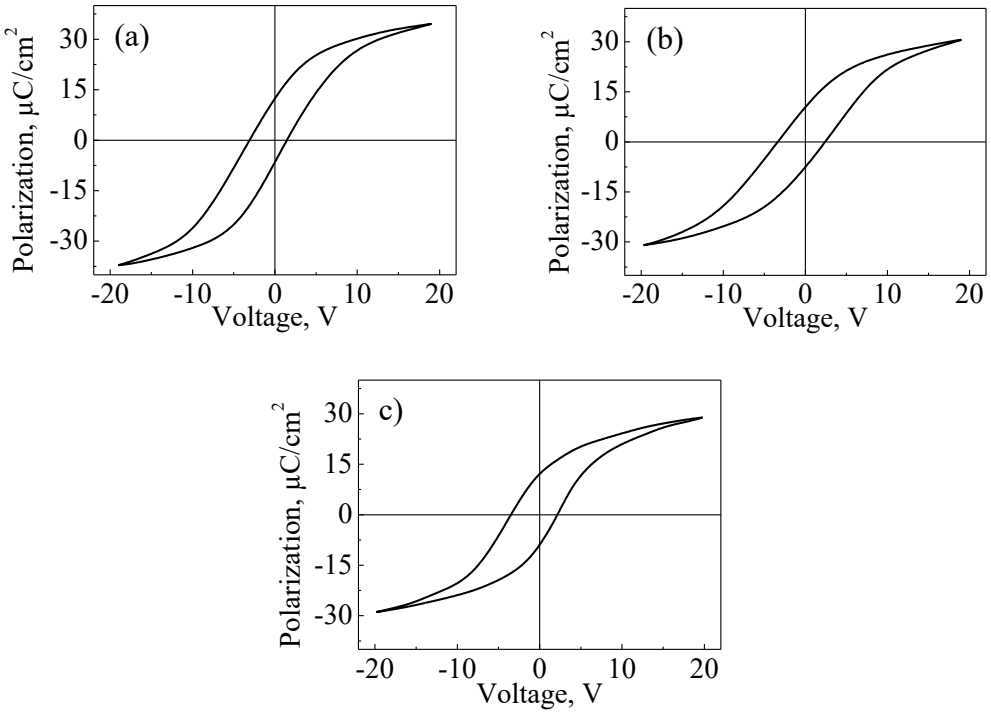

Fig. 3. Dielectric hysteresis loops after long-term aging (a), annealing at 400 °C (b) and subsequent aging for 1600 h (c)

The change in the value of E_{int} (and, consequently, the value of natural unipolarity or self-polarization P_{self}) was caused by a change in the temperature at which the crystallization (synthesis) of the perovskite phase of thin films (T_{sint}) occurred. Figure 4

shows the change in these parameters with T_{sint} varying in the range of 535–550 °C. It is evident that P_{self} and E_{int} reach their maximum values at 540–545 °C (Fig. 4(a,b), respectively) and then decrease sharply. We associate this behavior with the significant role of excess lead in the thin film bulk, presented in the form of its oxide (PbO) or dioxide (PbO_2), and a change in its content with increasing T_{sint} (Fig. 4(c)). It has been previously shown that such a change in the lead oxide content is associated with the competition of two mechanisms of crystallization of the perovskite phase, when the formation and growth of perovskite islands begins either from the free surface of the thin film, which is accompanied by the extrusion of excess lead oxide towards the lower interface, or by nucleation and growth from the lower interface of the film upwards and the extrusion of excess lead towards the surface of the film [35].

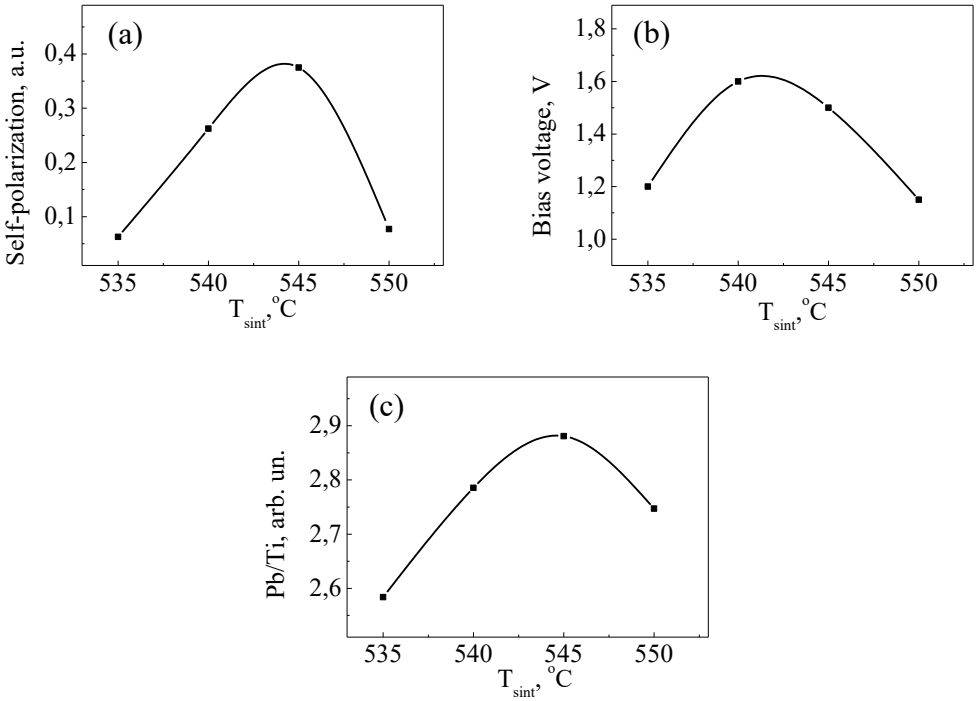

Fig. 4. Change in the values of self-polarization (a), internal field (b) and lead excess (in the form of the elemental ratio of Pb/Ti atoms) (c) depending on the T_{sint}

Discussion

To explain the obtained results, we will use the approach previously developed by the authors, according to which the formation of an internal field in thin PZT films during the crystallization of the perovskite phase is associated with the orienting action of the field of the negative space charge localized at deep traps in the film near the film-lower (platinum) electrode interface in the absence of the upper electrode [10]. Such a charge state of the film is shown schematically in Fig. 5(a), where the negative charges are electrons localized at deep traps and charged oxygen vacancies, in a first approximation, uniformly distributed over the thickness of the ferroelectric film. It is also assumed that the presence of excess lead oxide located at the film interfaces, in the intercrystallite space and at the boundaries of spherulitic blocks creates conditions for the formation of a sufficiently high concentration of oxygen vacancies [35].

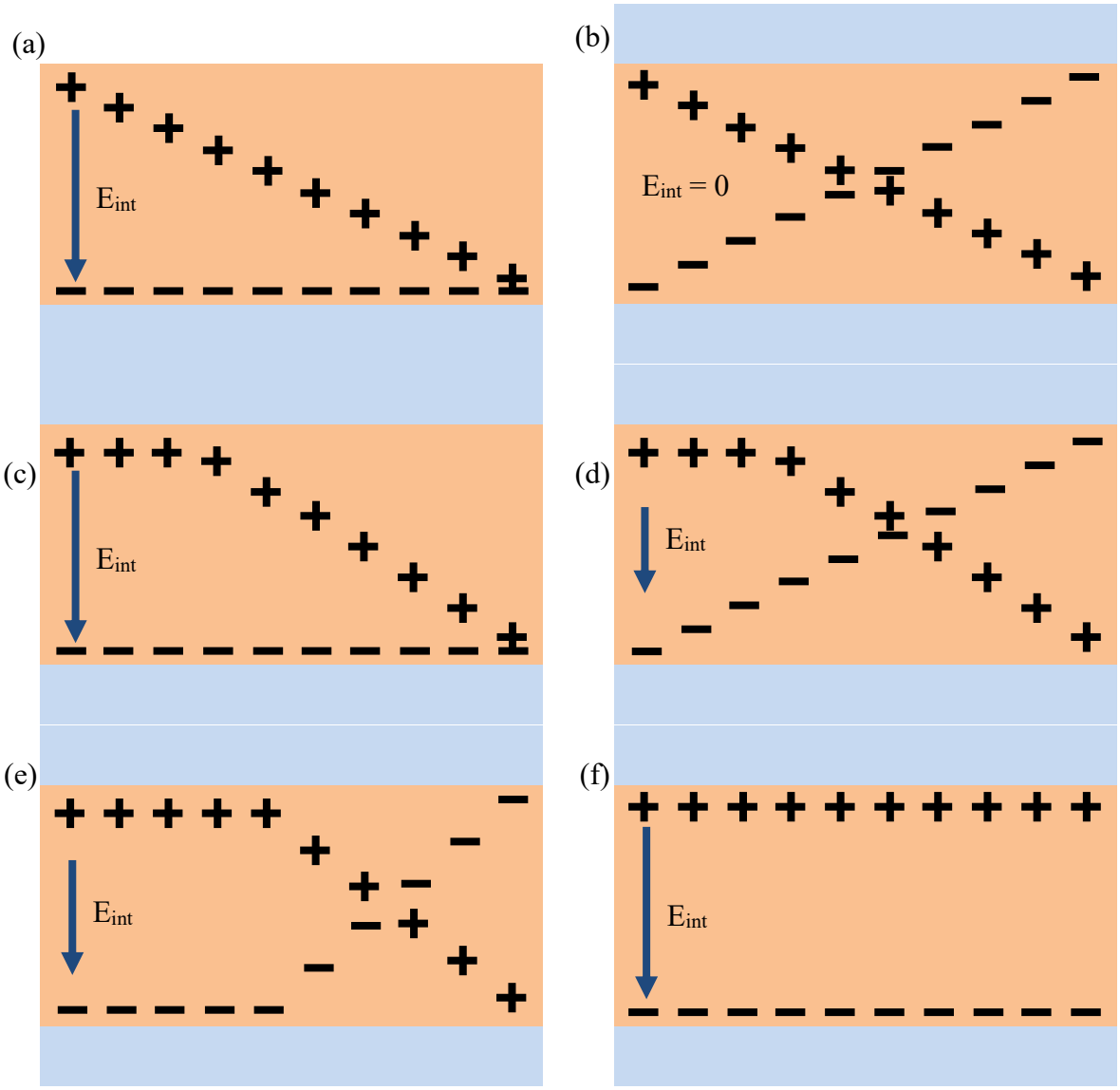

Fig. 5. Schematic representation of the distribution of positive and negative charges during the formation of a self-polarized state in a thin ferroelectric film: (a) in a freshly prepared sample, (b) after high-temperature annealing, (c) after aging of the self-polarized film, (d) after high-temperature annealing of the self-polarized film, (e) after subsequent aging, (f) limiting state as a result of aging. The magnitude and direction of the internal field (E_{int}) are indicated by arrows

Thus, the orientation of the electric field polarizing the ferroelectric is determined by the field of the negative space charge, which is sufficient to reorient some of the ferroelectric dipoles in the film. Figure 5(b) illustrates the process of hysteresis loop symmetrization, which occurs due to sample depolarization following high-temperature annealing, the depletion of deep traps, and the uniform distribution of the electron gas across the film's thickness. A similar state is also achieved by applying a strong alternating field.

It is assumed that the uniform distribution of charged oxygen vacancies in as-prepared samples is associated with their low diffusion rates in the perovskite lattice across the film thickness, and their ordering (or "ascending diffusion") can be caused by a mechanical stress gradient (the Gorsky effect) [32]. According to previous studies, this

gradient is formed during the crystallization and growth of spherulitic islands due to the difference in densities of the amorphous (or low-temperature pyrochlore) and perovskite phases [28,30]. Calculations show that in a non-uniformly deformed lattice at high rotation rates, the bending strain can reach fairly large values (~ 0.5–1 %) [28,30]. Figure 6 demonstrates that the mechanical stress gradient vector can be oriented either toward the lower (Fig. 6(a)) or upper (Fig. 6(b)) film interface, depending on which (upper or lower) film interface is near which nucleation and growth of perovskite islands occurs. In the first case, when the crystal lattice (growth axis) rotates toward the center of the spherulitic island, this leads to the diffusion of oxygen vacancies toward the free surface of the film (toward lattice compression) and will contribute to an increase in the internal field. In the second case, when the growth axis rotates away from the center and toward the periphery of the island, the movement of vacancies will occur in the opposite direction – toward the lower film interface, as a result of which the magnitude of the internal field will decrease. Thus, in a mechanically inhomogeneous crystal lattice, one can expect a noticeable diffusion of charged oxygen vacancies in the direction where lattice compression should be observed, Fig. 7. The results obtained in this work indicate that a variant is realized in the films in which the mechanical stress gradient determined the direction of diffusion of oxygen vacancies toward the free surface of the thin film (Fig. 6(a)).

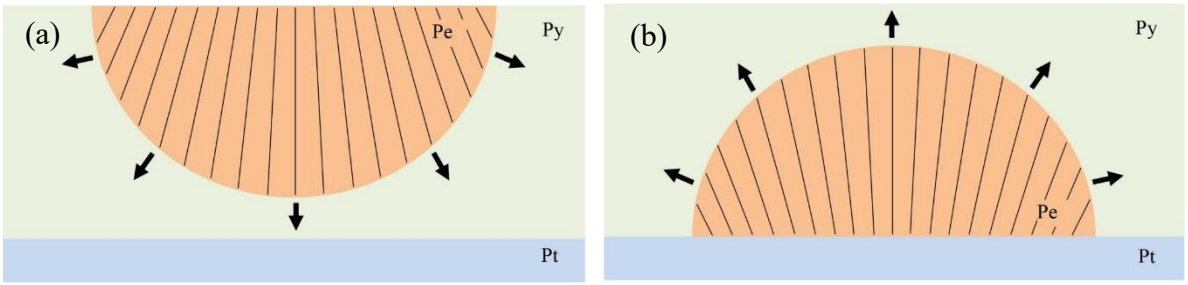

Fig. 6. Model of growth of spherulitic islands from the free surface of the film (a) and from the lower film-substrate interface (b)

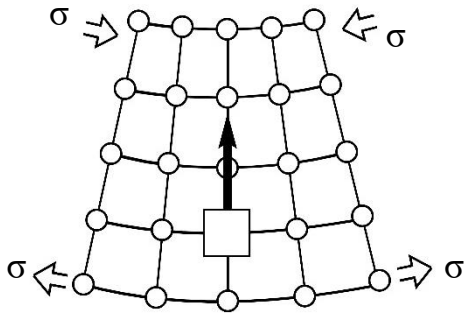

Fig. 7. Schematic model of the motion of an oxygen vacancy in a perovskite lattice under conditions of non-uniform (bending) deformation

The directed diffusion of charged oxygen vacancies during aging results in their gradual accumulation near the upper interface of the film, which is shown in Fig. 5(c). High-temperature annealing of the aged film results in the release of electrons from deep traps, as a result of which the internal field decreases (Fig. 5(d)), which corresponds to

a decrease in the hysteresis loop asymmetry (Fig. 3(b)), but maintaining a significant internal field (~ 9 kV/cm). Subsequent aging (3 months) leads to further accumulation of charged oxygen vacancies near the upper interface (Fig. 5(d)), an increase in the internal field (up to ~ 15 kV/cm), Fig. 3(c). It is assumed that in the presence of a sufficient concentration of charged oxygen vacancies, the initial value of the internal field (~ 23 kV/cm, Fig. 3(a)) is expected to be reached in the limit with the ordering of charged vacancies near the upper interface of the thin film (Fig. 5(e)). It should be noted that the difference between the unipolar state in freshly prepared films and films after their long-term aging lies in the formation of a stable macroscopic polar state caused by the diffusion of oxygen vacancies, which is extremely difficult to destroy under the influence of strong alternating fields and an increase in temperature.

The schematic charge redistribution shown in Fig. 8 reflects the change in excess lead oxide with T_{sint} (Fig. 4), which affects the mechanism of perovskite phase formation (Fig. 6). An increase in excess lead oxide leads to an increase in the concentration of oxygen vacancies, an increase in the space charge the internal field (Figs. 8(a,b)). A subsequent decrease in lead oxide leads to a redistribution of deep traps across the film thickness, a change in the position of the space charge, and a change in the concentration of oxygen vacancies, which affects the magnitude of the internal field (Fig. 8(c)).

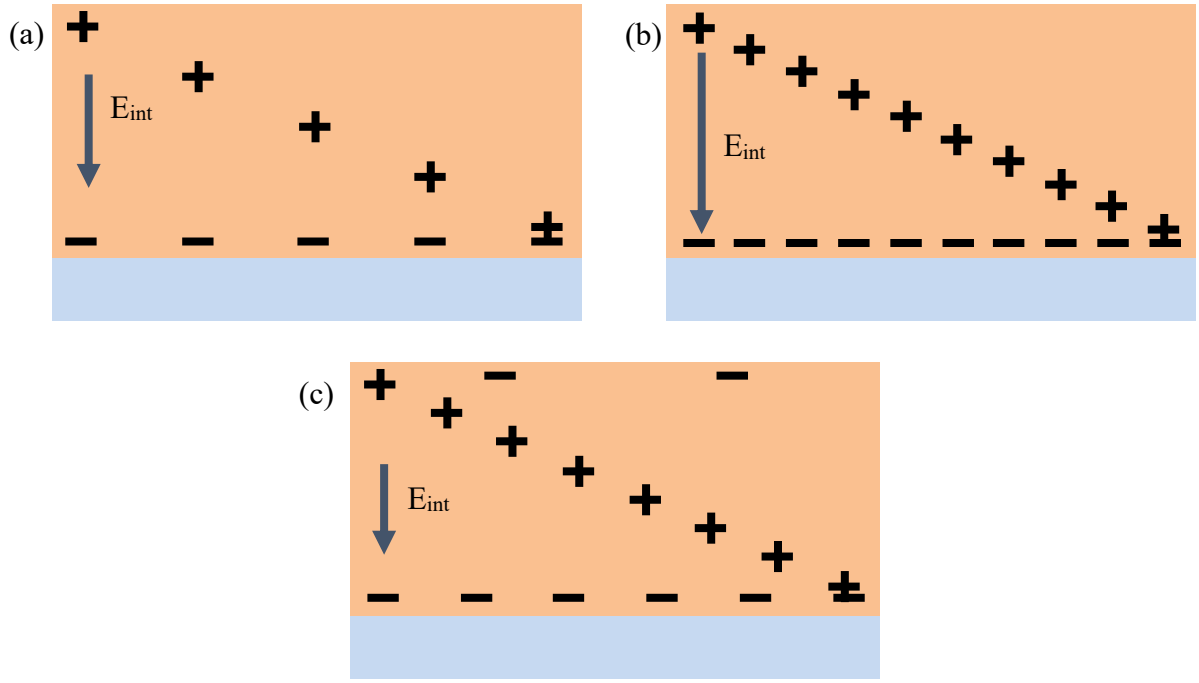

Fig. 8. Schematic distribution of charges in a thin film during the implementation of the mechanism of perovskite island growth from the free surface of the film: (a) with a small excess of lead oxide and a low concentration of separated charges, (b) with an increase in excess lead oxide and charge concentration, and (c) during the implementation of the mechanism of island growth from the lower interface of the film. The magnitude and direction of the internal field (E_{int}) are indicated by arrows

Estimates of the diffusion rate of oxygen vacancies and the internal field

To estimate the upward diffusion flux (I_V) of oxygen vacancies under the action of a mechanical stress gradient, we use the equation describing the Gorsky effect [31,32]:

$$I_V = - N_V \times D_V/(k_B T) \times \partial\sigma/\partial x \times \omega_V, \quad (1)$$

where N_V is the density of oxygen vacancies, D_V is their diffusion coefficient at room temperature, k_B is the Boltzmann constant, $\partial\sigma/\partial x$ is the mechanical stress gradient (σ) across the film thickness (x), and ω_V is the volume occupied by a vacancy in the perovskite lattice. To estimate the flux, reasonable values of oxygen vacancy concentration were used: ~ 0.01 % of the number of oxygen atoms in the octahedral sublattice of the perovskite structure, i.e. $N_V \sim 10^{24}$ m^{-3}, $D_V \sim 5\times10^{20}$ m^{-2} s^{-1} [36], $T \sim 295$ K, $\sigma \sim 300$ MPa at a growth axis rotation rate of ~ 0.6 deg/μm, $x \sim 0.5\times10^{-6}$ m [10], $\omega_V \sim 8\times10^{-30}$ m^{-3}. Then the value of I_V will be ~ 6×10^{10} m^{-2} s^{-1}.

As is well known, the flow of atoms (or vacancies) can be represented as the product of the density of atoms (vacancies) (N_V) and the velocity of their movement (υ), i.e. $I_V = N_V \times \upsilon$. Then the velocity of vacancies will be $\upsilon = I_V/N_V \sim 6\times10^{-12}$ m/s. This means that during the aging period (e.g., 3 months or ~ 10^7 s), the distance that oxygen vacancies will move will be 0.6×10^{-6} m or ~ 0.6 μm. Thus, virtually all of the available charged oxygen vacancies should move to the upper interface of the film.

However, judging by the experimental results, the internal field does not reach the value measured in as-prepared films. The most likely reason for this is the lack of charged oxygen vacancies in the thin film, caused by the fact that not all oxygen vacancies are charged at room temperature. This is due to the relatively high activation energies of electrons and charged vacancies (E_a). At room temperature, E_a is estimated to be ~ 0.22 eV [10]. This means that only 1.3 % of the oxygen vacancies in the thin film will be charged – $N_V^{2+} = 1.3\times10^{22}$ m^{-3}.

To estimate the concentration of charged oxygen vacancies that create a stable internal field, we use the relationship between the charge density ($\Delta\sigma$) and the internal field strength (ΔE_{int}):

$$\Delta\sigma \sim \varepsilon\varepsilon_0\Delta E_{int}, \quad (2)$$

where ε is the relative permittivity, which is ~ 700 at room temperature, and ε_0 is the permittivity. Thus, an increase in E_{int} = 10 kV/cm requires ~2×10^{16} m^{-2} of charged oxygen vacancies localized near the upper interface of the thin film. This means that the number of charged oxygen vacancies located throughout the thin film (~ 0.7×10^{16}), normalized per square meter of surface area, is several times lower than the required density.

In this regard, under conditions of a deficiency of charged oxygen vacancies, the formation of a field of ordered vacancies can occur in two stages. In the first stage, charged vacancies present in the film bulk accumulate relatively rapidly (over a period of ~10^6–10^7 s) near the upper film interface due to upward diffusion. In the second stage, the rate of increase in volume charge, which is significantly slower, will be determined by the activation energy of electrons/charged oxygen vacancies.

Conclusions

Experimental studies were conducted to examine changes in the internal field and self-polarization associated with the influence of the crystallization (synthesis) temperature of submicron spherulitic PZT films and their aging under the action of non-uniform mechanical stresses that form in the films as a result of crystallization of the perovskite phase from the amorphous (or intermediate pyrochlore phase) during high-temperature annealing. It was shown that the film aging process is accompanied by the directed

diffusion of oxygen vacancies, leading to the emergence of a stable internal field. Estimates were made of the diffusion rate of oxygen vacancies, as well as their concentration, necessary for the formation of an internal field in thin films. It was shown that a change in the crystallization (synthesis) temperature of the perovskite phase can lead to a change in the direction of the gradient vector of non-uniform mechanical stresses and the direction of diffusion of oxygen vacancies towards the substrate. The obtained results allow us to specify the physical mechanisms of both electrical and mechanical nature that lead to the formation of a internal field and self-polarized state and its stability in thin PZT films.

CRediT authorship contribution statement

Alsu R. Valeeva: investigation, data curation; **Michail V. Staritsyn**: investigation, data curation, writing – original draft; **Stanislav V. Senkevich**: data curation, writing – review & editing; **Eugenii Yu. Kaptelov**: investigation, data curation, writing – original draft; **Igor P. Pronin**: conceptualization, writing – review & editing, supervision; **Dmitrii A. Kiselev**: investigation, data curation, writing – original draft; **Sergey A. Nemov**: conceptualization, writing – review & editing.

Conflict of interest

The authors declare that they have no conflict of interest.

References

1. Izyumskaya N, Alivov Y-I, Cho S-J, Morkoç H, Lee H, Kang Y-S. Processing, structure, properties, and applications of PZT thin films. *Critical Reviews in Solid State and Materials Sciences.* 2007;32(3-4): 111–202.
2. Scott JF. Application of modern ferroelectrics. *Science.* 2007;315(5814): 954–959.
3. Balke N, Bdikin I, Kalinin SV, Kholkin AL. Electromechanical imaging and spectroscopy of ferroelectric and piezoelectric materials: state of the art and prospects for the future. *Journal of American Ceramic Society.* 2009;92(8): 1629–1647.
4. Vorotylov KA, Mukhortov VM, Sigov AS. *Integrated ferroelectric devices.* Moscow: Energoatomizdat; 2011. (In Russian)
5. Bukharaev AA, Zvezdin AK, Pyatakov AP, Fetisov YK. Straintronics: a new trend in micro- and nanoelectronics and materials science. *Physics-Uspekhi.* 2018;61(12): 1175–1212.
6. Yadav SK, Hemalatha J. Synthesis and characterization of magnetoelectric $Ba_2Zn_2Fe_{12}O_{22}$–$PbZr_{0.52}Ti_{0.48}O_3$ electrospun core–shell nanofibers for the AC/DC magnetic field sensor application. *Applied Physics A. Materials Science &Processing.* 2024;130(1): 67.
7. Song L, Glinsek S, Defay E. Toward low-temperature processing of lead zirconate titanate thin films: Advances, strategies, and applications. *Applied Physics Reviews.* 2021;8: 041315.
8. Li CL, Feng GH. Hydrothermal engineering of ferroelectric PZT thin films tailoring electrical and ferroelectric properties via TiO_2 and $SrTiO_3$ interlayers for advanced MEMS. *Micromachines.* 2025;16(8): 879.
9. Kholkin AL, Brooks KG, Taylor DV, Hiboux S, Setter N. Self-polarization effect in $Pb(Zr,Ti)O_3$ thin films. *Integrated Ferroelectrics.* 1998;22(1–4): 525–533.
10. Pronin IP, Tarakanov EA, Kaptelov EYu, Shaplygina TA, Afanasjev VP, Pankrashkin AV. Self-polarization and migratory polarization in lead zirconate titanate thin films. *Physics of the Solid State.* 2002;44(4): 769–773.
11. Liu L, Yi J, Xu K, Liu Z, Tang M, Dai L, Gao X, Liu Y, Wang S, Zhang Z, Shu L, Li J-F, Zhang S, Wang Y. High piezoelectric property with exceptional stability in self-poled ferroelectric films. *Nature Communications.* 2024;15: 10798.
12. Watts BE, Leccabue F, Tallarida G, Ferreri S, Fanciulli M, Padeletti G. Surface segregation mechanisms

in dielectric thin films. *Integrated Ferroelectrics.* 2004;62(1): 3–11.
13. Hiboux S, Muralt P. Origin of voltage offset and built-in polarization in in-situ sputter deposited PZT thin films. *Integrated Ferroelectrics.* 2001;36(1–4): 83–92.
14. Choi CH, Lee J, Park BH, Noh TW. Asymmetric switching and imprint in $(La,Sr)CoO_3/Pb(Zr,Ti)O_3/(La,Sr)CoO_3$ heterostructures. *Integrated Ferroelectrics.* 1997;18(1–4): 39–48.
15. Bruchhaus R, Pitzer D, Schreiter M, Wersing W. Optimized PZT thin films for pyroelectric IR detector arrays. *Journal of Electroceramics.* 1999;3(2): 151–162.
16. Pronin IP, Kaptelov EYu, Gol'tsev AV, Afanas'ev VP. The effect of stresses on self-polarization of thin ferroelectric films. *Physics of the Solid State.* 2003;45(9): 1768–1773.
17. Pertsev NA, Kukhar VG, Kohlstedt H, Waser R. Phase diagrams and physical properties of single-domain epitaxial Pb(Zr1–xTix)O3 thin films. *Physical Review B.* 2003;67(5): 054107.
18. Ogawa T, Senda A, Kasanami T. Controlling the crystal orientations of lead titanate thin films. *Jpn. J. Appl. Phys.* 1991;30(95): 2145–2148.
19. Bursian EV, Zaikovskii OI, Makarov KV. Polarization of a ferroelectric plate by bending. *Bulletin of the Russian Academy of Sciences: Physics.* 1969;33(7): 1017–1019.
20. Yudin PV, Tagantsev AK. Fundamentals of flexoelectricity in solids. *Nanotechnology.* 2013;24(43): 432001.
21. Gruverman A, Rodriguez BJ, Kingon AI, Nemanich RJ, Tagantsev AK, Cross JS, Tsukada M. Mechanical stress effect on imprint behavior of integrated ferroelectric. *Appl. Phys. Lett.* 2003;83(4): 728–730.
22. Kolosov VYu, Thölén AR. Transmission electron microscopy studies of the specific structure of crystals formed by phase transition in iron oxide amorphous films. *Acta Materialia.* 2000;48(8): 1829–1840.
23. Kolosov VY, Veretennikov LM, Startseva YB, Shwamm CL. Electron microscopy study of a chalcogenide-based polycrystalline condensate microstructure: the effect of composition and thickness on internal lattice bending. *Semiconductors.* 2005;39(8): 955–959.
24. Zhigalina OM, Khmelenin DN, Valieva YA, Kolosov VYu, Kuznetsov KA, Bokunyaeva AO, Vorotilov KA, Sigov AS. Structural features of PLZT films. *Crystallography Reports.* 2018;63(4): 646–655.
25. Savytskii D, Jain H, Tamura N, Dierolf V. Rotating lattice single crystal architecture on the surface of glass. *Scientific Reports.* 2016;6: 36449.
26. Lutjes NR, Zhou S, Antoja-Lleonart J, Noheda B, Ocelík V. Spherulitic and rotational crystal growth of Quartz thin films. *Scientific Reports.* 2021;11(1): 14888.
27. Da B, Cheng L, Liu X, Shigeto K, Tsukagoshi K, Nabatame T, Ding Z, Sun Y, Hu J, Liu J, Tang D, Zhang H, Gao Z, Guo H, Yoshikawa H, Tanuma S. Cylindrically symmetric rotating crystals observed in crystallization process of InSiO film. *Science and Technology of Advanced Materials: Methods.* 2023;3(1): 2230870.
28. Staritsyn MV, Pronin VP, Khinich II, Senkevich SV, Kaptelov EYu, Pronin IP, Elshin AS, Mishina ED. Microstructure of spherulitic lead zirconate titanate thin films. *Physics of the Solid State.* 2023;65(8): 1312–1318.
29. Kiselev DA, Staritsyn MV, Senkevich SV, Kaptelov EYu, Pronin IP, Pronin VP. Radially oriented lateral self-polarization in spherulitic lead zirconate titanate thin films. *Technical Physics Letters.* 2023;49(11): 45–47.
30. Pronin V. P., Staritsyn M.V., Kaptelov E.Yu., Senkevich S.V., Pronin I.P. Features of electronic images of spherulitic islands in thin PZT films. *Technical Physics Letters.* 2025;51(3): 1–4.
31. Gorsky WS. Theorie des elastischen Nachwirkung in ungeordneten Mischkristallen (elastische Nachwirkung zweiter Art). *Physikalische Zeitschrift Der Sowjetunion.* 1935;8: 457–471.
32. Kosevich AM. How a crystal flows. *Soviet Physics Uspekhi.* 1975;17: 920–930.
33. Okamura S, Miyata S, Mizutani Y, Nishida T, Shiosaki T. Conspicuous voltage shift of D-E hysteresis loop and asymmetric depolarization in Pb-based ferroelectric thin films. *Jpn J. Appl. Phys.* 1999;38;(95): 5364–5367.
34. Pronin IP, Kaptelov EYu, Senkevich SV, Sergeeva ON, Bogomolov AA, Kholkin AL. Electrical properties of heterophase PZT thin films with excess lead oxide. *Integrated Ferroelectrics.* 2009;106(1): 81–93.
35. Pronin VP, Senkevich SV, Kaptelov EYu, Pronin IP. Anomalous losses of lead in crystallization of the perovskite phase in thin PZT films. *Physics of the Solid State.* 2013;55: 105–108.
36. Holzlechner G., Kastner D., Slouka C., Hutter H., Fleig J. Oxygen vacancy redistribution in $PbZr_xTi_{1-x}O_3$ (PZT) under the influence of an electric field. *Solid State Ionics.* 2014;262: 625–629.

MATERIALS PHYSICS AND MECHANICS RESEARCH ARTICLE

Submitted: October 5, 2025 **Revised: November 10, 2025** **Accepted: December 5, 2025**

Configurational force distribution during perovskite phase growth in a ferroelectric film

M. Bakkar [1] ✉, A. Mhemeed Dbes [1], D.V. Avdonyushkin [2], A.S. Semenov [1,2]

[1] Peter the Great St. Petersburg Polytechnic University, St. Petersburg, Russia

[2] Institute for Problems in Mechanical Engineering of the Russian Academy of Sciences, St. Petersburg, Russia

✉ mamadyan1997@gmail.com

ABSTRACT

The propagation of the interphase boundary during the growth of the perovskite phase in a pyrochlore matrix in thin ferroelectric lead zirconate titanate films on a silicon substrate is studied using the methods of configurational force mechanics. A numerical solution of the boundary value problem of the growth of a perovskite inclusion in an initially pyrochlore film is obtained in axisymmetric and three-dimensional formulations. The growth of cylindrical, conical, and spherical inclusions is considered. The growth of single and multiple regularly and irregularly located inclusions were studied. A comparison of the solutions to the problem in linear-elastic and elastoplastic formulations was made. The dependence of the configurational force on the inclusion size and on the distance from the substrate is obtained. In the modeling, the interphase boundary rate was determined by a power-law dependence on the configurational force. Based on the results of finite-element computations of the spatial and temporal distribution of the configurational force and the evolution equation for the growth rate of the interphase boundary, the gradient of the growth axis angle deviation was determined, correlating with the experimental data obtained from X-ray diffraction analysis and scanning electron microscopy.

KEYWORDS

lead zirconate-titanate thin films • spherulitic microstructure • configurational forces • stress relaxation finite-element modeling and simulation

Funding. *This work has been supported by the grant of Russian Science Foundation (grant RSF 25-11-00274).*

Citation: Bakkar M, Mhemeed Dbes A, Avdonyushkin DV, Semenov AS. Configurational force distribution during perovskite phase growth in a ferroelectric film. *Materials Physics and Mechanics*. 2025;53(6): 25–43. http://dx.doi.org/10.18149/MPM.5362025_3

Introduction

Polycrystalline ferroelectric films with a perovskite structure, owing to their high electromechanical properties, have been widely used as FeRAM memory elements [1–5], offering high data storage density and fast operation, as well as in MEMS devices [5–7], microwave electronics [8,9], energy storage devices [1], infrared detectors [1,2], and optical modulators [2]. Thin-film coatings enable device miniaturization and high performance. Modern methods for fabricating thin ferroelectric films are multi-stage technologies based on radio-frequency magnetron deposition of amorphous films at low temperatures and subsequent heat treatment. The pyrochlore → perovskite phase transformation occurs during the final stage of film fabrication, during high-temperature annealing in air at 580 °C.

One of the primary mechanisms for forming the perovskite phase in thin films on silicon substrates is the growth of island structures (Fig. 1(a)) as spherulites [10,11].

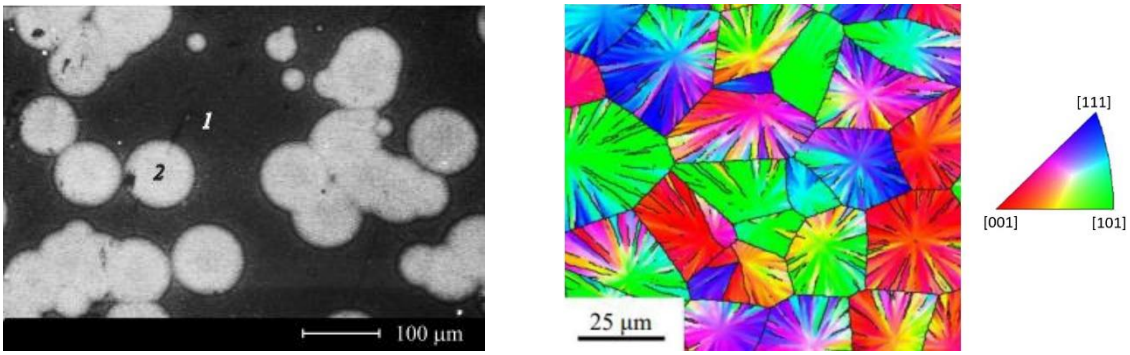

(a) (b)

Fig. 1. Formation of spherulitic structures in thin films of PZT: (a) at the initial stage of growth (data from an optical microscope, 1 – pyrochlore phase, 2 – perovskite phase), (b) at the final stage (maps of crystallographic orientations of growth axes based on the registration of backscattered electron diffraction)

As spherulitic islands merge, a blocky spherulitic microstructure of perovskite with linear boundaries is formed (Fig. 1(b)) [7]. In the case of the studied lead zirconate titanate (PZT) thin films, the phase transition from the pyrochlore phase to the perovskite structure results from a crystallization (recrystallization) process.

During the growth of a spherulite, a progressive deviation of the growth axis from the vertical (normal to the free surface of the film) in the meridional plane is observed. The main cause of this deviation is mechanical stresses arising in the thin film because of a change in volume (-8 %) [12] during the phase transition. The stresses arising during the growth process was evaluated in [12–14]. Due to the deviation of the growth axes, a structure with local axial symmetry is formed within the spherulite, determining the film properties at the macro level.

The relevance of studying residual stresses induced during the film production process and characteristic microstructural parameters of spherulites (size, thickness after shrinkage, angles of deviation of the growth axes, the presence and orientation of defects) is associated with their significant influence on the functional characteristics of ferroelectric films [15–17], dielectric properties [14–17] and hysteresis behavior [15–18].

One of the promising approaches to describing the kinetics of interphase boundaries is the approach of configurational force mechanics (configurational mechanics, mechanics in material space). The origins of configurational force mechanics go back to the work of J.D. Eshelby in 1951 [19], where the concept of a force acting on an elastic singularity (or defect) was introduced. It is defined as the negative gradient of the total energy of a body relative to the position of the defect in the material (not in physical space). The following terms were subsequently used for this force: a configurational force, a driving force, a thermodynamic force (or affinity), a non-Newtonian force, and a material force.

The mechanics of configurational forces have been actively developing since the 1980s as a branch of solid body mechanics, providing a natural description of the evolution of heterogeneities of various natures—from the movement of defects and crack growth to the development of new phase regions and the propagation of chemical reaction fronts. These processes have in common that they cannot be reduced to the displacement of material points under the action of mechanical forces but lead to a change in the configuration of the body due to the movement of defects and boundaries

relative to the material points, i.e., in the material space. Various theoretical and applied aspects of configurational mechanics can be found in [20–31].

The aim of this study is to investigate the kinetics of the pyrochlore → perovskite interphase boundary during high-temperature annealing by analyzing the spatial distribution of configurational forces during perovskite inclusion growth. The growth of inclusions with various initial configurations, including cylindrical, conical, and spherical, is considered. A solution to the problem is obtained in both linear-elastic and elastic-plastic formulations. The latter formulation allows for indirect consideration of dislocations, micropores, and microcracks. To evaluate the mutual influence of inclusions during growth, a solution to the problem for multiple irregular inclusions in a three-dimensional formulation is considered. The results are verified by comparing the calculated gradient of the growth axis deviation angle with experimental data.

Materials and Methods

The objects of the study were thin polycrystalline films of $Pb(Zr_{1-x}Ti_x)O_3$ (PZT) [15]. The composition of the binary solid solution $(1-x)PbZrO_3-xPbTiO_3$ corresponded to the morphotropic phase boundary (MPB), where tetragonal and rhombohedral phases coexist at a ratio of x(Ti/Zr) ≈ 46/54, leading to optimal piezoelectric properties.

The PZT thin films were fabricated in a two-step process using radio-frequency magnetron sputtering of a ceramic target. The substrate used was a <100> - oriented silicon wafer with sequentially deposited layers of silicon dioxide (SiO_2, ~ 300 nm thick) and platinum (Pt, 80 nm thick) [12]. The resulting film thickness was 500 nm, deposited at a temperature of 160 °C. As-deposited films were initially amorphous. Subsequent annealing (1 h) in an air atmosphere at temperatures above 450 °C resulted in the formation of a pyrochlore structure. The phase transformation from pyrochlore to perovskite began at 530 °C, initiating the formation of islands (perovskite inclusions). To obtain continuous perovskite films, the annealing temperature was increased to 580 °C [10].

The average size of the resulting spherulitic blocks ranged from 10 to 40 μm. This grain size was controlled by varying the target-to-substrate distance from 30 to 70 mm during deposition, which correspondingly varied the substrate temperature from 90 to 160 °C. The growth axis deviation angle was characterized using scanning electron microscopy (Lira 3 Tescan, EVO-40 Zeiss) in both backscattered electron and electron backscatter diffraction modes, as well as by θ-2θ X-ray diffraction (XRD) (Rigaku Ultima IV) [13]. The stress-strain state computations were performed using the finite element program ANSYS 2022 R2.

Model of perovskite phase growth in a thin film

The boundary-value problem describing the growth of a perovskite inclusion within an initially pyrochlore film on a silicon substrate was solved in axisymmetric and three-dimensional formulations, as shown in Fig. 2. The axisymmetric formulation is less computationally demanding and enables multivariate calculations with varying inclusion geometries, whereas the three-dimensional formulation provides a more accurate representation of the interactions between neighboring inclusions. In the computations, the inclusion shape (cylindrical, conical, or spherical) and its characteristic dimensions

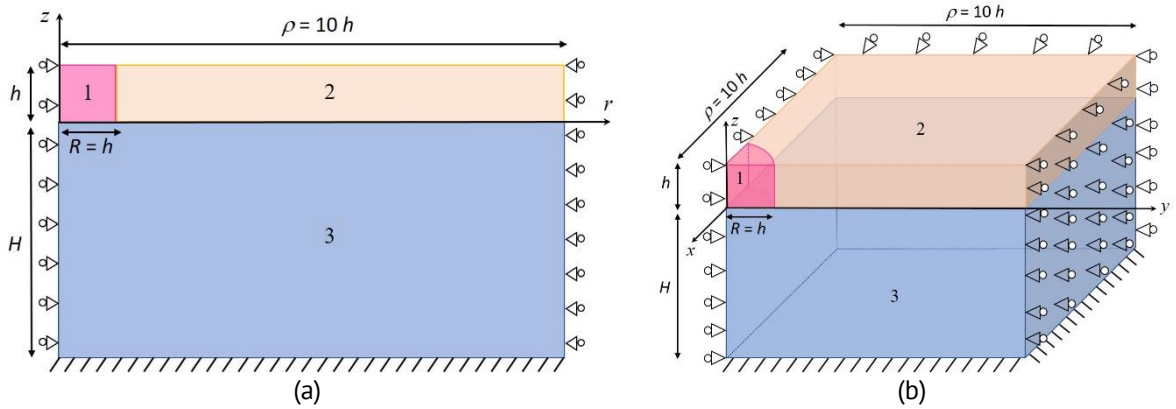

Fig. 2. Geometry parameters and boundary conditions for representative volume element of PZT film in (a) axisymmetric model, (b) 3D model. The material system consists of the perovskite inclusion 1, the pyrochlore matrix 2 and the silicon substrate 3

were varied, (R is the inclusion radius, 2ρ is the distance between inclusion centers, γ is the cone angle).

During the phase transition from pyrochlore to perovskite, there is an 8 % reduction in volume [12], which is the main source of stress in the film. The stresses are determined by the transformation strain tensor:

$$\boldsymbol{\varepsilon}^{tr} = \varepsilon^{*}\mathbf{1} = \frac{1}{3}\frac{\Delta V}{V}\mathbf{1}, \quad (1)$$

where $\mathbf{1}$ is the unit tensor, ΔV is the volume reduction under the phase transition, ε^{*}= 8/3 %. Note that the transformation strain tensor has nonzero value only in the inclusions. It is zero in the pyrochlore matrix and substrate. The constitutive equation of thermo-elasto-chemo-plasticity within the framework of infinitesimal mechanics is defined by the expression:

$$\boldsymbol{\sigma} = {}^{4}\boldsymbol{C}\colon(\boldsymbol{\varepsilon} - \boldsymbol{\varepsilon}^{tr} - \boldsymbol{\varepsilon}^{p} - \boldsymbol{\varepsilon}^{T}), \quad (2)$$

where $\boldsymbol{\sigma}$ is the stress tensor, ${}^{4}\boldsymbol{C}$ is the fourth-order elastic moduli tensor, $\boldsymbol{\varepsilon} = (\nabla\boldsymbol{u})^{S}$is the total strain tensor, $\boldsymbol{\varepsilon}^{p}$ is the plastic strain tensor defined at the active loading by relation:

$$\dot{\boldsymbol{\varepsilon}}^{p} = \frac{1}{H'}\frac{\partial F}{\partial \boldsymbol{\sigma}} \otimes \frac{\partial F}{\partial \boldsymbol{\sigma}}\colon\dot{\boldsymbol{\sigma}}, \quad (3)$$

with $F = \sqrt{3/2\mathrm{dev}(\boldsymbol{\sigma})\colon\mathrm{dev}(\boldsymbol{\sigma})} - H(\varepsilon^{p})$ is von Mises yield function, $\mathrm{dev}(\boldsymbol{\sigma}) = \boldsymbol{\sigma} - \frac{1}{3}\mathrm{tr}(\boldsymbol{\sigma})\mathbf{1}$ is the stress deviator, $H' = dH/d\varepsilon^{p}$ is the slope of the stress-strain curve (isotropic hardening is assumed), $\boldsymbol{\varepsilon}^{T}$ is the temperature strain tensor:

$$\boldsymbol{\varepsilon}^{T} = \alpha\Delta T\mathbf{1}, \quad (4)$$

here α is linear thermal expansion coefficient.

The appearance of mechanical stress slows down the advance of the interphase boundary. In the configurational force method, the rate of advance of the interphase boundary along the normal can be written as [14]:

$$V_N = A|f_N|^{n-1}f_N, \quad (5)$$

where V_N is the interface propagation velocity in interface normal direction, f_N is the configurational force:

$$f_N = \boldsymbol{N}\cdot[[-\boldsymbol{b}]]\cdot\boldsymbol{N}, \quad (6)$$

where $\boldsymbol{N}$ is the normal vector to the interface boundary, $\boldsymbol{b}$ is Eshelby energy-momentum tensor:

$$\boldsymbol{b} = \psi\mathbf{1} - \boldsymbol{\sigma}\cdot\boldsymbol{\varepsilon}, \quad (7)$$

where ψ is the volume density of free energy defined by expression:

$$\psi = \frac{1}{2}(\boldsymbol{\varepsilon} - \boldsymbol{\varepsilon}^{tr} - \boldsymbol{\varepsilon}^{p} - \boldsymbol{\varepsilon}^{T}) : {}^{4}\boldsymbol{C} : (\boldsymbol{\varepsilon} - \boldsymbol{\varepsilon}^{tr} - \boldsymbol{\varepsilon}^{p} - \boldsymbol{\varepsilon}^{T}) + \psi_0(T), \quad (8)$$

here $\psi_0(T)$ is the chemical free energy density, which depends on temperature. It is assumed that the jumps $[\![\varepsilon^*]\!] \neq 0$ and $[\![\psi_0]\!] \neq 0$ in the phase transformation.

The non-uniform configurational force distribution along the film thickness leads to different interface propagation velocities depending on the vertical coordinate *z*. This leads to the tilting of the initially vertical boundary (for linear dependencies $V_N(z)$) and the curvature of the initially straight boundary (for nonlinear dependencies $V_N(z)$). The orientation of the interphase boundary determines the orientation of the growth axis of the formed perovskite.

The main feature of the spherulite ferroelectric structure is the near to linear dependence of the rotation angle β of the growth axis on the coordinate along the radius of the spherulite. Assuming that the rotation is caused by the action of configurational forces, we can obtain an expression for the gradient of the growth axis angle [14]:

$$\frac{\partial \beta}{\partial r} = cos^{\,2}(\beta)\frac{n}{f}\frac{\partial f}{\partial z}. \quad (9)$$

The dependences $\beta(r, z = h)$ for various spherulites were measured experimentally [10] based on X-ray diffraction analysis and scanning electron microscopy methods. With linear changing β from r the value of $\frac{\partial \beta}{\partial r}$ is constant and can be used for validation of the model.

Results and Discussion

The purpose of the computations was to determine the stress distribution, and the associated configurational forces near the interphase boundary. Three types of inclusions were considered: cylindrical, conical, and spherical. The multi-variant finite element computations were performed for regular and non-regular inclusion systems with different sizes of perovskite inclusions. The material parameters [12] used in the solution process are given in Table 1.

Table 1. The material parameters used in the computations

	E, MPa	*v*	α, 1/°C	σ_{02}, MPa
Perovskite	70 000	0.3	$9.0 \cdot 10^{-6}$	500
Pyrochlore	70 000	0.3	$9.3 \cdot 10^{-6}$	-
Silicon substrate	109 000	0.3	$4.2 \cdot 10^{-6}$	-

The rate of radial change in the deviation angle of the growth axis is determined for the jump value $[\![\psi_0]\!]$ equal to 650 MJ/m^3. The data on the change in enthalpy from [32] for $La_2Ti_2O_7$ served as a guideline for setting this value.

Axisymmetric model

Cylindrical inclusion. The cylindrical representative volume element with the radius equal to half the distance between the centers of inclusions ($\rho = 10h = 5$ μm) is used for an axisymmetric formulation of the problem. To describe the evolution of the perovskite inclusion growth process, its radius *R* varied in the range from *h* to 10*h* with a step of *h*. The film thickness *h* was 0.5 μm, and the substrate thickness *H* in the model was 5 μm.

The significant excess of the actual substrate thickness relative to the model was taken into account by the fixed boundary condition on the bottom surface.

The boundary value problem was solved using the ANSYS APDL software package. The finite element mesh (Fig. 3) included maximum 200 elements through the film thickness and a total of 160 000 elements. A quadratic quadrilateral element formulation was used.

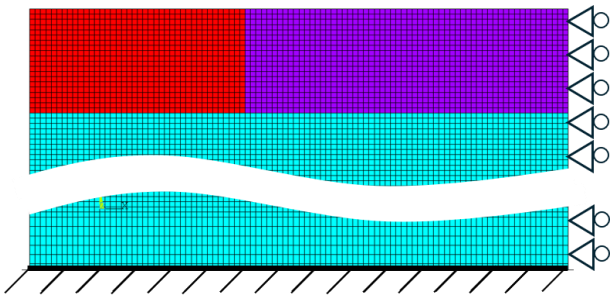

Fig. 3. Axisymmetric finite-element model of a *cylindrical* inclusion growth on a substrate

Configurational force was calculated using a component-wise stress formulation expressed in cylindrical coordinates:

$$f_N = \sigma_{rr}\varepsilon^* - \frac{1}{2E}\left[\!\left[\sigma_{\varphi\varphi}^2 + \sigma_{zz}^2 - 2\nu\sigma_{\varphi\varphi}\sigma_{zz}\right]\!\right] + f_0, \quad (10)$$

where $f_0 = [\![\psi_0]\!]$. To easily compare different formulations, only the stress-dependent part of configurational force is considered below, without f_0.

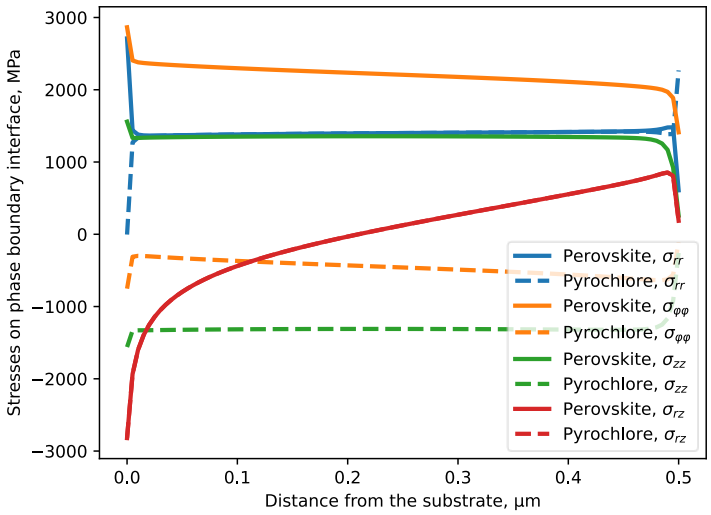

Fig. 4. Dependences of stress tensor components σ_{rr}, σ_{zz}, $\sigma_{\varphi\varphi}$, σ_{rz} [MPa] on the distance from the substrate (vertical coordinate *z*) for the inclusion radius *R* equal *5h* in the model of cylindrical growth of perovskite phase. Distance between inclusion centers 2ρ = 20*h*

This boundary value problem was solved in elastic and elastoplastic formulations. *Elastic solution*. The dependences of stress tensor components σ_{rr}, σ_{zz}, $\sigma_{\varphi\varphi}$ and σ_{rz} on the distance from the substrate (vertical coordinate *z*) for the inclusion radius *R* equal 5*h* are presented in Fig. 4. The distributions of stress components have a close to linear character over a significant part of the film thickness. Local deviations are observed only on the free surface and near the substrate.

The stress components σ_{rr} and σ_{rz} are continuous at the vertical interphase boundary. The stress components σ_{zz} and $\sigma_{\varphi\varphi}$ undergo a discontinuity (a jump) at the interphase boundary. Figure 4 shows the stress values both to the left of the boundary (in perovskite) and to the right of the boundary (in pyrochlore). Because of the high stress values at the interphase boundary, the circumferential $\sigma_{\varphi\varphi}$ and radial stress σ_{rr} components are the most critical. They are likely to be the main cause of the radial and ring cracks observed in the spherulitic structure.

The evolution of radial stress σ_{rr} and the configurational force f_N distributions with increasing inclusion radius R is shown in Fig. 5. With an increase in the radius of the inclusion R, the radial stress σ_{rr} change from a decreasing dependence on the distance from the substrate z for $R/h = 1$ to a monotonically increasing dependence for $R/h \geqslant 2$ (see Fig. 5(a)). Conversely, the configurational force increases steadily from 0 to $R/h \geqslant 8$, then starts decreasing at $R/h = 9$ as z grows (see Fig. 5(b)).

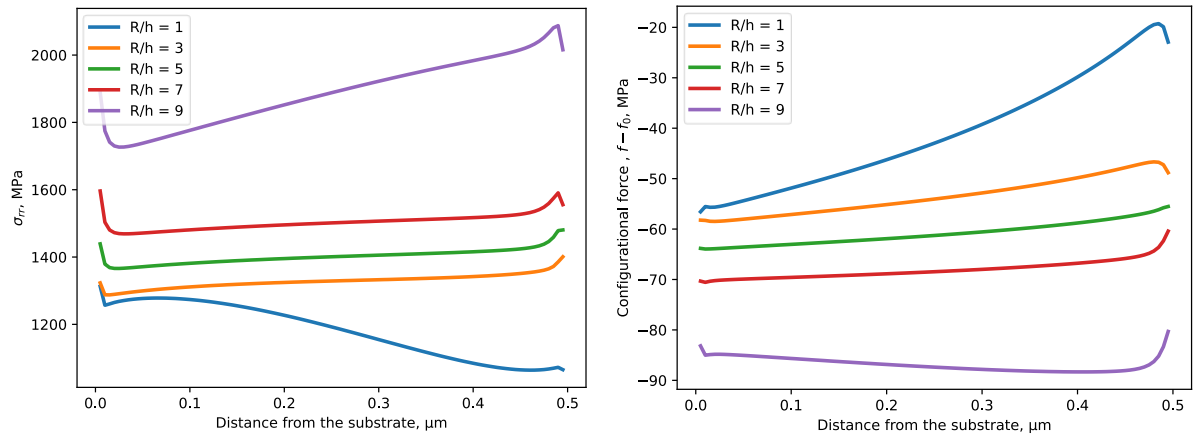

(a) (b)

Fig. 5. Dependences of (a) the radial stress component σ_{rr} [MPa] and (b) the configurational force f_N on the distance from the substrate (vertical coordinate z) for various ratios of the nucleation radius to the film thickness *R/h,* in a model of cylindrical growth of perovskite phase. Distance between inclusions $2\rho = 20h$

For cylindrical inclusions, the monotonically increasing configurational force $f_N(z)$ (Fig. 5(b)) leads in according with Eq. (5) to a progressive deviation of both the interphase boundary and the growth axis from the vertical with the increasing inclusion radius R. The initially cylindrical inclusion will gradually transform with increasing R, into a truncated conical inclusion with a larger radius on the free surface and a smaller radius on the substrate. It should also be noted that there is a surface layer in which the behavior of the angle differs slightly from that of the main part of the film. Growth angle deviation rate according to Eq. (9), with $n = 0.32$ and $z = h/2$ equals 1.1 deg/μm, which corresponds to the order of magnitude observed in experiments ~0.5÷1.4 deg/μm [10–14].

Elastoplastic solution. The elastoplastic formulation allows us to take into account qualitatively the elastic stress relaxation and the appearance of dislocations, micropores, and microcracks observed in experiments. To account for plastic deformation in perovskites, a basic isotropic hardening model based on the plastic flow theory is applied. The hardening modulus was taken to be one hundredth of the Young's modulus.

The resulting stresses and configurational forces for the case of an inclusion radius equal to 5h in the elastic–plastic formulation are presented in Fig. 6(a) and Fig. 6(b), respectively. The dependency of the configurational force $f_N(z)$ is significantly modified by plastic deformation in perovskite. Due to plastic deformations, the stress in perovskite decreases, which leads to a significant increase in configurational forces.

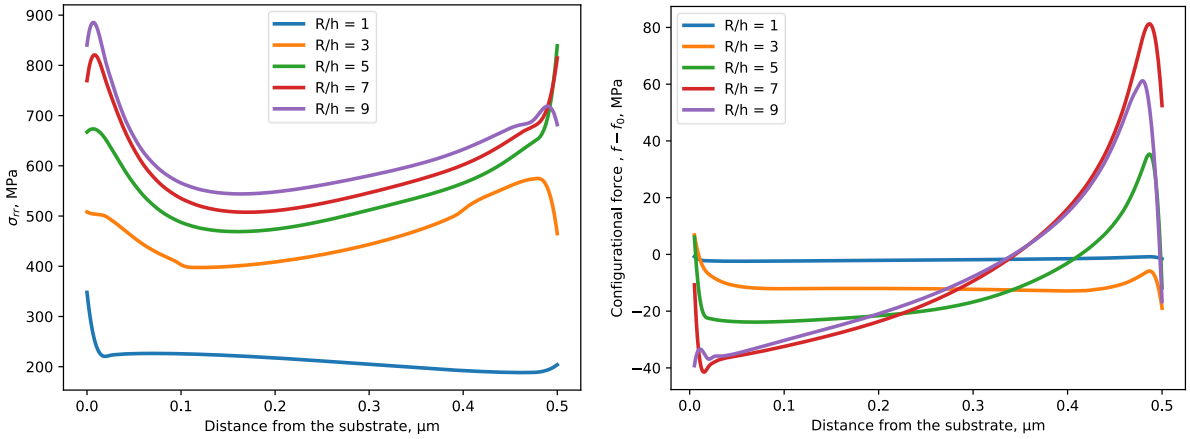

(a) (b)

Fig. 6. Dependence of (a) the radial stress component σ_{rr} [MPa] and (b) the configurational force f_N on the distance from the substrate (vertical coordinate z) for various ratios of the nucleation radius to the film thickness R/h in the model of cylindrical growth of perovskite phase. Distance between inclusion centers $2\rho = 20h$

Unlike the elastic solution, the monotonicity of the configurational force across the film thickness does not depend on the radial coordinate. This feature ensures a monotonic increase in the angle of rotation of the growth anisotropy (Fig. 7). Growth angle rotation rate according to Eq. (9), with $n = 0.07$ and $z = h/2$ equals 0.8 deg/μm, which corresponds to the order of magnitude observed in experiments ~0.5 ÷ 1.4 deg/μm.

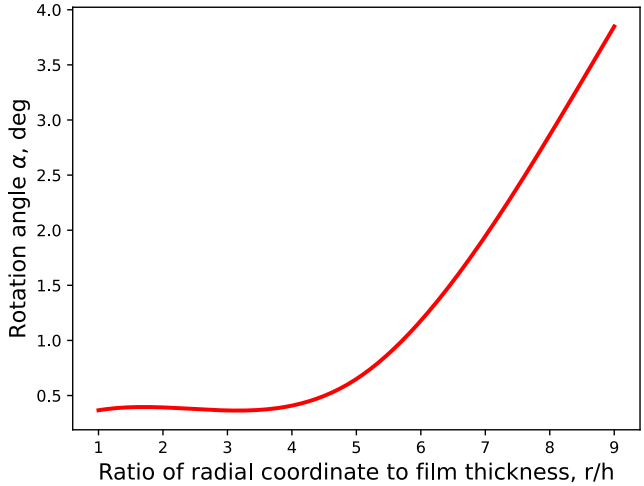

Fig. 7. Rotation angles along spherulite radius

Within the elastoplastic formulation, a distinct linear segment in the evolution of the anisotropy rotation angle is observed. In contrast, the purely elastic formulation reproduces only the order of magnitude of the effect, while failing to capture its qualitative behavior observed experimentally [14].

Conic inclusion. To simulate the growth process, a series of calculations was performed in which the cone solution angle varied from −30° to 30° in steps of 10°, and the radius of the lower base of the cone ranged from 1 to 9 units in steps of 2. A similar set of boundary conditions was analyzed for a cylindrical inclusion.

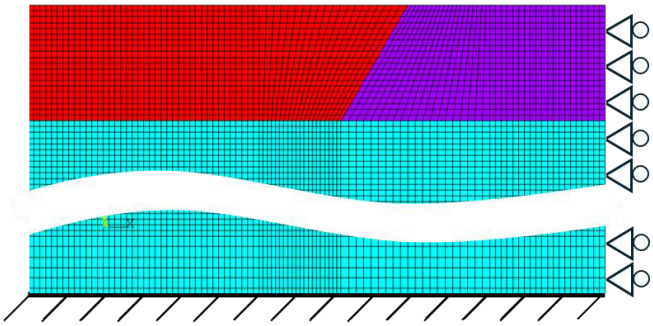

Fig. 8. Axisymmetric finite-element model of a *conic* inclusion growth on a substrate

The expression below is used to calculate the configurational forces for a conical inclusion, similar to Eq. (10):

$$f_N = \sigma_{NN}\varepsilon^* - \frac{1}{2E}\left[\!\left[\sigma_{\varphi\varphi}^2 + \sigma_{LL}^2 - 2\nu\sigma_{\varphi\varphi}\sigma_{LL}\right]\!\right] + f_0, \qquad (11)$$

where $f_0 = [\![\psi_0]\!]$, σ_{NN} is the normal stress to the conical interphase surface, σ_{LL} is the stress component along the cone generatrix.

The dependence of the configurational force on the radial coordinate in the case of a conical model does not differ qualitatively from the cylindrical inclusion model (see Fig. 9(b)). However, the size of the boundary region in which the behavior deviates significantly from linearity increases compared with the case of a cylindrical inclusion.

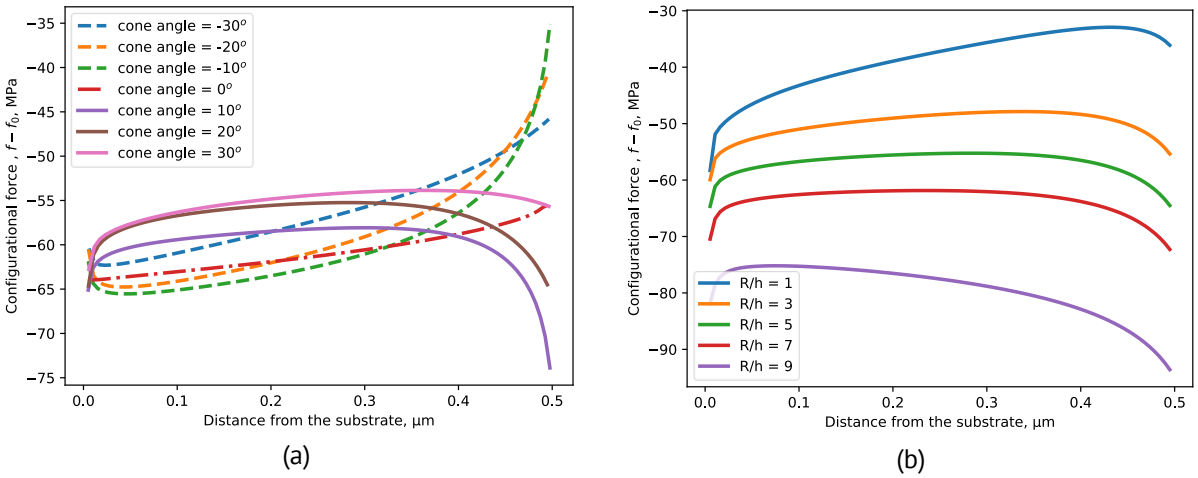

Fig. 9. Comparison of the configurational forces f_N at different (a) cone angles R/h = 5 and (b) ratios of inclusion radius to the film thickness R/h (cone angle 20°) in the model of conic growth of perovskite phase. Distance between inclusion centers $2\rho = 20h$

When the cone solution angle varies, the monotonicity of the configurational force distribution also changes. For positive angles, the interphase boundary velocity calculated using Eq. (5) is higher near the lower base of the cone. For negative angles, the maximum values are observed near the upper base. The dependence of the configurational force on the angle of the cone shows that the configurational forces tend to bring the inclusion to a near to cylindrical state (Fig. 9(a)).

Spherical inclusion. Two locations of the spherical inclusion were considered: on the free surface of the film and on the substrate (Fig. 10). The radii of spherical inclusions were considered equal to $h/3$. Boundary conditions similar to those in the cylindrical inclusion problem were used.

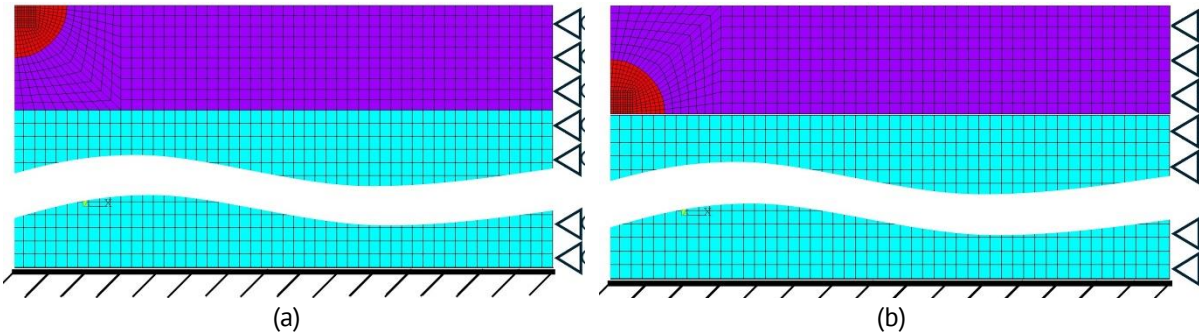

Fig. 10. Axisymmetric finite-element model of the growth of a spherical inclusion with a center on (a) the film free surface, (b) the substrate

From the dependence of the configuration force (Fig. 11), it can be seen that in a spherical inclusion on a substrate, growth in the direction of the film thickness prevails, while on the film surface, the inclusion grows in the radial direction. At large radius, the curvature of interphase boundary decreased, and the model of a spherical inclusion reduces to a conical inclusion.

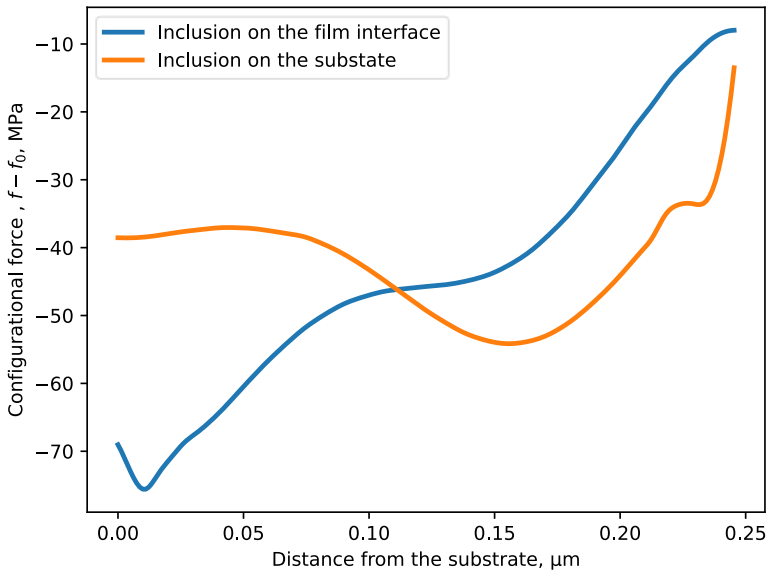

Fig. 11. Configurational forces for a spherical inclusion. The distance is measured from the lowest point of inclusion. Inclusion radius is equal to $h/3$

Three-dimensional model

Single cylindrical inclusion. A three-dimensional model was used to assess the interaction of nearby cylindrical perovskite inclusions on stress fields and configurational forces. The three-dimensional model has the same geometry and boundary conditions with the prior axisymmetric case (see Section "Axisymmetric model"). The *first model* corresponds to a single symmetrical perovskite inclusion (see Fig. 12) with a cylinder radius R varied from 0.5 to 4.5 μm, a film thickness h of 0.5 μm, and a substrate thickness of 5 μm. The radius of the cylinder was then increased incrementally in order to simulate the development of the perovskite phase. This case corresponds to the regular (periodic) inclusion system.

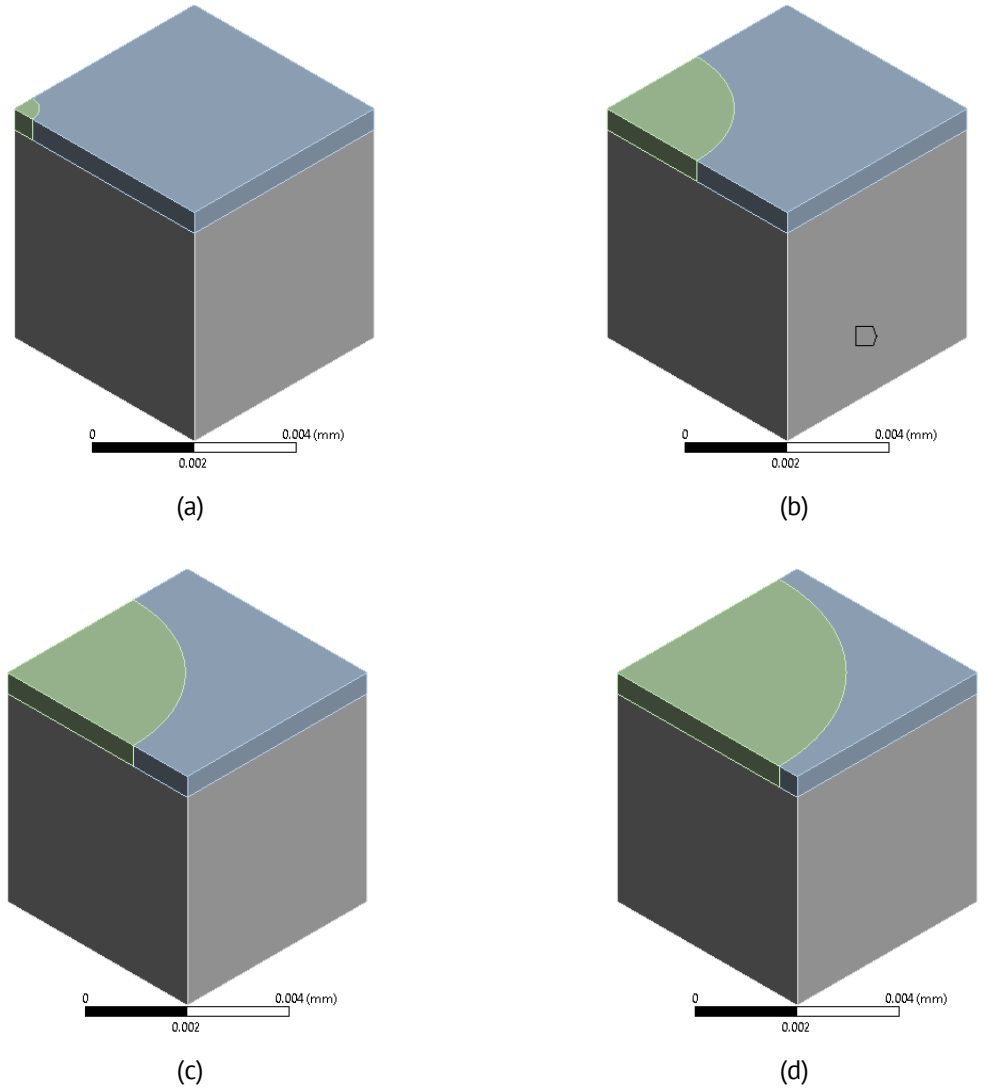

Fig. 12. 3D models of the cylindrical perovskite inclusion growth on a substrate: (a) $R/h = 1$, (b) $R/h = 5$, (c) $R/h = 7$, (d) $R/h = 9$. Distance between inclusion centers $2\rho = 20h$

The *second model* corresponds to the non-regular inclusion system with a more realistic scenario for the growth of perovskite inclusions in a pyrochlore matrix (Fig. 1(a)). The study focused on six adjacent perovskite inclusions. A key feature of the experiment was that the centers of these inclusions were positioned at varying distances from one

another. The considered model with an irregular (non-periodic) arrangement of inclusions allows for a more detailed study of the effects of interaction between inclusions, paying particular attention to such parameters as stress and configuration force.

Under identical boundary conditions, the differences in the radial, circumferential, and vertical stress values for the three-dimensional and two-dimensional axisymmetric models were 2, 9.7, and 2.7 %, respectively (compare Figs. 4 and 13) in elastic solutions, for an inclusion radius R/h = 5. Similar to the two-dimensional model, the maximum stress jump between the perovskite and pyrochlore phases was found to be the jump in vertical and circumferential stress.

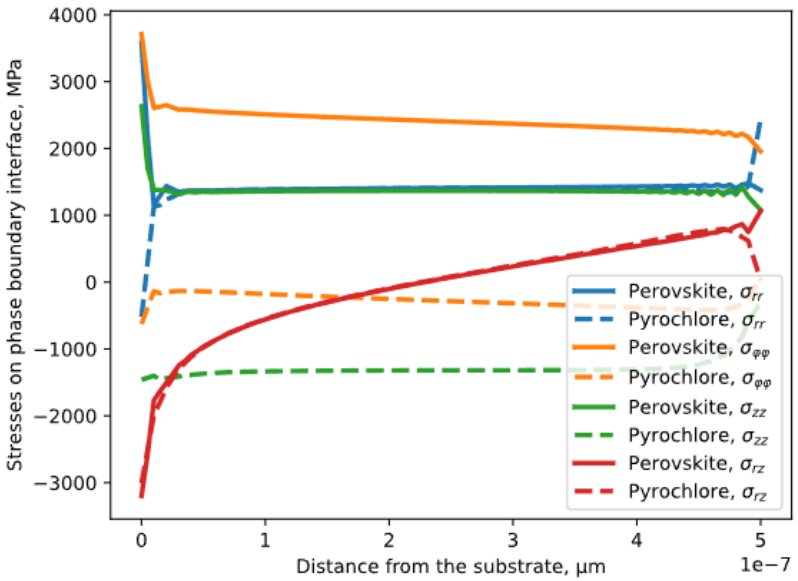

Fig. 13. Dependences of the stress tensor components σ_{rr}, σ_{zz}, $\sigma_{\varphi\varphi}$, σ_{rz} [MPa]on the distance from the substrate (vertical coordinate z) for the inclusion size R/h = 5h in the 3D model of cylindrical growth of the perovskite phase. The distance between inclusion centers is 2ρ = 20h

A comparison of the configurational forces in the three-dimensional and two-dimensional axisymmetric models revealed differences in the results only for inclusion radii R exceeding 0.90 of the half-distance between inclusions ρ. At smaller radii, the inclusions do not interact with each other. The results indicate that the maximum discrepancy in configuration forces between the two models in this case is 8 % (Fig. 14). This result demonstrates the potential of using a highly accurate two-dimensional symmetric model to reduce the computational costs associated with calculating configuration forces.

In order to comparison between three-dimensional models and a two-dimensional symmetric model with respect to configuration force, it was necessary to choose an inclusion radius that was nine times greater than the film height. This approach enabled the selection of the influence of inclusions on each other. In the case of small radii, inclusions do not affect each other. The findings indicate that the maximum disparity in configuration forces between the two models is 8 % in the studied case (Fig. 14). This result indicates the possibility of using a two-dimensional axisymmetric model to reduce the computational costs associated with calculating configuration forces.

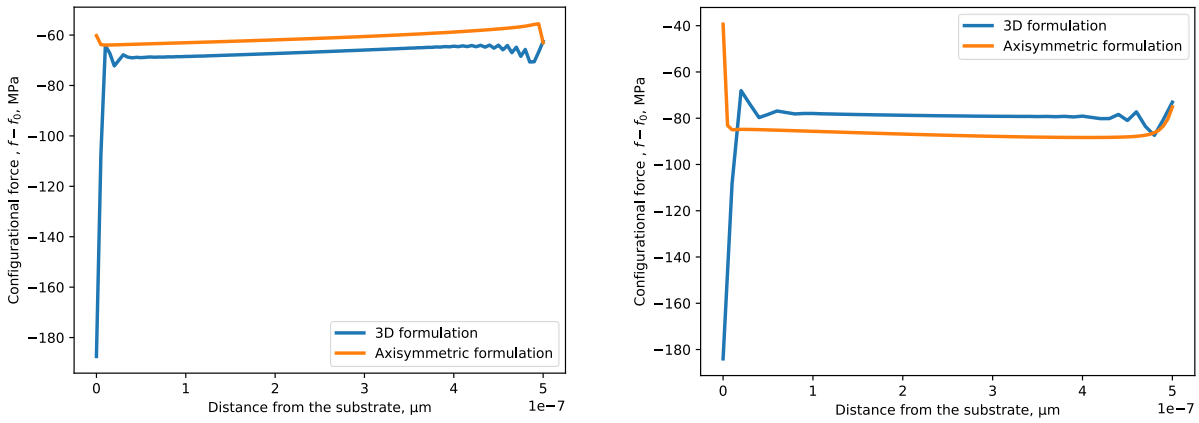

Fig. 14. Comparison of the two-dimensional symmetric with the 3D solution for the configuration force f_N for R/h=5 and R/h=9. The distance between inclusion centers is 2ρ = 20h

Multiple cylindrical inclusions. A three-dimensional simulation is considered using a representative configuration of six inclusions, the spatial arrangement of which was obtained from available literature (see Fig. 1). Within the three-dimensional model, the influence of inclusion distribution on both the stress-strain state and the configurational force was investigated. Changes in the distances between inclusions at successive growth stages were examined according to the attainment of radii of 2.5, 5, 7.5, and 10 μm.

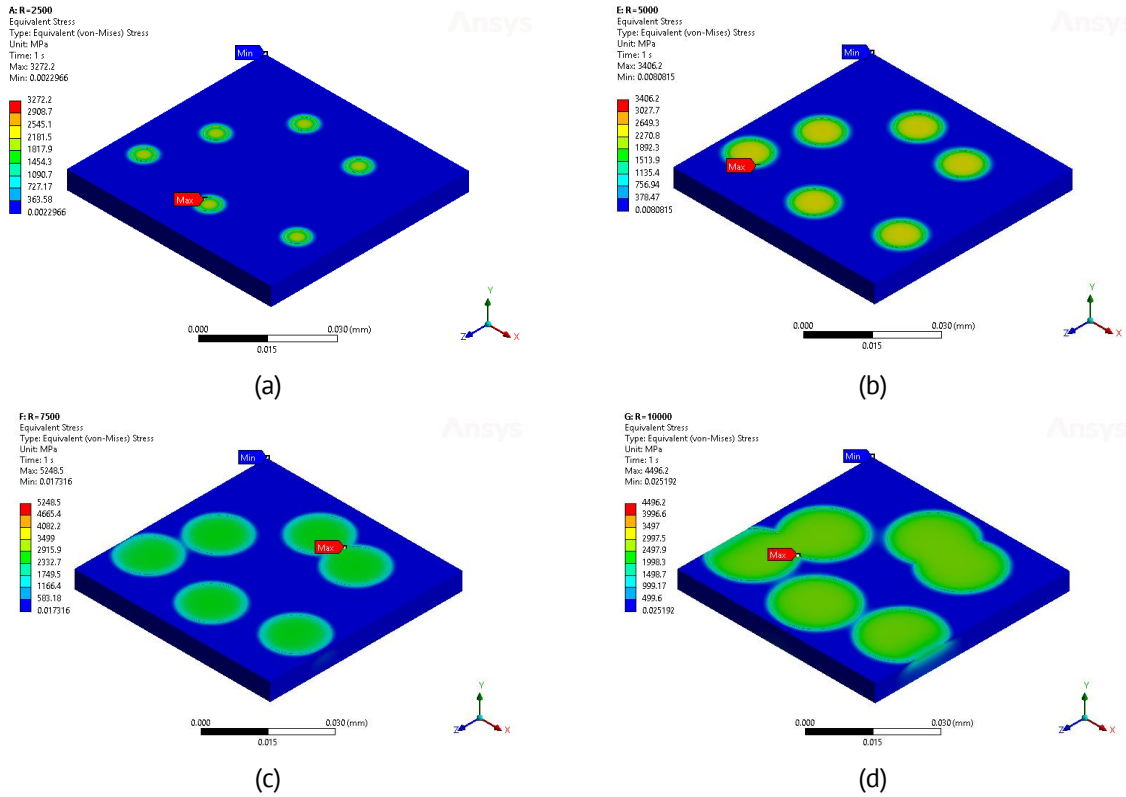

Fig. 15. Growth models of the perovskite phase in a film with a distribution of stress intensity fields according to Mises: (a) for cylindrical inclusions with a radius of 2.5 μm, (b) 5 μm, (c) 7.5 μm, and (d) 10 μm

The evolution of the von Mises stress intensity fields during the growth of six cylindrical inclusions is shown in Fig. 15. As the radius of the perovskite inclusion increases, the von Mises stress intensity increases simultaneously. This process continues until the intersection of two inclusions, where stress concentrators are formed (Fig. 15(c,d).

To determine the extent to which the distance between perovskite phase inclusions influences the configurational force, two stages of perovskite growth development were considered. At these stages, the radiuses of the cylindrical inclusion were R_1 = 2.5 μm and R_2 = 10 μm. Two paths were defined for the study the degree of influence when the distance between the inclusion centers was L_1 = 25.7 μm and L_2 = 34.4 μm. Consider points A_1, A_2, B_1 and B_2, which are defined as shown in Fig. 16. Point A_1 is located at the boundary of the perovskite and pyrochlore phases on the L_1 trajectory, when the perovskite phase develops for the R_1 cylinder radius. Point A_2 is located at the boundary of the perovskite and pyrochlore phases on the L_2 trajectory, when the perovskite phase develops within the R_1 cylinder radius. Point B_1 is located at the boundary between the perovskite and pyrochlore phases along trajectory L_1, when the perovskite phase develops within the radius of cylinder R_2. Point B_2 is located at the boundary between the perovskite and pyrochlore phases along trajectory L_2, when the perovskite phase develops within the radius of cylinder R_2.

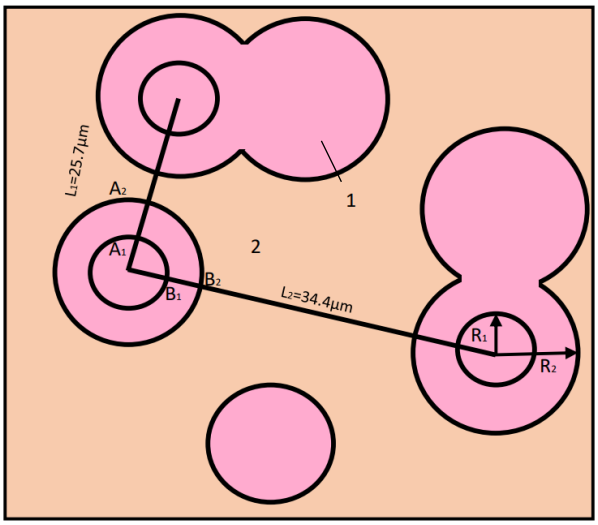

Fig. 16. Geometry parameters for representative volume element of PZT film for multiple cylindrical inclusions. 1 - perovskite inclusions, 2 - pyrochlore matrix

The study demonstrated that the configuration force is related to two geometric parameters: the first is the distance between the centers of the perovskite inclusions 2ρ, and the second is the radius of the perovskite inclusion R. The configuration force increase with decreasing perovskite inclusion radius and with decreasing distance between the centers of the perovskite inclusions.

The greatest configurational force was observed at point A_1 (Fig. 17(b)), which was located at the interphase boundary at the smaller radius and on the first path L_1. The next largest configurational force, which was 50 % lower, was at point B_1. The next largest

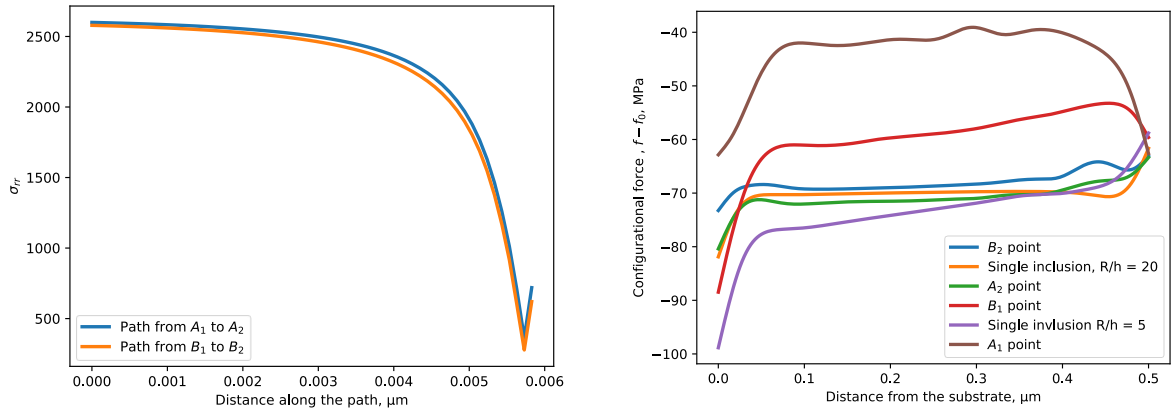

Fig. 17. Dependencies of (a) the radial stress σ_{rr} [MPa] vs the distance from the spherulite center and (b) the configurational force f_N vs the distance to the substrate (vertical coordinate z) at different ratios of the inclusion radius to the film thickness *R/h* in the 3D model of growth of 6 perovskite inclusions

configuration force, which was 16 % lower, was at point B_2. The configurational force, amounting to 7 % less, was observed at point A_2. It has been observed that configurational force in point B_2 exhibits a greater magnitude than in point A_2. This is explained by the influence of the perovskite inclusion, located at the other end of path L_1, on the configurational force.

The radial distributions of radial stresses σ_{rr} along two different orthogonal directions L_1 and L_2 differ very little (Fig. 17(a)). It is evident that as one moves away from the center of the spherulite, the radial stresses decrease.

Comparison of growth axis deviation angles for different deformation mechanisms and with experimental data

The rotation of the crystal-lattice growth axis in growing spherulitic islands, as well as in the resulting spherulitic block structure observed in experiments on PZT films [10–14], is a consequence of the significant mechanical stresses induced by changes in film density during crystallization of the perovskite phase. The growth axes exhibit axial symmetry and are oriented radially from the center of each spherulitic island toward its periphery.

The growth axis rotation rate $\frac{\partial \beta}{\partial r}$ measured in experiments using XRD analysis and scanning electron microscopy methods, lies in range of ~ 0.5÷1.4 deg/μm [10–14]. The rotation rate calculated from Eq. (7) with n = 0.32 and $z = h / 2$, is equal 0.4 deg/μm for axisymmetric elastic formulation (see section “Elastoplastic solution”) and 0.8 deg/μm for axisymmetric elastoplastic formulation (see section “Plastic solution”). These results are consistent to the order of magnitude observed in the experiments.

However, in addition to the mechanism of growth-axis rotation caused by the nonuniform distribution of configurational forces along the film thickness during the pyrochlore → perovskite phase transition, which was discussed in detail above, alternative mechanisms of film deformation are also possible. These include deviations of the perovskite growth axes due to:

1. bending of a multilayer plate (taking into account the compliance of the substrate) due to nonuniform initiated by the pyrochlore → perovskite phase transition [14];

2. bending of a multilayer plate due to polarization associated with the paraelectric → ferroelectric phase transform [33];
3. bending of a multilayer plate during cooling from 580 to 21 °C due to mismatches in coefficients of thermal expansion [34].

Growth axis rotation rate (bending plate curvature) for the first deformation mechanism was performed with assuming constant transformational deformation within the film based on Eqs. (18) from [14]:

$$\frac{\partial\beta}{\partial r} = \kappa^{tr} = \frac{\varepsilon^*}{H}\frac{6\frac{\bar{E}_{PZT}h}{\bar{E}_{Si}H}\left(1+\frac{h}{H}\right)}{1+2\frac{\bar{E}_{PZT}h}{\bar{E}_{Si}H}\left(2+3\frac{h}{H}+2\frac{h^2}{H^2}\right)+\frac{\bar{E}_{PZT}^2h^4}{\bar{E}_{Si}^2H^4}}, \quad (12)$$

where for double-layered plate $\bar{E}_i = \frac{E_i}{1-\nu_i}$, in the film i = PZT ($0 \le z \le h$), in the substate i = Si ($-H \le z \le 0$), $\varepsilon^{*Py\to Pe} = -0.0267$.

Equation (12) can also be used for calculating the rotation growth rate (plate curvature) for the second deformation mechanism, which arises from polarization associated with the paraelectric → ferroelectric phase transformation with $\varepsilon^{*Pa\to Fe} = 0.0073$ [35] ([36–38] provide data ranging from 0.0020 to 0.0191).

Equation (12) for calculating the rotation growth rate for the third deformation mechanism, which arises during cooling from 580 to 21 °C due to mismatches in coefficients of thermal expansion, has the form:

$$\frac{\partial\beta}{\partial r} = \kappa^{T} = \frac{(\alpha_{PZT}-\alpha_{Si})\Delta T}{H}\frac{6\frac{\bar{E}_{PZT}h}{\bar{E}_{Si}H}\left(1+\frac{h}{H}\right)}{1+2\frac{\bar{E}_{PZT}h}{\bar{E}_{Si}H}\left(2+3\frac{h}{H}+2\frac{h^2}{H^2}\right)+\frac{\bar{E}_{PZT}^2h^4}{\bar{E}_{Si}^2H^4}}. \quad (13)$$

In the rotation growth axis rate calculations according to Eqs. (10) and (11) the following parameter values were used E_{PZT} = 70 GPa, E_{Si} = 109 GPa, α_{PZT} = 9.0·10^{-6} 1/K, α_{Si} = 2.5·10^{-6} 1/K, h = 500 nm, H = 5 μm, $\varepsilon^{*Py\to Pe} = -0.0267$, $\varepsilon^{*Pa\to Fe} = 0.0073$, ΔT = 559 K. Calculations were performed assuming constant transformation deformation and thermal deformation in the film.

Comparison of the growth axis rotation rate caused by various deformation mechanisms is shown in Fig. 17. It can be seen that the dominant contribution arises from

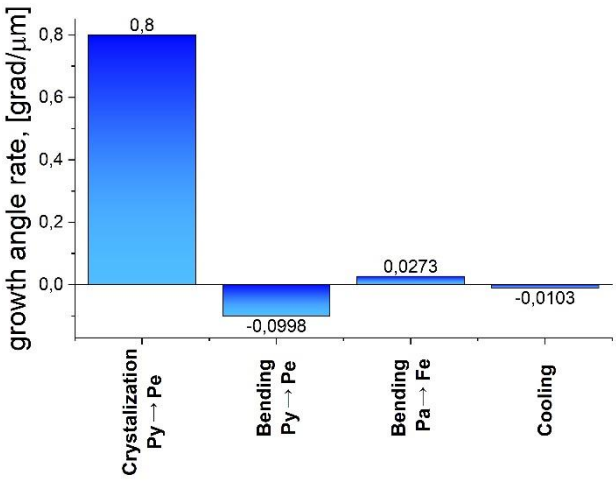

Fig. 18. Comparison of the growth axis rotation rate caused by various deformation mechanisms

nonuniform distribution of configurational forces along film thickness. The rotational rates resulting from plate bending due to nonuniform stress distribution, associated with pyrochlore → perovskite phase transition [14], bending due polarization associated with paraelectric → ferroelectric phase transition [33], bending during cooling due to mismatches in coefficients of thermal expansion are significantly smaller. Calculations were performed assuming the substate thickness equal 10 thickness of the film. As the substrate thickness increases and the film thickness decreases, the influence of the three deformation mechanisms under consideration will decrease.

Conclusion

The results of the interphase boundary propagation during the growth of the perovskite phase within a pyrochlore matrix in thin PZT films, carried out using configurational-force mechanics, are presented. The nonuniform distribution of configurational forces along the film thickness leads to a dependence of the interphase-boundary propagation velocity on the vertical coordinate. This, in turn, causes a progressive tilt and curvature of the interphase boundary away from the center of the spherulite, thereby determining the orientation of the growth axis of the emerging perovskite phase.

The growth of cylindrical, conical, and spherical inclusions was analyzed. For cylindrical inclusions, the dependence of the configurational force on distance from substate is nearly linear (monotonically increasing with distance from the substrate), which leads to a progressive deviation of both the interphase boundary and the growth axis from the vertical as the distance from the spherulite center increases. For conical inclusions with small cone angles, the configurational-force distribution along the height is monotonically increasing, whereas for large cone angles it becomes monotonically decreasing. This behavior indicates the existence of a characteristic slope toward which the growth axis asymptotically tends as the interphase boundary propagates. In spherical inclusions, more intensive growth in the vertical direction is observed near the substrate, while on the free surface growth in the radial direction dominates. At large radius, the model of a spherical inclusion reduces to a conical inclusion.

A comparison of the solutions obtained using linear elastic and elastic–plastic formulations showed that the latter yields lower values of configurational forces. The elastic–plastic formulation indirectly accounts for the presence of dislocations, micropores, and microcracks. Solving the problem within an elastic–plastic framework also demonstrated the possibility of a linear increase of the growth axis rotation angle, consistent with experimental observations.

A comparison of the numerical solutions obtained in axisymmetric and three-dimensional settings for an elementary representative volume (regular inclusions) demonstrated good agreement, with differences of less than 10 %.

The results of a comparison between the growth of single inclusions and multiple inclusions arranged regularly or irregularly are presented. The same radial distribution pattern (axial symmetry) is observed on the free surface of the film for different angles within an inclusion (a growing spherulite) surrounded by neighboring inclusions located at various distances.

The dominant influence on the growth axis rotation angle is exerted by the non-uniform distribution of the configurational force along the film thickness during the pyrochlore → perovskite phase transition. The rotation associated with plate bending caused by stress inhomogeneities initiated by the pyrochlore → perovskite phase transition, polarization during the paraelectric → ferroelectric phase transition, and due to differences in the thermal expansion coefficients of individual layers are much smaller (at least six times lower). This indicates that the distribution of configurational forces across the film thickness is the primary mechanism determining the orientation of the growth axis. The predicted rate of growth-axis deviation as a function of the distance from the spherulite center, obtained using this approach, correlates well with experimental data from X-ray diffraction analysis and scanning electron microscopy.

CRediT authorship contribution statement

Madyan Bakkar: investigation, writing – review & editing, original draft, data curation; **Alaa Mhemeed Dbes:** investigation, writing, review & editing; **Dmitrij V. Avdonyushkin:** investigation, data curation, writing; **Artem S. Semenov**: conceptualization, writing – review & editing, supervision.

Conflict of interest

The authors declare that they have no conflict of interest.

References

1. Uchino K. *Ferroelectric Devices*. New York: Decker; 2000.
2. Waser R. *Nanoelectronics and Information Technology: Advanced Electronic Materials and Novel Devices*. Berlin: Wiley-VCH; 2005.
3. Abdullaev DA, Milovanov RA, Volkov RL, Borgardt NI, Lantsev AN, Vorotilov KA, Sigov AS.Ferroelectric memory: state-of-the-art manufacturing and research. *Russian Technological Journal*. 2020;8(5): 44–67. (In Russian)
4. Ishiwara H, Arimoto Y, Okuyama M. *Ferroelectric Random Access Memories: Fundamentals and Applications*. Berlin: Springer; 2004.
5. Izyumskaya N, Alivov YI, Cho SJ, Morkoç H, Lee H, Kang YS. Processing, structure, properties, and applications of PZT thin films. *Critical Reviews in Solid State and Materials Sciences*. 2007;32(3–4): 111–202.
6. Eom CB, Trolier-McKinstry S. Thin-film piezoelectric MEMS. *MRS Bulletin*. 2012;37(11): 1007–1021.
7. Panda PK, Sahoo B. PZT to Lead Free Piezo Ceramics: A Review. *Ferroelectrics*. 2015;474(1):128–143.
8. Mukhortov VM, Yuz'uk YI. *Heterostructures Based on Nanosized Ferroelectric Films: Preparation, Properties and Applications*. Rostov-on-Don: Southern Scientific Center of the Russian Academy of Sciences; 2008. (In Russian)
9. Gevorgian S. *Ferroelectrics in Microwave Devices, Circuits and Systems*. London: Springer; 2009.
10. Staritsyn MV, Pronin VP, Khinich II, Senkevich SV, Kaptelov EY, Pronin IP, Elshin AS, Mishina ED. Microstructure of spherulitic lead zirconate titanate thin films. *Physics of the Solid State*. 2023;65(8): 1312–1318.
11. Kiselev DA, Staritsyn MV, Senkevich SV, Kaptelov EY, Pronin IP, Pronin VP. Radially oriented lateral self-polarization in spherulitic islands of lead zirconate titanate thin films. *Technical Physics Letters*. 2023;49(22): 8–11. (In Russian)
12. Kukushkin SA, Tentyilova IY, Pronin IP. Mechanism of the phase transformation of the pyrochlore phase into the perovskite phase in lead zirconate titanate films on silicon substrates. *Phys. Solid State*. 2012;54: 611–616.
13. Pronin VP, Ryzhov IV, Staritsyn MV, Senkevich SV, Kaptelov EY, Pronin IP. An influence of mechanical stresses on the phase state of spherulitic thin films of lead zirconate titanate. *Materials Physics and Mechanics*. 2024;52(6): 17–26.
14. Avdonyushkin DV, Staritsyn MV, Pronin VP, Semenov AS, Senkevich SV, Pronin IP. The Influence of Mechanical Stresses on Formation of Thin Spherulite PZT Films. To be published in *Physical Mesomechanics*. [Preprint] 2026.

15. Senkevich SV. *Features of Crystallization and Ferroelectric Properties of Thin Polycrystalline Lead Zirconate Titanate Films Obtained by a Two-Stage Method [dissertation].* Saint Petersburg; 2011. (In Russian)
16. Gushchina EV, Osipov VV, Borodin BR, Pavlov S, Tolmachev VA, Dunaevskiy MS, et al. Piezoelectric, conductive, and dielectric properties of magnetron sputtered $PbZr_{54}Ti_{46}O_3$ films studied by scanning probe microscopy and spectroscopic ellipsometry methods. *Ferroelectrics.* 2019;541(1):47–53.
17. Dolgintsev DM, Kaptelov EY, Senkevich SV, Pronin IP, Pronin VP. Microstructure and properties of polycrystalline PZT films obtained by RF magnetron sputtering with fine variation of the composition near morphotropic phase boundary. *Physics of Complex Systems.* 2021;2(3):101–109.
18. Lobanov SM, Semenov AS, Mamchits A. Modeling of Hysteresis in Single-Crystalline Barium Titanate with Allowance for Domain Structure Evolution. *Phys Mesomech.* 2023;26: 167–175.
19. Eshelby JD. The force on an elastic singularity. *Phil Trans Roy Soc London A.* 1951;244: 87–112.
20. Gurtin ME. On the nature of configurational forces. *Arch Ration Mech Anal.* 1995;131: 67–100.
21. Gurtin ME. *Configurational Forces as Basic Concepts of Continuum Physics.* New York: Springer; 2000.
22. Kienzler R, Herrmann G. *Mechanics in Material Space.* Berlin: Springer; 2000.
23. Maugin GA. *Material Inhomogeneities in Elasticity.* London: Chapman & Hall; 1993.
24. Maugin GA. Material forces: concepts and applications. *Appl Mech Rev.* 1995;48(5): 213–245.
25. Steinmann P, Scherer M, Denzer R. Secret and joy of configurational mechanics: From foundations in continuum mechanics to applications in computational mechanics. *Z Angew Math Mech.* 2009;89(8): 614–630.
26. Freidin AB. On configurational forces in the mechanics of phase and chemical transformations. *Journal of Applied Mathematics and Mechanics.* 2022;86(4): 571–583.
27. Freidin AB. On new phase inclusions in elastic solids. *ZAMM - Journal of Applied Mathematics and Mechanics.* 2007;87(2): 102–116.
28. Freidin AB, Vilchevskaya EN, Korolev IK. Stress-assist chemical reactions front propagation in deformable solids. *International Journal of Engineering Science.* 2014;83: 57–75.
29. Kabanova PK, Freidin AB. On the localization of a new phase domain in the vicinity of an elliptical hole. *ZAMM - Journal of Applied Mathematics and Mechanics.* 2024;104(3): e202301035.
30. Kabanova P, Morozov A, Freidin AB, Chudnovsky A. Numerical simulations of interface propagation in elastic solids with stress concentrators. In: Altenbach H, Bruno G, Eremeyev VA, Gutkin MYu, Müller WH. (eds.) *Mechanics of Heterogeneous Materials.* Springer; 2023. p.201–217.
31. Kabanova PK, Freidin AB. Numerical investigation of the evolution of new phase domains in an elastic solid. *Comput. Contin. Mech.* 2022;15(4): 466–479. (In Russian)
32. Helean KB, Ushakov SV, Brown CE, Navrotsky A, Lian J, Ewing RC, et al. Formation enthalpies of rare earth titanate pyrochlores. *Journal of Solid State Chemistry.* 2004;177(6): 1858–1866.
33. Korchagin AP, Semenov AS. Finite-element modeling of the polarization process of a ferroelectric multilayer structure due to the of microstresses during cooling. In: *Proceedings of the All-Russian Scientific Conference "Science Week PhizMech".* Saint Petersburg; 2023. p.273–276. (In Russian)
34. Valeeva AR, Kaptelov EY, Pronin IP, Senkevich SV, Pronin VP. Mechanical stresses in lead zirconate titanate thin films formed on substrates differing in temperature coefficients of linear expansion. *Physics of Complex Systems.* 2022;3(4): 159–166.
35. Semenov AS. *Multilevel Models of Ferroelectroelastic Materials and Their Application for Solution of Boundary Value Problems [dissertation].* Saint Petersburg; 2022. (In Russian)
36. Jaffe B, Cook WR, Jaffe H. *Piezoelectric Ceramics.* New York: Academic Press; 1971.
37. Micromechanical Model of a Polycrystalline Ferroelectrelastic Material with Consideration of Defects. *J Appl Mech Tech Phys.* 2019;60: 1125–1140.
38. Semenov AS. A microstructural model of ferroelectroelastic material with taking into account the defects' evolution. *St. Petersburg Polytechnical State University Journal. Physics and Mathematics.* 2021;14(1): 31–54.

MATERIALS PHYSICS AND MECHANICS RESEARCH ARTICLE

Submitted: October 18, 2025 Revised: November 11, 2025 Accepted: December 2, 2025

Development of theoretical basics and experimental verification of progressive methods of graphite oxidation with simultaneous grinding

S.B. Kargin [1], V.G. Artiukh [2], D.A. Kitaeva [2] ✉, N.V. Korihin [2], A.I. Kruglov [2]

[1] Pryazovskyi State Technical University, Mariupol, Russia

[2] Peter the Great St. Petersburg Polytechnic University, St. Petersburg, Russia

✉ dkitaeva@mail.ru

ABSTRACT

The first attempts of scientifically based analysis of grinding process belong to Rittinger and Kik. Results of theoretical and laboratory studies aimed to obtain finely dispersed graphite for manufacture of technological lubricants are presented. Modern very labor-intensive technology for grinding graphite is shown and its shortcomings are indicated. Theoretical analysis of possibility of changing graphite by progressive method of oxidative milling of graphite with help of hydrogen peroxide is given. Original method of laboratory research on oxidative grinding of graphite has been developed. Presented results of laboratory studies fully confirmed theoretical calculations that makes it possible to simplify process of obtaining colloidal graphite for technological lubricants. This eliminates operation of washing colloidal graphite from decomposition products of chromium mixture and sulfuric acid which takes place in manufacture of OGV lubricant.

KEYWORDS

graphite • grinding • acid medium • chromium mixture • lubricant • potassium bichromate • ammonia adsorption • hydrogen peroxide • cation-exchanger

Funding. *This work has been supported by the grant of the Russian Science Foundation, RSF 25-19-00921.*

Citation: Kargin SB, Artiukh VG, Kitaeva DA, Korihin NV, Kruglov AI. Development of theoretical basics and experimental verification of progressive methods of graphite oxidation with simultaneous grinding. *Materials Physics and Mechanics.* 2025;53(6): 44–52.
http://dx.doi.org/10.18149/MPM.5362025_4

Introduction

Graphite lubricants have become firmly established in practice of forging and stamping over past 20–30 years [1–3]. Main dispersion medium for them is water [4–6]. Degree of graphite grinding varies depending on severity of metal deformation conditions and it is in range of 1–30 μm [7–10]. Colloidal graphite in form of single dispersion has proven itself especially well for hot stamping [10–12]. Colloidal state is characterized by particle size of dispersed phase of less than 1 μm. Process of obtaining colloidal graphite is very laborious [13–15]. It should be noted that dispersion of graphite in water is mainly discussed when it is talked about modern lubricants used in stamping [16]. Gaseous products of oxidation which are formed in quantities (that are harmless to worker) are ideally meet requirements for lubrication of dies. Durability of die increases at least twice compared to its durability when lubricated with oils. There have been many publications on this topic since that time. Interest in grinding has especially increased due to sharp

expansion of production and consumption of powders and new technological possibilities for increasing their fineness [17–19].

Simple mechanical grinding of graphite does not lead to production of highly dispersed graphite. An obstacle is its ability to reverse process that is aggregation [20–22]. From our point of view, it is also necessary to chemically treat surface of particles in order to create polar groups of basic and acidic nature on them when crushing graphite. According to our observations, graphite (although quite strongly crushed by swelling (bulk density of 10 g/L) has an inert surface and therefore is not even wetted by water. It was enough to treat expanded graphite in acidic medium at pH = 10 with hydrogen peroxide for 10 h in cold environment so that graphite acquired hydrophilic character and ability to form stable aqueous suspension at 5 % concentration. Even better effect is obtained by oxidizing expanded graphite with chromium mixture.

Water-graphite lubricant OGV ('aquadag' type) is oxidized and crushed graphite with particle size of 1–2 μm in the form of 16–20 % aqueous suspension. Oxidation is carried out by strong oxidizing agent that is potassium bichromate in concentrated sulfuric acid. Aqueous graphite is stabilized with ammonia to pH = 10–11 and it is dispensed as finished lubricant after laborious operation of washing graphite from chromium salts and sulfuric acid. It is obvious that such lubricant can be practically ashless.

It must be assumed that surface of graphite particles in this case is dotted with carboxyl groups that is $COONY_4$ which can strongly decompose into ions: $COONY_4 \rightarrow COO^- + NH_4^+$, while negative charge remains on graphite particles value of which depends on depth of grinding and oxidation. Presence of negative charge on sufficiently small colloidal particles imparts stability of dispersion without additional stabilizer.

High lubricating properties of colloidal graphite are probably also associated with presence of polar groups on particle surface. Thanks to these groups, graphite acquires φ° ability to adsorb and even to chemically interact with the thinnest oxide film which is always present on surface of metal stamp [15,16,23]. Thus, graphite covers surface of stamp with even film that is well retained by chemisorption forces. The film is certainly destroyed when hot object touches this surface but graphite performs its separating function between metal and tool [24–27]. Moreover, graphite contributes to creation of gas cushion which enhances lubricating effect thanks to oxidizing due to oxygen of oxide film of workpiece [28–30].

Materials and Methods

Oxidative grinding of graphite using hydrogen peroxide

It has already been noted that oxidation and grinding of graphite during production of OGV lubricant is very laborious operation accompanied by production of toxic washing water when graphite is washed from chromium salts. Therefore, it is desirable to find out possibility of fine grinding of graphite in presence of "pure" oxidizing agent such as hydrogen peroxide or ozone. In case of positive result, it can be possible to get rid of washing operation and obtain finished products at the final stage by simply neutralizing crushed mass with ammonia.

Oxidizing ability of hydrogen peroxide, like any other oxidizing agent, is determined by normal potential φ°. Hydrogen peroxide accepts electrons from reducing agent (in acidic environment) according to equation: $H_2O_2 + 2H^+ + 2e = 2H_2O$ where $\varphi^{\circ} = 1.77$. Its oxidizing ability is lower in alkaline environment. Real potential can be kept equal to 1.77 by creating concentration of hydrogen ions equal to 1 g/L and concentration of peroxide equal to 1 mol/L, i.e. approximately 3–3.5 · 100 % solution. It was decided to carry out experiments on oxidative grinding at room temperature because grinding of graphite proceeds at ordinary temperature.

But what will be rate of oxidation reaction under these conditions? It will probably be close to zero. Where activation energy can be got from? There is only one hope left that is on active areas of graphite particles which are formed at moment of breaking bonds during crushing of larger particles.

Laboratory experiment on oxidative grinding of graphite was set up as follows. Metal rod 10 mm in diameter and 75 mm long was placed in glass conical flask with flat bottom. This rod with weight equal to 46 g was sealed inside glass tube. 40 g of graphite grade GS-1 by GOST 7022-76, 400 ml of distilled water, 4 g of concentrated phosphoric acid, and 5 ml of 33 % hydrogen peroxide were loaded into the flask. pH of aqueous pulp turned out to be equal to 1.6–1.7. The flask was placed on magnetic mixer and the rod was rotated at about 300 rpm. Grinding of graphite was carried out by friction of glass on glass. 5 ml of hydrogen peroxide was added to the flask every day. And thus, the mixer totally worked for 82 h. Sample was taken twice to determine nature of oxidation during oxidative grinding. The first sample was taken after 12 h of oxidation, the second one was taken after 65 h.

The sample was taken in the following way. The mixer was turned off, contents were allowed to stand for 5 min and upper dark layer was poured into a beaker. Contents of the beaker were allowed to settle overnight (18–20 h) and in the morning clear liquid returned to the grinding flask again. Precipitate of fine graphite in the beaker was thoroughly washed by centrifuge and test tubes until neutral reaction on universal indicator paper. The neutral sample was subjected to determination of oxidation nature.

Determination of nature of graphite oxidation

Moving equilibrium between solid phase and electrolyte solution was used to determine sign of charge of functional group of surface carbon atoms. If surface belong to hydroxyl groups and surface of particles has sign "+" then pH of aqueous phase shifts towards its increase when sodium chloride is added to graphite mixture:

$$R_{TB}OH + Na^+ + Cl^- \leftrightarrow RCl + Na^+ + OH^-. \quad (1)$$

When there are carboxyl groups on surface of graphite particles it results in pH of aqueous phase shifts to the lower side:

$$R_{TB} - COOH + Na^+ + Cl^- \leftrightarrow R - COONa + H^+ + Cl^-. \quad (2)$$

Thus, shift of pH value when sodium chloride solution is added to graphite suspension indicates nature of graphite oxidation.

Determination of pH shift of graphite suspension

After carefully washing out about 20 ml of graphite pulp its pH was determined on pH meter. pH of 5 % sodium chloride solution was determined in separate beaker. Then 2–3 ml of sodium chloride solution was poured into a cup with graphite pulp and pH meter electrodes lowered into it and pH of which was controlled. Pulp pH shift was noted. Experiments carried out with the first sample of graphite taken after 12 hours of oxidative milling showed upward shift of pH. Data is given in Table 1.

Table 1. Upward pH changes

pH graphite pulp	7.3
pH of NaCl solution	7.1
pH of pulp mixture and NaCl	8.2–8.4–8.5

Slowly (within 2 min) pH of solution increased while contents were mixed by gently shaking the glass. Experiments carried out with the second sample of graphite (taken after 65 h of oxidation and grinding) showed opposite picture where pH shift was obtained to a lower side. Results of experiment are given in Table 2.

Table 2. pH changes downward

pH graphite pulp	4.4
pH of NaCl solution	4.75
pH of pulp mixture and NaCl	3.8–3.7–3.6

It results in over time depth increase of graphite oxidation and surface carbocation atoms of graphite are transformed into carbanion ones. Presence of positive charge at nodal carbon atoms can be assumed due to benzene structure of six-membered graphite rings where carbon is in SP^2 hybridization.

Conjugation of P-electrons in benzene rings leads to their “contraction” to the center of the ring and, thus, electron density on nodal atoms that are common to two rings is depleted. Further oxidation leads to formation of carboxyl groups and graphite is converted into a cation-exchange substance. Schematically, this can be represented by following fragments in Fig. 1.

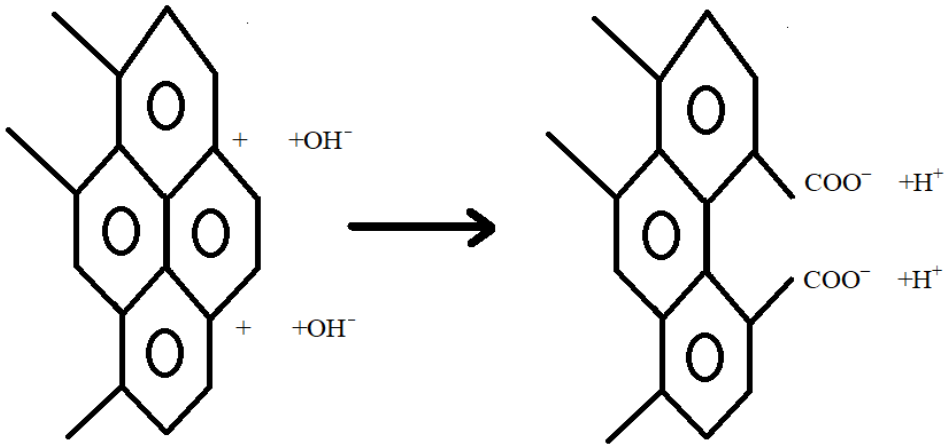

Fig. 1. Cation-exchange formation scheme

Determination of cation-exchange capacity of oxidizen graphite

Cation-exchange capacity was determined by method for determining capacity of ion exchange resins. Sample of graphite taken after 82 h of oxidative grinding (with weight equal to 1.212 g and pulp volume equal to 30 ml) was washed with hydrochloric acid and then with water until pH = 4.7. pH was measured in 5 % NaCl solution. It was equal to 4.5. Preliminarily, readings of pH meter were checked against standard buffer solution with pH = 6.86.

10 ml of sodium chloride was added to a cup with graphite pulp and lowered electrodes of pH meter. pH changed from 4.7 to 3.46 within 2 minutes. 0.100 N sodium hydroxide solution was added dropwise from the buret to the pulp. Results of titration are presented in Table 3.

Table 3. Results of titration

No	V_{NaOH}, ml	pH
1	0	3.46
2	0.2	4.0
3	0.3	4.4
4	0.4	5.0
5	0.5	5.8
6	0.6	6.8
7	0.7	7.4

Equivalent volume was taken to be equal to 0.5 ml. Pulp was washed twice with water, evaporated and dried in weighed beaker to determine mass of taken graphite. As a result, mass of graphite was equal to 1.212 g. Cation-exchange capacity of graphite Q was calculated by equation:

$$Q = \frac{V_{NaOH} \cdot N_{NaOH}}{m} = 0.041 \text{ mg·equal/g}, \quad (3)$$

where V_{NaOH} is volume of caustic soda used for titration, N_{NaOH} is normality of sodium hydroxide solution, m is mass of graphite.

Results of experiments convincingly indicate effect of oxidative grinding on quality of resulting material. Cation-exchange graphite with a clearly defined capacity is obtained as a result of oxidative grinding.

Results and Discussion

Calculations of state of oxidized graphite particles size and its maximum cation-exchange capacity

Main assumption. Maximum cation-exchange capacity will be if all corner and edge carbon atoms in graphite microcrystals contain carboxyl groups. One plane of graphite flake with scale of 1 Å: 1 cm can be taken. Carboxyl groups on extreme carbon atoms can be placed in Fig. 2:

1. Number of carboxyl groups is equal to number of units consisting of 4 C atoms along length of flake.
2. Along width, number of carboxyl groups is equal to twice number of units of 6 C atoms.
3. There are no carboxyl groups on the upper face of the flake.

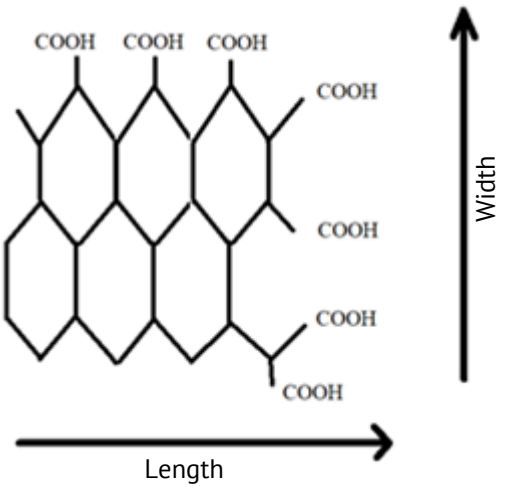

Fig. 2. Carboxyl groups

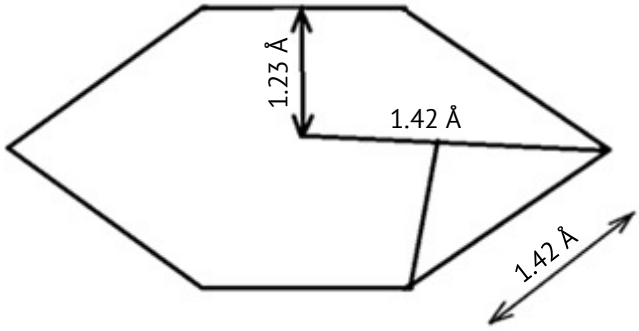

Fig. 3. Dimensions of six-membered ring of carbon atoms in graphite

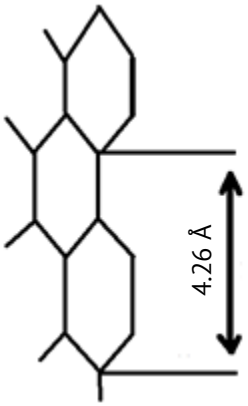

Fig. 4. Carboxyl groups

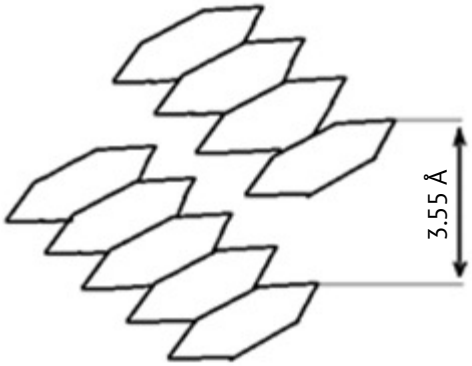

Fig. 5. Dimensions of six-membered ring of carbon atoms in graphite

Dimensions of six-membered ring of carbon atoms in graphite (Fig. 3) can be set to: length of C–C bond is 1.42 Å, width of six-membered ring is 2.46 Å. Distance between six-membered rings is 4.26 Å (Fig. 4). Fragment of graphite flake (Fig. 5) can be considered. Distance between planes in graphite is 3.55 Å. Calculations of ratio between carbon atoms and limiting number of carboxyl groups are described below.

The first case. Particle size is 0.1 μm that is equal to 1000 Å. Particle view can be set as cube for simplicity.

1. Number of links along the length = 1000 ÷ 2.46 = 406.
2. Number of links in width = 1000 ÷ 4.26 = 234.
3. Number of planes = 1000 ÷ 3.55 = 2.81.
4. Number of carbon atoms in plane: $406 \cdot 234 \cdot 6 = 5.7 \cdot 10^5$.
5. Number of carbon atoms in cube: $5.7 \cdot 10^5 \cdot 281 = 1.6 \cdot 10^8$.
6. Mass of atoms is $1.6 \cdot 10^8$ 12 = $1.92 \cdot 10^9$ amu.

Number of carboxyl groups:

1. Number of carboxyl groups in face along length and height is $406 \cdot 281 = 114086$.
2. Number of carboxyl groups in face along width and height is $234 \cdot 281 \cdot 2 = 131508$.

3. The total number of carboxyl groups is 114086·2 + 131508·2 = 491188.
4. Their mass is 491188·45 = $2.2 \cdot 10^7$ amu.
5. Cube weight is $1.92 \cdot 10^9 + 2.2 \cdot 10^7 = 1.94 \cdot 10^9$ amu.

It means that in $1.94 \cdot 10^9$ g of graphite there are $2.2 \cdot 10^7$ g of carboxyl groups. Carboxyl group equivalent is 45. Amount $2.2 \cdot 10^7$ can be converted into number of *r*-equivalents: $2.2 \cdot 10^7 \div 45 = 4.9 \cdot 10^5$. It is equal to $4.9 \cdot 10^8$ mg·equal. Proportion can be solved:

$$Q = X = \frac{4.9 \cdot 10^8}{1.94 \cdot 10^9} = 0.25 \text{ mg·equal/g}. \quad (4)$$

Similarly, for particle with size of 1 μm it can be got equal to 0.025 mg·equal.

The second case. Particle 2 μm long, 1 μm wide and 0.5 μm high can be taken. Cation-exchange capacity of 0.02 mg·equal/g can be obtained by repeating calculations. Calculation results for graphite particles of various sizes are summarized in Table 4. From Table 4 it follows that it is really possible to determine cation-exchange capacity of graphite only having particle size of less than 2 μm, i.e. almost practically for colloidal graphite. Cation-exchange capacity indicates the maximum particle size. Smaller particles provide obtained *Q* under condition of incomplete oxidation. So, if figure 0.04 was obtained in experiment to determine *Q* it means that particle size was no more than 1 μm. There may be smaller particles with lower degree of oxidation.

Table 4. Calculation results for graphite particles of various sizes

No	Particle size, μm, cube/plate	Capacity *Q*, mg·equal/g
1	0.1	0.25
2	0.05 × 0, 1 × 0.2	0.20
3	0.5	0.050
4	0.025 × 0, 5 × 1	0.040
5	1.0	0.025
6	0.5 × 1 × 2	0.020
7	2.0	0.012
8	1 × 2 × 4	0.01

Conclusions

1. Possibility of graphite oxidation with hydrogen peroxide of low concentration (0.3 – 0.4 %) at room temperature during its grinding has been proved.
2. Graphite acquires cation-exchange capacity due to formation of carboxyl groups on faces of colloidal particles.
3. Sample of colloidal graphite with cation-exchange capacity of 0.04 mg·equal/g was obtained after 82 h of oxidative grinding under laboratory conditions using magnetic stirrer.
4. Particle size of sample is estimated within limits not exceeding 1 μm using theoretical calculations.
5. These studies outline ways to simplify process of obtaining colloidal oxidized graphite by its oxidative grinding using “pure” oxidizing agents which are hydrogen peroxide and ozone. This eliminates operation of washing colloidal graphite from decomposition products of chromium mixture and sulfuric acid which takes place in manufacture of OGV lubricant.

CRediT authorship contribution statement

Sergey B. Kargin: writing – review & editing, original draft; **Viktor G. Artiukh**: investigation; **Daria A. Kitaeva**: data curation; **Nikolay V. Korihin**: data curation; **Adrei I. Kruglov**: data curation.

Conflict of interest

The authors declare that they have no conflict of interest.

References

1. Rukhov A, Bakunin E, Dyachkova T, Rukhov A, Istomin A, Obraztsova E, Kornev A, Burakova E, Smirnova A, Usol'tseva N. Graphite nanoplates as grease lubricant additive. *Fullerenes Nanotubes and Carbon Nanostructures.* 2022;30(1): 167–170.
2. Kumar N, Saini V, Bijwe J. Tribological Investigations of Nano and Micro-Sized Graphite Particles as an Additive in Lithium-Based Grease. *Tribology Letters.* 2020;68(4): 124.
3. Kargin S, Artyukh V, Ignatovich I, Dikareva V. Development and Efficiency Assessment of Process Lubrication for Hot Forging. *IOP Conference Series: Earth and Environmental Science.* 2017;90: 012190.
4. Joerger A, Morstein C, Dienwiebel M, Albers A. A numerical approach for the determination of graphite deformation behaviour by using microtribological pressure tests. *Wear.* 2021;476: 203652.
5. Ota J, Hait SK, Sastry MIS, Ramakumar SSV. Graphene dispersion in hydrocarbon medium and its application in lubricant technology. *RSC Advances.* 2015;5(66): 53326–53332.
6. Gotzias A, Lazarou YG. Graphene Exfoliation in Binary NMP/Water Mixtures by Molecular Dynamics Simulations. *ChemPlusChem.* 2024;89(6): e202300758.
7. Chizhevsky VB, Fadeeva NV, Kuranov PV. Processes of secondary enrichment of graphite in the foam layer and the influence of reagents on them. *Mining informational and analytical bulletin (scientific and technical journal).* 2003;(8): 160–162. (In Russian)
8. Pereira K, Yue T, Abdel Wahab M. Multiscale analysis of the effect of roughness on fretting wear. *Tribology International.* 2017;110: 222–231.
9. Vodzianskiy V, Artiukh V, Kargin S, Soloveva E. Machining of bearing trunnions of rolls by heavy lathes in conditions of repair production. *IOP Conference Series: Materials Science and Engineering.* 2020;918: 012129.
10. Mohd Nasir NA, Nazmi N, Mohamad N, Ubaidillah U, Nordin NA, Mazlan SA, Abdul Aziz SA, Shabdin MK, Yunus NA. Rheological Performance of Magnetorheological Grease with Embedded Graphite Additives. *Materials.* 2021;14(17): 5091.
11. Popov EM. Research of possibility of the Rostov region hydrocarbon raw materials usage for creation and manufacture carbonaceous materials. *Mining informational and analytical bulletin (scientific and technical journal).* 2009;(S6): 330–333. (In Russian)
12. Snitko SA, Yakovchenko AV, Sotnikov AL. Influence of wheel billet stamping schemes on power modes of forming press operation and wear of the deformation tool. Izvestiya. *Ferrous Metallurgy.* 2018;61(5): 385–392. (In Russian)
13. Obraztsova EYu, Rukhov AV, Bakunin ES, Bubnova EV, Rukhov AnV, Al-Ameri SNM, Zhabkina IA, Goncharova MS. Methodology and equipment for kinetic studies of electrochemical exfoliation of graphite. *Transactions TSTU.* 2023;29(4): 666–676. (In Russian)
14. Kolobov MYu, Bratkov IV, Gushchina TV, Chagin OV. Energy and resource saving technology production of sferical graphite. *Modern science-intensive technologies. Regional application.* 2023;2(74): 79–87. (In Russian)
15. Stebeleva OP, Kashkina LV, Vshivkova OA, Minakov AV. Application of high-speed hydrodynamic technology for the production of graphene nanosuspensions from natural graphites. *Siberian Aerospace Journal.* 2024;25(4): 521–530. (In Russian)
16. Belov VV, Slukin EY. Protective lubricant material for hot metal forming. Russian Patent RU 2741047 C1, 22 January 2021. (In Russian)
17. Zhang J, Wang A, Yin H. Preparation of graphite nanosheets in different solvents by sand milling and their enhancement on tribological properties of lithium-based grease. *Chinese Journal of Chemical Engineering.* 2020;28(4): 1177–1186.

18. Rudaev YaI, Kitaeva DA, Kodzhaspirov GE. Superplasticity in bulk forming processes. In: Gubaidullin DA, Elizarov AI, Lipachev EK. (eds.) *Proceedings of the XI All-Russian Congress on Fundamental Problems of Theoretical and Applied Mechanics, 20–24 August, Kazan, Russia.* Kazan: Kazan Federal University; 2015. p. 3252-3254. (In Russian)
19. Ghanbari H, Shafikhani MA, Daryalaal M. Graphene nanosheets production using liquid-phase exfoliation of pre-milled graphite in dimethylformamide and structural defects evaluation. *Ceramics International.* 2019;45(16): 20051–20057.
20. Bragina VI, Baksheeva II. Development of graphite ore beneficiation. *Mining informational and analytical bulletin (scientific and technical journal).* 2012;(9):133–137. (In Russian)
21. Al-Saadi DAY, Pershin VF, Salimov BN, Montaev SA. Modification of graphite greases graphene nanostructures. *Journal of Friction and Wear.* 2017;38: 355–358.
22. Pape F, Poll G. Investigations on Graphene Platelets as Dry Lubricant and as Grease Additive for Sliding Contacts and Rolling Bearing Application. *Lubricants.* 2020;8(1): 3.
23. Nikitchenko A, Artiukh V, Shevchenko D, Larionov A, Zubareva I. Application of Nonlinear Dynamic Analysis for Calculation of Dynamics and Strength of Mechanical Systems. In: Murgul V, Pasetti M. (eds.) *International Scientific Conference Energy Management of Municipal Facilities and Sustainable Energy Technologies (EMMFT 2018). Advances in Intelligent Systems and Computing, vol 983.* Cham: Springer; 2019. p. 496–510.
24. Solomonov KN. Application of CAD/CAM systems for computer simulation of metal forming processes. *Materials Science Forum.* 2012;704–705: 434–439.
25. Burlakov VI, Artiukh VG, Kitaeva DA, Korihin NV. Machinability of nitride ceramics with abrasive powders and their addition to diamond powder. *Materials Physics and Mechanics.* 2025;53(4): 99–110.
26. Gozbenko VE, Korchevin NA, Kargapoltsev SK, Karlina AI, Karlina YuI. Results of Research Replacement of Graphite by Petroleum Coke in Lubricated Compositions. In: *Proceedings of the VIII Science and Technology Conference "Contemporary Issues of Geology, Geophysics and Geo-ecology of the North Caucasus" (CIGGG 2018).* Paris: Atlantis Press; 2019. p. 126–131.
27. Bolotov AN, Novikova OO, Novikov VV. Effect of loading on tribotechnical characteristics of antifriction diamond-bearing mineral ceramics. *Materials Physics and Mechanics.* 2025;53(2): 104–112.
28. Li Z, Lu Sh, Zhang T, Mao Zh, Zhang Ch. A Simple and Low-Cost Lubrication Method for Improvement in the Surface Quality of Incremental Sheet Metal Forming. *Transactions of the Indian Institute of Metals.* 2018;71: 1715–1719.
29. Dan LA, Maslov VA, Trofimova LA, Kargin SB, Artiukh VG, Kitaeva DA, Korihin NV. About possibility of using the Roginsky-Schulz and Avrami-Erofeev equations in topokinetic analysis of carbothermic self-recovery of dispersed iron-graphite waste. *Materials Physics and Mechanics.* 2025;53(4): 111–119.
30. Torres H, Podgornik B, Jovičević-Klug M, Rodríguez Ripoll M. Compatibility of graphite, hBN and graphene with self-lubricating coatings and tool steel for high temperature aluminium forming. *Wear.* 2022;490–491: 204187.

MATERIALS PHYSICS AND MECHANICS RESEARCH ARTICLE

Submitted: August 23, 2023 **Revised: November 28, 2025** **Accepted: December 8, 2025**

Computational study of Ba-doped TiO_3 perovskites for solar energy applications

A. Kumar [1], R. Srivastava [2], A. Kumar [3], R. Kumar [4], S. Kumar [5], R. Chand [6], D. Saxena [7], A. Kumar [8] ✉

[1] Department of Physics, Mahamaya Government Degree College, Sherkot, Bijnor, Uttar Pradesh, India

[2] Department of Education Utkal Mani Gopabandhu Das, Faculty of Education, Swami Vivekananda, Subharti University, Meerut, UP, India

[3] Electrical Engineering, Subharti Polytechnic College, Swami Vivekanand, Subharti University, Meerut, UP, India

[4] Department of Mathematics, KVSCOS, Swami Vivekanand, Subharti University, Meerut, UP, India

[5] Department of Physics, SRM Institute of Science and Technology, Delhi NCR Campus Modinagar, UP, India

[6] Department of Applied Sciences (Physics), Meerut Institute of Engineering and Technology, Meerut Uttar Pradesh, India

[7] Department of Physics, Ismail National Mahila PG College, Meerut Uttar Pradesh, India

[8] Department of Physics, KVSCOS, Swami Vivekanand, Subharti University, Subhartipuram Meerut, India

✉ 01amankumar@gmail.com

ABSTRACT

The remarkable electrical and optical properties of barium doped TiO_3 perovskite make it an appealing material for optoelectronic applications. This study comprehensively investigates the structural, electrical, and optical characteristics of $BaTiO_3$ using density functional theory. The electrical characteristics, such as the energy band structure and density of states, were carefully examined. A band gap of 1.92 eV was discovered by the TB-mBJ functional, which is in good agreement with earlier experimental and theoretical findings. The partial density of states analysis reveals that the Ba-p, Ti-d, and O-p states have a significant impact on the material's electronic structure. By evaluating critical variables, the optical properties of $BaTiO_3$ were investigated. The TB-mBJ approximation indicates that the optical spectrum reveals $BaTiO_3$ has remarkable properties in the 4–5 eV energy range, making it suitable for solar energy harvesting. Its potential for integration into perovskite solar cells and other optoelectronic devices requiring high optical sensitivity is further corroborated by its low reflectance in this spectrum.

KEYWORDS

perovskite material • TB-mBJ • WIEN2K • GGA • density functional theory

Citation: Kumar A, Srivastava R, Kumar A, Kumar R, Kumar S, Chand R, Saxena D, Kumar A. Computational study of Ba-doped TiO_3 perovskites for solar energy applications. *Materials Physics and Mechanics.* 2025;54(6): 53–62. http://dx.doi.org/10.18149/MPM.5362025_5

Introduction

The chemical formula ABX_3, where A and B denote cations and X signifies an anion, characterizes perovskite materials. The materials in question demonstrate remarkable suitability for solar energy applications, attributed to their outstanding optoelectronic characteristics. These include a long carrier diffusion length, low trap state density, high

absorption coefficient, excellent intrinsic carrier mobility, and an appropriate band gap [1–3]. This development may result in solar cells that are more effective, greatly increasing energy conversion rates. In the near future, researchers hope that these developments will open the door to sustainable energy solutions. Increase their potential for photovoltaic applications by producing photovoltages higher than their band gap. ABO3 perovskites' optical and electronic characteristics can be tuned through cationic substitution at either the A or B site, providing a great deal of design flexibility for functional materials [4–7]. Among these, barium titanate ($BaTiO_3$), which crystallizes in the ABO_3 perovskite structure and experiences a tetragonal phase transition at about 120 ºC, is a classic ferroelectric material [8–10]. $BaTiO_3$ is a topic of theoretical and experimental interest due to its exceptional ferroelectricity, piezoelectricity, pyroelectricity, high dielectric constant, wide bandgap, and low electrical loss [11,12]. Moreover, it has exceptional chemical and mechanical stability over an extensive temperature range. This stability makes it an ideal candidate for various industrial applications, including aerospace and automotive sectors, where materials are often exposed to harsh conditions. Additionally, its resistance to corrosion further enhances its suitability for long-term use in demanding environments. Owing to these properties, $BaTiO_3$ finds applications in sensors, actuators, waveguides, high-performance computing, laser frequency doubling, nanoelectronics, and aerospace technologies [13]. The phase transitions of $BaTiO_3$ exhibit significant temperature dependence. At 120 ºC, the material changes from a cubic phase (*Pm3m*) to a tetragonal phase (*P4mm*). At 5 ºC finally, at around -90 ºC, it changes to a rhombohedral phase (*R3m*) [14,15]. These phase transitions are crucial for understanding the material's properties and potential applications, particularly in the fields of electronics and materials science. The ability to manipulate the phases by varying temperature allows for tailored performance in different environments. Structural modifications make $BaTiO_3$ highly suitable for various applications, for semiconductor applications in solar energy [16–20]. Enabling adjustments to its lattice structure [20]. Empirical studies have demonstrated that $BaTiO_3$ possesses a substantial bandgap of approximately 3.00 eV, which deviates from theoretical predictions [21,22]. To mitigate energy losses in photovoltaic applications, this structure ensures robust charge carrier mobility and an extended diffusion length. The lattice constants of cubic and tetragonal $BaTiO_3$ are estimated to be roughly 3.958 and 3.954 Å, respectively, based on theoretical simulations using the PBE-GGA. These values are crucial to understanding the material's phase transitions and structural features. This provides a platform for future research on the ferroelectric and piezoelectric properties of $BaTiO_3$ under various circumstances. The values are marginally lower than the experimental results, which span from 3.996 to 4.006 Å [11].

This study systematically investigates the electrical and optical properties of $BaTiO_3$ for prospective application in perovskite solar cells, employing density functional theory (DFT). The study seeks to evaluate its technological viability by examining critical aspects such as lattice constants (Å), electronic bandgaps (eV), and state density prior to structural optimisation. The The TB-mBJ potential is utilized to improve the precision of band structure calculations.

Materials and Methods

A first-principles analysis of $BaTiO_3$ was carried out [23,24]. The electronic structure of $BaTiO_3$ was better understood thanks to these computations, which also helped to clarify its phase transitions. The accuracy and dependability of the results were also confirmed by comparing them to experimental data. To improve computational accuracy, we used the TB-mBJ method to incorporate the exchange-correlation effects. mBJ potential, which is known for its exceptional accuracy and produces an approximate deviation of only 2 % in band structure estimations of perovskites and semiconductors [25,26]. High-resolution Brillouin zone sampling was used for structural and electronic characterization using a carefully optimized 7 × 7 × 7 k-point mesh, which was then further refined to a denser 10 × 10 × 10 k-grid for increased precision. The VESTA software was used for structural visualization and crystallographic analysis, allowing for a thorough depiction of the polyhedral framework inherent in perovskite lattice configurations [27–30].

Results and Discussion

Structure properties

The P4mm space group is used to describe the tetragonal perovskite structure in which the $BaTiO_3$ compound crystallizes. In this context, six oxygen anions (O^{2-}) coordinate the barium cation (Ba^{2+}) octahedrally, while the titanium cation (Ti^{4+}) coordinates twelve times. The basic skeletal network is formed by corner-sharing between the TiO_6 octahedra, as shown in Fig. 1. Furthermore, the titanium cation occupies a central position inside the octahedral units.

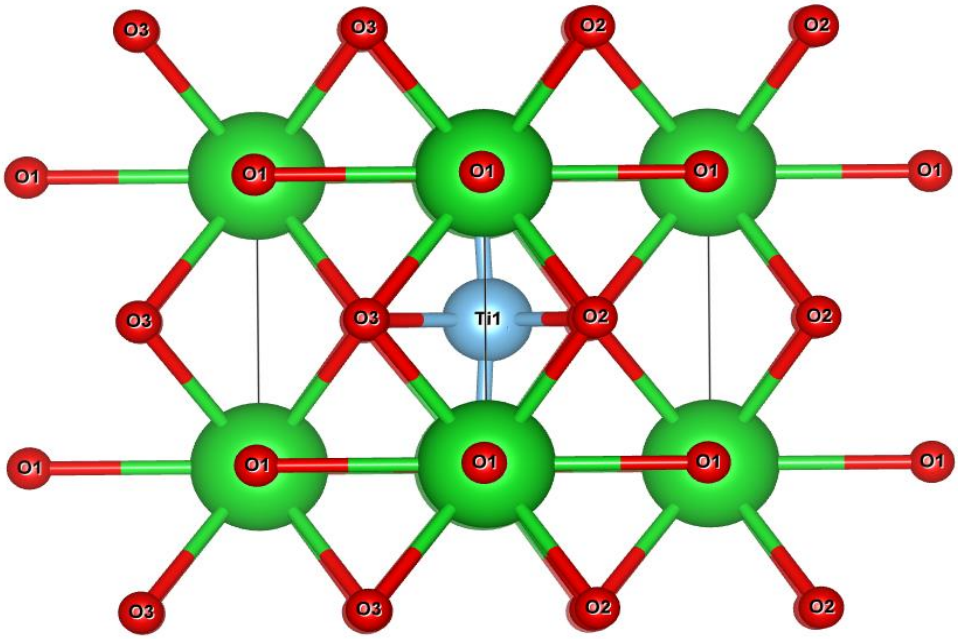

Fig. 1. Crystal structural of $BaTiO_3$ compound using VESTA simulation software

First-principles computing was used to improve the crystal structure and figure out the ground-state energy lattice parameters. The results showed that there was a strong

link between the lattice parameters and the physical properties of the material that were measured. The analysis also showed possible ways to improve the material's performance in a number of uses. The computed equilibrium lattice parameters, equilibrium volume and energy, bulk modulus, and first derivative for tetragonal $BaTiO_3$ are displayed in Table 1 and Fig. 2. These values are compared with existing experimental and theoretical datasets in a systematic way. The theoretical predictions match up very well with the reported experimental and computational results.

Table 1. Structural and electronic properties of $BaTiO_3$ compound using TB-mBJ approximation

Properties	$BaTiO_3$	Experimental
Lattice constant, Å	$a_0=b_0=4.068$	3.9988 [13]
	$c_0= 4.183$	4.0222 [13]
Space group	*P4mm* (99)	
Wyckoff position	Ba (0,0,0) Ti (0.5, 0.5, 0.5) O (0.5, 0.0, 0.48), (0.0, 0.5, 0.48) and (0.5, 0.5, 0.96)	
Minimum volume V_o, a.u^3	445.7012	
Minimum energy E_0, Ry	-18438.63743	
Bulk modulus B_0, GPa	159.3559	
First derivative of bulk modulus B_0', GPa	4.0942	
Band gap E_g, eV	1.92	1.56 [31,32]

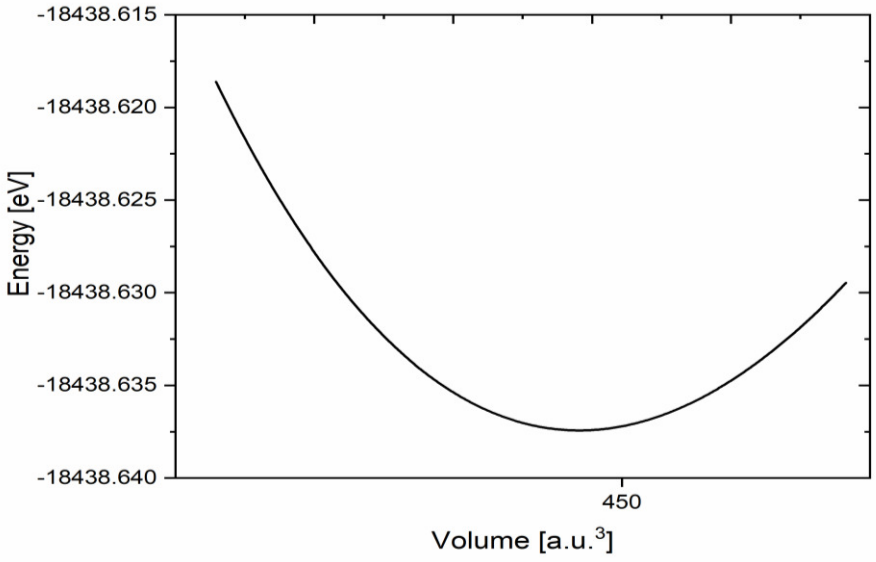

Fig. 2. Equilibrium volume V_s equilibrium energy curve of $BaTiO_3$ using Birch–Murnaghan equation of state (EOS) equation

Electronic properties

The electronic BS and DOS of $BaTiO_3$ have been investigated with help of TB-mBJ exchange potential [33–37]. The wave vector passes through high-symmetry points in the Brillouin zone along a particular k-point path. An estimate of the $BaTiO_3$ band structure is presented in Fig. 3. The Fermi energy located at origin. With the VBM point at the top and the CBM point at the bottom, the TB-mBJ approximation demonstrates that $BaTiO_3$ has an indirect

band gap. This method gives a band gap of 1.92 eV. This value matches what has been seen in experiments and $BaTiO_3$'s electronic properties, which are very important for using it in piezoelectric devices and ferroelectric materials. However, DFT calculations tend to underestimate the band gap because of the inherent problems with DFT-based methods, such as the fact that the energy derivative changes when the number of electrons changes. This underestimation happens because self-energy corrections and excited-state interactions are not handled well enough. The method used is correct. Figure 4 shows some important information that the study gives us.

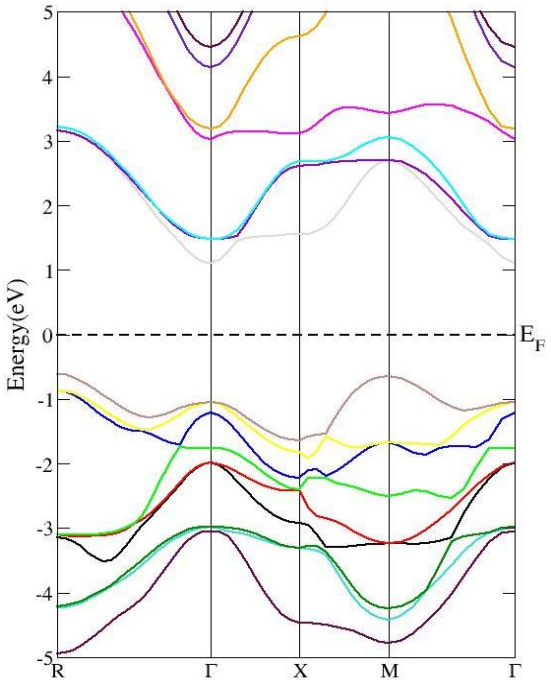

Fig. 3. Band structure of $BaTiO_3$

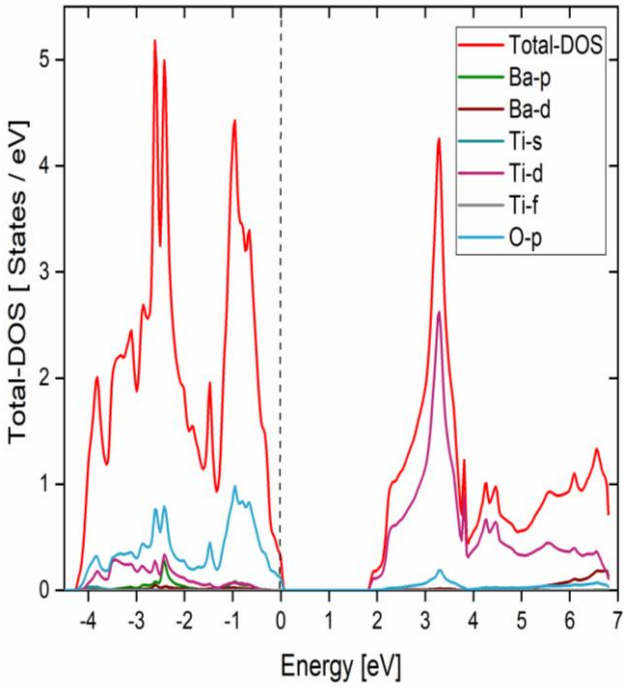

Fig. 4. Density of state of $BaTiO_3$

The impact of individual atomic orbitals on the DOS is displayed by the projected density of states (PDOS). According to the analysis, the titanium and oxygen orbitals make substantial contributions, especially in the valence band region. This realization aids in comprehending $BaTiO_3$ electrical characteristics and possible uses in piezoelectric devices. The unoccupied electronic states in this work have been analyzed using the PDOS, which takes into account contributions from the Ba-p, Ba-d, Ti-d, Ti-f, and O-p orbitals. 1.92 eV is found to be the calculated valence bandwidth for TB-mBJ in the tetragonal phase.

Optical properties

Figures 5(a–d) show the calculated optical properties of $BaTiO_3$. These elements include the optical conductivity σ(ω) shown in Fig. 5(b), the dielectric function $\varepsilon(\omega)$ shown in Fig. 5(a), the refractive index $n(\omega)$ shown in Fig. 5(c), and the reflectivity $R(\omega)$ shown in Fig. 5(d). Figure 5(a) shows the real and imaginary components of the dielectric functions with respect to the photon energy. The findings show that the optical responses of $BaTiO_3$ exhibit distinct behaviors across a range of energies. It is important to note

that the dielectric function's real part exhibits significant change that impacts both reflectivity and refractive index, whereas the peaks in the imaginary part are closely associated with absorption. For accurate optical property calculations to guarantee convergence, a dense and uniformly distributed k-point mesh is essential [38,39]. The dielectric function has two components: $\varepsilon_1(\omega)$, which represents the electronic polarization and structural features of the material's bands, and $\varepsilon_2(\omega)$, which accounts for all possible electronic transitions from the occupied state to the vacant state. These elements are essential for comprehending the interactions between materials and electromagnetic fields, especially in fields like photonics and optoelectronics.

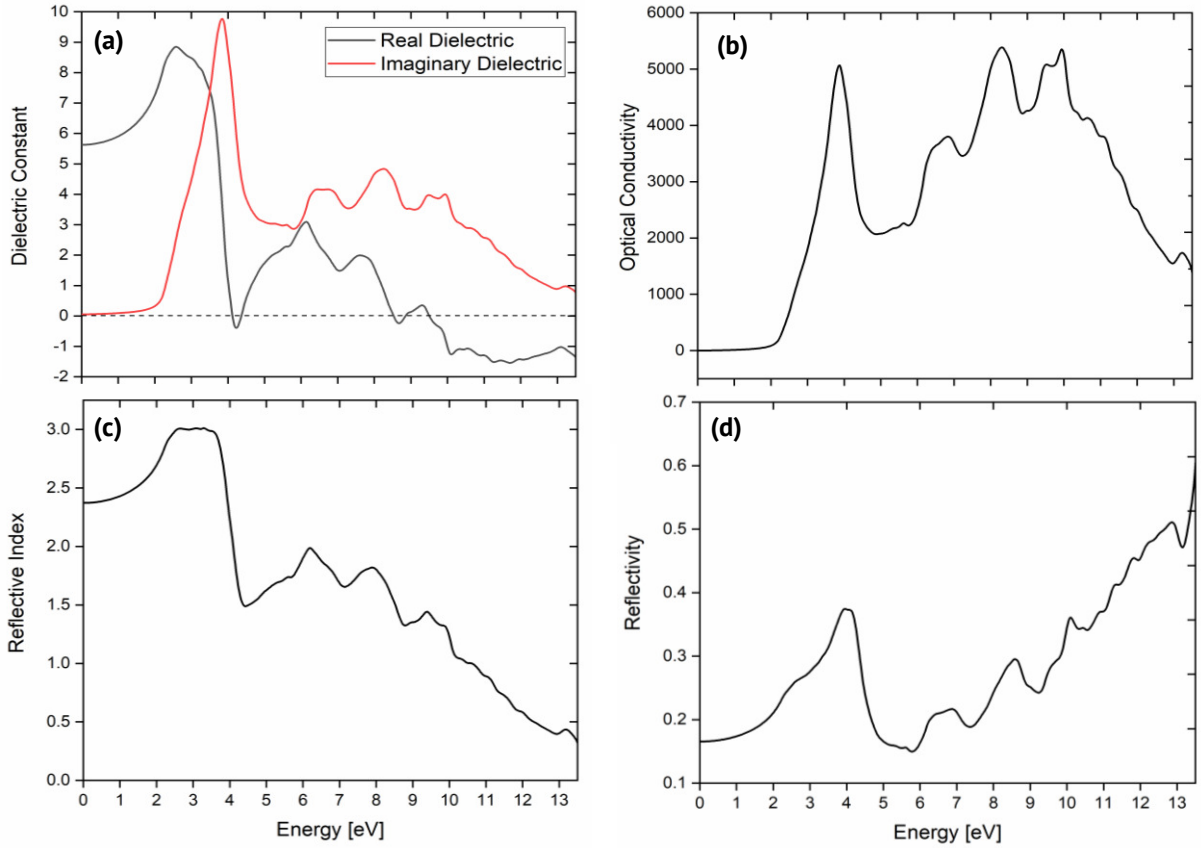

Fig. 5. Optical properties of (a) dielectric function $\varepsilon(\omega)$, (b) optical conductivity $\sigma(\omega)$, (c) refractive index $n(\omega)$, (d) reflectivity $R(\omega)$ for $BaTIO_3$

By examining the dielectric function, researchers can discover more about the optical characteristics and dynamics of various materials. This enables them to create increasingly sophisticated gadgets. $\varepsilon_1(0)$, in the TB-mBJ approximation is found to be 5.70. Moreover, $\varepsilon_1(\omega)$ shows negative values in the energy intervals of 4.0 and 9.50 to 13.5 eV, as shown in Fig. 5(a), suggesting the appearance of metallic properties in the UV spectrum. The relationship between energy dissipation from electronic transitions from the valence to the conduction band and the absorption spectrum is depicted in Fig. 5(a). Determine which orbitals are responsible for these changes by comparing the peaks in the $\varepsilon_2(\omega)$ curve with those in the DOS diagram in Fig. 4. It is possible to identify the electronic states that substantially influence the material's optical characteristics by examining these correlations. This knowledge is essential for customizing materials for

particular optoelectronic and photonic applications. The energy level at which $BaTiO_3$ exhibits optimal optical absorption and reduced polarization response is 3.90 eV, where $\varepsilon_2(\omega)$ reaches its maximum value based on the TB-mBJ approximation. Strong electronic transitions within the material are indicated by the distinct peaks in the optical conductivity $\sigma(\omega)$ of $BaTiO_3$. At photon energy of 8.5 eV, the optical conductivity reaches a maximum value of roughly 5500 $\Omega^{-1}cm^{-1}$, as illustrated in Fig. 5(b). Significant charge carrier excitation and energy dissipation mechanisms within this energy regime are suggested by the presence of such peaks. The optical transparency of $BaTiO_3$ is determined by its refractive index n(ω), which is directly related to its actual dielectric function, $\varepsilon_1(\omega)$, as shown in Fig. 5(c). The refractive index peaks at 2.4 at photon energies of 0 eV. $BaTiO_3$'s refractive index spectrum $n(\omega)$ exhibits two notable features.

The first is a noticeable peak that shows a strong optical response at about 3.0 eV. According to the Tb-mBJ approximation, the second is a region where the refractive index is less than unity and covers the photon energy range of 10.5 to 13.5 eV. Because of interactions with the electronic structure of the material, incident photons lose velocity when the refractive index rises above unity. This effect is further enhanced by a higher refractive index, which causes more. The first characteristic is a noticeable increase in the refractive index as the photon energy approaches the band gap. This indicates a stronger interaction between the material and light. The second characteristic is a distinct decrease in $n(\omega)$ with increasing energy level. This implies that as the material approaches the ultraviolet spectrum, its optical characteristics alter.

Generally speaking, any process that raises a material's electron density also raises its refractive index. The frequency-dependent optical reflectivity $R(\omega)$ of $BaTiO_3$, which is impacted by its complex dielectric functions, is displayed in Fig. 5(d). The amount of light that a substance reflects is known as its reflectivity. This property is essential for comprehending how the material behaves in a variety of applications, including electro-optic devices and capacitors. The changes in $R(\omega)$ disclose how various light frequencies interact with $BaTiO_3$'s dielectric characteristics, offering information about its possible applications in cutting-edge photonic technologies. It provides a comprehensive view of its light-responsiveness. Interestingly, under the Tb-mBJ approximation, $BaTiO_3$ shows noticeably increased reflectance.

The optical characteristics of $BaTiO_3$ demonstrate significant interaction with electromagnetic radiation, particularly within the UV-visible spectrum. The $\varepsilon_2(\omega)$ peak at 3.90 eV signifies pronounced interband transitions, corresponding to density of states contributions from O-2p to Ti-3d states. The refractive index $n(\omega)$ peaks at 2.4, showing strong light–matter interaction near the band edge, and decreases in the UV region. An abrupt increase in $\sigma(\omega)$ at around 8.5 eV indicates elevated optical conductivity resulting from excited carriers. The reflectivity $R(\omega)$ increases at elevated energies, indicating metallic characteristics. These findings illustrate the promise of $BaTiO_3$ in optoelectronic and photonic applications, particularly when using the TB-mBJ functional.

Conclusions

The structural, electronic, and optical characteristics of tetragonal $BaTiO_3$ are thoroughly examined in this first-principles investigation. The perovskite framework's stability is

confirmed by the optimized structural parameters, which also emphasize how important TiO_6 octahedral connectivity is to be preserving the crystal's integrity. These results support the potential of $BaTiO_3$ for use in ferroelectric and electronic devices. The indirect band gap of $BaTiO_3$ is 1.92 eV, according to electronic structure calculations performed with the TB-mBJ functional. Its use in sophisticated electronic and ferroelectric technologies is supported by the band structure and density of states (DOS) analyses, which provide important insights into its semiconducting behavior. To comprehend how the material interacted with electromagnetic radiation, the optical characteristics – such as the dielectric function, absorption coefficient, reflectivity, and refractive index – were assessed. In the ultraviolet region (4.0 and 9.5 – 13.5 eV), the real part of the dielectric function, $\varepsilon_1(\omega)$, exhibits negative values, signifying a shift toward metallic-like behavior. Strong optical absorption and electronic transitions are indicated by the imaginary part, $\varepsilon_2(\omega)$, peaking at 3.90 eV. A noticeable peak in the optical conductivity spectrum at 8.5 eV indicates strong interband transitions. With a notable peak at 3.0 eV, the refractive index exhibits a strong optical response, reaching a maximum value of 2.4 at 0 eV. It's interesting to note that the refractive index exhibits unusual dispersion behavior in the 10.5–13.5 eV range, falling below unity. The energy range where $\varepsilon_1(\omega)$ turns negative is represented by a clear peak in the reflectivity spectrum at 4.0 eV and a gradual increase beyond 5.0 eV. These findings confirm $BaTiO_3$ suitability for optoelectronic and photonic applications by highlighting the strong coupling between electronic transitions and optical responses.

CRediT authorship contribution statement

Anuj Kumar: writing – review & editing; **Ragini Srivastava**: supervision; **Amit Kumar**: data curation; **Rajiv Kumar**: data curation; **Sarvendra Kumar**: conceptualization; **Ramesh Chand**: supervision; **Deepti Saxena**: supervision; **Aman Kumar**: writing – original draft.

Conflict of interest

The authors declare that they have no conflict of interest.

References

1. Shrivastav N, Madan J, Pandey R, Shalan AE. Investigations aimed at producing 33% efficient perovskite–silicon tandem solar cells through device simulations. *RSC Advances.* 2021;11(59): 37366–37374.
2. Carrasco J, Illas F, Lopez N, Kotomin EA, Zhukovskii YF, Evarestov RA, Mastrikov Y, Piskunov S, Maier J. First-principles calculations of the atomic and electronic structure of F centers in the bulk and on the (001) surface of $SrTiO_3$. *Physical Review B.* 2006;73: 064106.
3. Noor NA, Mahmood Q, Rashid M, UlHaq B, Laref A, Ahmad SA. Ab-initio study of thermodynamic stability, thermoelectric and optical properties of perovskites $ATiO_3$ (A = Pb, Sn). *Journal of Solid State Chemistry.* 2018;263: 115–122.
4. Mahmood Q, Yaseen M, Haq BU, Laref A, Nazir A. The study of mechanical and thermoelectric behavior of $MgXO_3$ (X = Si, Ge, Sn) for energy applications by DFT. *Chemical Physics.* 2019;524: 106–112.
5. Mahmood Q, Haq BU, Yaseen M, Ramay SM, Ashiq MG, Mahmood A. First-principle study of mechanical, optical and thermoelectric properties of $SnZrO_3$ and $SnHfO_3$ for renewable energy applications. *Solid State Communications.* 2019;292: 17–23.

6. Noor A, Rashid M, Mahmood Q, Haq BU, Naeem MA, Laref A. Optoelectronic pressure dependent study of $MgZrO_3$ oxide and ground state thermoelectric response using Ab-initio calculations. *Opto-Electronics Review.* 2019;27(2): 194–201.
7. Wang D, Ye J, Kako T, Kimura T. Photophysical and photocatalytic properties of $SrTiO_3$ doped with Cr cations on different sites. *Journal of Physical Chemistry B.* 2006;110(32): 15824–15830.
8. Kumar S, Tiwari SC, Gupta A, Verma A, Kumar A. Comprehensive study of $BaAlO_3$ using FP-LMTO and PBE-GGA: Structural, electronic, and optical properties. *Semiconductors.* 2025;59: 495–501.
9. Evans DJ, Williams SR, Searles DJ. On the entropy of relaxing deterministic systems. *Journal of Chemical Physics.* 2011;135(19): 194107.
10. Aguado-Puente P, Junquera J. Ferromagneticlike closure domains in ferroelectric ultrathin films: First-principles simulations. *Physical Review Letters.* 2008;100: 177601.
11. Liu QJ, Zhang NC, Liu FS, Wang HY, Liu ZT. $BaTiO_3$: Energy, geometrical and electronic structure, relationship between optical constant and density from first-principles calculations. *Optical Materials.* 2013;35(12): 2629–2637.
12. Maldonado F, Rivera R, Villamaguan L, Maldonado J. DFT modelling of ethanol on $BaTiO_3$ (001) surface. *Applied Surface Science.* 2018;456: 276–289.
13. Akbar A, Imad K, Zahid A, Fawad K, Iftikhar A. First-principles study of $BiFeO_3$ and $BaTiO_3$ in tetragonal structure. *International Journal of Modern Physics B.* 2019;33(21): 1950231.
14. Xiao CJ, Jin CQ, Wang XH. Crystal structure of dense nanocrystalline $BaTiO_3$ ceramics. *Materials Chemistry and Physics.* 2008;111(2–3): 209–212.
15. Fan Z, Sun K, Wang J. Perovskites for photovoltaics: A combined review of organic–inorganic halide perovskites and ferroelectric oxide perovskites. *Journal of Materials Chemistry A.* 2015;3(37): 18809–18828.
16. Iram N, Sharma R, Ahmad J, Kumar A, Kumar A, Almutairi FN, Alturaifi HA. A DFT Manifestation of the physical, thermodynamic and thermoelectric properties in Sn-based halide perovskites. *Inorganic Chemistry Communications.* 2024;172: 113573.
17. Nechache R, Harnagea C, Li S, Cardenas L, Huang W, Chakrabartty J, Rosei F. Bandgap tuning of multiferroic oxide solar cells. *Nature Photonics.* 2015;9(1): 61–67.
18. Diéguez O, Rabe KM, Vanderbilt D. First-principles study of epitaxial strain in perovskites. *Physical Review B.* 2005;72: 144101.
19. King-Smith RD, Vanderbilt D. First-principles investigation of ferroelectricity in perovskite compounds. *Physical Review B.* 1994;49: 5828–5844.
20. Kumar A, Kumar A, Iram N. First-principles calculations to investigate structural, electronic, mechanical, and optical properties of $SrAlO_3$ compound. *Hybrid Advances.* 2024;6: 100211.
21. Gao H, Cao J, Liu L, Yang Y. Theoretical investigation on the structure and electronic properties of barium titanate. *Journal of Molecular Structure.* 2011;10003(1–3): 75–81.
22. Kumar A, Kumar R, Saxena D, Nautiyal VK, Kumar A, Iram N. Structural, electronic, magnetic and optical properties of $GdCuX_2$ (X = S, Se and Te) compounds. *Optical and Quantum Electronics.* 2024;56: 1742.
23. Kumar A, Kumar A, Jain P, Pundir SK, Singh N. TB-mBJ for doping concentration effects on magneto-optical properties in ZnMn *x* Sn (1-*x*) As 2 spintronics materials. *Optik.* 2024;315: 172039.
24. Kumar A, Gupta H, Kumar A, Kumar A, Sharma SK, Lal B, Iram N. Optoelectronic properties of Sb doped GaAs: DFT investigation. *Indian Journal of Physics.* [Preprint] 2024. Available from: doi.org/10.1007/s12648-024-03273-6
25. Kumar A, Kumar A, Iram N. First-principles calculations to investigate structural, electronic, mechanical and optical properties of $SrAlO_3$ compound. *Hybrid Advances.* 2024;6: 100211.
26. Kumar A, Kumar A, Kumar A, Iram N. Ab-initio study of hybrid perovskites $Cs_2AgGaCl_6$ for solar cells applications. *Hybrid Advances.* 2024;6: 100197.
27. Gautam R, Kumar A, Singh RP. First Principle Investigations on Electronic, Magnetic, Thermodynamic, and Transport Properties of $TlGdX_2$ (X = S, Se, Te). *Acta Physica Polonica A.* 2017;132(4): 1371–1378.
28. Annveer, Gautam R, Kumar A, Kumar A, Gautam YK, Saroj AL, Singh RP. Study of optoelectronic and thermoelectric spectra of $Tl(Nd/Gd)S_2$. *Journal of Materials Science: Materials in Electronics.* 2021;32: 727–744.
29. Bilc DI, Orlando R, Shaltaf R, Rignanese GM, Íñiguez J, Ghosez P. Hybrid exchange-correlation functional for accurate prediction of the electronic and structural properties of ferroelectric oxides. *Physical Review B.* 2008;77: 165107.
30. Blaha P, Schwarz K, Tran F, Laskowski R, Madsen GK, Marks LD. WIEN2k: An APW+lo program for calculating properties of solids. *Journal of Chemical Physics.* 2020;152: 23411–123417.

31. Kumar A, Kumar A, Kumar K, Singh RP, Singh R, Kumar R. The Electronic and Thermodynamic Properties of Ternary Rare Earth Metal Alloys. *East European Journal of Physics.* 2023;1: 109.
32. Wemple SH, DiDomenico M, Camlibel I. Dielectric and optical properties of melt-grown $BaTiO_3$. *Journal of Physics and Chemistry of Solids.* 1968;29(10): 1797–1803.
33. McCabe CJ, Halvorson MA, King KM, Cao X, Kim DS. Interpreting interaction effects in generalized linear models of nonlinear probabilities and counts. *Multivariate Behavioral Research.* 2022;57(2–3): 243–263.
34. Tran F, Blaha P. Accurate band gaps of semiconductors and insulators with a semilocal exchange-correlation potential. *Physical Review Letters.* 2009;102: 226401.
35. Barlidó P, Aull T, Huran AW, Tran F, Marques MAL. Large-scale benchmark of exchange-correlation functionals for electronic band gaps of solids. *Journal of Chemical Theory and Computation.* 2019;15(9): 5069–5079.
36. Momma K, Izumi F. VESTA 3 for visualization of crystal, volumetric and morphology data. *Journal of Applied Crystallography.* 2011;44: 1272–1276.
37. Kumar A, Gupta H, Kumar D, Sharma R, Kumar A, Sharma SK, Singh AP. Study of Structural and Electronic Properties of $CsMgCl_3$ Compound. *East European Journal of Physics.* 2024;1: 355.
38. Annveer, Gautam R, Kumar A, Kumar A, Singh PK, Singh RP. Magneto-optical effects in half metallic ferromagnets: Rare earth thallium tellurides ($TlXTe_2$; X = Tb-Er). *Optik.* 2020;223: 165317.
39. Kumar A, Guatam R, Chand S, Kumar A, Singh RP. First principle electronic, magnetic and thermodynamic characterization of heavy fermion ternary rare earth metal alloys. *Materials Physics and Mechanics.* 2019;42(1): 112–130.

MATERIALS PHYSICS AND MECHANICS RESEARCH ARTICLE

Submitted: August 18, 2025 **Revised: October 24, 2025** **Accepted: November 29, 2025**

Experimental and numerical study of energy absorption in bio-inspired scutoid cellular structures

Y. Sepahvand, F. Morshedsolouk ✉, A. Moazemi Goudarzi

Babol Noshirvani University of Technology, Babol, Mazandaran, Iran

✉ f.morshed@nit.ac.ir

ABSTRACT

This study investigates the compressive behavior and energy absorption of bio-inspired scutoid cellular structures made from polylactic acid to enhance mechanical energy absorbers used in impact protection. Seven four-cell scutoid specimens with varied transition point positions and wall thicknesses were fabricated using additive manufacturing and tested under quasi-static compression. Numerical simulations were conducted using finite element analysis in Abaqus to complement the experiments. Results show that scutoid structures outperform equivalent honeycomb designs in energy absorption efficiency, with the highest performance achieved when the transition point is located near the mid-height of the cells. Increasing wall thickness improves all key energy absorption indicators. Design of experiments reveals inner wall thickness as the most significant factor affecting energy absorption. The findings demonstrate that optimizing transition point location and wall thickness significantly enhances the crashworthiness of scutoid structures, making them promising candidates for lightweight energy absorbers.

KEYWORDS

PLA 3D-printed scutoid • energy absorption • crushing • explicit dynamics • crushing test

Citation: Sepahvand Y, Morshedsolouk F, Moazemi Goudarzi A. Experimental and numerical study of energy absorption in bio-inspired scutoid cellular structures. *Materials Physics and Mechanics*. 2025;53(6): 63–81. http://dx.doi.org/10.18149/MPM.5362025_6

Introduction

Mechanical energy absorbers are structures that convert all or part of the impact kinetic energy into potential strain energy. Since 1952, when a patent about a crumple zone was issued, mechanical energy absorbers have been used in various industries, such as automotive, railway, shipbuilding, and military industries [1]. Crumple zones, also known as crash boxes, are lightweight tubes that absorb collision energy and minimize the effect of collision impact on passengers, thereby increasing passengers' safety [2]. These energy-absorbing structures are usually subjected to axial compressive load, and the quasi-static compression test is a simple method to evaluate structures' energy absorption capability. Increasing the efficiency of energy absorbers is possible by either increasing the amount of absorbed energy (EA) or reducing the peak crushing force (PCF) in the quasi-static compression test. Researchers have been trying to enhance energy absorbers' efficiency by comprehending the behavior of conventional structures or introducing contemporary designs.

The first serious discussions and analyses of the compressive behavior of thin-walled circular tubes under quasi-static loads emerged during the 1960s with Alexander [3], who studied cylindrical tubes as a passive energy absorbing method and developed an empirical formula to predict the PCF for thin-walled cylinders. Abramovich

Publisher: Peter the Great St. Petersburg Polytechnic University

and Jones [4,5] performed a series of static and dynamic collapse tests on cylindrical and square tubes, modified Alexander's formula for the axisymmetric buckling failure mode of the cylinders and suggested the PCF empirical formula for the square tubes. Tak and Iqbal [6] compared the performance of square and circular tubes under impact load.

A great deal of previous research into energy-absorbing structures has mainly focused on enhancing tubes' energy absorption capacity by filling them with foam. For instance, Yamada et al. [7], Zarei et al. [8], and Zhibin et al. [9] investigated the absorbed energy and the collapse behavior of foam-filled aluminum tubes. Another method is using functionally graded foams and foams with different densities to improve the tube's energy absorption capacity [10]. However, filling tubes with lattice and cellular structures can improve the energy absorption performance of the tubes, as well. This idea was studied by Baykasoğlu et al. [11], Cetin and Baykasoğlu [12], and Tao et al. [13]. Moreover, Le et al. [14] and Nikkhah et al. [15] suggested a new stepwise lattice-filled structure to maintain a high compressive load after first buckling and improve the efficiency of the energy absorption. Hosseinpour et al. [16] conducted both numerical and experimental analyses on thin-walled auxetic cylindrical tubes (featuring Cylindrical Lozenge Grid, Square Grid, and Peanut Grid patterns) under quasi-static axial compression. Their findings emphasized that pattern type and rib thickness (porosity) significantly influence energy dissipation and failure modes, concluding that careful design can prioritize controlled and predictable deformation.

Other researchers suggested that the lower the PCF is, the higher the energy absorption efficiency is. They concluded that introducing imperfections, such as dents, grooves, or corrugation, may decrease the first buckling force, and consequently, the energy absorption process will be more efficient. Nikkhah et. al. [17], and Rogala et al. [18] reduced PCF by creating grooves on the circular, square. Whereas Tran et. al. [19], Taghipour et al. [20], and El-Baky et al. [21] argued that although holes can decrease PCF, they may cause major implications on energy absorption and can decrease the energy absorption capacity.

Following the introduction of the additive manufacturing method, many researchers use 3D-printed complicated structures for energy absorption applications, i.e., 3D-printed FGM structures are common shapes. Borovkov et al. [22] studied the mechanical properties of 3D printed meta materials. Baroutaji et al. [23] investigated a metal FGT 3D-printed circular section under transverse loading. By changing the FGT pattern they succeeded in improving the energy absorption capacity by 79%. Nian et al. [24,25] studied the energy absorption of the tube filled with FGM lattice and used an optimization method to increase the energy absorption. Similarly, Gharehbaghi and Farrokhabadi [26] utilized additive manufacturing to evaluate the energy absorption capability of a novel cruciform composite lattice structure made from continuous glass fiber reinforced polymer, highlighting the need for innovative printing paths to prevent debonding in complex cell joints. Focusing on enhanced structural topology, Gharehbaghi et al. [27] and Ghorbani et al. [28] introduced a new lattice structure for energy absorption applications. Ghorbani et al. [29] investigated a bone-inspired composite cellular structure fabricated using fused deposition modeling (FDM) 3D printing from glass fiber-reinforced polylactic acid (PLA).

Moreover, to date, several studies have begun to examine the use of bio-inspired cellular structures as energy absorbers. Among them, honeycomb is a well-known geometry that has been used for many structural applications. The structure of the basic form of the honeycomb is studied by Galehdari et al. [30] and Gu et al. [31]. While, Usta et al. [32], Feng et al. [33], Xia et al. [34], Nikhah et al. [35], and Tau et al. [36] studied the crushing behavior of the honeycombs with more complex geometries, i.e., graded honeycomb and hierarchical honeycomb.

A scutoid is a complex three-dimensional bio-inspired cellular structure that can be found in the epithelial tissues of organisms and is highly efficient in stabilizing packing structures [37]. Dehiri and Patel [38], for the first time, studied the compressive behavior of the aluminum scutoids self-packing cell numerically using ABAQUS software. To the authors' best knowledge, no experimental studies have been paired with numerical analyses. To fill the gap, this paper presents an experimental and numerical investigation of the compressive behavior and energy absorption characteristics of polymetric scutoid-based cellular structures under quasi-static compressive loading. For this purpose, sets of self-packing scutoids consisting of four cells are designed and fabricated through additive manufacturing using PLA filament and are tested under a quasi-static compression load. The energy absorption performance of these cellular structures is also studied numerically in the explicit dynamic module of Abaqus software.

Materials and Methods

A scutoid is composed of two parallel polygon or polygon-like shapes whose vertexes are connected through lines, curves, and at least a Y-shaped edge. The scutoid structures are widely observed in the living creatures' hard curved shells which have high compressive strength. The scutoid's transition point is the bifurcation point on the Y-shape edge (Fig. 1). Scutoids are efficient shapes in packing cellular shapes between two parallel surfaces.

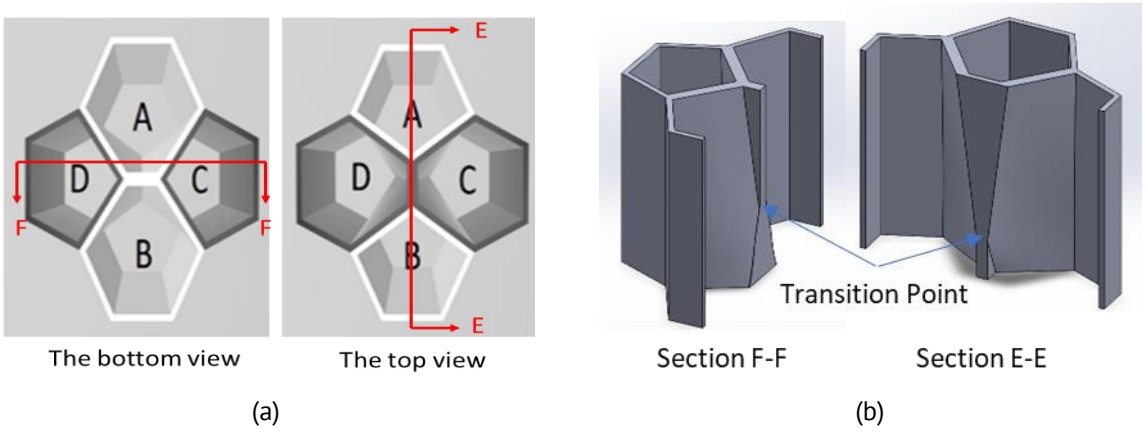

Fig. 1. The top and bottom view (a) and details of the self-packing four-cells scutoid (b)

In this research, the compressive behavior of a four-cell structure consisting of polymeric scutoids elements is investigated experimentally and numerically and the effect of the location of the transition point on the energy absorption and the crushing behavior is studied. Moreover, an equivalent honeycomb structure is used as a comparison basis. Seven cellular structures consisting of four self-packing scutoids are

modeled and their compressive behavior is analyzed in Abaqus software. These structures are also made through additive manufacturing and tested under a compressive load.

Scutoid structure design

The studied scutoid geometry is shown in Figs. 1 and 2. It is composed of two pentagons and two hexagons on the top and bottom planes. A hexagon on the top plane (or on the bottom plane) is connected to a polygon on the bottom plane (or on the top plane) by 4 lines and a Y-shaped edge (Fig. 1(a)). The transition point is defined as the bifurcation point of the Y-shape edge and is shown in Fig. 1(b) in the section views. The cells have two hexagonal and two pentagonal cross-sections in the top and bottom planes with an edge length of 6 mm. According to these dimensions, all specimens have the same relative density. As mentioned before, an equivalent honeycomb structure is also studied as a comparison basis.

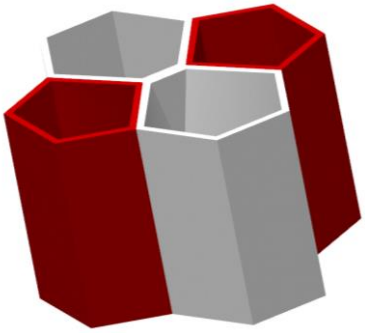

Fig. 2. The self-packing four-cells scutoid

All specimens have a fixed length of 20 mm, so for T20, the transition point is positioned 4 mm from the base. The scutoid specimens used in this study are divided into two distinct groups based on wall thickness configurations:

1. Group A: These models correspond to the specimens described in the Methodology section, where the inner walls have a thickness of 1 mm, which is twice the thickness of the outer walls at 0.5 mm.
2. Group B: This separate set of models was specifically designed to analyze the effect of wall thickness by using uniform wall thicknesses for both inner and outer walls.

For both groups, the specimens are labeled with the letter "T" followed by a number (e.g., T20, T30, ..., T80), which indicates the percentage height of the transition point relative to the total height of the scutoid. For example, T20 refers to a specimen whose transition point is located at 20% (0.2) of the total height from the base (lower) plane. The specimens in Group B are labeled with the transition point percentage followed by the wall thickness, for example, "T50 0.5 mm" indicates a specimen with a transition point at 50 % height and uniform wall thickness of 0.5 mm.

Additive manufacturing of specimens

Additive manufacturing can be used to create complex geometries. In this research, the four-cell scutoid specimens are fabricated using Dayan K36P 3D printer (Fig. 3). The 3D

models of the specimens were first designed in SOLIWORKS software and imported into ULTIMAKER CURA software in STL format. Then, the printer setup is implemented and the G-CODE files are developed to print the samples. The 3D printer settings for the specimens' fabrication are shown in Table 1.

Table 1. 3D printing process characterization

Filament material	PLA
Nozzle diameter, mm	0.5
Nozzle temperature, °C	200
Bed surface temperature, ˚C	50
Layer height, mm	0.2
Internal density, %	100

Fig. 3. The scutoid and honeycomb specimens fabricated by 3D printer

PLA material properties

The specimens are made of PLA using additive manufacturing. The PLA material properties are given in Table 2. In the finite element model, the mechanical behavior before the yield point is described by the elastic modulus, Poisson's ratio, and density. In the post-yield stage, the piecewise linear elastic-plastic model is defined by the experimental stress-strain curve of the standard specimen. Since no obvious fracture can be detected in the specimens during quasi-static experiments, the fracture and damage are not considered in the numerical simulations.

Table 2. The basic material parameters of PLA [33]

Density, kg/m^3	**Elastic modulus, GPa**	**Poisson's ratio**	**Yield strength, MPa**	**Initial yield strain**
1200	1.97	0.35	40	0.026

Experimental procedure

Energy absorption and crushing behavior of seven scutoid specimens and a honeycomb specimen were investigated under quasi-static compressive load. The specimens were made of PLA filament using an additive manufacturing process and were tested using SANTAM STM20 compression test device. As shown in Fig. 4 each specimen was placed between test machine platens, then, the upper platen moved downward with constant speed, while the lower platen was fixed. To fulfill the quasi-static criterion, the compression rate of 2 mm/min is applied. A load cell measured the crushing force at each displacement interval and the force–displacement diagrams are extracted, so that the behavior of the specimens during the test can be evaluated and compared.

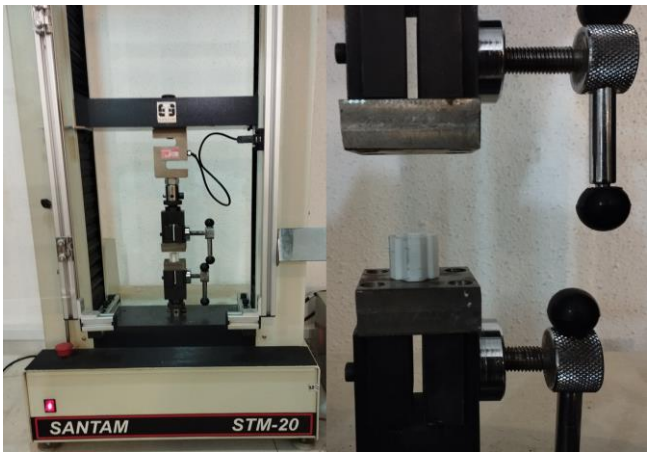

Fig. 4. SANTAM STM 20 Test Machine

Numerical modeling

The studied scutoid and honeycomb specimens are modeled in the SOLIDWORKS software, and the models are imported to the explicit dynamic module of the Abaqus software. As the models' walls are relatively thick compared to the dimensions of the specimens, the models are meshed with C3D10M solid elements. C3D10M is a 10-node modified quadratic tetrahedron which is well-suited for uniform mesh continuity and reduces computational time. To ensure the accuracy of element size, the mesh sensitivity analysis for the PCF parameter of the honeycomb specimen is conducted. Figure 5 shows the calculated PCF for the honeycomb specimen in relation to the element size. After performing the mesh size sensitivity analysis based on the PCF parameter, the mesh size of 0.3 mm is chosen and applied to all specimens, and the models are discretized with a total of 456,000-490,000 elements. Figure 6 shows a specimen that is meshed using this element size.

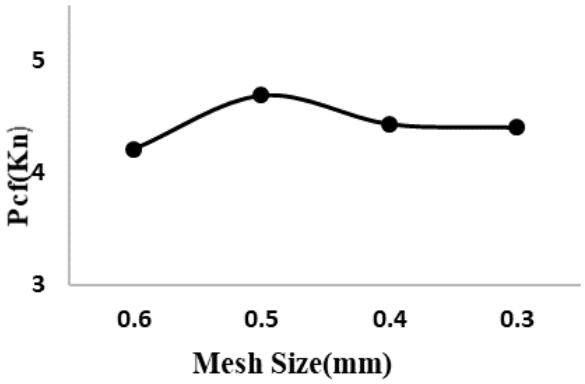

Fig. 5. Mesh sensitivity versus PCF

To model the quasi-static crushing test, two rigid plates are modeled at both ends of the specimens as the upper and lower platen of the compression test machine. The friction coefficient of 0.2 is defined in the contact surface between the rigid plates and the specimens [39,40]. The self-contact, i.e., the contact between the faces of the specimens itself, is also defined. The bottom rigid plate is assumed to be fixed and the upper rigid plate moves downward with constant speed.

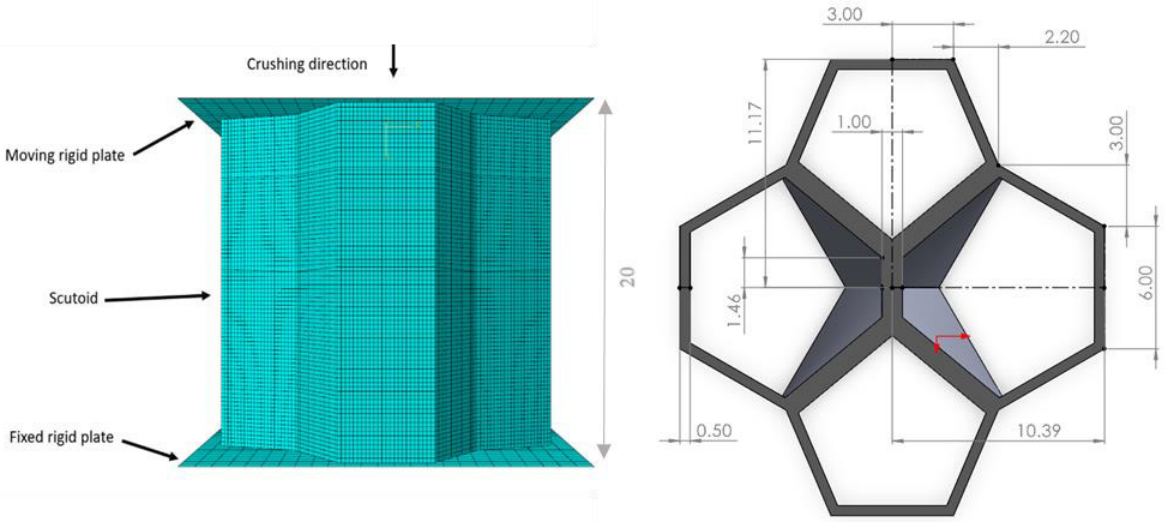

Fig. 6. Sample specifications of T50 (mm)

Moreover, to evaluate the accuracy of the quasi-static analysis in explicit dynamics, one should ensure that the total kinetic energy is small compared to the total internal energy and the ratio of kinetic energy to internal energy must be less than 5 % [41,42]. In Fig. 7, the kinetic energy to internal energy ratio is presented for the finite element crushing modeling of the honeycomb specimen, in which, the amount of kinetic energy is almost zero.

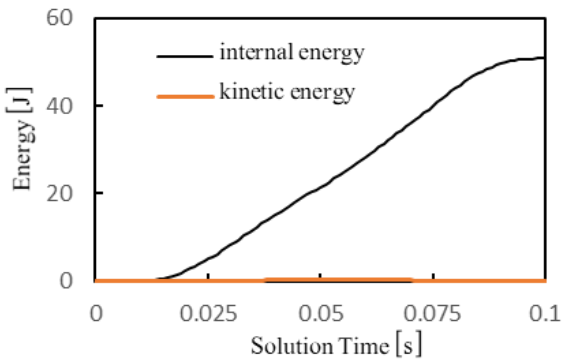

Fig. 7. A typical kinetic energy and internal energy versus solution time diagram

Results and Discussion

Numerical and experimental quasi-static compressive results

In this research, the crushing behavior and energy absorption of the 4-cell scutoids and honeycomb structures have been investigated in the quasi-static compression test. The crushing force-displacement curves for the honeycomb and scutoid specimens are extracted from the experiment and the numerical models. The numerical results for all specimens are illustrated in Fig. 8. The comparison of the force-displacement experimental and numerical diagrams is presented in Table 3. In which the bold line is the experimental result and the dashed line is the numerical result. The results indicate that the transition point location changes the compressive behavior and energy

absorption capability of the scutoids. The maximum crushing force for these specimens varies between 3.84 and 4.10 kN. The absorbed energy is between 34.69 and 39.67 and the crushing efficiency is between It varies from 62.84 to 71.28 %. The deformation of the specimens in different stages is, also, shown in Table 3.

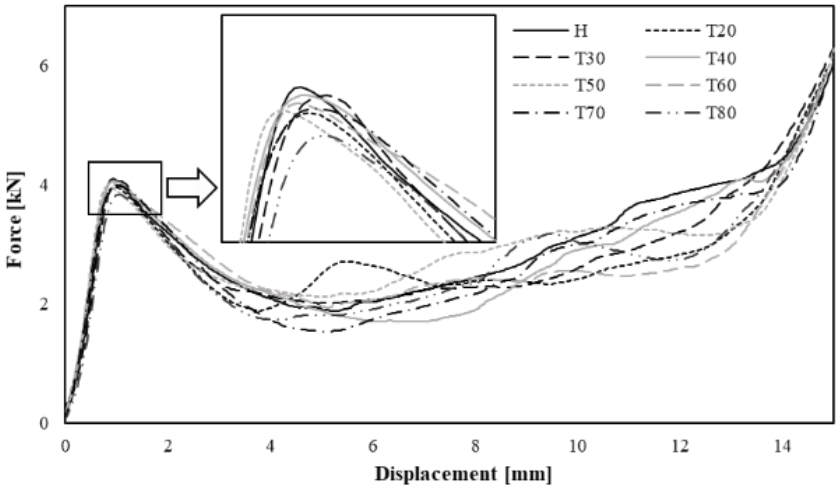

Fig. 8. The force-displacement curves from experiments for the honeycomb and scutoid specimens

Table 3. The comparison between the experimental and numerical results for the honeycomb specimen

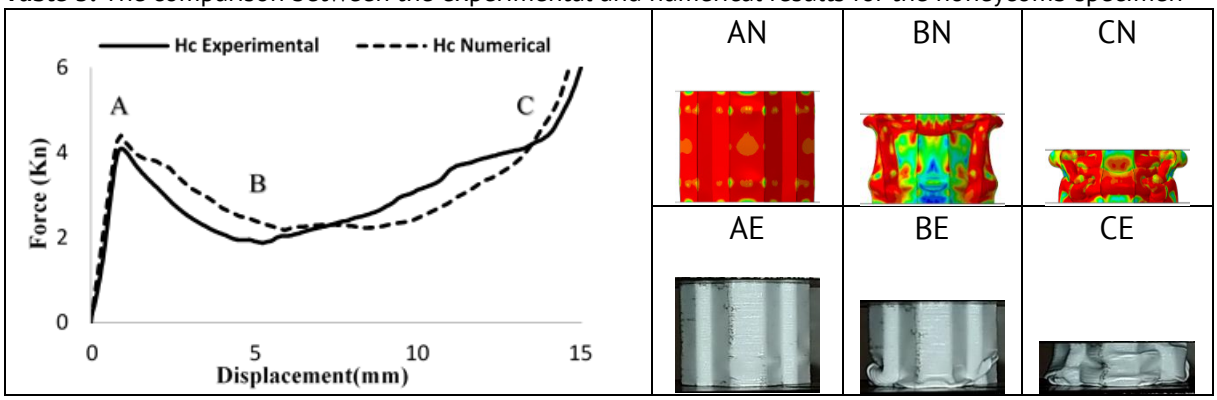

Under axial load, thin-walled cylindrical tubes usually fail in progressive folding buckling mode. While the failure modes for the square tubes are different. For the square tubes, the buckling shape develops when the load reaches the buckling load. By increasing the compressive load, the amplitude of the deformation increases, and many folds form simultaneously. Whereas, in progressive folding mode, each fold develops after the previous fold completion [43]. Chen [43] showed that the deformation modes of the uniform hexagonal honeycomb are similar to the symmetric deformation of the cylindrical tube.

The experimental and numerical results for the honeycomb and scutoid specimens are compared in Tables 3 and 4, respectively. The behavior of the studied honeycomb, in the numerical study, was like that of the cylindrical tubes. The buckling started by forming two folds on the honeycomb outer skin which is the thinnest part of the specimen. As the load increased, the folds grew larger. In contrast, in the experiment, due to the manufacturing imperfection at the ends, a fold started to form at the bottom first, and

another fold started to form after the first fold completion. The fluctuation in the experimental force-displacement curve is due to this phenomenon. From Table 4, it can be deduced that for all specimens, the buckling of all outer shells starts in the same manner. The outer shell first buckled in the upper and lower regions. Like the square tubes studied by Chen [43], the buckling shape amplitudes grew simultaneously.

Table 4. The comparison between the experimental and numerical results for the scutoid specimens (continued)

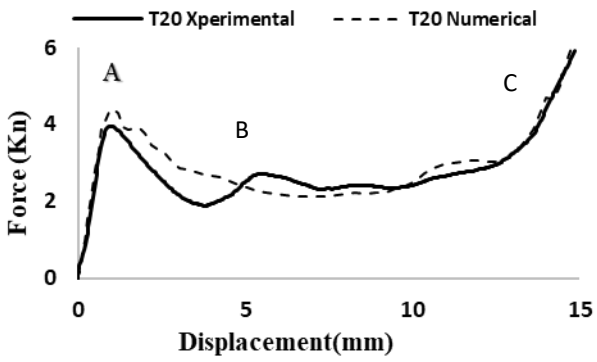	AN	BN	CN
	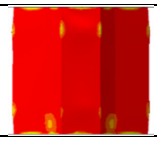	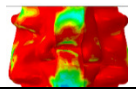	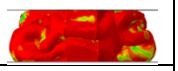
	AE	BE	CE
			
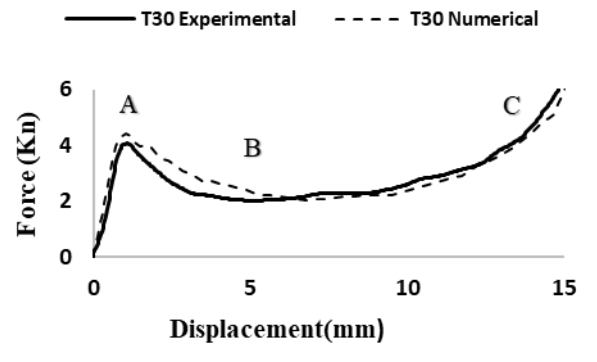	AN	BN	CN
	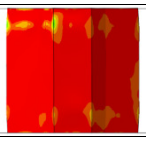	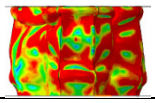	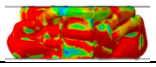
	AE	BE	CE
		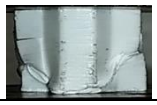	
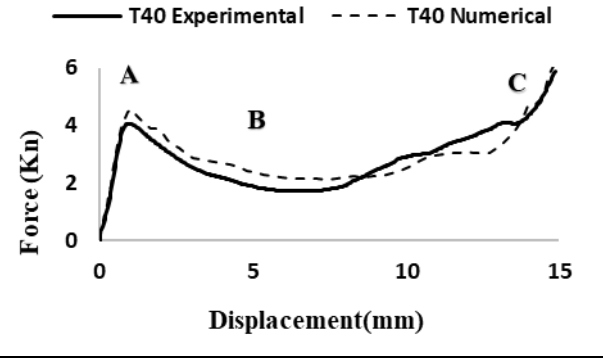	AN	BN	CN
	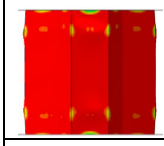	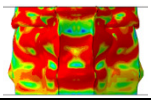	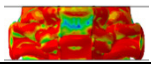
	AE	BE	CE
			
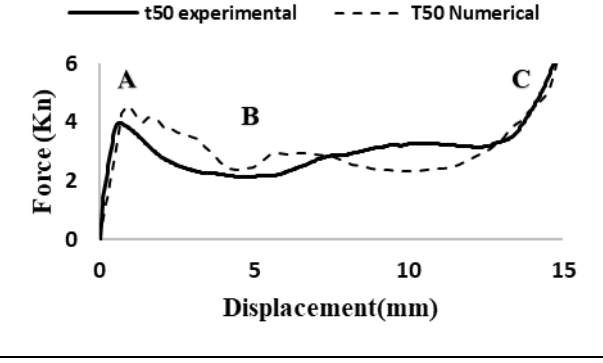	AN	BN	CN
	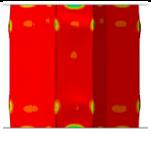	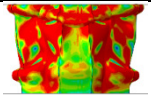	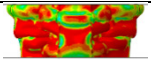
	AE	BE	CE
			

Table 4. The comparison between the experimental and numerical results for the scutoid specimens (continued)

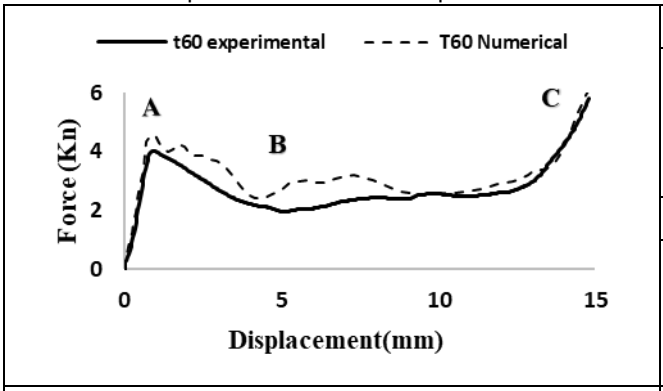	AN	BN	CN
	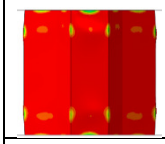	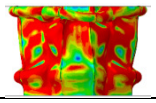	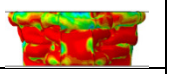
	AE	BE	CE
	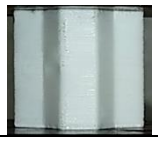		
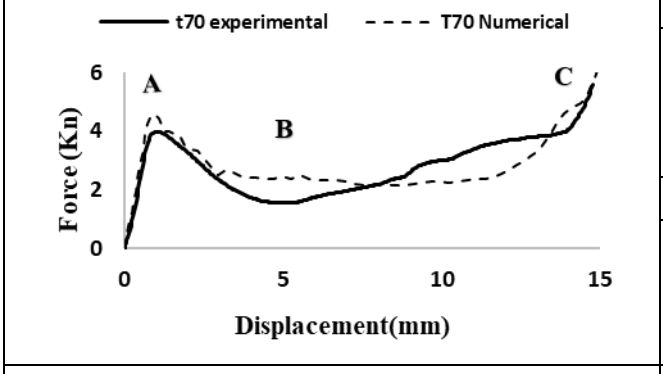	AN	BN	CN
	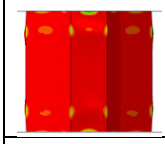	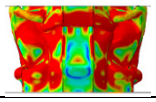	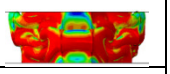
	AE	BE	CE
			
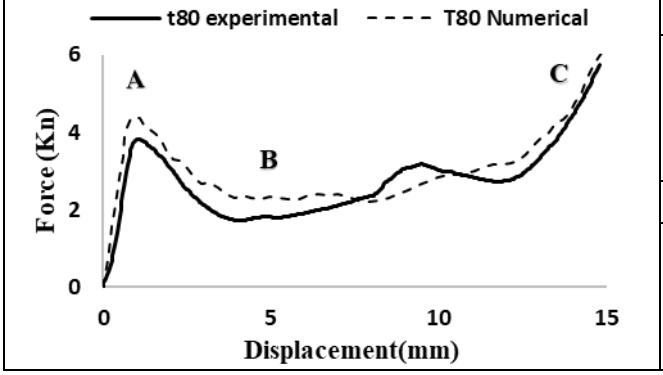	AN	BN	CN
	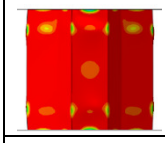	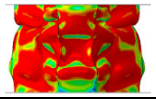	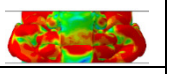
	AE	BE	CE
			

Energy absorption capacity assessment

The impact efficiency of the energy absorbers can be determined using various indices. Each of these indicators evaluates the behavior of the energy-absorbing structure by considering different aspects, i.e., Peak Crushing Force (PCF), Absorbed Energy (EA), Mean Crushing Force (MCF), Specific Absorbed Energy (SEA), and Crushing Efficiency (CLE) [44,45] as follows:

(1) $EA = \int_0^d F(x)dx$ (1)

(2) $SEA = \frac{EA}{m}$ (2)

(3) $MCF = \frac{EA}{d}$ (3)

(4) $CLE = \frac{MCF}{PCF}$ (4)

where $F(x)$, m and d are the collapse force at displacement x, the energy absorber mass and crushing length, respectively. Crushing length is the amount of force displacement in the crush test before densification. All indicators in the quasi-static collapse test are calculated until the beginning of the densification zone.

In this study, all specimens have the same mass, therefore, only PCF, EA, MCF and CLE are considered. For all samples, the amount of crushing length is the same and the effect of transition point can be determined better. Based on the force-displacement curves extracted from the numerical analysis, the energy absorption indices are calculated for T20 to T80, and the honeycomb specimens are shown in Table 5. Among these specimens, the amount of absorbed energy for the T50 specimen is higher than all the specimens. On the other hand, the amount of PCF for T80 and T20 is lower than all the structures. The reason is the collapse initiation in the inner shells in the top and bottom region, which leads to the collapse of some parts of the object in an inclined direction. Since the amount of energy divided by the crushing length gives the MCF value, the MCF value for the T50 specimen is, also, the highest, and the value of the crushing efficiency for T50, which is obtained by dividing the MCF by the PCF, is the highest.

Table 5. Energy absorption indices of scutoid specimens (experimental tests)

	***EA*, J**	***PCF*, KN**	***MCF*, KN**	***CLE*, %**	***SEA*, J/g**
T20	35.74	3.96	2.55	64.47	23.57
T30	37.49	4.05	2.68	66.12	24.80
T40	37.77	4.06	2.71	66.45	25.02
T50	40.56	3.97	2.90	72.98	26.87
T60	36.45	4.01	2.59	64.93	24.13
T70	37.49	3.98	2.68	67.28	24.78
T80	36.34	3.84	2.60	67.20	23.98
Hc	39.88	4.10	2.85	69.48	26.93

Failure mode assessment

In progressive buckling, the peak force indicates the beginning of the buckling process, which can be controlled by placing mechanisms to control the buckling onset and reduce the PCF value. When the crushing process starts, the structure enters the plastic region, the crushing load decreases, and the structure starts to fold. When the folding of this part of the member is completed, the load starts to increase until the plastic process occurs in the next place. This process is repeated until all the energy is absorbed or until the member cannot absorb any more energy. This stage is characterized by a sudden increase in load and is called densification.

In Figs. 9 and 10, the failure modes of 4-cell scutoids specimens and a honeycomb specimen from numerical analysis are presented. It should be noted that due to the lower thickness of the outer walls (0.5 mm), the commencement of the buckling and the failure of all specimens are when the outer walls of the specimens are buckled. For all specimens, the outer wall, first, buckled in the upper and lower regions in a symmetrical manner (Table 4 Point A). All specimens underwent the densification phase, which is the end of the energy absorption phase.

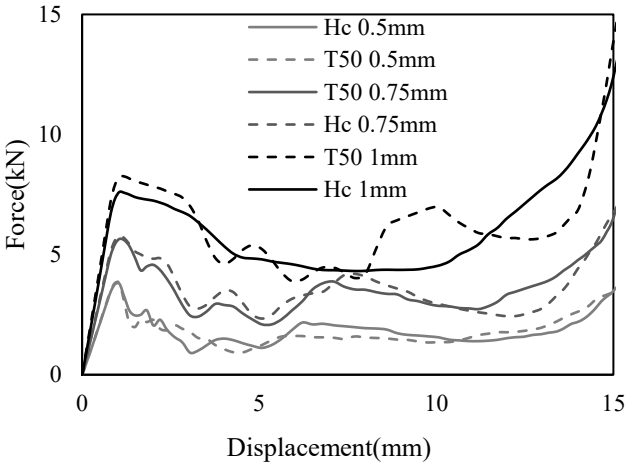

Fig.9. Force displacement diagram of T50 and Hc with diffrent thickness

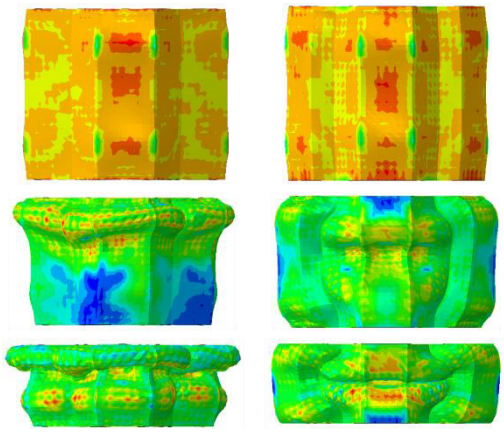

Fig. 10. Failure mode for T50 1mm and HC 1 mm from Group 2

Figure 11 compares the T50 and T20 specimens' deformation and the honeycomb specimen's deformation. T50 is the best specimen in energy absorption. The outer wall deformation of the three specimens is quite similar at the beginning. In the honeycomb specimen, after the outer shell buckling, increasing the displacement would cause the inner shells to buckle locally in the middle part. The inner shell buckling shape differed from the outer shell buckling shape. The outer shell buckled in a fold, whereas the inner shell buckled in 2 folds. In the T50 specimen, the outer shell buckling, also, affected the inner wall buckling, and the first two small buckling deformations on the outer wall shaped a two-fold deformation on the outer shells. The fold number of the inner shell of the T50 is 3 which is the biggest fold number of all specimens, and means that it deformed more effectively.

Scutoid specimens whose failure mode occurred away from the rigid plates have more energy absorption capacity, i.e., T40, T50, and T70 specimens. In addition to the energy absorption that was discussed, reducing the maximum crushing force is also required to increase the efficiency of the crushing load. In addition to these points, it has been pointed out that the type of external walls' failure mode has a great effect on the amount of energy absorption, for example, in specimens whose external walls are folded inwards during the crushing process, energy absorption is less, T20, T30, T60, and T80 specimens.

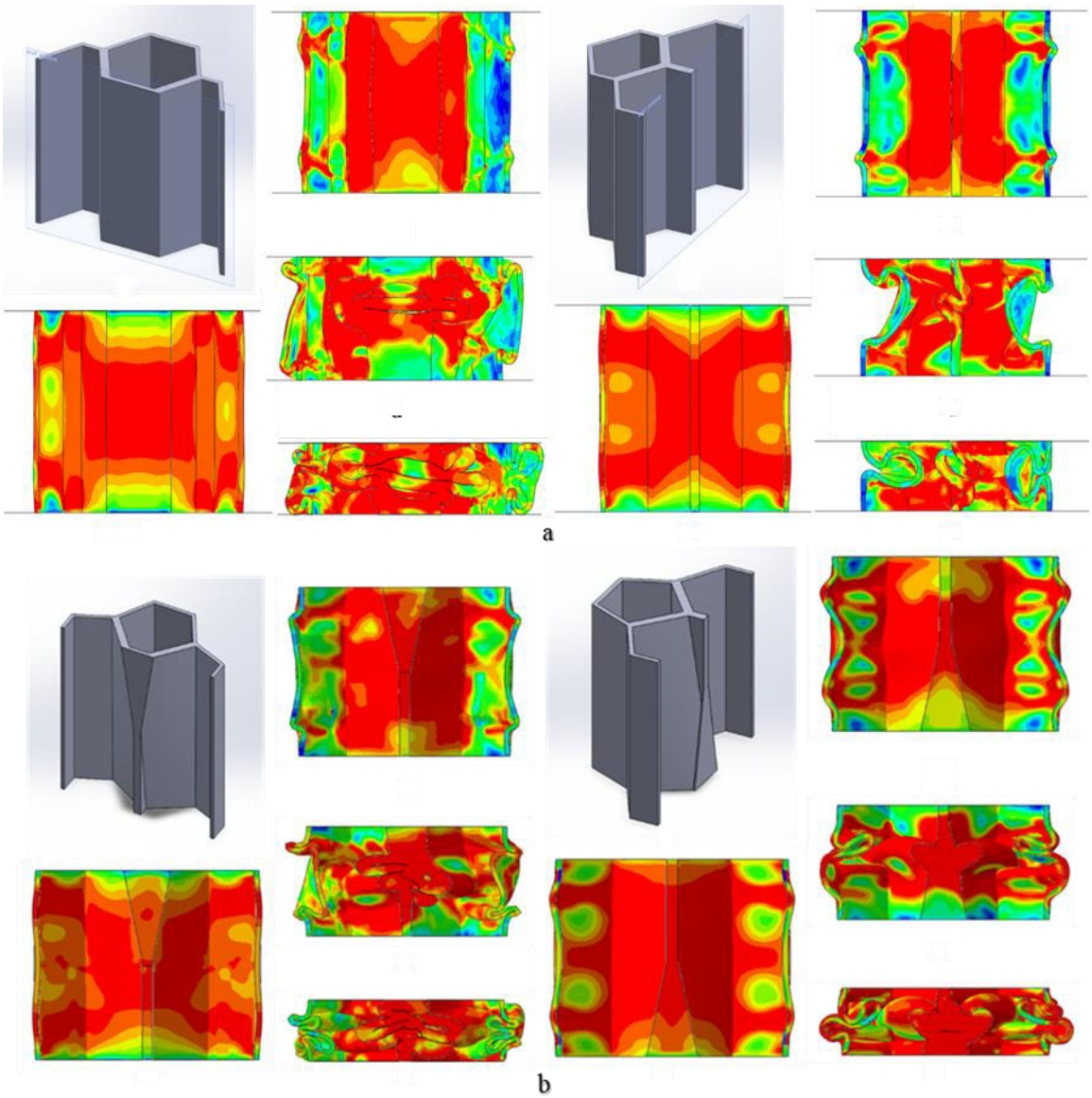

Fig. 11. A cut view of Hc specimen(a) and the T20 specimen (b)

The effect of thickness

In addition to the transition point location, the wall thickness also plays a significant role in the energy absorption characteristics of the scutoid and honeycomb structures. The force-displacement diagrams for the T50 0.5 mm, T50 0.75 mm, T50 1 mm, Hc 0.5 mm, Hc 0.75 mm, and Hc 1 mm specimens are presented in Fig. 9. T50 1 mm has higher PCF which makes it less efficient in energy absorption application compared to HC 1 mm, while better in the strength required applications. Although the deformation pattern for all specimens is alike in some aspects, the thicker specimens are more efficient in energy absorption due to more uniform loading pattern

Figure 10 shows a comparison of failure modes between a honeycomb structure (right) and a T50 scutoid structure (left), both with a wall thickness of 1 mm. The initial failure mode observed is local symmetric buckling at 5 mm of compression. The final failure mode is densification, which closely mirrors the modes observed in experimental specimens.

As shown in Table 6, increasing the wall thickness leads to higher values for all the evaluated energy absorption indices: EA, PCF, MCF, and CLE in both the T50 scutoid and the honeycomb specimens. This trend can be attributed to the increased resistance to deformation provided by thicker walls. Thicker walls require higher forces to initiate buckling and collapse, resulting in a higher PCF. Consequently, the structure absorbs more energy before failure, leading to an increase in EA. The MCF, which represents the average force sustained during the crushing process, also rises due to the enhanced resistance. This ultimately leads to an improvement in the CLE, indicating that thicker walls enable the structure to absorb energy more efficiently relative to the peak force. While the transition point location influences the deformation mode and fold formation, the wall thickness acts as a global factor affecting the overall strength and energy absorption capacity of both the scutoid and honeycomb structures.

Table 6. The effect of the thickness on scutoid energy absorption

	***EA*, J**	***PCF*, kN**	***MCF*, kN**	***CLE*, %**	***SEA*, J/g**
T50 0.5 mm	23.84	3.82	1.70	44.5	20.37
Hc 0.5 mm	24.581	3.78	1.75	46.4	21.31
T50 0.75 mm	46.44	5.59	3.31	59.3	28.3
Hc 0.75 mm	47.14	5.78	3.36	58.2	27.8
T50 1 mm	80.49	8.25	5.75	69.6	35.94
Hc 1 mm	78.31	7.60	5.60	73.5	36.48

Based on Fig. 12, at a wall thickness of 0.5 mm, the Specific Energy Absorption (SEA) of the honeycomb structure surpasses that of the T50 specimen. However, at a wall thickness of 0.75 mm, the T50 specimen exhibits a higher SEA than the honeycomb structure. This trend reverses again at a wall thickness of 1 mm, where the honeycomb structure demonstrates a greater SEA value compared to T50. While increasing the wall thickness generally leads to an increase in energy absorption for both specimen types, this enhancement does not consistently favor either the honeycomb or the T50 structure. The inconsistent very small superiority between the two structures with increasing thickness indicates that simply increasing thickness and mass does not guarantee a superior SEA performance for either configuration.

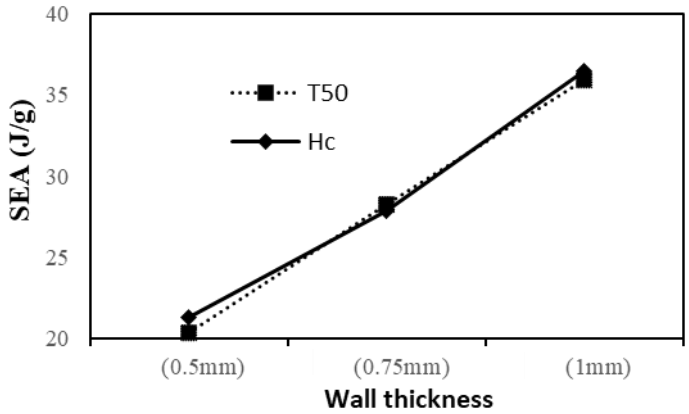

Fig. 12. The comparison of the SEA of T50 and HC from Group A

Figure 13 illustrates a comparative analysis of Specific Energy Absorption (SEA) values between our Group A (scutoids) and Group B (T50s and HCs) specimens and those reported by Cetin and Baykasoğlu for cubic lattice-filled specimens (LM 4 mm, 5 mm, and 6 mm). Notably, the HCS specimen exhibits the highest SEA among all samples. The scutoid from Group B specimens performs favourably relative to the specimens from Cetin and Baykasoğlu [12]. The scutoid and Hc specimens demonstrate competitive SEA values, generally outperforming the 4 mm and 5 mm LM specimens while exhibiting comparable performance to the 6 mm LM samples.

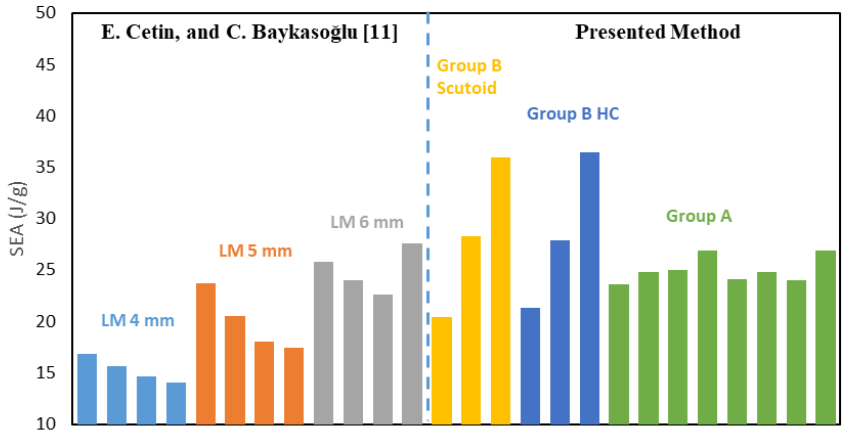

Fig. 13. Comparative analysis of Specific Energy Absorption (SEA) for scutoids & Hc, T50S, HCS, and cubic lattice-filled specimens (LM) with varying thicknesses. Based on [12]

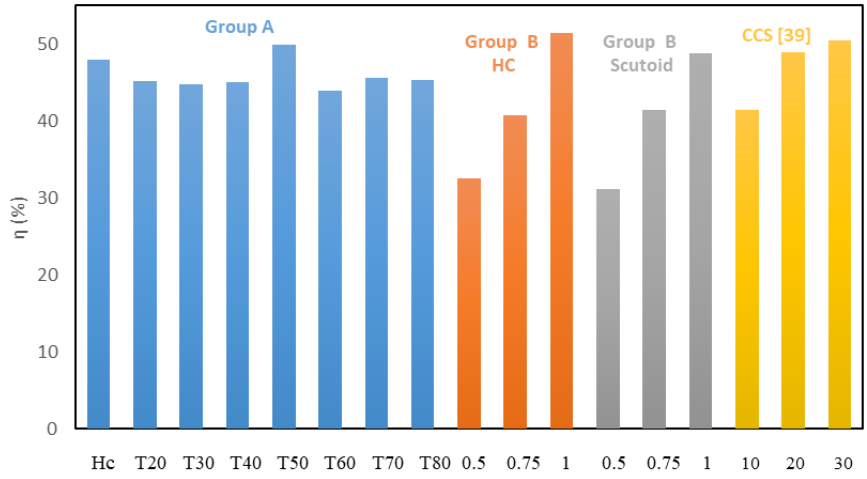

Fig. 14. Comparison of energy absorption efficiency (η) between scutoids, HC, T50, 3D cross–chiral auxetic materials. Based on [46]

Figure 14 presents a comparison of energy absorption efficiency(η), equivalent to CLE, between presented specimens and the 3D cross–chiral auxetic materials studied by Wang et al. [46] Scutoid specimens exhibit η values ranging from approximately 44 to 50 %, while HC specimen displays an η of around 48 %. The T50 specimens from Group B, with varying thicknesses, show a range of η from approximately 32 to 51 %. In comparison, the CCS specimens from Wang et al. [46] demonstrate η values between

roughly 41 and 50 %, indicating a comparable energy absorption efficiency to scutoid specimens.

DOE analysis

To systematically investigate the effects of key geometric parameters on crushing performance, a 2^3 full factorial Design of Experiments (DOE) was employed. The factors investigated were transition point height (h), inner wall thickness (t_{in}), and outer wall thickness (t_{out}), with crushing load efficiency (CLE) and specific energy absorption (SEA) as the primary response variables.

The DOE matrix consisted of eight simulation runs combining two levels of each factor (h = 20, 50 mm; t_{in} = 0.5, 1 mm; t_{out} = 0.5, 1 mm). The FEM simulations were performed according to this full factorial matrix, enabling systematic variation of parameters to capture their individual and interactive effects.

Analysis of Variance (ANOVA) was applied to the simulation results to identify statistically significant factors influencing CLE and SEA. The results confirm that inner wall thickness (t_{in}) is the most influential parameter for both responses. Increasing t_in improved both CLE and SEA due to the higher structural stiffness and delayed local buckling. Outer wall thickness (t_{out}) also played a meaningful role, particularly in SEA enhancement, while transition height (H) contributed less strongly but still showed a noticeable effect.

Updated ANOVA observations based on the 8-point dataset revealed the following relationships:

1. t_{in} ($p < 0.01$) and t_{out} ($p < 0.05$) significantly influenced CLE, accounting for 74 % of the total variance (R^2 = 0.74).
2. t_{in} ($p < 0.01$) and h ($p < 0.05$) dominated SEA variations, with a model fit of R^2 = 0.81.
3. A notable $h \times t_{out}$ interaction ($p < 0.1$) affected SEA, indicating non-linear sensitivity when both parameters increase simultaneously.

Table 7. The effect of the thickness on scutoid energy absorption

h, mm	t_{in}, mm	t_{out}, mm	CLE, %	SEA, J/g
20	0.5	0.5	49	21.38
20	1	0.5	64	23.51
20	0.5	1	62	28.29
20	1	1	73	34.34
50	0.5	0.5	45	20.38
50	1	0.5	70	35.94
50	0.5	1	68	31.84
50	1	1	70	78.31

The DOE matrix (Table 7) demonstrated:

1. The highest SEA occurred at t_{in} = 1 mm, t_{out} = 1 mm, h = 50 mm, with a value of 78.31 J/g.
2. The maximum CLE was also observed at t_{in} = 1 mm, t_{out} = 1 mm, h = 20 mm, yielding 73 %, though a similarly high value of 70 % appeared at h = 50 mm.

These results show that increasing both wall thicknesses enhances energy absorption, while transition height has a mixed influence—raising h improves SEA

substantially in thick-wall configurations but reduces CLE in thin-wall cases, highlighting a performance trade-off.

This DOE approach enabled efficient exploration of the geometric design space using a limited number of FEM simulations. The findings confirm the critical role of inner wall thickness in maximizing both crushing efficiency and energy absorption, while interactions with outer thickness and transition height must be considered for multi-objective optimization of crushing components.

Conclusions

In this research, the crushing behavior and crashworthiness of the scutoid structure have been investigated using numerical and experimental methods. Seven 4-cell self-packing scutoids and a 4-cell equivalent honeycomb were designed, fabricated using PLA filament through additive manufacturing, and tested under quasi-static compression. Numerical models were developed in Abaqus to simulate the crushing behavior, and the results were compared with experimental data, showing good agreement.

Seven four-cell self-packing scutoids and a four-cell equivalent honeycomb structure were designed and analyzed. The key findings of this study are:

1. Scutoid structures exhibited superior energy absorption capabilities compared to traditional honeycomb structures.
2. The energy absorption of scutoids was directly related to the number of folds formed during crushing. More folds resulted in higher energy absorption.
3. The location of the transition point in a scutoid significantly influenced its energy absorption efficiency. Scutoids with a transition point near the middle of their height demonstrated the highest energy absorption efficiency.
4. The honeycomb specimen exhibited a nearly symmetrical buckling shape in both the outer and inner shells.

Furthermore, the investigation into the effect of wall thickness on the T50 scutoid and honeycomb specimens revealed that increasing the wall thickness resulted in higher values for all the evaluated energy absorption indices (EA, PCF, MCF, and CLE). This finding highlights the significant role of wall thickness as a global factor influencing the overall strength and energy absorption capabilities of both the scutoid and honeycomb structures.

In conclusion, both the location of the transition point and the wall thickness are crucial design parameters that significantly impact the energy absorption performance of scutoid structures. By optimizing these parameters, it is possible to enhance the crashworthiness and energy absorption capabilities of these bio-inspired cellular structures for various applications.

CRediT authorship contribution statement

Sepahvand Yasin: writing – original draft, software, validation, formal analysis, investigation, data curation, writing – original draft; **Morshedsolouk Fattaneh:** methodology, data curation, supervision, writing – review & editing; **Moazemi Goudarzi Ali:** conceptualization, methodology, data curation, supervision.

Conflict of interest

The authors declare that they have no conflict of interest.

References

1. Bhutada S, Goel M. Crashworthiness parameters and their improvement using tubes as an energy absorbing structure: an overview. *International Journal of Crashworthiness*. 2022;27(6): 1569–1600.
2. Abdullah NAZ, Sani MSM, Salwani MS, Husain NA. A review on crashworthiness studies of crash box structure. *Thin-Walled Structures*. 2020;153: 106795.
3. Alexander JM. An approximate analysis of the collapse of thin cylindrical shells under axial loading. *The Quarterly Journal of Mechanics and Applied Mathematics*. 1960;13(1): 10–15.
4. Abramowicz W, Jones N. Dynamic axial crushing of circular tubes. *International Journal of Impact Engineering*. 1984;2(3): 263–281.
5. Abramowicz W, Jones N. Dynamic axial crushing of square tubes. *International Journal of Impact Engineering*. 1984;2(2): 179–208.
6. Tak SK, Iqbal MA. Axial compression behavior of thin-walled mild steel tubes subjected to axial impact. *Materials Physics and Mechanics*. 2021;47(5): 681–696.
7. Yamada Y, Banno T, Xie Z, Wen C. Energy absorption and crushing behaviour of foam-filled aluminium tubes. *Materials Transactions*. 2005;46(12): 2633–2636.
8. Zarei H, Kröger M. Optimization of the foam-filled aluminum tubes for crush box application. *Thin-Walled Structures*. 2008;46(2): 214–221.
9. Li Z, Yu J, Guo L. Deformation and energy absorption of aluminum foam-filled tubes subjected to oblique loading. *International Journal of Mechanical Sciences*. 2012;54(1): 48–56.
10. Najibi A, Ghazifard P, Alizadeh P. Numerical crashworthiness analysis of a novel functionally graded foam-filled tube. *Journal of Sandwich Structures and Materials*. 2021;23(5): 1635–1661.
11. Baykasoğlu A, Baykasoğlu C, Cetin E. Multi-objective crashworthiness optimization of lattice structure filled thin-walled tubes. *Thin-Walled Structures*. 2020;149: 106630.
12. Cetin E, Baykasoğlu C. Crashworthiness of graded lattice structure filled thin-walled tubes under multiple impact loadings. *Thin-Walled Structures*. 2020;154: 106849.
13. Tao C, Zhou X, Liu Z, Liang X, Zhou W, Li H. Crashworthiness study of 3D printed lattice reinforced thin-walled tube hybrid structures. *Materials*. 2023;16(5): 1871.
14. Le D, Novak N, Arjunan A, Baroutaji A, Estrada Q, Tran T, Le H. Crashworthiness of bio-inspired multi-stage nested multi-cell structures with foam core. *Thin-Walled Structures*. 2023;182: 110245.
15. Nikkhah H, Baroutaji A, Kazancı Z, Arjunan A. Evaluation of crushing and energy absorption characteristics of bio-inspired nested structures. *Thin-Walled Structures*. 2020;148: 106615.
16. Hosseinpour E, Goudarzi AM, Morshedsolouk F, Gharehbaghi H. Numerical and experimental study on the energy absorption characteristics of thin-walled auxetic cylindrical tubes with varying porosity. *Journal of Materials Research and Technology*. 2025;39: 400-417.
17. Nikkhah H, Baroutaji A, Olabi AG. Crashworthiness design and optimisation of windowed tubes under axial impact loading. *Thin-Walled Structures*. 2019;142: 132–148.
18. Rogala M, Gajewski J. Crashworthiness analysis of thin-walled square columns with a hole trigger. *Materials*. 2023;16(11): 4196.
19. Tran T, Baroutaji A, Estrada Q, Arjunan A, Le H, Thien N. Crashworthiness analysis and optimization of standard and windowed multi-cell hexagonal tubes. *Structural and Multidisciplinary Optimization*. 2021;63: 2191–2209.
20. Taghipoor H, Ghiaskar A, Shavalipour A. Crashworthiness performance of thin-walled square tubes with circular hole discontinuities under high-speed impact loading. *International Journal of Crashworthiness*. 2022;27(6): 1622–1634.
21. El-baky MAA, Allah MMA, Kamel M, Abd-Elaziem W. Energy absorption characteristics of E-glass/epoxy over-wrapped aluminum pipes with induced holes: experimental research. *Scientific Reports*. 2022;12(1): 21097.
22. Borovkov A, Maslov L, Zhmaylo M, Tarasenko F, Nezhinskaya L. Elastic properties of additively produced metamaterials based on lattice structures. *Materials Physics and Mechanics*. 2023;51(7): 42–62.

23. Baroutaji A, Arjunan A, Stanford M, Robinson J, Olabi AG. Deformation and energy absorption of additively manufactured functionally graded thickness thin-walled circular tubes under lateral crushing. *Engineering Structures*. 2021;226: 111324.
24. Nian Y, Wan S, Zhou P, Wang X, Santiago R, Li M. Energy absorption characteristics of functionally graded polymer-based lattice structures filled aluminum tubes under transverse impact loading. *Materials & Design*. 2021;209: 110011.
25. Nian Y, Wan S, Li X, Su Q, Li M. How does bio-inspired graded honeycomb filler affect energy absorption characteristics? *Thin-Walled Structures*. 2019;144: 106269.
26. Gharehbaghi H, Farrokhabadi A. Parametric study of the energy absorption capacity of 3D-printed continuous glass fiber reinforced polymer cruciform honeycomb structure. *Steel and Composite Structures*. 2022; 49(4): 393–405.
27. Gharehbaghi H, Farrokhabadi A, Noroozi Z. Introducing a new hybrid surface strut-based lattice structure with enhanced energy absorption capacity. *Mechanics of Advanced Materials and Structures*. 2024;31(14): 2955–2964.
28. Ghorbani F, Gharehbaghi H, Farrokhabadi A, Bolouri A. Evaluation of the mechanical properties and energy absorption in a novel hybrid cellular structure. *Aerospace Science and Technology*. 2024;148: 109105.
29. Ghorbani F, Gharehbaghi H, Farrokhabadi A, Bolouri A. Investigation of the equivalent mechanical properties of the bone-inspired composite cellular structure: analytical, numerical and experimental approaches. *Composite Structures*. 2023;309: 116720.
30. Galehdari SA, Kadkhodayan M, Hadidi-Moud S. Low velocity impact and quasi-static in-plane loading on a graded honeycomb structure: experimental, analytical and numerical study. *Aerospace Science and Technology*. 2015;47: 425–433.
31. Guo Y, Chen L, Zhu C, Liu H, Pan X, Du B, Zhao W, Li W. Fabrication and axial compression test of thermoplastic composite cylindrical sandwich structures with hierarchical honeycomb core. *Composite Structures*. 2021;275: 114453.
32. Usta F, Scarpa F, Türkmen HS. Edgewise compression of novel hexagonal hierarchical and asymmetric unit cells honeycombs metamaterials. *Materials Today Communications*. 2020;24: 101102.
33. Feng G, Li S, Xiao L, Song W. Energy absorption performance of honeycombs with curved cell walls under quasi-static compression. *International Journal of Mechanical Sciences*. 2021;210: 106746.
34. Xia P, Liu Q, Fu H, Yu Y, Wang L, Wang Q, Yu X, Zhao F. Mechanical properties and energy absorption of 3D printed double-layered helix honeycomb under in-plane compression. *Composite Structures*. 2023;315: 116982.
35. Nikkhah H, Crupi V, Baroutaji A. Crashworthiness analysis of bio-inspired thin-walled tubes based on Morpho wings microstructures. *Mechanics Based Design of Structures and Machines*. 2022;50(10): 3683–3700.
36. Tao Y, Li W, Wei K, Duan S, Wen W, Chen L, Pei Y, Fang D. Mechanical properties and energy absorption of 3D printed square hierarchical honeycombs under in-plane axial compression. *Composites Part B: Engineering*. 2019;176: 107219.
37. Gómez-Gálvez P, Vicente-Munuera P, Tagua A, Forja C, Castro AM, Letrán M, Valencia-Expósito A, Grima C, Bermúdez-Gallardo M, Serrano-Pérez-Higueras Ó. Scutoids are a geometrical solution to three-dimensional packing of epithelia. *Nature Communications*. 2018;9(1): 2960.
38. Dhari RS, Patel NP. On the crushing behaviour of scutoid-based bioinspired cellular structures. *International Journal of Crashworthiness*. 2022;27(4): 945–954.
39. Hu L, Luo Z, Yin Q. Negative Poisson's ratio effect of re-entrant anti-trichiral honeycombs under large deformation. *Thin-Walled Structures*. 2019;141: 283–292.
40. Wei L, Zhao X, Yu Q, Zhang W, Zhu G. In-plane compression behaviors of the auxetic star honeycomb: experimental and numerical simulation. *Aerospace Science and Technology*. 2021;115: 106797.
41. Chen J, Fang H, Liu W, Zhu L, Zhuang Y, Wang J, Han J. Energy absorption of foam-filled multi-cell composite panels under quasi-static compression. *Composites Part B: Engineering*. 2018;153: 295–305.
42. Tasdemirci A, Sahin S, Kara A, Turan K. Crushing and energy absorption characteristics of combined geometry shells at quasi-static and dynamic strain rates: experimental and numerical study. *Thin-Walled Structures*. 2015;86: 83–93.
43. Chen D-h. Crush mechanics of thin-walled tubes. Book. CRC Press; 2018.
44. Jones N. Energy-absorbing effectiveness factor. *International Journal of Impact Engineering*. 2010;37(6): 754–765.
45. Kotełko M, Ferdynus M, Jankowski J. Energy absorbing effectiveness–different approaches. *Acta Mechanica et Automatica*. 2018;12(1): 54–59.
46. Wang Q, Yang Z, Lu Z, Li X. Mechanical responses of 3D cross-chiral auxetic materials under uniaxial compression. *Materials & Design*. 2020; 186:108226.

MATERIALS PHYSICS AND MECHANICS RESEARCH ARTICLE

Submitted: September 16, 2025 Revised: November 1, 2025 Accepted: November 16, 2025

Physical and mechanical performance of surface treated areca fiber and nano alumina reinforced epoxy composites

S.B.R. Devireddy [1]✉, K. Sunil Ratna Kumar[2], R. Lalitha Narayana[3], T. Gopala Rao[1], V. Tara Chand[4]

[1] St. Ann's College of Engineering and Technology, Andhra Pradesh, India

[2] Sir C. R. Reddy College of Engineering, Andhra Pradesh, India

[3] Swarnandhra College of Engineering and Technology, Andhra Pradesh, India

[4] R.V.R. & J.C. College of Engineering, Andhra Pradesh, India

✉ sivabhaskararao@gmail.com

ABSTRACT

Areca palm stem fiber reinforced epoxy composites modified with alkaline surface treatment and nano alumina were investigated to evaluate improvements in physical and mechanical performance. Composite laminates were fabricated by the hand layup method with 20 wt. % areca palm stem fiber, while sodium hydroxide treatment levels (0, 3, 6, and 9 %) and nano alumina loadings (0, 2.5, 5, and 7.5 wt. %) were varied. The fabricated composite specimens containing 5 wt. % nano alumina, subjected to varying treatment concentrations, consistently exhibited reduced void content and enhanced density. Mechanical characterization showed a significant enhancement in strength and toughness due to the combined effects of fiber surface activation and nanoparticle reinforcement. A 6 % NaOH treatment with 5 wt. % nano alumina resulted in a 53.60 % increase in tensile strength and a 43.05 % increase in flexural strength compared to untreated composites. Maximum impact energy (5.81 J) and hardness (59.5 HV) were obtained at 7.5 wt. % nano alumina with 6 % NaOH-treated fibers. Scanning electron microscopy revealed reduced fiber pull-out and improved interfacial bonding, though voids and microcracks were observed at higher filler loadings.

KEYWORDS

areca fiber • mechanical properties • nanofiller • NaOH treatment • scanning electron microscope

Citation: Devireddy SBR, Sunil Ratna Kumar K, Lalitha Narayana R, Gopala Rao T, Tara Chand V. Physical and mechanical performance of surface treated areca fiber and nano alumina reinforced epoxy composites. *Materials Physics and Mechanics*. 2025;53(6): 82–96.
http://dx.doi.org/10.18149/MPM.5362025_7

Introduction

Natural plant fibers are abundantly available worldwide and offer numerous advantages, including high specific strength, renewability, excellent biodegradability, reduced energy processing requirements, low production costs, and favourable mechanical characteristics [1]. While natural fibers offer numerous advantages, they also present certain limitations, including weak interfacial adhesion with polymer matrices, high moisture absorption, and variability in mechanical properties [2,3]. These limitations pose a significant challenge, prompted extensive research into chemical and physical surface modification techniques to improve compatibility and maximize mechanical properties. Various chemical treatments such as alkali, benzyl chloride, silane, and acetylation have been employed to

modify fiber surfaces, mechanical interlocking and enhancing wettability with the polymer matrix [4,5]. Among chemical treatments, alkali treatment process enhances fiber surface roughness and removes hemicellulose and lignin, which in turn increases the number of reactive hydroxyl groups, thereby improving interfacial bonding with the polymer matrix [6]. Yousif et al. [7] demonstrated that alkaline treatment of kenaf fibers enhance the flexural strength by approximately 36 %, compared to 20 % improvement in untreated fibers through wax removal and surface roughening, which enhance interfacial adhesion and stress transfer efficiency.

Areca fiber is extracted from the husk of Areca catechu (betel nut), an abundant agricultural byproduct. In tropical regions like India, where betel nut cultivation is widespread, these fibers represent a substantial renewable resource with significant annual production potential [8,9]. Areca fibers exhibit excellent mechanical properties, including high strength, environmentally friendly, and an impressive strength-to-weight ratio, while also being cost-effective, biodegradable, and non-toxic [10]. Nayak and Mohanty [11] investigated the mechanical, mechanical behavior of thermoplastic composites reinforced with randomly oriented short areca sheath fibers. Their findings indicated that treating the areca fiber with benzyl chloride significantly improved its compatibility with the matrix, and an optimum fiber loading of 27 wt. % led to enhanced overall composite performance. Rahman et al. [12] reported that alkali treatment notably improved the tensile and flexural properties of coir and betel nut fiber composites in comparison with untreated counterparts. Yousif and Nirmal [13] observed that chemical treatment improved flexural properties by 28 % and increased hardness by 6 % relative to unreinforced polyester matrix.

The hybridization of natural fiber reinforced polymer composites with inorganic particulate fillers resulted in substantial enhancements in mechanical performance, physical characteristics, and wear resistance relative to traditional composite systems [14–17]. The incorporation of nanoparticles such as nano silica [18], nano alumina [19], carbon nanotubes [20], and nano titanium dioxide [21] into natural fiber reinforced epoxy composites is a significant research focus, aiming to combine the environmental advantages of natural fibers with the enhanced mechanical performance offered by nanoparticles. The addition of nanoparticles (e.g., nano alumina) can substantially enhance the mechanical performance of composites through improved filler-matrix interfacial bonding and more efficient stress distribution [22]. Kumar et al. [23] demonstrated that incorporating 3 wt. % nano clay into bamboo/epoxy laminates increased their flexural and tensile strengths by 27% and 40%, respectively, compared to the pure composite. Dhanasekar et al. investigated the effect of nano silica particles on the density, mechanical, and tribological properties of sisal/hemp hybrid nanocomposites. Their results demonstrated that a 6 wt. % nano silica content significantly enhanced tensile strength (48.13 % increase) and impact strength (1.9 times higher) compared to unreinforced composites [24]. Chowdary et al. [25] demonstrated that incorporating nano silica enhances the tensile and flexural performance of sisal and kevlar fiber reinforced polyester composites, with maximum tensile and flexural strengths observed at a 4 wt. % concentration. Patnaik et al. [26] studied the mechanical performance of epoxy composite reinforced with needle punch nonwoven jute fiber and

nano alumina. At 5 wt. % filler content, the composite exhibited a 30 % increase in tensile strength and 20% increases in flexural strength compared to the untreated composite.

The effects of nano alumina and sodium hydroxide treatments on the mechanical characteristics of areca fiber reinforced epoxy composites have not been explored in the literature. This research systematically examines the combined effects of sodium hydroxide treatment (at concentrations of 0, 3, 6, and 9 %) and nano alumina reinforcement (0, 2.5, 5, and 7.5 wt. %) on the physical and mechanical characteristics of epoxy-based areca fiber composites. The findings will provide fundamental insights for optimizing the mechanical performance and long term durability of APS fiber reinforced epoxy composites, facilitating their adoption in demanding industrial applications.

Materials and Methods

Materials

Areca fibers were selected as the reinforcement phase because they are derived from renewable biological sources, are naturally abundant, and intrinsic mechanical properties such as high specific strength and modulus. The Areca palm (Areca catechu) stems used in this study were obtained from a plantation in Chirala, Andhra Pradesh, India. The collected stems were subjected to a 14-day water retting treatment. Subsequently, the retted stalks were mechanically separated using a wooden mallet to extract the fibers. The extracted fibers were thoroughly rinsed under running water and subsequently air dried at room temperature for 48 h to eliminate residual moisture. Nano alumina particles were selected as the filler material due to their well-established ability to enhance mechanical properties and improve wear resistance in polymer matrices. Nano alumina particles used in the study were sourced from a supplier Fiber Source in Chennai, India. Figure 1 shows the reinforcement materials. Table 1 presents the physical characteristics of the nano alumina filler, while Table 2 summarizes the physical and mechanical properties along with the chemical composition of the areca palm stem fibers [8,27,28]. The epoxy resin matrix and hardener, procured from Sree Industrial Composite Products (Hyderabad, India), had a specified density of 1.1 g/cm^3. The densities of APS fibers and nano alumina were recorded as 1.34 and 3.96 g/cm^3, respectively.

Fig. 1. Reinforcement material (a) nano alumina and (b) APS fiber

Table 1. Properties of nano alumina powder

Property	Units	Value
Particle density	(g/cm^3)	3.96
Surface area	(m^2/g)	5.00–20.00
Thermal stability	°C	>1200
Thermal conductivity	W/m·K	30.00–35.00
Average particle size	nm	20–100
Crystal phase		α
Solubility in water	mg/L	0.01–0.1
Color		Off white

Table 2. Properties of areca palm stem fiber

Property	Units	Value
Density	g/cm^3	1.34
Cellulose	%	65.02
Hemicelluloses	%	8.26
Lignin	%	18.62
Tensile strength	MPa	320.00–876.00
Young's modulus	GPa	42.00–48.00
Elongation at failure	%	1.47–1.48

Sodium hydroxide treatment of fibers

Sodium hydroxide (NaOH) treatment was employed to modify areca fiber surfaces by enhancing their roughness and improving interfacial adhesion with the epoxy matrix. The fibers underwent alkali treatment using varying concentrations of sodium hydroxide (NaOH) (0, 3, 6, and 9 %). This alkali treatment was carried out to partially remove hemicellulose and lignin from the fiber surface. As a result, the surface roughness increased, which improved mechanical interlocking at the fiber–matrix interface. The surface treatment process involved immersing pre-cleaned areca fibers in an aqueous sodium hydroxide solution at room temperature (28 ± 2 °C) for 4 h to modify the fiber surface. After treatment, the fibers were thoroughly rinsed with distilled water until a neutral pH was reached, ensuring the removal of any residual alkali. Finally, the fibers were oven-dried at 70 ± 2 °C for 24 h to eliminate all moisture before their incorporation into composites.

Composites fabrication

The composite fabrication involved reinforcing surface modified continuous APS fibers into an epoxy matrix with nano alumina as a filler. Epoxy resin and hardener were mixed in a 10:1 ratio by weight. For composites containing nano alumina, the specified weight percentages of nanoparticles (2.5, 5, and 7.5 wt. %) were added to the resin, and the resulting resin–nanoparticle mixture was subjected to mechanical stirring for 5 min, followed by sonication for 30–45 min in pulse mode to ensure homogeneous dispersion and prevent nanoparticle agglomeration. The treated APS fibers were incorporated into the epoxy matrix using the hand layup technique. Prior to fabrication, a mold release agent was applied to the mold surface. The epoxy resin and layered APS fibers were then alternately arranged, ensuring thorough fiber wetting and eliminating air bubbles through controlled rolling process. The composites were then cured under light pressure

of 0.5 MPa at room temperature (28 ± 3 °C) for 24 h, followed by post-curing for physical and mechanical tests. Figure 2 displays the fabricated composite specimens for subsequent physical and mechanical testing. The process was systematically repeated for different sodium hydroxide (NaOH) treatment concentrations and nano alumina filler loadings. Table 3 summarizes the complete experimental design, including all parameter variations and composite compositions.

Fig. 2. Fabricated composite specimens

Table 3. Experimental parameters and their compositions

Sample	NaOH concentrations	Areca (wt. %)	Nano alumina (wt. %)	Total reinforcement	Matrix (wt. %)
C1	0	20	0	20.0	80.0
C2			2.5	22.5	77.5
C3			5.0	25.0	75.0
C4			7.5	27.5	72.5
C5	3	20	0	20.0	80.0
C6			2.5	22.5	77.5
C7			5.0	25.0	75.0
C8			7.5	27.5	72.5
C9	6	20	0	20.0	80.0
C10			2.5	22.5	77.5
C11			5.0	25.0	75.0
C12			7.5	27.5	72.5
C13	9	20	0	20.0	80.0
C14			2.5	22.5	77.5
C15			5.0	25.0	75.0
C16			7.5	27.5	72.5

Physical and mechanical testing

The developed APS fibers reinforced epoxy composites were subjected to extensive physical and mechanical characterization to evaluate their performance properties. FTIR

(Fourier transform infrared) spectroscopy was employed to characterize chemical composition alterations and surface functional group modifications in both untreated and NaOH treated fibers. FTIR spectra were acquired in the 4000–400 cm^{-1} spectral range using [specify instrument model/model number if available] spectroscopy to characterize functional groups and assess the effects of alkali treatment on fiber surface chemistry. The analysis provided critical evidence of chemical modification success and revealed correlations between surface chemistry and composite performance. The theoretical density ρ_{ct} of the APS fibers reinforced composites was determined using the rule of mixtures, based on the weight fractions and densities of the individual constituents as shown in Eq. (1). The composite density was measured according to ASTM D792 using the water displacement method. The calculation of theoretical density facilitated a comparison with the experimental density ρ_{ca} to estimate the void content V_v in the composites as shown in Eq. (2):

$$\rho_{\mathrm{ct}} = \frac{1}{(W_A/\rho_A) + (W_n/\rho_n) + (W_m/\rho_m)}, \quad (1)$$

$$V_v = \frac{\rho_{ct} - \rho_{ca}}{\rho_{ct}}, \quad (2)$$

where W_A, W_n, and W_m are weight fractions of areca, nano alumina, and matrix, respectively; ρ_A, ρ_{n}, ρ_m is density of areca, nano alumina, and matrix, respectively.

The mechanical properties of the fabricated APS fibers reinforced epoxy composites were comprehensively evaluated. Tensile and flexural properties were evaluated using a tensometer testing machine. Tensile properties were characterized according to ASTM D3039-76 using rectangular specimens (153 × 12.7 × 4 mm^3). Testing was conducted at a constant crosshead speed of 5 mm/min until failure, with strain measured using an extensometer to determine both tensile strength and elastic modulus. Flexural properties were determined via three-point bending tests conducted in accordance with ASTM D790-07. Rectangular specimens (125 × 12.7 × 4 mm^3) were loaded at a constant crosshead speed of 5 mm/min, with flexural strength and modulus calculated from the resulting load and displacement. The impact resistance of the hybrid composite samples was evaluated using the Izod impact tester. Impact resistance was evaluated using an Izod impact tester according to ASTM D256 standards, with notched specimens (64 × 12.7 × 4 mm^3). Surface hardness measurements were performed independently using a Vickers microhardness tester. A minimum of five specimens per composite configuration were tested for each mechanical property. Mean values with corresponding standard deviations are reported to ensure data reliability and enable statistical comparison. Finally, scanning electron microscopy (SEM) was used to evaluate the fracture surface morphology, which revealed various defects such as fiber pull-outs, interfacial bonding quality, nano-alumina dispersion, internal cracks, and voids.

Results and Discussion

Fourier transform infrared spectroscopy analysis

FTIR spectroscopy analysis was performed to investigate the chemical modifications in APS fibers following NaOH treatments at varying concentrations (0, 3, 6, and 9 %). Figure 3 displays the FTIR spectra, where characteristic absorption peaks corresponding to specific functional groups in the fiber composition are clearly identified. The broad

absorption peak observed around 3445 cm^{-1} is attributed to the O-H stretching vibrations, which correspond to the hydroxyl groups present in cellulose and hemicellulose. With increasing NaOH concentration, the intensity of these peak decreases, indicating the partial removal of hemicellulose and the exposure of cellulose components. The peak at 2891 cm^{-1} corresponds to C-H stretching vibrations, primarily from lignin and cellulose. A reduction in peak intensity with higher NaOH concentrations suggests effective delignification of the fibers. Another significant peak is observed at 1632 cm^{-1}, corresponding to the C=O stretching vibrations associated with lignin and other carbonyl-containing compounds. The decrease in intensity at this peak with increasing NaOH treatment concentration confirms the removal of lignin content, enhancing the fiber-matrix bonding potential. The differences in the FTIR spectra between untreated and treated fibers suggest that alkali treatment effectively modifies the fiber surface chemistry by removing impurities and enhancing the availability of reactive hydroxyl groups. This modification leads to improved interfacial bonding between the fibers and epoxy matrix, contributing to enhanced mechanical properties of the composites. Overall, the FTIR analysis confirms that alkali treatment positively affects the chemical structure of APS fibers.

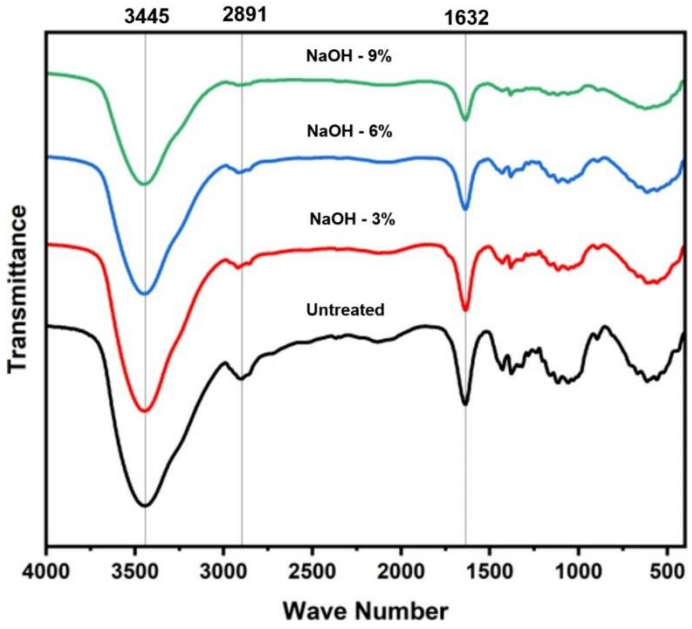

Fig. 3. FTIR spectra of untreated and treated APS fibers

Density and void content

Table 4 presents the density and void content analysis of APS fiber reinforced epoxy composites, evaluating the effects of different surface treatments and varying weight percentages of nano alumina filler. Among all tested compositions, the untreated APS fiber/epoxy composite containing 7.5 wt. % nano alumina filler had the maximum experimental density 1.141 g/cm^3. With sodium hydroxide (NaOH) treatment, the composite density progressively increased to 1.149 g/cm^3 (3 wt. % NaOH), 1.153 g/cm^3 (6 wt. % NaOH), and 1.146 g/cm^3 (9 wt. % NaOH), indicating a positive correlation between alkali concentration and densification. This increase in density suggests that NaOH treatment, by enhancing surface roughness and wettability, promotes superior

fiber–matrix adhesion, thereby reducing void content and improving composite compaction. The 9 % NaOH treatment resulted in a noticeable decrease in density, likely due to over-treatment damaging the cellulose crystalline structure and reduced fiber flexibility, which hindered proper matrix wetting and led to increased void formation [24]. The void content, a critical factor influencing the mechanical performance of composites, consistently decreased as the concentration of NaOH increased, until an optimal treatment level was achieved. Composite specimens incorporating 5 wt. % nano alumina, under varying treatment concentrations, consistently exhibited reduced void percentages of 24.75, 22.76, 22.11, and 21.63 %, respectively, in comparison to unfilled composites. This observation directly indicates an improvement in fiber-matrix interfacial adhesion, attributable to the alkali treatment's efficacy in eliminating surface impurities and augmenting fiber roughness. The observed decrease in void content with increasing nanofiller concentration is consistent with established scientific findings. This reduction in void content is mainly attributed to the high surface area-to-volume ratio of nanoparticles, which facilitates improved void filling and results in a denser, more compact composite matrix [29]. At higher void content, typically resulting from poor impregnation, the mechanical properties of composites can be severely compromised. These voids act as stress concentration points and reduce the material's ability to effectively transfer loads.

Table 4. Densities and void percentage of the nano alumina filled APS fiber composites

Sample	Theoretical density, g/cm^3	Actual density, g/cm^3	Void percentage, %
C1	1.141	1.067	6.481
C2	1.163	1.097	5.687
C3	1.185	1.123	5.284
C4	1.209	1.141	5.578
C5	1.141	1.076	5.672
C6	1.163	1.104	5.059
C7	1.185	1.130	4.643
C8	1.209	1.149	4.967
C9	1.141	1.082	5.195
C10	1.163	1.108	4.709
C11	1.185	1.134	4.327
C12	1.209	1.153	4.586
C13	1.141	1.078	5.467
C14	1.163	1.101	5.294
C15	1.185	1.127	4.951
C16	1.209	1.146	5.174

Tensile properties

The influence of NaOH treatment on the tensile strength and modulus of APS fiber reinforced epoxy composites is shown in Figs. 4 and 5, comparing untreated and chemically treated fibers across nano alumina filler content of 0, 2.5, 5, and 7.5 %. The tensile strength of APS fiber reinforced epoxy composites was significantly influenced by the nano alumina filler content and chemical treatments applied to the APS fibers. The tensile properties of the APS fiber-reinforced composites increase with nano alumina content, reaching an optimum at 5 wt. %, after which the properties

decrease at 7.5 wt. % filler loading. The integration of nano alumina into APS fiber reinforced epoxy composites has been shown to substantially reduce void formation, consequently leading to an enhancement of their tensile properties. At this optimal 5 wt. % nano alumina concentration, the peak tensile strength values recorded were 84.54 MPa for untreated composites, 90.42 MPa for 3 % NaOH treated composites, 97.63 MPa for 6 % NaOH-treated composites, and 92.59 MPa for 9 % NaOH treated composites. Compared to unfilled and untreated composites, the addition of 5 wt. % nano alumina led to tensile strength enhancements of 33.01, 42.25, 53.60, and 45.67 % for composites with untreated fibers, and those treated with 3, 6, and 9 % NaOH, respectively.

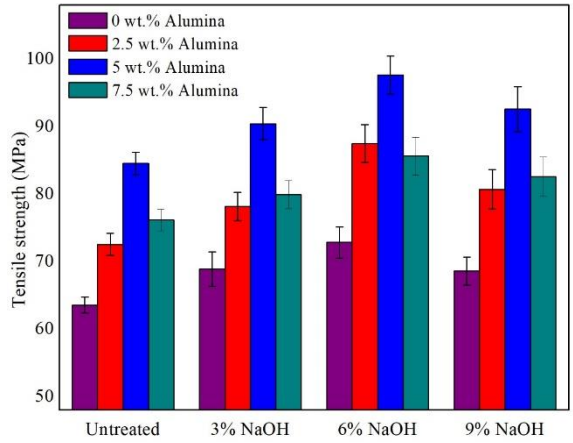

Fig. 4. Impact of nanofiller and surface treatment on tensile strength of composite

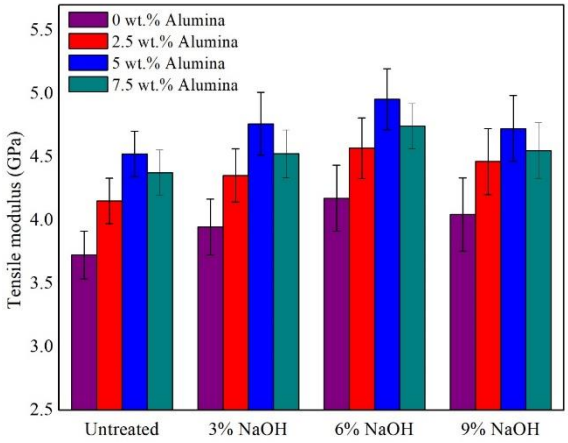

Fig. 5. Impact of nanofiller and surface treatment on tensile modulus of composites

By modifying the fiber-matrix interface, surface treatments on areca fibers strengthen adhesion and optimize stress transfer, resulting in enhanced ductility and overall mechanical performance. The 6 % NaOH-treated APS fiber composites exhibited optimal tensile modulus (4.956 GPa) at 5 wt. % filler loading. This tensile modulus value gradually decreased with other loadings: 4.743 GPa (7.5 wt. %), 4.57 GPa (2.5 wt. %), and 4.174 GPa (0 wt. %). The results revealed significant differences in tensile properties between untreated and NaOH treated APS fiber composites, with the extent of improvement varying systematically with NaOH concentration (3, 6, and 9 %). The study observed a reduction in tensile strength and tensile modulus of APS fiber reinforced epoxy composites at a 9 % NaOH concentration. This reduction is attributed to the removal of larger amounts of lignin, pectin, and other amorphous components at higher NaOH levels. Beyond an optimal concentration, such aggressive chemical treatment can degrade the cellulose structure itself, compromising fiber integrity [30]. This structural damage weakens the intrinsic tensile strength of the individual fibers, resulting in a direct decline in the composite's overall tensile properties.

Flexural properties

The flexural properties of APS fiber reinforced epoxy composites were evaluated as a function of surface treatment and nano alumina filler content (0–7.5 wt. %), with the results presented in Figs. 6 and 7. Optimal filler content was achieved with 5 wt. % nano

alumina, leading to the highest flexural strength and modulus values across all fiber treatments. The composites with 5 wt. % nano alumina exhibited the highest the flexural strengths observed were 128 ± 7.8 MPa for untreated APS fiber, 137 ± 5.4 MPa for 3 % NaOH treated, 146 ± 5.2 MPa for 6 % NaOH treated, and 141 ± 4.9 MPa for 9 % NaOH treated composites. At a 7.5 wt. % nano alumina loading, particle agglomeration becomes prominent, leading to weakened interfacial bonding, non-uniform dispersion, and increased void formation. These factors collectively contribute to the observed reduction in flexural properties compared to composites with lower filler concentrations. Compared to untreated and unfilled composites, the incorporation of 5 wt. % nano alumina resulted in flexural strength improvements of 26.02, 34.61, 43.05, and 38.47 % for the untreated, 3 % NaOH treated, 6 NaOH treated, and 9 % NaOH treated composites, respectively.

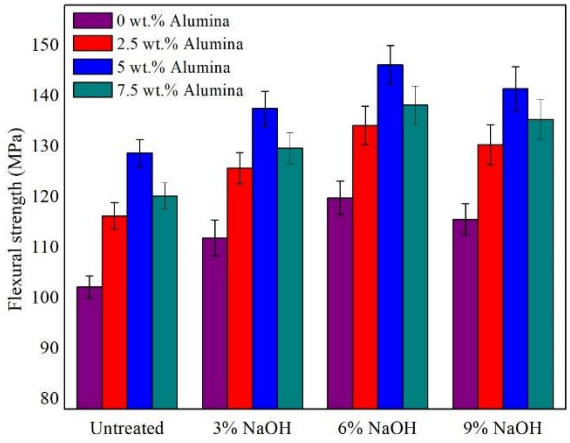

Fig. 6. Effect of nanofiller and surface treatment on flexural strength of composites

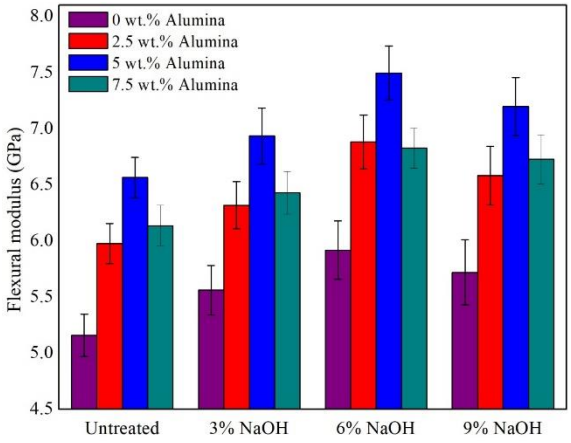

Fig. 7. Effect of nanofiller and surface treatment on flexural modulus of composites

The 5 wt. % of nano alumina filled APS fiber composites showing maximum flexural modulus values of about 6.563, 6.934, 7.496 and 7.196 GPa for untreated, 3 % NaOH, 6 % NaOH, and 9 % NaOH treated composites, respectively. Among these, the 6 % NaOH-treated composites showed the most significant improvement, with a 13.56 and 14.21 % increase in flexural strength and modulus, respectively, compared to the untreated composites. The results suggest the 6 % NaOH treatment is an optimal balance between surface modification and fiber integrity. However, the 9 % NaOH treated composites exhibited reduced flexural properties due to excessive delignification and potential fiber degradation at higher alkali concentrations. The optimal reinforcement observed at a 5 wt. % nano alumina loading is consistent with previously reported findings for similar nanofiller reinforced polymer composites [25,31]. This consistency suggests a common threshold for effective nanoparticle dispersion, beyond which agglomeration may occur, leading to a decline in composite properties.

Impact energy

Figure 8 displays the impact energy results for untreated and chemically treated APS fiber composites at varying nano-alumina filler concentrations (0, 2.5, 5, and 7.5 %). Among all tested compositions, the APS fiber composites containing 7.5 wt. % nano alumina had the highest impact energy. This increase in impact energy is attributed to the nanoparticles'

ability to deflect and absorb crack propagation, thereby increasing the material's resistance to sudden impacts [2]. At 7.5 wt. % nano alumina loading, the composites exhibited maximum impact energies of 5.32 (untreated), 5.68 (3 % NaOH treated), 5.81 (6 % NaOH treated), and 5.64 J (9 % NaOH treated), corresponding to a 6.8 % increase in impact energy for alkali-treated specimens compared to untreated composites. Composites incorporating 6 % NaOH treated fibers exhibited a marked increase in impact strength (5.81 kJ/m^2), substantially outperforming both untreated fibers and those treated with lower NaOH concentrations. The higher impact strength at this treatment level aligns with previous studies reporting that moderate alkali treatment enhances fiber–matrix bonding, whereas excessively high concentrations can degrade the fiber structure and reduce toughness [32].

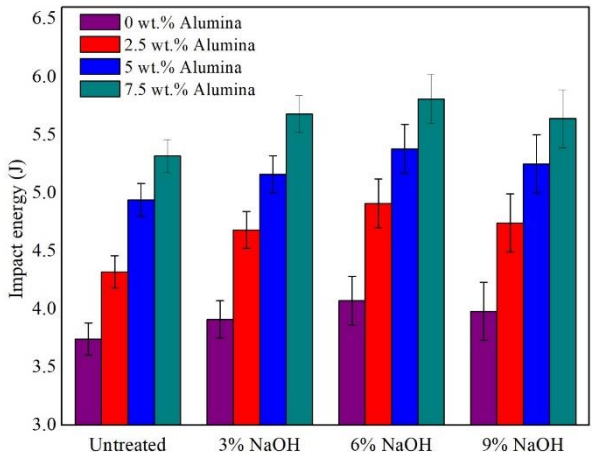

Fig. 8. Effect of nanofiller and surface treatment on impact energy of composites

Surface hardness

Vickers microhardness testing was utilized to evaluate the surface hardness of the APS fiber reinforced composites, offering quantitative insight into their resistance to plastic deformation under standardized indentation loads. Figure 9 presents a comparative analysis of surface hardness across various NaOH treatment conditions, evaluated for both unfilled composites and those reinforced with nano alumina. Surface hardness continued to increase with increasing nano alumina content, reaching its highest value at 7.5 wt. % loading, which confirms its effectiveness as a reinforcing filler. The increased surface hardness of the composites with higher weight fractions is primarily due to the inherent hardness of the alumina nanoparticles. These nanoparticles act as effective stiffening agents within the polymer matrix by restricting the mobility of polymer chains, consequently enhancing the material's resistance to surface penetration [33]. Surface hardness measurements revealed maximum values of 55.2 (untreated), 57.4 (3 % NaOH), 59.5 (6 % NaOH), and 58.7 HV (9 % NaOH) for composites containing 7.5 wt. % nano alumina. The 6 % NaOH treated composite exhibited the highest hardness, showing improvements of 7.98 % over untreated, 3.65 % over 3 % NaOH treated, and 1.36 % over 9 % NaOH treated specimens. The 6 % NaOH treated composites with 7.5 wt.% nano alumina exhibited superior surface hardness (59.5 HV), highlighting a synergistic effect between the optimized fiber surface modification and nanoparticle reinforcement.

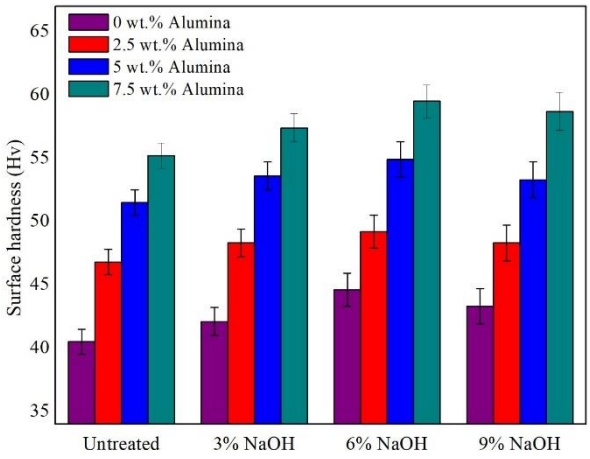

Fig. 9. Effect nanofiller and surface treatment on hardness of composites

Surface morphology

Scanning electron microscopy (SEM) analysis was performed to examine the surface morphology of untreated and NaOH treated APS fiber, as well as the fracture surfaces of the resulting APS fiber reinforced epoxy composites, to evaluate the effects of nano alumina and surface treatment on fiber microstructure and composite failure mechanisms. Figure 10(a) displays the SEM images of untreated APS fiber, revealing a relatively rough surface with visible waxy layers, impurities, and amorphous constituents such as hemicellulose and lignin. These surface characteristics can adversely affect reinforcement and matrix adhesion. Figure 10(b) presents the SEM micrographs of NaOH treated APS fiber, revealing significant modifications in the fiber surface morphology. The alkali treatment effectively removes pectin, impurities, and hemicelluloses, yielding a cleaner, rougher, and more fibrillated surface. This enhanced roughness and exposure of cellulosic fibrils improve fiber wettability with the epoxy matrix and facilitate mechanical interlocking, ultimately strengthening interfacial adhesion.

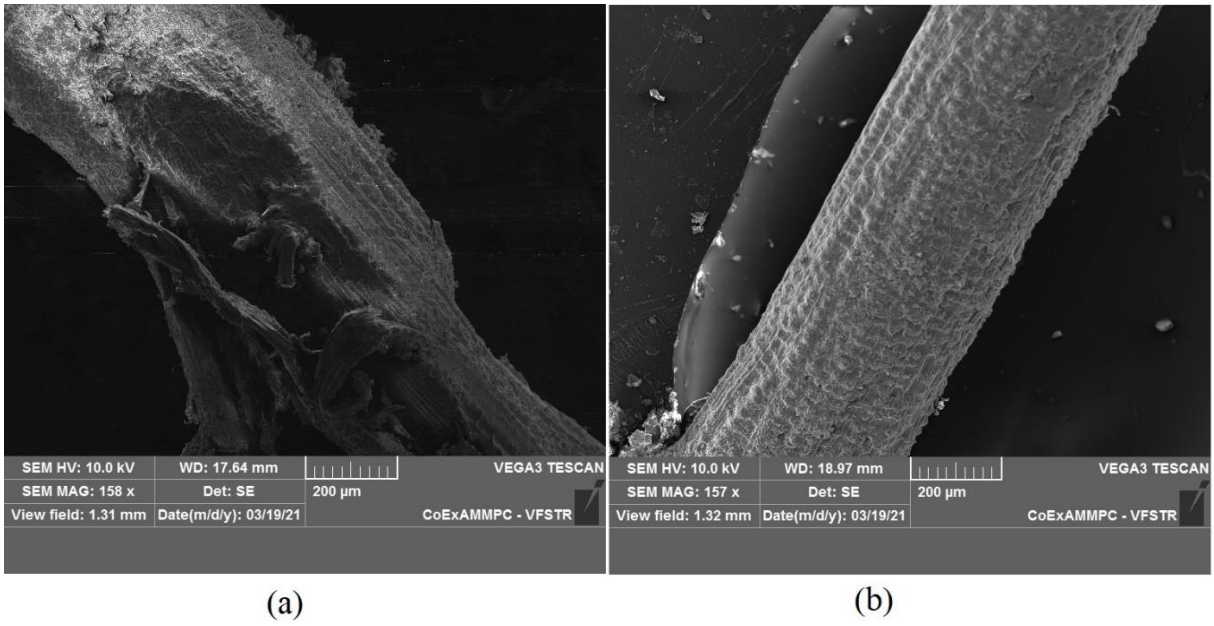

Fig. 10. SEM images of APS fiber (a) untreated, (b) 6% NaOH treated

Figure 11 shows the SEM images assessing the dispersion of nano alumina particles within the epoxy matrix. Figure 11(b,c) represents the uniform distribution of nanoparticles at 5 wt. % of nano alumina concentration for achieving optimal mechanical properties. In contrast, Fig. 11(d) shows the 7.5 wt. % nano alumina sample, where agglomeration of nanoparticles was observed. Such particle agglomeration can introduce defects, reduce the effective filler–matrix interfacial area, act as stress concentration points, and initiate microcracks. The micrographs display matrix fiber breakage, deformation, and crack propagation, providing direct visual evidence that supports the observed tensile properties.

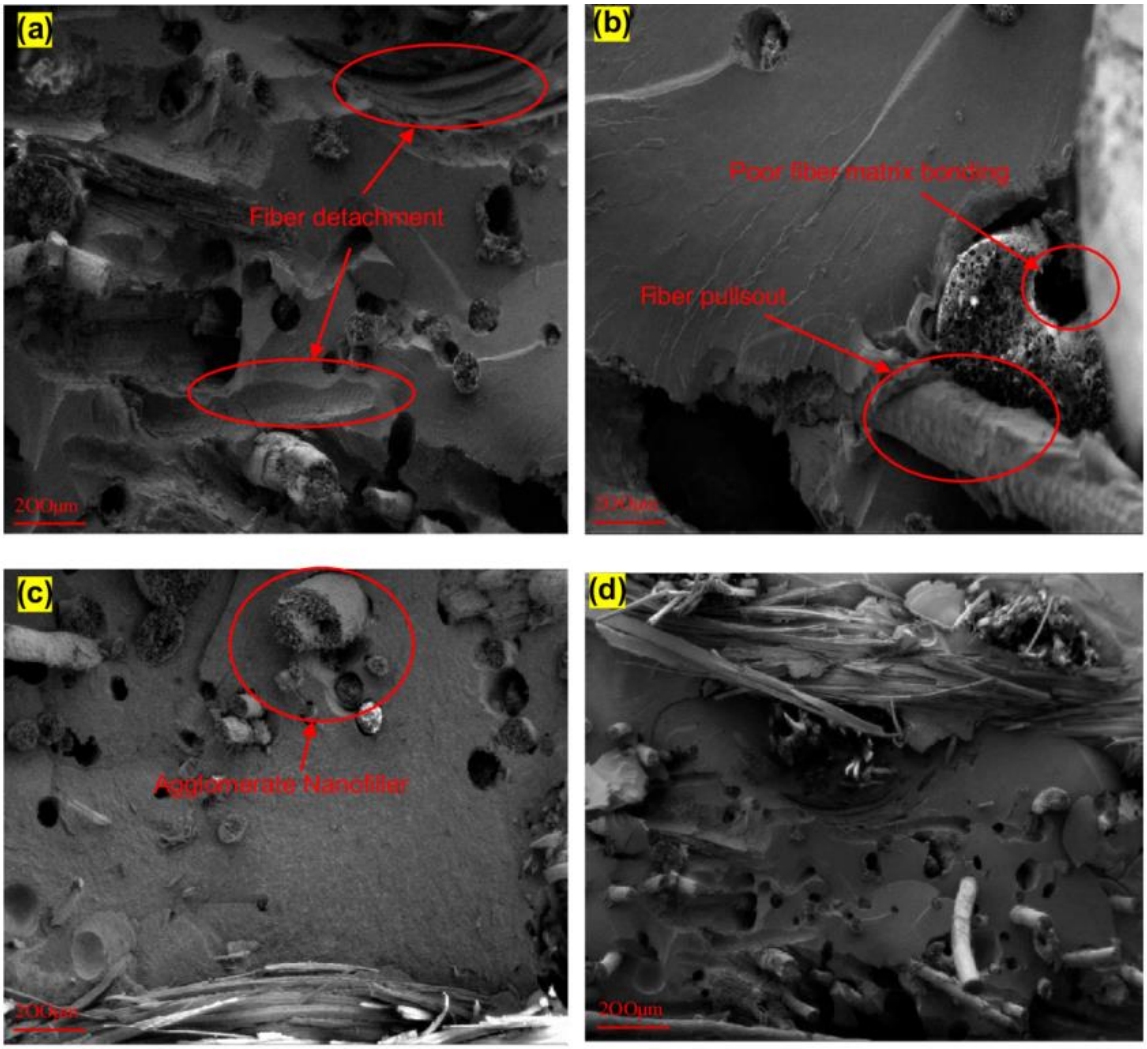

Fig. 11. SEM spectrographs of the tensile fracture surface of composites with (a) 0 % nano filler, (b) 2.5 % nano filler, (c) 5 % nano filler and (d) 7.5 % nano filler

Conclusion

This study evaluated the combined effects of alkali surface treatment and nano alumina reinforcement on the performance of APS fiber–reinforced epoxy composites. The results confirmed that both fiber surface modification and nanoparticle dispersion play critical roles in determining the mechanical response of the material. The main scientific conclusions are as follows:

1. Alkali treatment at 6 % NaOH provided the most effective fiber surface modification, producing a cleaner, fibrillated surface that enhanced fiber-matrix interfacial adhesion and stress transfer.
2. A synergistic reinforcement effect was observed between 6 % NaOH treatment and nano alumina addition, resulting in mechanical improvements greater than those achieved by either treatment alone.
3. The composite containing 5 wt. % nano alumina with 6 % NaOH-treated fibers delivered the highest overall tensile and flexural performance, with increases of 53.6 and 43.05 %, respectively, compared to the untreated composite.
4. Impact resistance and surface hardness were maximized at 7.5 wt. % nano alumina, indicating that energy absorption and indentation resistance benefit from higher filler loading, even though tensile and flexural properties begin to decline beyond 5 wt. % due to particle agglomeration.
5. Performance deterioration at 9 % NaOH and nano alumina levels above 5 wt.% confirmed two key failure mechanisms: (i) excessive alkali treatment damages the cellulose structure of fibers, and (ii) excess nanoparticles agglomerate, reducing interfacial area and inducing stress concentration.

CRediT authorship contribution statement

Siva Bhaskara Rao Devireddy: conceptualization, methods, writing – original draft; **Khandavalli Sunil Ratna Kumar**: data curation, formal analysis, writing – review & editing; **Ravi Lalitha Narayana**: investigation, resources, writing – review & editing; **Gopala Rao Thellaputta**: methodology, validation, writing – review & editing; **Vadlamudi Tara Chand**: project administration, supervision, writing – review & editing.

Conflict of interest

The authors declare that they have no conflict of interest.

References

1. Alotaibi MD, Alshammari BA, Saba N, Alothman OY, Sanjay MR, Almutairi Z, Jawaid M. Characterization of natural fiber obtained from different parts of date palm tree (Phoenix dactylifera L.). *Int J Biol Macromol.* 2019;135: 69–76.
2. Rajeshkumar G, Hariharan V, Indran S, Sanjay MR, Siengchin S, Maran JP, Al-Dhabi NA, Karuppiah P. Influence of Sodium Hydroxide (NaOH) Treatment on Mechanical Properties and Morphological Behaviour of Phoenix sp. Fiber/Epoxy Composites. *J Polym Environ.* 2021;29: 765–774.
3. Munde Y, Shinde AS, Siva I, Anearo P. Assessment of physical and vibration damping characteristics of sisal/PLA biodegradable composite. *Materials Physics and Mechanics.* 2023;51(7): 107–116.
4. Kabir MM, Wang H, Lau KT, Cardona F. Chemical treatments on plant-based natural fibre reinforced polymer composites: An overview. *Compos B Eng.* 2012;43(7): 2883–2892.
5. Godara MSS. Effect of chemical modification of fiber surface on natural fiber composites: A review. *Mater Today Proc.* 2019;18: 3428–3434.
6. Verma D, Goh KL. Effect of Mercerization/Alkali Surface Treatment of Natural Fibres and Their Utilization in Polymer Composites: Mechanical and Morphological Studies. *Journal of Composites Science.* 2021;5(7): 175.
7. Yousif BF, Shalwan A, Chin CW, Ming KC. Flexural properties of treated and untreated kenaf/epoxy composites. *Mater Des.* 2012;40: 378–385.
8. Venkateshappa SC, Jayadevappa SY, Puttiah PKW. Mechanical behavior of areca fiber reinforced epoxy composites. *Advances in Polymer Technology.* 2012;31(4): 319–330.

9. Kishore Chowdari G, Krishna Prasad DVV, Devireddy SBR. Physical and thermal behaviour of areca and coconut shell powder reinforced epoxy composites. *Mater Today Proc.* 2020;26: 1402–1405.
10. Dhanalakshmi S, Ramadevi P, Basavaraju B. A study of the effect of chemical treatments on areca fiber reinforced polypropylene composite properties. *Science and Engineering of Composite Materials.* 2017;24(4): 501–520.
11. Nayak S, Mohanty JR. Study of Mechanical, Thermal, and Rheological Properties of Areca Fiber-Reinforced Polyvinyl Alcohol Composite. *Journal of Natural Fibers.* 2019;16(5): 688–701.
12. Rahman MM, Mondol M, Hasan M. Mechanical Properties of Chemically Treated Coir and Betel Nut Fiber Reinforced Hybrid Polypropylene Composites. *IOP Conf Ser Mater Sci Eng.* 2018;438: 012025.
13. Yousif BF, Nirmal U. On the mechanical properties of a treated betelnut fibre-reinforced polyester composite. *Proc Inst Mech Eng C J Mech Eng Sci.* 2010;224(9): 1805–1814.
14. Jagadeesh P, Puttegowda M, Thyavihalli Girijappa YG, Rangappa SM, Siengchin S. Effect of natural filler materials on fiber reinforced hybrid polymer composites: An Overview. *Journal of Natural Fibers.* 2022;19(11): 4132–4147.
15. Jiang Z, Gyurova LA, Schlarb AK, Friedrich K, Zhang Z. Study on friction and wear behavior of polyphenylene sulfide composites reinforced by short carbon fibers and sub-micro TiO_2 particles. *Compos Sci Technol.* 2008;68(3–4): 734–742.
16. Rouway M, Nachtane M, Tarfaoui M, Chakhchaoui N, Omari LEH, Fraija F, Cherkaoui O. Mechanical Properties of a Biocomposite Based on Carbon Nanotube and Graphene Nanoplatelet Reinforced Polymers: Analytical and Numerical Study. *Journal of Composites Science.* 2021;5(9): 234.
17. Mikitaev AK, Kozlov GV. The efficiency of polymer nanocomposites reinforcement by disperse nanoparticles. *Materials Physics and Mechanics.* 2014;21(1): 51–57. (In Russian)
18. Sapiai N, Jumahat A, Jawaid M, Midani M, Khan A. Tensile and Flexural Properties of Silica Nanoparticles Modified Unidirectional Kenaf and Hybrid Glass/Kenaf Epoxy Composites. *Polymers.* 2020;12(11): 2733.
19. Raghavendra G, Ojha S, Acharya SK, Pal SK. Influence of micro/nanofiller alumina on the mechanical behavior of novel hybrid epoxy nanocomposites. *High Perform Polym.* 2014;27(3): 342–351.
20. Md Musthak, Madhavi M, Ahsanullah FM. Study on effects of E-glass fiber hybrid composites enhanced with multi-walled carbon nanotubes under tensile load using full factorial design of experiments. *Applied Nanoscience.* 2017;7: 283–289.
21. Prasad V, Joseph MA, Sekar K. Investigation of mechanical, thermal and water absorption properties of flax fibre reinforced epoxy composite with nano TiO_2 addition. *Compos Part A Appl Sci Manuf.* 2018;115: 360–370.
22. Divya GS, Suresha B. Impact of nano-silicon dioxide on mechanical properties of carbon fabric reinforced epoxy composites. *Mater Today Proc.* 2021;46: 8999–9003.
23. Kumar V, Kumar R. Improved mechanical and thermal properties of bamboo–epoxy nanocomposites. *Polym Compos.* 2012;33(3): 362–370.
24. Dhanasekar K, Krishnan AM, Kaliyaperumal G, De Poures MV, Chandramohan P, Parthipan N, Priya CB, Venkatesh R, Negash K. Influences of Nanosilica Particles on Density, Mechanical, and Tribological Properties of Sisal/Hemp Hybrid Nanocomposite. *Advances in Polymer Technology.* 2023;2023(1): 3684253.
25. Chowdary MS, Raghavendra G, Kumar MSRN, Ojha S, Boggarapu V. Influence of Nano-Silica on Enhancing the Mechanical Properties of Sisal/Kevlar Fiber Reinforced Polyester Hybrid Composites. *Silicon.* 2022;14: 539–546.
26. Kumar Patnaik T, Nayak SS. Investigation of physico-mechanical and thermo-mechanical analysis of alumina filled needle-punch nonwoven jute epoxy composites. *Polym Compos.* 2018;39(5): 1553–1561.
27. Sathyaseelan P, Sellamuthu P, Palanimuthu L. Influence of stacking sequence on mechanical properties of areca-kenaf fiber- reinforced polymer hybrid composite. *Journal of Natural Fibers.* 2022;19(1): 369–381.
28. Suresh PS, Dilip Kumar K, Dhanalakshmi S, Basavaraju B. Physical, chemical and surface morphological characterization of single areca sheath fiber. *IOP Conf Ser Mater Sci Eng* 2021;1065: 012020.
29. Pirayesh H, Khanjanzadeh H, Salari A. Effect of using walnut/almond shells on the physical, mechanical properties and formaldehyde emission of particleboard. *Compos B Eng.* 2013;45(1): 858–863.
30. Gu H. Tensile behaviours of the coir fibre and related composites after NaOH treatment. *Mater Des.* 2009;30(9): 3931–3934.
31. Karthick L, Rathinam R, Kalam SA, Loganathan GB, Sabeenian RS, Joshi SK, Ramesh L, Ali HM, Mammo WD. Influence of Nano-/Microfiller Addition on Mechanical and Morphological Performance of Kenaf/Glass Fibre-Reinforced Hybrid Composites. *J Nanomater.* 2022;2022(1): 9778224.
32. Kasinathan RK, Rajamani J. Investigation on mechanical properties of basalt/epoxy fiber reinforced polymer composite with the influence of turtle shell powder. *Polym Compos.* 2022;43(9): 6150–6164.
33. Lim SH, Zeng KY, He CB. Morphology, tensile and fracture characteristics of epoxy-alumina nanocomposites. *Materials Science and Engineering: A.* 2010;527(21–22): 5670–5676.

MATERIALS PHYSICS AND MECHANICS REVIEW

Submitted: July 8, 2025 **Revised: November 10, 2025** **Accepted: November 21, 2025**

Advancing sustainable construction: comprehensive analysis of the innovative geopolymer bricks

N.I. Vatin [1] ✉, **T.H. Gebre** [2]

[1] Peter the Great St. Petersburg Polytechnic University, St. Petersburg, Russia

[2] RUDN University, Moscow, Russia

✉ vatin@mail.ru

ABSTRACT

Innovative geopolymer brick is an alternative to conventional building materials, notably enhancing its mechanical properties and reducing construction costs. This research used a bibliographic approach based on specific keywords and the Scopus database to collect data, resulting in 490 papers that contain the keyword "geopolymer brick" used as sustainable construction materials between 2004 and 2024. The main approach includes scientometric analysis, in which the patterns of the acquired articles are examined with respect to different characteristics like countries with the highest number of publication sources, the most frequently occurring keywords, affiliations, authors, and articles with more research works that are relevant. Scientometric instruments, such as R-Studio and Vos Viewer, have been important in elucidating the complex network of geopolymer research. The scientometric review facilitates the exchange of innovative concepts and knowledge among scholars from different countries and promotes international collaboration in research. The use of scientific instruments not only amplifies the accuracy of the study analysis but also showcases the multidisciplinary character of modern research, establishing a pattern for forthcoming investigations. It is still necessary to carry out an extensive investigation of the novel geopolymer bricks as an innovative building material while taking the research gaps into account. To do this, it is necessary to examine the results of previous studies and identify the research components and development trends and future endeavours by highlighting the necessity for continued research and the advancement of geopolymers as a cutting-edge and ecologically responsible alternative in construction techniques across the globe.

KEYWORDS

geopolymer bricks • sustainable construction • environmental impact • innovative building materials scientometric analysis

Funding. *This research was funded by the Ministry of Science and Higher Education of the Russian Federation within the framework of the state assignment No. 075-03-2025-256 dated January 16, 2025, Additional agreement No. 075-03-2025-256/1 dated March 25, 2025, FSEG-2025-0008.*

Citation: Vatin NI, Gebre TH. Advancing sustainable construction: comprehensive analysis of the innovative geopolymer bricks. *Materials Physics and Mechanics*. 2025;53(6): 97–115.
http://dx.doi.org/10.18149/MPM.5362025_8

Introduction

For thousands of years, bricks have been an important part of construction and building projects. Even though burnt clay is a consistently workable and accessible material, its manufacture has always required a significant amount of energy and resources. The extraction of raw materials, consumption of energy techniques for manufacturing, and massive amounts of waste production associated with traditional building materials like clay bricks and concrete blocks all contribute significantly to increasing carbon emissions and resource degradation [1–4]. It is an urgent demand for innovative and

sustainable building materials in this era of mounting environmental concerns and the need to reduce the ecological footprint of human activity. Geopolymer bricks are more ecologically friendly than conventional bricks since they use less water and energy and produce fewer waste materials [5,6].

Numerous scholars are investigating the possibility of substituting traditional building materials with innovative, eco-friendly alternatives [7]. Sustainability has become more important in the construction industry as a result of growing environmental consciousness and the need to minimize the environmental impact of structures. Since the energy cost of their extraction, treatment, and disposal influences the environmental effect of construction, novel building materials are an important topic [8–10]. Among these innovations, the idea of Geopolymer Bricks has gained popularity recently. It was created with the same specifications as concrete bricks, fly ash bricks, lightweight bricks, and geopolymer bricks. The introduction of waste from industries in brick manufacturing was a breakthrough, and it produced opportunities for the reuse of waste, reducing the harmful impact on the environment [11]. The shift from conventional bricks to geopolymers is complemented by a concise examination of alternative brick varieties, including concrete bricks, fly ash bricks, and lightweight bricks [12–17]. The incorporation of waste materials from businesses into brick production is emphasized as a groundbreaking measure, not only mitigating environmental damage but also offering prospects for waste repurposing [18,19].

Geopolymers are known for their reduced impact on the carbon footprint as they can be created at low temperatures, unlike cement. Geopolymers are sustainable and environmentally friendly materials as they are prepared from waste materials from the industry, such as fly ash and slag. Apart from their raw material being industrial waste, they are reusable at the end of their life span. Scholars used a variety of waste resources, such as ceramic powder, glass powder [20], granulated blast furnace slag [21], mine tailings [22], fly ash [23] and others [24,25], as ingredients for a revolutionary geopolymer brick.

Geopolymers have an advantage over traditional construction materials as their better resistance to corrosion and chemical attack, which makes them a suitable option for the replacement of conventional construction materials. Cement uses raw materials from earth minerals, which makes it a limited and restricted production material as it can cause problems to the environment like mineral scarcity and air pollution on the other hand geopolymers act as a solution for the use of industrial waste without the requirement of a high temperature of about 900 to 1200 °C which is necessary for cement manufacturing process [26–30]. Apart from this, geopolymers can achieve the desired strength with a shorter curing period and less greenhouse gas emissions. The current review focuses on the scientometric analysis of the information available on the geopolymer brick in the Scopus database using R-Studio and Vos-viewer applications that provide essential information on the articles available in the database about the sources, affiliations, authors, and their relation with the different parameters [31,32]. The Scientometric Approach is used in this study to analyze the bibliometric dataset obtained from the Scopus Database. The scientometric analysis is a scientific methodology that uses a variety of statistical and computational tools to analyze patterns, trends, and relationships among scientific works, authors, institutions, and research topics. It involves

quantitative and qualitative assessments of scientific literature, publications, citations, and collaborations within a particular field or discipline.

The current study evaluated the positive impacts of innovative geopolymer bricks for building by conducting a scientometric analysis of published works that address the issue of advancing sustainable construction. Based on 490 publications published between 2004 and 2024, this article examines a growing collection of research on geopolymer bricks and provides a qualitative evaluation of the historical development of bricks. The study utilizes a scientometric methodology, using technologies like Web of Science, R-Studio, and Vos Viewer to carry out a comprehensive analysis of the current body of literature on geopolymer bricks [33,34]. The sheer magnitude of publications, affiliations, and authors exemplifies the growing interest and the worldwide scope of study in this field. India has emerged as a leading contender in the field of geopolymer brick papers, highlighting the global reach and importance of this area of study [35–38]. The introduction establishes the foundation for the next parts by concisely outlining the historical path of bricks, identifying the environmental obstacles presented by conventional materials, and offering geopolymers as a modern, environmentally friendly substitute [39–41]. These establishes are the framework for the extensive investigation of geopolymer bricks in the next parts, spanning their production methods, mechanical characteristics, uses, and the future potential of this revolutionary substance in the field of environmentally friendly building. This assessment is notable for its primary emphasis on resolving a crucial problem within the building industry—the ecological consequences linked to traditional construction binding materials such as cement [42]. The research suggests a revolutionary approach by promoting the use of geopolymers, particularly in the form of bricks, as a basic construction component. The article thoroughly examines alternative mix compositions, investigates the mechanical characteristics, and includes a full analysis of numerous experiments performed on geopolymer bricks. Moreover, the assessment provides insight into the most recent developments in geopolymer brick technology, clarifying its many uses in building projects.

The research investigation makes use of cutting-edge scientific instruments, including sophisticated scientometric analysis techniques like R-studio and Vos Viewer software, and it obtains its analytical data from the Scopus database. The collection of tools includes Network Visualization, Density Visualization, Topic Dendrogram, and Cluster Analysis, along with Bar Charts and Pie Chart representations. The use of this analytical toolbox enhances the research by offering a sophisticated comprehension of the current research evolution [43,44].

The study takes into account a wide range of elements and criteria, including Sources, Articles, Authors, Co-authors, Citations, Affiliations, and Keywords. This methodical approach guarantees a comprehensive examination of the topic, enhancing the understanding of the interrelated aspects of geopolymer bricks in infrastructure. This comprehensive evaluation distinguishes itself from past reviews by thoroughly exploring the complex interactions among crucial material qualities rather than focusing just on physical aspects and future research directions. The study utilizes advanced scientometric analysis to pioneer multidisciplinary methodologies, setting a new standard in research methodology [45–48]. By prioritizing cost-effective solutions, this study investigates the elements that impact the qualities of geopolymer bricks, ultimately improving their

availability for a wide variety of building projects. The analysis highlights the significant role of geopolymers, especially in brick manufacturing, as a critical aspect in providing environmentally friendly choices for building projects [49–53]. These choices not only foster sustainable infrastructure development but also conform to environmentally conscious practices. In addition to its academic importance, this review plays a crucial role in sharing information and promoting cooperation within the construction sector [54–57]. By serving as a catalyst, it stimulates innovation and advancement, leading to beneficial transformations in the field of building materials and processes.

Literature search methods

Literature Search

This section should clearly outline which bibliographic databases and time frames were used for the literature search, providing examples of keywords, phrases, and search queries employed to identify relevant studies. Observing the articles on innovative geopolymer bricks as a sustainable construction material for the record of 490 articles in Web of Science throughout the period of 2004 to 2024, the researchers evaluated their significance to conclude the investigation of the current study. These articles are published in 182 different sources with an overall number of authors as 1536. The most relevant source is identified as CONSTRUCTION AND BUILDING MATERIALS with a total of 103 articles on the topic of geopolymer brick, followed by JOURNAL OF BUILDING ENGINEERING and JOURNAL OF CLEANER PRODUCTION with several articles 33 and 23 respectively. The top three Authors were identified as ABDULLAH MM, SAHMARAN M, and KADIR AA with the number of articles as 20, 19, and 18 respectively. The most relevant Affiliations are UNIV MALAYSIA PERLIS, SWINBURNE UNIV TECHNOL, and HACETTEPE UNIV with 54, 27, and 25 articles respectively. India is the country with the maximum number of publications in geopolymer bricks, with 59 articles followed by China (57), and Malaysia (39).

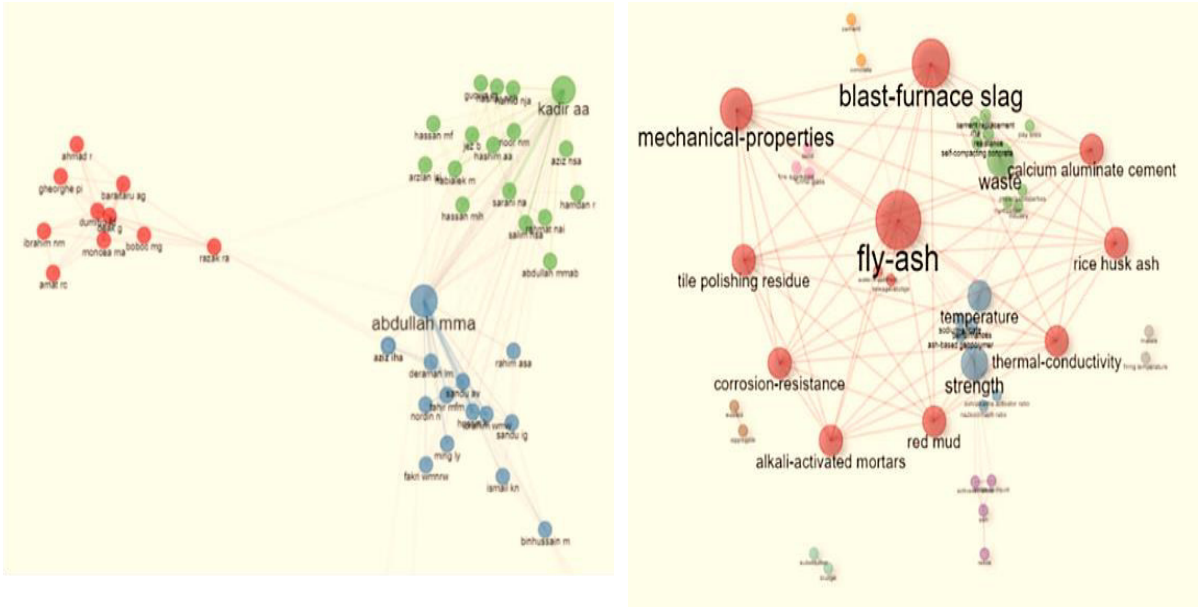

(a) (b)

Fig. 1. (a) Author co-relation (b) Author keywords reoccurrence network

After screening for the most relevant affiliation UNIV MALAYSIA PERLIS, 31 articles were obtained for the research related to geopolymer brick with the contribution of 81 authors, among which 20 articles are published by ABDULLAH MMA as shown in Fig. 1(a). It was seen in Fig. 1(b) in the network analysis that most of the work in these articles was done on the fly ash and blast furnace slag, considering their mechanical properties. Over the last few decades, the growth of industries and increased population demands have given a tremendous rise to the emissions of greenhouse gases, which CO_2 is a major contributor which results in about 8 % of CO_2 emissions every year due to cement manufacturing and the use of cement-based products [58–61]. It is estimated to have a production of 6.1 billion metric tons of cement in the world by 2050 to fulfil the demands of the population.

Data collection and processing

Based on information gathered from the majority of existing literature, which was used in Fig. 2 out the results' scientific foundation, Scopus was selected as the bibliographic database since it is thorough and well-organized, making it an effective tool for in-depth scientific investigation. The dataset obtained was further screened to scrutinize the unwanted articles. The obtained articles were saved in a CSV format so that they could be adjusted in the Vos Viewer and R Studio software for required analysis. The procedure is shown in Fig. 2 using a flowchart. Due to the nature of the research procedure, the data contained in the obtained file was processed and displayed using networks, clustering, and graphics.

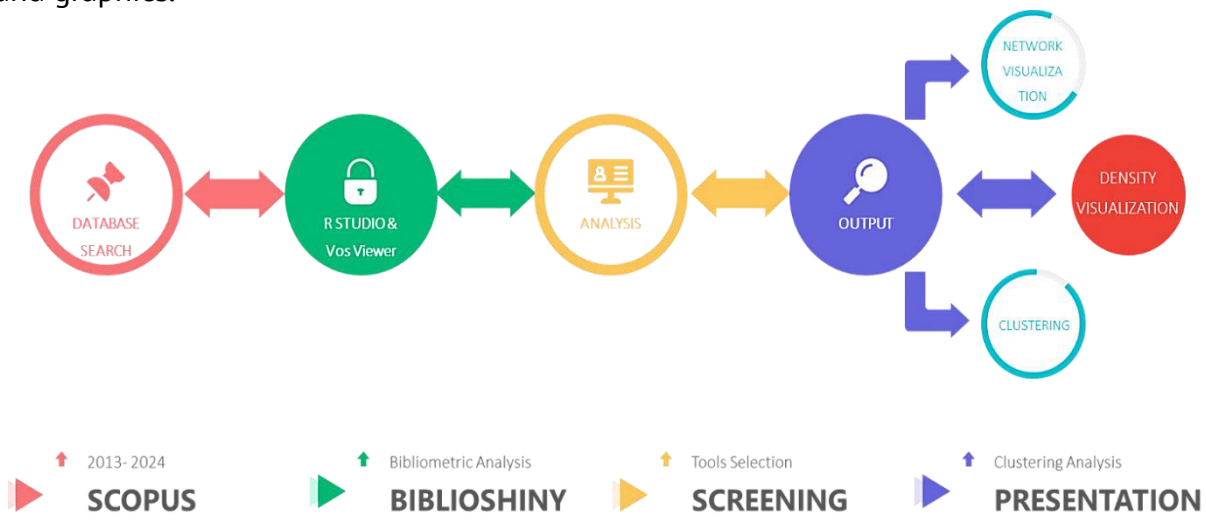

Fig. 2. Research methodology flowchart

Result and Analysis

Scopus database analysis

For the identification of important research fields in the geopolymer bricks topic, an analysis was performed in the Scopus database, as shown in Fig. 3. In the year range of 2013 to 2023, a total of 85 documents were received. Boost in the research can be seen after 2018-2019, where 15.3 % of articles were published in the years 2020 and 2021

each, 17.65 % in the year 2022, and 31.77 % in 2023, as shown in Fig. 4. This rise in the frequency indicates the increasing interest of researchers in the field of geopolymer.

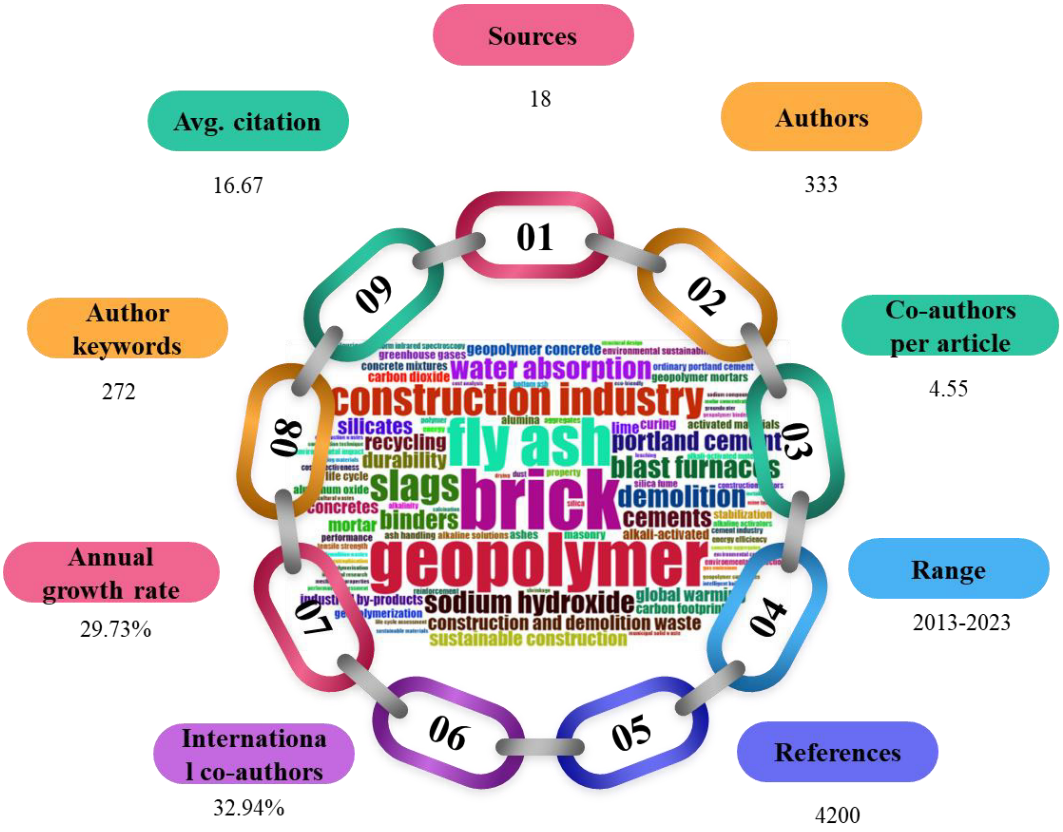

Fig. 3. Main Information received in the scientometric analysis in R studio

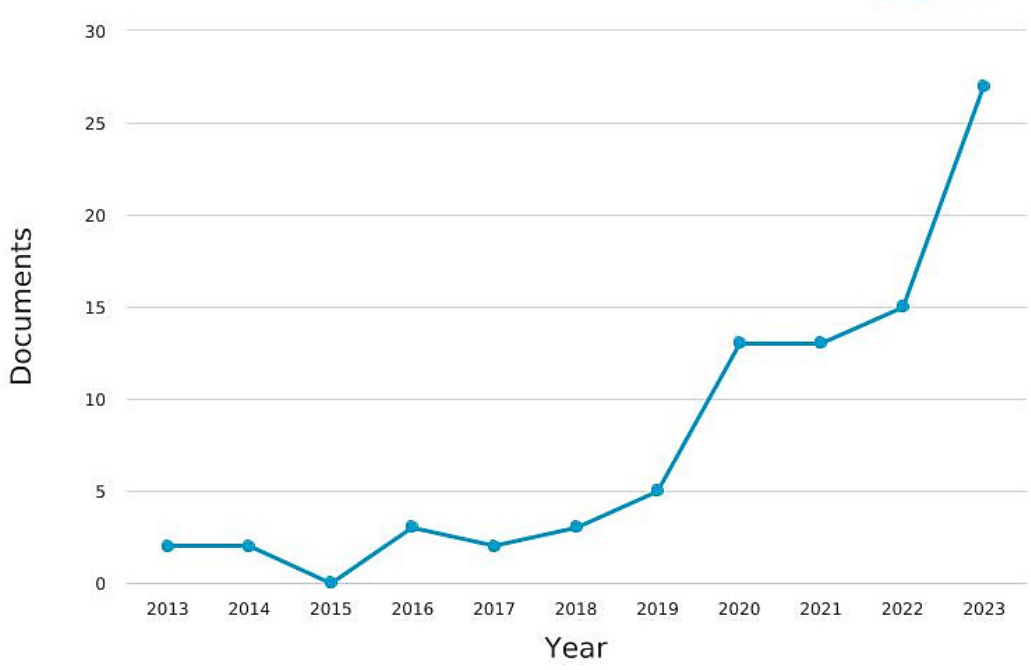

Fig. 4. Articles published per year in geopolymer brick topic

The renown and significance of a paper for other researchers can be determined by its citations. In this dataset, the Construction and Building Materials Journal contains the maximum cite-score for the articles related to the topic of geopolymer brick which shows that the articles published in this journal are more popular for containing important information as shown in Fig. 5.

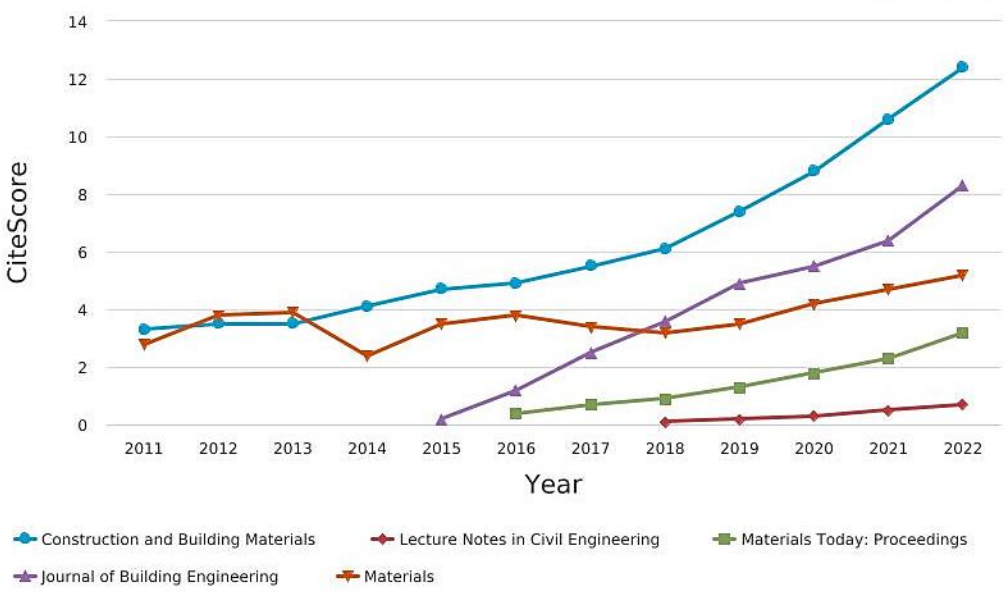

Fig. 5. Cite-score obtained in different sources of the dataset

Apart from the cite score, the most relevant source list is also topped by the Construction and Building Materials Journal, which contains 20 % of the articles available in the dataset. This relevancy is followed by LECTURE NOTES IN CIVIL ENGINEERING and MATERIALS TODAY: PROCEEDINGS with 9.4 and 7 %, respectively.

Research and innovation trends by year

Geopolymer bricks, as an innovative building material, have been the subject of relevant research studies over recent decades. The frequency of documents published per year is a symbol of consistent research in the concerned field. This consistency was maintained by the Construction and Building Materials till 2017. Thereafter, it was surpassed by Materials Today: Proceedings and later since 2020-21 Materials Journal has been holding the top position for the publication of maximum documents per year in the concerned field as shown in Fig. 6.

Analysis of articles from the author

A maximum of 6 articles were published by Sahmaran, H followed by Kul, A, and Khan, S.A with 5 and 4 articles, respectively, as shown in Fig. 7(a). Figure 7(b) shows that a maximum of 8 articles were received from Hacettepe Universitesi, followed by Ankara and Hana Bin Khalifa University, with 4 articles each. India has contributed to this topic with a maximum of 30 articles in the dataset, making 35.29 % of the whole, as shown in

Fig. 7(c). In the funding institutes shown in Fig. 7(d), a maximum contribution of 4 articles was seen from the Qutar National Research Fund.

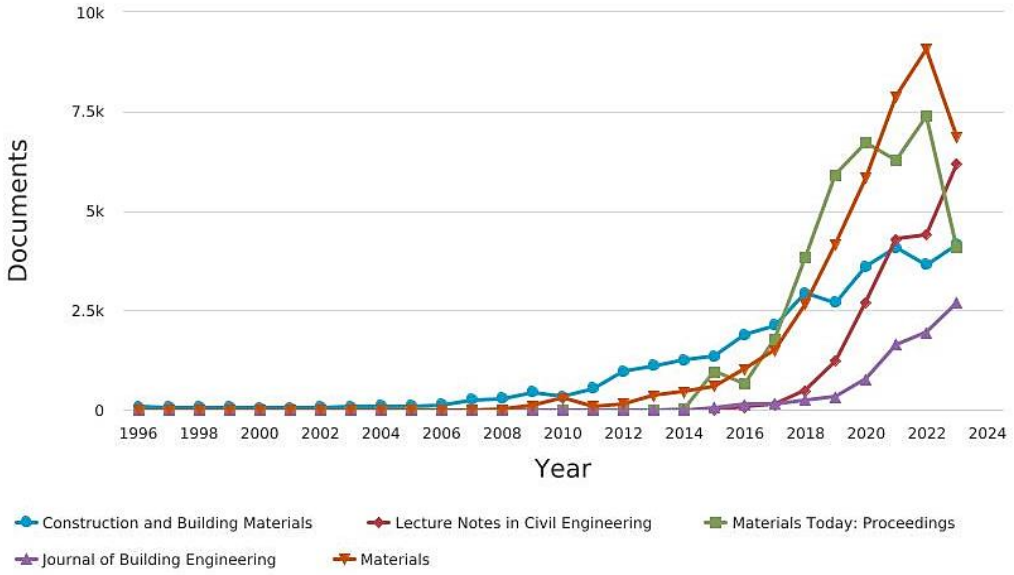

Fig. 6. Year-wise document publication in the sources

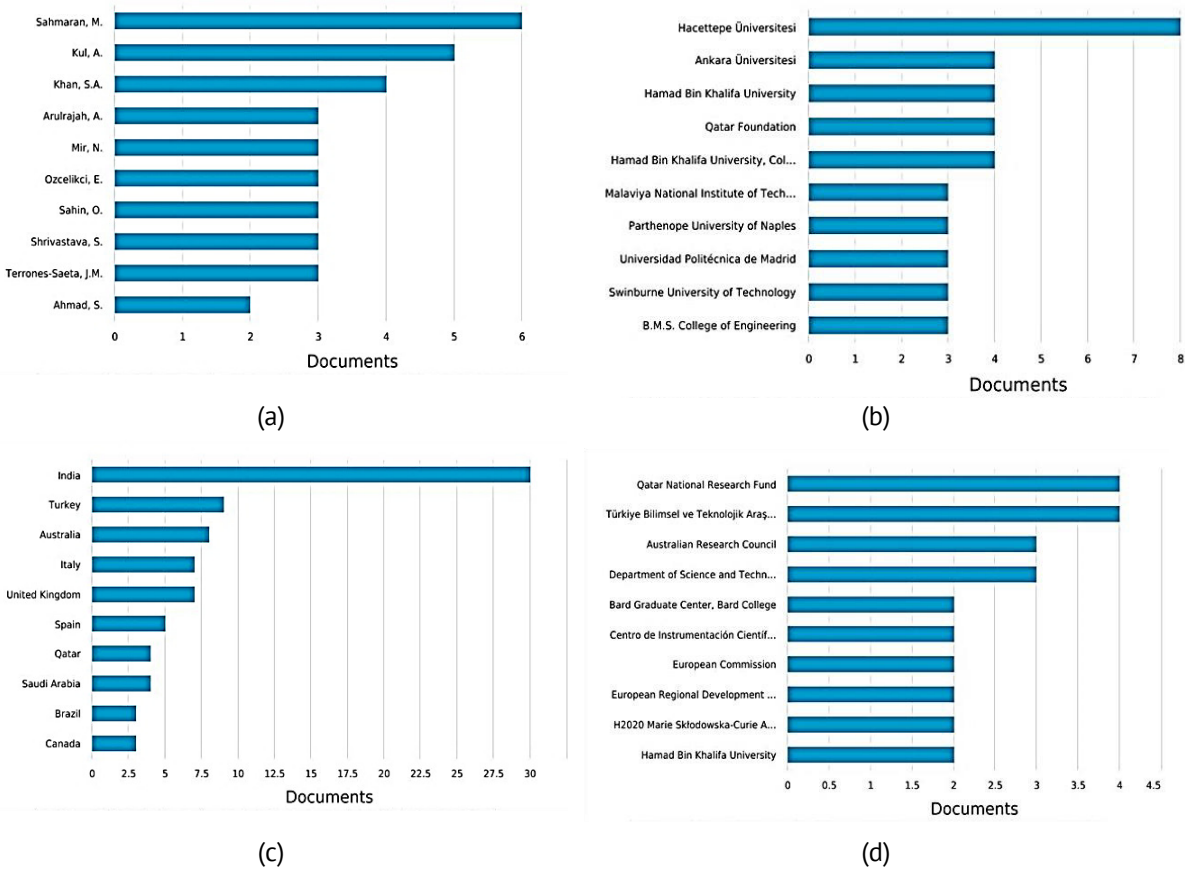

Fig. 7. (a) Author-wise document publication; (b) affiliation-wise document publication; (c) country-wise document publication; (d) funding institute-wise document publication

In the document type analysis of Fig. 8(a), 62.4 % are articles, 23.5 % are conference papers, 8.2 % are review papers, and 4.7 % are book chapters. In the discipline of the research in Fig. 8(b), a maximum of 36.1 % are from Engineering, 31 % are from material science, and others are from diverse fields of environment, computing, chemicals, and Business management.

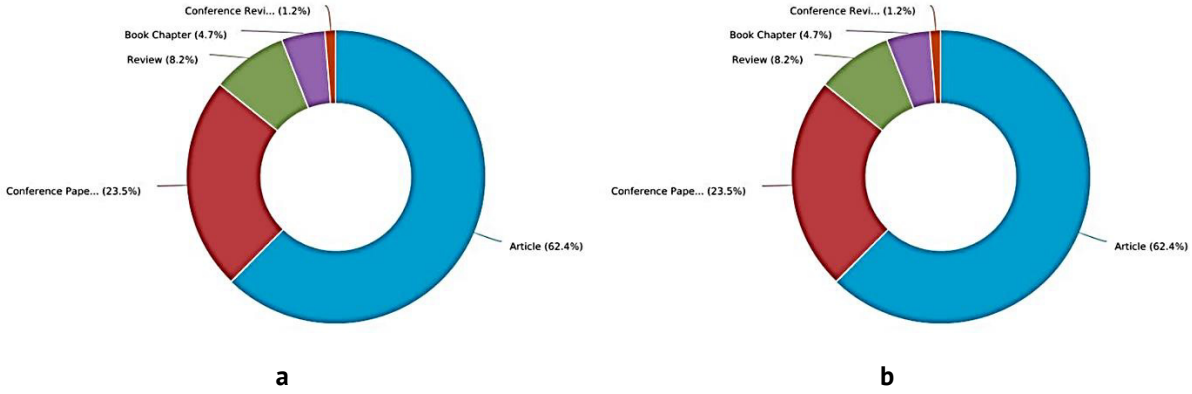

Fig. 8. (a) Document type in the dataset; (b) subject type in the dataset

The most relevant documents obtained in this dataset are Lignola GP, 2017 published in Compos Part B: ENG, Ahmari S, 2013 published in Construction Building Materials, and Tang Z, 2020 published in Conservation and Recycling Journal with an overall citation score of 190, 158, and 135 respectively which can be seen in Fig. 9.

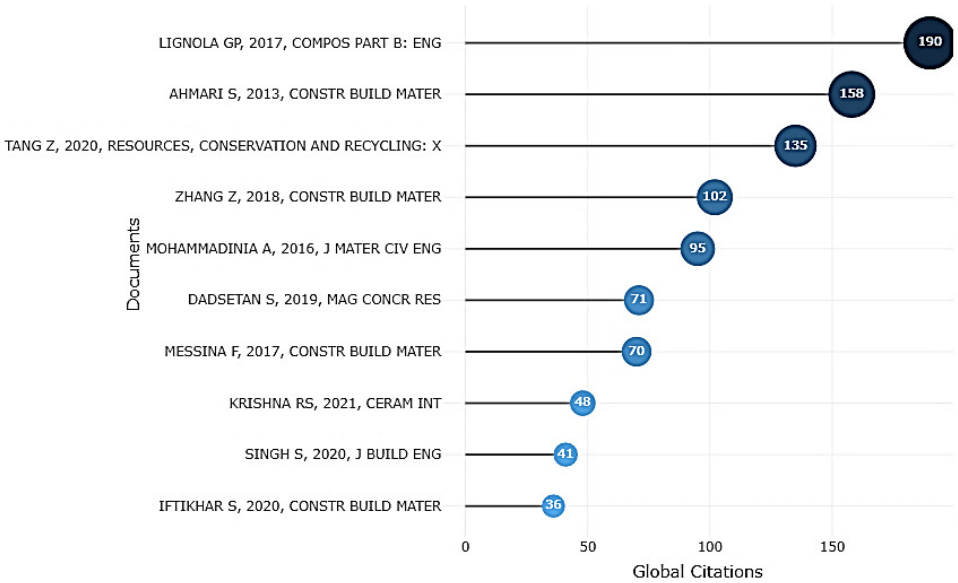

Fig. 9. Cite-score of the top ten articles

Analysis of co-occurrence network

The co-occurrence network of the keywords in Fig. 10 is a representation of the author's keywords, showing the importance and relevance of the keywords that are mostly used. The terms "geopolymers," "inorganic polymers," "brick," "sustainable development," and "fly ash" are most commonly used in the researchers examined in this collection. Out of

861, 60 keywords, 10 occurrences, co-occurrences, all of the keywords, and complete counting match the criterion.

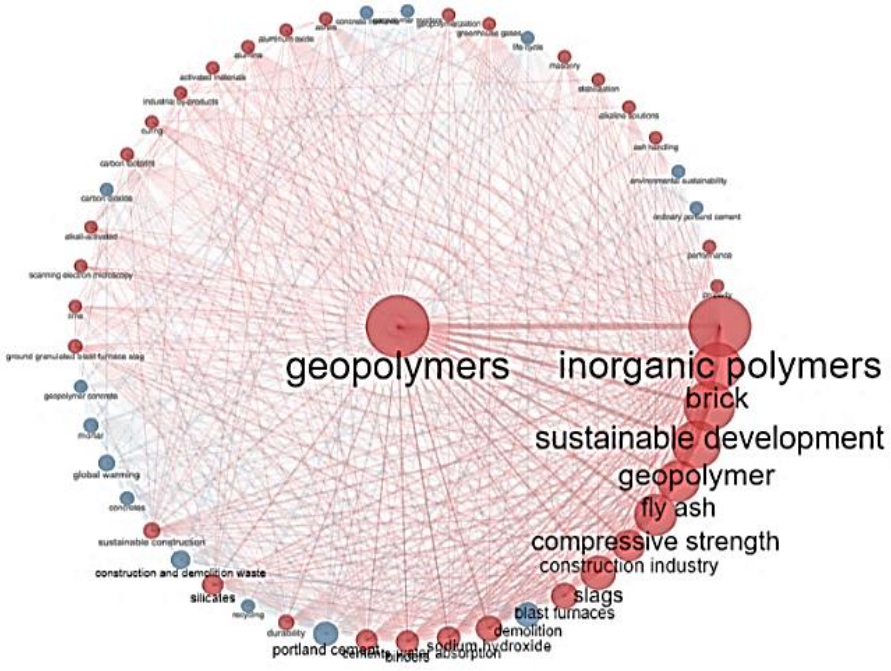

Fig. 10. Co-occurrence network of the author keywords

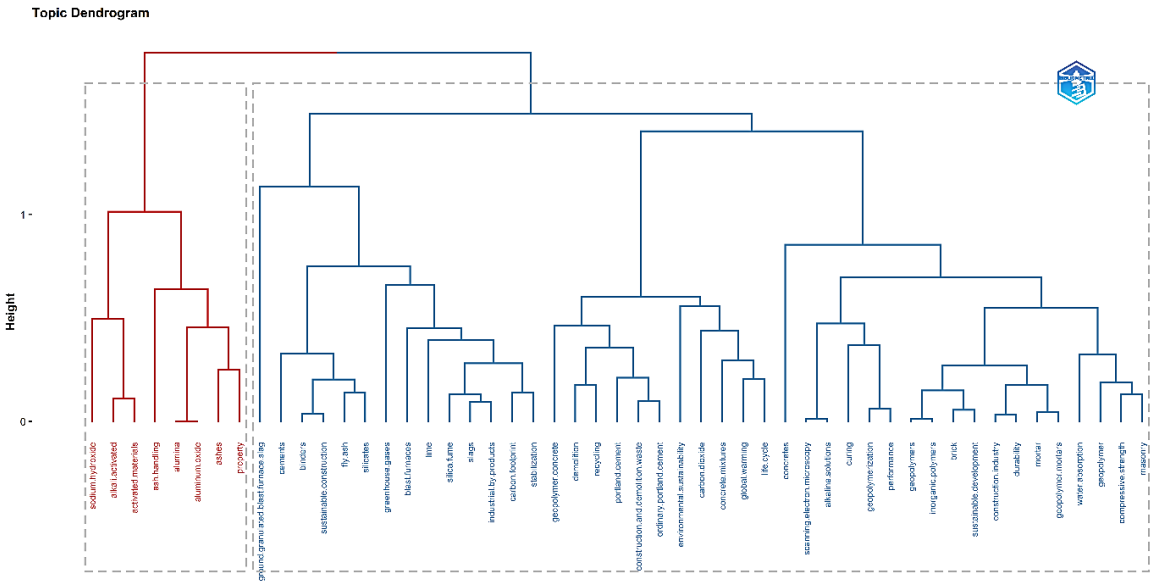

Fig. 11. Topic dendrogram as per multiple correspondence analysis.

Hierarchical clustering is presented in the topic dendrogram in Fig. 11. Two colours, blue and red, represent the clusters with similarities. 1st group of clusters shown in red represents the clusters of primary units in the geopolymer formation. In contrast, different subgroups of the blue-coloured group represent the other ingredients, processes, analysis, and final output obtained in the different clusters, which have similarities. Co-

authorship and authors network analysis was done using Vos Viewer with max author per doc as 5 and min documents of the author as 1, taking minimum citation score as 10, and a total of 64 Authors met the threshold.

Network visualization represents the clusters of authors in Fig. 12(b) with higher numbers of citations, which can be easily identified in the density visualization. Arulrajah, Arul Zhang, Lianyang and Li Wengui are the authors with the most citations and the highest temperatures in heat density visualization.

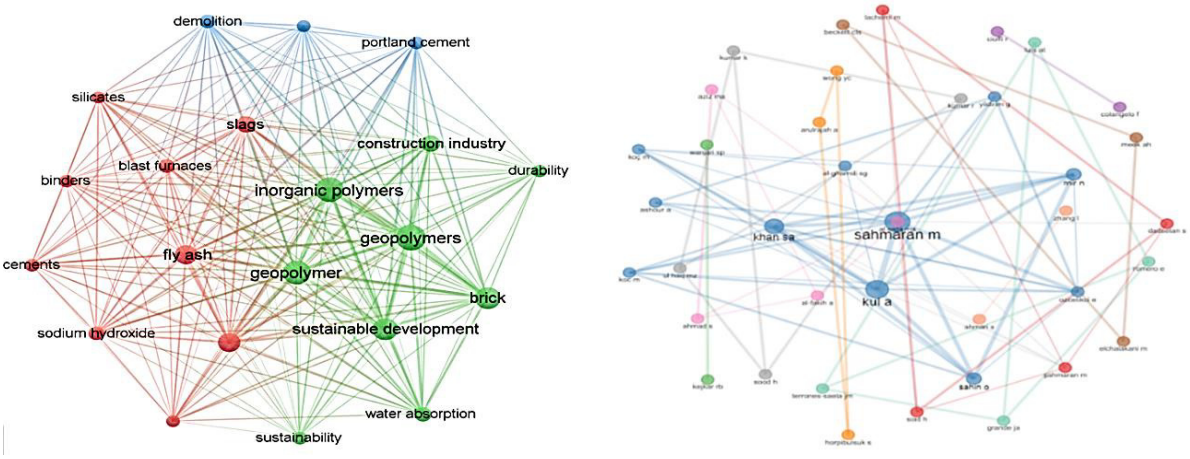

(a) (b)

Fig. 12. (a) Author keywords network visualization; (b) Author co-occurrence network

A structure of collaboration networks in the application of geopolymers in the field of advancing sustainable construction is revealed by the Co-Authorship visualization and Co-Authorship density visualization network, as shown in Fig. 13(a,b), respectively, and can be helpful in organising future scientific collaboration. Bibliographic coupling and countries clustering analysis was done in Vos Viewer with full counting, taking countries with minimum documents as 2 and minimum citation as 10. Out of a total of 35, 19 met the threshold. Network visualization of bibliographic coupling and countries shows the maximum number of research articles from India, followed by Australia and Turkey, which can be interpreted in the heat density visualization, as shown in Fig. 14. The most minor research is shown in countries located at a farther place with small diameters, such as Egypt, France, Brazil, and Poland.

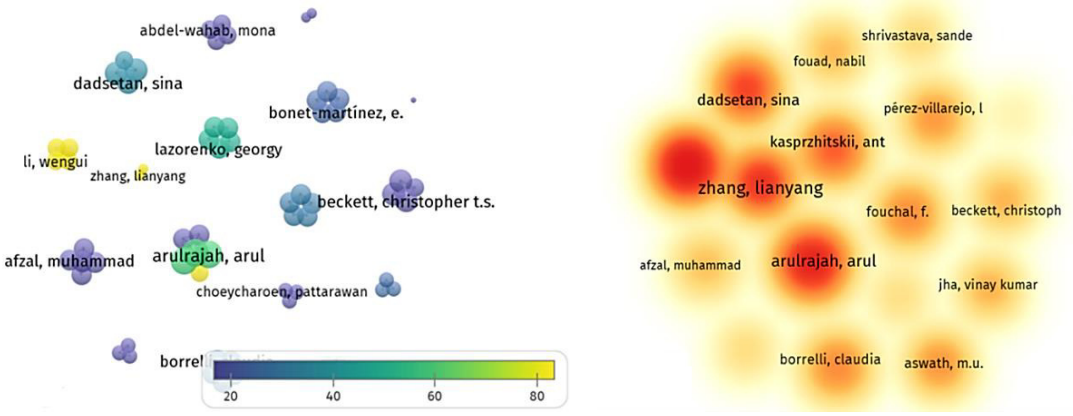

(a) (b)

Fig. 13. (a) Co-authorship network visualization; (b) co-authorship density visualization

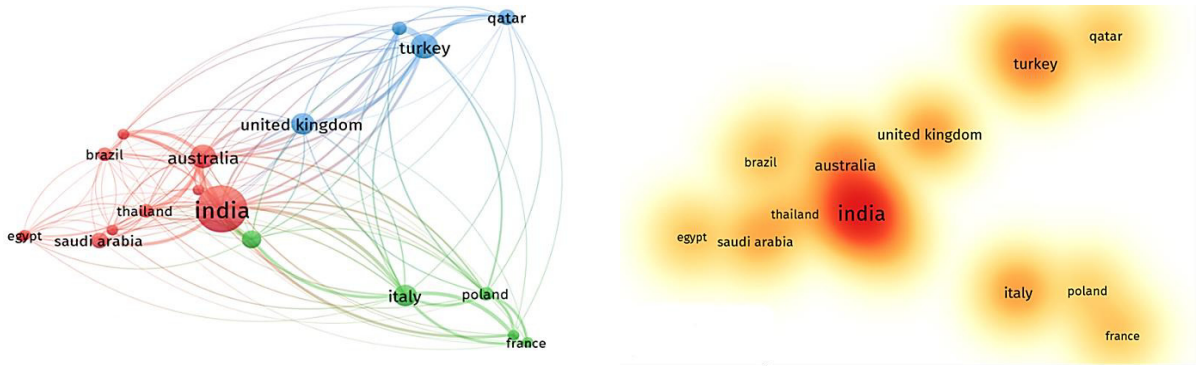

(a) (b)

Fig. 14. (a) Bibliographic coupling network of countries; (b) bibliographic coupling density visualization

Physio-mechanical properties

Compressive strength. The compressive strength of the brick was seen to vary according to the type and proportion of the materials and activator used. The most common and important thing that makes this research sustainable is the use of waste materials from industries, which is common in almost all research papers. The compressive strength of the brick was seen to vary from 2.1 to 42 MPa, as reported by different researchers [62–64]. The bricks with less compressive strength are suitable for interior works where they don't have to carry the load. Otherwise, the bricks with good strength can be utilized in the load-carrying members of the structure. The proportion of the materials depends upon availability. If the percentage of fly ash and ground granulated ballast furnace slag is suitable, then the complete replacement of soil and other ingredients in the conventional bricks will be achieved. The optimum percentage was seen to be between 10 to 30% for good compressive strength. If we only use GGBS (25 %) and fly ash (75 %) with 30 % NaOH and 70 % Na_2SiO_3, a good increase in compressive strength can be achieved with better durability properties [58] and detailed mechanical properties performed by researchers are shown in Table 1.

Durability and chemical resistance. The inclusion of silica-added brick kiln rice husk ash and activators such as NaOH and Na_2SiO_3 solution resulted in increased durability. A reduction in water absorption was seen by 34 %, which is considerable in preventing harmful ingredient absorption, especially in the case of coastal regions. The acidic environment of coastal regions is well known to cause issues for building materials by reducing their durability. Because of this, it's critical that building materials be chemically resistant. Even a 10 to 15 % proportion of pozzolanic materials in geopolymer bricks will give them good resistance to such environments [19]. In addition, resistance to abrasion was seen in comparison to conventional brick [71]. Finding the ideal amount of mine tailings in the brick will allow for the control of leaching properties [72]. While employing low-reactive copper mine tailings does not significantly improve compressive strength, durability qualities can be improved [73].

Flexural strength. It is evident that geopolymer bricks have higher flexural strength than conventional materials. The use of fly ash (FA) and ladle furnace slag (LFS) with varying percentages of silica fume along with sodium silicate and sodium hydroxide as

Table 1. Summary of geopolymer brick studies with optimized compositions and properties

Authors	Ingredients	Activator	Test	Optimum %	Comp. strength, MPa	Time	Ref.
Haq et al. 2024	Rice husk ash (rha), ground granulated blast furnace slag (ggbs), red mud, and recycled washed sand as filler	Sodium hydroxide (NaOH) and sodium silicate (Na_2SiO_3)	Compressive strength and water absorption	60 % rha, 20 % ggbs, and 20 % red mud	27.34	28	[65]
Mortada et al. 2023	Calcium hydroxide	Calcium hydroxide	Compressive strength	1 wt. % of nano-silica	42	28	[66]
Ahmad et al. 2022	Fly ash	–	Compressive strength and water absorption	–	40	7 and 28	[67]
Shilar et al. 2023	Granite waste powder and iron chips	Sodium hydroxide	Compressive strength and water absorption	20 %	10.1	7 and 28	[68]
Morsy et al. 2022,	Rice straw ash,soil	Sodium hydroxide	Compressive strength, thermal conductivity, and water absorption	10 % sodium hydroxide and 20 % RSA	2.1	28	[5]
Li et al. 2022	Brick powder	Na_2O	Compressive and flexural strengths, bulk density, water absorption and softening coefficient	6 % Na_2O	31.1	7	[69]
Kakodkar et al. 2023,	Iron ore tailings	–	Compressive strength	10 % fly ash and 30 % GGBS with 50 %	11.15	28	[70]

activators was seen to increase the flexural strength of the brick [74]. Apart from fly ash, if waste fibre cement is being used with a suitable activator, it has the capability of increasing the flexural strength of the geopolymers to about 20 % of its compressive strength [75]. Additional strength and sustainability can be achieved using carbon or steel fiber reinforcement as a replacement for steel in the concrete [76]. Geopolymer bricks have a vast application among the various structural units, and their performance is far better than that of traditional clay bricks and fly ash bricks [77,78]. The application is determined by the ratio of materials to be used and the improved properties, such as increased flexural strength for use in the building's beams or increased compressive

strength for use as paver bricks. For high resistance to chemicals and water absorption, the application can be made on the structure's exposed surface likewise after serving the life span as a main unit in the structures, the geopolymer recycled brick aggregate-filled steel tubes can be made with good strength as compared to the traditional concrete-filled steel tubes [79].

Discussion and Recommendations

The findings showed that there is a notable and consistently rising trend in the research study on the subject of geopolymers as cutting-edge building materials, indicating that the researchers are fully aware of and interested in the potential benefits and applications of geopolymers as advancing sustainable construction. The statistical analysis and mapping of the bibliographic databases and time periods utilized for the literature search were carried out by a systematic review, which also provided examples of the keywords, phrases, and search queries used to find relevant studies. The ability to fully and accurately connect divergent sections of the literature is lacking in previous review studies. The researchers assessed the relevance of the 490 publications on innovative geopolymer bricks as a sustainable building material published in Web of Science between 2004 and 2024 in order to wrap up the inquiry of the current study. There are 1536 writers total, and these papers are published in 182 distinct sites. Researchers from China, Malaysia, and India have made significant contributions to the field of geopolymer brick research by collaborating extensively with other researchers in the discipline and utilizing their knowledge. Table 1 summarizes studies on geopolymer bricks with optimized compositions and properties. Several researches observed the compressive strength of bricks based on the ideal constituent proportions to replace the traditional brick. The analysis carried out in this study suggests the following investigations for the future.

In anticipation, the recognition of forthcoming avenues for study underscores the need for economically viable resolutions and a more profound comprehension of the variables impacting the characteristics of geopolymer bricks. The ever-evolving characteristics of this domain need ongoing investigation, ingenuity, and cooperation to tackle developing obstacles and unleash the whole capabilities of geopolymer technology in the realm of building.

Fundamentally, this assessment not only consolidates preexisting information but also functions as a catalyst for the spread of knowledge, promoting cooperation within the construction sector and driving innovation and advancement. The use of scientometric instruments not only enhances the analysis but also signifies the amalgamation of conventional and state-of-the-art approaches in furthering our comprehension of geopolymer brick study. As we find ourselves at the intersection of historical significance and groundbreaking advancements, the investigation into geopolymer bricks arises as an illuminating beacon, directing the building sector towards a more environmentally friendly and enduring future.

Conclusion

The investigation of geopolymer bricks as a groundbreaking and environmentally friendly substitute for conventional building materials is a revolutionary expedition that mirrors the changing demands of the construction sector. The current study evaluated the positive impacts of innovative geopolymer bricks for building by conducting a scientometric analysis of 490 papers published between 2004 and 2024 that address the issue of advancing sustainable construction.

There are numerous strong connections among the research communities in China, Malaysia, and India, all of which have made substantial contributions. With 59 publications, India leads the world in geopolymer brick publications, followed by China (57), Malaysia (39), and other countries.

These research articles have been published in 182 different sources, and there are 1536 authors in total. Having 103 articles on the subject of geopolymer brick, CONSTRUCTION AND BUILDING MATERIALS is the most relevant source. Journal of Building Engineering and Journal of Cleaner Production, with multiple articles 33 and 23, are the following two most relevant sources.

The extensive contributions from writers such as Abdullah MM, Sahmaran M, and Kadir AA, in conjunction with affiliations such as Univ Malaysia Perlis, highlight the worldwide cooperation that drives geopolymer research. Significantly, India emerges as a prominent participant, exemplifying the extensive acknowledgment of the potential of geopolymer technology in tackling the obstacles presented by traditional building materials.

The environmental issues linked to the manufacturing of conventional cement-based products, notably the concerning amounts of carbon dioxide emissions, provide a striking context for the environmentally beneficial characteristics of geopolymer bricks. Through the use of lower temperatures throughout the manufacturing process and the inclusion of industrial byproducts such as fly ash and slag, geopolymers effectively reduce their carbon footprint. The inherent durability of geopolymers and their capacity for being repurposed after their life span establishes geopolymers as a tempting option for building methods that prioritize environmental consciousness.

Scientometric instruments, such as R-Studio and Vos Viewer, have been important in elucidating the complex network of geopolymer research. The methodical technique, as shown in the flowchart, guarantees a meticulous screening procedure, enabling a sophisticated study of sources, affiliations, authors, and keywords. The use of scientific instruments not only amplifies the accuracy of the study but also showcases the multidisciplinary character of modern research, establishing a pattern for forthcoming investigations.

The main fields of study on geopolymer bricks used as building materials and any knowledge gaps were outlined in a qualitative evaluation. This thorough analysis broadens the framework's understanding and helps researchers identify high-impact journals and scholars. It also clarifies current patterns in the field's investigation of novel applications for geopolymer brick as construction materials.

The use of waste resources not only enhances sustainability but also establishes geopolymer bricks as feasible substitutes for traditional building materials. The

compressive strength, which varies from 2.1 to 42 MPa in different experiments, highlights the versatility and robustness of geopolymer bricks, rendering them appropriate for use in paver bricks, beams, and exposed surfaces. The versatility, along with the environmentally conscious characteristics, establishes geopolymer bricks as a fundamental element in the development of a sustainable future.

CRediT authorship contribution statement

Nikolai Ivanovich Vatin: conceptualization, drafting of the paper, methodology, formal analysis, writing – review & editing, revising it critically for intellectual content; **Tesfaldet H. Gebre**: writing – review & editing, drafting of the paper, formal analysis, revising it critically for intellectual content.

Conflict of interest

The authors declare that they have no conflict of interest.

References

1. Iftikhar S, Rashid K, Haq EU, Zafar I, Alqahtani FK, Khan MI. Synthesis and Characterization of Sustainable Geopolymer Green Clay Bricks: An Alternative to Burnt Clay Brick. *Constr Build Mater*. 2020;259: 119659.
2. Esparham A, Vatin NI, Kharun M, Hematibahar M. A Study of Modern Eco-Friendly Composite (Geopolymer) Based on Blast Furnace Slag Compared to Conventional Concrete Using the Life Cycle Assessment Approach. *Infrastructures*. 2023;8(3): 58.
3. Ibraheem M, Butt F, Waqas RM, Hussain K, Tufail RF, Ahmad N, Usanova K, Musarat MA. Mechanical and Microstructural Characterization of Quarry Rock Dust Incorporated Steel Fiber Reinforced Geopolymer Concrete and Residual Properties after Exposure to Elevated Temperatures. *Materials*. 2021;14(22): 6890.
4. Amran M, Lee YH, Fediuk R, Murali G, Mosaberpanah MA, Ozbakkaloglu T, Lee YY, Vatin N, Klyuev S, Karelia M. Palm Oil Fuel Ash-Based Eco-Friendly Concrete Composite: A Critical Review of the Long-Term Properties. *Materials*. 2021;14(22): 7074.
5. Shilar FA, Ganachari SV, Patil VB, Almakayeel N, Yunus Khan TM. Development and Optimization of an Eco-Friendly Geopolymer Brick Production Process for Sustainable Masonry Construction. *Case Studies in Construction Materials*. 2023;18: e02133.
6. Madani H, Ramezanianpour AA, Shahbazinia M, Ahmadi E. Geopolymer Bricks Made from Less Active Waste Materials. *Constr Build Mater* 2020;247: 118441.
7. Hodhod OA, Alharthy SE, Bakr SM. Physical and Mechanical Properties for Metakaolin Geopolymer Bricks. *Constr Build Mater* 2020;265: 120217.
8. Moonphukhiao A, Samran B, Chaiwichian S. Preparation and characterization of geopolymer/activated carbon composite materials used as a bone substitute material. *Materials Physics and Mechanics*. 2025;53(1): 150–158.
9. Subash N, Avudaiappan S, Adish Kumar S, Amran M, Vatin N, Fediuk R, Aepuru R. Experimental Investigation on Geopolymer Concrete with Various Sustainable Mineral Ashes. *Materials*. 2021;14(24): 7596.
10. Arunachelam N, Maheswaran J, Chellapandian M, Murali G, Vatin NI. Development of High-Strength Geopolymer Concrete Incorporating High-Volume Copper Slag and Micro Silica. *Sustainable*. 2022;14(13).
11. Wang Q, Ahmad W, Ahmad A, Aslam F, Mohamed A, Vatin NI. Application of Soft Computing Techniques to Predict the Strength of Geopolymer Composites. *Polymers*. 2022;14(6): 7601.
12. Nematollahi B, Ranade R, Sanjayan J, Ramakrishnan S. Thermal and Mechanical Properties of Sustainable Lightweight Strain Hardening Geopolymer Composites. *Archives of Civil and Mechanical Engineering*. 2017;17: 55–64.
13. Kuppusamy Y, Jayaseelan R, Pandulu G, Kumar VS, Murali G, Dixit S, Vatin NI. Artificial Neural Network with a Cross-Validation Technique to Predict the Material Design of Eco-Friendly Engineered Geopolymer Composites. *Materials*. 2022;15(10): 3443.

14. Gailitis R, Sprince A, Kozlovskis T, Radina L, Pakrastins L, Vatin N. Long-Term Properties of Different Fiber Reinforcement Effect on Fly Ash-Based Geopolymer Composite. *Crystals*. 2021;11(7): 760
15. Kumar VS, Ganesan N, Indira PV, Murali G, Vatin NI. Flexural Behaviour of Hybrid Fibre-Reinforced Ternary Blend Geopolymer Concrete Beams. *Sustainability*. 2022;15(10): 3443.
16. Wang S, Xue Q, Zhu Y, Li G, Wu Z, Zhao K. Experimental Study on Material Ratio and Strength Performance of Geopolymer-Improved Soil. *Construction and Building Materials*. 2020;267: 120469.
17. Al-Ghouti MA, Khan M, Nasser MS, Al-Saad K, Heng OE, Recent Advances and Applications of Municipal Solid Wastes Bottom and Fly Ashes: Insights into Sustainable Management and Conservation of Resources. *Environ Technol Innov*. 2021;21: 101267.
18. Bhogayata AC, Arora NK. Utilization of Metalized Plastic Waste of Food Packaging Articles in Geopolymer Concrete. *J Mater Cycles Waste Manag*. 2019;21: 1014–1026.
19. Matsimbe J, Dinka M, Olukanni D, Musonda I, A Bibliometric Analysis of Research Trends in Geopolymer. *Materials*. 2022;15(19): 6979.
20. Dhamija P, Bag S, Role of Artificial Intelligence in Operations Environment: A Review and Bibliometric Analysis. *TQM Journal*. 2020;32: 869–896.
21. Uysal M, Aygörmez Y, Canpolat O, Cosgun T, Faruk Kuranlı Ö. Investigation of Using Waste Marble Powder, Brick Powder, Ceramic Powder, Glass Powder, and Rice Husk Ash as Eco-Friendly Aggregate in Sustainable Red Mud-Metakaolin Based Geopolymer Composites. *Construction and Building Materials*. 2022;361: 129718.
22. Mahakhud R, Priyadarshini M, Prakash Giri J. Utilization of Ground Granulated Blast-Furnace Slag Powder in Brick Industry: A New Generation Building Material. *Materials Today: Proceedings*. [Preprint] 2023. Available from: doi.org/10.1016/j.matpr.2023.03.707.
23. Nikvar-Hassani A, Hodges R, Zhang L. Production of Green Bricks from Low-Reactive Copper Mine Tailings: Durability and Environmental Aspects. *Construction and Building Materials*. 2022;337: 127571.
24. Ahmed MM, El-Naggar KAM, Tarek D, Ragab A, Sameh H, Zeyad AM, Tayeh BA, Maafa IM, Yousef A. Fabrication of Thermal Insulation Geopolymer Bricks Using Ferrosilicon Slag and Alumina Waste. *Case Studies in Construction Materials*. 2021;15: e00737.
25. Ahmad M, Rashid K. Novel Approach to Synthesize Clay-Based Geopolymer Brick: Optimizing Molding Pressure and Precursors' Proportioning. *Construction and Building Materials*. 2022;322: 126472.
26. Das D, Gołąbiewska A, Rout PK. Geopolymer Bricks: The next Generation of Construction Materials for Sustainable Environment. *Construction and Building Materials*. 2024;445: 137876.
27. Youssef N, Lafhaj Z, Chapiseau C. Economic Analysis of Geopolymer Brick Manufacturing: A French Case Study. *Sustainability*. 2020;12(18): 7403.
28. Hematibahar MH, Kharun M, Fediuk RS, Vatin NI, Porvadov MG, Sabitov LS. Predicting the flexural strength of 3D-printed geopolymer reinforced concrete using machine learning techniques. *Materials Physics and Mechanics*. 2025;53(4): 22–34.
29. Saeed A, Najm HM, Hassan A, Sabri MMS, Qaidi S, Mashaan NS, Ansari K. Properties and Applications of Geopolymer Composites: A Review Study of Mechanical and Microstructural Properties. *Materials*. 2022;15(22): 8250.
30. Amran M, Al-Fakih A, Chu SH, Fediuk R, Haruna S, Azevedo A, Vatin N. Long-Term Durability Properties of Geopolymer Concrete: An In-Depth Review. *Case Stud. Constr. Mater.* 2021;15: e00661.
31. Qin Z, Shi Q, Qin D, Wang H, Luo Y, Wang W. Performance comparison of geopolymer and clay-cement grouting pastes and goaf effect evaluation of grouting backfilling method. *Front. Mater.* 2023;10: 1301504.
32. Rihan Maaze M, Shrivastava S. Design Development of Sustainable Brick-Waste Geopolymer Brick Using Full Factorial Design Methodology. *Constr Build Mater*. 2023;370: 130655.
33. Zheng Y, Xiao Y. A Comparative Study on Strength, Bond-Slip Performance and Microstructure of Geopolymer/Ordinary Recycled Brick Aggregate Concrete. *Constr Build Mater*. 2023;366: 130257
34. Pilien VP, Promentilla MAB, Leaño JL, Oreta AWC, Ongpeng JMC. Confinement of Concrete Using Banana Geotextile-Reinforced Geopolymer Mortar. *Sustainability*. 2023;15(7): 6037.
35. Elemam WE, Tahwia AM, Abdellatief M, Youssf O. Kandil MA. Durability, Microstructure, and Optimization of High-Strength Geopolymer Concrete Incorporating Construction and Demolition Waste. *Sustainability*. 2023;15: 15832.
36. Hosseinbor J, Madani H, Norouzifar MN. Improving the Characteristics of Less Active Geopolymer Binders Utilizing Ground Granulated Blast-Furnace Slag under Different Curing Conditions. *Sustainability*. 2023; 15(16): 12165.
37. Azimi Z, Toufigh V. Influence of Blast Furnace Slag on Pore Structure and Transport Characteristics in Low-Calcium Fly-Ash-Based Geopolymer Concrete. *Sustainability*. 2023;15(18): 13348.

38. Samarina T, Guagneli L, Takaluoma E, Tuomikoski S, Pesonen J and Laatikainen O. Ammonium removal by metakaolin-based geopolymers from municipal and industrial wastewaters and its sequential recovery by stripping techniques. *Front. Environ. Sci.* 2020;10: 1033677.
39. Chen L, Wang T, Li F, Zhou S. Preparation of geopolymer for *in-situ* pavement construction on the moon utilizing minimal additives and human urine in lunar regolith simulant. *Front. Mater.* 2024;11: 1413432.
40. Medpelli D, Seo D-K. Synthesis and Characterization of Dispersible Geopolymer Nanoaggregates. *Front. Chem.* 2020;9: 751085.
41. Singh N, Colangelo F, Farina I. Sustainable Non-Conventional Concrete 3D Printing—A Review. *Sustainability*. 2023;15(13): 10121.
42. Tukaziban A, Shon CS, Zhang D, Kim JR, Kim JH. Chung, CW. Synthesis and Evaluation of Geopolymer Mixtures Containing Chronologically Aged Basic Oxygen Furnace Slags. *Sustainability*. 2023;15(24): 16934.
43. Zhang J, Fernando S, Law DW, Gunasekara C, Setunge S, Sandanayake M, Zhang G. Life Cycle Assessment for Geopolymer Concrete Bricks Using Brown Coal Fly Ash. *Sustainability*. 2023;15(9): 7718.
44. Popovich J, Chen S, Iannuzo N, Ganser C, Seo D-K and Haydel SE. Synthesized Geopolymers Adsorb Bacterial Proteins, Toxins, and Cells. *Front. Bioeng. Biotechnol.* 2020;8: 527.
45. Kang X, Gan Y, Chen R, Zhang C. Sustainable Eco-Friendly Bricks from Slate Tailings through Geopolymerization: Synthesis and Characterization Analysis. *Constr Build Mater*. 2021;278: 122337.
46. Cong M, Zhang S, Sun D, Zhou K. Optimization of Preparation of Foamed Concrete Based on Orthogonal Experiment and Range Analysis. *Front. Mater.* 2021;8: 778173.
47. Robayo-Salazar R, Martínez F, Vargas A, Mejía de Gutiérrez R. 3D Printing of Hybrid Cements Based on High Contents of Powders from Concrete, Ceramic and Brick Waste Chemically Activated with Sodium Sulphate (Na_2SO_4). *Sustainability*. 2023;15(13): 9900.
48. Zhao X, Wang H, Gao H, Liang L, Yang J. Synthesis, Stability and Microstructure of a One-Step Mixed Geopolymer Backfill Paste Derived from Diverse Waste Slags. *Sustainability*. 2023;15(8): 6708.
49. Ivanović M, Knežević S, Mirković MM, Kljajević L, Bučevac D, Pavlović VB, Nenadović M. Structural Characterization of Geopolymers with the Addition of Eggshell Ash. *Sustainability*. 2023;15(6): 5419.
50. Zhang M, Qiu X, Shen S, Wang L, Zang Y. Mechanical and Thermal Insulation Properties of RGFRP Fiber-Reinforced Lightweight Fly-Ash-Slag-Based Geopolymer Mortar. *Sustainability*. 2023;15(9): 7200.
51. Nagaraju TV, Bahrami A, Azab M and Naskar S. Development of sustainable high performance geopolymer concrete and mortar using agricultural biomass—A strength performance and sustainability analysis. *Front. Mater.* 2023;10: 1128095.
52. Yatsenko EA, Goltsman BM, Novikov YV, Trofimov SV, Ryabova AV, Smoliy VA, Klimova LV. Recycling of Coal Combustion Waste through Production of Foamed Geopolymers with Improved Strength. *Sustainability*. 2023;15(23): 16296.
53. Haq Md ZU, Sood H, Kumar R, Merta I. Taguchi-Optimized Triple-Aluminosilicate Geopolymer Bricks with Recycled Sand: A Sustainable Construction Solution. *Case Studies in Construction Materials*. 2024;20: e02780.
54. Mortada Y, Masad E, Kogbara RB, Mansoor B, Seers T, Hammoud A, Karaki A. Development of Ca(OH)2-Based Geopolymer for Additive Manufacturing Using Construction Wastes and Nanomaterials. *Case Studies in Construction Materials*. 2023;19: e02258.
55. Ahmad M, Rashid K, Hameed R, Ul Haq E, Farooq H, Ju M, Physico-Mechanical Performance of Fly Ash Based Geopolymer Brick: Influence of Pressure – Temperature – Time. *Journal of Building Engineering*. 2022;50: 104161.
56. Li C, Tan G, Weng H, Shi J, Li S, Xie J. Feasibility of using FA and GGBS-derived geopolymer for high liquid limit soil stabilization. *Front. Mater.* 2025;12: 1643683.
57. Morsy MI, Alakeel KA, Ahmed AE, Abbas AM, Omara AI, Abdelsalam NR, Emaish HH. Recycling Rice Straw Ash to Produce Low Thermal Conductivity and Moisture-Resistant Geopolymer Adobe Bricks. *Saudi J Biol Sci*. 2022;29: 3759–3771.
58. Li Y, Shen J, Lin H, Lv J, Feng S, Ci J. Properties and Environmental Assessment of Eco-Friendly Brick Powder Geopolymer Binders with Varied Alkali Dosage. *Journal of Building Engineering*. 2022;58: 105020.
59. Kakodkar S, Sawaiker U. Composite Material Design for Bricks Manufacturing. *Mater Today Proc*. 2023;05: 663.
60. Usman Kankia M, Baloo L, Danlami N, Zawawi NA, Bello A, Muhammad SI. Microstructural Analysis and Compressive Strength of Fly Ash and Petroleum Sludge Ash Geopolymer Mortar under High Temperatures. *Sustainability*. 2023;15(12): 9846.
61. Aperador W, Bautista-Ruiz J, Sánchez-Molina J. Geopolymers Based on a Mixture of Steel Slag and Fly Ash, Activated with Rice Husks and Reinforced with Guadua Angustifolia Fibers. *Sustainability*. 2023;15(16): 12404.

62. Dai BB, Zou Y, He Y, Lan M, Kang Q. Solidification Experiment of Lithium-Slag and Fine-Tailings Based Geopolymers. *Sustainability*. 2023;15(5): 4523.
63. Hwalla J, Bawab J, El-Hassan H, Abu Obaida F, El-Maaddawy T. Scientometric Analysis of Global Research on the Utilization of Geopolymer Composites in Construction Applications. *Sustainability*. 2023;15(14): 11340.
64. Muhammad MK, Mohd Arif Zainol MRR, Ikhsan J Zawawi MH, Abas MA, Mohamed Noor N, Abdul Razak N, Sholichin M, Assessment of Debris Flow Impact Based on Experimental Analysis along a Deposition Area. *Sustainability*. 2023;15(17): 13132.
65. Nisa AU, Singh P. An Alkali Activated Geopolymer Concrete Brick Incorporated with Devri Stone Quarry Dust. *Mater Today Proc*. [Preprint] 2023. Available from: doi.org/10.1016/j.matpr.2023.03.085.
66. Hussain S, Amritphale S, Matthews J, Paul N, Matthews E, Edwards R. Advanced Solid Geopolymer Formulations for Refractory Applications. *Materials*. 2024;17(6): 1386.
67. Łach M, Róg G, Ochman K, Pławecka K, Bąk A, Korniejenko K. Assessment of Adhesion of Geopolymer and Varnished Coatings by the Pull-Off Method. *Eng*. 2022;3(1): 42-59.
68. Mukhametkaliyev T, Ali MH, Kutugin V, Savinova O, Vereschagin V. Influence of Mixing Order on the Synthesis of Geopolymer Concrete. *Polymers*. 2022;14(21): 4777.
69. Boros A, Korim T. Development of Geopolymer Foams for Multifunctional Applications. *Crystals*. 2022;12(3): 386.
70. Migunthanna J, Rajeev P, Sanjayan J. Waste Clay Bricks as a Geopolymer Binder for Pavement Construction. *Sustainability*. 2022;14(11): 6456.
71. Aurelie Tchouateu Kamwa R, Tchadjie Noumbissie L, Tome S, Idriss E, Giogetti Deutou Nemaleu J, Tommes B, Woschko D, Janiak C, Etoh MA. A Comparative Study of Compressed Lateritic Earth Bricks Stabilized with Natural Pozzolan-Based Geopolymer Binders Synthesized in Acidic and Alkaline Conditions. *Constr Build Mater*. 2023;400: 132652.
72. Mahdi SN, Babu RDV, Hossiney N, Abdullah MMAB. Strength and Durability Properties of Geopolymer Paver Blocks Made with Fly Ash and Brick Kiln Rice Husk Ash. *Case Studies in Construction Materials*. 2022;16: e00800.
73. Ahmari S, Zhang L. Durability and Leaching Behavior of Mine Tailings-Based Geopolymer Bricks. *Constr Build Mater*. 2013;44: 743–750.
74. Kabantsev O, Cajamarca-Zuniga D. Proposal for improving the solid clay brick contact surface to increase the initial shear strength of masonry. *Materials Today: Proceedings*. [Preprint] 2023. Available from: doi.org/10.1016/j.matpr.2023.05.640.
75. Yong-Sing N, Yun-Ming L, Cheng-Yong H, Abdullah MMAB, Rojviriya C, Khalid MS, Shee-Ween O, Wan-En O, Yong-Jie H. Interaction of Silica Fume on Flexural Properties of 10 Mm-Thickness Geopolymers Based on Fly Ash and Ladle Furnace Slag under the Thermal Conditions. *Journal of Building Engineering* 2023;69: 106331.
76. Naenudon S, Vilaivong, Zaetang Y, Tangchirapat W, Wongsa A, Sata V, Chindaprasirt P. High Flexural Strength Lightweight Fly Ash Geopolymer Mortar Containing Waste FIber Cement. *Case Studies in Construction Materials* 2022;16: e01121.
77. George G, Shreeram PK, Minalan AS, Lokesh K, Mano M, Prince A. Numerical Investigation on the Flexural Behavior of Geopolymer Concrete Beam Reinforced with Different Types of Fiber-Reinforced Polymer Bars. *Mater Today Proc*. 2023;16: e01121.
78. Cajamarca-Zuniga D, Kabantsev OV, Campos D. Geometric characterization of solid ceramic bricks for construction in Ecuador. *Structural Mechanics of Engineering Constructions and Buildings*. 2023;19(3): 329-336.
79. Zheng Y, Xiao Y, Wang C, Li Y. Behavior of Square Geopolymer Recycled Brick Aggregate Concrete Filled Steel Tubular Stub Columns under Axial Compression. *Constr Build Mater*. 2023;363: 129823.

MATERIALS PHYSICS AND MECHANICS RESEARCH ARTICLE

Submitted: September 11, 2025 **Revised: October 28, 2025** **Accepted: November 28, 2025**

Polylactic acid filaments reinforced with natural fique fibers for 3D printing applications

S. Gomez Suarez [1], R.E. Guzman-Lopez [1], R.A. Gonzalez-Lezcano [2]✉

[1] Universidad Pontificia Bolivariana, Bucaramanga, Colombia

[2] Universidad CEU San Pablo, Madrid, Spain

✉ rgonzalezcano@ceu.es

ABSTRACT

3D printing offers advantages in terms of geometry customization and material waste reduction; however, the formulation of polymeric composite materials with improved mechanical properties remains a challenge. This study analyzes the use of natural fique fibers as reinforcement in polylactic acid filaments for additive manufacturing applications. In order to improve their compatibility with the polymer matrix, the fibers were subjected to an alkalization treatment and then incorporated into the polylactic acid at a 10 wt. % using a single-screw extruder. The composite filament was characterized by scanning electron microscopy for morphological analysis, differential scanning calorimetry, and thermogravimetric analysis. The test specimens for mechanical evaluation were manufactured by 3D printing and subjected to tensile testing according to ASTM D638-22 using a universal testing machine. In addition, statistical analysis was performed using ANOVA to determine the significance of the differences between pure polylactic acid and the reinforced composite. The differential scanning calorimetry results showed an increase in the glass transition temperature and cold crystallization temperature due to the incorporation of the fibers. Thermogravimetric analysis showed lower thermal stability of the composite, reflected in a reduction in the degradation temperature. Morphological observations indicated low interfacial adhesion between the fibers and the matrix, which contributed to the decrease in tensile strength. However, the composite material had a higher modulus of elasticity, indicating an increase in structural rigidity.

KEYWORDS

fique fibres • 3D printing • biocomposite filaments • polymer–fibre composites • PLA reinforcement

Citation: Gomez Suarez S, Guzman-Lopez RE, Gonzalez-Lezcano RA. Polylactic acid filaments reinforced with natural fique fibers for 3D printing applications. *Materials Physics and Mechanics*. 2025;53(6): 116–129. http://dx.doi.org/10.18149/MPM.5362025_9

Introduction

3D printing, also known as additive manufacturing, is a technique that has revolutionised the industrial sector by making it possible to create prototypes and complex objects quickly and with highly customised designs, building them layer by layer [1]. Among the materials most commonly used in this process, polylactic acid (PLA) stands out for its biodegradability, ease of printing, and low level of shrinkage during cooling. However, its limitations in terms of mechanical strength, fragility, and thermal stability restrict its application in more demanding conditions, which has driven the search for polymer formulations and composites with improved properties [2]. A promising strategy for improving the properties of PLA is to reinforce it with natural fibers. Materials such as bamboo, kenaf, flax, hemp, and sisal stand out for their high mechanical strength, greater thermal stability, biodegradability, and low cost, making them viable alternatives for expanding the applications of additive manufacturing [3].

The incorporation of natural fibers into polymer matrices reduces the density of the composite, favoring the manufacture of lighter parts. In addition, these composite materials have a lower environmental impact compared to pure synthetic polymers, which is advantageous for sectors such as the automotive industry, construction, and consumer goods [4]. The incorporation of natural fibers as reinforcement in polymeric materials not only reduces the cost of filaments, but also improves their degradability. In addition, this type of reinforcement gives printed parts a distinctive appearance that may be attractive to certain users or sectors, especially when accompanied by an appropriate marketing strategy [5]. The use of natural resources as reinforcement has generated interest due to their availability and their potential to modify the mechanical and thermal behavior of the material [6].

However, one of the main limitations in the manufacture of filaments with natural fibers is the incompatibility between the two phases: natural fibers are hydrophilic, while the polymer matrix is usually hydrophobic. This difference in their chemical nature can cause adhesion problems, affecting stress transfer and, consequently, the mechanical performance of the composite material, can cause adhesion problems, which can intensify when certain fiber content levels are exceeded, reducing the mechanical properties of the material [7]. Due to this limitation associated with the incompatibility between the polymer matrix and natural fibers, various treatments have been studied with the aim of improving the interfacial adhesion between the two phases [8].

In addition to compatibility between material components, processing conditions during 3D printing also play a decisive role in the behavior of natural fiber-reinforced thermoplastic composites. High temperatures in the print nozzle can degrade the fibers, negatively affecting the mechanical properties of the final product. Therefore, it is necessary to optimize parameters such as temperature and layer spacing to obtain appropriate mechanical performance according to the application requirements. Likewise, the presence of natural fibers can modify the crystallinity of the matrix, influencing its thermal stability and resistance to degradation [9,10].

There are numerous developments and studies on filaments made from polylactic acid and reinforced with natural fibres for use in 3D printing. Celik et al. [11] produced polylactic acid filaments reinforced with hemp fibres, evaluating their thermal, morphological and mechanical properties. The results showed that the addition of hemp fibres deteriorated the thermal properties after 3D printing, although the flexural strength increased slightly. Additionally, Faidallah et al. [12] evaluated filaments made from PLA reinforced with 7 % by weight of hemp and jute fibres, achieving tensile strengths of 38.8 and 62.38 MPa, respectively. These values represent significant improvements compared to the original and recycled pure PLA filaments.

Selvan et al. [13] developed a PLA composite reinforced with flax fibres, highlighting its mechanical properties. The 3D printing parameters were optimised, achieving a tensile strength of 61.13 MPa and an impact strength of 12.77 kJ/m^2. On the other hand, Wu et al. [14] fabricated 3D printing filaments from PLA and rice husk (RH), incorporating PLA modified with acrylic acid (PLA-g-AA) and rice husk treated with a coupling agent (TRH) to improve the properties of PLA/RH biocomposites. The results showed that PLA-g-AA/TRH biocomposites exhibited superior tensile properties to PLA/RH due to improved compatibility between the polymer and the reinforcement.

Suteja et al. [15] developed PLA composites reinforced with continuous fibres from pineapple leaves for 3D printing, improving the mechanical properties of thermoplastic materials. Rafiee et al. [16] created PLA composite filaments reinforced with birch fibres, highlighting their printability and potential in additive manufacturing. However, they pointed out the need to optimise extrusion and printing parameters to improve the strength and resolution of the final products, as, although the biocomposite filaments were printable, they require high settings to achieve maximum performance.

In turn, Aumnate et al. [17] manufactured PLA/kenaf biocomposite filaments, improving their mechanical properties through treatment with plasticizers. These filaments showed an increase in tensile strength and elongation, making them suitable for 3D printing applications in sustainable textiles, prosthetics, and medical devices.

Despite the aforementioned advances in the field of natural fiber-reinforced filaments for 3D printing, no studies have been found that use fique fiber as reinforcement. Similar approaches using advanced 3D-printed PLA structures have been reported in [18], and the extrusion process in FDM printing has been modeled to optimize performance [19]. Fique fiber, which comes from a plant native to Colombia, stands out for its exceptional mechanical properties, particularly its high strength [20], making it a promising option for the development of biocomposite filaments for 3D printing. Its incorporation could lead to significant improvements in both performance and functionality.

Therefore, this study develops and characterizes a PLA filament reinforced with 10 % by weight of alkali-treated fique fibers, manufactured by extrusion for application in 3D printing. The morphological and thermal properties of the filament were evaluated, as well as the mechanical properties of the material once printed.

Materials and Methods

Materials

Long fique fibres were supplied by the company Ecofibras, located in Santander, Colombia. Subsequently, they were cut to sizes of 1 to 2 mm (Fig. 1(a)). The average diameter of the fibres was 187.8 µm, according to the micrograph obtained by scanning electron microscopy (SEM), presented in Fig. 1(b).

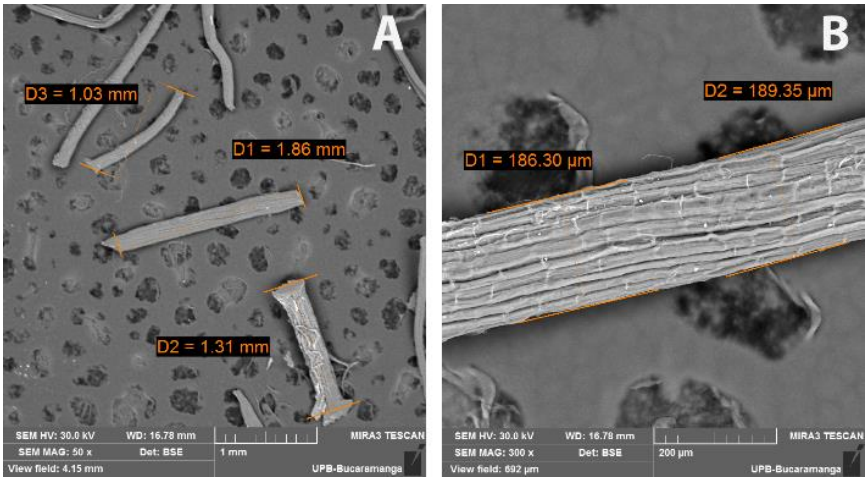

Fig. 1. SEM-images of fique fibres: (a) length of fibres after cutting; (b) average diameter of fibres

The PLA used was of 2003D grade, from renewable resources and presented in roll form. According to the manufacturer's specifications, this material has a density of 1240 kg/m³, a melt flow rate of 6 g / 10 min (measured at 210 °C with a load of 2.16 kg). Before use, PLA was dried at 60 °C for 4 h and then processed into fragments of 1 to 2 mm in size.

Alkalinisation treatment

The fique fibers were subjected to an alkalization treatment using a 10 % by weight aqueous solution of sodium hydroxide (NaOH). The fiber/solution ratio was 1:10. The fibers were kept immersed in the solution for 30 min at room temperature. After this time, the solution was decanted and the fibers were washed repeatedly with distilled water and a small amount of acetic acid (CH_3COOH) until the alkaline residues were removed, confirming neutralization using pH indicator paper.

Subsequently, and unrelated to the previous immersion time, the fibers were subjected to a manual mechanical reduction process, decreasing their diameter to a range of 10–20 µm. Finally, the fibers were placed in a Petri dish and dried at room temperature for 24 h. To remove residual moisture, the samples were then dried in an oven at 60 °C for 6 h, until they reached a constant weight. Figure 2 shows the microfibrils obtained after the mechanical reduction process.

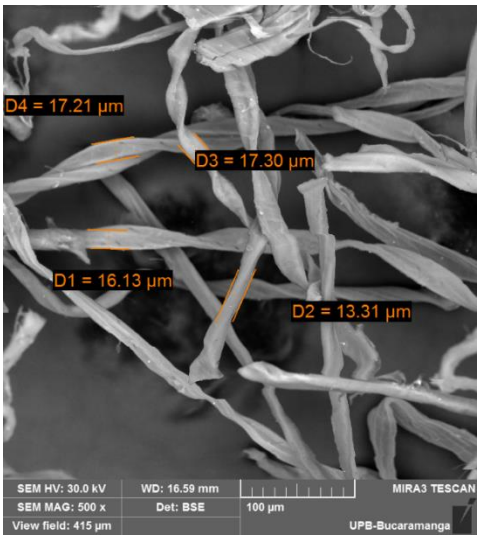

Fig. 2. SEM-images of microfibrils obtained by mechanical reduction

Filament processing

For the manufacture of the filament, a Wellzoom single-screw extruder, model Filament Extruder Line II, equipped with a 1.75 mm diameter nozzle, was used. The extrusion process was carried out at 205 °C, within the range recommended by the manufacturer for PLA and below the maximum degradation temperature of fique (337 °C), according to the study by Guzmán et al. [21], in which fique fibres were subjected to an alkalinisation treatment similar to the one used in this work. Before extrusion, the screw was preheated at 180 °C for 30 min. Extrusion was performed with a screw rotation speed of 10 rpm, which generated an exit speed at the nozzle of 8.46 mm/s.

The filament was manufactured with a 10 % weight fraction of the fique fibre. The procedure consisted of feeding the two components directly into the extruder in alternating layers, starting with 40 g of PLA, followed by 4 g of fique fibres, repeating this pattern successively.

Figure 3 shows the filament produced, from which continuous filaments of 180 cm in length were obtained. These filaments were used to manufacture the specimens for mechanical characterisation, by means of 3D printing.

Fig. 3. Extruded filament

Scanning electron microscopy

Scanning electron microscopy (SEM) was used to evaluate the adhesion between PLA and fique fibre in the extruded filament. The filament was sectioned into small fractions using a Ted Pella microtome and coated with a thin layer of gold using a Cressington Sputtering machine. This coating was done to improve the electrical conductivity of the material and to guarantee the quality of the observations during the analysis. A Tescan MIRA 3 FEG-SEM scanning electron microscope was used to capture micrographs at different focal planes, with magnifications of up to 1000X.

Thermal characterisation of the filament

A differential scanning calorimetry (DSC) analysis was performed on a 3 mg sample of the fique fibre filament and pure PLA using a TA INSTRUMENTS Discovery apparatus. The test was carried out in a nitrogen atmosphere with a flow rate of 20 ml/min, covering a temperature range of 25 to 300 °C and using a heating and cooling rate of 5 °C/min.

Thermogravimetric analysis

These findings are in line with other analyses that associate thermal degradation with printing defects in composite structures, and with studies showing that 3D printing defects strongly influence strength. The analysis was carried out in dry synthetic air atmosphere, with gas flow (25 mL/min) with a TGA5500 equipment of TA Instruments, applying a temperature increase of 5 °C/min until reaching 600 °C. TGA thermograms and derivative curves (DTG) were obtained for the filament of fique fibre with PLA, as well as for pure PLA.

Filament printing

The specimens for the mechanical characterisation of the biocomposite were manufactured by 3D printing using a Creality Ender 3 V2 and Creality Slicer 4.8 software. During the process, temperatures of 200 °C were set at the extruder and 70 °C at the printing bed, (according to the results of the thermal analysis). The use of supports for the model was not necessary, and the printing was performed at a controlled speed of 30 mm/s to ensure high precision in the details. Additionally, similar procedures have been validated for ABS-based fiber composites with infill variations. The parameters defined in the Crealty Slicer 4.8. software for 3D printing are shown in Table 1.

Table 1. Parameters defined in the printer

Quality	
Layer height, mm	0.2
Shell	
Wall thickness, mm	0.8
Wall line count	2.0
Top/bottom thickness, mm	0.8
Top thickness, mm	0.8
Botton thickness, mm	0.8
Top/bottom pattern, mm	lines
Infill	
Infill density, %	100
Infill line distance, mm	0.4
Infill pattern	lines
Minimun infill area, mm^2	0
Speed	
Print speed, mm/s	30
Infill speed, mm/s	30
Outer wall speed, mm/s	30
Travel speed, mm/s	120
Travel	
Retraction distance, mm	4
Retraction speed, mm/s	25
Cooling	
Fan speed, %	100
Regular fan speed at heigth, mm	0.6
Mimimun layer time	10

Tension test

The tensile test was performed using an MTS universal testing machine, model C43.104, following the guidelines of ASTM D638-22, entitled "Standard Test Method for Determining Tensile Properties of Plastics". Type V test specimens were used for this study, which are suitable when the amount of material available is limited. Five test specimens 3.2 mm thick and with the geometry specified in Fig. 4 (all dimensions expressed in mm) were prepared for both the PLA/fiche fiber composite and pure PLA in order to compare their mechanical behavior. The tests were performed at a crosshead displacement speed of 5 mm/min, as recommended by the standard. The values presented correspond to the average of the five tests performed for each material.

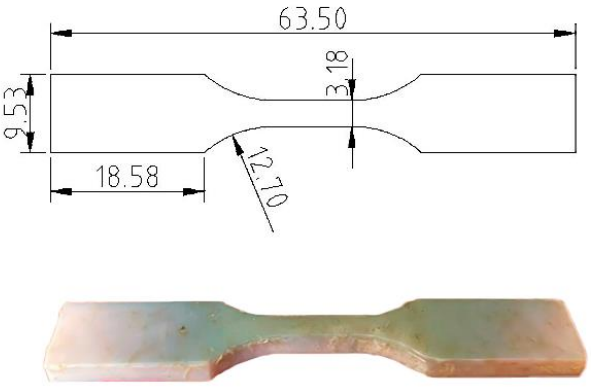

Fig. 4. Geometry of the specimen stress

Statistical analysis

The existence of statistically significant differences between the maximum stress and modulus of elasticity of the PLA–fique composite material and pure PLA were evaluated using analysis of variance (ANOVA). In this study, the ANOVA procedure was applied, which establishes that if the p-value obtained is lower than the adopted significance level (0.05), then it is concluded that the means of the mechanical properties differ statistically significantly.

Results

Morphological analysis

Figure 5 shows the adhesion and distribution of the fique fibre in the PLA matrix that makes up the manufactured filament. Scanning electron microscopy (SEM) images revealed significant voids at the matrix-fibre interface, showing poor interaction and suggesting inefficient charge transfer between the two components. Fibre agglomerates were also detected in some areas, pointing to inhomogeneous dispersion during the extrusion process.

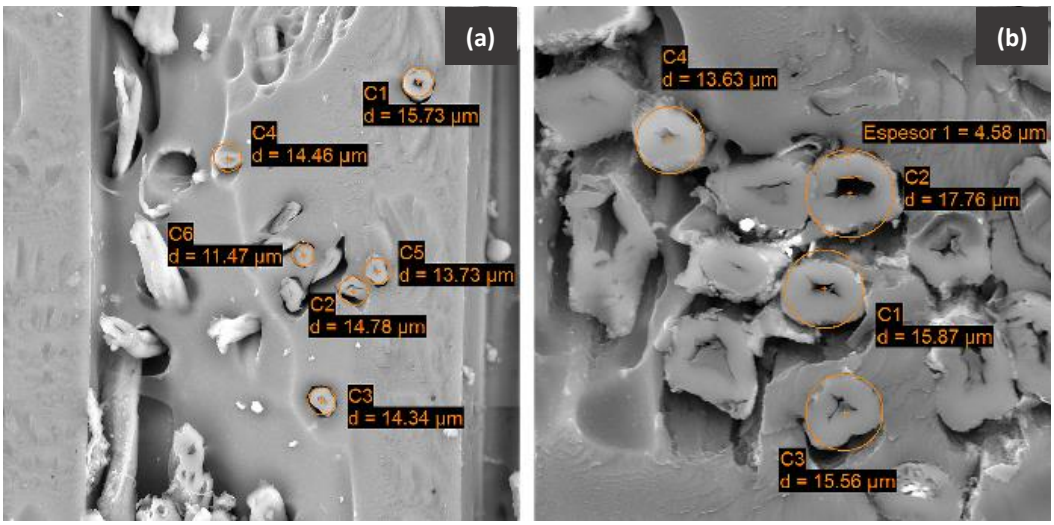

Fig. 5. Fibre-matrix adhesion micrograph: (a) 800X; (b) 1000X

This behaviour was also reported by Mazurt et al. [22] in their study on PLA filament composites reinforced with natural fibres (wood, bamboo and cork), where they observed the lack of continuity of the material and the presence of gaps between the applied filaments, which resulted in an increased porosity of the materials and subsequently affected their mechanical properties.

Thermogravimetric analysis

Thermogravimetric analysis (TGA) (Fig. 6) reveals that the incorporation of fique fibre reduces the thermal stability of PLA. In pure PLA, degradation starts at 290 °C and ends at 400 °C, while in the composite it occurs between 260 and 370 °C, advancing the decomposition process. In terms of mass loss, the pure PLA experiences a reduction of 94.63 %, while the composite loses 89.67 %, suggesting the presence of carbonaceous residues from the fique fibre, with possible effects on its thermal and structural stability. These findings are in line with other analyses that associate thermal degradation with printing defects in composite structures, and with studies showing that 3D printing defects strongly influence strength.

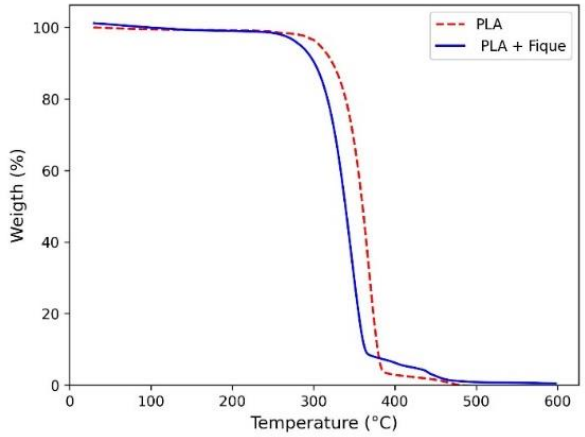

Fig. 6. TGA curves

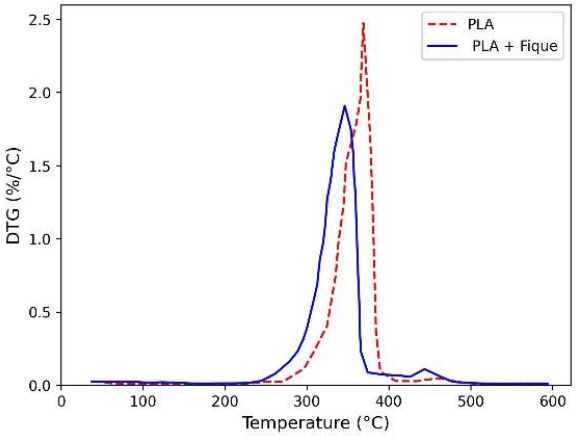

Fig. 7. DTG analysis curves

Differential thermogravimetric analysis (DTG) (Fig. 7) shows that pure PLA exhibits a single degradation peak at 380 °C, indicating rapid decomposition. In contrast, the PLA composite with fique exhibits a broader and shifted peak at 345 °C, indicating a more complex degradation process due to the decomposition of the lignocellulosic components of the fibre. The lower intensity of the peak in the composite indicates a reduction in the degradation rate, associated with the generation of carbonaceous residues that slow down the process.

Differential scanning calorimetry

The (differential scanning calorimetry) DSC analysis, represented in Fig. 8, shows that the incorporation of fique fibre modifies the thermal properties of PLA. The glass transition temperature (T_g) increased from 59.5 to 64 °C, suggesting a restriction in the mobility of the polymer chains due to the interaction with the fibre. Likewise, the cold crystallisation temperature (T_{cc}) increased from 103 to 107.5 °C, indicating a nucleating effect of the

fibre influencing the reorganisation of the polymer chains. Finally, the melting temperature (T_m) showed a slight increase from 155.5 to 156.5°C, suggesting that the addition of fique does not significantly alter the crystalline phase of PLA. Numerical simulations of PLA during additive manufacturing have confirmed similar thermomechanical behaviour.

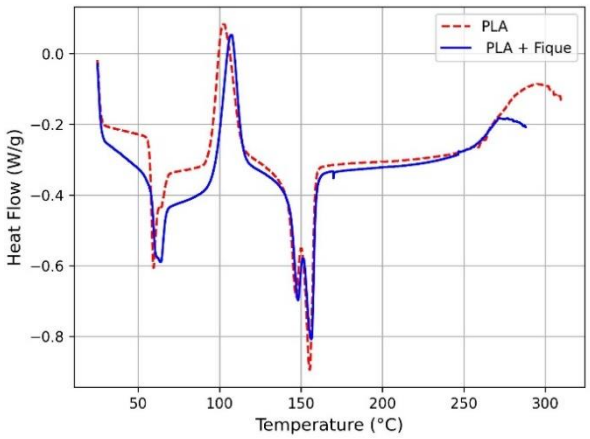

Fig. 8. DSC curves

The existence of statistically significant differences between the maximum tensile stress and the modulus of elasticity of the PLA composite reinforced with fique fibre and those of pure PLA was evaluated using an ANOVA (Analysis of Variance). According to this technique, when the p-value obtained is lower than the established significance level (0.05), it is concluded that the mean values of the mechanical properties differ significantly.

These results are consistent with those reported by Celik et al. [11], who observed similar behaviour in a PLA filament reinforced with hemp fibre. In their study, T_g increased from 55.86 to 59.7 °C, which aligns with the increase recorded in this work. Similarly, T_{cc} increased from 93.99 to 97.55 °C. Regarding Tm, although a slight decrease from 176.21 to 175.98 °C was observed, the variation was minimal and without significant impact, as also occurred in the present study.

The 3D-printing temperature settings for the PLA filament reinforced with fique fibre were established based on the thermal analysis of the material. The bed temperature was set at 70 °C to ensure proper adhesion of the first layer and to minimise deformation, as this value exceeds the glass transition temperature (T_g) of the composite, providing sufficient softening of the material at the interface.

The extrusion temperature was set at 200 °C, a value higher than the melting temperature (Tm), which guarantees adequate material flow during deposition, yet low enough to remain well below the degradation temperature identified through TGA, thus preventing thermal decomposition during printing.

Mechanical characterization

Figure 9 shows the stress–strain curves of pure PLA and the composite reinforced with fique fibre. Pure PLA exhibits the typical behaviour of thermoplastics, with an initial linear elastic response followed by plastic deformation until reaching its maximum strength,

after which it quickly loses its load-bearing capacity and fractures in a brittle manner. In contrast, the composite with fique fibre presents a well-defined elastic response but with a lower capacity for plastic deformation before fracturing.

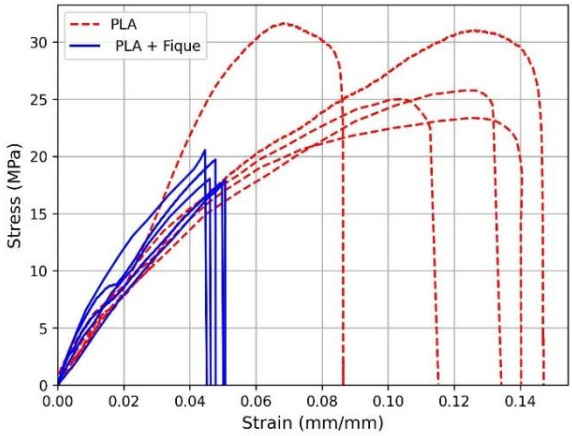

Fig. 9. Stress-strain curves

Figure 10 compares the tensile stress and modulus of elasticity of pure PLA and fique fibre reinforced composite. The tensile stress of the composite was 18.76 ± 1.30 MPa, which represents a 31.5 % reduction compared to neat PLA (27.36 ± 3.73 MPa). In contrast, its modulus of elasticity increased, reaching 593.10 ± 165.65 MPa compared to 441.34 ± 103.64 MPa in pure PLA.

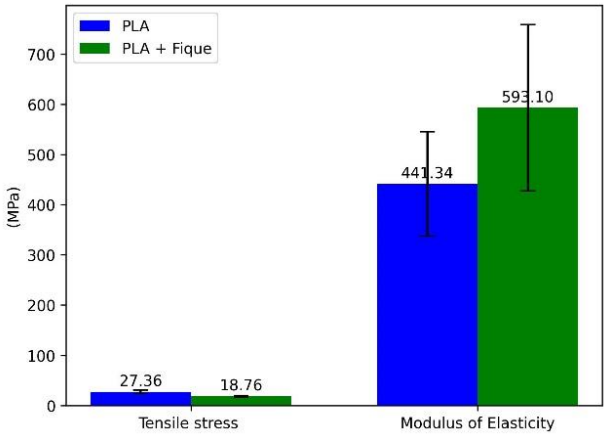

Fig. 10. Comparison of modulus of elasticity and tensile stress of PLA and PLA + Fique

The differences in tensile stress are due to poor interfacial adhesion between the fibers and the polymer matrix, as evidenced by electron microscopy images. This low adhesion hinders stress transfer, creating weak areas that reduce the strength of the composite material. Furthermore, the irregular distribution of fibers in the PLA matrix exacerbates this phenomenon, as their irregular accumulation produces stress concentrations, poor impregnation, and pore formation, further compromising the mechanical properties of the material. On the other hand, thermal analysis revealed that the incorporation of fique reduces the thermal stability of the material, accelerating its degradation.

The phenomenon of poor interfacial adhesion between the fibers and the polymer matrix—previously described through microscopic observations—could affect the structural integrity of the filament during 3D printing, negatively influencing its mechanical performance. Pitchaimani et al. [23] observed similar behavior in PLA filaments reinforced with short banana fiber, where poor interfacial adhesion reduced tensile properties by 31 % and resulted in brittle behavior, consistent with the results of this study. Comparable studies on biodegradable composites support these findings, highlighting the importance of interfacial adhesion in PLA and natural fiber systems, while other studies have reported greater thermal and mechanical stability with lignocellulosic reinforcements.

The increase in the modulus of elasticity is a key characteristic of the polylactic acid (PLA) composite reinforced with fique fibers, as discussed in the literature. This increase is due to the fact that the fique fibers, when integrated into the PLA polymer matrix, act as reinforcements. This mechanical reinforcement limits the deformation of the material under load and transfers the stresses to the more rigid fibers, resulting in a substantial improvement in the overall strength and stiffness of the composite material. Additionally, the increase in the glass transition temperature (T_g) and cold crystallization temperature (T_{cc}) of PLA with fique indicates a restriction in the mobility of the polymer chains, which favors greater crystallinity in the matrix. This effect contributes directly to the increase in the stiffness of the material, reflected in a higher modulus of elasticity.

The dual utility of fique in materials engineering is further supported by studies focused on its intrinsic properties. The fique fiber is particularly valuable not only for its structural reinforcement capabilities but also for its proven characteristics of sustainability and thermal performance, making it suitable for advanced material design. Research has confirmed the potential of Fique as a sustainable material and thermal insulation for buildings, along with studies detailing its decomposition and thermal conductivity [24]. Furthermore, the physical and mechanical properties of Fique, specifically its low thermal conductivity and high breaking strain, are essential for understanding its performance as a reinforcement and an insulating agent [25]. Its strong resistance to breaking provides the necessary mechanical reinforcement for load transfer and stiffness, while its low thermal conductivity contributes to the overall improved thermal profile of the resulting biocomposite.

Statistical analysis

Table 2 presents the ANOVA test results. These results show that the tensile stress of PLA, compared to PLA composite reinforced with natural fique fibre, has a p-value lower than 0.05, indicating statistically significant differences between the two materials. However, for the modulus of elasticity, no statistically significant differences were observed (p-value = 0.121), which means that the addition of fique fibre does not significantly affect the stiffness of the material under the evaluated conditions

Table 2. ANOVA test results

Property	Source	Sum of squares	Degrees of freedom	Mean square	FO	P
Tensile stress	Material	184.6	1	184.61	23.6	0.001
	Residuals	62.5	8	7.81		
	Total	247.1	9			
Modulus of elasticity	Material	57580	1	57580	3.02	0.121
	Residuals	152736	8	19092		
	Total	210316	9			

Conclusions

The article developed and characterized a PLA filament reinforced with 10 wt. % of alkali-treated fique fiber, analyzing its morphological, thermal, and mechanical behavior to assess its suitability for 3D printing applications. Based on the experimental evidence, the following scientific conclusions are established:

1. The incorporation of fique fiber generated measurable changes in the thermal transitions of PLA, specifically increasing the glass transition temperature (T_g) and cold crystallization temperature (T_{cc}). These modifications indicate a restriction in the mobility of the polymer chain, demonstrating that fique fibers act as nucleating agents that promote crystallization. This behavior coincides with the response observed in other lignocellulose-reinforced PLA systems, positioning fique as a functional thermal modifier.
2. Despite improvements in crystallinity-related transitions, the composite exhibited lower thermal stability, as confirmed by thermogravimetric analysis (TGA). The earlier onset of degradation suggests that the fiber introduces thermolabile components, such as hemicellulose and residual lignin. This finding is crucial for defining safe processing ranges, underscoring the need to optimize fiber purification or consider the use of thermal stabilizers.
3. Mechanically, fique-reinforced PLA achieved a significant increase in stiffness, reflected in an elastic modulus higher than that of pure PLA. This confirms that fique fibers provide effective reinforcement to support the load, transferring stress to the more rigid fiber domains and limiting deformation. This behavior demonstrates the mechanical potential of fique as a reinforcement for biodegradable structural composites.
4. However, a decrease in maximum tensile stress was observed, indicating premature failure of the composite. SEM analysis revealed insufficient fiber-matrix interfacial bonding, pores, and fiber detachment. These microstructural defects act as stress concentration points, explaining the loss of strength despite the increase in stiffness. This highlights the urgent need for improved surface treatments or compatibilizers to maximize mechanical performance.
5. Extrusion and 3D printing tests demonstrated that the developed filament is processable and compatible with standard FDM parameters, with no clogging or thermal degradation during printing. Although it has lower thermal stability, the material maintained its structural integrity during extrusion and layer deposition, demonstrating its potential for the additive manufacturing of biodegradable components with moderate mechanical requirements.
6. The results confirm that fique fiber is a technically viable and promising reinforcement for PLA-based biocomposite filaments, offering sustainability advantages due to its

availability, biodegradability, and high intrinsic strength. A solid foundation is established for understanding its behavior in filament form and identifies key areas for future optimization, such as refinement of chemical treatment, fiber dispersion strategies, and interfacial compatibilization.

7. Future research should focus on improving interfacial adhesion and thermal stability. As these two aspects currently limit tensile strength and processing robustness. Methods such as silane treatments, coupling agents, fiber microrefining, or reactive extrusion could significantly improve performance, enabling the development of high-strength biodegradable filaments suitable for engineering applications.

This study allowed the development and characterisation of a PLA filament reinforced with 10% by weight of fique fibre, evaluating its viability for 3D printing applications. The results showed that the incorporation of fique significantly modifies the thermal and mechanical properties of PLA.

It was observed that the addition of fique fibre increases the glass transition temperature and cold crystallisation temperature, indicating a restriction in the mobility of the polymer chains. However, it also reduces the thermal stability of the material, bringing forward its degradation. In terms of mechanical behaviour, the composite showed higher stiffness compared to pure PLA, although with a decrease in the maximum tensile stress, attributed to the low interfacial adhesion between the matrix and the fibre.

The results obtained show the need to improve the compatibility between the fique fibre and the polymeric matrix. The SEM analysis showed a low interfacial adhesion, with the presence of spaces and voids that affected the mechanical properties. Despite these limitations, the filament obtained proved to be suitable for 3D printing, opening up new opportunities for its application in the manufacture of sustainable and biodegradable parts.

CRediT authorship contribution statement

Sergio Gomez Suarez: review & editing, Writing – original draft; conceptualization, investigation, data curation; **Rolando Enrique Guzman-Lopez**: writing – review & editing, writing – original draft; conceptualization, investigation, data curation; **Roberto Alonso Gonzalez-Lezcano**: writing – review & editing, writing- original draft; conceptualization, supervision.

Conflict of interest

The authors declare that they have no conflict of interest.

References

1. Sözen A, Doğru A, Demir M, Özdemir HN, Seki Y. Production of waste jute doped PLA (polylactic acid) filament for fff: effect of pulverization. *Int. J. 3D Print. Technol. Digit. Ind.* 2023;7(1): 124–128.
2. Vijayan M. Advancements in Biofiller-Reinforced PLA Composites for 3D Printing: A Review. *Int. J. Res. Appl. Sci. Eng. Technol.* 2024;12(10): 748–761.
3. Ramachandran A, Mavinkere Rangappa S, Kushvaha V, Khan A, Seingchin S, Dhakal HN. Modification of Fibers and Matrices in Natural Fiber Reinforced Polymer Composites: A Comprehensive Review. *Macromol. Rapid Commun.* 2022;43(17): 2100862.

4. Ahmad MN, Ishak MR, Mohammad Taha M, Mustapha F, Leman Z. A Review of Natural Fiber-Based Filaments for 3D Printing: Filament Fabrication and Characterization. *Materials*. 2023;16(11): 4052.
5. Subramani R, Mustafa MA, Ghadir GK, Al-Tmimi HM, Alani ZK, Rusho MA, Rajeswari N, Haridas D, Rajan AJ, Kumar AP. Exploring the use of Biodegradable Polymer Materials in Sustainable 3D Printing. *Appl. Chem. Eng.* 2024;7(2): 3870.
6. Pereira DF, Branco AC, Cláudio R, Marques AC, Figueiredo-Pina CG. Development of Composites of PLA Filled with Different Amounts of Rice Husk Fibers for Fused Deposition Modeling. *J. Nat. Fibers*, 2023;20(1): 2162183.
7. Agaliotis EM, Ake-Concha BD, May-Pat A, Morales-Arias JP, Bernal C, Valadez-Gonzalez A, Herrera-Franco PJ, Proust G, Koh-Dzul JF, Carrillo JG, Flores-Johnson EA. Tensile Behavior of 3D Printed Polylactic Acid (PLA) Based Composites Reinforced with Natural Fiber. *Polymers*. 2022;14(19): 3976.
8. Hamat S, Ishak MR, Salit MS, Yidris N, Showkat Ali SA, Hussin MS, MS Abdul Manan, Suffin MQZA, Ibrahim M, Khalil ANM. The Effects of Self-Polymerized Polydopamine Coating on Mechanical Properties of Polylactic Acid (PLA)–Kenaf Fiber (KF) in Fused Deposition Modeling (FDM). *Polymers*. 2023;15(11): 2525.
9. Ivey M, Melenka GW, Carey Jason P, Ayranci C. Characterizing short-fiber-reinforced composites produced using additive manufacturing. *Adv. Manuf. Polym. Compos. Sci.* 2017;3(3): 81–91.
10. Muchhala N, Desai S, Suryawanshi VB, Tayade R. Parametric Study on Manufacturing of Continuous Glass Fibers Reinforced Polylactic Acid (PLA) Filaments for 3D Printing. *Key Eng. Mater.* 2023;969: 31–38.
11. Celik E, Uysal M, Gumus OY, Tasdemir C. 3D-Printed biocomposites from hemp fibers reinforced polylactic acid: Thermal, morphology, and mechanical performance. *BioResources*. 2024;20(1): 331–356.
12. Faidallah RF, Hanon MM, Salman ND, Ibrahim Y, Babu MN, Gaaz TS, Szakál Z, Oldal I. Development of Fiber-Reinforced Polymer Composites for Additive Manufacturing and Multi-Material Structures in Sustainable Applications. *Processes*. 2024;12(10): 2217.
13. Thamizh Selvan S, Mohandass M, Senthil Kumar VS. Pattern optimization for 3D printing of composite filament materials with natural fibers and polylactic acid. *Proc. Inst. Mech. Eng. Part E J. Process Mech. Eng.* [Preprint] 2024. Available from: doi.org/10.1177/095440892412814.
14. Wu CS, Tsou CH. Fabrication, characterization, and application of biocomposites from poly(lactic acid) with renewable rice husk as reinforcement. *J Polym Res*. 2019;26: 44.
15. Suteja J, Firmanto H, Soesanti A, Christian C. Properties investigation of 3D printed continuous pineapple leaf fiber-reinforced PLA composite. *J. Thermoplast. Compos. Mater.* 2022;35(11): 2052–2061.
16. Rafiee M, Abidnejad R, Ranta A, Ojha K, Karakoç A, Paltakari J. Exploring the possibilities of FDM filaments comprising natural fiber-reinforced biocomposites for additive manufacturing. *AIMS Mater. Sci.* 2021;8(4): 524–537.
17. Aumnate C, Soatthiyanon N, Makmoon T, Potiyaraj P. Polylactic acid/kenaf cellulose biocomposite filaments for melt extrusion based-3D printing. *Cellulose*. 2021;28(13): 8509–8525.
18. Pogrebnoi AV. Study of polylactide 3D-printed samples with double-layer weave. *Materials Physics and Mechanics*. 2022;48(2): 289–299.
19. Kudryashova OB, Toropkov NE, Lerner MI, Vorozhtsov AB. Mathematical model of extrusion in FDM 3D printing technology. *Materials Physics and Mechanics*. 2022;50(3): 388–400.
20. Muñoz-Blandón O, Ramírez-Carmona M, Rendón-Castrillón L, Ocampo-López C. Exploring the Potential of Fique Fiber as a Natural Composite Material: A Comprehensive Characterization Study. *Polymers*, 2023;15(12): 2712.
21. Guzmán RE, Gómez S, Amelines O, Aparicio GM. Superficial modification by alkalization of cellulose Fibres obtained from Fique leaf. *IOP Conf. Ser. Mater. Sci. Eng.* 2018;437: 012015.
22. Mazur KE, Borucka A, Kaczor P, Gądek S, Bogucki R, Mirzewiński D, Kuciel S. Mechanical, Thermal and Microstructural Characteristic of 3D Printed Polylactide Composites with Natural Fibers: Wood, Bamboo and Cork. *J Polym Environ*. 2022;30: 2341–2354.
23. Mohamed Shafeer PP, Pitchaimani J, Doddamani M. A short banana fiber— PLA filament for 3D printing: Development and characterization. *Polym. Compos.* 2025;46(6): 4863–4880
24. Sánchez GFG, López REG, Gonzalez-Lezcano RA. Fique as a Sustainable Material and Thermal Insulation for Buildings: Study of Its Decomposition and Thermal Conductivity. *Sustainability*. 2021;13(13): 7484.
25. Guzmán-López RE, Cavada AMP, De Isidro Gordejuela F, González-Lezcano RA. Physical and mechanical properties of Fique: Thermal conductivity and breaking strain. *The Journal Of Strain Analysis For Engineering Design*. 2025;60(5): 323–335.

MATERIALS PHYSICS AND MECHANICS RESEARCH ARTICLE

Submitted: August 28, 2024 **Revised: September 12, 2025** **Accepted: October 30, 2025**

Multi-physics simulation to estimate exposure time for microwave-assisted metallic cast

A. Kumar ✉, **A.K. Bagha**, **S. Sharma**

Dr. B. R. Ambedkar National Institute of Technology Jalandhar, Punjab, India

✉ ashishkumar.me.22@nitj.ac.in

ABSTRACT

Microwave casting utilizes microwave energy to heat and cast metallic materials. This technique is novel and efficient in comparison to traditional methods. This technique has been applied to cast various metallic materials. There are some factors like dielectric characteristics of processing material, casting setup design, and choices of susceptor and mold, that affect the microwave heating rate. Consequently, determining the optimal exposure time for cast experimentally can be challenging. To address this, simulation studies are valuable. This study involves finite element modeling of microwave casting experimental setup. Using finite element simulations, the exposure times are predicted that are required to cast various metallic powders (Ni, stainless steel SS-316, and Cu) under identical parametric conditions in an electromagnetic environment. The impacts of microwave heating are analyzed through electric field configuration, resistive losses, and thermal distribution within the applicator cavity. The electric field intensity is observed to be maximum (4.46 × 104 V/m) in the susceptor zone, resulting in the highest resistive losses (4.9 × 109 W/m^3) in that area. Under the specified conditions, the exposure times to cast Ni, SS-316 and Cu powder into dimensions of 150 × 35 × 3 mm^3, are predicted as 2280, 2080, and 1125 s respectively. Experimental results confirm these times with an average percentage error of 13.83 %, demonstrating a close correlation between predicted and actual exposure times.

KEYWORDS

microwave casting • exposure time • FE model • simulation

Acknowledgments. *The author(s) would like to thank and acknowledge Indian Science Technology and Engineering Facilities Map (I-STEM), a program sponsored by the Office of the Principal Scientific Adviser to the Govt. of India, for enabling access to COMSOL Multiphysics 5.6 software suite to carry out this work.*

Citation: Kumar A, Bagha AK, Sharma S. Multi-physics simulation to estimate exposure time for microwave-assisted metallic cast. *Materials Physics and Mechanics*. 2025;53(6): 130–144.
http://dx.doi.org/10.18149/MPM.5362025_10

Introduction

Over the years, materials have been fabricated through traditional casting processes and are extensively used for industrial applications [1,2]. In these processes, conventional heating sources are used to heat the materials from the exterior to the interior core. This results in several drawbacks, such as non-uniform heating, high energy consumption, long processing time, material wastage, and, most importantly, not being suitable to the environment [3]. Over the last two decades, researchers from all around the world have been trying to develop a novel technique that can provide advantages of energy efficiency, unique heating abilities, and an eco-friendly working environment; however, they are facing challenges. Microwave-assisted casting is an advanced manufacturing technique that offers numerous benefits over traditional methods. The conventional heating processes rely on conduction or convection to transfer heat from a source to a target. Whereas microwave heating directly converts energy into heat within the material

itself. This method eliminates the need for heating furnaces and other heat transfer mediums. Microwaves are absorbed by the material, causing its particles to interact and generate heat throughout the entire volume, resulting in more uniform heating [4]. This efficient heating process reduces energy consumption and improves overall operational efficiency. Microwave-assisted casting offers significant energy advantages, with the required energy being only about one-third of that in conventional casting. Combined with direct volumetric heating, shorter processing times, and reduced heat losses, this highlights its superior energy efficiency. Additionally, microwave heating is relatively simple to implement, requires less setup compared to traditional methods, and produces less waste or hazardous by-products, making it a greener technology [5,6].

The electromagnetic waveform that has a frequency between 300 to 300 GHz is termed as microwaves. The microwave heating phenomenon relies on the principle of dielectric heating [7]. The depth of penetration (skin depth) of microwaves into materials, is crucial for effective microwave processing. For metallic materials, the skin depth is very small, so direct exposure to microwaves results in insufficient heating [8].

Earlier it was believed that processing metallic materials with microwave energy was impossible because metals reflect microwaves and do not interact effectively with them. To address this challenge, the concept of microwave hybrid heating (MHH) was developed [9,10]. This approach uses a susceptor [11–13], a microwave-absorbing material with a high dielectric loss factor. The susceptor is utilized to initially transfer heat to the metal until it reaches its critical temperature (T_c). Once the metal reaches this temperature, it begins to absorb microwaves effectively with increased penetration depth. Microwave-assisted metal casting uses microwave energy to melt and process metal-based materials. It can be classified into in-situ and ex-situ castings [14–17]. A variety of metals, alloys and metal matrix composites (MMCs) were cast through MHH are listed below in Table 1.

It is revealed from the literature that the casting of materials using microwave energy is dependent upon various process parameters such as casting setup design and geometry, dielectric characteristics of casting material and operating conditions [14]. Based on

Table 1. Parametric description of various microwave casts reported earlier

Sr. No.	Authors	Material	Weight / size, g/mm	Susceptor	Applicator frequency, GHz	Power, W	Exposure time, s
1.	Gangwar, et al. [18]	Alum. Alloys 6063/6063A	150	Silicon carbide (SiC)	2.45	900	700
2.	Kaushal [19]	MMC	50 × 12	Charcoal powder	2.45	900	900
3.	Lingappa, et al. [20]	Al 1050	250	Silicon carbide (SiC)	2.45	900	1200
4.	Mishra and Sharma [21]	AA 7039	–	Silicon carbide (SiC)	2.45	1400	930
5.	Mishra and Sharma [22]	Copper	–	Silicon carbide (SiC)	2.45	1400	900
6.	Shashank, et al. [23]	Brass	600	Silicon carbide (SiC)	2.45	900	1500
7.	Marahadige, et al. [24]	Brass	–	Silicon carbide (SiC)	2.45	3300	1020
8.	Ram, et al. [25]	SS-316	60 × 20 × 5	Charcoal powder	2.45	900	1200
9.	Singh, et al. [26]	MMC	50×20×6	Charcoal powder	2.45	900	1500
10.	Kumar, et al. [27]	MMC	–	Charcoal powder	2.45	900	350
11.	Pal, et al. [28]	MMC	–	Pulverized charcoal	2.45	900	1900
12.	Nandwani, et al. [29]	MMC	55 × 12 × 5	Activated charcoal	2.45	900	1200
13.	Kaushal, et al. [30]	MMC	–	Charcoal powder	2.45	900	660–1020

selected process parameters, the heating rate of specimens is also affected. Therefore, it is difficult to estimate the optimal exposure time for microwave cast experimentally. Moreover, experimental measurement of parameters like electromagnetic distribution, thermal history and heat transfer mechanism within the cavity is also challenging. In these cases, simulation studies can be more effective for predicting and understanding the complex multi-physics involved in microwave heating phenomena. Simulation tools can incorporate detailed models of these phenomena, allowing for a more comprehensive understanding and prediction of the heating behavior. Multi-physics coupled model can provide insights into how different parametric conditions influence the heating rate during the process [31].

In [32–36], FE simulations are successfully modelled and validated by researchers for microwave processing and melting of metallic materials using parametric variations. However, there is limited research reported on predicting the optimal exposure time for microwave casts of different sizes and materials. In this context, in this work, the FE simulation model of a microwave casting setup is designed through the COMSOL multi-physics tool. The FE model examines the MHH effects and predicts the exposure time required to cast different metallic powders (Ni, SS-316, and Cu) in an electromagnetic environment. The impacts of MHH are analyzed within the applicator cavity through electric field configuration, resistive heating, and thermal distribution. Based on these predicted exposure times, the specimens are cast experimentally using microwave casting. The study includes the comparison of the simulated outcomes with the experimental findings.

FE model

Microwave-assisted casting involves multi-physics phenomena, including electromagnetic field interactions and heat transfer. An FE model of microwave casting is developed using the COMSOL multi-physics tool [37]. This study involved creating a 3D geometry of the experimental setup by considering the actual experimental conditions. After the geometry is established, material properties are allocated to each component based on the actual specifications. The model geometry is then discretized into smaller elements to approximate the behavior of the entire system.

3D geometric model

Microwave-assisted casting experimental setup composed of microwave applicator and casting setup. Casting setup includes the metallic powder, mold, refractory brick, susceptor and masking brick. Figure 1 represents the schematic diagram of the casting setup.

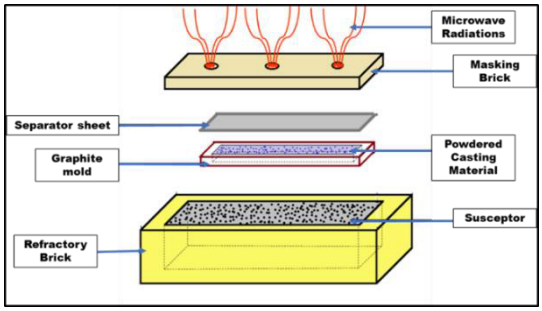

Fig. 1. Schematic diagram of refractory brick casting setup

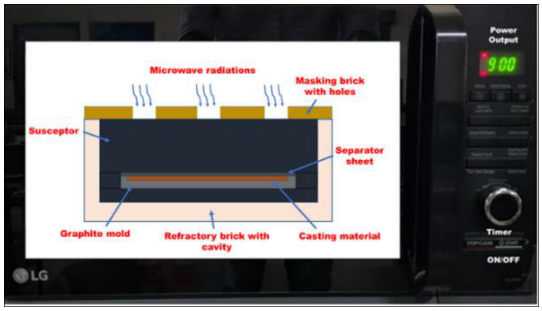

Fig. 2. Schematic diagram of experimental setup

To simplify the FE model, the following assumptions are taken into consideration (Fig. 2):

1. The waveguide and microwave cavity walls are constructed from stainless steel.
2. The microwave cavity is assumed to be filled with air.
3. The microwave oven operates at a frequency of 2.45 GHz and 900 W power output.
4. The port is excited by a transverse electric field.
5. The surrounding temperature is assumed to be 20 ºC.
6. The material properties are considered isotropic and homogeneous.
7. The dielectric and thermo-physical characteristics of the materials are assumed to be constant.
8. Mass transfer is disregarded in the study.
9. The powder material is modeled as a bulk or plate form to simplify the computational model and reduce complexity.

These simplified assumptions reduce computational complexity but may cause deviations in temperature distribution, heating uniformity, and exposure time. Ignoring mass transfer and modeling the powder as bulk can also lead to minor differences between simulated and experimental results.

Figure 3 represents the 3D geometric model of the microwave casting experimental setup modeled in COMSOL. A mold is designed with a cavity to hold the casting material. The mold is covered with the separator sheet to avoid the contamination of casting material through the susceptor. A refractory brick with a cavity is designed to contain a susceptor and prepared mold.

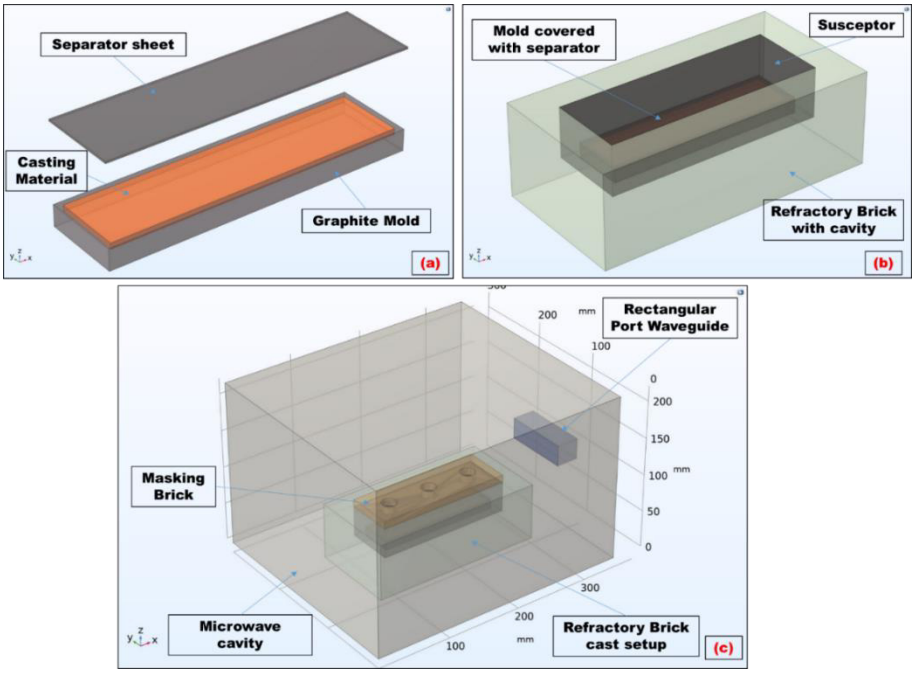

Fig. 3. 3D geometric model (a) mold and separator sheet, (b) refractory brick casting setup, (c) casting setup inside the microwave cavity

The refractory brick is covered with the masking brick with holes to allow selective microwave hybrid heating (SMHH). The complete refractory brick casting setup is placed at the optimized location within the applicator cavity. Microwave enters the cavity through rectangular port waveguide.

Table 2 displays the dimensional specifications for the components of the geometric model utilized in the experimental setup. The properties of materials are essential in microwave heating. Table 3 provides the input values for these properties in the simulated model. Relative permeability is assumed unity for all materials.

Table 2. Dimensions of the 3D geometric model

Geometry	Size, mm³
Waveguide port (TE_{10})	30 × 85 × 28
The cavity of applicator	345 × 300 × 200
Mold (cavity)	156 × 41× 10 (150 × 35 × 3)
Refractory brick (cavity)	224 × 114 × 75 (174 × 62 × 40)
Masking brick (holes)	174 × 62 × 10 (3 × Ø 25 × 10)
Separator sheet	156 × 41 × 1

Table 3. Material properties [11,32,38]

Material properties	Density (ρ), kg/m³	Electrical conductivity (σ), S/m	Relative permeability (μ_r)	Relative permittivity (ε_r)	Heat capacity at constant pressure (C_p), J/(kg·K)	Thermal conductivity (k), W/(m·K)
Ni Powder	8902	14577	1	1	440	90.9
Charcoal powder	1300	0.02	1	2.5	4186.8	0.478
Air	1	0	1	1	0	0
Stainless steel	7850	1.339e6	1	1	490	16.5
Alumina	2770	1e-14	1	4.3	885	0.32
Graphite	2100	1300	1	15	830	470
Cu powder	8700	5.998e7	1	1	385	400

Governing equations

MHH is dictated by Maxwell's electromagnetic wave equation. The following equation governs the propagation of microwaves from the port to the cavity of the applicator.

$$\nabla \times \mu_r^{-1}(\nabla \times E) - k_0^2\left(\varepsilon_r - \frac{j\sigma}{\omega\varepsilon_0}\right)E = 0, \quad (1)$$

where E is the electric field (V/m), k_0 is wave number of free space, ε_r is relative permittivity, ε_0 is the permittivity of free space, μ_r is the relative magnetic permeability, and σ is an electrical conductivity (S/m).

The relative permittivity is given as:

$$\varepsilon_r = \varepsilon' - j\varepsilon", \quad (2)$$

where ε' and ε'' are the dielectric constant and energy factor, respectively.

The relative magnetic permeability of any material during magnetization is calculated as:

$$\mu_r = \mu' - \mu", \quad (3)$$

where μ' and μ'' are magnetic field penetration into the material and magnetic loss tangent, respectively.

When an electromagnetic wave interacts with any dielectric material, the wave energy gets converted into heat can be defined as follows:

$$Q_e = Q_{rh} + Q_{ml}, \quad (4)$$

where Q_e, Q_{rh} and Q_{ml} are electromagnetic losses (W/m^3), resistive heat losses (W/m^3) and magnetic losses (W/m^3) respectively.

The resistive Q_{rh} and magnetic heat losses Q_{ml} are computed through the following:

$$Q_{rh} = \frac{1}{2} Re(J \cdot E^*), \quad (5)$$

where ω is angular frequency, J is current density (A/m^2), R_e is the Nusselt number, and E^* is electric field intensity;

$$Q_{ml} = \frac{1}{2} Re(i\omega B \cdot H^*), \quad (6)$$

where H^* and B represents the magnetic field intensity (A/m) and magnetic flux density (Wb/m^2), respectively.

The average power P_{avg} required for the conversion of electric energy into heat energy is given by the following equation:

$$P_{avg} = tan\,\delta\, E_{avg}, \quad (7)$$

where

$$E_{avg} = \frac{1}{2} \varepsilon_0 \varepsilon' E^2. \quad (8)$$

Meshing and boundary conditions

Discretizing the entire model geometry into numerous small segments is referred to as meshing. These subdivisions typically have simple shapes, such as triangles, quadrilaterals, tetrahedrons, or hexagons. To achieve convergence and accurate simulation results, mesh size is a critical factor. Mesh quality is assessed on a scale from 0 to 1, where 1 represents perfectly regular or structured elements, and 0 indicates distorted elements.

Figure 4(a) illustrates the mesh geometry. In the present FE model, a physics-controlled mesh is preferred over a user-defined mesh to ensure high-quality and accurate meshing. The physics-controlled mesh offers a range from extremely coarse to extremely fine mesh quality. For the current model, a fine mesh quality has been chosen. The finalized geometry includes 12 domains, 81 boundaries, 156 edges, and 96 vertices. The mesh comprises 760 edge elements, 4,992 boundary elements and 23,720 domain elements. The mesh quality statistics was evaluated, yielding an average elemental quality value of 0.6602, which, according to literature, falls within the acceptable range for achieving numerically accurate simulation results [11,12]. Figure 4(b) represents the mesh quality stat for the current FE model.

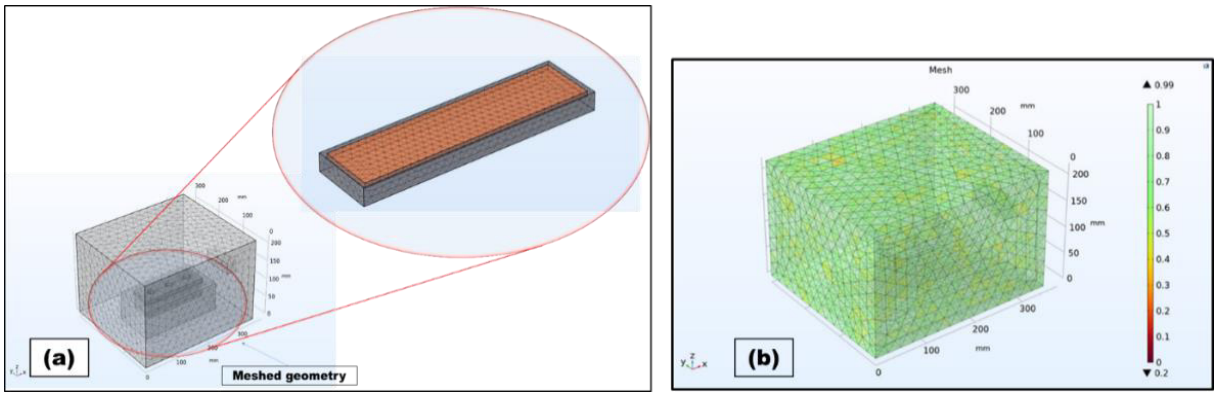

Fig. 4. (a) Mesh geometry; (b) mesh quality statistics for fine meshing

After completing the meshing process, boundary conditions are applied to the FE simulation model. Figure 5 represents the impedance and port boundary conditions [9,34,39]. As microwaves interact with the walls of the applicator cavity, they penetrate through the skin depth of the metallic material. In this simulation study, metallic walls of the applicator cavity are assigned as an impedance boundary conditions. The port boundary condition is assigned to the waveguide through which the microwave enters the cavity of the applicator.

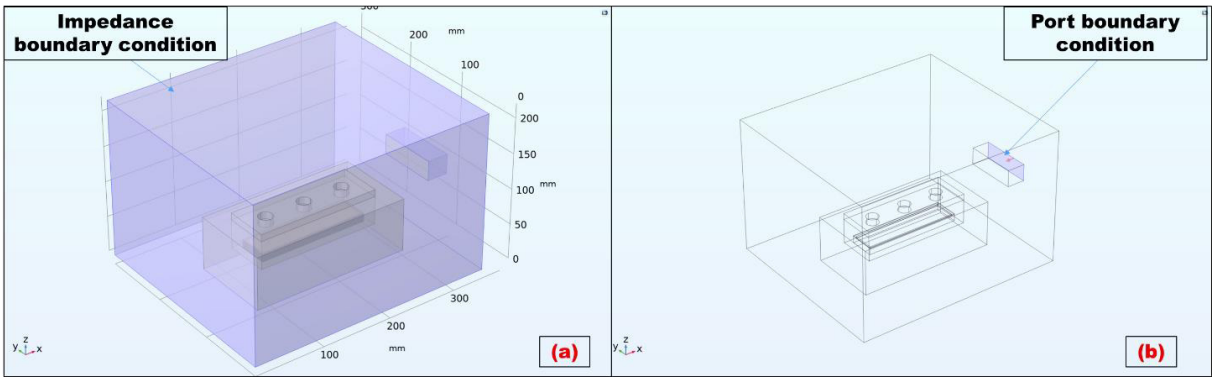

Fig. 5. (a) Impedance boundaries; (b) port boundary

Experimental study

This section describes the experimental process used to achieve microwave casting. Table 4 outlines the parameters used in the experimental process for microwave-assisted casting.

Table 4 Microwave casting process parameters

Process parameters	Overview
Microwave-type	Domestic microwave oven (Make: LG, MC3286BLT)
Cast specimen material	Ni, SS-316 and Cu powder
Power output (frequency)	900 W (2.45 GHz)
Surrounding temperature	20 °C
Susceptor	Powdered activated charcoal (AR)
Mold, separator sheet	Graphite
Refractory and masking brick	Alumina

Figure 6 represents the experimental setup which is used to achieve the microwave casting. A household microwave oven is utilized as a source of microwave energy for microwave metallic cast. To cast metallic materials using the MHH approach, a refractory brick casting setup is designed. In this work, fine metallic powders of Ni, SS-316 and Cu are taken as a cast material. The metal powder is packed in a microwave-absorbing graphite mold. A thin layer of refractory coating is applied to the interior surface of the mold to prevent the specimen from sticking. The graphite separator sheet (~ 1 mm thick) serves as a barrier between metallic powder and susceptor. Activated charcoal AR powder (molecular mass of 12.01 g/mol, density of 1.8–2.1 g/cm^3) is taken as susceptor. Activated charcoal powder is taken as a susceptor due to its high dielectric loss, thermal stability, cost-effectiveness, and easy of availability. The cavity of the alumina brick is used to contain the mold and the susceptor. The prepared mold is correctly positioned within the

cavity of the refractory brick and is surrounded by susceptor material. To facilitate SMHH, the cavity filled with the susceptor is then covered with masking alumina bricks with cylindrical openings. The cast setup is placed at the optimal location within the microwave oven to begin the heating process.

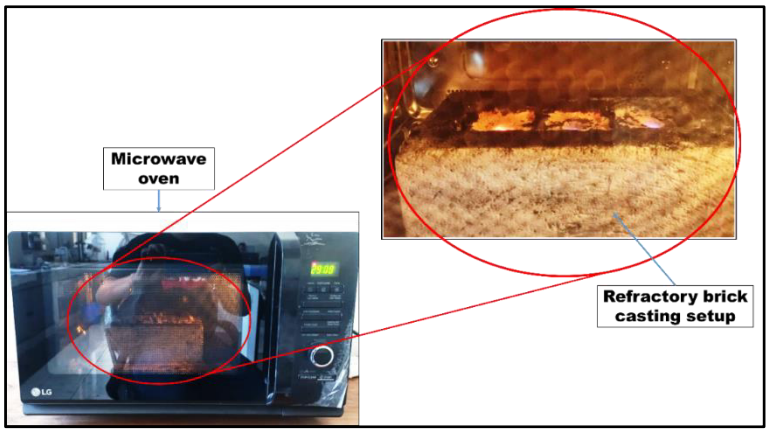

Fig. 6. Experimental setup

Results and Discussion

Simulation results

Firstly, the results in the form of electric field intensity, resistive losses, and thermal profile, obtained from the FE simulation are explained. Then the thermal profiles are compared for the different metallic casts including Ni, SS-316 and Cu.

Electric field distribution

As microwave radiations are the standing waveform; therefore, when these waves encounter any target, anti-nodal and nodal positions are developed. Nodal positions tend to cold spot regions or no heating zones and anti-nodal corresponds to the hot spot zones where the maximum heating takes place. The distribution of the electric field helps in predicting the optimum place to locate the casting setup inside the cavity to maximize

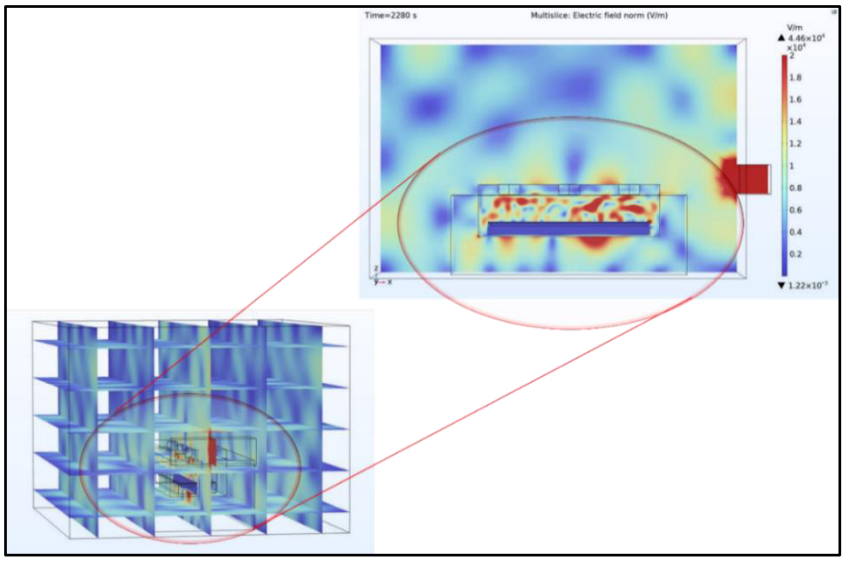

Fig. 7. Distribution of electric field

the microwave heating of the metallic cast [33,40]. The distribution of the electric field during the casting process is represented in Fig. 7, when the casting setup is located at the centremost location of the applicator cavity. The maximum intensity of the electric field is represented in red color and blue color represents the minimum electric field region. The maximum electric field strength is observed in the susceptor zone with a value of 4.46×10^4 V/m. This maximum electric field strength is likely to enhance the heating of this zone. In the free space of the applicator cavity, the value of electric field intensity is minimum as 1.22×10^{-3} V/m.

Resistive losses

The amount of energy transformed into heat energy through the absorber material is termed as resistive or joule heating. It is also responsible for heat dissipation through microwave-absorbing material. Figure 8 represents the resistive heating contour for the susceptor heating. It was observed that the resistive heating loss is maximized (4×10^9 W/m^3) within the susceptor zone. Therefore, in this zone, the maximum amount of energy of interaction between microwave and particles of charcoal powder is converted into heat. In the other domains such as microwave cavity filled with air, refractory brick and masking brick, zero losses as observed due to their non-interactive behavior with microwaves. This resistive heating phenomenon highlights the significance of SMHH.

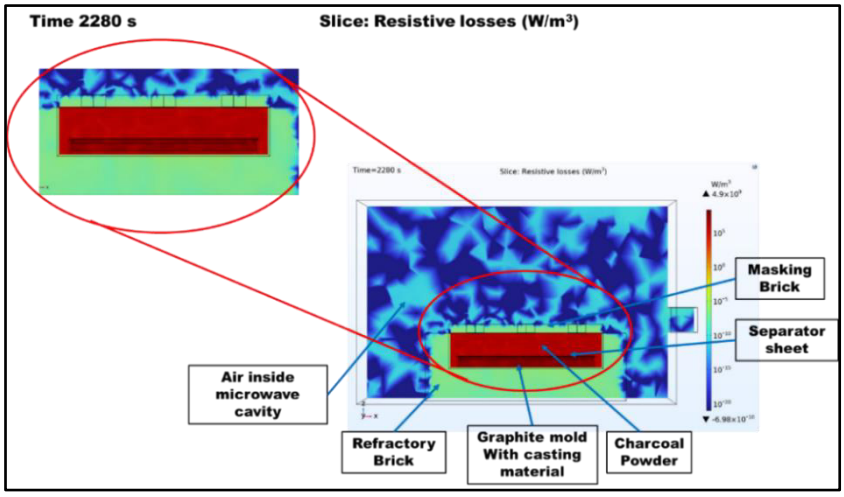

Fig. 8. Resistive heating (W/m^3)

Thermal profile

The simulation results of the thermal profile of the susceptor domain undergoing through microwave heating process are represented in Fig. 9. The thermal profiles have been plotted at four random time intervals of 360, 720, 1440 and 2280 s.

Figure 9 shows that the susceptor heats up more rapidly near the openings in the masking brick, which allows microwave radiation to enter the cavity. This illustrates the significance of SMHH. Due to interactions of microwaves with susceptor, there is a rapid increase in its temperature. The temperature of the susceptor reached around 1560 °C in 2280 s. The increased temperature of the susceptor helps in transferring the heat to the metallic powder through graphite mold via a conductive mode of heat transfer.

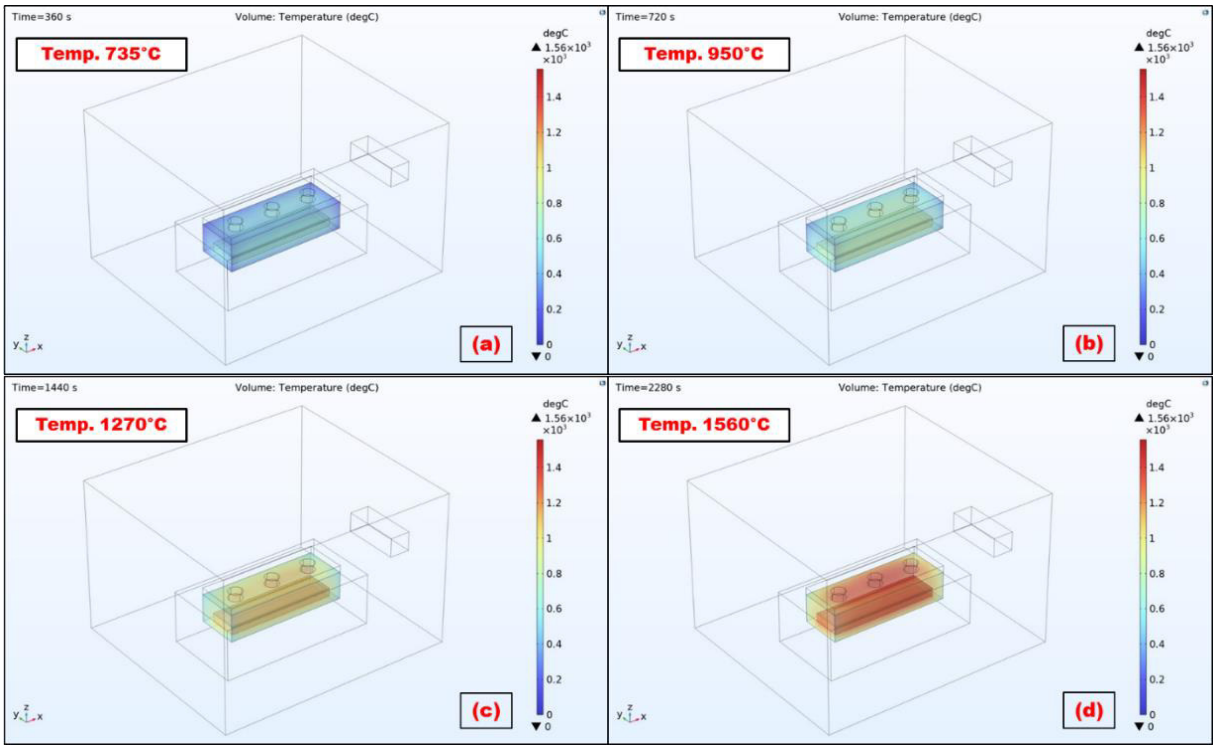

Fig. 9. Temperature distribution of charcoal inside the cavity at: (a) 360 s; (b) 720 s; (c) 1440 s; (d) 2280 s

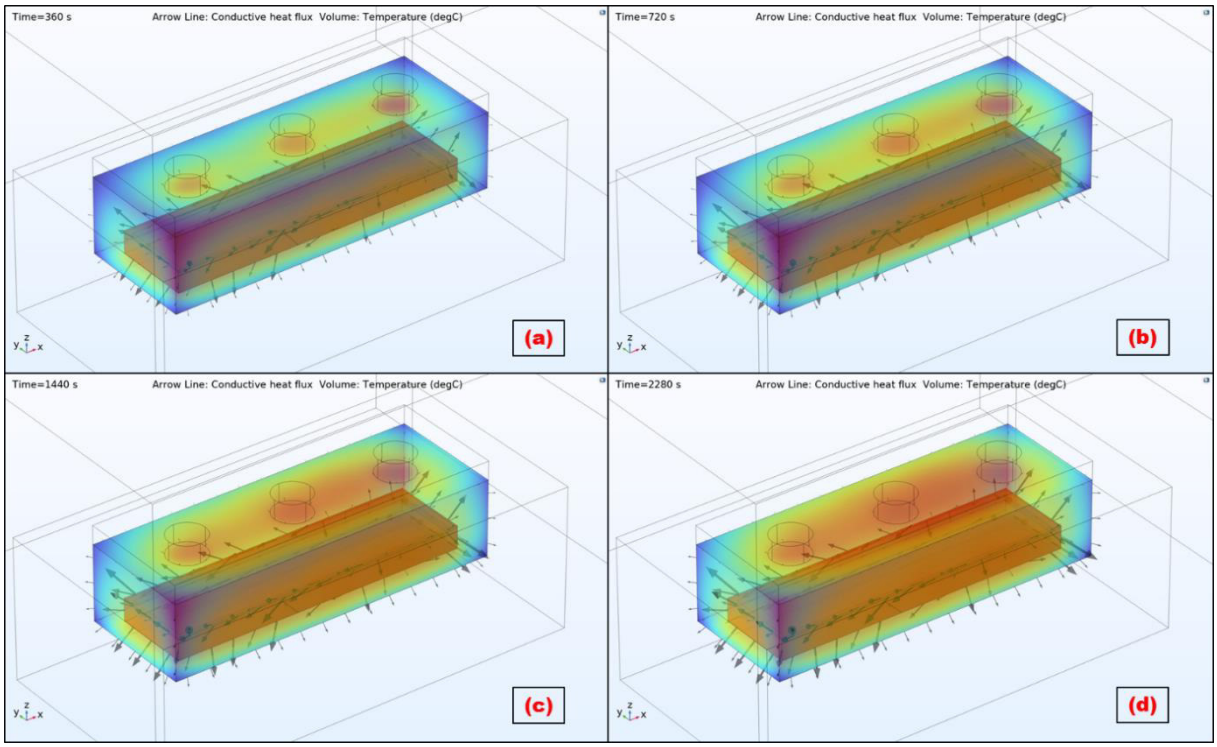

Fig. 10. Conductive heat transfer in susceptor domain at: (a) 360 s; (b) 720 s; (c) 1440 s; (d) 2280 s

The analysis of Fig. 10 illustrates the volumetric heating of the susceptor domain and the conductive flow of heat transfer through the susceptor inside the cavity. The black arrows indicate the direction of conductive heat flux, with the length of the arrow representing the magnitude of heat transfer. It is observed from Fig. 10 that the length of arrows increases with the increased temperature of the susceptor. This indicates that

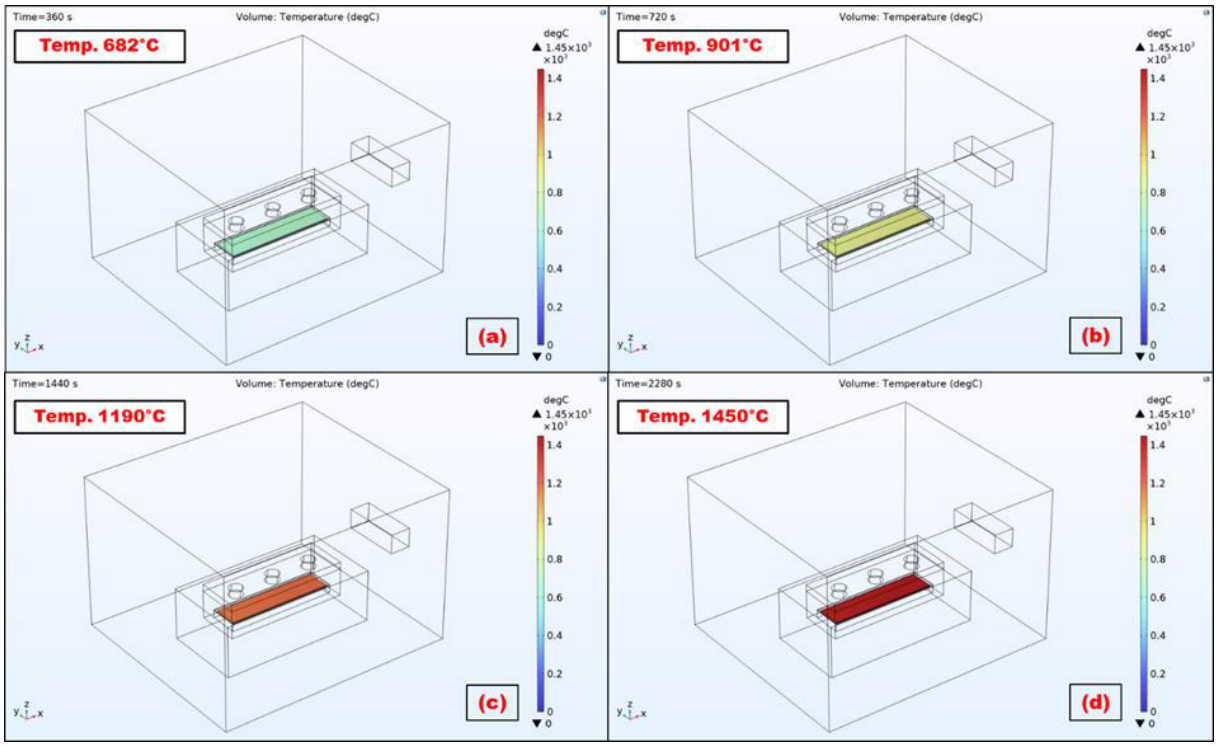

Fig. 11. Volumetric temperature distribution of Ni cast at: (a) 360 s; (b) 720 s; (c) 1440 s; (d) 2280 s

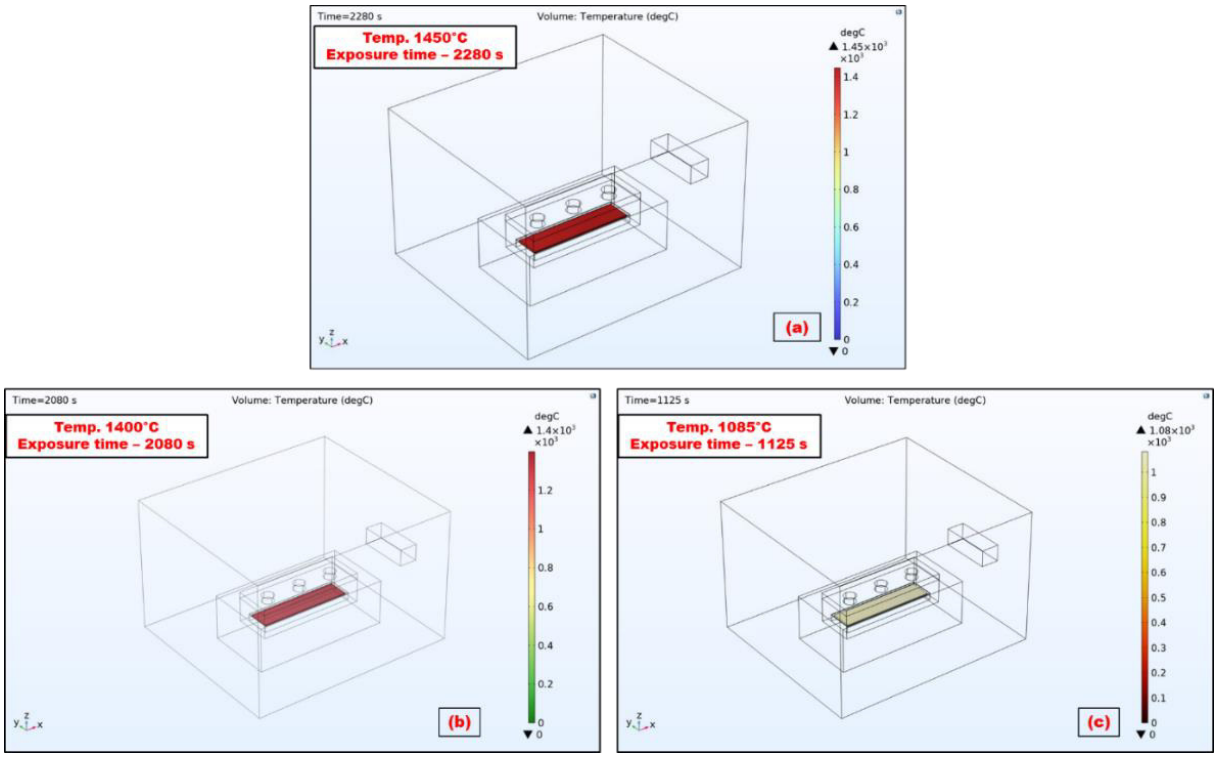

Fig. 12. Thermal profile for metallic cast: (a) Ni; (b) SS-316; (c) Cu

the magnitude of heat transfer through the susceptor rises with its temperature. The conductive heat transfer helps in raising the temperature of metallic powder inside the mold. As a result, the penetration depth of metallic powder to microwaves gets increased and it also starts absorbing the microwaves. The simulation results of thermal profile of

Ni powder undergoing through microwave heating process is represented in Fig. 11. According to the simulation results, the volumetric temperature of Ni cast approaches its melting point, approximately 1450 ºC, within 2280 s. The uniform heating is observed throughout the complete volume of the cast at these different time intervals. This highlights the significance of volumetric heating through microwave energy.

The MHH simulations are performed for SS-316 and Cu cast specimens using the same FE model. The properties of SS-316 and Cu powder are assigned instead of Ni Powder. For simulation, the properties of SS-316 powder are taken same as that of stainless steel used for cavity wall. The MHH effects in the form of electric field strength, and resistive losses are observed to be unaffected with change in cast material properties. Figure 12 represents the temperature profiles of Ni, SS-316 and Cu cast specimens corresponding to their melting temperatures. The simulation results reveal that uniform heating is achieved across the entire volume of all three cast specimens in the electromagnetic environment. The melting temperature of Ni, SS-316 and Cu cast specimens is achieved in 2280 s, 2080 s, and 1125 s respectively.

Fabrication of metallic cast using microwave casting

The Ni, SS-316, and Cu powders have been effectively cast utilizing a custom-designed refractory brick casting experimental setup. The setup is positioned within the applicator and the maximum power level is activated. Once the power is activated, the susceptor begins to absorb the microwave radiation. As a result, the susceptor starts to heat up. The heat produced by the interaction between microwaves and the susceptor causes a temperature increase in the metallic powder within the mold through conduction. As the temperature of metallic powder reaches its critical value, it also begins to absorb the microwave radiation with increased skin depth. The hybrid heating of metallic powder using susceptor and microwave radiation helps in reaching the melting temperature of the cast. The applicator power is switched off after reaching the optimum exposure time. The setup is cooled within the applicator to achieve proper bonding during solidification. The specimens cast using microwave radiation with their exposure time and sizes are discussed in Table 5.

Table 5. Sizes and exposure time for casts

Sr. No	Material	Size, mm^3	Exposure time, s	Metallic cast
1	Ni powder	120 × 32 × 2	1980	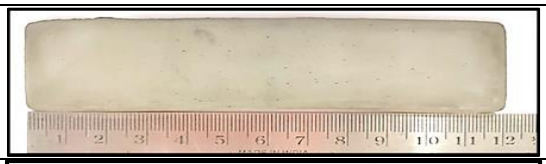
2	SS-316 powder	148 × 33 × 2	1740	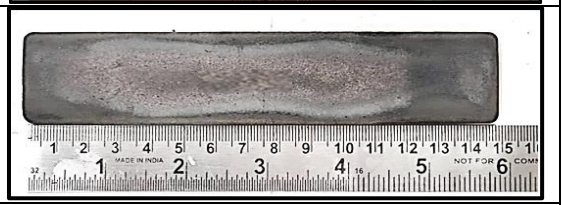
3	Cu powder	135 × 32 × 2	1260	

In microwave-assisted casting, Cu exhibits a shorter exposure time. This is primarily due to its high thermal conductivity and electrical conductivity, which enable faster heat transfer and more efficient energy absorption from the susceptor. In contrast, Ni and SS-316 have lower thermal conductivities and higher specific heat capacities, causing slower temperature rise and requiring longer exposure times to achieve complete melting.

Comparison of simulated and experimental exposure time

Table 6 represents the comparison of experimental and simulated exposure time for different cast specimens including Ni, SS-316 and Cu. It is observed from Table 6 that experimental and simulated exposure time for different metallic casts shows a close co-relation. The percentage error between experimental and simulated exposure time for Ni, SS-316 and Cu cast are observed as 13.15, 16.34 and 12.00 % respectively. The average percentage error is measured as 13.83 %. The deviation arises from using idealized material properties and modeling the powder as a homogenized bulk, neglecting porosity, particle morphology, and microstructural evolution. The FE model assumes isotropic and constant dielectric and thermo-physical properties, ignoring temperature-dependent variations. Additionally, the use of simplified boundary conditions and modeling assumptions may further limit the ability of FE model to fully capture the microwave-thermal interactions and real experimental conditions of the MHH process.

Table 6. Comparison of simulated and experimental exposure time

Sr. No	Metallic 9owder	Size of experimental cast, mm^3	Size of simulated cast, mm^3	Experimental exposure time, s	Simulated exposure time, s	Percentage error, %
1	Ni	120 ×32 × 2	150 × 35 × 3	1980	2280	13.15
2	SS-316	148 × 33× 2	150 × 35 × 3	1740	2080	16.34
3	Cu	136 × 32× 2	150 × 35 × 3	1260	1125	12.00

Conclusions

This study explores the microwave casting of metallic powders using an energy-efficient microwave heat source. An FE model of the experimental setup was created to predict the optimal exposure time for cast within the electromagnetic environment. Analysis of the simulation results indicated that the highest concentrations of electric field intensity are detected in the susceptor zone. The maximum electric field strength was recorded at 4.46×10^4 V/m. This high electric field strength increases heating in the susceptor zone through microwave irradiation, resulting in maximum resistive losses of 4.9×10^9 W/m^3 in that area. Consequently, conductive heat transfer through the susceptor raises the temperature of the metallic powder inside the mold. The simulations demonstrated that as the temperature of the susceptor increases, the magnitude of heat transfer through the susceptor to metallic powder also rises. The FE model accurately predicted the exposure times needed to cast various metallic powders. Experimental validation confirmed these predictions, showing a strong agreement between simulated and actual exposure times, with an average percentage error of 13.83 %. This demonstrates the effectiveness of the simulation in optimizing microwave casting processes and highlights its potential to improve efficiency and accuracy in metal casting applications.

CRediT authorship contribution statement

Ashish Kumar: writing – review & editing, writing – original draft; **Ashok K. Bagha**: writing – review & editing; **Sumit Sharma**: writing – review & editing.

Conflict of interest

The authors declare that they have no conflict of interest.

References

1. Kashyap S, Tripathi H, Kumar N. Mechanical properties of marble dust reinforced aluminum matrix structural composites fabricated by stir casting process. *Materials Physics and Mechanics.* 2022;48(2): 282–288.
2. Sulardjaka S, Nugroho S, Iskandar N. Mechanical properties of AlSiMg/SiC and AlSiMgTiB/SiC produced by semi-solid stir casting and high pressure die casting. *Materials Physics and Mechanics.* 2021;47(1): 31–39.
3. Salonitis K, Zeng B, Mehrabi HA, Jolly M. The Challenges for Energy Efficient Casting Processes. *Procedia CIRP.* 2016;40: 24–29.
4. Mishra RR, Sharma AK. Microwave-material interaction phenomena: Heating mechanisms, challenges and opportunities in material processing. *Composites Part A: Applied Science and Manufacturing.* 2016;81: 78–97.
5. Bhoi NK, Singh H, Pratap S, Jain PK. Microwave material processing: A clean, green, and sustainable approach. In: Kumar K, Zindani D, Davim P. (eds.) *Sustainable Engineering Products and Manufacturing Technologies.* Academic Press; 2019. p.3–23.
6. Kaushal S, Singh S, Bohra S, Gupta D, Jain V, Kapoor M. Sustainable microwave processing and surface characterization of powdered tungsten reinforced copper metal matrix (Cu-Wx) castings. *Results in Surfaces and Interfaces.* 2024;16: 100249.
7. Thostenson ET, Chou TW. Microwave processing: fundamentals and applications. *Composites - Part A: Applied Science and Manufacturing.* 1999;30(9): 1055–1071.
8. El Khaled D, Novas N, Gazquez JA, Manzano-Agugliaro F. Microwave dielectric heating: Applications on metals processing. *Renewable and Sustainable Energy Reviews.* 2018;82: 2880–2892.
9. Lingappa SM, Srinath MS, Amarendra HJ. Melting of bulk non-ferrous metallic materials by microwave hybrid heating (MHH) and conventional heating: a comparative study on energy consumption. *Journal of the Brazilian Society of Mechanical Sciences and Engineering.* 2018;40(1): 1.
10. Mishra RR, Sharma AK. A Review of Research Trends in Microwave Processing of Metal-Based Materials and Opportunities in Microwave Metal Casting. *Critical Reviews in Solid State and Materials Sciences.* 2016;41(3): 217–255.
11. Rawat S, Samyal R, Bedi R, Bagha AK. Comparative performance of various susceptor materials and vertical cavity shapes for selective microwave hybrid heating (SMHH). *Physica Scripta.* 2022;97(12): 125704.
12. Patel DK, Bhoi HS, Kumar N. Microwave Heating Capabilities of Different Susceptor Material: Experimental and Simulation Study. *Silicon.* 2022;14: 6621–6635.
13. Boiprav OV, Bogush VA, Lynkou LM. Electromagnetic radiation reflection, transmission and absorption characteristics of microwave absorbers based on dilatant liquids and powdered activated wood charcoal. *Materials Physics and Mechanics.* 2023;51(6): 127–134.
14. Bhatt SC, Ghetiya ND. Review on effect of tooling parameters on microwave processing of metallic materials with special emphasis on melting/casting application. *International Journal of Metalcasting.* 2022;16: 2097–2127.
15. Stalin B, Ravichandran M, Balasubramanian M, Chairman CA, Pritima D, Dhinakaran V. Processing of MMC through conventional sintering and spark plasma sintering process: A review. *IOP Conference Series: Materials Science and Engineering.* 2020;988(1): 012092.
16. Singh S, Gupta D, Jain V. Fabricating In Situ Powdered Nickel–Alumina Metal Matrix Composites Through Microwave Heating Process: A Sustainable Approach. *International Journal of Metalcasting.* 2021;15: 969–982.
17. Bhatt S, Suthar S, Mistry D, Ghetiya N. Experimental study on microwave Ex-situ casting of AA 6061. *Materials Today: Proceedings.* 2021;44(1): 1312–1315.
18. Gangwar V, Singh H, Kumar S. Influence of Process Parameter on Microstructure, Residual Stress, Microhardness and Porosity of AA-6063 Microwave Cast. *International Journal of Metalcasting.* 2022;16: 826–841.

19. Kaushal S. Microstructure and Tribological Characterization of Composite Castings Developed through In-situ Microwave Hybrid Heating. *Inter Metalcast.* 2022;16: 2150–2161.
20. Lingappa MS, Srinath MS, Amarendra HJ. Microstructural and mechanical investigation of aluminium alloy (Al 1050) melted by microwave hybrid heating. *Materials Research Express.* 2017;4(7): 076504.
21. Mishra RR, Sharma AK. On mechanism of in-situ microwave casting of aluminium alloy 7039 and cast microstructure. *Materials & Design.* 2016;112: 97–106.
22. Mishra RR, Sharma AK. Experimental investigation on in-situ microwave casting of copper. *IOP Conference Series: Materials Science and Engineering.* 2018;346: 012052.
23. Lingappa M S, Srinath M S, Amarendra H J. Microstructural Investigation and Characterization of Bulk Brass Melted by Conventional and Microwave Processing Methods. *Materials Science Forum.* 2017;890: 356–361.
24. Marahadige SL, Sridharmurthy SM, Jayraj AH, Mahabaleshwar US, Lorenzini G, Lorenzini E. Development of copper alloy by microwave hybrid heating technique and its characterization. *International Journal of Heat and Technology.* 2018;36(4): 1343–1349.
25. Ram VK, Nandwani S, Vardhan S, Bahl S, Samyal R, Bagha AK. Microwave casting of stainless still through microwave hybrid heating. *IOP Conference Series: Materials Science and Engineering.* 2022;1248: 012047.
26. Singh S, Gupta D, Jain V. Processing of Ni-WC-8Co MMC casting through microwave melting. *Materials and Manufacturing Processes.* 2018;33(1): 26–34.
27. Kumar R, Bhowmick H, Gupta D, Bansal S. Development and characterization of multiwalled carbon nanotube-reinforced microwave sintered hybrid aluminum metal matrix composites: An experimental investigation on mechanical and tribological performances. *Proceedings of the Institution of Mechanical Engineers, Part L: Journal of Materials: Design and Applications.* 2021;235(10): 2310–2323.
28. Pal J, Gupta D, Singh TP. Processing and characterization of SS316 based metal matrix composite casting through microwave hybrid heating. *Proceedings of the Institution of Mechanical Engineers, Part C: Journal of Mechanical Engineering Science.* 2022;236(20): 10508–10527.
29. Nandwani S, Vardhan S, Bahl S, Yadav AK, Samyal R, Bagha AK. Evaluating the dynamic characteristics of microwave-casted metal matrix composite material by using experimental modal analysis. *Proceedings of the Institution of Mechanical Engineers, Part E: Journal of Process Mechanical Engineering.* 2023;238(4): 1580–1590.
30. Kaushal S, Bohra S, Gupta D, Jain V. On Processing and Characterization of Cu–Mo-Based Castings Through Microwave Heating. *International Journal of Metalcasting.* 2020;15: 530–537.
31. Bykov NY, Obraztsov NV, Hvatov AA, Maslyaev MA, Surov AV. Hybrid modeling of gas-dynamic processes in AC plasma torches. *Materials Physics and Mechanics.* 2022;50(2): 287–303.
32. Tamang S, Aravindan S. 3D numerical modelling of microwave heating of SiC susceptor. *Applied Thermal Engineering.* 2019;162: 114250.
33. Mishra RR, Sharma AK. Multi-physics simulation of in situ microwave casting of 7039 Al alloy inside different applicators and cast microstructure. *Proceedings of the Institution of Mechanical Engineers, Part E: Journal of Process Mechanical Engineering.* 2019;233(3): 617–629.
34. Sharma MV, Nekraje G, Bhuvan V, Hebbale AM, Srinath MS. Simulation studies on melting characteristics of bulk alloy Al-1050 during in-situ microwave casting process. *Materials Today: Proceedings.* 2022;52: 407–412.
35. Bhatt SC, Ghetiya ND, Joshi M. Multiphysics simulation and validation of microwave melting characteristics of AA6061 by finite element analysis. *Advances in Materials and Processing Technologies.* 2021;8(3): 1557–1568.
36. Bhatt SC, Ghetiya ND. 3D Multiphysics simulation of microwave heating of bulk metals with parametric variations. *Chemical Engineering and Processing - Process Intensification.* 2023;184: 109271.
37. Pryor RW. *Multiphysics Modeling using COMSOL*. Jones and Bartlett; 2011.
38. Thakur A, Bedi R. Microwave joining of copper pipes using selective microwave hybrid heating process: Simulation and experimental study. *Materials Today Communications.* 2024;38: 108154.
39. Lin B, Li H, Chen Z, Zheng C, Hong Y, Wang Z. Sensitivity analysis on the microwave heating of coal: A coupled electromagnetic and heat transfer model. *Applied Thermal Engineering.* 2017;126: 949–962.
40. Liu S, Fukuoka M, Sakai N. A finite element model for simulating temperature distributions in rotating food during microwave heating. *Journal of Food Engineering.* 2013;115(1): 49–62.

MATERIALS PHYSICS AND MECHANICS RESEARCH ARTICLE

Submitted: August 5, 2025 **Revised: October 20, 2025** **Accepted: November 10, 2025**

Elastodynamic response of photothermoelastic plate with moisture due to various sources

R. Kumar [1], N. Sharma [2], V. Rani [2]✉

[1] Kurukshetra University, Kurukshetra, India

[2] Maharishi Markandeshwar (Deemed to be University), Mullana-Ambala, India

✉ vineeta.jaglan@gmail.com

ABSTRACT

This current study examines how carrier density and moisture sources cause deformation in an isotropic photothermoelastic moisture plate. We develop simplified two-dimensional equations describing the interaction of heat, moisture, and charge carriers within the material. These equations are expressed in a dimensionless form and solved analytically using Laplace and Fourier transformations to obtain the main field quantities—displacement, stress, temperature, carrier density, and moisture distribution. The theoretical results are validated for silicon material and illustrated graphically. The analysis demonstrates that both carrier density and moisture significantly affect the stress, temperature, and carrier concentration within the plate. Moisture tends to stabilize stress variations and reduce temperature fluctuations, while relaxation times strongly influence oscillation patterns in all field quantities. These results underscore the integrated role of thermal, moisture, and photoelastic effects in shaping the mechanical behavior of semiconducting materials. The proposed model aids in analyzing coupled thermoelastic, moisture, and carrier effects in semiconductors, offering improved prediction of transient responses essential for enhancing thermal stability and reliability in electronic and photonic devices.

KEYWORDS

isotropic • photothermoelastic • Laplace transform • Fourier transform • carrier density source •moisture source

Citation: Kumar R, Sharma N, Rani V. Elastodynamic response of photothermoelastic plate with moisture due to various sources. *Materials Physics and Mechanics*. 2025;53(6): 145–163.
http://dx.doi.org/10.18149/MPM.5362025_11

Introduction

Advances in modern technology have considerably expanded the use of semiconducting materials in diverse engineering and applied physics applications. The study of wave propagation in semiconducting media is of both academic and technological significance owing to its relevance to optoelectronic and thermomechanical processes. In recent years, the photothermal excitation of short elastic pulses has become a central topic of research, finding applications in photoacoustic microscopy, thermal wave imaging, thermoelastic parameter determination, non-destructive device evaluation, laser drilling monitoring, and laser-induced annealing and melting phenomena in semiconductors. When a laser beam irradiates a semiconductor surface, part of the absorbed energy excites electrons to higher energy states. The recombination of electron–hole pairs through non-radiative transitions produces photoexcited free carriers that influence the local thermal and elastic fields. Consequently, photothermal (PT) and photoacoustic (PA) techniques have emerged as powerful diagnostic tools for investigating the internal dynamics of semiconductor materials.

Publisher: Peter the Great St. Petersburg Polytechnic University

Over the last few decades, PA and PT methods have evolved into highly sensitive and versatile techniques for characterizing semiconductors and microelectronic structures. These methods exhibit excellent sensitivity to the kinetics of photoexcited carriers and have been employed for precise analysis of carrier transport, recombination, and diffusion mechanisms (Mandelis [1]; Almond and Patel [2]; Nikolic and Todorović [3]; Mandelis and Michaelian [4]). In most semiconductor systems, an absorbed modulated laser beam generates electron-hole pairs, producing carrier-diffusion or plasma waves that significantly contribute to the PT and PA responses. These plasma waves induce periodic thermal and elastic disturbances, resulting in coupled thermoelastic and plasma wave propagation. The subsequent deformation of the crystal lattice alters the potential profiles of the conduction and valence bands, producing complex photo-induced mechanical behavior. Todorović [5–7] proposed theoretical models that linked carrier recombination and transport phenomena with the deformation and mechanical response of semiconductor media.

Considerable theoretical developments have since been made in the field of generalized thermoelasticity and its extensions. Sharma [8] examined boundary value problems in generalized thermodiffusive elastic media, while Sharma et al. [9] obtained the fundamental solution for electro-microstretch viscoelastic solids and explored wave motion. Othman et al. [10] analyzed magneto-thermoelastic behavior in perfectly conducting half-spaces subjected to magnetic and thermal fields, and Marin et al. [11] extended Saint-Venant's principle to micropolar thermoelastic diffusion models. Zenkour and Abbas [12] utilized the Green–Naghdi model to investigate thermal shock in fiber-reinforced anisotropic media under magnetic influence. Lotfy [13] applied a two-temperature model to study magneto-thermoelastic interactions, while Sharma and Sharma [14] and Abbas et al. [15] extended these formulations to bio-heat transfer and microstretch elastic media.

Further research integrated electromagnetic, fractional, and relaxation phenomena into photothermal and magneto-thermoelastic analyses. Hobiny and Abbas [16,17] employed the coupled thermoelastic–plasma wave theory using the Green–Naghdi framework and its fractional-order extensions. Marin et al. [18] developed porothermoelastic models using fractional calculus and thermal relaxation parameters. Lotfy et al. [19] and Abbas [20,21] studied the combined effects of electromagnetic, thermal, and photonic fields on semiconductor response to laser-induced heating. Recent studies by Sharma and Kumar [22,23], Lotfy et al. [24], and Mahdy et al. [25] examined photothermoelastic deformations caused by inclined loads, ramp-type heating, Hall currents, and time-fractional heat conduction effects.

Sharma and Khator [26,27] explored renewable energy challenges and microgrid planning for prosumer markets, while several studies advanced semiconductor thermoelastic modeling: Lotfy [28] studied Hall current and microtemperature effects in magneto-thermoelastic semiconductors; Hobiny et al. [29] examined wave propagation using the hyperbolic two-temperature model; El-Sapa et al. [30] applied a nonlocal variable-conductivity approach at the nanoscale; Raddadi et al. [31] modeled photoacoustic wave generation via carrier diffusion; and Sharma et al. [32] investigated micropolar thermoviscoelasticity incorporating nonlocal and hyperbolic two-temperature effects under the MGT framework.

The coupling of heat and moisture diffusion known as hygro-thermoelasticity has also received significant attention due to its relevance in porous and hygroscopic materials such as composites, foams, biotissues, and concrete. Foundational studies by Szekeres [33,34] and Szekeres and Engelbrecht [35] established analogies between heat and moisture transfer, later expanded by Sih et al. [36] to analyze coupled hygro-thermoelastic behavior. More recently, Alhashash et al. [37] and El-Sapa et al. [38] developed mathematical–physical models describing the effects of moisture diffusivity in semiconducting media under two-temperature and nonlocal frameworks. Lotfy et al. [39] and Alshehri and Lotfy [40] investigated the interaction between photoacoustic waves and moisture diffusivity in hydro-poroelastic semiconductors.

Kumar and Devi [41] and Kumar et al. [42,43] investigated thick circular plates through modified couple stress and photothermoelastic frameworks, considering factors such as porosity, phase lag, and fractional behavior. Abbas et al. [44,45] and Lotfy et al. [46] explored thermoelastic half-spaces incorporating diffusion, voids, and Hall current influences. Alzahrani and Abbas [47] and Sharma et al. [48] analyzed semiconductor half-spaces exhibiting nonlocal and phase-lag thermoelastic responses.

The novelty of the present work lies in the combined analysis of carrier density and moisture diffusivity effects on the deformation of an isotropic photothermoelastic moisture (IPTM) plate, an aspect that has not been extensively reported in prior literature. Unlike earlier studies that focused separately on thermal or photothermal interactions, the current formulation incorporates simultaneous contributions from carrier generation, moisture transport, and relaxation mechanisms. The governing field equations are derived using generalized thermoelasticity and diffusion theories, introducing suitable non-dimensional parameters and potential functions to simplify the coupled system. The equations are solved analytically using Laplace and Fourier transform techniques to obtain expressions for temperature, carrier density, moisture concentration, and normal stress. The results are numerically inverted to retrieve time-domain responses, and graphical analyses are presented to demonstrate the effects of carrier density, moisture diffusivity, and relaxation times on the deformation characteristics of the IPTM plate, which offers novel perspectives on the multiphysical coupling mechanisms in semiconductor materials.

Basic equations

Following the formulations of Todorovic [5–7], Szekeres [33,34], and Alenazi et al. [49], the constitutive relations and field equations are developed for a homogeneous, isotropic, and linearly elastic photothermoelastic material with moisture. The model neglects body forces, carrier photogeneration, and internal heat or moisture sources, while incorporating finite relaxation effects for heat, carrier, and moisture diffusion.

$$t_{ij} = 2\mu e_{ij} + \delta_{ij}(\lambda e_{kk} - \gamma_t T - \gamma_n N - \gamma_m M), \tag{1}$$

$$\left(2\mu e_{ij,j} + \lambda e_{kk,i} - \gamma_t T_{,i} - \gamma_n N_{,i} - \gamma_m M_{,i}\right) + F_i = \rho \frac{\partial^2 u_i}{\partial t^2}, \tag{2}$$

$$D_e N_{,ii} - \frac{\partial N}{\partial t} - \frac{N}{\tau} + \delta \frac{T}{\tau} = 0, \tag{3}$$

$$\rho C_e\left(D_t T_{,ii} + D_t^m M_{,ii}\right) + \frac{E_g N}{\tau} = \left(1 + \tau_o \frac{\partial}{\partial t}\right)\left[\rho C_e \dot{T} + \gamma_t T_o \dot{e}_{kk}\right], \tag{4}$$

$$K_m\left(D_m M_{,ii} + D_m^t T_{,ii}\right) + \frac{E_g N}{\tau} = \left(1 + \tau^o \frac{\partial}{\partial t}\right)\left[K_m \dot{M} + \gamma_m D_m M_o \dot{e}_{kk}\right]. \quad (5)$$

where t_{ij} are components of stress tensor; e_{ij} are components of strain tensor, λ end μ are Lame's constants, δ_{ij} is kronecker delta, $\gamma_t = (3\lambda + 2\mu)\alpha_t - \alpha_t$ are linear thermal expansion coefficients, $\gamma_n = (3\lambda + 2\mu)\alpha_n - \alpha_n$ are electronic deformation coefficients, $\gamma_m = (3\lambda + 2\mu)\alpha_m - \alpha_m$ are moisture expansion coefficients, F_i are the components of body force per unit volume, u_i are components of displacement, ρ is the medium density, D_e are the coefficients of carrier diffusion; $N = n\text{-}n_0$, n_0 are the carrier concentration at equilibrium, τ is the photogenerated carrier lifetime, $\delta = \frac{\partial n_0}{\partial T}$ is thermal activation coupling parameter, T is the temperature distribution, C_e is the specific heat, $D_t = K/\rho C_e$ is temperature diffusivity, where K is a coefficient of thermal conductivity, D_t^m is coupled moisture diffusivity, E_g is the semiconductor energy gap, $\tau_o$is the thermal relaxation time, τ^o is the moisture relaxation time, T_0 is the reference temperature, K_m is moisture diffusion constant, D_m is moisture diffusivity, D_m^t is coupled thermal diffusivity, M_0 is the reference moisture. Partial derivatives and time derivatives are denoted by the symbols "," and "." respectively.

Formulation of the problem and model assumptions

We investigate a homogeneous, isotropic, thermally conducting, infinite photothermoelastic moisture Cartesian plate with finite thickness 2d having an initial uniform temperature T_o. The origin of the coordinate system may be any point on the middle plane, and the middle plane of the plate coincides with the x_1x_2-plane, consequently $-d \le x_3 \le d$ and $-\infty < x_1, x_2 < \infty$. The boundary surface of the plate is subjected to carrier density source and moisture source. We limit our analysis to the x_1x_3-plane, which we assume the plane of incident, so that the physical field elements vary with x_1, x_3, t. Consequently, displacement components, temperature distribution, carrier density distribution and moisture distribution are provided by:

$$\vec{u} = \left(u_1(x_1, x_3, t), 0, u_3(x_1, x_3, t)\right), T = T(x_1, x_3, t), N = N(x_1, x_3, t), M = M(x_1, x_3, t). \quad (6)$$

The governing Eqs. (2)–(5) and constitutive relation (1) for IPTM plate utilizing Eq. (6), adopt the following form:

$$(\lambda + \mu)\frac{\partial e}{\partial x_1} + \mu \Delta u_1 - \gamma_t \frac{\partial T}{\partial x_1} - \gamma_n \frac{\partial N}{\partial x_1} - \gamma_m \frac{\partial M}{\partial x_1} = \rho \frac{\partial^2 u_1}{\partial t^2}, \quad (7)$$

$$(\lambda + \mu)\frac{\partial e}{\partial x_3} + \mu \Delta u_3 - \gamma_t \frac{\partial T}{\partial x_3} - \gamma_n \frac{\partial N}{\partial x_3} - \gamma_m \frac{\partial M}{\partial x_3} = \rho \frac{\partial^2 u_3}{\partial t^2}, \quad (8)$$

$$D_e \Delta N - \frac{\partial N}{\partial t} - \frac{N}{\tau} + \delta \frac{T}{\tau} = 0, \quad (9)$$

$$\rho C_e [D_t \Delta T + D_t^m \Delta M] + \frac{E_g N}{\tau} = \left(1 + \tau_o \frac{\partial}{\partial t}\right)\left[\rho C_e \frac{\partial T}{\partial t} + \gamma_t T_o \frac{\partial e}{\partial t}\right], \quad (10)$$

$$K_m [D_m \Delta M + D_m^t \Delta T] + \frac{E_g N}{\tau} = \left(1 + \tau^o \frac{\partial}{\partial t}\right)\left[K_m \frac{\partial M}{\partial t} + \gamma_m D_m M_o \frac{\partial e}{\partial t}\right], \quad (11)$$

$$t_{11} = (\lambda + 2\mu)\frac{\partial u_1}{\partial x_1} + \lambda \frac{\partial u_3}{\partial x_3} - \gamma_t T - \gamma_n N - \gamma_m M, \quad (12)$$

$$t_{33} = (\lambda + 2\mu)\frac{\partial u_3}{\partial x_3} + \lambda \frac{\partial u_1}{\partial x_1} - \gamma_t T - \gamma_n N - \gamma_m M, \quad (13)$$

$$t_{31} = \mu\left(\frac{\partial u_1}{\partial x_3} + \frac{\partial u_3}{\partial x_1}\right), \quad (14)$$

where $e = \frac{\partial u_1}{\partial x_1} + \frac{\partial u_3}{\partial x_3}$ and $\Delta = \frac{\partial^2}{\partial x_1^2} + \frac{\partial^2}{\partial x_3^2}$.

The model is formulated under the following physical and mathematical assumptions:

The plate is homogeneous, isotropic, and linearly elastic, with uniform mechanical, thermal, and electronic properties. All field variables temperature, carrier density, and moisture concentration are considered small perturbations around a uniform equilibrium state, allowing the governing equations to be linearized. Finite relaxation times are incorporated for heat, carrier, and moisture fluxes to represent finite-speed propagation and realistic transient behavior. Body forces, carrier photogeneration, and internal heat or moisture sources within the medium are neglected.

The problem is treated as two-dimensional, assuming no variation along the x_2-axis, and all field variables are continuous and differentiable, ensuring the applicability of Laplace and Fourier transforms. The plate is initially stress-free and thermally uniform, and its bounding surfaces are subjected to prescribed, time-dependent carrier-density and moisture loadings.

The dimensionless quantities are defined in the following way:

$$(x_1', x_3', u_1', u_3') = \eta_1 C_o (x_1, x_3, u_1, u_3),\ (t_{11}', t_{33}', t_{31}') = \frac{1}{\lambda+2\mu}(t_{11}, t_{33}, t_{31}),$$
$$\left(t', \tau_o', \tau^{o\prime}\right) = \eta_1 C_o^2 (t, \tau_o, \tau^o),\ \ T' = \frac{\gamma_t}{\lambda+2\mu} T, \tag{15}$$
$$N' = \frac{\gamma_n}{\lambda+2\mu} N,\ \ e' = e\ ,\ \ M' = M,$$

where $\eta_1 = \frac{\rho C_e}{K}, C_o^2 = \frac{\lambda+2\mu}{\rho}$.

Using the dimensionless quantities provided by Eq. (15) in Eqs. (7)–(14) and, after prime deprivation, we obtain:

$$f_{11}\frac{\partial e}{\partial x_1} + f_{12}\Delta u_1 - \frac{\partial T}{\partial x_1} - \frac{\partial N}{\partial x_1} - f_{13}\frac{\partial M}{\partial x_1} = \frac{\partial^2 u_1}{\partial t^2}, \tag{16}$$

$$f_{11}\frac{\partial e}{\partial x_3} + f_{12}\Delta u_3 - \frac{\partial T}{\partial x_3} - \frac{\partial N}{\partial x_3} - f_{13}\frac{\partial M}{\partial x_3} = \frac{\partial^2 u_3}{\partial t^2}, \tag{17}$$

$$\Delta N - f_{14}\frac{\partial N}{\partial T} - f_{15}N + f_{16}T = 0, \tag{18}$$

$$\Delta T + f_{17}\Delta M + f_{18}N = \left(1 + \tau_o \frac{\partial}{\partial t}\right)\left[f_{19}\frac{\partial T}{\partial t} + f_{20}\frac{\partial e}{\partial t}\right], \tag{19}$$

$$\Delta M + f_{21}\Delta T + f_{22}N = \left(1 + \tau^o \frac{\partial}{\partial t}\right)\left[f_{23}\frac{\partial M}{\partial t} + f_{24}\frac{\partial e}{\partial t}\right], \tag{20}$$

$$t_{11} = \frac{\partial u_1}{\partial x_1} + f_{25}\frac{\partial u_3}{\partial x_3} - T - N - f_{13}M, \tag{21}$$

$$t_{33} = \frac{\partial u_3}{\partial x_3} + f_{25}\frac{\partial u_1}{\partial x_1} - T - N - f_{13}M, \tag{22}$$

$$t_{31} = f_{12}\left(\frac{\partial u_1}{\partial x_3} + \frac{\partial u_3}{\partial x_1}\right), \tag{23}$$

where $f_{11} = \frac{\lambda+\mu}{\rho C_o^2}$, $f_{12} = \frac{\mu}{\rho C_o^2}$, $f_{13} = \frac{\gamma_m}{\rho C_o^2}$, $f_{14} = \frac{1}{\eta_1 D_e}$, $f_{15} = \frac{1}{D_e \eta_1^2 C_o^2 \tau}$, $f_{16} = \frac{\delta\gamma_n}{D_e \tau \gamma_t \eta_1^2 C_o^2}$,
$f_{17} = \frac{D_t^m \gamma_t}{D_t(\lambda+2\mu)}$, $f_{18} = \frac{E_g \gamma_t}{\tau\gamma_n \rho C_e D_t \eta_1^2 C_o^2}$, $f_{19} = \frac{1}{D_t \eta_1}$, $f_{20} = \frac{\gamma_t^2 T_o}{\rho C_e D_t \eta_1 (\lambda+2\mu)}$, $f_{21} = \frac{D_m^t(\lambda+2\mu)}{D_m \gamma_t}$,
$f_{22} = \frac{E_g(\lambda+2\mu)}{\tau\gamma_n K_m D_m \eta_1^2 C_o^2}$, $f_{23} = \frac{1}{D_m \eta_1}$, $f_{24} = \frac{\gamma_m M_o}{K_m \eta_1}$, $f_{25} = \frac{\lambda}{\lambda+2\mu}$.

According to Helmholtz's decomposition, u_1 and u_3 have the following non-dimensional connections to the potential functions Φ and Ψ:

$$u_1 = \frac{\partial \Phi}{\partial x_1} - \frac{\partial \Psi}{\partial x_3},\ u_3 = \frac{\partial \Phi}{\partial x_3} + \frac{\partial \Psi}{\partial x_1}. \tag{24}$$

With the assistance of Eq. (24), Eqs. (16)–(17) provide:

$$\left(\Delta - \frac{\partial^2}{\partial t^2}\right)\Phi - T - N - f_{13}M = 0, \tag{25}$$

$$\Delta\Psi - \frac{1}{f_{12}}\frac{\partial^2 \Psi}{\partial t^2} = 0. \tag{26}$$

Define Laplace and Fourier Transform as:

$$\hat{f}(x_1, x_3, \mathfrak{s}) = \int_0^\infty f(x_1, x_3, t) e^{-\mathfrak{s}t} dt, \tag{27}$$

$$\tilde{f}(\xi, x_3, \mathfrak{s}) = \int_{-\infty}^\infty \hat{f}(x_1, x_3, \mathfrak{s}) e^{i\xi x_1} dx_1, \tag{28}$$

where $\mathfrak{s}$ is Laplace transform parameter and ξ is Fourier transform parameter.

After executing Laplace and Fourier transforms provided by Eqs. (27)–(28) to Eqs. (25), *(18)–(20)* and (26), we obtain the following:

$$\left(-\xi^2 + \frac{d^2}{dx_3^2} - \mathfrak{s}^2\right)\widetilde{\Phi} - \tilde{T} - \tilde{N} - f_{13}\widetilde{M} = 0, \tag{29}$$

$$\left(-\xi^2 + \frac{d^2}{dx_3^2}\right)\tilde{N} - f_{14}\mathfrak{s}\tilde{N} - f_{15}\tilde{N} + f_{16}\tilde{T} = 0, \tag{30}$$

$$-\xi^2\tilde{T} + \frac{d^2\tilde{T}}{dx_3^2} + f_{17}\left(-\xi^2\tilde{M} + \frac{d^2\tilde{M}}{dx_3^2}\right) + f_{18}\tilde{N} = (1 + \tau_o\mathfrak{s})\left[f_{19}\mathfrak{s}\tilde{T} + f_{20}\mathfrak{s}\left(-\xi^2 + \frac{d^2}{dx_3^2}\right)\widetilde{\Phi}\right], \tag{31}$$

$$-\xi^2\widetilde{M} + \frac{d^2\tilde{M}}{dx_3^2} + f_{21}\left(-\xi^2\tilde{T} + \frac{d^2\tilde{T}}{dx_3^2}\right) + f_{22}\tilde{N} = (1 + \tau^o\mathfrak{s})\left[f_{23}\mathfrak{s}\widetilde{M} + f_{24}\mathfrak{s}\left(-\xi^2 + \frac{d^2}{dx_3^2}\right)\widetilde{\Phi}\right], \tag{32}$$

$$\left[\left(-\xi^2 + \frac{d^2}{dx_3^2}\right) - \frac{1}{f_{12}}\mathfrak{s}^2\right]\widetilde{\Psi} = 0. \tag{33}$$

Employing transforms defined by Eqs. (27)–(28) on Eqs. (24) and (21)–(23), the displacement and stress components are obtained as follows:

$$\tilde{u}_1 = -i\xi\widetilde{\Phi} - \frac{d\widetilde{\Psi}}{dx_3}, \tag{34}$$

$$\tilde{u}_3 = \frac{d\widetilde{\Phi}}{dx_3} - i\xi\widetilde{\Psi}, \tag{35}$$

$$\tilde{t}_{11} = -i\xi\tilde{u}_1 + f_{25}\frac{d\tilde{u}_3}{dx_3} - \tilde{T} - \tilde{N} - f_{13}\widetilde{M}, \tag{36}$$

$$\tilde{t}_{33} = \frac{d\tilde{u}_3}{dx_3} - i\xi f_{25}\tilde{u}_1 - \tilde{T} - \tilde{N} - f_{13}\widetilde{M}, \tag{37}$$

$$\tilde{t}_{31} = f_{12}\left(\frac{d\tilde{u}_1}{dx_3} - i\xi\tilde{u}_3\right). \tag{38}$$

Algebraic simplifications of Eqs. (29)–(32) result in:

$$(\mathfrak{B}_1 D^8 + \mathfrak{B}_2 D^6 + \mathfrak{B}_3 D^4 + \mathfrak{B}_4 D^2 + \mathfrak{B}_5)\left(\widetilde{\Phi}, \tilde{T}, \tilde{N}, \widetilde{M}\right) = 0, \tag{39}$$

where $D = \frac{d}{dx_3}$, $\mathfrak{B}_1 = f_{17}f_{21} - 1$, $\mathfrak{B}_2 = \mathfrak{R}_1 + \mathfrak{R}_4 - \mathfrak{B}_1\xi^2 - \mathfrak{B}_1\mathfrak{s}^2 + f_{13}\mathfrak{R}_{11}$,

$\mathfrak{B}_3 = \mathfrak{R}_2 - \mathfrak{R}_1\xi^2 - \mathfrak{R}_1\mathfrak{s}^2 + \mathfrak{R}_5 - \mathfrak{R}_8 + f_{13}\mathfrak{R}_{12}$,

$\mathfrak{B}_4 = \mathfrak{R}_3 - \mathfrak{R}_2\xi^2 - \mathfrak{R}_2\mathfrak{s}^2 + \mathfrak{R}_6 - \mathfrak{R}_9 + f_{13}\mathfrak{R}_{13}$,

$\mathfrak{B}_5 = -\mathfrak{R}_3\xi^2 - \mathfrak{R}_3\mathfrak{s}^2 + \mathfrak{R}_7 - \mathfrak{R}_{10} + f_{13}\mathfrak{R}_{14}$,

and

$\mathfrak{R}_1 = (3 - 3f_{17}f_{21})\xi^2 + f_{19}r_1 + f_{23}r_2 + f_{14}\mathfrak{s} + f_{15} - f_{14}f_{17}f_{21}\mathfrak{s} - f_{15}f_{17}f_{21}$,

$\mathfrak{R}_2 = 3f_{17}f_{21}\xi^4 - 3\xi^4 + 2f_{15}f_{17}f_{21}\xi^2 + 2f_{14}f_{17}f_{21}\mathfrak{s}\xi^2 - 2f_{14}\mathfrak{s}\xi^2 - 2f_{15}\xi^2 - 2f_{19}r_1\xi^2 - -2f_{23}r_2\xi^2 - f_{14}f_{19}r_1\mathfrak{s} - f_{14}f_{23}r_2\mathfrak{s} - f_{15}f_{19}r_1 - f_{15}f_{23}r_2 - f_{19}f_{23}r_1r_2 + f_{16}f_{18} - -f_{16}f_{17}f_{22}$,

$\mathfrak{R}_3 = \xi^6 - f_{17}f_{21}\xi^6 + f_{15}\xi^4 + f_{14}\mathfrak{s}\xi^4 - f_{14}f_{17}f_{21}\mathfrak{s}\xi^4 - f_{15}f_{17}f_{21}\xi^4 + f_{19}r_1\xi^4 + f_{23}r_2\xi^4 + +f_{14}f_{19}r_1\mathfrak{s}\xi^2 + f_{14}f_{23}r_2\mathfrak{s}\xi^2 + f_{15}f_{19}r_1\xi^2 + f_{15}f_{23}r_2\xi^2 + f_{16}f_{17}f_{22}\xi^2 - f_{16}f_{18}\xi^2 + +f_{19}f_{23}r_1r_2\xi^2 + f_{14}f_{19}f_{23}r_1r_2\mathfrak{s} + f_{15}f_{19}f_{23}r_1r_2 - f_{16}f_{18}f_{23}r_2$,

$\mathfrak{R}_4 = f_{17}f_{24}r_2 - f_{20}r_1$,

$\mathfrak{R}_5 = 3f_{20}r_1\xi^2 - 3f_{17}f_{24}r_2\xi^2 + f_{14}f_{20}r_1\mathfrak{s} - f_{14}f_{17}f_{24}r_2\mathfrak{s} + f_{15}f_{20}r_1 - f_{15}f_{17}f_{24}r_2 + +f_{20}f_{23}r_1r_2$,

$\mathfrak{R}_6 = 3f_{17}f_{24}r_2\xi^4 - 3f_{20}r_1\xi^4 - 2f_{15}f_{20}r_1\xi^2 - 2f_{14}f_{20}r_1\mathfrak{s}\xi^2 - 2f_{20}f_{23}r_1r_2\xi^2 + +2f_{14}f_{17}f_{24}r_2\mathfrak{s}\xi^2 + 2f_{15}f_{17}f_{24}r_2\xi^2 - f_{14}f_{20}f_{23}r_1r_2\mathfrak{s} - f_{15}f_{20}f_{23}r_1r_2$,

$\mathfrak{R}_7 = f_{20}r_1\xi^6 - f_{17}f_{24}r_2\xi^6 + f_{14}f_{20}r_1\mathfrak{s}\xi^4 + f_{15}f_{20}r_1\xi^4 + f_{20}f_{23}r_1r_2\xi^4 - -f_{14}f_{17}f_{24}r_2\mathfrak{s}\xi^4 - f_{15}f_{17}f_{24}r_2\xi^4 + f_{14}f_{20}f_{23}r_1r_2\mathfrak{s}\xi^2 + f_{15}f_{20}f_{23}r_1r_2\xi^2$,

$\Re_8 = f_{16}f_{20}r_1 - f_{16}f_{17}f_{24}r_2,$
$\Re_9 = 2f_{16}f_{17}f_{24}r_2\xi^2 - 2f_{16}f_{20}r_1\xi^2 - f_{16}f_{20}f_{23}r_1r_2,$
$\Re_{10} = f_{16}f_{20}r_1\xi^4 - f_{16}f_{17}f_{24}r_2\xi^4 + f_{16}f_{20}f_{23}r_1r_2\xi^2,$
$\Re_{11} = f_{20}f_{21}r_1 - f_{24}r_2,$
$\Re_{12} = 3f_{24}r_2\xi^2 - 3f_{20}f_{21}r_1\xi^2 + f_{14}f_{24}r_2\mathfrak{s} - f_{14}f_{20}f_{21}r_1\mathfrak{s} + f_{15}f_{24}r_2 - f_{15}f_{20}f_{21}r_1 + +f_{19}f_{24}r_1r_2,$
$\Re_{13} = 3f_{20}f_{21}r_1\xi^4 - 3f_{24}r_2\xi^4 - 2f_{14}f_{24}r_2\mathfrak{s}\xi^2 + 2f_{14}f_{20}f_{21}r_1\mathfrak{s}\xi^2 - 2f_{15}f_{24}r_2\xi^2 + +2f_{15}f_{20}f_{21}r_1\xi^2 - 2f_{19}f_{24}r_1r_2\xi^2 - f_{14}f_{19}f_{24}r_1r_2\mathfrak{s} - f_{15}f_{19}f_{24}r_1r_2 - f_{16}f_{20}f_{22}r_1 + +f_{16}f_{18}f_{24}r_2,$
$\Re_{14} = f_{24}r_2\xi^6 - f_{20}f_{21}r_1\xi^6 - f_{14}f_{20}f_{21}r_1\mathfrak{s}\xi^4 + f_{14}f_{24}r_2\mathfrak{s}\xi^4 - f_{15}f_{20}f_{21}r_1\xi^4 + +f_{15}f_{24}r_2\xi^4 + f_{19}f_{24}r_1r_2\xi^4 + f_{14}f_{19}f_{24}r_1r_2\mathfrak{s}\xi^2 + f_{15}f_{19}f_{24}r_1r_2\xi^2 - f_{16}f_{18}f_{24}r_2\xi^2 + +f_{16}f_{20}f_{22}r_1\xi^2,$
with $r_1 = \mathfrak{s}(1 + \tau_o\mathfrak{s}),\ r_2 = \mathfrak{s}(1 + \tau^o\mathfrak{s}).$

The general solution of Eq. (39) is expressed as:

$$\left(\tilde{\Phi}, \tilde{T}, \tilde{N}, \tilde{M}\right) = \sum_{i=1}^{4}(1, \alpha_i^{\circ}, \beta_i^{\circ}, \gamma_i^{\circ})\,\bar{C}_i^{\circ}\cosh m_i^{\circ} x_3, \tag{40}$$

where $m_i^{\circ}(i = 1, 2, 3, 4)$ are roots of $\mathfrak{B}_1D^8 + \mathfrak{B}_2D^6 + \mathfrak{B}_3D^4 + \mathfrak{B}_4D^2 + \mathfrak{B}_5 = 0$ and the coupling parameters $\alpha_i^{\circ}, \beta_i^{\circ}, \gamma_i^{\circ}$ are given by:

$$\alpha_i^{\circ} = \sum_{i=1}^{4}\frac{\Re_4 m_i^{\circ 6} + \Re_5 m_i^{\circ 4} + \Re_6 m_i^{\circ 2} + \Re_7}{\mathfrak{B}_1 m_i^{\circ 6} + \Re_1 m_i^{\circ 4} + \Re_2 m_i^{\circ 2} + \Re_3}, \tag{41}$$

$$\beta_i^{\circ} = \sum_{i=1}^{4}\frac{\Re_8 m_i^{\circ 4} + \Re_9 m_i^{\circ 2} + \Re_{10}}{\mathfrak{B}_1 m_i^{\circ 6} + \Re_1 m_i^{\circ 4} + \Re_2 m_i^{\circ 2} + \Re_3}, \tag{42}$$

$$\gamma_i^{\circ} = \sum_{i=1}^{4}\frac{\Re_{11} m_i^{\circ 6} + \Re_{12} m_i^{\circ 4} + \Re_{13} m_i^{\circ 2} + \Re_{14}}{\mathfrak{B}_1 m_i^{\circ 6} + \Re_1 m_i^{\circ 4} + \Re_2 m_i^{\circ 2} + \Re_3}. \tag{43}$$

Additionally, Eq. (33) has a solution provided by:

$$\tilde{\Psi} = \bar{C}_5^{\circ}\sinh m_5^{\circ} x_3, \tag{44}$$

where m_5° is a root of equation $D^2 + \mathfrak{B}_6 = 0$, where $\mathfrak{B}_6 = -\left(\xi^2 + \frac{1}{f_{12}}\mathfrak{s}^2\right)$.

Expressions for displacement and stress components are obtained with the help of Eqs. (34)–(38), (40) and (44) as:

$$\tilde{u}_1 = -\mathrm{i}\xi\sum_{i=1}^{4}\bar{C}_i^{\circ}\cosh m_i^{\circ} x_3 - \bar{C}_5^{\circ} m_5^{\circ}\cosh m_5^{\circ} x_3, \tag{45}$$

$$\tilde{u}_3 = \sum_{i=1}^{4}\bar{C}_i^{\circ} m_i^{\circ}\sinh m_i^{\circ} x_3 - \mathrm{i}\xi\bar{C}_5^{\circ}\sinh m_5^{\circ} x_3, \tag{46}$$

$$\tilde{t}_{33} = \sum_{i=1}^{4}\left(m_i^{\circ 2} - \xi^2 f_{25} - \alpha_i^{\circ} - \beta_i^{\circ} - f_{13}\gamma_i^{\circ}\right)\bar{C}_i^{\circ}\cosh m_i^{\circ} x_3 + +\mathrm{i}\xi(f_{25} - 1)\bar{C}_5^{\circ} m_5^{\circ}\cosh m_5^{\circ} x_3, \tag{47}$$

$$\tilde{t}_{11} = \sum_{i=1}^{4}\left(-\xi^2 + m_i^{\circ 2} f_{25} - \alpha_i^{\circ} - \beta_i^{\circ} - f_{13}\gamma_i^{\circ}\right)\bar{C}_i^{\circ}\cosh m_i^{\circ} x_3 + +\mathrm{i}\xi(f_{25} - 1)\bar{C}_5^{\circ} m_5^{\circ}\cosh m_5^{\circ} x_3, \tag{48}$$

$$\tilde{t}_{31} = -2\mathrm{i}\xi\sum_{i=1}^{4} f_{12}\bar{C}_i^{\circ} m_i^{\circ}\sinh m_i^{\circ} x_3 - (m_5^2 + \xi^2)\bar{C}_5^{\circ}\sinh m_i^{\circ} x_3. \tag{49}$$

Boundary restrictions

The boundary restrictions for an isotropic photothermoelastic moisture plate subjected to carrier density source and moisture source are considered as:

$$\left.\begin{aligned} &t_{33} = 0,\\ &t_{31} = 0,\\ &T = 0,\\ &N = \mathrm{F}_3(x_1, x_3, t),\\ &M = \mathrm{F}_4(x_1, x_3, t), \end{aligned}\right\} \tag{50}$$

where

$$\mathrm{F}_3(x_1,x_3,t)=\mathrm{F}_{30}\delta(x_1)(\cosh x_3)H(t-a), \tag{51}$$
$$\mathrm{F}_4(x_1,x_3,t)=\mathrm{F}_{40}\delta(x_1)(\cosh x_3)\frac{\sin\pi t}{\eta}. \tag{52}$$

Here, $\delta(\,)$ is Dirac delta function, $H(\,)$ is Heaviside step function, F_{30} is the magnitude of the carrier density source, F_{40} is the constant moisture applied on the boundary.

Applying Laplace and Fourier transform defined by Eqs. (27)-(28) on Eqs. (50)–(52), we obtain:

$$\left.\begin{array}{l}\tilde{t}_{33}=0,\\ \tilde{t}_{31}=0,\\ \tilde{T}=0,\\ \widetilde{N}=\tilde{\mathrm{F}}_3(\xi,x_3,\mathfrak{s}),\\ \widetilde{M}=\tilde{\mathrm{F}}_4(\xi,x_3,\mathfrak{s}),\end{array}\right\}\ \text{at } x_3=\pm d\,, \tag{53}$$

where

$$\tilde{\mathrm{F}}_3(\xi,x_3,\mathfrak{s})=\mathrm{F}_{30}(\cosh x_3)\frac{e^{-\mathfrak{s}a}}{\mathfrak{s}}, \tag{54}$$
$$\tilde{\mathrm{F}}_4(\xi,x_3,\mathfrak{s})=\mathrm{F}_{40}(\cosh x_3)\left(\frac{\eta\pi}{\pi^2+\eta^2\mathfrak{s}^2}\right)(1+e^{-\eta\mathfrak{s}}). \tag{55}$$

Substituting the values of $\tilde{t}_{33},\tilde{t}_{31},\tilde{T},\widetilde{N},\widetilde{M}$ from Eqs. (47), (49) and (40) in the transformed boundary restrictions (53), along with Eqs. (54)–(55), yield:

$$\sum_{i=1}^{5}(a_i^{\diamond}\bar{C}_i^{\diamond}\cosh m_i^{\diamond}x_3)=0, \tag{56}$$
$$\sum_{i=1}^{5}(b_i^{\diamond}\bar{C}_i^{\diamond}\sinh m_i^{\diamond}x_3)=0, \tag{57}$$
$$\sum_{i=1}^{4}\alpha_i^{\diamond}\bar{C}_i^{\diamond}\cosh m_i^{\diamond}x_3=0, \tag{58}$$
$$\sum_{i=1}^{4}\beta_i^{\diamond}\bar{C}_i^{\diamond}\cosh m_i^{\diamond}x_3=\tilde{\mathrm{F}}_3(\xi,x_3,\mathfrak{s}), \tag{59}$$
$$\sum_{i=1}^{4}\gamma_i^{\diamond}\bar{C}_i^{\diamond}\cosh m_i^{\diamond}x_3=\tilde{\mathrm{F}}_4(\xi,x_3,\mathfrak{s}), \tag{60}$$

where $a_i^{\diamond}=m_i^{\diamond 2}-\xi^2 f_{25}-\alpha_i^{\diamond}-\beta_i^{\diamond}-f_{13}\gamma_i^{\diamond}$, $b_i^{\diamond}=-2\mathrm{i}\xi f_{12}m_i^{\diamond}$, $i=1,2,3,4$, and $a_5^{\diamond}=\mathrm{i}\xi(f_{25}-1)m_5^{\diamond}$ and $b_5^{\diamond}=-\left(m_5^{\diamond 2}+\xi^2\right)f_{12}$.

Equations (56)–(60) are expressed in matrix form as:

$$A^{\diamond}\bar{C}_i^{\diamond}=\bar{B}, \tag{61}$$

where

$$A^{\diamond}=\begin{bmatrix}a_1^{\diamond}\mathcal{C}_1 & a_2^{\diamond}\mathcal{C}_2 & a_3^{\diamond}\mathcal{C}_3 & a_4^{\diamond}\mathcal{C}_4 & a_5^{\diamond}\mathcal{C}_5\\ b_1^{\diamond}\mathcal{S}_1 & b_2^{\diamond}\mathcal{S}_2 & b_3^{\diamond}\mathcal{S}_3 & b_4^{\diamond}\mathcal{S}_4 & b_5^{\diamond}\mathcal{S}_5\\ \alpha_1^{\diamond}\mathcal{C}_1 & \alpha_2^{\diamond}\mathcal{C}_2 & \alpha_3^{\diamond}\mathcal{C}_3 & \alpha_4^{\diamond}\mathcal{C}_4 & 0\\ \beta_1^{\diamond}\mathcal{C}_1 & \beta_2^{\diamond}\mathcal{C}_2 & \beta_3^{\diamond}\mathcal{C}_3 & \beta_4^{\diamond}\mathcal{C}_4 & 0\\ \gamma_1^{\diamond}\mathcal{C}_1 & \gamma_2^{\diamond}\mathcal{C}_2 & \gamma_3^{\diamond}\mathcal{C}_3 & \gamma_4^{\diamond}\mathcal{C}_4 & 0\end{bmatrix},\ \bar{C}_i^{\diamond}=\begin{bmatrix}\bar{C}_1^{\diamond}\\ \bar{C}_2^{\diamond}\\ \bar{C}_3^{\diamond}\\ \bar{C}_4^{\diamond}\\ \bar{C}_5^{\diamond}\end{bmatrix},\ \bar{B}=\begin{bmatrix}0\\ 0\\ 0\\ \tilde{\mathrm{F}}_3(\xi,d,\mathfrak{s})\\ \tilde{\mathrm{F}}_4(\xi,d,\mathfrak{s})\end{bmatrix}, \tag{62}$$

and $\mathcal{C}_i=\cosh m_i^{\diamond}d\,,\mathcal{S}_i=\sinh m_i^{\diamond}d$.

From Eq. (62), we determine:

$$\bar{C}_i^{\diamond}=\frac{\bar{\Delta}_i^{\diamond}}{\bar{\Delta}^{\diamond}}\,,\ i=1,2,3,4,5,$$
$$\bar{\Delta}^{\diamond}=\mathcal{C}_2\mathcal{C}_3\mathcal{C}_4(b_1^{\diamond}a_5^{\diamond}\mathcal{S}_1\mathcal{C}_5-a_1^{\diamond}b_5^{\diamond}\mathcal{S}_5\mathcal{C}_1)\mathfrak{R}_{29}-\mathcal{C}_1\mathcal{C}_3\mathcal{C}_4(b_2^{\diamond}a_5^{\diamond}\mathcal{S}_2\mathcal{C}_5-a_2^{\diamond}b_5^{\diamond}\mathcal{S}_5\mathcal{C}_2)\mathfrak{R}_{30}+ \tag{63}$$
$$+\mathcal{C}_1\mathcal{C}_2\mathcal{C}_4(b_3^{\diamond}a_5^{\diamond}\mathcal{S}_3\mathcal{C}_5-a_3^{\diamond}b_5^{\diamond}\mathcal{S}_5\mathcal{C}_3)\mathfrak{R}_{31}-\mathcal{C}_1\mathcal{C}_2\mathcal{C}_3(b_4^{\diamond}a_5^{\diamond}\mathcal{S}_4\mathcal{C}_5-a_4^{\diamond}b_5^{\diamond}\mathcal{S}_5\mathcal{C}_4)\mathfrak{R}_{32}\,.$$

where $\bar{\Delta}_i^{\diamond}$ = determinant of $A^{\diamond}$ when i^{th} column of $A^{\diamond}$ is replaced by $\bar{B}$, which yield the following:

$$\bar{\Delta}_1^{\diamond}=\mathfrak{R}_{33}\tilde{\mathrm{F}}_3+\mathfrak{R}_{34}\tilde{\mathrm{F}}_4;\ \bar{\Delta}_2^{\diamond}=\mathfrak{R}_{35}\tilde{\mathrm{F}}_3+\mathfrak{R}_{36}\tilde{\mathrm{F}}_4;$$
$$\bar{\Delta}_3^{\diamond}=\mathfrak{R}_{37}\tilde{\mathrm{F}}_3+\mathfrak{R}_{38}\tilde{\mathrm{F}}_4;\ \bar{\Delta}_4^{\diamond}=\mathfrak{R}_{39}\tilde{\mathrm{F}}_3+\mathfrak{R}_{40}\tilde{\mathrm{F}}_4; \tag{64}$$
$$\bar{\Delta}_5^{\diamond}=\mathfrak{R}_{41}\tilde{\mathrm{F}}_3+\mathfrak{R}_{42}\tilde{\mathrm{F}}_4,$$

where

$$\mathfrak{R}_{29}=\bar{r}_1^{\diamond}\gamma_2^{\diamond}+\bar{r}_2^{\diamond}\gamma_3^{\diamond}+\bar{r}_3^{\diamond}\gamma_4^{\diamond}\,,$$

$\mathfrak{R}_{30} = \bar{r}_1^{\diamond}\gamma_1^{\diamond} + \bar{r}_4^{\diamond}\gamma_3^{\diamond} + \bar{r}_5^{\diamond}\gamma_4^{\diamond},$
$\mathfrak{R}_{31} = -\bar{r}_2^{\diamond}\gamma_1^{\diamond} + \bar{r}_4^{\diamond}\gamma_2^{\diamond} + \bar{r}_6^{\diamond}\gamma_4^{\diamond},$
$\mathfrak{R}_{32} = \bar{r}_3^{\diamond}\gamma_1^{\diamond} - \bar{r}_5^{\diamond}\gamma_2^{\diamond} + \bar{r}_6^{\diamond}\gamma_3^{\diamond},$
$\mathfrak{R}_{33} = (a_2^{\diamond}b_5^{\diamond}\mathcal{S}_5\mathcal{C}_2 - a_5^{\diamond}b_2^{\diamond}\mathcal{S}_2\mathcal{C}_5)\mathcal{C}_3\mathcal{C}_4\bar{\bar{r}}_1^{\diamond} + (a_3^{\diamond}b_5^{\diamond}\mathcal{S}_5\mathcal{C}_3 - a_5^{\diamond}b_3^{\diamond}\mathcal{S}_3\mathcal{C}_5)\mathcal{C}_2\mathcal{C}_4\bar{\bar{r}}_4^{\diamond} +$
$+(a_4^{\diamond}b_5^{\diamond}\mathcal{S}_5\mathcal{C}_4 - a_5^{\diamond}b_4^{\diamond}\mathcal{S}_4\mathcal{C}_5)\mathcal{C}_2\mathcal{C}_3\bar{\bar{r}}_6^{\diamond},$
$\mathfrak{R}_{34} = (a_2^{\diamond}b_5^{\diamond}\mathcal{S}_5\mathcal{C}_2 - a_5^{\diamond}b_2^{\diamond}\mathcal{S}_2\mathcal{C}_5)\mathcal{C}_3\mathcal{C}_4\bar{\bar{r}}_1^{\diamond} + (a_3^{\diamond}b_5^{\diamond}\mathcal{S}_5\mathcal{C}_3 - a_5^{\diamond}b_3^{\diamond}\mathcal{S}_3\mathcal{C}_5)\mathcal{C}_2\mathcal{C}_4\bar{\bar{r}}_2^{\diamond} +$
$+(a_4^{\diamond}b_5^{\diamond}\mathcal{S}_5\mathcal{C}_4 - a_5^{\diamond}b_4^{\diamond}\mathcal{S}_4\mathcal{C}_5)\mathcal{C}_2\mathcal{C}_3\bar{\bar{r}}_3^{\diamond},$
$\mathfrak{R}_{35} = (a_5^{\diamond}b_1^{\diamond}\mathcal{S}_1\mathcal{C}_5 - a_1^{\diamond}b_5^{\diamond}\mathcal{S}_5\mathcal{C}_1)\mathcal{C}_3\mathcal{C}_4\bar{\bar{r}}_1^{\diamond} + (a_5^{\diamond}b_3^{\diamond}\mathcal{S}_3\mathcal{C}_5 - a_3^{\diamond}b_5^{\diamond}\mathcal{S}_5\mathcal{C}_3)\mathcal{C}_1\mathcal{C}_4\bar{\bar{r}}_2^{\diamond} +$
$+(a_4^{\diamond}b_5^{\diamond}\mathcal{S}_5\mathcal{C}_4 - a_5^{\diamond}b_4^{\diamond}\mathcal{S}_4\mathcal{C}_5)\mathcal{C}_1\mathcal{C}_3\bar{\bar{r}}_3^{\diamond},$
$\mathfrak{R}_{36} = (a_5^{\diamond}b_1^{\diamond}\mathcal{S}_1\mathcal{C}_5 - a_1^{\diamond}b_5^{\diamond}\mathcal{S}_5\mathcal{C}_1)\mathcal{C}_3\mathcal{C}_4\bar{\bar{r}}_1^{\diamond} + (a_5^{\diamond}b_3^{\diamond}\mathcal{S}_3\mathcal{C}_5 - a_3^{\diamond}b_5^{\diamond}\mathcal{S}_5\mathcal{C}_3)\mathcal{C}_1\mathcal{C}_4\bar{\bar{r}}_4^{\diamond} +$
$+(a_5^{\diamond}b_4^{\diamond}\mathcal{S}_4\mathcal{C}_5 - a_4^{\diamond}b_5^{\diamond}\mathcal{S}_5\mathcal{C}_4)\mathcal{C}_1\mathcal{C}_3\bar{\bar{r}}_5^{\diamond},$
$\mathfrak{R}_{37} = (a_2^{\diamond}b_5^{\diamond}\mathcal{S}_5\mathcal{C}_2 - a_5^{\diamond}b_2^{\diamond}\mathcal{S}_2\mathcal{C}_5)\mathcal{C}_1\mathcal{C}_4\bar{\bar{r}}_2^{\diamond} + (a_5^{\diamond}b_1^{\diamond}\mathcal{S}_1\mathcal{C}_5 - a_1^{\diamond}b_5^{\diamond}\mathcal{S}_5\mathcal{C}_1)\mathcal{C}_2\mathcal{C}_4\bar{\bar{r}}_4^{\diamond} +$
$+(a_5^{\diamond}b_4^{\diamond}\mathcal{S}_4\mathcal{C}_5 - a_4^{\diamond}b_5^{\diamond}\mathcal{S}_5\mathcal{C}_4)\mathcal{C}_1\mathcal{C}_2\bar{\bar{r}}_5^{\diamond},$
$\mathfrak{R}_{38} = (a_5^{\diamond}b_1^{\diamond}\mathcal{S}_1\mathcal{C}_5 - a_1^{\diamond}b_5^{\diamond}\mathcal{S}_5\mathcal{C}_1)\mathcal{C}_2\mathcal{C}_4\bar{\bar{r}}_2^{\diamond} + (a_2^{\diamond}b_5^{\diamond}\mathcal{S}_5\mathcal{C}_2 - a_5^{\diamond}b_2^{\diamond}\mathcal{S}_2\mathcal{C}_5)\mathcal{C}_1\mathcal{C}_4\bar{\bar{r}}_4^{\diamond} +$
$+(a_4^{\diamond}b_5^{\diamond}\mathcal{S}_5\mathcal{C}_4 - a_5^{\diamond}b_4^{\diamond}\mathcal{S}_4\mathcal{C}_5)\mathcal{C}_1\mathcal{C}_2\bar{\bar{r}}_6^{\diamond},$
$\mathfrak{R}_{39} = (a_5^{\diamond}b_2^{\diamond}\mathcal{S}_2\mathcal{C}_5 - a_2^{\diamond}b_5^{\diamond}\mathcal{S}_5\mathcal{C}_2)\mathcal{C}_1\mathcal{C}_3\bar{\bar{r}}_3^{\diamond} + (a_3^{\diamond}b_5^{\diamond}\mathcal{S}_5\mathcal{C}_3 - a_5^{\diamond}b_3^{\diamond}\mathcal{S}_3\mathcal{C}_5)\mathcal{C}_1\mathcal{C}_2\bar{\bar{r}}_5^{\diamond} +$
$+(a_5^{\diamond}b_1^{\diamond}\mathcal{S}_1\mathcal{C}_5 - a_1^{\diamond}b_5^{\diamond}\mathcal{S}_5\mathcal{C}_1)\mathcal{C}_2\mathcal{C}_3\bar{\bar{r}}_6^{\diamond},$
$\mathfrak{R}_{40} = (a_5^{\diamond}b_1^{\diamond}\mathcal{S}_1\mathcal{C}_5 - a_1^{\diamond}b_5^{\diamond}\mathcal{S}_5\mathcal{C}_1)\mathcal{C}_2\mathcal{C}_3\bar{\bar{r}}_3^{\diamond} + (a_2^{\diamond}b_5^{\diamond}\mathcal{S}_5\mathcal{C}_2 - a_5^{\diamond}b_2^{\diamond}\mathcal{S}_2\mathcal{C}_5)\mathcal{C}_1\mathcal{C}_3\bar{\bar{r}}_5^{\diamond} +$
$+(a_5^{\diamond}b_3^{\diamond}\mathcal{S}_3\mathcal{C}_5 - a_3^{\diamond}b_5^{\diamond}\mathcal{S}_5\mathcal{C}_3)\mathcal{C}_1\mathcal{C}_2\bar{\bar{r}}_6^{\diamond},$
$\mathfrak{R}_{41} = -b_1^{\diamond}\mathcal{S}_1\mathcal{C}_2\mathcal{C}_3\mathcal{C}_4(a_2^{\diamond}\bar{\bar{r}}_1^{\diamond} + a_3^{\diamond}\bar{\bar{r}}_4^{\diamond} + a_4^{\diamond}\bar{\bar{r}}_6^{\diamond}) + b_2^{\diamond}\mathcal{S}_2\mathcal{C}_1\mathcal{C}_3\mathcal{C}_4(a_1^{\diamond}\bar{\bar{r}}_1^{\diamond} + a_3^{\diamond}\bar{\bar{r}}_2^{\diamond} - a_4^{\diamond}\bar{\bar{r}}_3^{\diamond}) +$
$+b_3^{\diamond}\mathcal{S}_3\mathcal{C}_1\mathcal{C}_2\mathcal{C}_4(a_1^{\diamond}\bar{\bar{r}}_4^{\diamond} - a_2^{\diamond}\bar{\bar{r}}_2^{\diamond} + a_4^{\diamond}\bar{\bar{r}}_5^{\diamond}) + b_4^{\diamond}\mathcal{S}_4\mathcal{C}_1\mathcal{C}_2\mathcal{C}_3(a_1^{\diamond}\bar{\bar{r}}_6^{\diamond} + a_2^{\diamond}\bar{\bar{r}}_3^{\diamond} - a_3^{\diamond}\bar{\bar{r}}_5^{\diamond}),$
$\mathfrak{R}_{42} = b_1^{\diamond}\mathcal{S}_1\mathcal{C}_2\mathcal{C}_3\mathcal{C}_4(a_2^{\diamond}\bar{r}_1^{\diamond} + a_3^{\diamond}\bar{r}_2^{\diamond} + a_4^{\diamond}\bar{r}_3^{\diamond}) - b_2^{\diamond}\mathcal{S}_2\mathcal{C}_1\mathcal{C}_3\mathcal{C}_4(a_1^{\diamond}\bar{r}_1^{\diamond} + a_3^{\diamond}\bar{r}_4^{\diamond} + a_4^{\diamond}\bar{r}_5^{\diamond}) +$
$+b_3^{\diamond}\mathcal{S}_3\mathcal{C}_1\mathcal{C}_2\mathcal{C}_4(-a_1^{\diamond}\bar{r}_2^{\diamond} + a_2^{\diamond}\bar{r}_4^{\diamond} + a_4^{\diamond}\bar{r}_6^{\diamond}) - b_4^{\diamond}\mathcal{S}_4\mathcal{C}_1\mathcal{C}_2\mathcal{C}_3(a_1^{\diamond}\bar{r}_3^{\diamond} - a_2^{\diamond}\bar{r}_5^{\diamond} + a_3^{\diamond}\bar{r}_6^{\diamond}),$
where
$\bar{r}_1^{\diamond} = \alpha_3^{\diamond}\beta_4^{\diamond} - \alpha_4^{\diamond}\beta_3^{\diamond},\ \bar{r}_2^{\diamond} = \alpha_4^{\diamond}\beta_2^{\diamond} - \alpha_2^{\diamond}\beta_4^{\diamond},\ \bar{r}_3^{\diamond} = \alpha_2^{\diamond}\beta_3^{\diamond} - \alpha_3^{\diamond}\beta_2^{\diamond},$
$\bar{r}_4^{\diamond} = \alpha_4^{\diamond}\beta_1^{\diamond} - \alpha_1^{\diamond}\beta_4^{\diamond},\ \bar{r}_5^{\diamond} = \alpha_1^{\diamond}\beta_3^{\diamond} - \alpha_3^{\diamond}\beta_1^{\diamond},\ \bar{r}_6^{\diamond} = \alpha_1^{\diamond}\beta_2^{\diamond} - \alpha_2^{\diamond}\beta_1^{\diamond},$
$\bar{\bar{r}}_1^{\diamond} = \alpha_4^{\diamond}\gamma_3^{\diamond} - \alpha_3^{\diamond}\gamma_4^{\diamond},\ \bar{\bar{r}}_2^{\diamond} = \alpha_1^{\diamond}\gamma_4^{\diamond} - \alpha_4^{\diamond}\gamma_1^{\diamond},\ \bar{\bar{r}}_3^{\diamond} = \alpha_1^{\diamond}\gamma_3^{\diamond} - \alpha_3^{\diamond}\gamma_1^{\diamond},$
$\bar{\bar{r}}_4^{\diamond} = \alpha_2^{\diamond}\gamma_4^{\diamond} - \alpha_4^{\diamond}\gamma_2^{\diamond},\ \bar{\bar{r}}_5^{\diamond} = \alpha_1^{\diamond}\gamma_2^{\diamond} - \alpha_2^{\diamond}\gamma_1^{\diamond},\ \bar{\bar{r}}_6^{\diamond} = \alpha_3^{\diamond}\gamma_2^{\diamond} - \alpha_2^{\diamond}\gamma_3^{\diamond}.$

Inserting the values of $\bar{C}_i^{\diamond}$ from Eq. (63) in Eqs. (40), (45)–(47), and (49) ascertain the displacement components, temperature distribution, carrier density distribution, moisture, and stress components as:

$\tilde{u}_1 = \frac{1}{\bar{\Delta}_i^{\diamond}}\left(\mathfrak{S}_{15}^{\diamond}\tilde{\mathrm{F}}_3 + \mathfrak{S}_{16}^{\diamond}\tilde{\mathrm{F}}_4\right),\ \tilde{u}_3 = \frac{1}{\bar{\Delta}_i^{\diamond}}\left(\mathfrak{S}_{17}^{\diamond}\tilde{\mathrm{F}}_3 + \mathfrak{S}_{18}^{\diamond}\tilde{\mathrm{F}}_4\right),\ \tilde{T} = \frac{1}{\bar{\Delta}_i^{\diamond}}\left(\mathfrak{S}_{19}^{\diamond}\tilde{\mathrm{F}}_3 + \mathfrak{S}_{20}^{\diamond}\tilde{\mathrm{F}}_4\right),$
$\tilde{N} = \frac{1}{\bar{\Delta}_i^{\diamond}}\left(\mathfrak{S}_{21}^{\diamond}\tilde{\mathrm{F}}_3 + \mathfrak{S}_{22}^{\diamond}\tilde{\mathrm{F}}_4\right),\ \tilde{M} = \frac{1}{\bar{\Delta}_i^{\diamond}}\left(\mathfrak{S}_{23}^{\diamond}\tilde{\mathrm{F}}_3 + \mathfrak{S}_{24}^{\diamond}\tilde{\mathrm{F}}_4\right),\ \tilde{t}_{33} = \frac{1}{\bar{\Delta}_i^{\diamond}}\left(\mathfrak{S}_{25}^{\diamond}\tilde{\mathrm{F}}_3 + \mathfrak{S}_{26}^{\diamond}\tilde{\mathrm{F}}_4\right),$
$\tilde{t}_{31} = \frac{1}{\bar{\Delta}_i^{\diamond}}\left(\mathfrak{S}_{27}^{\diamond}\tilde{\mathrm{F}}_3 + \mathfrak{S}_{28}^{\diamond}\tilde{\mathrm{F}}_4\right),$
where
$\mathfrak{S}_{15}^{\diamond} = -\mathrm{i}\xi\sum_{i=0}^{3}\bar{\mathrm{R}}_{2i+1}^{\diamond} - m_5^{\diamond}\bar{\mathrm{R}}_9^{\diamond},\ \mathfrak{S}_{16}^{\diamond} = -\mathrm{i}\xi\sum_{i=1}^{4}\bar{\mathrm{R}}_{2i}^{\diamond} - m_5^{\diamond}\bar{\mathrm{R}}_{10}^{\diamond},$
$\mathfrak{S}_{17}^{\diamond} = \sum_{i=5}^{8}m_{i-4}^{\diamond}\bar{\mathrm{R}}_{2i+1}^{\diamond} - \mathrm{i}\xi\bar{\mathrm{R}}_{19}^{\diamond},\ \mathfrak{S}_{18}^{\diamond} = \sum_{i=5}^{8}m_{i-4}^{\diamond}\bar{\mathrm{R}}_{2i+2}^{\diamond} - \mathrm{i}\xi\bar{\mathrm{R}}_{20}^{\diamond},\ \mathfrak{S}_{19}^{\diamond} = \sum_{i=0}^{3}\alpha_{i+1}^{\diamond}\bar{\mathrm{R}}_{2i+1}^{\diamond},$
$\mathfrak{S}_{20}^{\diamond} = \sum_{i=0}^{3}\alpha_{i+1}^{\diamond}\bar{\mathrm{R}}_{2i+2}^{\diamond},\ \mathfrak{S}_{21}^{\diamond} = \sum_{i=0}^{3}\beta_{i+1}^{\diamond}\bar{\mathrm{R}}_{2i+1}^{\diamond},\ \mathfrak{S}_{22}^{\diamond} = \sum_{i=0}^{3}\beta_{i+1}^{\diamond}\bar{\mathrm{R}}_{2i+2}^{\diamond},$
$\mathfrak{S}_{23}^{\diamond} = \sum_{i=0}^{3}\gamma_{i+1}^{\diamond}\bar{\mathrm{R}}_{2i+1}^{\diamond},\ \mathfrak{S}_{24}^{\diamond} = \sum_{i=0}^{3}\gamma_{i+1}^{\diamond}\bar{\mathrm{R}}_{2i+2}^{\diamond},\ \mathfrak{S}_{25}^{\diamond} = \sum_{i=0}^{4}a_{i+1}^{\diamond}\bar{\mathrm{R}}_{2i+1}^{\diamond},$
$\mathfrak{S}_{26}^{\diamond} = \sum_{i=0}^{4}b_{i+1}^{\diamond}\bar{\mathrm{R}}_{2i+2}^{\diamond},\ \mathfrak{S}_{27}^{\diamond} = \sum_{i=5}^{9}b_{i-4}^{\diamond}\bar{\mathrm{R}}_{2i+1}^{\diamond},\ \mathfrak{S}_{28}^{\diamond} = \sum_{i=5}^{9}b_{i-4}^{\diamond}\bar{\mathrm{R}}_{2i+2}^{\diamond},$
where
$\bar{\mathrm{R}}_1^{\diamond} = \mathfrak{R}_{33}\mathcal{C}_1, \bar{\mathrm{R}}_2^{\diamond} = \mathfrak{R}_{34}\mathcal{C}_1, \bar{\mathrm{R}}_3^{\diamond} = \mathfrak{R}_{35}\mathcal{C}_2, \bar{\mathrm{R}}_4^{\diamond} = \mathfrak{R}_{36}\mathcal{C}_2, \bar{\mathrm{R}}_5^{\diamond} = \mathfrak{R}_{37}\mathcal{C}_3, \bar{\mathrm{R}}_6^{\diamond} = \mathfrak{R}_{38}\mathcal{C}_3,$
$\bar{\mathrm{R}}_7^{\diamond} = \mathfrak{R}_{39}\mathcal{C}_4, \bar{\mathrm{R}}_8^{\diamond} = \mathfrak{R}_{40}\mathcal{C}_4, \bar{\mathrm{R}}_9^{\diamond} = \mathfrak{R}_{41}\mathcal{C}_5, \bar{\mathrm{R}}_{10}^{\diamond} = \mathfrak{R}_{42}\mathcal{C}_5, \bar{\mathrm{R}}_{11}^{\diamond} = \mathfrak{R}_{33}\mathcal{S}_1, \bar{\mathrm{R}}_{12}^{\diamond} = \mathfrak{R}_{34}\mathcal{S}_1,$
$\bar{\mathrm{R}}_{13}^{\diamond} = \mathfrak{R}_{35}\mathcal{S}_1, \bar{\mathrm{R}}_{14}^{\diamond} = \mathfrak{R}_{36}\mathcal{S}_1, \bar{\mathrm{R}}_{15}^{\diamond} = \mathfrak{R}_{37}\mathcal{S}_1, \bar{\mathrm{R}}_{16}^{\diamond} = \mathfrak{R}_{38}\mathcal{S}_1, \bar{\mathrm{R}}_{17}^{\diamond} = \mathfrak{R}_{39}\mathcal{S}_1, \bar{\mathrm{R}}_{18}^{\diamond} = \mathfrak{R}_{40}\mathcal{S}_1,$

$\overline{\mathrm{R}}_{19}^{\diamond} = \Re_{41}\mathcal{S}_1, \overline{\mathrm{R}}_{20}^{\diamond} = \Re_{42}\mathcal{S}_1.$

Particular cases

Case 1: For carrier density source $\mathrm{F}_{40} = 0$ yield:

$$\left(\tilde{u}_1, \tilde{u}_3, \tilde{T}, \tilde{N}, \tilde{M}, \tilde{t}_{33}, \tilde{t}_{31}\right) = \frac{1}{\Delta_i^{\diamond}}\left(\mathfrak{S}_{15}^{\diamond}, \mathfrak{S}_{17}^{\diamond}, \mathfrak{S}_{19}^{\diamond}, \mathfrak{S}_{21}^{\diamond}, \mathfrak{S}_{23}^{\diamond}, \mathfrak{S}_{25}^{\diamond}, \mathfrak{S}_{27}^{\diamond}\right)\tilde{\mathrm{F}}_3. \tag{66}$$

Case 2: For moisture source $\mathrm{F}_{30} = 0$ yield:

$$\left(\tilde{u}_1, \tilde{u}_3, \tilde{T}, \tilde{N}, \tilde{M}, \tilde{t}_{33}, \tilde{t}_{31}\right) = \frac{1}{\Delta_i^{\diamond}}\left(\mathfrak{S}_{16}^{\diamond}, \mathfrak{S}_{18}^{\diamond}, \mathfrak{S}_{20}^{\diamond}, \mathfrak{S}_{22}^{\diamond}, \mathfrak{S}_{24}^{\diamond}, \mathfrak{S}_{26}^{\diamond}, \mathfrak{S}_{28}^{\diamond}\right)\tilde{\mathrm{F}}_4. \tag{67}$$

Special case

In absence of moisture impact i.e. when $D_t^m = 0, K_m = 0, \gamma_m = 0$ yield the corresponding results for isotropic photothermoelastic plate, then Eq. (39) takes the form:

$$\left(D^6 + \mathfrak{B}_{p1}D^4 + \mathfrak{B}_{p2}D^2 + \mathfrak{B}_{p3}\right)\left(\widetilde{\Phi}, \tilde{T}, \widetilde{N}\right) = 0, \tag{68}$$

where

$\mathfrak{B}_{p1} = \Re_{p1} - \Re_{p3} - \xi^2 - \mathfrak{s}^2$; $\mathfrak{B}_{p2} = \Re_{p2} - \xi^2\Re_{p1} - \mathfrak{s}^2\Re_{p1} - \Re_{p4} - \Re_{p6}$,

$\mathfrak{B}_{p3} = -\xi^2\Re_{p2} - \mathfrak{s}^2\Re_{p2} - \Re_{p5} - \Re_{p7}$,

where

$\Re_{p1} = -2\xi^2 - f_{13}\,\mathfrak{s} - f_{14} - \mathcal{r}_1 f_{17}$,

$\Re_{p2} = \xi^4 + f_{13}\mathfrak{s}\xi^2 + f_{14}\xi^2 + f_{17}\mathcal{r}_1\xi^2 + f_{13}f_{17}\mathcal{r}_1\mathfrak{s} + f_{14}f_{17}\mathcal{r}_1 - f_{15}f_{16}$,

$\Re_{p3} = f_{18}\mathcal{r}_1$; $\Re_{p4} = -2f_{18}\mathcal{r}_1\xi^2 - f_{13}f_{18}\mathcal{r}_1\mathfrak{s} - f_{14}f_{18}\mathcal{r}_1$,

$\Re_{p5} = f_{18}\mathcal{r}_1\xi^4 + f_{13}f_{18}\mathcal{r}_1\mathfrak{s}\xi^2 + f_{14}f_{18}\mathcal{r}_1\xi^2$,

$\Re_{p6} = -f_{15}f_{18}\mathcal{r}_1$, $\Re_{p7} = f_{15}f_{18}\mathcal{r}_1\xi^2$.

The general solution of Eq. (68) is represented as:

$$\left(\widetilde{\Phi}, \tilde{T}, \widetilde{N}\right) = \sum_{i=1}^{3}\left(1, \alpha_{pi}, \beta_{pi}\right)\bar{C}_{pi}\cosh m_{pi}\,x_3, \tag{69}$$

where $m_{pi}(i = 1, 2, 3)$ are roots of $D^6 + \mathfrak{B}_{p1}D^4 + \mathfrak{B}_{p2}D^2 + \mathfrak{B}_{p3} = 0$.

The coupling parameters α_{pi}, β_{pi} are given by:

$$\alpha_{pi} = \sum_{i=1}^{3}\frac{\Re_{p3}m_{pi}^4 + \Re_{p4}m_{pi}^2 + \Re_{p5}}{m_{pi}^4 + \Re_{p1}m_{pi}^2 + \Re_{p2}}, \tag{70}$$

$$\beta_{pi} = \sum_{i=1}^{3}\frac{\Re_{p6}m_{pi}^2 + \Re_{p7}}{m_{pi}^4 + \Re_{p1}m_{pi}^2 + \Re_{p2}}\ . \tag{71}$$

In this case, $\widetilde{\Psi} = \bar{C}_{p4}\sinh m_{p4}x_3$, where m_{p4} is a root of equation $D^2 + \mathfrak{B}_{p4} = 0$, $\mathfrak{B}_{p4}$ is same as $\mathfrak{B}_6$ and m_{p4} is same as $m_5^{\diamond}$.

Transformed boundary restrictions in this case lead to:

$$\tilde{t}_{33} = 0,\ \ \tilde{t}_{31} = 0,\ \ \tilde{T} = 0,\ \ \widetilde{N} = \tilde{\mathrm{F}}_3(\xi, x_3, \mathfrak{s}) \text{ at } x_3 = \pm d. \tag{72}$$

Utilizing these revised boundary restrictions, we compute the associated results as

$$\begin{aligned}
&\tilde{u}_1 = \frac{1}{\Delta_p}\left(\overline{\mathfrak{S}}_{p1}\tilde{\mathrm{F}}_3\right),\ \ \tilde{u}_3 = \frac{1}{\Delta_p}\left(\overline{\mathfrak{S}}_{p2}\tilde{\mathrm{F}}_3\right),\\
&\tilde{T} = \frac{1}{\Delta_p}\left(\overline{\mathfrak{S}}_{p3}\tilde{\mathrm{F}}_3\right),\ \ \widetilde{N} = \frac{1}{\Delta_p}\left(\overline{\mathfrak{S}}_{p4}\tilde{\mathrm{F}}_3\right),\\
&\tilde{t}_{33} = \frac{1}{\Delta_p}\left(\overline{\mathfrak{S}}_{p5}\tilde{\mathrm{F}}_3\right),\ \ \tilde{t}_{31} = \frac{1}{\Delta_p}\left(\overline{\mathfrak{S}}_{p6}\tilde{\mathrm{F}}_3\right),
\end{aligned} \tag{73}$$

where

Δ_p is determinant of matrix A_p which is given by:

$$A_p = \begin{bmatrix} a_{p1}\mathcal{C}_{p1} & a_{p2}\mathcal{C}_{p2} & a_{p3}\mathcal{C}_{p3} & a_{p4}\mathcal{C}_{p4} \\ b_{p1}\mathcal{S}_{p1} & b_{p2}\mathcal{S}_{p2} & b_{p3}\mathcal{S}_{p3} & b_{p4}\mathcal{S}_{p4} \\ \alpha_{p1}\mathcal{C}_{p1} & \alpha_{p2}\mathcal{C}_{p2} & \alpha_{p3}\mathcal{C}_{p3} & 0 \\ \beta_{p1}\mathcal{C}_{p1} & \beta_{p2}\mathcal{C}_{p2} & \beta_{p3}\mathcal{C}_{p3} & 0 \end{bmatrix},$$

with

$\overline{\mathcal{S}}_{p1} = -\mathrm{i}\xi \sum_{i=1}^{3} \overline{\mathrm{R}}_i^p - m_{p4}\mathrm{R}_4^p,\ \overline{\mathcal{S}}_{p2} = \sum_{i=1}^{3} m_{pi}\overline{\mathrm{R}}_{i+4}^p - \mathrm{i}\xi \mathrm{R}_8^p,\ \overline{\mathcal{S}}_{p3} = \sum_{i=1}^{3} \alpha_{pi}\overline{\mathrm{R}}_i^p,$
$\overline{\mathcal{S}}_{p4} = \sum_{i=1}^{3} \beta_{pi}\overline{\mathrm{R}}_i^p,\ \overline{\mathcal{S}}_{p5} = \sum_{i=1}^{4} a_{pi}\overline{\mathrm{R}}_i^p, \overline{\mathcal{S}}_{p6} = \sum_{i=1}^{4} b_{pi}\overline{\mathrm{R}}_{i+4}^p,$

and

$\overline{\mathrm{R}}_1^p = \overline{\mathfrak{R}}_{p8}\mathcal{C}_{p1},\ \overline{\mathrm{R}}_2^p = \overline{\mathfrak{R}}_{p9}\mathcal{C}_{p2}, \overline{\mathrm{R}}_3^p = \overline{\mathfrak{R}}_{p10}\mathcal{C}_{p3},\ \overline{\mathrm{R}}_4^p = \overline{\mathfrak{R}}_{p11}\mathcal{C}_{p4},$
$\overline{\mathrm{R}}_5^p = \overline{\mathfrak{R}}_{p8}\mathcal{S}_{p1},\ \overline{\mathrm{R}}_6^p = \overline{\mathfrak{R}}_{p9}\mathcal{S}_{p2},\ \overline{\mathrm{R}}_7^p = \overline{\mathfrak{R}}_{p10}\mathcal{S}_{p3},\ \overline{\mathrm{R}}_8^p = \overline{\mathfrak{R}}_{p11}\mathcal{S}_{p4},$

where

$\overline{\mathfrak{R}}_{p8} = a_{p2}b_{p4}\alpha_{p3}\mathcal{C}_{p2}\mathcal{C}_{p3}\mathcal{S}_{p4} - a_{p3}b_{p4}\alpha_{p2}\mathcal{C}_{p2}\mathcal{C}_{p3}\mathcal{S}_{p4} +$
$+a_{p3}\mathcal{C}_{p4}\left(b_{p3}\alpha_{p2}\mathcal{C}_{p2}\mathcal{S}_{p3} - b_{p2}\alpha_{p3}\mathcal{C}_{p3}\mathcal{S}_{p2}\right),$
$\overline{\mathfrak{R}}_{p9} = -a_{p1}b_{p4}\alpha_{p3}\mathcal{C}_{p1}\mathcal{C}_{p3}\mathcal{S}_{p4} + a_{p3}b_{p4}\alpha_{p1}\mathcal{C}_{p1}\mathcal{C}_{p3}\mathcal{S}_{p4} +$
$+a_{p4}\mathcal{C}_{p4}\left(b_{p1}\alpha_{p3}\mathcal{C}_{p3}\mathcal{S}_{p1} - b_{p3}\alpha_{p1}\mathcal{C}_{p1}\mathcal{S}_{p3}\right),$
$\overline{\mathfrak{R}}_{p10} = a_{p1}b_{p4}\alpha_{p2}\mathcal{C}_{p1}\mathcal{C}_{p2}\mathcal{S}_{p4} - a_{p2}b_{p4}\alpha_{p1}\mathcal{C}_{p1}\mathcal{C}_{p2}\mathcal{S}_{p4} +$
$+a_{p4}\mathcal{C}_{p4}\left(b_{p2}\alpha_{p1}\mathcal{C}_{p1}\mathcal{S}_{p2} - b_{p1}\alpha_{p2}\mathcal{C}_{p2}\mathcal{S}_{p1}\right),$
$\overline{\mathfrak{R}}_{p11} = a_{p1}\mathcal{C}_{p1}\left(b_{p2}\alpha_{p3}\mathcal{C}_{p3}\mathcal{S}_{p2} - b_{p3}\alpha_{p2}\mathcal{C}_{p2}\mathcal{S}_{p3}\right) +$
$-a_{p2}\mathcal{C}_{p2}\left(b_{p1}\alpha_{p3}\mathcal{C}_{p3}\mathcal{S}_{p1} - b_{p3}\alpha_{p1}\mathcal{C}_{p1}\mathcal{S}_{p3}\right) + a_{p3}\mathcal{C}_{p3}\left(b_{p1}\alpha_{p2}\mathcal{C}_{p2}\mathcal{S}_{p1} - b_{p2}\alpha_{p1}\mathcal{C}_{p1}\mathcal{S}_{p2}\right).$

Numerical outcomes and interpretation

For the mathematical calculations, we implement the isotropic Silicon (Si) material constants (Alenazi et al. [49], Table 1).

Table 1. Material constants for the isotropic Silicon (Si) material

Symbol, Unit	Value	Symbol, Unit	Value
$\lambda, \mathrm{N/m^2}$	$6.4 \cdot 10^{10}$	E_g, eV	1.11
$\mu, \mathrm{N/m^2}$	$6.5 \cdot 10^{10}$	$D_t^m, \mathrm{m^2(\%H_2O)/s(K)}$	$2.1 \cdot 10^{-7}$
$\alpha_t, \mathrm{K^{-1}}$	$4.14 \cdot 10^{-6}$	T_o, K	800
$\alpha_n, \mathrm{m^3}$	$-9 \cdot 10^{-31}$	$K_m, \mathrm{(kg/msM)}$	$2.2 \cdot 10^{-8}$
$\alpha_m, \mathrm{cm/cm(\%H_2O)}$	$2.68 \cdot 10^{-3}$	$D_m, \mathrm{m^2\ s^{-1}}$	$0.35 \cdot 10^{-2}$
$\rho, \mathrm{kg/m^3}$	2330	$D_m^t, \mathrm{m^2 s(K)/(\%H_2O)}$	$0.648 \cdot 10^{-6}$
$D_\mathrm{e}, \mathrm{m^2/s}$	$2.5 \cdot 10^{-3}$	$k, \mathrm{Wm^{-1}K^{-1}}$	150
τ, s	$5 \cdot 10^{-5}$	$n_o, \mathrm{m^{-3}}$	10^{10}
$\delta, \mathrm{m^{-3}\ K^{-1}}$	0.5	m_o	10 %
$C_\mathrm{e}, \mathrm{J/(kgK)}$	695		

The Matlab (R2014a) software is utilized for computing in the following scenarios:
Photothermoelastic moisture plate with $\tau_o = .03, \tau^o = .02$ (IPTMT1);
Photothermoelastic moisture plate with $\tau_o = .05, \tau^o = .04$ (IPTMT2);
Photothermoelastic moisture plate with $\tau_o = .03, \tau^o = .04$ (IPTMT3);
Photothermoelastic moisture plate with $\tau_o = 0, \tau^o = 0$ (IPTMT4);
Photothermoelastic without moisture plate $\tau_o = .03, \tau^o = 0$ (IPTWMT1);
Photothermoelastic without moisture plate $\tau_o = .05, \tau^o = 0$ (IPTWMT2).

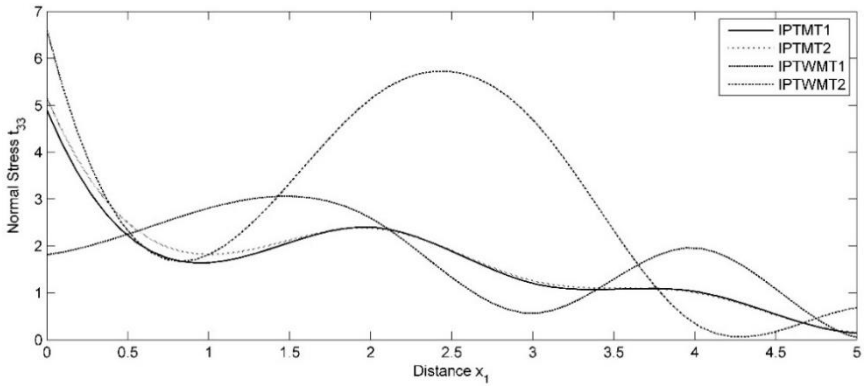

Fig. 1. Variation of normal stress t_{33} w.r.t. x_1 owing to carrier density source

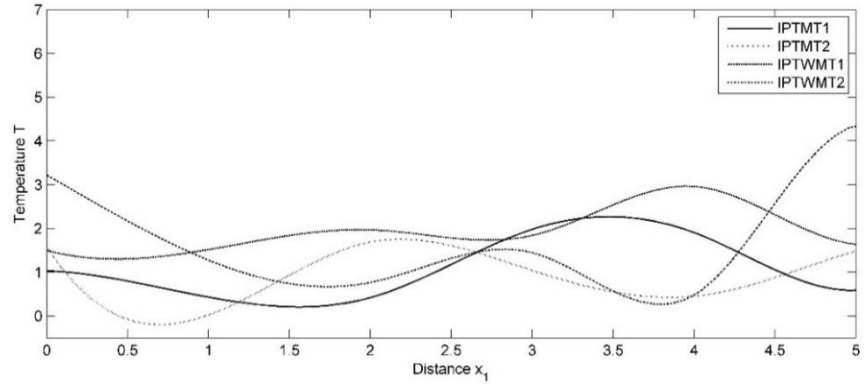

Fig. 2. Variation of temperature *T* w.r.t. x_1 owing to carrier density source

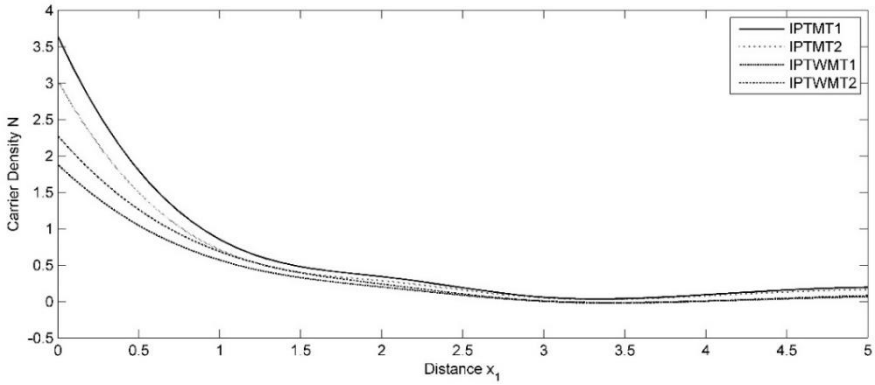

Fig. 3. Variation of carrier density *N* w.r.t. x_1 owing to carrier density source

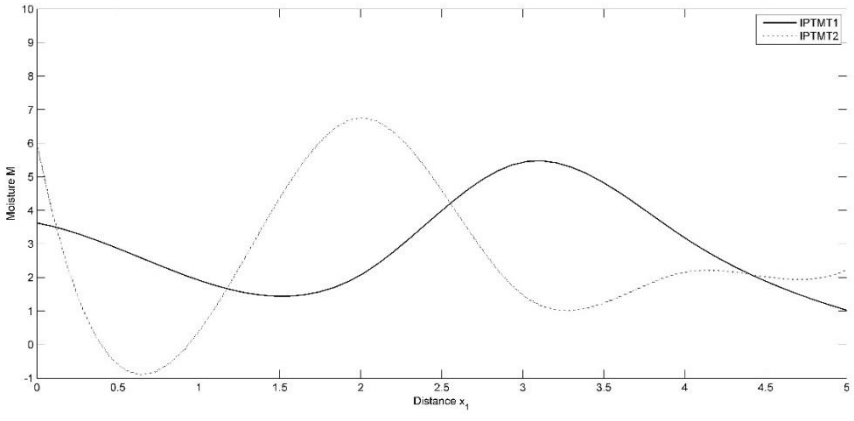

Fig. 4. Variation of moisture *M* w.r.t. x_1 owing to carrier density source

Figures 1–4 represent how moisture affects the field variables (t_{33}, T, N, M) when there is carrier density source. Figures 5–8 represent the impact of relaxation times in case of carrier density source and Figures 9–12 represent the impact of relaxation times in case of moisture source on the same field variables (t_{33}, T, N, M).

In all the figures, the solid line (———) represents IPTMT1, the dotted (⋯⋯⋯) line represents IPTMT2, the solid line containing the center symbol square (— ▫ —) indicates to IPTMT3 and the solid line containing the center symbol triangle (— △ —) represents IPTMT4, the dash (— — —) line corresponds to IPTWMT1, the dash dot (— · — · —) line corresponds to IPTWMT2.

Figure 1 displays the variation of normal stress t_{33} with x_1. With the exception of the IPTMT1 model, t_{33} for the IPTMT2, IPTWMT1, and IPTWMT2 models exhibit a declining trend in proximity to the source. Across the entire domain, t_{33} reflects identical behavior with less fluctuations for the IPTMT1 and IPTMT2 models whereas it fluctuates more and displays an opposing oscillatory pattern for the IPTWMT1 and IPTWMT2 models.

Figure 2 presents the variation of temperature *T* with x_1. *T* exhibits a large-scale oscillating behavior for the IPTWMT2 model. T for IPTWMT1 and IPTWMT2 demonstrates a decreasing tendency initially, and it tracks the opposite trend for $0.5 \leq x_1$. T for IPTMT1 and IPTMT2 displays an overall opposing oscillating pattern, with the exception of some limited region where their behavior aligns.

Figure 3 shows how the carrier density *N* changes with x_1. Close to the source, all models exhibits a decreasing trend in *N*, with the IPTMT1 model showing the steepest decline. *N* for all models possess a pattern of minor oscillations within the range $1.5 \leq x_1 \leq 3$, followed by a slight and monotonic increasing trend thereafter.

Figure 4 depicts the variation of moisture *M* with x_1. In the range $0 \leq x_1 \leq 3$, *M* for IPTMT2 exhibits more pronounced oscillatory trend, followed by slight oscillations thereafter. *M* for IPTMT2 decreases within the range $0 \leq x_1 \leq 1.5$, transitioning into oscillatory behavior beyond this interval.

Figure 5 demonstrates the variation of normal stress t_{33} with x_1. All models indicate a declining pattern in t_{33} near the source, with the IPTMT3 model showing the highest magnitude and the IPTMT4 model depicting the smallest magnitude. As x_1 increases t_{33} continues to decline with minor oscillations with slight variations in magnitude across the models.

Figure 6 illustrates how temperature *T* varies with x_1. With the exception of a limited initial segment, *T* for IPTMT1 and IPTMT2 reflect the opposite oscillatory patterns. *T* for the IPTMT3 and IPTMT4 models exhibit an opposite fluctuating behavior within the range $0 \leq x_1 \leq 3$ but beyond this interval their trends aligns.

Figure 7 depicts the variation of carrier density *N* with x_1. Close to the source, all models reveal a decreasing trend in *N*, with IPTMT3, reaching the highest magnitude and IPTMT2 the lowest. As the distance increases, *N* begins to oscillate slightly, tends to converge, and shows an increasing trend across all models.

Figure 8 shows how moisture *M* changes along x_1. *M* for IPTMT1 and IPTMT2 exhibit opposite oscillatory patterns throughout the entire domain, except for an initial small region where their responses temporarily align. On the other hand, *M* for IPTMT3 and IPTMT4 display inverse oscillatory behaviors within the range $0 \leq x_1 \leq 2.25$, subsequently exhibiting comparable behavior thereafter.

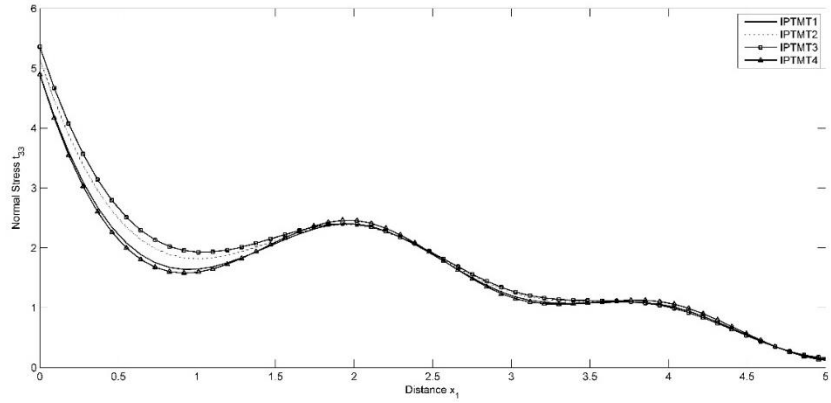

Fig. 5. Impact of relaxation times on normal stress t_{33} due to carrier density source

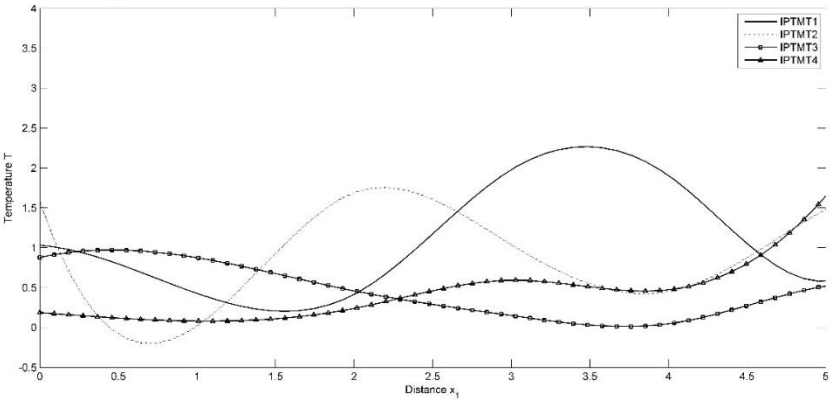

Fig. 6. Impact of relaxation times on temperature *T* due to carrier density source

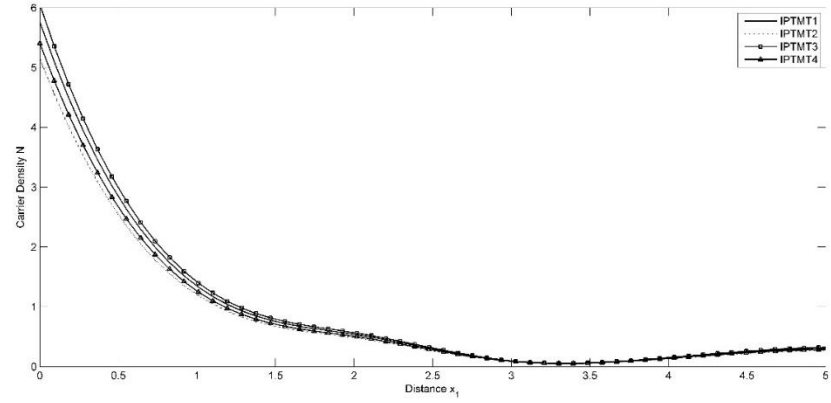

Fig. 7. Impact of relaxation times on carrier density *N* due to carrier density source

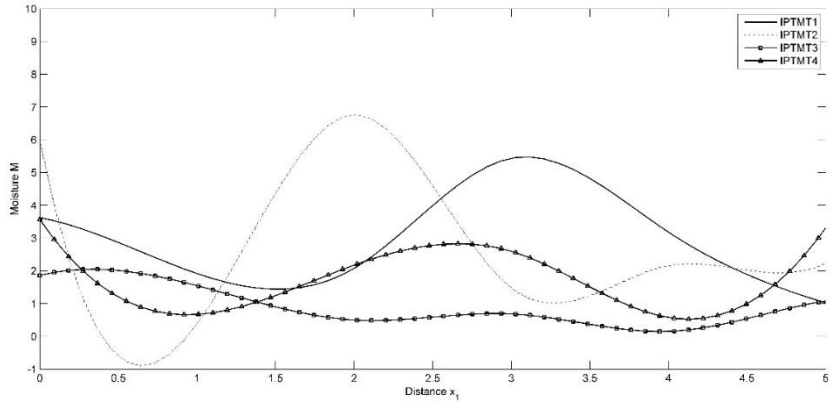

Fig. 8. Impact of relaxation times on moisture *M* due to carrier density source

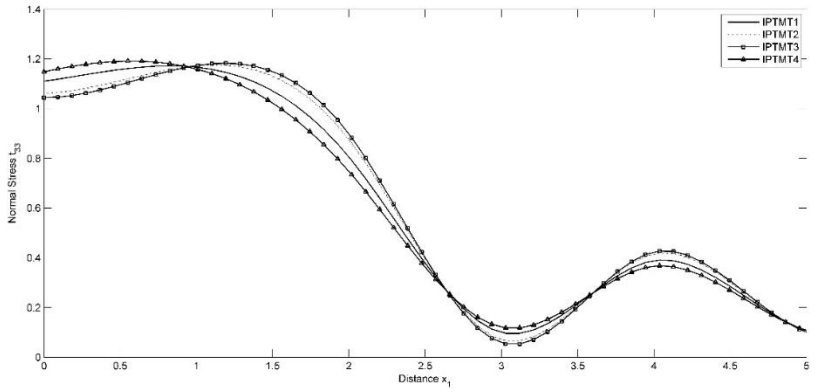

Fig. 9. Impact of relaxation times on normal stress t_{33} due to moisture source

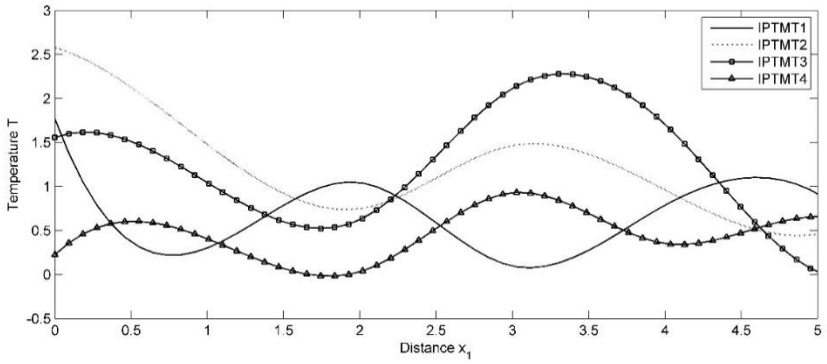

Fig. 10. Impact of relaxation times on temperature *T* due to moisture source

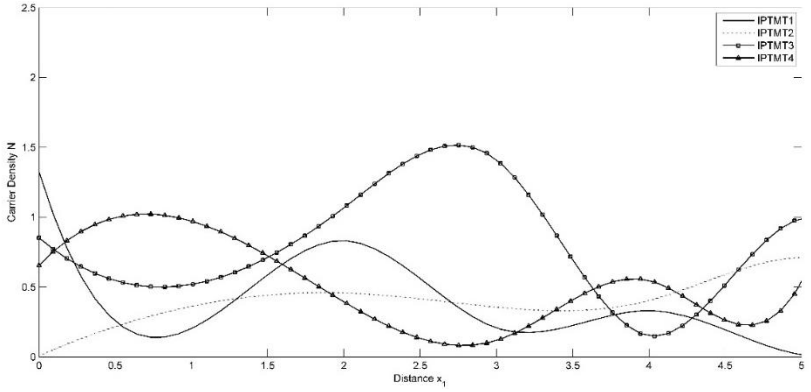

Fig. 11. Impact of relaxation times on carrier density *N* due to moisture source

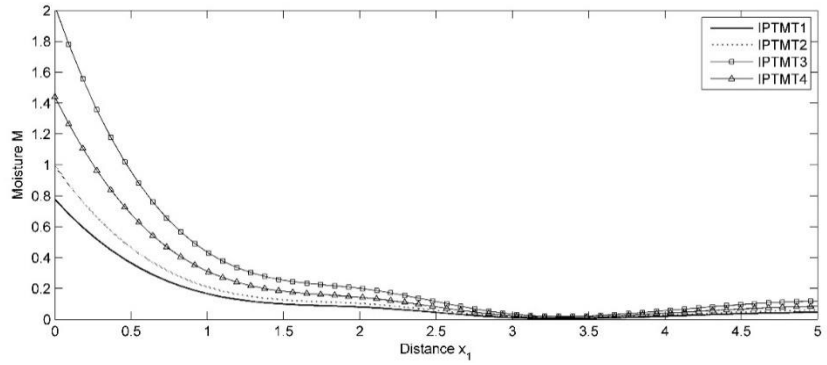

Fig. 12. Impact of relaxation times on moisture *M* due to moisture source

Figure 9 displays the variation of normal stress t_{33} with x_1. t_{33} exhibits an increasing tendency near the vicinity of the source across all models. With the increasing distance, t_{33} begins to decrease in reverse order and reveals an oscillating tendency with magnitudes varying between models.

Figure 10 shows the variation of temperature T with x_1. T for IPTMT1 and IPTMT2 exhibit an initial decline, followed by opposite oscillatory trend in the range $0.75 \leq x_1 \leq 5$. Meanwhile, T for IPTMT3 and IPTMT4 displays a similar oscillatory behavior in the range $0 \leq x_1 \leq 4$, and beyond this range, it transitions into an opposite oscillatory behavior.

Figure 11 illustrates how the carrier density N varies with x_1. Close to the source, N for IPTMT1 and IPTMT3 models follow a declining trend, though N for IPTMT2 and IPTMT4 shows an increasing pattern. N for IPTMT3 and IPTMT4 demonstrate more pronounced oscillations compared to IPTMT1 and IPTMT2 models. N for IPTMT1 displays significant oscillations in the range $0 \leq x_1 \leq 3$, and slight oscillation around $3 \leq x_1$. N for IPTMT2 follows an increasing trend in the range $0 \leq x_1 \leq 2$, and maintains a relatively mild oscillatory pattern beyond this range. The oscillatory pattern of N for IPTMT3 and IPTMT4 is opposing with high variation in magnitude.

Figure 12 displays the variation of moisture M with x_1. Near the source, M for all the models exhibit a decreasing trend, with the IPTMT3 model showing the highest magnitude and IPTMT1 model the lowest and display slight oscillations within the range $1 \leq x_1 \leq 3$. Near the source, there is a notable difference in magnitude for all the models, while away from the source, the magnitudes tend to converge, and all models exhibit a consistent upward trend, accompanied by slight amplitude variations.

Conclusions

This study investigates the deformation in an isotropic IPTM plate due to the influence of a carrier density source and a moisture source. General equations are used to derive the governing equations and constitutive relations for the plate under consideration. To simplify the analysis, non-dimensional variables and potential functions are employed. Analytical solutions for the resulting equations are obtained through Laplace and Fourier transforms, and numerical inversion techniques are applied to retrieve the solutions in the physical domain. Graphical representations illustrate the effects of moisture, relaxation times, and source terms on various physical fields such as stress, temperature, carrier density, and moisture distribution. Based on the numerical results, the following key conclusions can be drawn.

Carrier density source. The presence of moisture leads to a more stable pattern of normal stress, showing reduced fluctuations. Moisture presence also slightly attenuates temperature variations. Carrier density maintains comparable behavior, with higher magnitude induced by moisture. Moisture content oscillates more strongly with larger thermal and moisture relaxation times ($\tau_o = 0.05$, $\tau^o = 0.04$), near the source. For all models, normal stress display oscillations. Near the source, normal stress reaches higher values, for smaller thermal and higher moisture relaxation times ($\tau_o = 0.03$, $\tau^o = 0.04$). Near the source, Temperature and Moisture fluctuations are more pronounced and attain extremes for higher thermal and moisture relaxation times ($\tau_o = 0.05$, $\tau^o = 0.04$), while at greater distances, stronger fluctuations occur under smaller relaxation times ($\tau_o = 0.03$,

$\tau^o = 0.02$). Carrier density for all models initially decreases monotonically then transitions into a slight oscillatory phase and subsequently shows a modest increase, amplified under smaller thermal and higher moisture relaxation times.

Moisture source. Normal stress intensifies near the source, and its peaks and valleys occur at identical positions across all models. It has peaks for lower thermal and higher moisture relaxation times ($\tau_o = 0.03$, $\tau^o = 0.04$) and lower overall magnitude when relaxation effects are absent. Near the source, temperature fluctuations are more pronounced for smaller thermal and moisture relaxation times ($\tau_o = 0.03$, $\tau^o = 0.02$). At greater distances, temperature shows stronger fluctuations with increased magnitude for lower thermal and higher moisture relaxation times ($\tau_o = 0.03$, $\tau^o = 0.04$). Carrier density exhibits pronounced oscillations across the domain under the conditions of high moisture relaxation time ($\tau_o = 0.03$, $\tau^o = 0.04$) and when relaxation times are disregarded ($\tau_o = 0$, $\tau^o = 0$). Moisture concentration undergoes a monotonic decrease in all cases, with higher attenuation magnitude corresponding to lower thermal and higher moisture relaxation times ($\tau_o = 0.03$, $\tau^o = 0.04$). However, with distance, the moisture profile transitions into an oscillatory form that eventually converges, subsequently exhibiting a minor increasing trend.

The proposed method offers a unified analytical approach to study coupled thermoelastic, moisture, and photo-induced effects in semiconducting materials. It is particularly relevant for microelectronic, optoelectronic, and photovoltaic devices, where thermal loading, carrier excitation, and moisture exposure affect performance and reliability. The model aids in optimizing thermal management and structural stability, providing deeper insight into transient behavior under realistic operating conditions.

CRediT authorship contribution statement

Rajneesh Kumar: conceptualization, supervision, literature review, methodology, software, visualization, investigation; **Nidhi Sharma**: assistance in methodology refinement, analysis and interpretation of the study; **Vineeta Rani**: writing, draft preparation, validation and visualization.

Conflict of interest

The authors declare that they have no conflict of interest.

References

1. Mandelis A. *Photoacoustic and thermal wave phenomena in semiconductors*. New York: Elsevier Science; 1987.
2. Almond DP, Patel PM. *Photothermal science and techniques*. London: Chapman & Hall; 1996.
3. Nikolic PM, Todorovic DM. Photoacoustic and electroacoustic properties of semiconductors. *Progress in Quantum Electronics*. 1989;13(2): 107–189.
4. Mandelis A, Michaelian KH. Photoacoustic and photothermal science and engineering. *Optical Engineering*. 1997;36(2): 301–302.
5. Todorovic D. Photothermal and electronic elastic effects in micro electromechanical structures. *Review of Scientific Instruments*. 2003;74(1): 578–581.
6. Todorovic D. Plasma, thermal, and elastic waves in semiconductors. *Review of Scientific Instruments*. 2003;74(1): 582–585.
7. Todorovic D. Plasmaelastic and thermoelastic waves in semiconductors. *Journal de Physique IV (Proceeding)*. 2005;125: 551–555.

8. Sharma K. Boundary value problem in generalized thermodiffusive elastic medium. *Journal of Solid Mechanics.* 2010;2(4): 348–362.
9. Sharma S, Sharma K, Bhargava RR. Wave motion and representation of fundamental solution in electro-microstretch viscoelastic solids. *Materials Physics and Mechanics.* 2013;17(2): 93–110.
10. Othman MIA, Lotfy K, Farouk RM. Transient disturbance in a half-space under generalized magneto-thermoelasticity with internal heat source. *Acta Physica Polonica A.* 2009;116(2): 185–192.
11. Marin M, Abbas JA, Kumar R. Relaxed Saint-Venant principle for thermoelastic micropolar diffusion. *Structural Engineering and Mechanics.* 2014;51(4): 651–662.
12. Zenkour AM, Abbas IA. Thermal shock problem for a fiber-reinforced anisotropic half-space placed in a magnetic field via G–N model. *Applied Mathematics and Computation.* 2014;246: 482–490.
13. Lotfy K. Two-temperature generalized magneto-thermoelastic interactions in an elastic medium under three theories. *Applied Mathematics and Computation.* 2014;227: 871–888.
14. Sharma S, Sharma K. Influence of heat sources and relaxation time on temperature distribution in tissues. *International Journal of Applied Mechanics and Engineering.* 2014;19(2): 427–433.
15. Abbas IA, Othman MIA. Plane waves in generalized thermo-microstretch elastic solid with thermal relaxation using finite element method. *International Journal of Thermophysics.* 2012;33: 2407–2423.
16. Hobiny A, Abbas IA. A GN model on photothermal interactions in a two-dimensional semiconductor half-space. *Results in Physics.* 2019;15: 102588.
17. Hobiny A, Abbas IA. Fractional order GN model on photo-thermal interaction in a semiconductor plane. *Silicon.* 2020;12: 1957–1964.
18. Marin M, Hobiny A, Abbas IA. The effects of fractional time derivatives in porothermoelastic materials using finite element method. *Mathematics.* 2021;9(14): 1606.
19. Lotfy K, El-Bary AA. Magneto-photo-thermo-microstretch semiconductor elastic medium due to photothermal transport process. *Silicon.* 2022;14: 4809–4821.
20. Abbas IA. A GN model based upon two-temperature generalized thermoelastic theory in an unbounded medium with a spherical cavity. *Applied Mathematics and Computation.* 2014;245: 108–115.
21. Abbas IA. A GN model for thermoelastic interaction in a microscale beam subjected to a moving heat source. *Acta Mechanica.* 2015;226: 2527–2536.
22. Sharma N, Kumar R. Photo-thermoelastic investigation of semiconductor material due to distributed loads. *Journal of Solid Mechanics.* 2021;13(2): 202–212.
23. Sharma N, Kumar R. Photothermoelastic deformation in dual phase lag model due to concentrated inclined load. *Italian Journal of Pure and Applied Mathematics.* 2022;48–2022: 1147–1160.
24. Lotfy K, El-Bary AA, El-Sharif AH. Ramp-type heating microtemperature for a rotator semiconducting material during photo-excited processes with magnetic field. *Results in Physics.* 2020;19: 103338.
25. Mahdy AMS, Lotfy K, Ismail EA, El-Bary AA, Ahmed M, El-Dahdouh AA. Analytical solutions of time-fractional heat order for a magneto-photothermal semiconductor medium with Thomson effects and initial stress. *Results in Physics.* 2020;18: 103174.
26. Sharma S, Khator S. Power generation planning with reserve dispatch and weather uncertainties including penetration of renewable sources. *International Journal of Smart Grid and Clean Energy.* 2021;10(4): 292–303.
27. Sharma S, Khator S. Micro-grid planning with aggregator's role in the renewable inclusive prosumer market. *Journal of Power and Energy Engineering.* 2022;10(4): 47–62.
28. Lotfy K, El-Bary AA, Hassan W, Ahmed MH. Hall current influence of microtemperature magneto-elastic semiconductor material. *Superlattices and Microstructures.* 2020;139: 106428.
29. Hobiny A, Abbas IA, Marin M. The influences of the hyperbolic two-temperatures theory on waves propagation in a semiconductor material containing spherical cavity. *Mathematics.* 2022;10(1): 121.
30. El-Sapa S, Becheikh N, Chtioui H, Lotfy K, Seddeek MA, El-Bary AA, El-Dali A. Moore–Gibson–Thompson model with the influence of moisture diffusivity of semiconductor materials during photothermal excitation. *Frontiers in Physics.* 2023;11: 1224326.
31. Raddadi MH, Lotfy K, Mahdy AMS, El-Bary AA, Elidy ES. A novel model of photoacoustic and thermalelectronic waves in semiconductor material. *AIP Advances.* 2025;15(1): 015207.
32. Sharma K, Marin M, Kumar R. Thermomechanical deformation in a micropolar thermoviscoelastic solid under the Moore–Gibson–Thompson heat equation with non-local and hyperbolic two-temperature effects. *Journal of Computational Applied Mechanics.* 2025;56(4): 720–736.
33. Szekeres A. Analogy between heat and moisture. *Computers & Structures.* 2000;76(1-3): 145–152.

34. Szekeres A. Cross-coupled heat and moisture transport: Part 1 – Theory. *Journal of Thermal Stresses.* 2012;35(1–3): 248–268.
35. Szekeres A, Engelbrecht J. Coupling of generalized heat and moisture transfer. *Periodica Polytechnica Mechanical Engineering.* 2000;44(1): 161–170.
36. Sih GC, Michopoulos JG, Chou SC. *Hygrothermoelasticity*. Netherlands: Springer; 1986.
37. Alhashash A, Elidy ES, El-Bary AA, Tantawi RS, Lotfy K. Two-temperature semiconductor model photomechanical and athermal wave responses with moisture diffusivity process. *Crystals.* 2022;12(12): 1770.
38. El-Sapa S, Lotfy K, El-Bary AA, Ahmed MH. Moisture diffusivity and photothermal excitation in non-local semiconductor materials with laser pulses. *Silicon.* 2023;15: 4489–4500.
39. Lotfy K, Mahdy AMS, El-Bary AA, Elidy ES. Magneto-photo-thermoelastic excitation of rotating semiconductor medium based on moisture diffusivity. *Computer Modeling in Engineering & Sciences.* 2024;141(1): 107–126.
40. Alshehri HM, Lotfy K. A photo thermoacoustic diffusion model for hydro poroelastic nanocomposite semiconductor medium with chemical potential. *Physics of Fluids.* 2025;37(1): 017121.
41. Kumar R, Devi S. A problem of thick circular plate in modified couple stress theory of thermoelastic diffusion. *Cogent Mathematics.* 2016;3(1): 1217969.
42. Kumar R, Kaushal S, Dahiya V. Porosity and phase lags response of thick circular plate in modified couple stress thermoelastic medium. *ZAMM – Journal of Applied Mathematics and Mechanics.* 2021;101(12): e202100098.
43. Kumar R, Sharma N, Chopra S. Axisymmetric deformation of thick circular plate under Moore–Gibson–Thompson photothermoelastic model. *Advances in Materials Research.* 2025;14(1): 1–30.
44. Abbas IA, Kumar R, Chawla V. Response of thermal source in a transversely isotropic thermoelastic half-space with mass diffusion by using a finite element method. *Chinese Physics B.* 2012;21(8):084601.
45. Abbas IA, Kumar R. Response of thermal source in initially stressed generalized thermoelastic half-space with voids. *Journal of Computational and Theoretical Nanoscience.* 2014;11: 1472–1479.
46. Lotfy K, Elshazly IS, Halouani B, Sharma S, Ailawalia P, El-Bary AA. Influence of Hall current and acoustic pressure on nano-structured DPL thermoelastic plates under ramp heating in a double-temperature model. *Open Physics.* 2025;23(1): 20250125.
47. Alzahrani FS, Abbas IA. Photo-thermo-elastic interactions without energy dissipation in a semiconductor half-space. *Results in Physics.* 2019;15: 102805.
48. Sharma S, Marin M, Altenbach H. Elastodynamic interactions in thermoelastic diffusion including non-local and phase lags. *ZAMM – Journal of Applied Mathematics and Mechanics.* 2025;105(1): e202401059.
49. Alenazi A, Ahmed A, El-Bary AA, Tantawi RS, Lotfy K. Moisture photo-thermoelasticity diffusivity in semiconductor materials: a novel stochastic model. *Crystals.* 2023;13(1): 42.

MATERIALS PHYSICS AND MECHANICS RESEARCH ARTICLE

Submitted: October 3, 2025 **Revised: November 7, 2025** **Accepted: November 17, 2025**

Rayleigh waves in a rotating inhomogeneous half-space with magnetic effect under impedance and variable amplitudes of corrugation

A.I. Anya

Veritas University, Abuja, Bwari-Abuja, Nigeria

anyaa@veritas.edu.ng

ABSTRACT

A mathematical model investigating the dispersions of Rayleigh wave on an inhomogeneous rotating half-space with magnetic field influence, impedance and variable amplitudes of corrugation is presented. Normal mode approach and non-dimensionalization principles were employed to the equations of motion. Derivations of the analytical solutions of the stresses and displacement components occasioned by the wave on the material were achieved. Variable amplitudes of corrugation due to a linear function incorporated as the amplitude of the trigonometric Fourier series and the impedance conditions enriches the material characterizations and paved way in formulating the structure or nature of corrugation at the boundary. Thus, dispersion relations of Rayleigh waves due to homogeneous impedance and inhomogeneous impedance were analytically given and graphically depicted with the variations of the physical parameters.

KEYWORDS

variable amplitude of corrugation • inhomogeneous fiber-reinforcement • magnetism • rotation of the medium homogeneous and inhomogeneous impedance boundaries • dispersion of Rayleigh wave

Citation: Anya AI. Rayleigh waves in a rotating inhomogeneous half-space with magnetic effect under impedance and variable amplitudes of corrugation. *Materials Physics and Mechanics*. 2025;53(6): 164–181. http://dx.doi.org/10.18149/MPM.5362025_12

Introduction

Mechanical wave propagation is dependent on the physical composition of materials. Scientists in the fields of seismology and geophysical analysis usually devote and maintain clear position in examining compositions associated with most materials before employing them into structural and engineering constructions or applications. This is largely pertinent to ensure quality occasioned by such materials through which waves and in particular surface waves modulate. These materials are classed into two forms; anisotropic and isotropic materials and following which homogeneous and inhomogeneous characterization of the materials would ensue. Also, the inhomogeneity of these materials hugely depends on the nature of the deformation which typically lies in the form of growth or decay of the material parameters or other geometrical considerations of the interacting material constants.

Furthermore, mathematics, physics, and geophysics scientists have maintained constant researches in this field of solid mechanics by exploring and developing models that could necessitate great insights about the behaviors of these materials when acted upon by stress and other environmental factors. Given this, the consideration of just isotropic material may not holistically define or describe exact continuum information in composites. Part of

Publisher: Peter the Great St. Petersburg Polytechnic University

this line of thought yielded examination on anisotropic material exhibitions. Anisotropic materials exist as composites, for instance, the Fiber-reinforced composites, and the orthotropic materials, etc., to mention but a few, are highly regarded for engineering applications due to their high positive mechanical properties. On this note, Spencer [1] developed and presented a work that hinged on deformation of fiber-reinforced material as a composite whose characterizations in terms of tensile strength, weightlessness (leading to flexibility), and so on, endears them to various industrial applications.

In a different vein, fiber-reinforced composites, also, might not give definite results in terms of its behavior if the environmental factors or other physical interacting quantities like magnetic fields Abd-Alla et al. [2] or maybe rotation Schoenberg et al. [3] surrounding it are not factored into the mathematical model equations characterizing a particular phenomenon. This is solely because they have a way of giving near accurate predictions of the model problem needed for insightful reach of decisions. Aside the surrounding characterizations, researchers equally exploit other mechanical properties such as the impedance [4], which act like a resistance to the motion of matter or acoustic energy on a material alongside appropriate boundary conditions which could be planar or non-planar like the corrugated boundary [5] to enrich the understating of some complex mechanical structures and surface wave (Stoneley wave, Love wave and Rayleigh wave) propagations along and across interfaces of materials. Hence, the basic mechanical reasoning behind this design of corrugation is to positively enhance the stiffness-to-weight ratio of the material by giving optimal geometric representation rather than addition of more material. Thus, increase in bending stiffness, energy absorption, and anisotropic behavior exhibitions cum buckling resistance are some of the key principles behind corrugation of materials. While variable corrugation shapes or geometries of different heights, or even hierarchical construction on materials, allows for further enhancement and optimization of the mechanical properties of the material for a particular performance needs.

In the foregoing, several authors have made contributions to further the investigations associated with these corrugated-impedance boundary effects on materials along with other interesting wave phenomena. Singh et al. [6] and Singh et al. [7,8] worked on qP-wave at a corrugated interface between two different initial stress elastic semi-infinite material, influence of corrugated boundary surfaces reinforcement, hydrostatic stress, heterogeneity and anisotropy on Love type wave propagation and also on the effect of loose bonding and corrugation on Rayleigh-type wave modulation. More so, Das et al. [9] dealt with surface waves in an inhomogeneous material which included gravity. Abd-Alla et al. [10] investigated impact of rotation on a non-homogeneous infinite elastic cylinder of orthotropic material under magnetic influences. Chattopadhyay et al. [11] opined the dispersion equation of Love wave based on irregularity in the thickness of non-homogeneous crustal layer. Following this trend, Roy et al. [12] worked on the propagation and reflection of plane waves in a rotating magneto-elastic fiber-reinforced semi space with surface stress. Singh et al. [13], Gupta et al. [14], Anya et al. [15–18] dealt on magnetic effects on surface waves in a rotating non-homogeneous half-space with grooved-impedance boundary conditions and non-local effects, respectively. Likewise, Maleki et al. [19] developed model tests on determining the effect of various geometrical aspects on horizontal impedance function of

surface footings. Chowdhury et al. [20] examined the dispersion of Stoneley waves through the irregular common interface of two hydrostatic stressed MTI media. Singh et al. [21,22] contributed their investigation on Rayleigh wave at an impedance boundary of an incompressible micropolar and orthotropic solid, respectively while Sahu et al. [23] dealt on the Mathematical analysis of Rayleigh waves at the imperfect boundary between orthotropic and micropolar media. Giovannini [24] worked on the theory of dipole-exchange spin-wave propagation in periodically corrugated films. And Rakshit et al. [25,26] also proposed a stress analysis for the irregular surface of visco-porous piezoelectric half-space subjected to a moving load. Subsequently, Gupta et al. [27] presented different theories of thermo-elasticity under the Rayleigh wave propagation along an isothermal boundary while Kaushal et al. [28] examined wave propagation under the influence of voids and non-free surfaces in a micropolar elastic medium. Also, Sharma et al. [29] dealt on the fractional strain analysis on reflection of plane waves at an impedance boundary of non-local swelling porous thermo-elastic medium. Sharma et al. [30] further made input on the effect of rotation for generalized thermo-viscoelastic Rayleigh-Lamb wave propagating on materials while its counterpart Shaw et al. [31] utilized eigen function expansion approach to examine Rayleigh wave propagation in an orthotropic magneto-thermoelastic half-space. Moreover, Othman et al. [32–34] incorporated effects of magnetic field on a rotating thermo-elastic medium with some other physical properties like voids, relaxation time and reinforcement of fibers to study wave propagation on structures. Thus, we observed keenly that all these investigations were associated with singular or part investigations of the interacting physical quantities of rotation, micropolar effects, homogeneity, inhomogeneity, magnetism, corrugation, etc., which fall short as constituted in this present investigation where the corrugation effects possess variable amplitudes whilst considering different ideas of impedance characterizations in generating the dispersions of Rayleigh wave.

In view of the literatures posited above, the present investigation is geared towards exploring a mathematical model and analysis on the dispersion of Rayleigh wave for a rotating inhomogeneous fiber-reinforced solid with magnetic influences under impedance and variable amplitudes of corrugation. Following this, the variable amplitude of corrugation is conceived to be a linear function of the horizontal coordinate and incorporated at the point of the constant amplitude using the Trigonometric Fourier series cosine terms. The equations of motion were derived using the stress-strain relations of a fiber-reinforced material through the fundamental governing laws of motion of Physics. In addition, the analytical solution is developed by utilizing the eigenvalue method also called normal mode method. We developed both the homogeneous and inhomogeneous impedance conditions at the boundary via which the two dispersion relations of the Rayleigh wave were analytically derived and presented. Graphical results depicting the impact of the contributing physical parameters of inhomogeneity, rotation of the medium, corrugation parameters (variable amplitude parameters), wavenumber, and magnetic effect on the two dispersion relations of the Rayleigh wave due to homogeneous and inhomogeneous impedance were achieved. We observe that particular cases found in the literature can be obtained from our results as special cases especially when we neglect one of the parameters associated with the variable amplitudes of corrugation leading to constant or uniform amplitude of corrugation model.

The mathematical model and formulations

In this section, we introduce the basic fields' equations characterizing the mathematical model. In line with this, the mathematical formulations of the model using the constitutive equations of fiber-reinforced material in its homogeneous form as introduced by Spencer [1] and the magnetic field effect, Abd-Alla et al. [2] and Anya et al. [35,36] are given below:

$$\sigma_{ij} = \lambda\varepsilon_{kk}\delta_{ij} + 2\mu_T\varepsilon_{ij} + \alpha\left(f_k f_m \varepsilon_{km}\delta_{ij} + \varepsilon_{kk} f_i f_j\right) + 2(\mu_L - \mu_T)\left(f_i f_k \varepsilon_{kj} + \right.$$
$$\left. + f_j f_k \varepsilon_{ki}\right) + \beta\left(f_k f_m \varepsilon_{km} f_i f_j\right), i = j = k = m = 1,2,3, \quad (1)$$

$$F_i = \mu_0 H_0^2\left(e_{,1} - \varepsilon_0\mu_0\ddot{u}_1, e_{,2} - \varepsilon_0\mu_0\ddot{u}_2, 0\right),\ i = 1,2,3, \quad (2)$$

where σ_{ij} denotes the stress tensor, ε_{ij} prescribe the strain tensor, u_i represents the displacement vector, λ stipulate the Lames constant, $(\alpha, \beta, (\mu_L - \mu_T))$ are the fiber-reinforced parameters, δ_{ij} entails the Kronecker-delta function; and F_i implies the magnetic force such that $F_i = (F_1, F_2, F_3)$. However, the strain is equally defined to be mathematically represented as $\varepsilon_{ij} = \frac{1}{2}\left(u_{i,j} + u_{j,i}\right)$ and $f = (f_1, f_2, f_3)$ such that $f = (1,0,0)$ prescribe the fiber-reinforced directions. H_i is the magnetic vector field defined to be $H_i = H_0\delta_{i3} + h_i$, $h_i = (0,0,-e)$, $e = u_{i,i}$, $i = 1,2$. Also, h_i is induced magnetic field such that ε_0 and μ_0 connotes the electric permeability and the magnetic permeability, as the case maybe, owing to the Maxwell's theory of electromagnetism. This model postulates its analysis in 2-D such that x_1x_2-plane becomes the plane of consideration and such that $h_i(x_1, x_2, x_3) = -u_{k,k}\delta_{i3}$. Owing to all these formulations, the governing equations of motion for the rotating Schoenberg et al. [3] homogeneous fiber-reinforced material under magnetic field are thus, presented:

$$\sigma_{ij,j} + F_i = \rho\{\ddot{u}_i + \Omega_j u_j \Omega_i - \Omega^2 u_i - 2\varepsilon_{ijk}\Omega_j\dot{u}_k\}. \quad (3)$$

The parameters in Eq. (3) like the ε_{jim} represents the Levi-Civita tensor (alternating symbol) and Ω stipulates the rotation of the medium. Einstein summation indices are used and where index after comma represents partial rate of change with respect to coordinate and superscript dot stipulate partial rate of change with respect to time. Since our formulation is making use of the deformation in the x_1x_2-plane, we take $x_3 = 0$ and $\Omega(0,0,1)$ as the rotation (which purely involved the Coriolis and centrifugal forces arising from a rotating coordinate frame) of the half-space about the x_3-axis. It then means that the displacements $u_1 \neq 0$ and $u_2 \neq 0$, for any change in plane and coordiantes of consideration.

Furthermore, the material is originally presumed to be inhomogeneous but the fiber-reinforced medium so presented in Eq. (1) is homogeneous. It suffices that the parameters of the homogeneous fiber-reinforced material be considered to decay or grow such that the rate of the occurrence is proportional to its value at that instance. This would ultimately introduce the inhomogeneity into the model. This is such that the elastic module, elastic parameters, and density of the half-space take the representation: $(\lambda, \alpha, \mu_L, \mu_T, \beta, \rho) = (\lambda_0, \alpha_0, \mu_{L0}, \mu_{T_0}, \beta_0, \rho_0)e^{-mx_2}$, Khan et al. [37] and Munish et al. [38]. In the given proportionality above, m describes the inhomogeneity of the fiber-reinforced material.

Thus, employing these inhomogeneous parameters into Eq. (1), the component forms of the equations of motion of the wave are presented:

$$(\lambda + 2\alpha + 4\mu_L - 2\mu_T + \beta + \mu_0 H_0^2)u_{1,11} + (\alpha + \lambda + \mu_L + \mu_0 H_0^2)u_{2,21} + \mu_L u_{1,22} - -m\mu_T(u_{1,2} + u_{2,1}) = \{\rho + \varepsilon_0\mu_0^2 H_0^2\}\ddot{u}_1 - \rho\Omega^2 u_1 - 2\Omega\dot{u}_2\}, \quad (4)$$

$$(\alpha + \lambda + \mu_L + \mu_0 H_0^2)u_{1,12} + \mu_L u_{2,11} + (\lambda + 2\mu_T + \mu_0 H_0^2)u_{2,22} - m(\lambda + \alpha)u_{1,1} - -m(\lambda + 2\mu_T)u_{2,2} = \{\rho + \varepsilon_0\mu_0^2 H_0^2\}\ddot{u}_2 - \rho\{\Omega^2 u_2 + 2\Omega\dot{u}_1\}, \quad (5)$$

$$\mu_L u_{3,11} + \mu_T u_{3,22} - m\mu_T u_{3,2} = \rho\ddot{u}_3. \quad (6)$$

We can restructure Eqs. (4)–(6) as follows:

$$G_1 u_{1,11} + G_2 u_{2,21} + G_3 u_{1,22} - mG_4(u_{1,2} + u_{2,1}) = \{\{\rho + \varepsilon_0\mu_0^2 H_0^2\}\ddot{u}_1 - \rho(\Omega^2 u_1 + 2\Omega\dot{u}_2)\}, \quad (7)$$

$$G_2 u_{1,12} + G_3 u_{2,11} + G_5 u_{2,22} - mG_6 u_{1,1} - mG_7 u_{2,2} = \{\{\rho + \varepsilon_0\mu_0^2 H_0^2\}\ddot{u}_2 - \rho(\Omega^2 u_2 - 2\Omega\dot{u}_1)\}, \quad (8)$$

$$G_3 u_{3,11} + G_4 u_{3,22} - mG_4 u_{3,2} = \rho\ddot{u}_3, \quad (9)$$

where $G_1 = (\lambda + 2\alpha + 4\mu_L - 2\mu_T + \beta + \mu_0 H_0^2)$, $G_2 = (\alpha + \lambda + \mu_L + \mu_0 H_0^2)$, $G_3 = \mu_L$, $G_4 = \mu_T$, $G_5 = (\lambda + 2\mu_T + \mu_0 H_0^2)$, $G_6 = (\lambda + \alpha)$, $G_7 = (\lambda + 2\mu_T)$.

If we employ $m = 0$ into Eqs. (7)–(9), the homogeneous material characterizing the equations of the wave motion is recovered. In addition, let us define the following dimensionless variables: $(x_1', x_2', u_1', u_2') = c_0(x_1, x_2, u_1, u_2)$, $c_0^2, = G_1/\rho, (t') = c_0^2 t$, $\Omega' = \Omega/c_0^2$, $\sigma_{ij}' = \sigma_{ij}/\rho c_0^2$, and employ them into Eqs. (7)–(9). Dropping the sign " ′" from the equations results to the dimensionless form of the equations of the wave motion below:

$$u_{1,11} + G_{12}u_{2,21} + G_{13}u_{1,22} - mG_{24}(u_{1,2} + u_{2,1}) = \left\{\left\{1 + \frac{\varepsilon_0\mu_0^2 H_0^2}{\rho}\right\}\ddot{u}_1 - \rho\Omega^2 u_1 - 2\rho\Omega\dot{u}_2\right\} \quad (10)$$

$$G_{12}u_{1,12} + G_{13}u_{2,11} + G_{15}u_{2,22} - mG_{26}u_{1,1} - mG_{27}u_{2,2} = \{\{1 + \varepsilon_0\mu_0^2 H_0^2/\rho\}\ddot{u}_2 - \rho\Omega^2 u_2 + 2\rho\Omega\dot{u}_1\}, \quad (11)$$

$$G_{13}u_{3,11} + G_{14}u_{3,22} - mG_{24}u_{3,2} = \ddot{u}_3,$$

$$(G_{12}, G_{13}, G_{14}, G_{15}, G_{16}, B_{17}) = ((G_2, G_3, G_4, G_5, G_6, G_7)/G_1), \quad (12)$$

$$(G_{24}, G_{26}, G_{27}) = (G_{14}, G_{16}, G_{17})\rho^{1/2}/G_1^{3/2}.$$

Analytical solution of the problem and normal mode analysis

This section employs the eigenvalue approach also called the normal mode solution approach in the derivation of the analytical solutions of the displacement components and subsequently, the normal and shear stresses on the rotating inhomogeneous impedance-corrugated fiber-reinforced solid. Thus, adopting the fact that this approach of normal mode analysis be applicable, the waves have their displacement components as:

$$u_i = (\hat{u}_i(x_2))e^{\omega t + ibx_1};\ i = 1,2. \quad (13)$$

Employing Eq. (13) into Eqs. (10)–(12), three ordinary differential equations (ODEs) in the x_2 coordinates are given:

$$(G_{13}D^2 - mG_{24}D - b^2 - g1)\hat{u}_1 + (iG_{12}bD - mG_{24}bi - 2\rho\Omega\omega)\hat{u}_2 = 0, \quad (14)$$

$$(iG_{12}bD - mbiG_{26} + 2\rho\Omega\omega)\hat{u}_1 + (G_{15}D^2 - mG_{27}D - G_{13}b^2 - g1)\hat{u}_2 = 0, \quad (15)$$

$$(G_{14}D^2 - mG_{24}D - (G_{13}b^2 + \rho\omega^2)\hat{u}_3 = 0. \quad (16)$$

In Eqs. (14)–(15), $g1 = (1 + \varepsilon_0\mu_0^2 H_0^2/\rho)\omega^2 + \rho\Omega^2)$. Note that D^2 entails second order ordinary derivative with respect to x_2. For non-trivial solution, Eqs. (14)–(15) produce 4th order ordinary differential equation below where $\hat{u}_1, \hat{u}_2$ becomes the dependent variables and x_2 the independent variable. That is, the determinant of the coefficients of $\hat{u}_1, \hat{u}_2$ are equated to zero whereas $(\hat{u}_1, \hat{u}_2) \neq 0$. Observe that Eq. (16) is

uncoupled with Eqs. (14)–(15) and thus, we neglect it from forming the associated characteristic equation below. This is because we based our analysis in a plane geometry. However, its solution can be easily obtained by using quadratic formula:

$$(d_{11}D^4 + d_{12}D^3 + d_{13}D^2 + d_{14}D + d_{15})(\hat{u}_1, \hat{u}_2) = 0, \tag{17}$$

where $d_{1i}, i = 1,2,3,4,5$ are complex coefficients which depends on the parameters of the solid half-space. Assume that $\eta_i, i = 1,2,3,4$ be positive roots of Eq. (17), thus, the normal mode analysis gives the solutions of $\hat{u}_1, \hat{u}_2$ as follows:

$$(\hat{u}_1, \hat{u}_2) = (K_n, K_{1n})e^{-\eta_n x_2}, \quad n = 1,2,3,4, \tag{18}$$

where K_n and K_{1n} functions of the wavenumber b in the direction of the horizontal coordinate x_1 and ω is the complex frequency associated with the propagation of the wave. Utilizing Eq. (18) into Eqs. (10)–(11), a relation below is achieved:

$$\begin{aligned} &K_{1n} = H_{1n}K_n, \\ &H_{1n} = (G_{13}\eta_n^2 + mG_{24}\eta_n - b^2 - g1 - (2\rho\Omega\omega - iG_{12}b\eta_n - mbiG_{26}), \\ &(G_{15}\eta_n^2 - G_{13}b^2 + mG_{27}\eta_n - g1 + (2\rho\Omega\omega + iG_{12}b\eta_n + mbiG_{24}), n = 1,2,3,4. \end{aligned} \tag{19}$$

Thus, the complete solutions of the displacements and stresses utilized for the model problem follows:

$$\begin{aligned} &u_1 = K_n e^{-\eta_n x_2 + \omega t + ibx_1}; u_2 = H_{1n}K_n e^{-\eta_n x_2 + \omega t + ibx_1}, \\ &\sigma_{11} = \left\{ib\left(1 - \left(\frac{\mu_0 H_0^2}{G_1}\right)\right) - \eta_n H_{1n} G_{16}\right\} K_n e^{-(\eta_n + m)x_2 + \omega t + ibx_1}, \\ &\sigma_{22} = \{ibG_{16} - \eta_n H_{1n} G_{17}\} K_n e^{-(\eta_n + m)x_2 + \omega t + ibx_1}, \\ &\sigma_{12} = (ibH_{1n} - \eta_n) G_{13} K_n e^{-(\eta_n + m)x_2 + \omega t + ibx_1}, \\ &\sigma_{21} = G_{13}(ibH_{1n} - \eta_n) K_n e^{-(\eta_n + m)x_2 + \omega t + ibx_1}, n = 1,2,3,4. \end{aligned} \tag{20}$$

Impedance-corrugated conditions of the half-space and dispersions of Rayleigh waves

This section is anchored on formulations and derivations associated with the impedance and corrugated conditions through which dispersion of Rayleigh wave on the fiber-reinforced half-space is explored. Following Asano [5], the corrugated boundary in trigonometric Fourier series denoted $x_2 = \xi(x_1)$ is such that$\xi(x_1) = \xi_l e^{ilbx_1} + \xi_{-l} e^{-ilbx_1}$, $l = 1,2,3,4, \ldots$, where ξ_l and ξ_{-l} gives the Fourier expansion coefficients and l is the series expansion order. Asano represented the parameters a, F_l and I_l in the form $\xi_1^{\pm} = \frac{a}{2}$, $\xi_l^{\pm} = \frac{F_l + I_l}{2}, l = 2,3 \ldots$, such that $\xi(x_1) = a\cos b\, x_1 + F_2 \cos 2\, bx_1 + I_2 \sin 2\, bx_1 + \cdots + + F_l \cos l\, bx_1 + I_l \sin l\, bx_1$; F_l and I_l gives the Fourier cosine and sine Fourier coefficients, respectively, and through which the corrugated boundary surface in cosine terms by Asano become $\xi(x_1) = a\cos b\, x_1$. a denote the constant amplitude of the corrugation and b is wavenumber such that $2\pi/b$ gives the wavelength. However, we are interested in variable amplitudes of corrugation of the boundary of the material such that the wavelength of the wave for the corrugated surface equal π/b. This is actually half of the wavelength for a non-variable or uniform amplitude of the wave as given by Asano [5]. For this to occur, we need to redefine the amplitude of the corrugated surface such that $\bar{\xi}_1^{\pm} = (a + cx_1)/2$, and $\bar{\xi}(x_1) = \bar{\xi}_l e^{ilbx_1} + \bar{\xi}_{-l} e^{-ilbx_1}$, $l = 1,2,3,4, \ldots$, through which we can obtain $\bar{\xi}(x_1) = (a + cx_1)\cos b\, x_1 + F_2 \cos 2\, bx_1 + I_2 \sin 2\, bx_1 + \ldots + F_l \cos l\, bx_1 + I_l \sin l\, bx_1$.

Here, $\bar{\xi}_l^{\pm} = (F_l + I_l)/2, l = 2,3 \ldots$ Subsequently, we then assume the corrugated

surface boundary to be in the form of cosine term $\bar{\xi}(x_1) = (a + cx_1)\, cos\, b\, x_1$. Here, $(a + cx_1)$ become the variable amplitudes of the corrugated surface and $b$the wave number. Also, a, c are terms associated with amplitudes such that if $c = 0$, we recover the amplitude associated with Asano [5] model. To visualize these scenarios and its geometry, we illustrate $\xi(x_1) = a\, cos\, b\, x_1$ with uniform or constant amplitude of corrugation; $\bar{\xi}(x_1) = (a + cx_1)\, cos\, b\, x_1$ and its derivative – $\bar{\xi}'_1 \, sin\, b_1 \, cos\, b_1$ with variable amplitudes of corrugation graphically in Fig. 1, respectively:

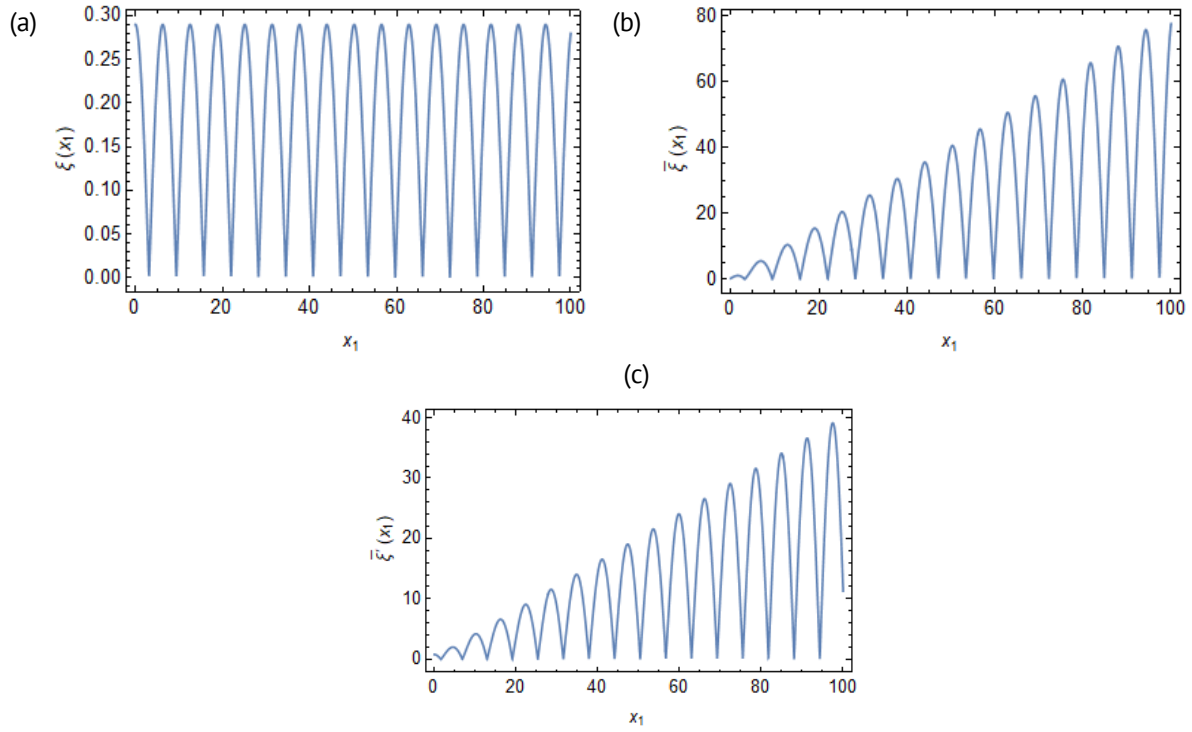

Fig. 1. (a) Uniform amplitude of corrugation; (b) variable amplitude of corrugation; (c) Rate of change of (b) with respect to x_1

(a) Homogenous boundary conditions on the impedance, considering corrugated fibre-reinforced inhomogeneous material: $u_1 = 0$, $u_2 = 0$, at $x_2 = \bar{\xi}(x_1)$, for all x_1 coordinate and at any time t. Conditions on stresses w.r.t $x_2 = \bar{\xi}(x_1)$ gives the following: $\sigma_{22} - \bar{\xi}'(x_1)\sigma_{21} + \bar{\sigma}_{22} + \omega Z_2 u_2 = 0$, that is $\sigma_{22} + \bar{\sigma}_{22} - \bar{\xi}'(x_1)\sigma_{21} + \omega Z_2 u_2 = 0$, $\sigma_{22} + \mu_0 H_0^2(u_{1,1} + u_{2,2}) - \bar{\xi}'(x_1)\sigma_{21} + \omega Z_2 u_2 = 0$, where $\bar{\sigma}_{22} = \mu_0 H_0^2(u_{1,1} + u_{2,2})$, gives Maxwell's additional stress on the fibre-reinforced inhomogeneous material, Abd-Alla et al. [2], Anya et al. [35,36] and Azhar et al. [39]. The tangential stress condition or shear stress follows: $\sigma_{12} - \bar{\xi}'(x_1)\sigma_{11} + \omega Z_1 u_1 = 0$ for all x_1 coordinate and at any time t.

(b) Inhomogeneous boundary conditions on the impedance, considering corrugated fibre-reinforced inhomogeneous material: $u_1 = 0$, $u_2 = 0$, at $x_2 = \bar{\xi}(x_1)$, for all x_1 coordinate and at any time t. Conditions on stresses w.r.t $x_2 = \bar{\xi}(x_1)$ gives the following:
$\sigma_{22} - \bar{\xi}'(x_1)\sigma_{21} + \bar{\sigma}_{22} + \omega Z_2 u_2 = 0$ that is $\sigma_{22} + \bar{\sigma}_{22} - \bar{\xi}'(x_1)\sigma_{21} + \omega Z_2 u_2 = 0$,
$\sigma_{22} + \mu_0 H_0^2(u_{1,1} + u_{2,2}) - \bar{\xi}'(x_1)\sigma_{21} + \omega Z_2 u_2 = 0$, where $\bar{\sigma}_{22} = \mu_0 H_0^2(u_{1,1} + u_{2,2})$, gives Maxwell's additional stress on the fibre-reinforced inhomogeneous material, Abd-Alla et al. [2], Anya et al. [35,36] and Azhar et al. [39]. The tangential stress condition or shear stress

follows: $\sigma_{12} - \bar{\xi}'(x_1)\sigma_{11} + \omega Z_1 u_1 = 0$ for all x_1 coordinate and at any time t. In (b) above, $\bar{Z}_1$ and $\bar{Z}_2$ are the impedance parameters, Anya et al. [35,36] and Ailawalia et al. [40]. We assume that these impedance parameters $\bar{Z}_1$ and $\bar{Z}_2$ are inhomogeneous. This is such that $(\bar{Z}_1, \bar{Z}_2) = (Z_1, Z_2)e^{-mx_2}$. But note that Z_1, Z_2 are homogeneous at the boundary of (a). Hence, these assumptions imply the following two sets of four equations from (a) and (b) above, respectively. They are presented below as (c) and (d), respectively.

(c) Homogenous boundary conditions on the impedance considering fiber-reinforced inhomogeneous material:

$$K_n = 0, \tag{21}$$

$$H_{1n}K_n = 0, \tag{22}$$

$$\{ibG_{16} - \eta_n H_{1n}G_{17}\}e^{-(\eta_n+m)\bar{\xi}(x_1)}K_n + [(a+cx_1)b\sin b\,x_1 - c\cos b\,x_1]\{(ibH_{1n} - -\eta_n)G_{13}\} \times\times e^{-(\eta_n+m)\bar{\xi}(x_1)}K_n + \{\mu_0 H_0^2(ib - \eta_n H_{1n})\}e^{-(\eta_n+m)\bar{\xi}(x_1)}K_n + +\{\omega H_{1n}Z_2K_n\} = 0, \tag{23}$$

$$\Big\{\{ibH_{1n} - \eta_n\}G_{13} + [(a+cx_1)b\sin b\,x_1 - c\cos b\,x_1]\{ib\big(1 - (\mu_0 H_0^2/G_1)\big) - -\eta_n H_{1n}G_{16}\}\Big\} \times K_n e^{-(\eta_n+m)\bar{\xi}(x_1)} + \{\omega Z_1\}K_n = 0. \tag{24}$$

(d) Inhomogenous boundary conditions on the impedance considering fiber-reinforced inhomogeneous material:

$$K_n = 0, \tag{25}$$

$$H_{1n}K_n = 0, \tag{26}$$

$$\{ibG_{16} - \eta_n H_{1n}G_{17}\}e^{-\eta_n\bar{\xi}(x_1)}K_n + [(a+cx_1)b\sin b\,x_1 - c\cos b\,x_1]\{(ibH_{1n} - -\eta_n)G_{13}\}e^{-\eta_n\bar{\xi}(x_1)}K_n + \{\omega H_{1n}Z_2K_n + \mu_0 H_0^2(ib - \eta_n H_{1n})\}e^{-\eta_n\bar{\xi}(x_1)}K_n = 0, \tag{27}$$

$$\{\{ibH_{1n} - \eta_n\}G_{13}K_n + [(a+cx_1)b\sin b\,x_1 - c\cos b\,x_1]\{ib(1 - (\mu_0 H_0^2/G_1)) - -\eta_n H_{1n}G_{16}\}K_n + \{\omega Z_1\}\}K_n e^{-\eta_n\bar{\xi}(x_1)} = 0, \quad n = 1,2,3,4. \tag{28}$$

For non-trivial solutions in (a) and (b), the determinants $|K_{ij}| = 0, \quad i = j = 1,2,3,4$ and for $K_n \neq 0$, gives the novel respective two dispersion relations $|\nabla|$ of the Rayleigh wave for: (a) homogeneous conditions on the impedance and (b) inhomogeneous conditions on the impedance.

Computational results and Discussion

This section devotes wholly on depicting our analytical solution graphically. To achieve this, we employ the numerical fiber-reinforced constants as given by Othman et al. [41] and some other parameters below to demonstrate the variations or effects of the physical quantities of impedance, rotation, inhomogeneity, magnetic fields, variable amplitudes of corrugated parameters and the wavenumber on the two dispersions of Rayleigh wave considering when the impedance applied on the material is homogeneous and when the impedance applied is inhomogeneous. It should be noted that the fiber-reinforced solid half-space is inhomogeneous: $\lambda = 7.59 \cdot 10^9$ kg m^{-1}s^{-2}, $\mu_L = 2.45 \cdot 10^9$ kg m^{-1}s^{-2}, $\mu_T = 1.89 \cdot 10^9$ kg m^{-1}s^{-2}, $\rho = 7.8 \cdot 10^3$ kg m^{-3}, $\alpha = -1.28 \cdot 10^9$ kg m^{-1}s^{-2}, $\beta = 0.32 \cdot 10^9$ kg m^{-1}s^{-2}, $\omega = (0.02 + \mathrm{i})$ rad/s, $a = 0.29$.

Figure 2 entails the variation of magnetic field H_0 on the dispersions $|\nabla|$ of Rayleigh wave as against x_1 coordinate, considering (a) homogeneous impedance and (b) inhomogeneous impedance on an inhomogeneous solid half-space such that all other physical parameters of impedance Z_i, $i = 1,2$, rotation Ω of the medium,

inhomogeneity$m$, corrugated parameters (a, c and b) i.e. parameters linked with the variable amplitudes of corrugation and wavenumber, respectively, are assumed to be in fixed state on the inhomogeneous fiber-reinforced solid half-space. Hence, increase in the magnetic field H_0 results to a corresponding increase in the behavior of the dispersions $|\nabla|$. In fact, the minima amplitudes of the dispersions $|\nabla|$ are attained when we neglect the magnetic field on the material. While the maxima amplitudes of the dispersions $|\nabla|$ are attained at $x_1 = 0.7$ and $x_1 = 0.6$ for an increasing magnetic field H_0 application especially on Fig. 2(a) and Fig. 2(b), respectively. Also, we observe that the dispersion relations $|\nabla|$ decrease for an extended x_1 coordinate such that the behavior of the dispersions $|\nabla|$ due to (a) homogeneous impedance and (b) inhomogeneous impedance on an inhomogeneous solid half-space are alike in every aspect except in their respective dispersion amplitudes and a difference in behavior when $x_1 \geq 1.4$. Physically, this has shown that the presence of external magnetic field influences the wave propagation especially as a push to the material characterizations and thus, impacts the wave attenuation and velocity of propagation. Hence, low magnetic fields on the model tend to give reduced influences of propagation as observed.

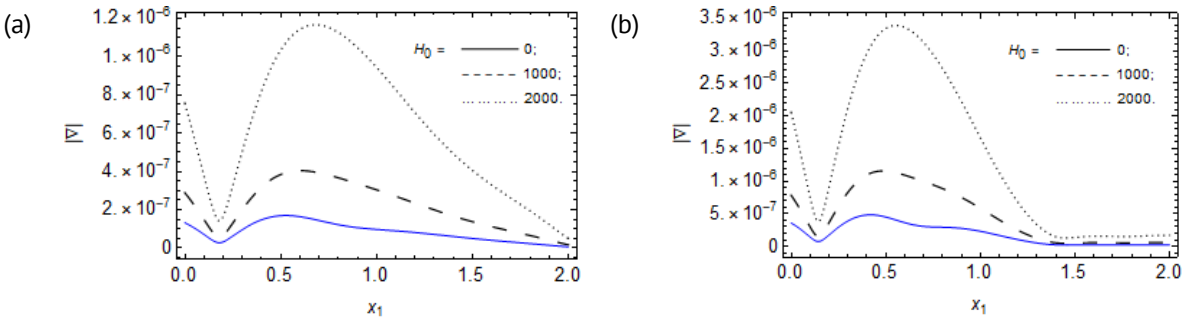

Fig 2. Variation of magnetic field $H_0(A/m)$ on the dispersions $|\nabla|$ of Rayleigh wave against x_1, considering (a) homogeneous impedance; (b) inhomogeneous impedance on an Inhomogeneous solid half-space

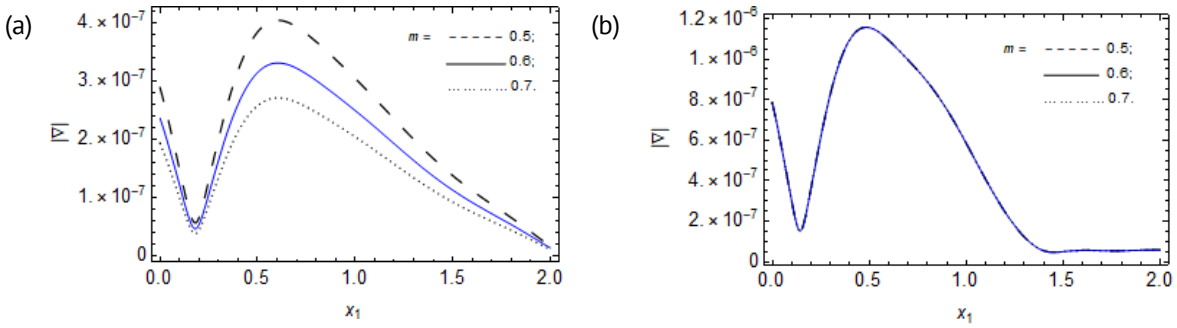

Fig. 3. Variation of inhomogeneous parameter m on the dispersions $|\nabla|$ of Rayleigh wave against x_1, considering (a) homogeneous impedance and (b) inhomogeneous impedance on an Inhomogeneous solid half-space

Consequently, Fig. 3 demonstrates the effect of the inhomogeneous parameter $m$on the dispersions $|\nabla|$ of Rayleigh wave against$x_1$coordinate, considering (a) homogeneous impedance and (b) inhomogeneous impedance on an inhomogeneous solid half-space through a constant applications of the physical quantities of magnetic field H_0, impedance $Z_i,\ i = 1,2$, rotation Ω of the medium, corrugated parameters (a, c and b) i.e. parameters associated with the variable amplitudes of corrugation and wavenumber, respectively, on the material.

This is such that an increase in the inhomogeneity m result to a sequential decrease in behavior of the dispersion relation $|\nabla|$ of the wave due to homogeneous impedance that is Fig. 3(a) while the dispersion $|\nabla|$ due to inhomogeneous impedance; Fig. 3(b) possess negligible behavior. That is, the minima value of dispersion due to the homogeneous impedance is attained when the inhomogeneity m increase. However, both considerations; Fig. 3(a) and Fig. 3(b) attain their maxima values of dispersions $|\nabla|$close to $x_1 = 0.6$ and $x_1 = 0.5$, respectively. For extended length of the material both dispersions decreases whilst noticing a difference in behavior for $x_1 \geq 1.4$ and the short dispersion amplitudes of the Rayleigh wave due to homogeneous impedance as compared with the dispersion amplitudes of the Rayleigh wave due to inhomogeneous impedance. This could be physically attributed to the characterizations of the solid half-space owing to fiber-reinforcement, homogeneous impedance and inhomogeneous impedance considerations on the inhomogeneous fiber-reinforced. Thus, it suffices to infer that the impact of the wave velocity and attenuation on the homogeneous characterization of the material would be pronounced as compared with the inhomogeneous material for the considered same physical parameters of the model.

More so, Fig. 4 depicts the effect of rotation Ω of the medium on the dispersions$|\nabla|$ of Rayleigh wave against x_1 coordinate, considering (a) homogeneous impedance and (b) inhomogeneous impedance on an inhomogeneous solid half-space especially when the quantities of magnetic field H_0, impedance Z_i, $i = 1{,}2$, inhomogeneous parameter m, corrugated parameters (a, c) i.e. parameters associated with the variable amplitudes of corrugation and wavenumber b are unchanged on the solid half-space.

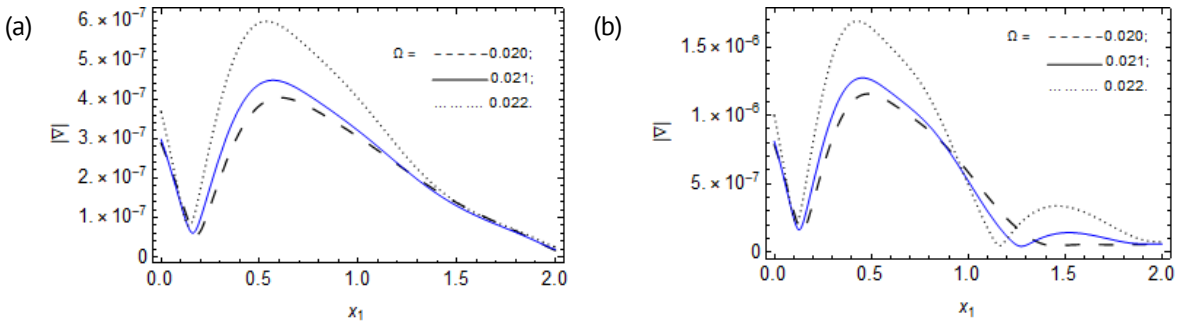

Fig. 4. Variation of rotation Ω, rad/s on the dispersions $|\nabla|$ of Rayleigh wave against x_1, considering (a) homogeneous impedance and (b) inhomogeneous impedance on an Inhomogeneous solid half-space

We observe that both conditions possess mixed behaviors in some domains of the Rayleigh wave dispersion profile when the rotation increase. That is, the two dispersions tend to move in upward trend for an increase in rotation within the domain $0 \leq x_1 < 1$ whilst possessing mixed behavior (increase and decrease) and after which the increase ensues again in a minimal manner, sequentially. However, for an increase in rotation, an outright decrease in behavior equally occur within the domain $0.95 < x_1 < 1.25$ in Fig. 3(b). Near $x_1 = 0.55$ and $x_1 = 0.45$ gives the positions of the maxima values of the dispersions of the Rayleigh wave on the material for Fig. 3(a) and Fig. 3(b), respectively. Hence, we can infer that the maxima values occur when the rotation is large on the material. And again, the amplitude of the dispersion due to inhomogeneous impedance is large as compared with the amplitude of the dispersion due to homogeneous

impedance, i.e., both has very close behavior aside their amplitudes and the behavior around the extended length of the material say from $x_1 > 1.4$. Realistically and across the length of the material, it is evident that the wave modulation is being impacted by rotation of the medium in a higher proportion.

Nevertheless, Fig. 5 connotes the impact of a associated with the variable amplitude of corrugation on the dispersions $|\nabla|$ of Rayleigh wave as against x_1 coordinate, considering (a) homogeneous impedance and (b) inhomogeneous impedance on the inhomogeneous medium. This is feasible only on the constant application of the physical parameters of rotation Ω, magnetic field H_0, impedance Z_i, $i = 1,2$, inhomogeneous parameter m, corrugated parameter c (parameter associated with the variable amplitudes of corrugation) and wavenumber $b$on the inhomogeneous solid half-space. Following this, Fig. 5(a) and Fig. 5(b) decrease sequentially in the domains $0.5 < x_1 \leq 2$ and $0.6 < x_1 \leq 1.1$, respectively when the parameter a associated with the variable amplitude of corrugation increase. We equally note mix behavior in both cases in the domain $0 < x_1 \leq 0.1$. Fig. 5(b) increases again for an increase in a from $x_1 > 1.3$ before mix behavior ensued. More so, the maxima profiles of the dispersions in Fig. 5(a) and Fig. 5(b) of the Rayleigh wave were attain close to $x_1 = 0.35$ and $x_1 = 0.3$, respectively, especially when a associated with the variable amplitude of corrugation increase. Generally, the dispersions of the wave tend to decrease along the length of the material as the wave propagate. We note that both cases have differences in dispersion amplitudes on the considered length of the solid medium and as well as in behaviors for extended length of the material.

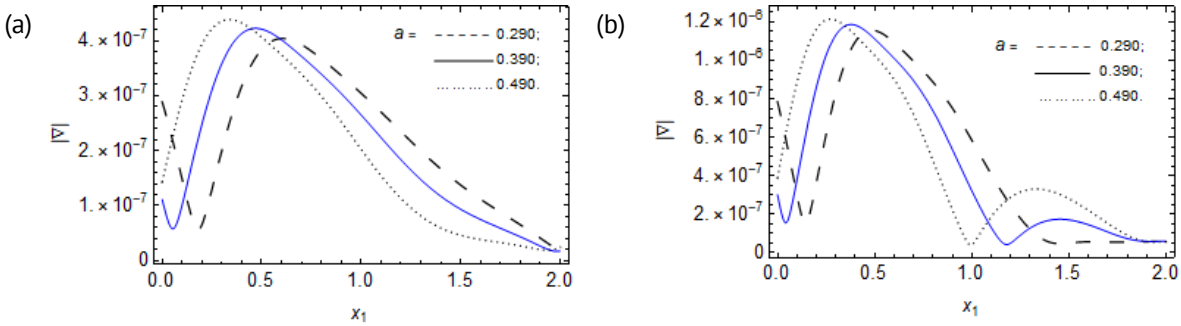

Fig. 5. Variation of a associated with the variable amplitude of corrugation on the dispersions $|\nabla|$ of Rayleigh wave against x_1, considering (a) homogeneous impedance and (b) inhomogeneous impedance on an Inhomogeneous solid half-space

In a similar analysis, Fig. 6 demonstrates the effect of c associated with the variable amplitude of corrugation on the dispersions $|\nabla|$ of Rayleigh wave as against x_1 coordinate, considering (a) homogeneous impedance and (b) inhomogeneous impedance on the inhomogeneous medium. This is such that the physical parameters of rotation Ω, magnetic field H_0, impedance Z_i, $i = 1,2$, inhomogeneous parameter m, corrugated parameter a (parameter associated with the variable amplitudes of corrugation) and wavenumber b remain steady on the material. Hence, we note that parameter c associated with the variable amplitude of corrugation gradually increase the dispersions of the Rayleigh wave when increased in both cases especially within the domain $0 < x_1 \leq 0.8$ for Fig. 6(a) and $0 < x_1 \leq 1.4$ for Fig. 6(b), and after which a very gradual decrease and

a uniform behavior, respectively, occurs. In addition, for the dispersion due to homogeneous impedance, the parameter $c$decrease the dispersion relations of the Rayleigh wave in the domain $0.8 < x_1 \leq 2$ when increased whilst observing uniform behavior for the inhomogeneous impedance case when $x_1 > 1.4$. More so, for an increase in c associated with the variable amplitude of corrugation, the maxima profiles of the dispersions of the Rayleigh wave were recorded close to $x_1 = 0.49$. Thus, we can deduce that the dispersions of the wave tend to decrease along the length of the material as the wave propagate whilst noting that both cases have differences in dispersion profiles in terms of their amplitudes and behaviors at the extended length of the coordinate.

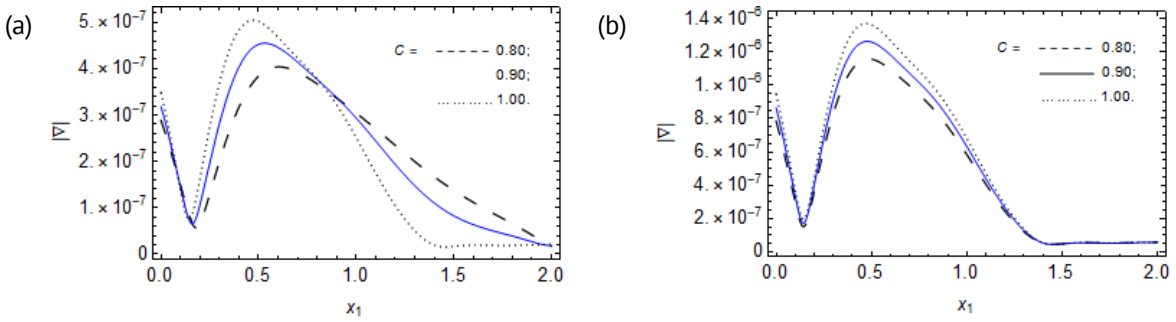

Fig. 6. Variation of c associated with the variable amplitude of corrugation on the dispersions $|\nabla|$ of Rayleigh wave against x_1, considering (a) homogeneous impedance and (b) inhomogeneous impedance on an Inhomogeneous solid half-space

Be that as it may, Fig. 7 depicts the impact of the wavenumber b (associated with the corrugation) on the dispersions $|\nabla|$ of Rayleigh wave as against x_1 coordinate, considering (a) homogeneous impedance and (b) inhomogeneous impedance on the inhomogeneous medium when the parameters of rotation Ω, magnetic field H_0, impedance Z_i, $i = 1{,}2$, inhomogeneous parameter m, corrugated parameters (a, c) (parameters associated with the variable amplitudes of corrugation) are in fixed state on the medium.

We deduce that the dispersion profiles of the Rayleigh wave in both cases show some outright mixed behaviors (uniform, decrease and increase) in certain domains of the horizontal coordinate x_1 when the wavenumber b increase. However, an outright downward trend ensues in the domain $0.5 < x_1 \leq 1.8$ in Fig. 7(b) when the wavenumber

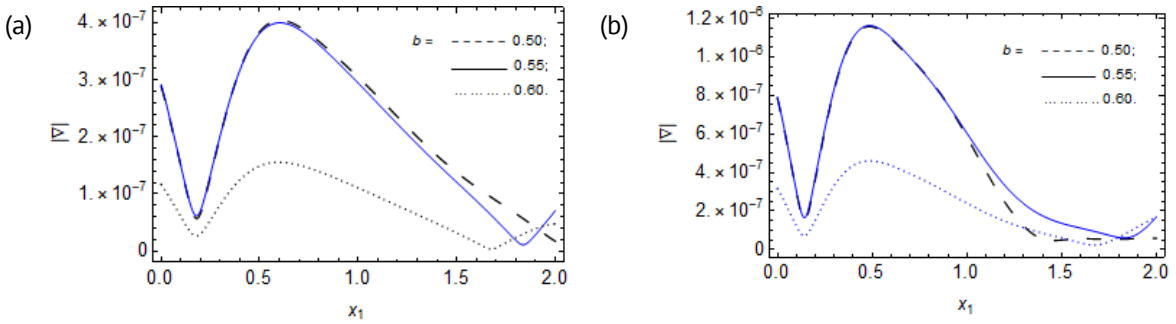

Fig. 7. Variation of wavenumber b associated with the corrugation on the dispersions $|\nabla|$ of Rayleigh wave against x_1, considering (a) homogeneous impedance and (b) inhomogeneous impedance on an Inhomogeneous solid half-space

b increase. The maxima values in Fig. 7(a) and Fig. 7 (b) occur near $x_1 = 0.6$ and $x_1 = 0.5$, respectively while the minima values of the dispersions occur when b is large. When $b = 0.5$ and along the extended length of the material, there exist gradual upward trend different from the initial behavior of the dispersions. We equally observe as in Fig. 6, that Fig. 7 possess reduce amplitude of dispersion for the dispersion due to homogeneous impedance as compared with the amplitude of dispersion occasioned by the inhomogeneous impedance. This can be attributed to the homogeneous impedance and inhomogeneous impedance considerations on the inhomogeneous fiber-reinforced solid. Thus, owing to the considered geometry, it is inferred that the number of cycles or wavelengths per unit of distance (wave number) has huge influence on the wave propagation on the material such that mixed occurrences of the Rayleigh wave were recorded across certain positions on the material.

In a different vein, Fig. 8 depicts the effect of impedance Z_2 on the dispersions$|\nabla|$of Rayleigh wave as against$x_1$coordinate, considering (a) homogeneous impedance and (b) inhomogeneous impedance on the inhomogeneous medium when the parameters of wavenumber b, rotation Ω, magnetic field H_0, impedance Z_i, $i = 1$, inhomogeneous parameter$m$, corrugated parameters (a, c) (parameters associated with the variable amplitudes of corrugation) are unchanged on the solid medium. Figure 8 shows that increase in the impedance Z_2 yield negligible behavior in terms of increase and decrease on both considered dispersions of Fig. 8(a) and Fig. 8(b), respectively. However, they dispersions in both cases are uniformly distributed in this instance of increase in Z_2. They attain maxima values close to $x_1 = 0.6$ and $x_1 = 0.5$, respectively at any of the given Z_2. This can be attributed to the material exhibition where the resistant-like phenomena of the impedance is felt or witnessed. However, Fig. 8(a) has a reduced dispersion amplitude as compared with Fig. 8(b). This can be attributed to the homogeneous impedance and inhomogeneous impedance considerations on the inhomogeneous fiber-reinforced medium.

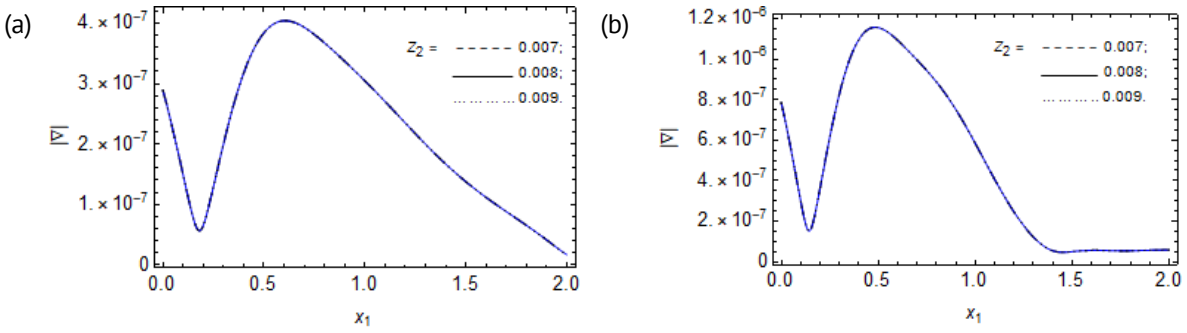

Fig. 8. Variation of impedance Z_2 on the dispersions $|\nabla|$ of Rayleigh wave against x_1, considering (a) homogeneous impedance and (b) inhomogeneous impedance on an Inhomogeneous solid half-space

In a similar vein, Fig. 9 demonstrates the effect of impedance Z_1 on the dispersions$|\nabla|$ of Rayleigh wave as against x_1 coordinate, considering (a) homogeneous impedance and (b) inhomogeneous impedance on the inhomogeneous medium when the parameters of wavenumber b, rotation Ω, magnetic field H_0, impedance Z_i, $i = 2$, inhomogeneous parameter m, parameters associated with the variable amplitudes of corrugation (a, c) remain constantly applied on the solid. In the light of this, Fig. 9 shows

that increase in the impedance Z_1 yield negligible behavior on both considered dispersions of (a) and (b), respectively in terms of decrease an increase. They attain maxima values close to $x_1 = 0.6$ and $x_1 = 0.5$, respectively at any of the given Z_1. This can be attributed to the material characteristics where a resistant-like phenomena of the impedance is witnessed. However, Fig. 9(a) has a reduced dispersion amplitude as compared with Fig. 9(b). This can be attributed to the homogeneous impedance and inhomogeneous impedance considerations on the inhomogeneous fiber-reinforced medium. We can say that this analysis on Z_1 is alike to analysis on Fig. 8 with uniform distributed dispersions at this instance.

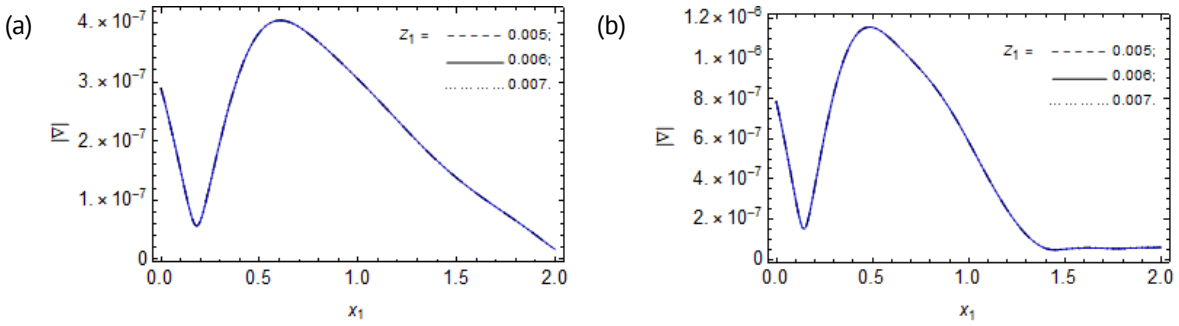

Fig. 9. Variation of impedance Z_1 on the dispersions $|\nabla|$ of Rayleigh wave against x_1, considering (a) homogeneous impedance and (b) inhomogeneous impedance on an Inhomogeneous solid half-space

Conclusions

The present investigation aimed at exploring a mathematical model and its analysis, occasioned by the dispersion relation of Rayleigh wave in a rotating inhomogeneous half-space with variable corrugation amplitudes and impedance conditions under magnetic influence. The impedance conditions were made to be in two characterizations i.e., homogeneous impedance and inhomogeneous impedance conditions at the boundary of the material. We employed the constitutive relations for a fiber-reinforced material alongside an exponentially decaying function of the material parameters characterizing the inhomogeneity, rotation of the medium and magnetism in deriving the equations of motion of the wave on the material. Through this, the analytical solution of the model was derived using the normal mode analysis. Subsequently, using the corrugated-impedance boundary conditions, the two dispersion relations of Rayleigh wave for homogeneous impedance and inhomogeneous impedance conditions were formulated. The graphical depictions of these two dispersion relations of Rayleigh wave where the variations of the physical parameters of rotation, inhomogeneity, magnetic field, impedance, wavenumber and variable amplitudes of corrugation parameters were carried out are illustrated. This is such that:

1. An increase in the magnetic field H_0 give rise to increase in the behavior for the two dispersion relations of the Rayleigh wave on the inhomogeneous fiber-reinforced medium, that is, dispersion due to inhomogeneous impedance and dispersion due to homogeneous impedance increases for increase in H_0.
2. Increase in the inhomogeneity m result to a sequential decrease in behavior of the dispersion relation of the wave due to homogeneous impedance while the dispersion due

to inhomogeneous impedance possesses negligible behavior at this instance.
3. A larger portion of the dispersion profiles witnessed increase in behavior when the rotation Ω increase. However, the rotation Ω of the medium yielded mix behaviors on the dispersion relation of the Rayleigh wave especially in certain domains of the horizontal coordinate when increased.
4. The parameter a associated with the variable amplitude of corrugation caused both decreasing behavior and increasing behavior on both dispersion relations of the wave in certain domains of the horizontal coordinate especially when increased. While the parameter c which is also associated with the variable amplitude of corrugation caused an upward trend on both dispersion relations of the Rayleigh wave when increased. This occurrence ensued especially to a larger extent in the domain of the horizontal coordinate where a very slight mix behavior occurs afterwards. In addition, for the dispersion due to homogeneous impedance, the parameter $c$decrease the dispersion relations of the Rayleigh wave in the domain $0.8 < x_1 \leq 2$ when increased whilst observing uniform behavior for the inhomogeneous impedance case when $x_1 > 1.4$.
5. The wavenumber associated with the variable corrugated surfaces tend to cause a decrease in behavior to the dispersions of the waves to a large extent when increased while noting some mixed behaviors in both cases towards the extended part of the material.
6. Impedance parameters, that is, both the normal and horizontal impedances behaved alike such that they pulled a resistant-like measure on the material by exhibiting a negligible impact when increased on the material in terms of increase and decrease. However, we can equally adduce that the dispersions in both cases were uniformly distributed in this instance.

Thus, it is imperative to state that this model and its analysis invoke special cases found in the literature when the variable amplitude parameter $c$is neglected, i.e., at $c = 0$, models related to Asano [4] are gotten for constant or uniform amplitude of corrugation as occasioned in Fig. 1(a). Hence, we adduce that this study should be beneficial to the investigation and characterization of new and old materials, mathematics of wave phenomena cum solution, and the entire research community working in the directions similar to surface waves on solid materials. Also, the most immediate and realistic engineering applications where the joint interactions of Rayleigh wave, magnetic influences, rotation and fiber reinforcement becomes eminent or applicable is in the design and failure analysis of rotating machinery components designed from composite materials, like those in aerospace materials especially in rotor blades, non-destructive testing using surface waves, and making of piezo-magneto-electric sensors and actuator technologies.

CRediT authorship contribution statement

Augustine I. Anya: conceptualization, methodology, investigation, writing – review & editing, writing – original draft, data curation.

Conflict of interest

The author declares that there is no conflict of interest.

References

1. Spencer AJM. *Deformations of fiber-reinforced materials*. Oxford: Oxford University Press; 1972.
2. Abd-Alla AM, Abo-Dahab SM, Khan A. Rotational effects on magneto-thermoelastic Stonely, Love, and Rayleigh waves in fiber-reinforced anisotropic general viscoelastic media of higher order. *CMC – Computers, Materials & Continua.* 2017;53(1): 49–72.
3. Schoenberg M, Censor D. Elastic waves in rotating media. *Quarterly of Applied Mathematics.* 1973;15: 115–125.
4. Singh B. Reflection of Elastic Waves from Plane Surface of a Half-space with Impedance Boundary Conditions. *Geosciences Research.* 2017;2(4): 242–253.
5. Asano S. Reflection and refraction of elastic waves at a corrugated interface. *Bulletin of the Seismological Society of America.* 1966;56(1): 201–221.
6. Singh SS, Tomar SK. qP-wave at a corrugated interface between two dissimilar pre-stressed elastic half-spaces. *Journal of Sound and Vibration.* 2008;317(3–5): 687–708.
7. Singh AK, Das A, Kumar S, Chattopadhyay A. Influence of corrugated boundary surfaces, reinforcement, hydrostatic stress, heterogeneity and anisotropy on Love-type wave propagation. *Meccanica.* 2015;50: 2977–2994.
8. Singh AK, Mistri KC, Pal MK. Effect of loose bonding and corrugated boundary surface on propagation of Rayleigh-type wave. *Latin American Journal of Solids and Structures.* 2018;15(1): e01.
9. Das SC, Acharya DP, Sengupta PR. Surface waves in an inhomogeneous elastic medium under the influence of gravity. *Romanian Journal of Technical Sciences. Applied Mechanics.* 1992;37(5): 539–551.
10. Abd-Alla AM, Abo-Dahab SM, Alotaibi HA. Effect of the rotation on a non-homogeneous infinite elastic cylinder of orthotropic material with magnetic field. *Journal of Computational and Theoretical Nanoscience.* 2016;13(7): 4476–4492.
11. Chattopadhyay A. On the dispersion equation for Love waves due to irregularity in the thickness of the non-homogeneous crustal layer. *Acta Geologica Polonica.* 1975;23: 307–317.
12. Roy I, Acharya DP, Acharya S. Propagation and reflection of plane waves in a rotating magneto-elastic fiber-reinforced semi-space with surface stress. *Mechanics and Mechanical Engineering.* 2018;22(4): 939–957.
13. Singh D, Sindhu R. Propagation of waves at an interface between a liquid half-space and an orthotropic micropolar solid half-space. *Advances in Acoustics and Vibration.* 2011;2011(1): 159437.
14. Gupta RR. Surface wave characteristics in a micropolar transversely isotropic half-space underlying an inviscid liquid layer. *International Journal of Applied Mechanics and Engineering.* 2014;19(1): 49–60.
15. Anya AI, Akhtar MW, Abo-Dahab SM, Kaneez H, Khan A, Jahangir A. Effects of a magnetic field and initial stress on reflection of SV-waves at a free surface with voids under gravity. *Journal of the Mechanical Behavior of Materials.* 2018;27(5–6): 20180002.
16. Anya AI, Khan A. Reflection and propagation of plane waves at free surfaces of a rotating micropolar fiber-reinforced medium with voids. *Geomechanics and Engineering.* 2019;18(6):605–614.
17. Anya AI, Khan A. Reflection and propagation of magneto-thermoelastic plane waves at free surfaces of a rotating micropolar fiber-reinforced medium under GL theory. *International Journal of Acoustics and Vibration.* 2020;25(2): 190–199.
18. Anya AI, Khan A. Plane waves in a micropolar fiber-reinforced solid and liquid interface for non-insulated boundary under magneto-thermo-elasticity. *Journal of Computational Applied Mechanics.* 2022;53(2): 204–218.
19. Maleki F, Jafarzadeh F. Model tests on determining the effect of various geometrical aspects on horizontal impedance function of surface footings. To be published in *Scientia Iranica.* [Preprint] 2023. Available from: doi.org/10.24200/SCI.2023.59744.6403.
20. Chowdhury S, Kundu S, Alam P, Gupta S. Dispersion of Stoneley waves through the irregular common interface of two hydrostatic stressed MTI media. *Scientia Iranica.* 2021;28(2): 837–846.
21. Singh B, Kaur B. Rayleigh surface wave at an impedance boundary of an incompressible micropolar solid half-space. *Mechanics of Advanced Materials and Structures.* 2022;29(25): 3942–3949.
22. Singh B, Kaur B. Rayleigh-type surface wave on a rotating orthotropic elastic half-space with impedance boundary conditions. *Journal of Vibration and Control.* 2020;26(21–22): 1980–1987.
23. Sahu SA, Mondal S, Nirwal S. Mathematical analysis of Rayleigh waves at the nonplanner boundary

between orthotropic and micropolar media. *International Journal of Geomechanics.* 2023;23(3): 04022313.
24. Giovannini L. Theory of dipole-exchange spin-wave propagation in periodically corrugated films. *Physical Review B.* 2022;105(21): 214426.
25. Rakshit S, Mistri KC, Das A, Lakshman A. Effect of interfacial imperfections on SH-wave propagation in a porous piezoelectric composite. *Mechanics of Advanced Materials and Structures.* 2022;29(25): 4008–4018.
26. Rakshit S, Mistri KC, Das A, Lakshman A. Stress analysis on the irregular surface of visco-porous piezoelectric half-space subjected to a moving load. *Journal of Intelligent Material Systems and Structures.* 2022;33(10): 1244–1270.
27. Gupta V, Kumar M, Goel Sh. Study of different theories of thermoelasticity under the Rayleigh wave propagation along an isothermal boundary. *Materials Physics and Mechanics.* 2025;53(1): 22–37.
28. Kaushal S, Kumar R, Kochar A. Wave propagation under the influence of voids and non-free surfaces in a micropolar elastic medium. *Materials Physics and Mechanics.* 2022;50(2): 226-238.
29. Sharma S, Batra D, Kumar R. Fractional strain analysis on reflection of plane waves at an impedance boundary of a non-local swelling porous thermoelastic medium. *Materials Physics and Mechanics.* 2025;53(1): 1–21.
30. Sharma JN, Othman MIA. Effect of rotation on generalized thermo-viscoelastic Rayleigh–Lamb waves. *International Journal of Solids and Structures.* 2007;44(13): 4243–4255.
31. Shaw S, Othman MIA. Characteristics of Rayleigh wave propagating in an orthotropic magneto-thermoelastic half-space: An eigen function expansion method. *Applied Mathematical Modelling.* 2019;67: 605–620.
32. Othman MIA, Zidan MEM, Hilal MIM. Effect of magnetic field on a rotating thermoelastic medium with voids under thermal loading due to laser pulse with energy dissipation. *Canadian Journal of Physics.* 2014;92(11): 1359–1371.
33. Othman MIA, Song YQ. The effect of rotation on 2-D thermal shock problems for a generalized magneto-thermoelastic half-space under three theories. *Multidiscipline Modeling in Materials and Structures.* 2009;5(1): 43–58.
34. Othman MIA, Saied SM. The effect of rotation on two-dimensional problem of a fiber-reinforced thermoelastic medium with one relaxation time. *International Journal of Thermophysics.* 2012;33(2): 160–171.
35. Anya AI, Nwachioma C, Ali H. Magnetic effects on surface waves in a rotating non-homogeneous half-space with grooved and impedance boundary characteristics. *International Journal of Applied Mechanics and Engineering.* 2023;28(4): 26–42.
36. Anya AI, Khan A. Propagation and reflection of magneto-elastic plane waves at the free surface of a rotating micropolar fiber-reinforced medium with voids. *Journal of Theoretical and Applied Mechanics.* 2019;57(4): 869–881.
37. Khan A, Anya AI, Kaneez H. Gravitational effects on surface waves in non-homogeneous rotating fiber-reinforced anisotropic elastic media with voids. *International Journal of Applied Science and Engineering Research.* 2015;4: 620–632.
38. Munish S, Sharma A, Sharma A. Propagation of SH waves in double non-homogeneous crustal layers of finite depth lying over a homogeneous half-space. *Latin American Journal of Solids and Structures.* 2016;13(14): 2628–2642.
39. Azhar E, Ali H, Jahangir A, Anya AI. Effect of Hall current on reflection phenomenon of magneto-thermoelastic waves in a non-local semiconducting solid. To be published in *Waves in Random and Complex Media.* [Preprint] 2023. Available from: doi.org/10.1080/17455030.2023.2182146.
40. Ailawalia P, Sachdeva SK, Pathania D. A two dimensional fiber-reinforced micropolar thermoelastic problem for a half-space subjected to mechanical force. *Theoretical and Applied Mechanics.* 2015;42(1): 11–25.
41. Othman MIA, Lofty Kh. The effect of magnetic field and rotation on the 2-D problem of a fiber-reinforced thermoelastic medium under three theories with influence of gravity. *Mechanics of Materials.* 2013;60: 129–143.

Nomenclatures

b is wavenumber;
$a,\ c$ are parameters associated with variable amplitude of corrugation;
σ_{ij} is stress tensor;
ε_{ij} is strain tensor;
u_i is displacement vector;
δ_{ij} is Kronecker-Delta function;
λ is Lame's constant;
α, β, $(\mu_L - \mu_T)$ are fiber-reinforced parameters;

F_i is Magnetic force;
ε_0 is electric permeability;
μ_0 is Magnetic permeability;
H_i is Magnetic vector field;
Ω is Rotation parameter of the medium;
ρ is density;
x_i are coordinates;
$Z_1,\ Z_2$ are impedance parameters.

Appendix

$d_{11} = G_{13}G_{15}$;
$d_{12} = -m(G_{15}G_{24} + G_{13}G_{27})$;
$d_{13} = (-b^2i^2\rho G_{12}^2 - b^2\rho G_{15} - \rho\omega^2 G_{15} + \rho^2\Omega^2 G_{15} + m^2\rho G_{24}G_{27} - \omega^2 G_{15}H_0^2\varepsilon_0\mu_0^2 +$
$+G_{13}(-\rho\omega^2 + \rho^2\Omega^2 - b^2\rho G_{13} - \omega^2 H_0^2\mu_0^2))/\rho$;
$d_{14} = (m(b^2i^2\rho G_{12}G_{26} + G_{24}(\rho\omega^2 - \rho^2\Omega^2 + b^2i^2\rho G_{12} + b^2\rho G_{13} + \omega^2 H_0^2\mu_0^2) +$
$+G_{27}(\rho(b^2 + \omega^2 - \rho\Omega^2) + \omega^2 H_0^2\varepsilon_0\mu_0^2)))/\rho$;
$d_{15} = \frac{1}{\rho^2}(b^2\rho^2\omega^2 + \rho^2\omega^4 - b^2\rho^3\Omega^2 - 2\rho^3\omega^2\Omega^2 + 4\rho^4\omega^2\Omega^2 + \rho^4\Omega^4 - 2bim\rho^3\omega\Omega G_{26} +$
$+bim\rho^2 G_{24}(2\rho\omega\Omega - bimG_{26}) + b^2\rho\omega^2 H_0^2\mu_0^2 + \rho\omega^4 H_0^2\mu_0^2 - \rho^2\omega^2\Omega^2 H_0^2\mu_0^2 + \rho\omega^4 H_0^2\varepsilon_0\mu_0^2 -$
$-\rho^2\omega^2\Omega^2 H_0^2\varepsilon_0\mu_0^2 + \omega^4 H_0^4\varepsilon_0\mu_0^4 + b^2\rho G_{13}(\rho(b^2 + \omega^2 - \rho\Omega^2) + \omega^2 H_0^2\varepsilon_0\mu_0^2))$.

MATERIALS PHYSICS AND MECHANICS RESEARCH ARTICLE

Submitted: June 2, 2025 **Revised: September 26, 2025** **Accepted: November 7, 2025**

Diagnostics of coating and adhesive properties on load-bearing elements of complex shape

S.N. Yakupov ✉

Institute of Mechanics and Engineering Russian Academy of Sciences, Kazan, Russia

✉ samat.mech.eng@gmail.com

ABSTRACT

Protective coatings are used to solve many technical and economic problems. Information on known methods and approaches to studying the mechanical and adhesive properties of coatings is provided. It is noted that modern thin-walled structures, as a rule, have a complex geometry. In this case, protective coatings are formed directly on the surfaces of load-bearing elements. Known adhesion meters have a number of limitations. There are practically no works on determining the mechanical properties of coatings and adhesive formed on surfaces of complex shapes. An effective two-dimensional experimental - theoretical approach to diagnosing the rigidity and adhesive properties of a thin-layer coating formed directly on the surface of a load-bearing element of complex shape is described. At the theoretical stage of the study, the spline version of the finite element method is effective, when varying the properties of the material, we approach the shape of the experimental dome of the considered loading stage.

KEYWORDS

load-bearing element • protective coating • mechanical and adhesive properties • deformed surface diagnostics • complex structure and geometry

Acknowledgements. *Samat Yakupov performed the work at the grant expense the Academy Sciences the Tatarstan Republic, provided to young candidates of sciences (postdoctoral fellows) for the defending purpose a doctoral dissertation, performing research work, as well as performing labor functions in scientific and educational organizations in the Tatarstan Republic within the framework the State Program the Tatarstan Republic "Scientific and Technological Development of the Tatarstan Republic".*

Citation: Yakupov SN. Diagnostics of coating and adhesive properties on load-bearing elements of complex shape. *Materials Physics and Mechanics.* 2025;53(6): 182–189.
http://dx.doi.org/10.18149/MPM.5362025_13

Introduction

On the role of protective coatings

Since the 20 th century, thin-walled structures have garnered significant attention. To ensure the reliable operation of such structures, which are often exposed to diverse environments, physical fields, and substantial loads, maximizing the protection of their components from external influences is crucial. Protective coatings are commonly employed for this purpose. Research in this direction remains highly relevant.

Protective coatings are widely employed to address a multitude of technical and economic challenges. The degradation or failure of these protective coatings leads to the exposure of the surface of load-bearing structural components. Consequently, the load-bearing element becomes directly subjected to the effects of the surrounding environment and physical fields. This, in turn, results in the development of various corrosion defects, scratches, localized depressions, and the like on the surface of these structural components [1,2]. These defects induce alterations in the stiffness properties

Publisher: Peter the Great St. Petersburg Polytechnic University

of thin-walled structural elements and give rise to stress concentrations in the defect regions [3,4].

The requisite properties of coatings, including smart coatings, are achieved through the development of sophisticated thin-film composite structures and adhesives [5–8]. Various methods and approaches have been devised for applying coatings to the surface of load-bearing components.

However, during structural operation, various defects also emerge within the coatings themselves, arising from the environment, physical fields, and deformation of the load-bearing component. Local delaminations also develop in multilayer composites. All of these factors induce significant alterations in the structure and stiffness properties of both the coating and the adhesive [9].

Modern coatings are typically formed directly onto the surfaces of load-bearing thin-walled structures, which generally possess a non-planar geometry. During operation, the coating deforms in concert with the load-bearing component. Research into the mechanical properties of coatings and adhesives on complex-shaped surfaces, considering the deformations of the load-bearing components, is notably scarce. Consequently, when determining the mechanical properties of coatings and adhesives, it is essential to account for the shape and deformation of the load-bearing component [10].

On methods and approaches for investigating the mechanical properties of coatings

When selecting coatings, adhesives, and their application technologies, based on a specified service life and operational conditions, questions arise concerning the determination of their structure, geometric parameters, and physico-mechanical characteristics. To ensure the integrity of coatings on structural components, it is crucial to effectively design and reliably assess both the initial mechanical properties and those acquired during operation for protective coatings and adhesives. The challenges of assessing the mechanical properties of coatings and the adhesion of coatings to load-bearing components, as well as investigating the patterns of change in coating and adhesion characteristics under the influence of the environment, physical fields, and operational factors, are highly relevant. The instrumentation for evaluating the mechanical properties of coatings remains underdeveloped. The "indenter" method, while capable of determining material properties in the vicinity of a point of interest, exhibits limited effectiveness when investigating coatings with complex structures [11]. In [12], the indentation method is noted as an effective tool for studying the mechanical properties of polyethylene. This method can be used to determine such material properties as hardness, elastic modulus and rheological characteristics. However, the "indenter" method, which allows determining the properties of the material in the vicinity of the point under consideration, is ineffective when studying coatings of complex structure. Indentation methods, as well as the stretch test method, which consists of stretching a material sample until it breaks to assess its strength and plasticity, are noted in [13]. Adhesion assessments based on the destruction of the coating in the area of application of the indenter are considered in [14,15]. The advent of powerful computers has facilitated the increasing prevalence of computational modeling. Molecular approaches to investigating the mechanical properties of thin structures are currently in their nascent

stages. Difficulties arise in describing the complex structure and defects of coatings at the nano- and macro-scales [16]. Uniaxial tensile testing of specimens is a standard method [17–19]. However, when investigating the stiffness properties of complex-structured coatings, uniaxial testing often reveals a significant scatter in test results [20]. On the topic under consideration, there exist inventor's certificates (A.c.) and patents for inventions, including: A.c. 1742671 USSR, publ. 23.06.92; A.c. 1458766 USSR, publ. 5.02.89; SU 601599 A, 05.04.1978; SU 1441243 A1, 30.11.1988; SU 765697 A, 23.09.1980; US Patents US 5764068A, 09.06.1998 and Japan JP 8313422 A, 29.11.1996, which provide solutions to certain questions related to this subject. When investigating the properties of complex-structured coatings, the experimental-theoretical method of investigation proves indispensable. In particular, for studying initially flat thin coatings with complex structures, a two-dimensional shell approach is recommended [21]. This method can also be employed to determine the mechanical characteristics of nano-coatings within a "coating-substrate" system without separating the coating from the substrate [22]. The experimental-theoretical method has been further developed for investigating initially spherical and cylindrical coatings with variable radii [23].

On approaches to determining the adhesion of coatings to a load-bearing element

Determining the adhesion of coatings to load-bearing structural components has received considerable attention. A review of standard methods for assessing the adhesive strength of special coatings is given in [24]. The interaction between the adhesion strength and the tensile properties of coated laminates is noted in [25]. It is obvious that the adhesion strength of the coating is affected by both the properties and the technology of coating application [26,27]. An analysis of some adhesion assessment methods for heat-protective coatings is given in [28]. A technique for assessing the adhesion of thin-film coatings is considered in [29]. Some aspects of increasing the adhesion of metal coatings are presented in [30]. The effect of temperature on the adhesion of films to substrates is noted in [31]. The choice of adhesion assessment method for antifriction coatings is considered in [32]. In [33], it is noted that grinding and sandblasting are effective in improving the adhesion strength.

The following methods are known for determining adhesion properties: the tear-off method, which allows determining, in particular, the adhesion of the paint and varnish coating to various substrates; the method of lattice cuts, including *X*-shaped cuts and parallel cuts for visual assessment of coating delamination.

Methods have been developed to determine the adhesion strength of coatings to substrates, as evidenced by inventor's certificates and patents, including: A.c. USSR No. 183459, publ. 17.06.1966; Patent RF No. 689411, publ. 10.05.1995; Patent RF No. 2207544, publ. 27.06.2003. However, these methods suffer from drawbacks such as low accuracy, technological complexity, and low throughput. A known method for assessing the adhesion of elastic films utilizes "bubble" parameters [34], but this approach, along with its inherent limitations, exhibits a scatter in results.

Specialized instruments known as adhesiometers (e.g., PSO-XMG series) are available for evaluating coating adhesion to substrates [35]. However, these devices

exhibit limitations, notably the difficulty in ensuring measurement consistency when studying the influence of different factors, among others.

A method for evaluating coating adhesion to a flat substrate has been developed [36]. Further developments of this method, refining the results of adhesion studies on substrates, are detailed in [37].

Modern thin-walled structures are typically characterized by complex geometries, harmoniously blending functional purpose with architectural expressiveness. In these designs, protective coatings are formed directly on the surfaces of load-bearing elements. Notably, research is scarce regarding the determination of mechanical properties of coatings and adhesives on complexly shaped surfaces.

An algorithm for diagnosing the mechanical and adhesive properties of a coating system on a complex surface of a structural element is outlined below. This algorithm assumes the availability of experimental coating pull-off data, specifically the parameters defining the dome shape and base as a function of air pressure introduced through a central aperture in the structural element.

Algorithm for determining mechanical and adhesion properties of a coating on a load-bearing surface of a structural element of complex shape

Numerical investigation tool

Established software packages can be utilized during the theoretical phase of the investigation. However, when examining the mechanical and adhesive properties of a coating applied to the surface of a load-bearing element with complex geometry, the spline-based finite element method proves most effective [38].

A load-bearing structural element of complex geometry 1 with a protective coating 2 is under consideration (Fig. 1(a)). The structural element 1 is parameterized by parameters t^1, t^2, t^3 of a parallelepiped 3 [39], where:

, (1)

and the coating 2 is parameterized by parameters t^1, t^2 of a rectangle 4 (Fig. 1(b)) [37–39]:

$r = \bar{r}(t^1, t^2)$. (2)

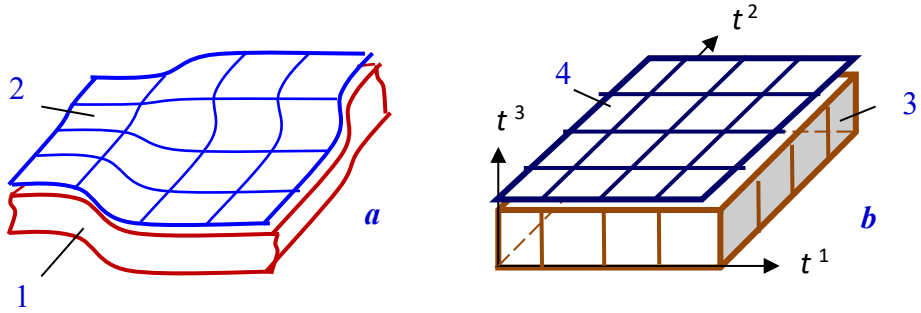

Fig. 1. A scheme of parametrization

A distinction is made between thin-walled structural elements of complex canonical geometry, where the mid-surface is described by analytical formulas, and elements of complex non-canonical geometry, where the mid-surface is not described analytically,

but rather specified point-by-point. When considering thin-walled elements with complex non-canonical geometry, challenges arise in the parameterization stage [40]. For cases where the structural element geometry is not analytically described, an experimental parameterization approach can be employed, as exemplified by Patents of the Russian Federation Nos. 2374697 and 2665499.

By differentiating expression (1) with respect to t^1 и t^2 for all nodal and integration points, the coordinate vectors $\bar{r}_1$ и $\bar{r}_2$, the first fundamental metric tensor a_{ij} and the fundamental determinant a are calculated for the coating:

$$\bar{r}_1 = \frac{\partial \bar{r}}{\partial t^1},\ \bar{r}_2 = \frac{\partial \bar{r}}{\partial t^2},\ \bar{m} = \frac{[\bar{r}_1,\bar{r}_2]}{\sqrt{a}},\ a_{11} = \bar{r}_1\bar{r}_1,\ a_{12} = \bar{r}_1\bar{r}_2,\ a_{22} = \bar{r}_2\bar{r}_2,\ a = a_{11}a_{22} - a_{12}^2\,. \quad (3)$$

Subsequently, Christoffel symbols of the second kind are calculated:

$$a\Gamma_{11}^1 = \frac{a_{22}}{2}\frac{\partial a_{11}}{\partial t^1} - a_{12}\left(\frac{\partial a_{12}}{\partial t^1} - \frac{1}{2}\frac{\partial a_{11}}{\partial t^2}\right), a\Gamma_{12}^1 = \frac{1}{2}\left(a_{22}\frac{\partial a_{11}}{\partial t^2} - a_{12}\frac{\partial a_{22}}{\partial t^1}\right),$$
$$a\Gamma_{22}^1 = a_{22}\left(\frac{\partial a_{12}}{\partial t^2} - \frac{1}{2}\frac{\partial a_{22}}{\partial t^1}\right) - \frac{a_{12}}{2}\frac{\partial a_{22}}{\partial t^2}, a\Gamma_{11}^2 = a_{11}\left(\frac{\partial a_{12}}{\partial t^1} - \frac{1}{2}\frac{\partial a_{11}}{\partial t^2}\right) - \frac{a_{12}}{2}\frac{\partial a_{11}}{\partial t^1}, \quad (4)$$
$$a\Gamma_{12}^1 = \frac{1}{2}\left(a_{11}\frac{\partial a_{22}}{\partial t^1} - a_{12}\frac{\partial a_{11}}{\partial t^2}\right), a\Gamma_{22}^2 = \frac{a_{11}}{2}\frac{\partial a_{22}}{\partial t^2} - a_{12}\left(\frac{\partial a_{12}}{\partial t^2} - \frac{1}{2}\frac{\partial a_{22}}{\partial t^1}\right),$$

along with the components of the second fundamental metric tensor b_{ij}:

$$b_{11} = \bar{m}\frac{\partial^2\bar{r}}{(\partial t^1)^2},\ b_{12} = \bar{m}\frac{\partial^2\bar{r}}{\partial t^1\partial t^2},\ b_{22} = \bar{m}\frac{\partial^2\bar{r}}{(\partial t^2)^2}. \quad (5)$$

Tangential forces T^{ik} and bending moments M^{ik} for the coating in a physically linear formulation can be expressed as [41]:

$$T^{ik} = \frac{Eh}{2(1-\nu^2)}(a^{ij}a^{ks} + \nu c^{ij}c^{ks})\left[\nabla_j u_s - b_{js}w + \nabla_s u_j - b_{sj}w + (\nabla_j w + b_j^l u_l)(\nabla_s w + b_j^m u_m)\right],$$
$$M^{ik} = \frac{Eh^3}{12(1-\nu^2)}\left(a^{ij}a^{ks} + \nu c^{ij}c^{ks}\right)\left[-\nabla_j(\nabla_s w + b_s^l u_l) - b_j^m(\nabla_s u_m - b_{sm}w)\right], \quad (6)$$
$$c^{ii} = 0,\ c^{12} = -c^{21} = 1/\sqrt{a};\ i,j,k,s,l,m = 1,2,$$

where T^{ik}, M^{ik} are tangential forces and bending moments, E is the elastic modulus of of the coating; ν is Poisson's ratio, h is the coating thickness, $u = u_1$, $v = u_2$, w are the components of displacements of the middle surface of the coating, ∇_i is the symbol of covariant differentiation with respect to a_{ij}; a^{ij} are the contravariant components of the first fundamental metric tensor.

The governing relations are derived from Lagrange's variational equation:

$$\delta W - \delta A = 0, \quad (7)$$

where δW is the variation of the shell's strain potential energy, δA is the variation of the work done by external forces acting on the structural element.

The solution within each mesh cell is represented using an interpolating Hermite bicubic spline, and the problem is then reduced to solving a system of algebraic equations:

$$[B]\{U\} = \{R\}, \quad (8)$$

where $[B]$ is the stiffness matrix of a system with a banded structure, $\{U\}$ is the vector of unknowns, $\{R\}$ is the load vector.

Diagnostic algorithm

Initially, the stiffness characteristics of the coating are investigated. The components of parameterization are calculated using Eqs. (1)–(5) for the initial state of the load-bearing element with a coating (Fig. 1). Further, for each loading stage, based on the experimentally determined coordinates of the dome base (Fig. 2), a numerical model of coating deformation under pressure p is constructed – all components of

parameterization are calculated using Eqs. (1)–(5); in nodes coinciding with the dome base, displacements are zeroed, the load is applied to elements located under the dome, and the stress-strain state calculation is performed according to Eq. (8).

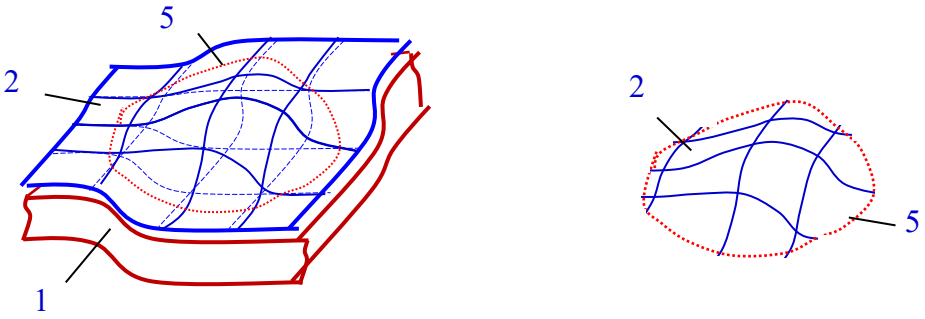

Fig. 2. Formation of a dome

The source material employed in this study was Class F fly ash sourced from Raichur Thermal Power Corporation Limited (RTPCL), Karnataka, India. The fly ash confirmed to IS 3812 2003 (part 1&2) [26].

At each loading stage *p*, using the iterative adjustment method – by varying material properties (Young's modulus *E* and Poisson's ratio ν), the shape of the experimental dome at the considered loading stage is approached. This determines process the distribution of the stress-strain state of the coating. When required, curves "strain ε – stress σ", "Young's modulus *E* – strain ε" are constructed. Thus, the mechanical properties of the coating are determined.

Next, the adhesion properties of the coating to the surface of the load-bearing element are investigated. In general, the coating detachment forces T_{otr} vary significantly along the contour. Knowing the tangential forces T^{ik} at the calculation nodes along line 5 of the dome base (Fig. 2) from the current loading stage solution, we can determine the local value of the normal adhesion stress η_{otr} at the surface of the load-bearing element 1 (Fig. 1) using the following equation:

$$\eta_{otr} = T_{otr}(\bar{m}_0 \times \bar{m}_i)/\left[h_0(1-\varepsilon_1-\varepsilon_2)\right], \quad (9)$$

where $T_{otr} = f(T^{ik})$ is the detachment force, which depends on the values of tangential forces T^{ik} at each point along line 5 of the dome base; h_0 is the coating thickness before deformation, ε_1, ε_2 is the coating deformation in the normal and tangential directions along line 5 of the dome base.

Conclusions

Employing protective coatings is an effective strategy for safeguarding structural load-bearing elements from environmental and physical field exposure. The requisite properties of coatings, including smart coatings, are achieved through the development of sophisticated composite structures and adhesives.

Selecting coatings, adhesives, and their application technologies raises questions regarding the determination of their parameters. The available tools for assessing the mechanical properties of coatings remain underdeveloped.

To determine the mechanical and adhesive properties of a coating system with a complex structure applied to a load-bearing element with complex geometry, a two-dimensional approach proves effective. This approach involves an experimental-theoretical method rooted in a spline-based finite element method (FEM).

An algorithm for diagnosing the mechanical and adhesive properties of coatings on the surface of complexly shaped load-bearing structural elements is described. This algorithm serves as a reliable tool for researchers, designers, and practicing engineers alike.

CRediT authorship contribution statement

Samat N. Yakupov: writing – review & editing, writing – original draft.

Conflict of interest

The author declares that he has no conflict of interest.

References

1. Collins JA. *Failure of Materials in Mechanical Design. Analysis, Prediction, Prevention.* NewYork: John Wiley & Sons; 1981.
2. Yakupov SN. Influence of Scratches on the Stiffness Properties of Thin-walled Elements. *Lobachevskii Journal of Mathematics.* 2019;40(6): 834–839.
3. Neuber H. *Theory of Notch Stress.* Michigan: J.W. Edwards; 1946.
4. Peterson RE. *Stress Concentration Factors.* New York: John Wiley & Sons; 1974.
5. Montemor MF. Functional and smart coatings for corrosion protection: A review of recent advances. *Surface and Coatings Technology.* 2014;258: 17–37.
6. Taylor SR, Shiflet GJ, Scully JR, Buchheit RG, W, Van Ooij WG, Sieradzki K, Diaz R, Brinker CJ, Moran AL. Increasing coating functionality using nanodimensioned materials. In: *Nanotechnology Applications in Coatings. (ACS Symposium Series).* American Chemical Society; 2009. p. 126–155.
7. Yakupov SN, Yakupov NM. Thin-layer films and coatings. *Journal of Physics: Conference Series.* 2017;857: 012056.
8. Belyaev AK, Galyautdinova AR, Smirnov SA, Bessonov NM. Analytical and numerical solution to the problem of hydrogen diffusion in rotating cylindrical elastic bodies. *Materials Physics and Mechanics.* 2022;50(1): 56–65.
9. Yakupov NM, Kharislamova LU. Stiffness of Compositions with Delaminations and the Influence of Ultraviolet on Adhesion. *Lobachevskii Journal of Mathematics.* 2019;40(6): 840–845.
10. Yakupov SN, Gubaidullin RI, Yakupov NM. Investigation of the influence of the nature of surface deformation on coating adhesion. *Journal of Physics: Conference.* 2021;1954: 012053.
11. Tsui TY, Oliver W, Pharr GM. Nanoindentation Hardness of Soft Films on Hard Substrates: Effects of the Substrate. *MRS Online Proceedings Library.* 1997;473: 57–62.
12. Vinogradova AA, Gogolinskiy KV, Shchiptsova EK. A study of applicability of instrumented indentation method to determine the mechanical properties of thermoplastic. *Industrial laboratory. Diagnostics of materials.* 2025;91(5): 67–76. (In Russian)
13. Wang YM, Weng WX, Chi MH, Lui BL, Li Q. Investigation into the evolution of interface fracture toughness of thermal barrier coatings with thermal exposure treatment by wedge indentation. *Journal of Materials Research.* 2020;35: 1715–1725.
14. Vidakis N, Antoniadis A, Bilalis N. The VDI 3198 indentation test evaluation of a reliable qualitative for layered compounds. *Journal of Materials Processing Technology.* 2003;143–144: 481–485.
15. Hatic D, Cheng X, Stephani T, Rauhut M, Gäbler J, Bethke R, King H, Hagen H. Use of machine learning for automatic Rockwell adhesion test classification based on descriptive and quantitative features. *Surface and Coatings Technology.* 2021;427: 127762.
16. Yanovsky YuG, Nikitina EA, Nikitin SM, Karnet YuN. Quantum mechanical studies of the mechanism of deformation of carbon nanotubes. *Nanoscience and Technology: An International Journal.* 2010;1(1): 1–29.

17. State Standard. GOST 14236-81. *Polymer films. Tensile testing method.* Moscow: Publishing house of standards; 1989. (In Russian)
18. State Standard. GOST 29088-91. *Polymer cellular elastic materials. Determination of conditional strength and elongation at break.* Moscow: Publishing house of standards; 1991. (In Russian)
19. American Society for Testing and Materials. ASTM D 412-41. *Standard Test Methods for Vulcanized Rubber and Thermoplastic Elastomers-Tension*. West Conshohocken; 2016.
20. Kupriyanov VN. *Film – fabric materials for building structures*. Kazan: KISI; 1989.
21. Jakupov NM, Nurullin RG, Nurgaliev AR, Jakupov SN. *Method of determining strength of thin-layer materials*. Russian Patent RU 2310184 C2, 10 November 2007. (In Russian)
22. Yakupov SN. Mechanical characteristics of thin titanium oxide coatings in the "coating – polymer film" system. *Mechanics of Composite Materials and Structures*. 2010;16: 436–444. (In Russian)
23. Yakupov NM, Galimov NK, Yakupov SN. Methodology of studying non-planar films and membranes of complex structure. *Zavodskaya Laboratoriya. Diagnostika Materialov.* 2019;85(2): 55–59. (In Russian)
24. Zaytsev AN, Aleksandrova YP, Yagopolskiy AG. Comparative Analysis of Methods for Assessing Adhesion Strength of Thermal Spray Coatings. *BMSTU Journal of Mechanical Engineering.* 2021;5: 48–59. (In Russian)
25. Luo X, Smith GM, Sampath S. On the Interplay between Adhesion Strength and Tensile Properties of Thermal Spray Coated Laminates– Part I: High Velocity Thermal Spray Coatings. *Journal of Thermal Spray Technology.* 2018;27: 296–307.
26. Mittal KL. *Adhesion Measurement of Films and Coatings.* London: CRC Press; 1995.
27. Mittal KL. *Adhesion Measurement of Films and Coatings, Volume 2.* London: CRC Press;2001.
28. Fedorova EN, Sukhodoeva NV, Moskvichev VV, Ogoreltceva NV, Klimkin YuO. Methods for characterizing the interfacial adhesion in thermal barrier coating systems. *Industrial laboratory. Diagnostics of materials.* 2022;88(12): 51–63. (In Russian)
29. Topolyanskiy P, Ermakov S, Topolyansky A. Adhesion characteristics of thin-film coating deposited by finishing plasma hardening. *Voronezh Scientific-Technical Bulletin.* 2022;3(3): 11–27. (In Russian)
30. Kolesnik LL, Zhuleva TS, Predtechenskiy PO, Hlaing MK, Aung ZP. Processing of metallization technology aluminum oxide ceramics for electro-vacuum devices elements and power electronics devices. *Journal of Physics: Conference Series.* 2017;872: 012018.
31. Bovaldinova KA, Feldstein MM, Sherstneva NE, Moscalets AP, Khokhlov AR. Thermo-switchable pressure-sensitive adhesives with strong tunable adhesion towards substrate surfaces of different hydrophilicity. *Polymer.* 2017;125: 10–20.
32 Lunin EA, Zakharova NV, Trifanov IV. Selecting a method for determining the adhesion of an antifriction coating. *Current issues in aviation and astronautics.* 2019;2: 613–615. (In Russian)
33. Ito K, Shima T, Fujioka M. Improvement of Oxidation Resistance and Adhesion Strength of Thermal Barrier Coating by Grinding and Grit-Blasting Treatments. *Journal of Thermal Spray Technology.* 2020;29: 1728–1740.
34. Bilbi B. Fracture. In: Taplin J. (eds.). *Fracture Mechanics. The destruction of the materials*. Moscow: Mir;1979. p.222–224. (In Russian)
35. Bousfield DW, Coleman PS, Hassler JC, Osgood AK. *Devices and methods for testing tack uniformity of a coating on a substrate*. US6050139A (Patent), 2000.
36. Gol'dshtejn RV, Jakupov NM, Nurullin RG, Jakupov SN, Jakupova RN. *Method of determining adhesion of film substrate*. RU 2421707 C1 (Patent), 2011. (In Russian)
37. Yakupov SN. Experimental-Theoretical Approach to Determining the Film–Substrate Adhesion. *Mechanic of Solids.* 2017;52: 587–593.
38. Yakupov NM. Method of calculating shells of complex geometry. *Research in Shell Theory. Seminar Proceedings*. 1984;17(2):4–17. (In Russian)
39. Yakupov SN, Kiyamov HG, Yakupov NM, Mukhamedova IZ. A new variant of the fem for evaluation the strenght of structures of complex geometry with heterogeneous material structure. *Case Studies in Construction Materials.* 2023;19: e02360.
40. Badriev IB, Paimushin VN. Refined models of contact interaction of a thin plate with positioned on both sides deformable foundations. *Lobachevskii Journal of Mathematics.* 2017;38: 779–793.
41. Galimov KZ. *Foundations of Nonlinear Theory of Thin Shells*. Kazan: Kazan University Press; 1975. (In Russian)

MATERIALS PHYSICS AND MECHANICS RESEARCH ARTICLE

Submitted: November 5, 2025 **Revised: December 3, 2025** **Accepted: December 6, 2025**

Influence of the core-sleeve boundary interface on the composite Al-Al wire properties

A.E. Medvedev [1]✉, A.F. Shaikhulova [1], M.M. Motkov [2], M.Yu. Murashkin [1]

[1] Ufa University of Science and Technology, Ufa, Russia

[2] Siberian Federal University, Krasnoyarsk, Russia

✉ medvedevandreyrf@gmail.com

ABSTRACT

The influence of the core-sleeve boundary interface on the mechanical properties and electrical conductivity of the composite all-aluminium wires made of electromagnetically cast Al-0.5 wt. % Fe and Al-1.7 wt. % Fe alloys was studied. For the comparison all-aluminium wires made of same materials were studied as well. Structural analysis was presented by the scanning electron microscopy of the composite all-aluminium wires cross-section, as well as by the fractographic analysis of the failed tensile samples. It was demonstrated that the effect of the core-sleeve boundary increases with the increase in amount of alloying elements in the composite all-aluminium wires components. The core-sleeve boundary in the composite all-aluminium wires acts as a buffer for the deformation thus the amount of the deformation, that otherwise would be distributed gradually in the all-aluminium wires, is distributed uneven between the core and the sleeve of the composite all-aluminium wires, accumulating more within the composite all-aluminium wires sleeve. The major influence of the core-sleeve boundary is noted in yield strength and ductility of the wires, while electrical conductivity and especially ultimate tensile strength remain mostly unaffected.

KEYWORDS

aluminium alloys • electromagnetic crystallization • composite wire • mechanical strength • ductility electrical conductivity

Funding. *The research was supported by the Russian Science Foundation grant No. 25-19-00633, https://rscf.ru/project/25-19-00633/.*

Acknowledgements. *The authors express special gratitude to the Center for Collective Use "Nanotech" of the Federal State Budgetary Educational Institution of Higher Education "Ufa University of Science and Technology".*

Citation: Medvedev AE, Shaikhulova AF, Motkov MM, Murashkin MYu. Influence of the core-sleeve boundary interface on the composite Al-Al wire properties. *Materials Physics and Mechanics*. 2025;53(6): 190–200. http://dx.doi.org/10.18149/MPM.5362025_14

Introduction

Aluminum and its alloys may replace copper as electrically conductive materials because they are lightweight, commercially available, exhibit high electrical conductivity, and are resistant to corrosion [1]. The downside of the aluminium alloys is their relatively low strength, making it important to find either new alloys or methods of their production. One result of the search for new conductive materials has been the concept of creating hybrid (composite) materials [2,3]. This way two or more different materials could be united into one product, theoretically combining all the advantages of each individual component without their disadvantages [4,5].

This approach, for example, has been implemented in the form of a specific cable architecture consisting of a core and an outer layer made of various aluminum alloys, such as an all-aluminum alloy cable (AAAC) [6] and an aluminum cable steel-reinforced

(ACSR) [7]. In these cases, hybridization of the final product is achieved through the mechanical assembly of different materials. The most obvious approach to the hybridization of aluminum alloys is the creation of composite materials from various aluminum alloys [8,9]. Combining them in a certain proportion can help overcome the tradeoff between strength and conductivity, providing both high mechanical strength and high electrical conductivity in a composite aluminum alloy [10]. Previous studies have shown the potential of this approach to produce Al-Al composite wire [11].

The other way to create composite aluminium alloys is the application of cold bonding, for example, the accumulative roll bonding (ARB) [12–14]. Such approaches make it possible to obtain gradient microstructures that provide effective control over a complex of structurally sensitive characteristics. The main advantages of this approach are the possibility to produce continuous products and the high deformation value required for the mechanical bonding of materials [15]. Unfortunately, ARB is not suitable for wire production.

Research into the production of composite conductors made from two alloys using the "core-sleeve" design has shown that the drawing process used to produce them has not yet resulted in a monolithic blank [16]. This is apparently due to the fact that a single drawing pass of such composite blanks can only achieve a deformation of 30 %, whereas reliable joining of different metals/alloys to create a composite sample using ARB requires a deformation of at least 50 % at elevated temperatures (0.3–0.4 of a melting temperature) [17].

Therefore, composite conductors made from aluminum alloys currently contain an interface between their components. In this regard, it is important to determine how the presence and the length of the interface between components influences the properties of such conductors.

In this study, the composite aluminium wires made of Al-0.5 wt. % Fe and Al-1.7 wt. %Fe were compared to the all-aluminium wires made of same materials. The length of the core-sleeve boundary interface was chosen so that the fraction of the core would be 10 % in the cross-section. The choice of the materials was based on the fact that these alloys belong to immiscible systems and that the absence of the solid solution effect and the associated diffusion processes will allow to isolate the influence of the boundary interface, without taking into consideration potential diffusion transitions of alloying elements through it.

Materials and Methods

Two alloys of the Al-Fe system with an iron content of 0.5 and 1.7 wt. % were used as research material. Initial samples were produced in the form of rods of a diameter of 11 mm by continuous casting in an electromagnetic mold (EMC) [18]. The chemical composition of the alloy samples is presented in Table 1.

Table 1. Chemical composition of alloys of the Al-Fe system (wt. %)

Alloy	Fe	Si	Cu	Mg	Zn	∑Ti,Mn,Cr	Al
Al-0.5Fe	0.50	0.04	0.01	0.01	0.02	⩽ 0.02	Rem.
Al-1.7Fe	1.65	0.03	0.01	-	0.03		

Samples of 11 mm in diameter wire rod of the Al-Fe alloys were made on the basis of primary aluminum grade A85 (not less than 99.85 wt. % Al) and Fe80Al20 alloys in proportions selected to match the required Fe concentrations. After the melt temperature reached more than 800 °C, continuous casting was carried out in an EMC installation at a speed of 12.4 mm/s.

Part of the Al-0.5Fe and Al-1.7Fe alloys samples were cold drawn (CD) down to 3 mm diameter, creating all-aluminium wires (Al-0.5Fe AAW and Al-1.7Fe AAW). The other part of the Al-1.7Fe and Al-0.5Fe alloys rods were cold drawn down to 10 mm diameter. The section of these rods with 300 mm in length was cut off. Then the hole of 3.2 mm in diameter was drilled along the longitudinal axis of the cut samples, creating the tubes. The inner surface of the tubes and the outer surface of the wires of both samples were cleaned and degreased, after which the wire was put into the corresponding tube. The combined billet was subjected to CD with an area reduction of 91 %. Total area reduction was achieved in 10 passes, resulting in the 3 mm diameter composite all-aluminium wires of the following compositions: Al-0.5Fe core and Al-0.5Fe sleeve; Al-1.7Fe core and Al-1.7Fe sleeve (Al-0.5Fe CAAW and Al-1.7Fe CAAW, respectively). Thus, the fraction of the core in the cross-section of CAAW was 10 %, and the length of the core-sleeve boundary interface was 30 % of the outer wire diameter. The evaluation of the core fraction in the cross-section of the wire using scanning electron microscopy (SEM) images. This cross-section corresponds to the length of the interface being the 30 % of the outer wire diameter.

The heat resistance of wire samples was assessed in accordance with the requirements of the IEC 62641:2023 standard [19]. To do this, after CD, samples were annealed at a temperature of 230 °C for 1 h, followed by cooling in air. The microstructure was studied using scanning electron microscopy (SEM) on a Tescan Mira microscope at an accelerating voltage of 10–20 kV in back-scattered (BSE) and secondary electrons (SE) modes. To obtain statistically reliable results, tensile tests were carried out on three samples for each state, on a universal tensile machine Instron 5982 at room temperature and at a speed of 100 mm/min. Based on the test results, the values of the yield strength ($\sigma_{0.2}$), ultimate tensile strength (σ_{UTS}) and elongation to failure (δ) were determined [20].

The specific electrical resistance of the material under study was measured in accordance with IEC 60468:1974 [21]. Straightened samples of at least 1 m in length were selected. The electrical conductivity value of the samples relative to annealed copper (International Annealed Copper Standard) was calculated using the equation:

$$IACS = \rho_{Cu}/\rho_{Al} \times 100\ [\%], \quad (1)$$

where ρ_{Al} is the experimentally determined value of the specific electrical resistance of the aluminum alloy sample, ρ_{Cu} is the specific electrical resistance of annealed copper, equal to 17.241 nΩm.

Results and Discussion

The cross-section of the Al-0.5Fe CAAW and Al-1.7Fe CAAW is presented on Fig. 1. The initial placement of the core wire was designed to be coaxial, the displacement of the core wire from the center of the sleeve is probably due to the bending of the drill instrument during preparation of the tube (see Materials and Methods section). Gaps in

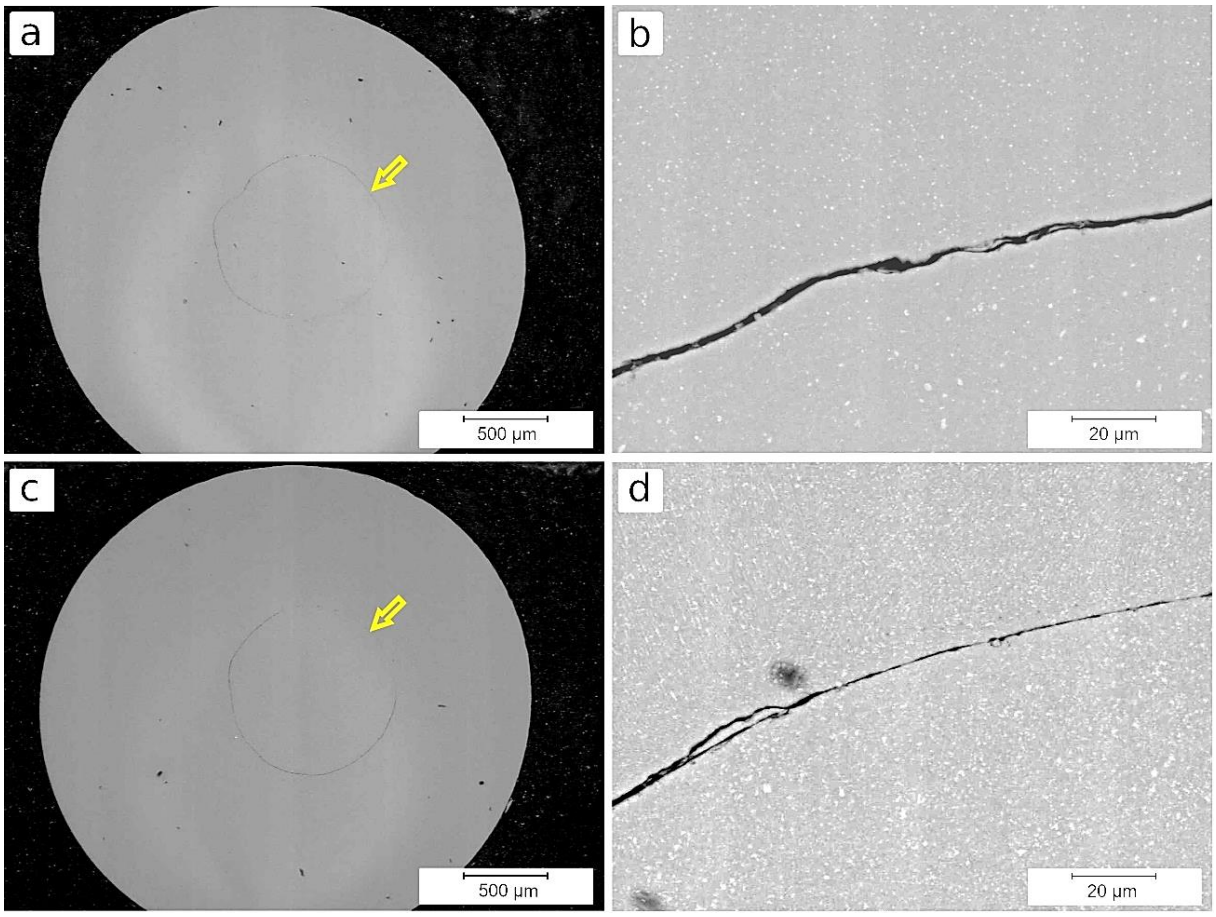

Fig. 1. Cross-section of the Al-0.5Fe CAAW (a,b) and Al-1.7Fe CAAW (c,d), SEM BSE. Yellow arrows point at the core of the CAAW

core-sleeve boundary interface are the consequence of the drilling a hole in the initial billet, and surface quality depends on the drillling method and tool. Still, for the better CAAW performance improving the contact surface quality may be recommended. Nevertheless, this doesn't affect the performance of the CAAWs, since the fraction of the core in both alloys is 10 ± 1 %. Cross-section of the wires shows deviation from the circular shape, although it also doesn't affect the overall CAAW performance.

Al-1.7Fe CAAW (Fig. 1(c,d)) demonstrates notably higher, compared to Al-0.5Fe CAAW (Fig. 1(a,b)), fraction of the second phase particles, being of the Al_xFe_y nature, most probably Al_2Fe or Al_6Fe [22,23]. Figure 1 also demonstrates the core-sleeve boundary of the CAAWs. The applied pressure and temperature were clearly not enough to form a continuous bond between materials, leaving the gap from 30 to 300 nm in width (Fig. 1(b,d)). In works related to ARB it is stated that the deformation value at each pass should be at least 50 % in order to mechanically bond the contact materials, while in this case it was notably lower [12]. It would be promising to increase the deformation value of each drawing pass or even include the extrusion stage in order to close the gap on the core-sleeve boundary. Based on the previous study it is safe to say that annealing at 230 °C didn't affect the core-sleeve boundary [24].

Table 2 contains the data of the mechanical and physical properties of the composite all-aluminium wires (CAAWs), as well as data for the all-aluminium wires (AAWs).

Table 2. Physical and mechanical properties of the CAAW

Sample	Electrical conductivity		σ_{YS}		σ_{UTS}		δ	
	Value, % IACS	Δ, %	Value, MPa	Δ, %	Value, MPa	Δ, %	Value, %	Δ, %
Al-0.5Fe								
CAAW	57.2±0.2	2.1	170 ± 3	0.0	201 ± 1	1.5	3.7 ± 0.3	30.2
AAW [25]	58.4±0.2		170 ± 12		204 ± 14		5.3 ± 0.3	
CAAW+230 °C, 1 h	58.5±0.2	1.2	168 ± 17	4.0	207 ± 18	3.4	2.2 ± 0.4	47.8
AAW+230 °C, 1 h [25]	59.2±0.2		175 ± 11		200 ±16		4.6 ± 0.4	
Al-1.7Fe								
CAAW	51.5±0.2	0.9	150 ± 22	36.2	293 ± 1	0.7	6.6 ± 0.2	25.8
AAW [25]	52.0±0.2		235 ± 18		295 ± 19		4.9 ± 0.5	
CAAW+230 °C, 1 h	54.4±0.2	2.9	171 ± 21	31.6	260 ± 13	17.4	2.5 ± 0.2	35.9
AAW+230 °C, 1 h [25]	52.8±0.2		250 ± 14		315 ± 17		3.9 ± 0.3	

Table 2 also contains the values of the difference (in percent) in electrical conductivity and mechanical properties between the AAWs and CAAWs in the similar conditions. This information is contained in the Δ columns and is calculated as a value of the AAW subtracted from the values of the CAAW relative to the CAAW values.

In case of Al-0.5Fe alloys the difference in properties between CAAW and AAW is relatively small. Difference in σ_{YS} and σ_{UTS} lies within the error value for both CD and annealed states and could be regarded as insignificant. The Al-0.5Fe CAAW is characterized by lower electrical conductivity compared to the AAW in both states, although this difference decreases after annealing. Since electrical conductivity is sensitive to the structural defects, both on micro- and macroscale, it is natural for the aluminium wire with the core-sleeve boundary to have lower conductivity.

Al-1.7Fe CAAW is characterized by significantly lower, than in Al-1.7Fe AAW σ_{YS} in both CD and annealed states, meaning that the presence of the core-sleeve boundary contributes the faster deformation build-up [26]. In the annealed state CAAW is characterized by higher electrical conductivity and lower ductility compared to the AAW. The effect of decreased ductility in the annealed Al-1.7Fe alloys was documented in previous studies, although the exact mechanism of it is yet not clear [27,28]. One possible explanation could be the annealing-induced change of the texture formed during cold drawing, that could influence the electrical conductivity by 1 % IACS [29,30]. While Al-0.5Fe alloy demonstrates almost complete indifference (with an exception for the ductility) to the presence of the core-sleeve boundary, Al-1.7Fe demonstrates certain amount of sensitivity to the presence of such boundary.

Figure 2 presents the engineering stress-strain curves for the Al-0.5Fe alloy wires (a) and Al-1.7Fe alloy wires (b). The form and the shape of the Al-0.5Fe curves, as well as levels of the σ_{UTS} are very similar. The curves for the Al-1.7Fe are spread more, with the difference in both elongations to failure and σ_{UTS}, supporting the core-sleeve boundary having more significant influence in the Al-1.7Fe alloy rather than Al-0.5Fe. For both Al-0.5Fe and Al-1.7Fe (AAW and CAAW) alloys annealing results in the decrease of the elongation to failure. On Fig. 2(b) it could be seen that AAW to CAAW transition increases the ductility of the Al-1.7Fe alloy wire, which is contrary for the Al-0.5Fe alloy wires. Since

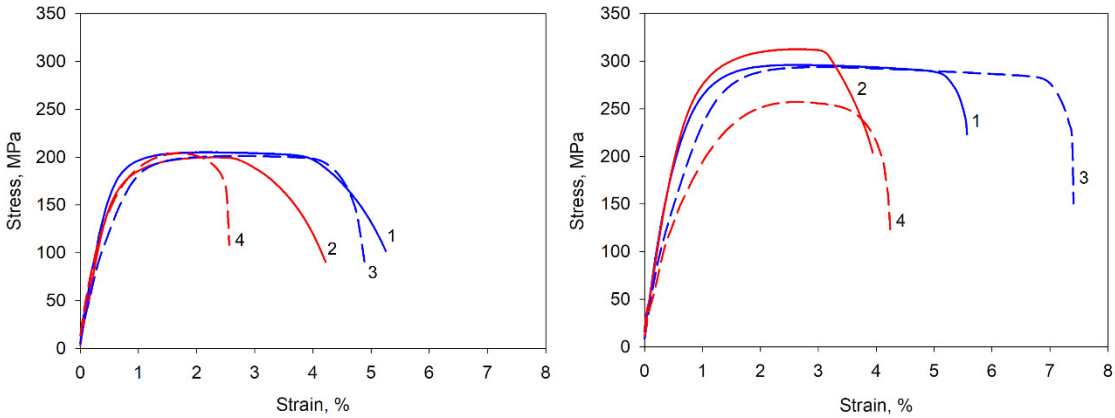

Fig. 2. Engineering stress-strain curves foe the Al-0.5Fe (a) and Al-1.7Fe (b) alloy wires:
1 – AAW in cold-drawn state; 2 - AAW after annealing at 230 °C for 1 h; 3 – CAAW in cold-drawn state;
4 - CAAW after annealing at 230 °C for 1 h

the reason for the different behavior of the AAW and CAAW may as well be attributed to the behavior of their individual components, fractography analysis was conducted.

Figure 3 demonstrates the overview of the fracture images of Al-Fe AAW (a,c) and CAAW (b,d) after tensile tests. Al-0.5Fe AAW demonstrates higher value of relative reduction, which corresponds to higher value of elongation to failure (Table 2). Similar behavior is demonstrated by the sleeve of the CAAWs (Fig. 3(b,d)).

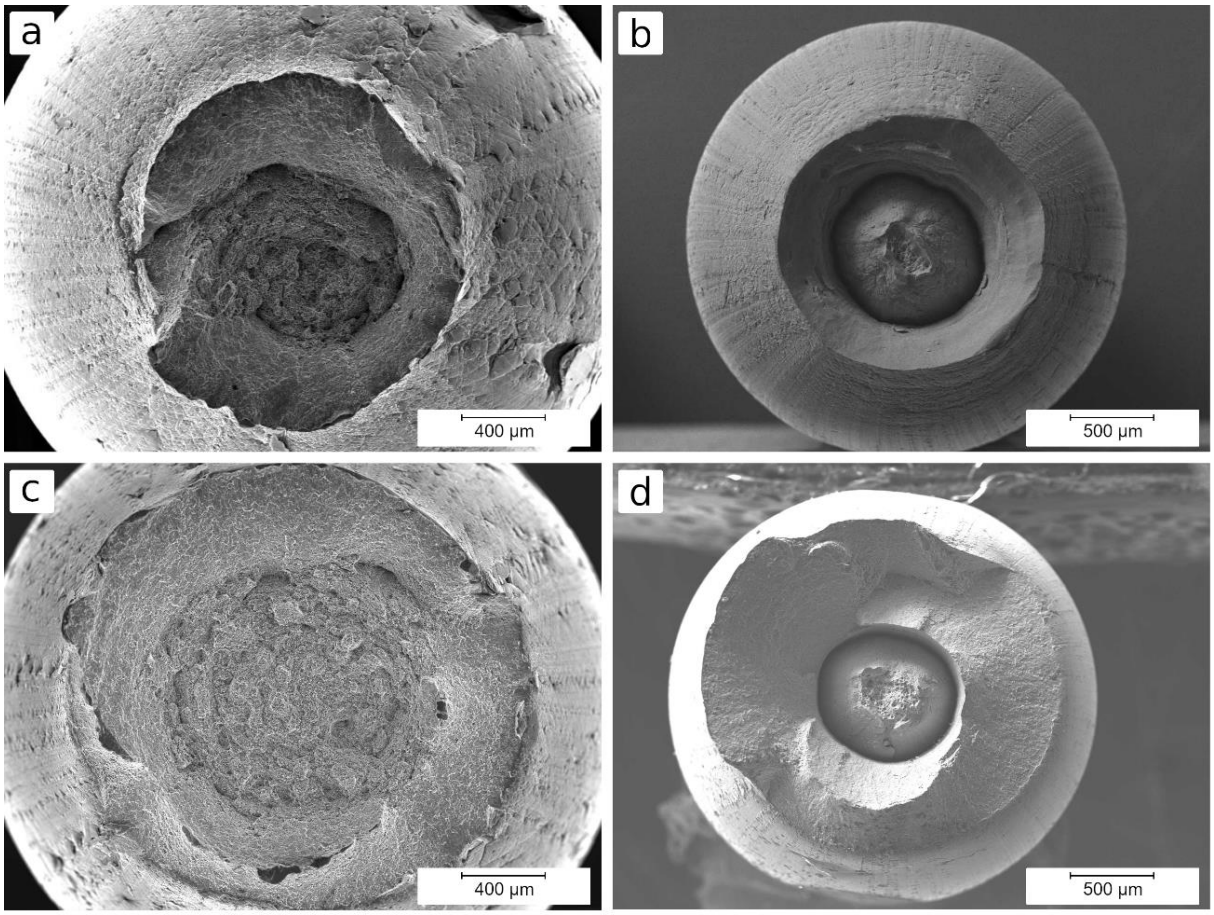

Fig. 3. Fractographic images of the (a) Al-0.5Fe AAW, (b) Al-0.5Fe CAAW, (c) Al-1.7Fe AAW and (d)Al-1.7Fe CAAW, SEM

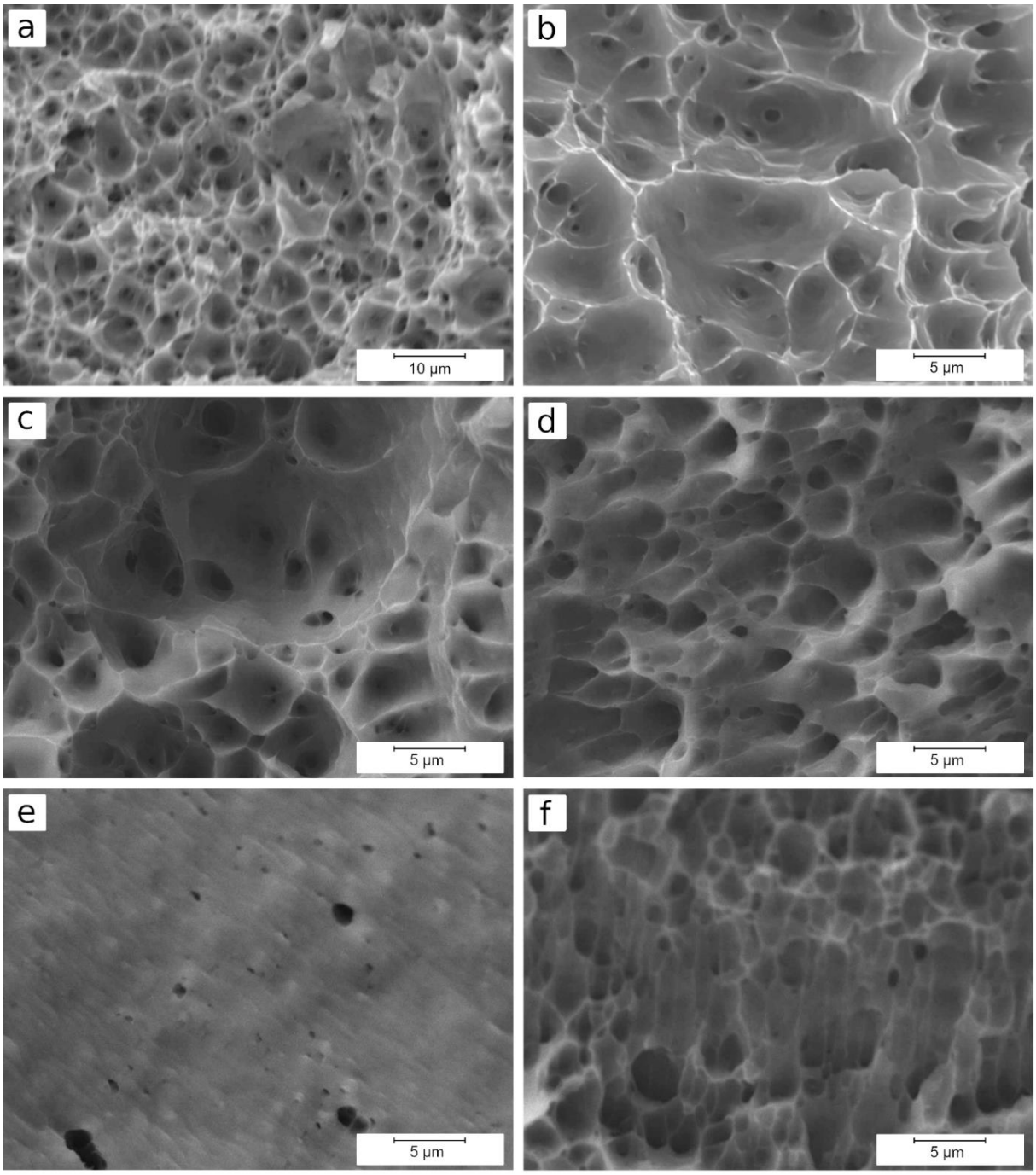

Fig. 4. Fractographic images of the Al-0.5Fe alloy wires in the initial state (a,c,e) and after annealing at 230 °C for 1 h (b, d, f), SEM: (a,b) AAW center, (c,d) CAAW core, (e,f) CAAW sleeve

Figure 4 demonstartes the fracture surface of the Al-0.5Fe wires in cold-drawn state and after annealing. The fracture of the Al-0.5Fe AAW (Fig. 4(a)), as well as fracture of the core (Fig. 4(c)) and sleeve (Fig. 4(e)) of the Al-0.5Fe CAAW are ductile in nature. Both Al-0.5Fe AAW and core of the Al-0.5Fe CAAW are characterized by the dimples, notably smaller in Al-0.5Fe AAW. The presence of the core-sleeve interfcae in the Al-0.5Fe CAAW may cause the uneven deformation within the core and sleeve of the composite wire, resulting in lowed deformation value of the core material and thus larger dimple size. The fracture surface of the Al-0.5Fe CAAW may support this hypothesis – the dimples in this region are the smallest among all three, and the fracture has smoothened surface,

probably caused by the flow of the metal during the last stage of the composite wire fraction – the core in Al-0.5Fe CAAW fractured first, the sleeve fractured later.

Annealing of the Al-0.5Fe AAW resulted in slightly lower, within the error range, ductility, with the same character of the fracture – ductile (Fig. 4(b,d,f)) for the AAW, CAAW core and CCAW sleeve, respectively). The size of the dimples is comparable to ones in the cold-drawn AAW. Annealing seem to have no effect on the core of the Al-0.5Fe CAAW, while the size and the character of the dimples in the sleeve have changed – the became larger and more pronounced. Since it was assumed that the sleeve of the CAAW accumulated higher deformation value, it is safe to asssume that the sleeve structure experienced recovery and\or recrystallization, resulting in the different dimple morphology.

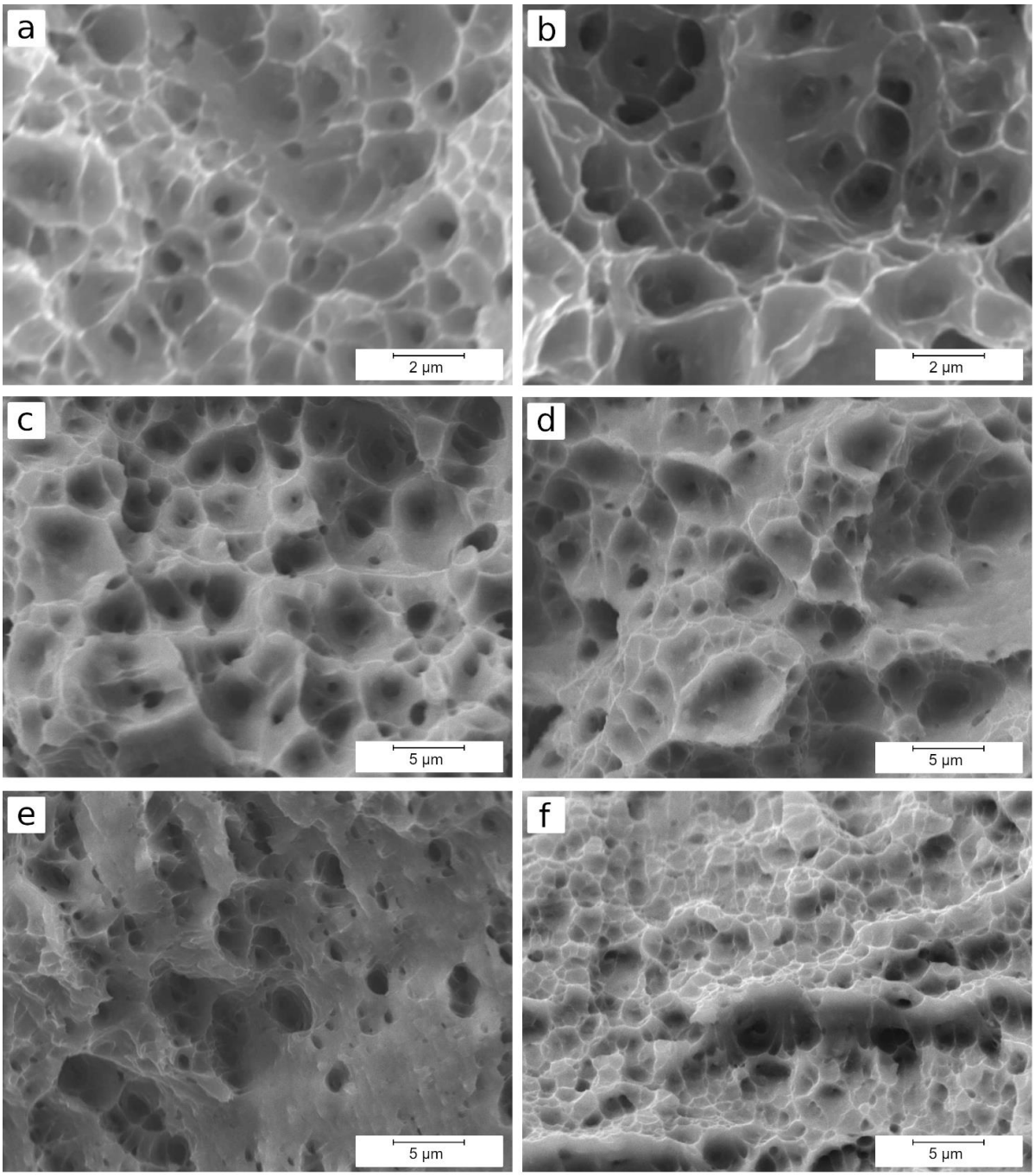

Fig. 5. Fractographic images of the Al-1.7Fe alloy wires in the initial state (a,c,e) and after annealing at 230 °C for 1 h (b,d,f), SEM: (a,b) AAW center, (c,d) CAAW core, (e,f) CAAW sleeve

Figure 5 demonstartes the fracture surface of the Al-1.7Fe wires in CD state and after annealing. The fracture of the Al-1.7Fe AAW (Fig. 4(a)), as well as fracture of the core (Fig. 4(c)) and sleeve (Fig. 4(e)) of the Al-1.7Fe CAAW are ductile in nature, similar to the Al-0.5Fe wires.

The dimple size in the Al-1.7Fe AAW is notably lower than that of Al-1.7Fe CAAW core or sleeve. It would appear that the core-sleeve boundary interface has accomodated certain amount of deformation that went directly into the material structure in AAW. Thus, less deformed core and sleeve of the Al-1.7Fe CAAW allowed higher degree of deformation before fracture and conaeequently ductilty (Fig. 2(b)).

Annealing of Al-1.7Fe wires doesn't demonstrate notable effect on the type of the AAW fracture. The dimple size remains the same. In the Al-1.7Fe CAAW influence of the annealing is similar to one in Al-0.5Fe CAAW – the form and size of simples in the core remains the same, while the sleeve demonstrates changes (in case of Al-1.7Fe CAAW - diminishing) in dimple size. This effet is most probably connected to higher accumulated deformation in the Al-1.7Fe CAAW sleeve and is manifested by increased ductility of the annealed CAAW (Fig. 2(b)).

Conclusions

In this study the core-sleeve boundary interface was introduced into the Al-0.5Fe and Al-1.7Fe alloys wires. The fraction of the core in the cross section was 10 %, and the length of the interface is 30% of the outer wire diameter. Composite all-aluminium wires (CAAW) were subjected to annealing at 230 °C for 1 h. Following conclusions were drawn:
1. In this particular case the gap width ranged from nanometer scale up to 300 nm. Presene of the core-sleeve boundary interface mildly affects the mechanical strength and electrical conductivity of the CAAW. This effect almost absent in Al-0.5Fe alloy wires, and more prominent in the Al-1.7Fe wires. Since amount of the Fe determines the intensity of the structural defects in Al-Fe alloys, the core-sleeve boundary interface impact in composite wires depends on the sensitivity of a given alloy to deformation and heat treatment.
2. It would seem that the presence of the core-sleeve boundary interface attributes to the slower build-up of the structural defects, which is supported by the lower angle of the strain-stress curve elastic region for both Al-0.5Fe and Al-1.7Fe CAAW. This could be due to the fact that core-sleeve boundary interface helps to accomodate some amount of deformation during tensile tests, that otherwise would impact the alloy itself since the pressence of this boundary affect mainly ductility and ultimate tensile strength of the CAAWs.

CRediT authorship contribution statement

Andrey E. Medvedev: writing – review & editing, writing – original draft; **Aygul F. Shaikhulova**: investigation; **Mikhail M. Motkov**: data curation; **Maxim Yu. Murashkin**: conceptualization.

Conflict of interest

The authors declare that they have no conflict of interest.

References

1. Dursun T, Soutis C. Recent developments in advanced aircraft aluminium alloys. *Mater Des*. 2014;56: 862–871.
2. Beygelzimer Y, Kulagin R, Estrin Y. Severe plastic deformation as a way to produce architectured materials. In: Estrin Y, Bréchet Y, Dunlop J, Fratzl P. (eds.) *Architectured Materials in Nature and Engineering. Springer Series in Materials Science, vol 282*. Cham: Springer; 2019, p.231–255.
3. Estrin Y, Krishnamurthy VR, Akleman E. Design of architectured materials based on topological and geometrical interlocking. *Journal of Materials Research and Technology*. 2021;15: 1165–1178.
4. Ragazin A, Aryshenskii E, Aryshenski V, Rasposienko D, Lukyanchuk A, Konovalov S. Effect of Hafnium on the Microstructure Formation during High-Temperature Treatment of High-Magnesium Aluminum Alloys Microalloyed with Scandium and Zirconium. *Phys Mesomech*. 2025;28: 535–546.
5. Soleymani S, Abdollah-Zadeh A, Alidokht SA. Microstructural and tribological properties of ultra fine grained hybrid composite produced by friction stir processing. *Materials Physics and Mechanics*. 2013;17(1): 6–10.
6. Kalombo RB, Araújo JA, Ferreira JLA, da Silva CRM, Alencar R, Capra AR. Assessment of the fatigue failure of an All Aluminium Alloy Cable (AAAC) for a 230 kV transmission line in the Center-West of Brazil. *Eng Fail Anal*. 2016;61: 77–87.
7. Zhang J, Li X, Zhao L, Li Z, Wang S, Yao P, Dai P. Analysis of Temperature Rise Characteristics and Fatigue Damage Degree of ACSR Broken Strand. *Energy Engineering*. 2023;120(3): 617–631.
8. Udensi SC, Anioke AU. An in-depth investigation of factors responsible for optimal performance in stir-cast Aluminum metal matrix composites. *Sci Afr*. 2024;26: e02452.
9. Parvizi P, Jalilian M, Dearn KD. Beyond traditional conductors: Aluminium conductor composite core's role in next-generation high temperature-low sag technologies – A review. *Electric Power Systems Research*. 2025;239: 111251.
10. Huang Y, Liu Y, Xiao Z, Huang Y. A trade-off between mechanical strength and electrical conductivity of Al–Zn–Mg–Cu alloy via Ag alloying and retrogression re-aging heat treatment. *Materials Science and Engineering: A*. 2023;880: 145230.
11. Yang C, Masquellier N, Gandiolle C, Sauvage X. Multifunctional properties of composition graded Al wires. *Scr Mater* 2020;189: 21–24.
12. Yousefi Mehr V, Toroghinejad MR. On the texture evolution of aluminum-based composites manufactured by ARB process: a review. *Journal of Materials Research and Technology*. 2022;21: 1095–1109.
13. Mei XM, Mei QS, Li JY, Li CL, Wan L, Chen F, Chen ZH, Xu T, Wang YC, Tan YY. Solid-state alloying of Al-Mg alloys by accumulative roll-bonding: Microstructure and properties. *J Mater Sci Technol*. 2022;125: 238–251.
14. Satjabut P, Uthaisangsuk V. Effects of Initial Microstructure on Mechanical Properties of AA1050/AA2024 Laminated Metal Composite Fabricated by Accumulative Roll Bonding Process. *Metals and Materials International*. 2025;31: 1460–1478.
15. Toroghinejad MR, Jamaati R, Dutkiewicz J, Szpunar JA. Investigation of nanostructured aluminum/copper composite produced by accumulative roll bonding and folding process. *Mater Des*. 2013;51: 274–279.
16. Sajjadi Nikoo S, Qods F, Yousefieh M. Microstructure evolution and mechanical properties of the AA2024/AA5083 ultra-fine grained composite fabricated via accumulative roll bonding (ARB) method. *J Mater Res*. 2023;38: 2519–2533.
17. Gashti SO, Fattah-Alhosseini A, Mazaheri Y, Keshavarz MK. Effects of grain size and dislocation density on strain hardening behavior of ultrafine grained AA1050 processed by accumulative roll bonding. *J Alloys Compd*. 2016;658: 854–861.
18. Li J, Nian Y, Liu X, Zong Y, Tang X, Zhang C, Zhang L. Application of electromagnetic metallurgy in continuous casting: A review. *Progress in Natural Science: Materials International*. 2024;34(1): 1–11.
19. International Electrotechnical Commission. IEC 62641:2023. *Conductors for overhead lines - Aluminium and aluminium alloy wires for concentric lay stranded conductors*. IEC; 2023.
20. ASTM International. ASTM E8/E8M-22. *Tension Testing of Metallic Materials*. ASTM; 2022.
21. Lee JE, Bae DH, Chung WS, Kim KH, Lee JH, Cho YR. Effects of annealing on the mechanical and interface properties of stainless steel/aluminum/copper clad-metal sheets. *J Mater Process Technol*. 2007;187–188: 546–549.
22. Saller BD, Hu T, Ma K, Kurmanaeva L, Lavernia EJ, Schoenung JM. A comparative analysis of solubility, segregation, and phase formation in atomized and cryomilled Al–Fe alloy powders. *J Mater Sci*. 2015;50: 4683–4697.
23. Saller BD, Sha G, Yang LM, Liu F, Ringer SP, Schoenung JM. Iron in solution with aluminum matrix after non-equilibrium processing: an atom probe tomography study. *Philos Mag Lett*. 2017;97(3): 118–124.

24. Medvedev AE, Zhukova OO, Khafizova ED, Motkov MM, Murashkin MYu. Composite Coaxial Wire Produced from Electromagnetically Cast Al–Fe Alloys. *Russian Journal of Non-Ferrous Metals*. 2024;65: 307–317.
25. Medvedev A, Zhukova O, Fedotova D, Murashkin M. The mechanical properties, electrical conductivity, and thermal stability of a wire made of Al–Fe alloys produced by casting into an electromagnetic crystallizer. *Frontier Materials & Technologies*. 2022;3–1: 96–105.
26. Selyutina NS. Influence of Mg and Cu on the dynamic yield stress of aluminium alloys. *Materials Physics and Mechanics*. 2021;47(3): 408–415.
27. Medvedev A, Murashkin M, Enikeev N, Medvedev E, Sauvage X. Influence of morphology of intermetallic particles on the microstructure and properties evolution in severely deformed al-fe alloys. *Metals*. 2021;11(5): 815.
28. Medvedev A, Zhukova O, Enikeev N, Kazykhanov V, Timofeev V, Murashkin M. The Effect of Casting Technique and Severe Straining on the Microstructure, Electrical Conductivity, Mechanical Properties and Thermal Stability of the Al–1.7 wt. % Fe Alloy. *Materials*. 2023;16(8): 3067.
29. Hou JP, Li R, Wang Q, Yu HY, Zhang ZJ, Chen QY, Ma H, Wu XM, Li XW, Zhang ZF. Breaking the trade-off relation of strength and electrical conductivity in pure Al wire by controlling texture and grain boundary. *J Alloys Compd*. 2018;769: 96–109.
30. Wang S, Hou JP, Zhang ZJ, Gong BS, Qu Z, Wang H, Zhou XH, Jiang HC, Wang Q, Li XW, Zhang ZF. Grain design in ultra-fine Al wire with remarkable combination of strength and conductivity: Ultra-fine-long grains with super strong 〈111〉 texture. *Scr Mater*. 2024;238: 115746.

MATERIALS PHYSICS AND MECHANICS RESEARCH ARTICLE

Submitted: September 1, 2025 **Revised: October 28, 2025** **Accepted: November 12, 2025**

Effect of welding parameters and response surface method based on prediction of maximum temperature generated during friction stir welding of AA3003

A. Belaribi [1], I. Chekalil [2], A. Miloudi [1]✉, M.A. Ben Messaoud [1], A. Zoukel [3]

[1] University of Djillali Liabes, Sidi Bel Abbès, Algeria

[2] King Fahd University of Petroleum and Minerals, Dhahran, Saudi-Arabia

[3] University of Laghouat, Laghouat, Algeria

✉ miloudidz@yahoo.fr

ABSTRACT

Friction stir welding generates significant temperature increases, leading to microstructural changes that influence the mechanical properties of the material. Temperature control is therefore essential to ensure the quality of the welded joint. This study aims to model and predict the maximum temperature generated during the friction stir welding of aluminum alloy 3003, based on three key operating parameters: rotation speed, feed rate, and tool inclination angle. The response surface method was used to develop a robust predictive model and evaluate the individual and combined effects of these parameters on the thermal response. The results reveal that the most influential parameters are, in order, rotation speed, tool inclination angle, and feed rate. They also indicate that the maximum temperature increases significantly with rotational speed and angle of inclination. In contrast, it decreases as the feed rate increases. The model obtained has excellent predictive power, validated by a low root mean square error of 4.41 °C and a coefficient of determination R^2 of 0.972.

KEYWORDS

FSW • T_{max} • RSM • prediction • rotation speed

Citation: Belaribi A, Chekalil I, Miloudi A, Ben Messaoud MA, Zoukel A. Effect of welding parameters and response surface method based on prediction of maximum temperature generated during friction stir welding of AA3003. *Materials Physics and Mechanics*. 2025;53(6): 201–212.
http://dx.doi.org/10.18149/MPM.5362025_15

Introduction

Since the advent of the friction stir welding (FSW) process in 1991 [1], much research has been carried out in both academic and industrial fields for its application in the aerospace sector, and its extension to other sectors and application on other metallic materials such as steel, magnesium and its alloys. In addition to welding, the friction stir welding process has been successfully used to repair cracks [2] and improve material behavior by modifying the microstructure [1–4]. Similarly, FSW welds have significantly higher fatigue strength than other welding techniques [5]. FSW welded assemblies have very good mechanical strength, averaging 80 % of that of the base material [6]. Moreover, the microstructure of the alloys remains little changed compared to liquid phase welding techniques.

This technique uses a non-consumable rotating tool to generate frictional heat, softening materials without melting and producing high-quality, defect-free welds [7–10]. Despite these advantages, achieving better joint quality remains a major challenge. Several

methods have been explored to improve the performance of FSW joints: Underwater friction stir welding (UWFSW) has been applied to AA5083 alloy to improve its mechanical and corrosion resistance [11,12]. At the same time, heat treatments have been used to optimize AA2014-AA7075 heterogeneous joints [13]. These two approaches have resulted in tensile strengths and hardnesses exceeding those of conventional processes, highlighting the crucial role of thermal control on the final performance of joints.

Peak temperature in the weld zone significantly affects weld quality, as excessive temperatures can dissolve precipitates in precipitation-hardened alloys, leading to reduced mechanical properties [14,15]. Typical FSW peak temperatures for aluminum alloys range from 200–550 °C depends on process parameters. The temperature rise during FSW welding leads to microstructural changes that influence the material properties. Temperature control is therefore essential to guarantee the quality of the welded joint. Accurate prediction of this temperature ensures optimal weld strength and minimizes defects [14].

Numerous studies have focused on predicting the rate of heat generation and maximum temperature during friction stir welding (FSW), intending to assess the quality of the resulting joints. Khalifa et al. [16] predicted the FSW temperature of 6061 T6 aluminum. They showed that welding speed is responsible for 63 % of the temperature variation. Selvaraj [17] used a regression model to predict peak temperature during friction stir welding of steel. The results showed that the peak temperature reached is related to rotational speed (*N*) and inversely proportional to welding speed (*S*).

Using finite element modeling, Meyghani et al. [18] investigated the influence of the friction coefficient on thermal behavior during friction stir welding (FSW). Their results showed that the temperature reached during the process is directly impacted by the value of this coefficient. In the same context, Palanivel et al. [19] developed a finite element (FE) model to predict temperature distribution during friction stir welding (FSW). The results show that simulated values deviate from experimental measurements by around 3 %.

Chamoret et al. [20] have developed a 3D nonlinear thermal model to simulate the thermal history during FSW welding of AISI 316L. The simulated temperature distributions were compared with experimental values and showed good agreement.

The studies presented above demonstrate that welding speed has a significant impact on heat generation and peak temperature during friction stir welding (FSW), while the effect of tool penetration and the interaction between these parameters has not been sufficiently investigated.

Other studies suggest that rotation speed most significantly affects peak temperature during FSW, followed by welding speed and axial force. Increasing rotational speed boosts frictional heat generation, raising peak temperatures, while higher welding speeds decrease heat input per unit length, leading to lower temperatures. For example, in FSW of AA6061, Dadi et al. [21] and Meyghani et al. [22] reported peak temperatures ranging from approximately 300 to 467.4 °C under different process parameters. Specifically, a minimum temperature of about 300 °C was observed at 600 rpm, 130 mm/min, and a constant axial force of 3 kN, while the maximum of 467.4 °C was reached at 1200 rpm, 70 mm/min, and a constant axial force of 7 kN. These findings emphasize the key role of rotational speed in controlling temperature when axial force is systematically varied or kept constant within the experimental setup.

Saravanakumar et al. [23] examined the influence of the rotation speed/feed speed ratio (*N*/*S*) on weld quality. Their results showed that an increase in this ratio led to an increase in the maximum temperature during welding. This increase in temperature caused the core and core zone to widen, leading to a reduction in joint hardness.

Response surface methodology (RSM) is the most widely used soft computing technique for modeling the performance parameters of the FSW process. It develops second-degree polynomial regression equations to predict these parameters [24]. RSM has been crucial in estimating the performance of aluminum alloy welding, including yield strength [25], elongation [26,27], weld joint hardness [28], ultimate tensile strength (UTS) [26,29–31], among others. For AA6061-T6, a thermo-mechanical model using RSM predicted a peak temperature of ~ 453 °C under stable welding conditions, validated with experimental data [32].

The AA3003 alloy is frequently used in oil storage and gasoline transportation systems, heat exchangers, and marine equipment. Its light weight and good corrosion resistance make it a material of choice for manufacturing components such as automotive evaporators and radiators.

Numerous studies have explored the effect of welding parameters on the mechanical strength of AA3003 alloy joints welded by FSW. Chekalil and Miloudi [33] studied the effect of rotation speed, feed rate, and tool inclination angle on the mechanical strength of friction stir-welded (FSW) joints in AA3003 alloy. However, no study has yet evaluated the combined effect of these parameters on the thermal evolution during welding of this alloy. Continuing this work, we maintained the same welding conditions to analyze their influence on the temperature evolution during the FSW process.

In this article, the effect of three main parameters, namely the tool rotation speed (*N*), the feed rate (*S*), and the angle of inclination (θ), on the maximum temperature generated during friction stir welding of AA 3003 aluminum was investigated using the response surface method (RSM) with 27 experiments in the factorial design. The equation obtained makes it possible to predict the maximum temperature based on these parameters.

Methods

The friction stir welding tool was manufactured from X210Cr12 steel with a breaking strength of σ_m = 870 MPa, selected based on preliminary tests conducted by Chekalil and Miloudi [33] on the tool itself to validate the design. The chosen geometry is similar to that of a conical pin, with the following dimensions: d = 5 mm, D = 6.8 mm, and length = 1.7 mm. It features a concave shoulder with a 3° angle and a diameter of 19.5 mm.

Two AA3003 aluminum alloy plates with dimensions 210 × 110 × 2 mm^3 were butt-welded along the rolling direction (RD) in a single pass using friction stir welding (FSW). The mechanical characteristics of aluminum alloy 3003 were determined by tensile tests carried out on an INSTRON 8500 servo-hydraulic machine with a capacity of ± 100 kN. The rational curve for the alloy is shown in Fig. 1. This test was used to determine the main mechanical characteristics of the base material, which are listed in Table 1.

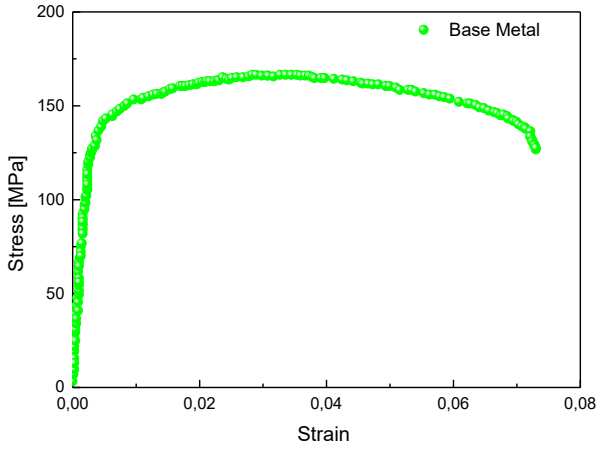

Fig. 1. Rational curves of the tensile test for aluminium alloy 3003

Table 1. Mechanical properties of the material before welding (σ_e is yield stress, σ_U is ultimate tensile strength, σ_m is rupture strength, *A* is elongation, *E* is the Young modulus)

Microhardness, HV	σ_e, MPa	σ_U, MPa	σ_m, MPa	*A*, %	*E*, GPa
51.0	130.0	160.0	127.0	5.6	60.0

Chekalil et al. [34] characterized the different microstructural zones of an AA 3003 FSW joint under the same welding conditions. This analysis was carried out under optimal welding conditions (*N* = 1400 rpm, *S* = 400 mm/min, and θ = 1.5°).

The chemical composition of the alloy was determined by A COXEM scanning electron microscope (SEM) with 15Kv voltage and x2000 magnification. Table 2 represents the chemical composition of the material used.

Table 2. Chemical composition of aluminum alloy 3003

Element	Al	Mn	Si	Fe	Cu	Ti	Zn	Mg	Cr
%	96.7	1.3	0.9	0.9	0.13	0.1	0.03	0	0

We note that the welded joint presents a very heterogeneous microstructure. Indeed, the thermal gradient and the deformation gradient imply a gradient of the microstructures across the weld. The micrographs observation in the direction orthogonal to the welding direction allowed us to distinguish 4 main zones. The core is located in the center of the weld. In this zone the grain size is the finest with an equi-axial shape thanks to the deformation generated by the pin. The ZATM (thermo-mechanically affected zone) is close to the core, reveals elongated grains with a relatively large size. This reformulation is caused by the flow of materials around the pin and below the shoulder. The ZAT (thermal affected zone) is characterized by large grains with an equi-axial geometry. This coarsening is the result of the heat flow generated by the tool. Finally, the base metal is recrystallized and presents an equi-axial grain structure.

The design of experiment was used for the statistical design of the tests. The three process parameters considered were rotation speed N (rpm), feed rate S (mm/min), and tilt angle θ (°). Table 3 below shows the values of each parameter for each level. The maximum temperature T_{max} (°C) reached during welding was chosen as the main response variable to measure the thermal impact of the process.

Table 3. Parameter values for each level

Parameter	Level 1	Level 2	Level 3
N, rpm	1000	1500	2000
S, mm/min	100	200	400
θ, °	0.5	1.5	2.5

The FSW welding operation is carried out in conjunction with a thermal characterization procedure, which involves the measurement of temperatures on both sides of the joint: advance (AS) and retract (RS), temperature evolution was monitored using Type-K thermocouples with a temperature capability ranging from -40 to 1200 °C and connected to a thermal recorder, which will be installed on the sheets, at a distance of 2 and 4 mm from the center of the joint, using Thermigrease TG 20033 thermal paste to ensure optimum heat transfer. The positioning of the thermocouples and sampling are illustrated in Fig. 2.

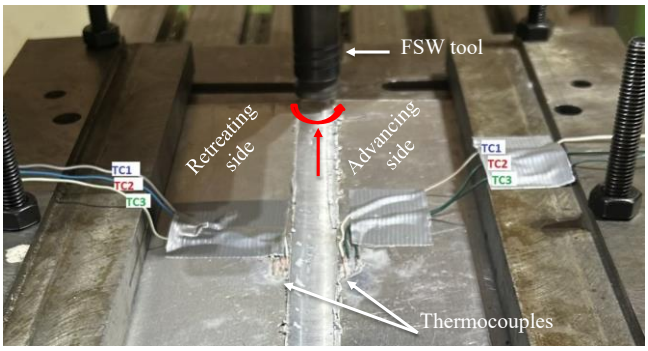

Fig. 2. Thermocouple and sampling positioning

Figure 3 illustrates the evolution of the thermal cycle in the forward (AS) and reverse (RS) directions. Examination of this figure reveals a rapid increase in temperature as the tool approaches the thermocouple, and a slow decrease as it moves away from it. This evolution is observed independently of the position of the thermocouple. In addition, it has been observed that the temperature gradient intensifies significantly the closer one gets to the center of the weld. In addition, it was found that temperatures measured on the advancing side are slightly higher than those on the retreating side, with a difference of up to a few ten degrees.

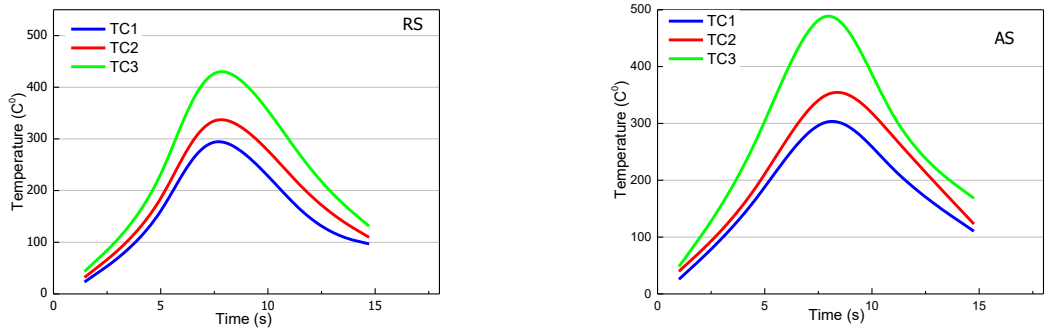

(a) (b)

Fig. 3. Temperature evolution during FSW of alloy 3003 on the advancing (a) and retreating sides (b) at several distances from the weld center

This thermal asymmetry between the advancing (AS) and retreating (RS) sides is a well-known feature of the FSW process [35], associated with the direction of rotation of the tool relative to the workpiece feed. This increased heat dissipation manifests itself mainly on the AS side. All the maximum temperatures analyzed in the rest of this study correspond to measurements taken on the feed side, which is the most thermally stressed zone. The experiment matrix was determined by MODDE 5.0 software, following a 3^3 full factorial design (27 trials). The results of the 27 tests are presented in Table 4.

Table 4. Experimental design results.

N°	N, rpm	S, mm/min	θ, °	T_{max}, °C
1	1000	200	0,5	207
2	1500	200	0,5	242
3	2000	200	0,5	323
4	1000	300	0,5	198
5	1500	300	0,5	221
6	2000	300	0,5	274
7	1000	400	0,5	184
8	1500	400	0,5	200
9	2000	400	0,5	263
10	1000	200	1,5	216
11	1500	200	1,5	254
12	2000	200	1,5	310
13	1000	300	1,5	203
14	1500	300	1,5	239
15	2000	300	1,5	282
16	1000	400	1,5	194
17	1500	400	1,5	213
18	2000	400	1,5	260
19	1000	200	2,5	295
20	1500	200	2,5	342
21	2000	200	2,5	397
22	1000	300	2,5	236
23	1500	300	2,5	300
24	2000	300	2,5	366
25	1000	400	2,5	216
26	1500	400	2,5	272
27	2000	400	2,5	316

Results and Discussion

The polynomial mathematical model developed for optimizing the maximum temperature during FSW welding is a second-degree model of the form:

$$y = a_0 + \sum_{i=1}^{3} a_i x_i + \sum_{1 \le j \le 3} a_{ij} x_j + \sum_{i=1}^{3} a_{ii} x_i^2 + e \quad , \qquad (1)$$

where a_0 is the predicted response value at the center of the experimental range, a_i represents the effect of the factor x_i, and a_{ij} represents the interaction between the factor x_i and x_j.

The mathematical model developed establishes a relationship between the input parameters (N, S and θ) and the output variable (T_{max}). To calculate the model coefficients, a regression method based on the least-squares criterion is used. The

mathematical model proposed by MODDE 5.0 is as follows: $T_{max} = 3{,}366664 \times 10^{-5} \times \times N^2 - 0.000111667 \times N \times S + 0.01016668 \times N \times \theta + 0{,}01080576 \times N + +0.000241664 \times S^2 - 0.0875002 \times S \times \theta - 0.1062476 \times S + 27.0833 \times \theta^2 - -35.36096 \times \theta + 212.270165$.

The values of the coefficients associated with the maximum welding temperature parameters in the mathematical model show the degree of influence of each factor. Model (1) was used to predict the evolution of T_{max} as a function of the input parameters (N, S and θ) as shown in Fig. 4 below, where the central curves represent the predicted values, and the other two curves show the 95 % confidence interval of the predicted response.

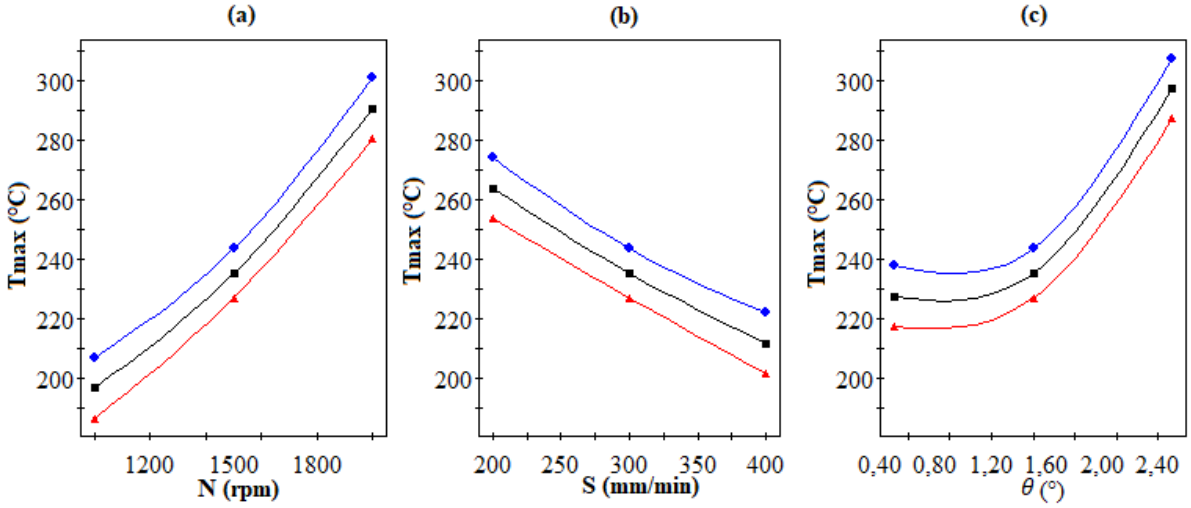

Fig. 4. Evolution of predicted T_{max} as a function of welding parameters

Analysis of Fig. 4(a) suggests that an increase in rotation speed N leads to a sharp rise in T_{max}. Indeed, a 100 % increase in rotational speed leads to an increase of around 155 % in T_{max}. This temperature is highest when the speed is equal to 2000 rpm. On the other hand, it is minimal for low values of N. This correlation can be explained by the fact that higher rotational speeds cause greater mechanical deformation and generate more heat through friction. This heating reduces the mechanical strength of the alloys and increases their ductility.

Figure 4(c) illustrates the effect of inclination angle on T_{max}. It can be clearly seen that T_{max} is constant in the interval between 0.5° and 1.5°, after which T_{max} increases with increasing θ. The maximum value of T_{max} is obtained at an angle of 2.5°. This inclination increases the force applied to the trailing edge of the tool, which contributes to raising the temperature.

Concerning the impact of feed speed, Fig. 4(b) shows that as S increases, T_{max} decreases. A 100 % increase in feed speed results in an 18 % decrease in maximum temperature. Furthermore, it can be observed that the temperature is lowest for extreme values of S, whereas T_{max} is recorded for low values S, which is contrary to the results previously published by Mimmi et al. [36]. In fact, a low feed rate increases contact time and heat input, resulting in more intense and prolonged heating. This heat is essential

to reach the optimum plasticity temperature, which allows complete plastic flow of the material and eliminates critical interface defects such as kissing bonds.

In this stage of the analysis, we expand our comments by considering the interaction between two factors while keeping the third constant. The response variation of T_{max} is visualized as Iso curves in Fig. 5.

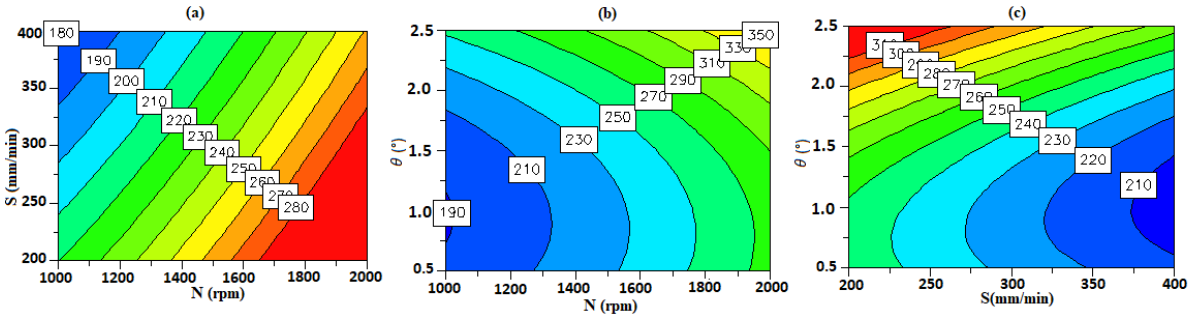

Fig. 5. Prediction of T_{max} as a response to two factors interaction

Figure 5(a) shows the effect of the two factors S and N acting simultaneously on T_{max}, moving from their minimum to their maximum values, while the third factor (θ) is kept constant. Analysis of the graph in this figure suggests that as N increases, T_{max} also increases until it reaches the maximum value of 280 °C, while S lies between 200 and 320 mm/min. On the other hand, low T_{max} values are recorded for low N values around 1000 rpm and high S values between 340 and 400 mm/min.

Concerning the impact of rotation speed and tilt angle on T_{max}, Fig. 5(b) shows that as N increases, T_{max} rises to reach a maximum value of 350 °C. It can also be seen that T_{max} is at its highest for extreme values of θ. On the other hand, low values of T_{max} are recorded for low values of N and θ; they are recorded for values of N between 1000 and 1300 rpm, and θ between 0.5 and 1.2°.

Figure 5(c) illustrates the variation of T_{max} as a function of S and θ. Analysis of this curve shows that maximum temperatures are reached at a feed speed of between 200 and 260 mm/min and a rotation angle of between 2.2 and 2.5°. On the other hand, low values are reached at high feed speeds and low rotation angles, in the range [380–400 mm/min] and [2.2–2.5°], respectively. Consequently, it can be concluded from this analysis that a maximum value of T_{max} is obtained for a value of N between 1650 and 2000 rpm, while keeping the value of S constant between 340 and 400 mm/min.

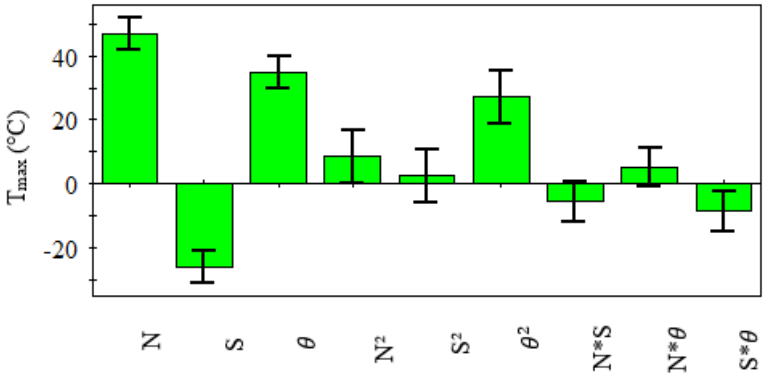

Fig. 6. Parameters with the greatest influence on T_{max}

In order to identify the parameters that have the greatest influence on the maximum temperature generated during welding, an analysis of variance (ANOVA) was performed based on the model established using the response surface methodology (RSM). This approach allows for a quantitative assessment of the individual impact of each factor, as well as their interaction and quadratic effects. The results of this analysis are summarized in Fig. 6, which highlights the relative contributions of the different terms in the model.

Statistical analysis has shown that the most influential parameter is rotational speed, while tilt angle is less important, and feed rate has the least influence. In other parts, the model coefficients allow us to evaluate the interaction effect between the different factors of the process and the response. We note that the factors (N,θ) are the most significant. On the other hand, the factors (N,S) and, as well as (θ,S) are the weakest. We can also note that the effect of the coefficients following S^2 is negligible.

Model validation is a fundamental step in experimental design. It involves comparing the maximum values of the measured temperatures with the responses calculated by the model. As shown in Fig. 7, the more the points are aligned with the first bisector, the higher the descriptive quality of the model. The root-mean-square error (RMSE) is 8.84°C, and the estimates are generally conservative. However, the results obtained by the model are closer to reality.

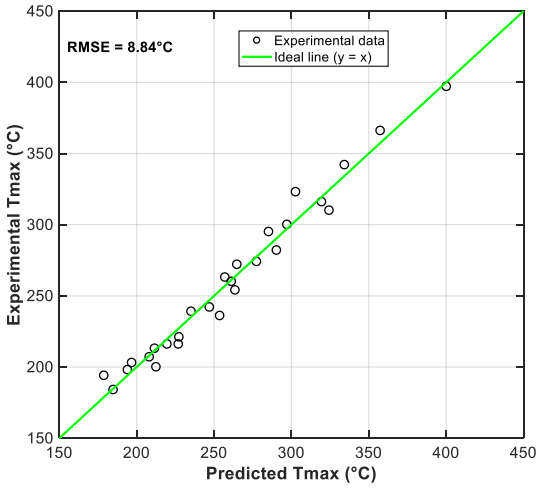

Fig. 7. Model performance

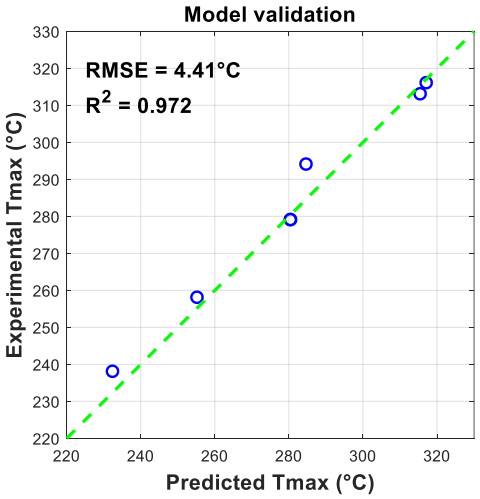

Fig. 8. Model validation

This second step allows us to study the generalization qualities of the proposed model, meaning its predictive behavior. Six additional experimental tests were carried out. The conditions for these tests were randomly selected within the variation ranges of the process parameters. Figure 8 illustrates a comparison between the six experimental results and those predicted by the proposed model.

Figure 8 demonstrates that the results obtained using the proposed model are in agreement with the experimental results, even when compared to those of the RSM model development. The model therefore provides a better prediction of the maximum temperature generated during FSW welding of aluminum alloy AA3003. This is confirmed by a coefficient of determination R^2 of 0.972 and a low root-mean-square error (RMSE) of 4.41 °C.

After studying the generalization of the model, a stage of optimizing these parameters becomes more interesting. This involves determining the optimum values for the tool's rotational speed (*N*), feed rate (*S*), and angle of inclination (θ) (Table 5). These three factors contribute to improving the quality of the FSW joint. These values are obtained by maximizing YS, UTS, and RS [33]. The optimum parameters identified were N = 1.423.93 rpm, S = 400 mm/min, and θ = 1.2885°. This analysis step identifies the maximum temperature during FSW welding of AA 3003 and ensures that it remains compatible with achieving good mechanical performance.

Table 5. T_{max} for optimal process parameters

N, rpm	S, mm/min	θ, °	σ_U, MPa	σ_e, MPa	σ_m, MPa	T_{max}, °C
1087.13	399.997	0.7508	116.771	49.9487	83.489	182.15331
1685.85	200.015	1.3552	122.24	41.8872	91.1325	278,262731
1694.02	200	1.281	122.59	41.7067	91.047	276.562232
1900	400	2.0999	122.156	39.5626	86.7125	277.875911
1423.93	400	1.2885	121.186	55.3134	94.6581	201.440827
1799.9	200	1.4948	122.716	41.8335	89.989	297.858791
1600	400	1.5	118.225	42.2038	94.8028	220.242196

For these optimum values, the corresponding maximum temperature is 201.44 °C. Figure 9 shows the various possible combinations of rotational speeds, feed rates, and angles of rotation to achieve this temperature.

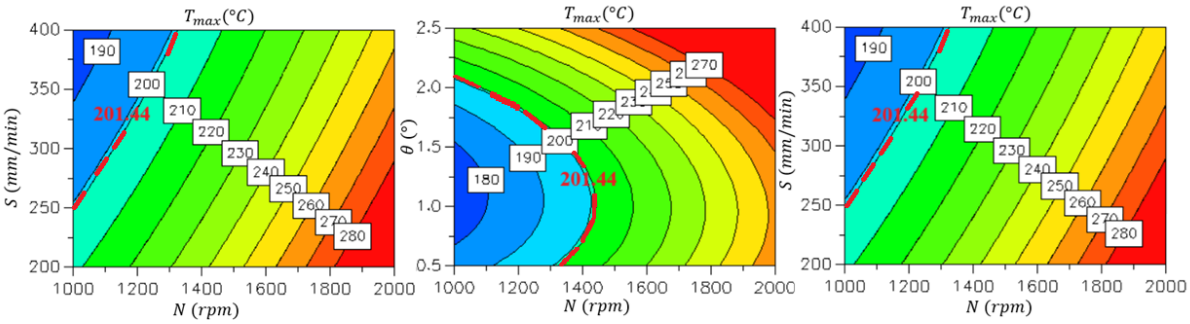

Fig. 9. T_{max} corresponding to the optimal values

Conclusion

The aim of our study is therefore to develop a mathematical model using response surface methodology (RSM). This model enables the prediction of the maximum temperature generated during FSW welding of AA3003 alloy as a function of rotational speed, feed rate, and tool inclination angle. It also enables the effect of these parameters on the evolution of the maximum temperature to be determined.

The model developed enabled us to obtain a better prediction of T_{max}. This model is an effective tool for selecting optimum FSW process parameters. Statistical analysis has shown that the most influential parameter is rotational speed, while tilt angle is less important, and feed rate has the least influence. Although response surface methodology

(RSM) is simple to implement and has a low computational cost, it is important to explore new approaches, such as artificial intelligence methods, to minimize prediction error.

CRediT authorship contribution statement

Belaribi Amina: writing – review & editing, writing – original draft, data curation; **Chekalil Ismail:** data curation, investigation, writing – review & editing; **Miloudi Abdelkader:** conceptualization, data curation, writing – original draft; **Ben Messaoud Mohamed Abdelghani:** data curation, writing – review & editing; **Zoukel Abdelhalim:** supervision.

Conflict of interest

The authors declare that they have no conflict of interest.

References

1. Mishra RS, Ma ZY. Friction stir welding and processing. *Materials Science and Engineering R: Reports.* 2005;50(1–2): 1–78.
2. Masroor Z, Rauf AA, Mustafa F, Hussain SW. Crack Repairing of Aluminum Alloy 2024 by Reinforcement of Al_2O_3 and B_4C Particles using Friction Stir Processing. In: *2019 Sixth International Conference on Aerospace Science and Engineering (ICASE), Islamabad, Pakistan, 2019*. IEEE; 2019. p.1–6.
3. Nasiri Z, Sarkari Khorrami M, Mirzadeh H, Emamy M. Enhanced mechanical properties of as-cast Mg-Al-Ca magnesium alloys by friction stir processing. *Materials Letters.* 2021;296: 129880.
4. Nouri Z, Taghiabadi R, Moazami-Goudarzi M. Mechanical properties enhancement of cast Al-8.5Fe-1.3V-1.7Si (FVS0812) alloy by friction stir processing. *Archives of Civil and Mechanical Engineering.* 2020;20: 141.
5. Lomolino S, Tovo R, Dos Santos J. On the fatigue behaviour and design curves of friction stir butt-welded Al alloys. *International Journal of Fatigue.* 2005;27(3): 305–316.
6. Ma YE, Xia ZC, Jiang RR, Li WY. Effect of welding parameters on mechanical and fatigue properties of friction stir welded 2198 T8 aluminum–lithium alloy joints. *Engineering Fracture Mechanics.* 2013;114: 1–11.
7. Yang D, Jiang H, Ai S, Yang T, Zhi Z, Jing D, et al. Detection method for weld defects in time-of-flight diffraction images based on multi-image fusion and feature hybrid enhancement. *Engineering Applications of Artificial Intelligence.* 2024;138: 109442.
8. Merzoug M, Ghazi A, Lousdad A, Benamara N, Miloudi A, Boulenouar A. Effect of the parameters affecting the properties during friction stir welding of AA 5083 H111 alloy. *Materials Physics and Mechanics.* 2023;51(5): 115–125.
9. Mimmi A, Merzoug M, Ghazi A, Dellal N. Mechanical behavior of structures welded with friction stir lap welding process. *Materials Physics and Mechanics.* 2023;51(2): 151–163.
10. Belaziz A, Bouamama M, Elmeguenni Imane, Zahaf S. Experimental study of the roughness variation of friction stir welding FSW. *Materials Physics and Mechanics.* 2023;51(3): 115–125.
11. Saravanakumar R, Rajasekaran T, Pandey C. Underwater Friction Stir Welded Armour Grade AAA5083 Aluminum Alloys: Experimental Ballistic Performance and Corrosion Investigation. *Journal of Materials Engineering and Performance.* 2023;32: 10175–10190.
12. Saravanakumar R, Rajasekaran T, Pandey C. Mechanical and Microstructural Characteristics of Underwater Friction Stir Welded AAA5083 Armor-Grade Aluminum Alloy Joints. *Journal of Materials Engineering and Performance.* 2022;31: 8459–8472.
13. Kumar R, Upadhyay V, Pandey C. Effect of Post-Weld Heat Treatments on Microstructure and Mechanical Properties of Friction Stir Welding Joints of AAA2014 and AAA7075. *Journal of Materials Engineering and Performance.* 2023;32: 10989–10999.
14. Anandan B, Manikandan M. Machine learning approach for predicting the peak temperature of dissimilar AAA7050-AAA2014A friction stir welding butt joint using various regression models. *Materials Letters.* 2022;325: 132879.
15. Sandeep R, Natarajan A. Prediction of peak temperature value in friction lap welding of aluminium alloy 7475 and PPS polymer hybrid joint using machine learning approaches. *Materials Letters.* 2022;308: 131253.

16. Khalifa RB, Toumi O. Prediction of the friction stir welding temperature and ultimate tensil stress for 6061 T6 aluminum. *Journal of Mechanical Engineering Science*. 2025;239(14): 5622–5635.
17. Selvaraj M. Regression model for obtaining peak temperature and heat generation during friction stir welding of stainless steel. *Materials Today: Proceedings*. 2022;62: 633–637.
18. Meyghani B, Awang MB, Poshteh RGM, Momeni M, Kakooei S, Hamdi Z. The Effect of Friction Coefficient in Thermal Analysis of Friction Stir Welding (FSW). *IOP Conference Series: Materials Science and Engineering*. 2019;495: 012102.
19. Palanivel V, Johnson P, Munimathan A, Arumugam ST. Finite element analysis of friction stir welding process to predict temperature distribution. *Revista Materia*. 2024;29(4): e29465.
20. Chamoret D, Lebaal N, Roman A, Schlegel D, Langlade C. Thermal aspects in friction stir process of AISI 316L: Numerical and experimental investigation. *Mechanics of Advanced Materials and Structures*. 2020;27(1): 74–79.
21. Dadi SSO, Patel C, Appala Naidu B. Effect of friction-stir welding parameters on the welding temperature. *Materials Today: Proceedings*. 2021;38: 3358–3364.
22. Meyghani B, Awang M, Wu CS. Finite element modeling of friction stir welding (FSW) on a complex curved plate. *Journal of Advanced Joining Processes*. 2020;1: 100007.
23. Saravanakumar R, Rajasekaran T, Pandey SM, Sirohi S, Pandey C. Effects of welding parameter on the microstructure and mechanical properties of friction stir-welded non-heat treatable alloy AAA5083. *Journal of Adhesion Science and Technology*. 2024;2024: 1–19.
24. Medhi T, Hussain SAI, Roy BS, Saha SC. An intelligent multi-objective framework for optimizing friction-stir welding process parameters. *Applied Soft Computing*. 2021;104: 107190.
25. Elatharasan G, Kumar VSS. An Experimental Analysis and Optimization of Process Parameter on Friction Stir Welding of AA 6061-T6 Aluminum Alloy using RSM. *Procedia Engineering*. 2013;64: 1227–1234.
26. Heidarzadeh A. Tensile behavior, microstructure, and substructure of the friction stir welded 70/30 brass joints: RSM, EBSD, and TEM study. *Archives of Civil and Mechanical Engineering*. 2019;19(1): 137–146.
27. Senthil SM, Parameshwaran R, Ragu Nathan S, Bhuvanesh Kumar M, Deepandurai K. A multi-objective optimization of the friction stir welding process using RSM-based-desirability function approach for joining aluminum alloy 6063-T6 pipes. *Structural and Multidisciplinary Optimization*. 2020;62: 1117–1133.
28. Rathinasuriyan C, Kumar VSS. Optimisation of submerged friction stir welding parameters of aluminium alloy using RSM and GRA. *Advances in Materials and Processing Technologies*. 2020;7(4): 696–709.
29. Jayaraman M, Sivasubramanian R, Balasubramanian V, Lakshminarayanan AK. Prediction of Tensile Strength of Friction Stir Welded A356 Cast Aluminium Alloy Using Response Surface Methodology and Artificial Neural Network. *International Journal of Materials and Structural Integrity*. 2008;9(1–2): 45–58.
30. Rajakumar S, Muralidharan C, Balasubramanian V. Optimization of the friction-stir-welding process and tool parameters to attain a maximum tensile strength of AA7075-T6 aluminium alloy. *Proceedings of the Institution of Mechanical Engineers, Part B: Journal of Engineering Manufacture*. 2010;224(8): 1175–1191.
31. Singh HN, Kaushik A, Juneja D. Optimization of process parameters of friction stir welded joint of AA6061 and AA6082 by response surface methodology (RSM). *International Journal of Research in Engineering and Innovation*. 2019;03: 417–427.
32. Yang T, Wei X, Zhou J, Jiang H, Liu X, Man Z. The Formation Mechanism of Residual Stress in Friction Stir Welding Based on Thermo-Mechanical Coupled Simulation. *Symmetry*. 2025;17: 917.
33. Chekalil I, Miloudi A, Planche MP, Ghazi A. Prediction of mechanical behavior of friction stir welded joints of AA3003 aluminum alloy. *Fracture and Structural Integrity*. 2020;14: 153–168.
34. Chekalil I, Chadli R, Miloudi A, Ghazi A, Planche MP, Mekid S, Raza MS. Effect of corrosion environments on the mechanical properties of friction stir welded aluminum alloy AA3003. *Journal of Materials Research and Technology*. 2024;33: 2353–2364.
35. Li K, Jarrar F, Sheikh-Ahmad J, Ozturk F. Using coupled Eulerian Lagrangian formulation for accurate modeling of the friction stir welding process. *Procedia Engineering*. 2017;207: 574–579.
36. Mimmi A, Merzoug M, Ghazi A. Prediction of the temperature recorded in lap joint at during the friction stir welding. *Engineering Review*. 2023;43: 82–92.

MATERIALS PHYSICS AND MECHANICS RESEARCH ARTICLE

Submitted: May 9, 2025 **Revised: May 20, 2025** **Accepted: June 22, 2025**

Investigating the effect of process parameters on EDM performance of Inconel 725 alloy

Himanshu [1] ✉, R. Arora [1], Kushdeep [2]

[1] Maharishi Markandeswar (Deemed to be) University, Haryana, India

[2] School of Engineering and Technology (SET), CGC University, Punjab, India

✉ kumar.d041789@gmail.com

ABSTRACT

In aerospace and automotive sectors, electrical discharge machining is essential for shaping hard-to-machine materials like Inconel 725. Using Taguchi's L16 orthogonal array, this study examines how electrode shape (round and square), peak current (8 and 12 A), pulse-on time (100 and 200 μs), and pulse-off time (1.2 and 1.6 μs) affect material removal rate and surface roughness. The study found that raising peak current from 8 to 12 A considerably improved material removal rate from 0.0593 to 0.1417 mm^3/min. The maximum material removal rate was reached with a round electrode, 12 A current, 200 μs pulse-on, and 1.2 μs pulse-off duration. However, this setting resulted in the roughest surface finish (9.407 μm). However, the square electrode had better surface quality, with the lowest SR value of 5.965 μm at 8 A, 100 μs pulse-on, and 1.6 μs pulse-off. enhanced pulse-on time (200 μs), enhanced material removal rate by 47.77 %, but shorter pulse-off time (1.2 μs) led to more efficient erosion owing to higher discharge frequency. The findings help precision machine advanced alloys like Inconel 725 by emphasizing the need for electrical discharge machining parameter selection to balance high material removal rate and surface integrity.

KEYWORDS

Inconel 725 alloy • electrical discharge machining • DOE • material removal rate • surface roughness

Citation: Himanshu, R. Arora, Kushdeep. Investigating the effect of process parameters on EDM performance of Inconel 725 alloy. *Materials Physics and Mechanics*. 2025;53(6): 213–223.
http://dx.doi.org/10.18149/MPM.5362025_16

Introduction

Machining plays a very important role in manufacturing and production sector especially in the automobile sector whereby accuracy, reliability and efficiency are very vital in maintaining competitiveness [1]. The automobile industry is a technology-driven industry in which parts are required to maintain high levels of performance and tight tolerances. The current trend of lightweight, electric mobility and engine economy of vehicles has sharply increased the demand of machining of complex geometries of the hard and heat-resistant materials [2]. Modern engines, gearboxes, turbochargers, brakes, and so on require sophisticated and accurate machining solutions. Traditional machining methods, stable as they are in various applications, are facing limitations to suit these emerging demands, especially with materials that have outstanding hardness, toughness or heat resistance [3]. As the modern manufacturing industry moves towards the more advanced materials, the typical methods of machining, including turning, milling, and drilling, often become unsuitable, particularly in dealing with superalloys or composites [4]. This shortcoming has led to the development and implementation of non-conventional machining (NCM). The methods, including electrical discharge machining (EDM), laser

beam machining (LBM) and ultrasonic machining (USM), have certain advantages over the common methods [5]. Non-conventional machining eliminates direct contact between the tool and the workpiece and hence prevents issues related to mechanical forces such as tool wear and workpiece deformation. These methods are especially suited to machining complex shapes, finer cavities or very hard and brittle materials [6]. The wide use in the industrial segment has made EDM unique in dealing with electrically conductive materials which are hard to produce. Figure 1 illustrates the principle of working of the EDM process.

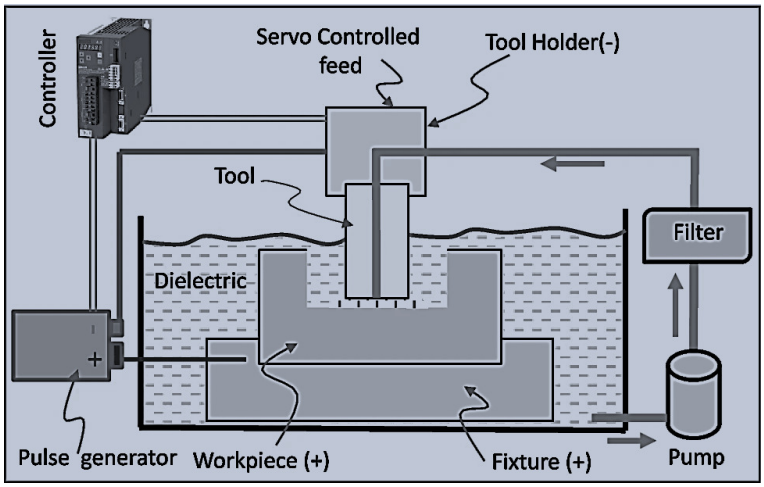

Fig. 1. EDM working principle. Based on [6]

Electrical discharge machining (EDM) is a thermoelectric process in which the material is removed by means of high-frequency electrical discharges between a profiled electrode and an electrically conductive workpiece by being placed in a dielectric fluid [7]. This is mostly suitable for materials that are difficult to cut with conventional tools due to their hardness or heat-resistant nature. The application of EDM in die and mold fabrication, aerospace components, medical implants and military apparatus has mainly been attributed to its ability to produce high precision components with complex geometries and excellent surface finishing [8]. Mechanical force is not necessary in machining, so EDM is ideal in complicated parts and thin-walled parts, which reduces the possibility of distortion. Inconel 725 is a nickel-based superalloy that is difficult to machine conventionally but extremely important in high-performance engineering [9]. Inconel 725 has been known to have high corrosion resistance, high strength, and pitting, stress corrosion cracking, and crevice corrosion resistance [10]. It has excellent mechanical properties in high temperatures, making it a best option in demanding conditions such as deep-sea oil and gas exploration, aircraft engines, sea gears and chemical processing [11]. Nickel, chromium, and molybdenum are high in concentration, and they provide resistance to oxidation and heat deterioration in addition to strength. However, these individual characteristics make machining on traditional procedures very difficult. Its ability to work-harden together with the lack of heat conductivity and extreme abrasiveness of the material leads to expedited wear on the tool as well as poor surface quality in a conventional machining operation. The electrical conductivity of Inconel 725 and the fact that EDM can machine thermally resistant materials has made

the process of machining the alloy using electrical discharge machining (EDM) an effective process [12]. Even though EDM is an appropriate choice, the achievement of the best results in terms of material removal rate (*MRR*) and surface roughness (*SR*) remains a challenge. The performance and the quality of product of EDM process highly depend on some factors such as discharge current, pulse-on time, pulse-off time and flushing pressure [13]. These directly influence the energy per spark, the stability of the spark production, and the ablation of debris of the inter-electrode gap. The improper choice of these parameters could lead to the negative consequences of unstable machining, excessively worn tool, recast layer formation, or even damage of the workpiece. These issues have led to the optimization of EDM parameters becoming an important area of research in order to overcome these difficulties and enhance the productivity and surface quality of components machined using EDM. The process can be refined to meet desired performance goals either by increasing the rate at which material is removed to enhance productivity, or reducing the surface roughness to enhance functionality by optimization of the EDM input variables [14]. However, the complexity and non-linearity of the interaction between the parameters of EDM make the conventional methods of selecting parameters through trial-and-error not efficient in time and cost. This has seen the adoption of statistical and multi-objective optimization techniques that ease the process of making decision-making accurate and reliable. This helps the researchers to determine which factors are paramount and they should be given priority in the optimization process [15]. The study is structured to investigate how the EDM parameters (discharge current, pulse-on time, pulse-off time, Flushing pressure) influence the machining rate of material (*MRR*) and surface roughness (*SR*) when machining Inconel 725 [16].

The results of this study aim at testing the effects of EDM parameters on MRR and surface roughness experimentally, and ANOVA is employed solely in designing the experiments (DOE). The better parameters that will be achieved through this research will be used to curb down manufacturing cost, increase the tool life and ensure reliability of components in the crucial sectors of the aerospace, automotive, marine and oil and gas industries. The predictive model developed in this study will be beneficial in real-time parameter selection in an industrial setup to promote smart manufacture systems and intelligent machining systems.

Materials and Methods

Workpiece Material

The material used in this study is Inconel 725 which is a nickel-based superalloy with high mechanical strength, corrosion resistant and temperature resistant characteristics. Inconel 725 is mainly employed in the aerospace, marine, and petroleum industries because it is resistant to pitting, stress-corrosion cracking and crevice corrosion. The chemical structure of Inconel 725 majorly contains Nickel (Ni), Chromium (Cr), Molybdenum (Mo), Niobium (Nb), and Iron (Fe) that make it have the best properties. The machining workpiece was a rectangular block with a size of 25 × 20 × 10 mm^3. It was good in electrical conductivity therefore the alloy could be machined using the EDM technique.

Tool electrode

The tool electrode is very important in the EDM process, because it is the direct determinant of the shape accurateness and the quality of the surface of the machined component. Copper was used as the tool electrode material in this study because it is highly conductive to electricity, moderately melts, and has excellent wear resistance. Two electrode shapes were taken into consideration: round-shaped electrode (R1) and square-shaped electrode (S1). The two electrodes were made in a similar fashion so that the cross-sectional area would be the same and mounted on the EDM machine so that they were aligned well. Fresh copper electrodes were applied in the experiments to each test to reduce the influence of electrode wear on machining performance and keep trials consistent [17]. The procedure assists in ensuring that the conditions of electrical discharge are uniform during the tests.

EDM machine setup

The tests were carried out using a die-sinking EDM machine that had servo control and parameter setting features (digital). The experiment structure of the EDM process is shown in Fig. 2. The machine table was then strictly clamped, and the electrode was inserted in the tool holder. The dielectric fluid was kerosene that was required to assist in the erosion process of the spark as well as to clean up the particles of debris that were generated in the inter-electrode gap [18]. The temperature of the dielectric fluid under our experimental conditions was passively kept at ambient laboratory temperatures. Data To maintain machining conditions and to avoid temperature increase caused by machining heat, the kerosene was constantly circulated and filtered during machining.

Fig. 2. EDM experimental setup

Characterization detail

Experimental design - DOE

The experiment trials were designed using Taguchi robust design method. Four process parameters were analyzed using orthogonal array of L16 (24) at two levels using the least amount of experiments [19]. This design method is beneficial to determine the main effects and interactions as well as the optimization of the EDM process. The EDM process

is inputted to examine four parameters of the process based on literature review and initial trial:

1. Electrode shape (R1, S1).
2. Discharge current (I): 8 and 12 A.
3. Pulse-on time (T_{on}): 100 and 200 µs.
4. Pulse-off time (T_{off}): 1.2 and 1.6 µs.

At these two levels, these parameters were varied and the experimental matrix was created based on Taguchi L16 orthogonal array that is efficient in investigating more than a number of parameters at a lower cost [20]. Every combination of parameters was tried once and the results of MRR and surface roughness were measured. All trials of EDM were held at the constant duration of 10 min under constant conditions of dielectric flushing. This time was chosen because it was necessary to be able to compare machining with a stable condition and measure the material removal to compare it with *MRR* and surface roughness evaluation.

Response parameter

Two primary performance indicators were chosen as output responses to evaluate machining performance. Material removal rate (*MRR*) indicates the volume of material removed per unit time and was calculated using the equation [21]:

$$MRR = \frac{W_i - W_f}{\rho \, x \, t}, \quad (1)$$

where W_i is the initial weight of the workpiece, W_f is the final weight after machining, ρ is the density of Inconel 725 (8.4 g/cm^3), and t is the machining time in minutes.

Surface roughness (*SR*): surface finish was obtained through Taylor Hobson surface profilometer. The roughness was established at the surface at three points depending on the trial, and the mean was taken so that there is consistency and loss of error in the experiment is minimal [22].

Results and Discussion

Test results for workpiece

A progression of electrical discharge machining (EDM) tests was carried out in order to test the machining characteristics of Inconel 725 once the composition of the workpiece was established along with the powder used. The Taguchi method was used to develop the experimental design, and an L16 Orthogonal Array (OA) was chosen to combine the parameters [23–25]. The major EDM parameters that were taken into consideration in this study were peak current, pulse-on time, pulse-off time and powder concentration which were all to be varied in two levels. In particular, the levels were the following: peak current (8 and 12 A), pulse-on time (100 and 200 µs), pulse-off time (1.2 and 1.6 µs), and electrode shape (round and square). Prior to the commencement of the experiment the work-piece was put to test, and the report of the testing is in Table 1.

The electrode material was made of copper, and the workpiece material was Inconel 725. After defining parameters and level values, machining tests were conducted according to the combinations that are defined in L16 OA matrix. After the completion of

Table 1. Test results for composition of work-piece

Elements	Max. limit of impurities, %
Silicon (Si)	0.048
Manganese (Mn)	0.107
Phosphorus (P)	0.009
Sulfur (S)	0.006
Chromium (Cr)	20.76
Molybdenum (Mo)	7.294
Nickel (Ni)	57.860
Aluminum (Al)	0.176
Niobium (Nb)	2.985
Titanium (Ti)	1.562

Table 2. Values of various responses

Tool shape	*I*, A	T_{on}, µs	T_{off}, µs	*MRR*, mm³/min	*SR*, µm
R1	8	100	1.2	0.0648	6.323
R1	8	100	1.6	0.0722	5.977
R1	8	200	1.2	0.066	6.84
R1	8	200	1.6	0.095	6.771
R1	12	100	1.2	0.0959	8.478
R1	12	100	1.6	0.0988	8.98
R1	12	200	1.2	0.1417	9.407
R1	12	200	1.6	0.115	8.06
S1	8	100	1.2	0.0593	7.389
S1	8	100	1.6	0.0658	5.965
S1	8	200	1.2	0.0691	7.079
S1	8	200	1.6	0.0883	7.454
S1	12	100	1.2	0.0924	7.668
S1	12	100	1.6	0.0863	7.708
S1	12	200	1.2	0.0956	8.119
S1	12	200	1.6	0.0987	7.801

Fig. 3. Specimen after machining at EDM

experiments, the weighing of the work piece and electrode was done using a precision weighing machine to ascertain material removal rate (*MRR*) [26]. Table 2 gives the values of the surface roughness (*SR*) [27] measured by a surface roughness tester. Figure 3 displays the pictures of the specimen at the end of doing the experiments.

The objective of the experimental study was lower EDM parameters of Inconel 725 based on the L16 Orthogonal Array (OA) system of Taguchi by using an electrode shape, maximum current, pulse-on time, and pulse-off time as input variables. Material removal rate (*MRR*) and surface roughness (*SR*) were measured to identify what effect each parameter had on machining performance. The findings revealed that increased peak current (12 A) resulted in significant rise in *MRR* with values of 0.1417 mm^3/min when using the round electrode (R1) at pulse-on time of 200 µs and pulse-off time of 1.2 µs. This was because the more the current, the greater the amount of discharge energy and thus the higher the erosion of the workpiece material. Nevertheless, the increase in current led to the increase in the roughness of the surface to its maximum depth of 9.407 µm since the excessive heat would lead to deeper craters and the deposition of molten material. Pulse-on time was also a significant aspect of *MRR* enhancement with 200 µs pulse-on time considered better in enhancing *MRR* than 100 µs because of higher energy transfer per spark. A reduced pulse-off time (1.2 µs) also increased *MRR*, and enabled more frequent discharges per unit time, and also reduced the period between discharges between sparks. The findings further indicated that round electrodes (R1) had higher *MRR* than square electrodes (S1) as a result of the better distribution of the spark and smooth wear properties. On the other hand, square electrodes gave a better surface finish and less surface roughness values were registered in a number of trials. An example is that when the square electrode was used, pulse-on = 8 A, pulse-off = 100 µs and *SR* = 5.965 µm was recorded, but when the round electrode was used, *SR* = 5.977 µm was observed (Fig. 4). In general, the experiment showed that increased current and the length of pulse-on affect MRR positively and adversely affect surface roughness, whereas shorter pulse-off time positively affects machine performance. Electrode shape is also a major factor that influences machining performance with round electrodes showing better MRR and square electrodes showing better surface quality. The results indicate

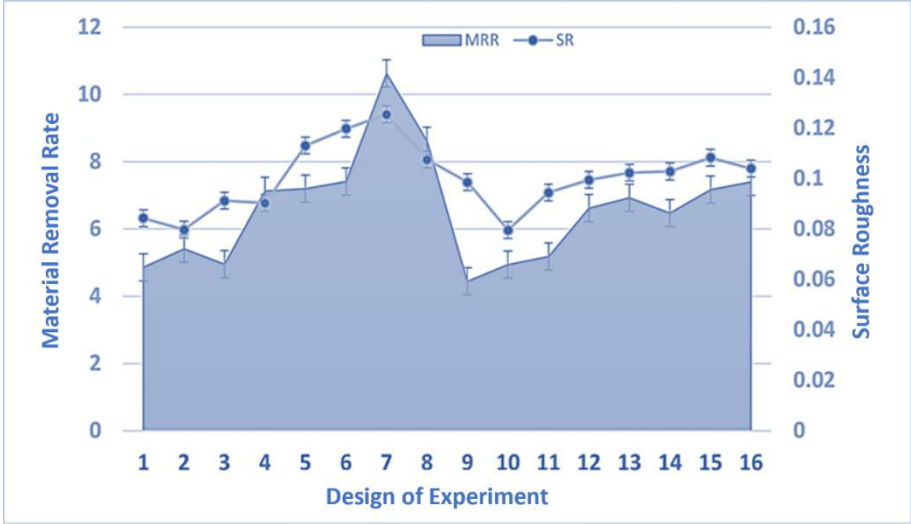

Fig.4 Specimen after machining at EDM

that parameter optimization is needed to realize an optimal combination of machining efficiency and surface integrity during machining Inconel 725 by using EDM [28–30].

Experimental analysis of EDM parameters for Inconel 725

The experimental research aimed at optimization of EDM parameters of Inconel 725 with the help of Taguchi L16 Orthogonal Array (OA). The performance of machining was compared in terms of material removal rate (*MRR*) and surface roughness (*SR*) with the main input variables being electrode shape, peak current, pulse-on time and pulse-off time. The results obtained (Table 2) were processed to establish the effect of each parameter.

Influence of peak current on MRR and surface roughness

The rate of removal of material per current (*MRR*) was higher with higher current (12 as compared to 8 A). An example is that at 8 A, *MRR* was between 0.0593 and 0.095 mm^3/min whereas at 12 A, the rate was maximum (0.1417 mm^3/min). This can be attributed to the fact that the discharge energy increases with increase in current thereby increasing material erosion. Nonetheless, as current was increased, surface roughness (*SR*) also increased with more deeply cratered and more deposition of molten material. *SR* was 5.965 to 7.454 µm at 8 A, and 9.407 µm at 12 A. Excessive thermal damage was due to the increased energy input, which resulted in a rough surface finish [31].

Effect of pulse-on and pulse-off time

Pulse-on time was very important in affecting *MRR*. At 200 µs pulse-on time, *MRR* was greater than when pulse-on time was 100 µm. Case: *MRR* at R1 electrode of 12 A was 0.0959 mm^3/min (100 µs) and then 0.1417 mm^3/min (200 µs). The longer the pulse-on the more energy will be transferred and thus the material removed will be more. The reason behind a higher MRR was a shorter pulse-off time (1.2 µs) than a pulse-off time of 1.6 µs since short pulse-off time implies more discharges/second, and thus, continuous erosion of the material occurred. Example: *MRR* at 12 A and 200 µs was 0.0956 mm^3/min (1.2 µs pulse-off) vs. 0.0987 mm^3/min (1.6 µs pulse-off) with S1 electrode [32].

Influence of electrode shape (round vs. square)

Round (R1) and square (S1) electrodes did not have equal machining efficiencies. Round electrodes recorded higher *MRR* in the majority of applications, perhaps because they have a higher distribution of spark, as well as uniform wear. Available data: using the round electrode (R1) at 12 A, 200 µs, 1.2 µs pulse-off, the electrode attained 0.1417 mm^3/min, whereas the square electrode (S1) had 0.0956 mm^3/min at the same conditions. In the majority of cases, surface roughness was reduced under square electrodes [33–35]. Sample: *SR* = 5.965 µm and *SR* = 5.977 µm were obtained with square and round electrodes, respectively, at 8 A, 100 µs, 1.6 µs pulse-off.

Conclusions

1. Material removal rate with an increase in peak current by 8 to 12 A was significantly enhanced. The highest *MRR* of 0.1417 mm^3/min was achieved with 12 A current, 200 µs pulse-on time and 1.2 µs pulse-off time using the round electrode (R1).
2. The longer pulse-on time augmented spark energy and *MRR*. To illustrate, at 12 A upsurge in pulse-on time, 100 to 200 µs, caused a 47.77 percent augmentation in *MRR* of 0.0959 to 0.1417 mm^3/min. spark duration plays a vital role in the removal of materials.
3. Fewer pulse-off (1.2 µs) reduced spark discharges and enhanced MRR. At pulse-on of S1, 12 A, 200 µs, *MRR* was 0.0956 mm^3/min at 1.2 µs, a little smaller than 0.0987 at 1.6 µs. Smaller pulse-off times resulted in better erosion since the idle time was minimized.
4. Experiments were all conducted with better MRR with the round electrode (R1). Under the same conditions (12 A, 200 µs, 1.2 µs), R1 showed the most highest *MRR* (0.1417 mm^3/min) in comparison with the one of S1 (0.0956 mm^3/min). This may be due to reduced tool wear and homogeneity of spark in round electrodes.
5. Most studies have found that the square electrode (S1) was of better quality in terms of surface. Short pulse-on of 8 A, pulse-off of 100 µs and pulse-on of 1.6 us, S1 was able to achieve a surface roughness of 5.965 µm, a little more improved than the 5.977 µm of R1, which showed that S1 has advantages in surface quality.
6. Optimal conditions of maximal MRR uses are: round electrode (R1), 12 A current, 200 µs pulse-on time, and 1.2 µs pulse-off time. In order to enhance surface polish, apply square electrode (S1), 8 A current, 100 µs pulse-on time, and 1.6 µs pulse-off time, as result will be *SR* = 5.965 µm.

CRediT authorship contribution statement

Himanshu : conceptualization, writing – review & editing, writing – original draft; **Ravish Arora:** supervision**,** review & editing; **Kushdeep** : data curation, writing – review & editing.

Conflict of interest

The authors declare that they have no conflict of interest.

References

1. De Oliveira Junior CA, Diniz AE, Bertazzoli R. Correlating tool wear, surface roughness and corrosion resistance in the turning process of super duplex stainless steel. *J Braz. Soc. Mech. Sci. Eng.* 2014;36: 775–785.
2. Kumar D, Singh S, Angra S. Dry sliding wear and microstructural behavior of stir-cast Al6061-based composite reinforced with cerium oxide and graphene nanoplatelets. *Wear.* 2023;516: 204615.
3. Kareem H, Raju H, Thethi HP, Tyagi LK, Kumari V. Advancements in Aluminum-Based Composite Manufacturing: Leveraging La_2O_3 Reinforcement through Friction Stir Process. *E3S Web of Conferences.* 2024;507: 01036.
4. Kumar D, Angra S, Singh S. Synthesis and characterization of DOE-based stir-cast hybrid aluminum composite reinforced with graphene nanoplatelets and cerium oxide. *Aircraft Engineering and Aerospace Technology.* 2023;95(10): 1604–1613.
5. Czelusniak T, Higa CF, Torres RD, Laurindo CAH, de Paiva Júnior JMF, Lohrengel A, Amorim FL. Materials used for sinking EDM electrodes: a review. *J Braz. Soc. Mech. Sci. Eng.* 2019;41: 14.

6. Aghdeab SH, Al-Habaibeh A. Investigating the effect of process parameters on surface roughness of AISI M2 steel in EDM using deep learning neural networks. *Int J Adv Manuf Technol*. 2025;137: 251–262.
7. Kumar D, Singh S, Angra S. Synergistic effects of graphene and ceria nanoparticulates on microstructure and mechanical behavior of stir-cast hybrid aluminum composite. *Trans Indian Inst Met*. 2024;77: 2699–2709.
8. Khleif AA. Computer vision aided electrode wear estimation in electrical discharge machining process. *Journal of Engineering Science and Technology*. 2022;17(1): 0197–0206.
9. Kumar D, Angra S, Singh S. High-temperature dry sliding wear behavior of hybrid aluminum composite reinforced with ceria and graphene nanoparticles. *Engineering Failure Analysis*. 2023;151: 107426.
10. Mukhtarova KS, Shakhov RV, Mukhtarov SK. Effect of high-pressure torsion and annealing on the microstructure and microhardness of Inconel 718 produced by selective laser melting. *Materials Physics and Mechanics*. 2025;53(1): 109–116.
11. Amin MA, El-Bagoury N, Saracoglu M, Ramadan M. Electrochemical and corrosion behavior of cast re-containing inconel 718 alloys in sulphuric acid solutions and the effect of Cl. *International Journal of Electrochemical Science*. 2014;9(9): 5352–5374.
12. Praveen DV, Raju DR, Raju MVJ. Optimization of machining parameters of wire-cut EDM on ceramic particles reinforced Al-metal matrix composites - A review. *Materials Today: Proceedings*. 2020;23: 495–498.
13. Malhotra P, Tyagi RK, Singh NK, Singh B. Experimental investigation and effects of process parameters on EDM of Al7075 / SiC composite reinforced with magnesium particles. *Materials Today: Proceedings*. 2020;21: 1496–1501.
14. Baburaja K, Teja Sainadh S, Sri Karthik D, Kuldeep J, Gowtham V. Manufacturing and machining challenges of hybrid aluminium metal matix composites. *IOP Conference Series: Materials Science and Engineering*. 2017;225: 012115.
15. Kataria M, Mangal SK. Excellence of al-metal matrix composite fabricated by gas injection bottom pouring vacuum stir casting process. *Indian Journal of Engineering and Materials Sciences*. 2020;27(2): 234–245.
16. Sharath BN, Madhu KS, Pradeep DG, Madhu P, Premkumar BG, Karthik S. Effects of tertiary ceramic additives on the micro hardness and wear characteristics of Al2618 + Si3N4-B4C-Gr hybrid composites for automotive applications. *Journal of Alloys and Metallurgical Systems*. 2023;3: 100014.
17. Bhatt RJ, Raval HK. Investigation on flow forming process using Taguchi-based grey relational analysis (GRA) through experiments and finite element analysis (FEA). *Journal of the Brazilian Society of Mechanical Sciences and Engineering*. 2018;40(11): 1–24.
18. Ali S, Suswagata K, Sahoo P. WEDM Characteristics of Stir-Cast Al-TiB2 Metal Matrix Composites. *Arab J Sci Eng*. 2024;49: 15037–15057.
19. Kumar D, Singh S, Angra S. Synergistic corrosion protection of stir-cast hybrid aluminum composites reinforcing CeO_2 and GNPs nano-particulates. *Aircraft Engineering and Aerospace Technology*. 2023;95(10): 1706-1715.
20. Ravikumar R, Amirthagadeswaran KS, Senthil P. Parametric optimization of squeeze cast AC2A-Ni Coated SiC p composite using taguchi technique. *Advances in Materials Science and Engineering*. 2014;2014: 160519.
21. Girisha PL, Koti V, Madgule M. Optimization of stir casting and drilling process parameters of hybrid composites. *Journal of Alloys and Metallurgical Systems*. 2023;3: 100023.
22. Rayjadhav SB, Naik VR. Characterization of Developed Al 6061-Sic Metal Matrix Composites Produced By the Stir Casting Method. *International Journal of Innovative Research in Science, Engineering and Technology*. 2016;2(3): 92–103.
23. Kumar N, Bharti A. Optimization of powder metallurgy process parameters to enhance the mechanical properties of AZ91 magnesium alloy. *Materials Physics and Mechanics*. 2022;48(3): 315–327.
24. Sabil M, Prabhakar DAP. Optimisation of Extrusion Temperature and Infill Density of PLA material by using L16 Orthogonal Array. *Australian Journal of Mechanical Engineering*. 2022;22(2): 241–257.
25. Selvaraj DP. Optimization of surface roughness of duplex stainless steel in dry turning operation using taguchi technique. *Materials Physics and Mechanics*. 2018;40(1): 63–70.
26. Mohammadi A, Fadaie Tehrani A, Emanian E. A new approach in turning with wire electrical discharge machining to evaluate the effects of machining parameters on material removal rate. In: *Proceedings of the 1st Tehran International Congress on Manufacturing Engineering (TICME 2005), Tehran, Iran*. 2005. p.12–15.
27. Kishore G, Parthiban A, Mohana Krishnan A, Radha Krishnan B. Investigation of the surface roughness of aluminium composite in the drilling process. *Materials Physics and Mechanics*. 2021;47(5): 739–746.
28. Janardhanan NK, Perianna H. Investigation on the effect of inclination angle of electrochemical machined deep inclined holes by hybrid multi genetic-based criteria decision making. *Int J Adv Manuf Technol*. 2025;138: 4019–4041.

29. Wang L, Hu X, Li H, Qu N, Wang J. Experimental investigation on the machining performance of honeycomb seal structures by using electrochemical discharge machining. *Journal of Manufacturing Processes*. 2024;124: 226–239.
30. Fernandes GHN, Ferreira ER, França PHP, Barbosa LMQ, Benedetti Filho E, Martins PS, Machado ÁR. Internally cooled tools as an innovative solution for sustainable machining: Temperature investigation using Inconel 718 superalloy. *CIRP Journal of Manufacturing Science and Technology*. 2024;50: 269–284.
31. Tolcha MA, Lemu HG. Parametric optimizing of electro-discharge machining for LM25Al/VC composite material machining using deterministic and stochastic methods. *Int J Adv Manuf Technol*. [Preprint] 2024. Available from: doi.org/10.1007/s00170-024-13221-7.
32. Han J, Gao X, Zhou Y, Li Z, Gao M, Hao Y, Zhang Q. Optimization of Process Parameters in Ultrasonic Vibration-Assisted Powder-Mixed Electrical Discharge Machining of TiN Ceramics. *J. of Materi Eng and Perform*. 2025;34: 21197–21210.
33. Kulkarni A, Dongre G. A Comparative Investigation of Dielectrics for Near Dry EDM Process Optimization. To be published in *J. Inst. Eng. India Ser. D*. [Preprint] 2025. Available from: doi.org/10.1007/s40033-025-00903-z.
34. Thamizhvalavan P, Varatharajulu M, Baskaran J. Parametric optimization of abrasive waterjet machining for aluminum 7075/boron carbide/zirconium silicate hybrid composites. To be published in *Proceedings of the Institution of Mechanical Engineers, Part E: Journal of Process Mechanical Engineering*. [Preprint] 2025. Available from: doi.org/10.1177/09544089241312610.
35. Chakraborty T, Acherjee B, Mandal A. Emerging frontiers in electro-discharge machining: A comprehensive review of research trends, challenges, and innovative solutions. *Forsch Ingenieurwes*. 2025;89: 68.

MATERIALS PHYSICS AND MECHANICS

53 (6) 2025

УЧРЕДИТЕЛИ

Санкт-Петербургский политехнический университет Петра Великого
Адрес: 195251, Санкт-Петербург, Политехническая ул., д. 29

Институт проблем Машиноведения Российской академии наук
Адрес: 199178, Санкт-Петербург, Большой пр-кт В.О., д. 61

ИЗДАТЕЛЬ

Санкт-Петербургский политехнический университет Петра Великого
Адрес: 195251, Санкт-Петербург, Политехническая ул., д. 29

Журнал зарегистрирован в Федеральной службе по надзору в сфере связи, информационных технологий и массовых коммуникаций (РОСКОМНАДЗОР), свидетельство ПИ №ФС77-69287 от 6 апреля 2017 года.

АДРЕС И ТЕЛЕФОН РЕДАКЦИИ

199178, Санкт-Петербург, Большой пр-кт В.О., д. 61

Тел. редакции: +7(812)552 77 78, доб. 224

E-mail редакции: mpmjournal@spbstu.ru

Компьютерная верстка Л.И. Гузилова

Подписано в печать 30.12.2025 г. Выход в издания в свет: 30.01.2026 г.
Формат 60x84/8. Печать цифровая
Усл. печ. л. 10,0. Тираж 100. Заказ___.
Цена: Бесплатно

Отпечатано в **Издательско-полиграфическом центре Политехнического университета Петра Великого**
Адрес: 195251, Санкт-Петербург, Политехническая ул., 29
Тел.: +7(812)552 77 17

MPM SCIENTIFIC JOURNAL

MPM, Vol. 53, No. 6, 2025